AD-A259 898

PL-TR-92-2217

ON THE DYNAMICS OF SPACE PLASMAS

Jay Albert
Chung Chan
Michael B. Silevitch
Elena Villalón

Northeastern University
360 Huntington Avenue
Boston, Massachusetts 02115

01 September 1992

Final Report
06 March 1989 — 01 September 1992

APPROVED FOR PUBLIC RELEASE; DISTRIBUTION UNLIMITED

PHILLIPS LABORATORY
Directorate of Geophysics
AIR FORCE MATERIEL COMMAND
HANSCOM AIR FORCE BASE, MA 01731-5000

92-29315

225 pp

"This technical report has been reviewed and is approved for publication."

WILLIAM J. BURKE
Contract Manager

NELSON C. MAYNARD
Branch Chief

RITA C. SAGALYN
Division Director

This report has been reviewed by the ESC Public Affairs Office (PA) and is releasable to the National Technical Information Service (NTIS).

Qualified requestors may obtain additional copies from the Defense Technical Information Center.

If your address has changed, or if you wish to be removed from the mailing list, or if the addressee is no longer employed by your organization, please notify PL/TSI, Hanscom AFB, MA 01731-5000. This will assist us in maintaining a current mailing list.

Do not return copies of this report unless contractual obligations or notices on a specific document requires that it be returned.

REPORT DOCUMENTATION PAGE

Form Approved
OMB No. 0704-0188

1. AGENCY USE ONLY *(Leave blank)*	2. REPORT DATE	3. REPORT TYPE AND DATES COVERED
	01 September 1992	Final (03.06.89 - 09.01.92)

4. TITLE AND SUBTITLE
"On the Dynamics of Space Plasmas"

5. FUNDING NUMBERS
PE 62101F
PR 7601
TA 50
WU CA

Contract
F19628-89-K-0014

6. AUTHOR(S)
Jay Albert, Chung Chan, Michael Silevitch
Elena Villalon

7. PERFORMING ORGANIZATION NAME(S) AND ADDRESS(ES)
Northeastern University
360 Huntington Avenue
Boston, MA 02115

8. PERFORMING ORGANIZATION REPORT NUMBER

9. SPONSORING/MONITORING AGENCY NAME(S) AND ADDRESS(ES)
Phillips Laboratory
Hanscom AFB, MA 01731-5000

Contract manager: William Burke GPSG

10. SPONSORING/MONITORING AGENCY REPORT NUMBER
PL-TR-92-2217

11. SUPPLEMENTARY NOTES

12a. DISTRIBUTION/AVAILABILITY STATEMENT
Approved for public release;
distribution unlimited

12b. DISTRIBUTION CODE

13. ABSTRACT *(Maximum 200 words)*

The research was focused into three related areas. These were:

A) An examination of stochastic electron acceleration mechanisms in the ionosphere and the resulting dynamics of magnetospheric (i.e., Radiation Belt) particles and waves.

B) A study of nonadiabatic particle orbits and the electrodynamic structure of the coupled magnetosphere-ionosphere auroral arc syste.

C) An experimental investigation of the wake signatures created by a solid body immersed in a flowing plasma.

14. SUBJECT TERMS
Electron acceleration Space interactions Auroral Arcs
Wave particle interaction Substorm dynamics

15. NUMBER OF PAGES
226

16. PRICE CODE

17. SECURITY CLASSIFICATION OF REPORT	18. SECURITY CLASSIFICATION OF THIS PAGE	19. SECURITY CLASSIFICATION OF ABSTRACT	20. LIMITATION OF ABSTRACT
Unclassified	Unclassified	Unclassified	SAR

Table of Contents

Introduction

This document is a final report describing the research activities performed under the contract F 19628-89-K-0014, *"On the Dynamics of Space Plasmas"*. The research was focused into three related areas. These were:

A) An examination of stochastic electron acceleration mechanisms in the ionosphere and the resulting dynamics of magnetospheric (i.e., Radiation Belt) particles and waves.

B) A study of nonadiabatic particle orbits and the electrodynamic structure of the coupled magnetosphere-ionosphere auroral arc system.

C) An experimental investigation of the wake signatures created by a solid body immersed in a flowing plasma.

In the next section we present a more detailed description of the three research areas. Following that is a list of the refereed publications which resulted from the research investigations. Copies of the publications themselves are then added.

Description of Research

In this section we present a more detailed synopsis of the research areas which were investigated during the period of the contract.

A) An examination of stochastic electron acceleration mechanisms in the ionosphere and the resulting dynamics of magnetospheric (i.e., Radiation Belt) particles and waves.

In this area we have studied the following problems:

(1) <u>The interaction of high frequency electromagnetic waves (EM) with plasma particles in a constant magnetic field</u>. This theory is of interest to ionospheric modification research. The EM waves can be radiated from the ground and will propagate in the ionosphere. They interact with the ambient electrons and may accelerate them to high energies. We have published three papers in scientific journals and two articles in conference proceedings.

(2) <u>The mode conversion of EM waves into electrostatic (ES) cyclotron waves in the ionosphere</u>. We consider an inhomogeneous plasma and wave frequencies in the range $\Omega_e \leq \omega \leq 2\Omega_e$, where Ω_e is the electron gyrofrequency. By using a WKB analysis of the wave equation in a warm plasma we estimate the energy transmission coefficients and

power absorbed by the ES waves. We have published two papers containing this theory. The radio window idea of mode conversion into ES waves has been tested in the HIPAS-UCLA facility in Alaska. The electrostatic waves can interact very efficiently with the ambient plasma producing density cavities and acceleration of electrons to high energies.

(3) The interaction of electrons and VLF waves in the Radiation Belts. The interaction of electrons and whistler waves near the equator inside the plasmasphere is investigated by using quasilinear theory. The waves propagate at arbitrary angles with respect to the inhomogeneous geomagnetic field. The cyclotron instability is due to the resonance interaction of waves and particles at multiple harmonics of the cyclotron frequency. The magnetosphere can be treated as a gigantic maser whose mirrors are the ionospheric regions and the earth's surface in the conjugate hemispheres. The waves' amplitudes grow to large values due to interactions with the energetic particles, which anisotropic velocity distributions provide the free source of energy. It is also a mechanism for the removal of energetic electrons, which are precipitated into the ionosphere and lost from the trap. This theory is of interest to active magnetospheric experiments such as CRRES which can test the efficiency of wave particle interactions in the Radiation Belts. We have published three articles in scientific journals and three in conference proceedings.

(4) The interaction of protons and whistler waves in the equatorial regions of the magnetosphere. Experiments performed by U.S. and Russian scientists [H.C. Koons, Journal Geophysics Research, **82**, 1163, 1977; R.A. Kovrazhkin, et al., JETP Lett., **39**, 228, 1984], have shown that protons can precipitate from the Radiation Belts as a result of their interaction with VLF waves. The waves are launched from satellites and have frequencies which are close to the equatorial electron gyrofrequency. Waves and particles can interact through multiple harmonics of the proton gyrofrequency in the inhomogeneous geomagnetic field. For protons that satisfy the second order resonance condition the change in pitch-angle can be very large which will precipitate them into the ionosphere. We have published two articles in conference proceedings and are in the process of preparing a paper to be submitted to a major journal.

(5) The development of a relativistic Hamiltonian formalism of magnetospheric wave particle interactions including background inhomogeneities. We are also studying wave-particle interactions in the Earth's magnetosphere, and particularly have in mind protons and VLF waves, motivated by observed precipitation of protons by VLF waves near the electron cyclotron frequency [Kovrazhkin, et al., JETP Lett., **39**, 228, 1984]. An important application is the upcoming WISP (Waves in Space) experiment. Previous work [Ginet and Albert, Phys. Fluids, **B3**, 2994, 1991] reduced the resonant test particle problem to one dimension in resonance-averaged canonical variables, for the

approximation of a constant background geomagnetic field $\mathbf{B}_0$. We are generalizing this to realistic, slow varying $\mathbf{B}_0$, which is especially crucial in the paradigm of Shklyar [Planet. Space Sci. **34**, 1091, 1986], who gives a schematic theory of nonrelativistic proton pitch-angle scattering by a perfectly ducted electrostatic wave. The resonance function, $\omega - k_\parallel v_z - \ell\Omega$, is a function of distance along the field line, so that many isolated resonances occur. It is important to study the result of a resonant interaction as the particle enters and leaves the resonant region. The work of Ginet and Albert, among others, shows that the behavior depends strongly on the degree of tuning of the resonance.

We have extended the relativistic, electromagnetic Hamiltonian formalism of Ginet and Albert to account for local background inhomogeneity. The price is an additional degree of freedom in the description, which can no longer be reduced to an autonomous (time-independent) pair of equations of resonant motion. The analytic solutions of the homogeneous case no longer hold exactly, and can only be used as guides. Nevertheless, resonance averaging is still fruitful, yielding a non-autonomous pair of equations (with distance along the field line replacing time). This is accomplished by exploiting several constants of the motion, which can be found explicitly to lowest and first order in the wave amplitude, or exactly if an iteration method is used to solve a certain implicit equation. This set is much easier to solve numerically than the full set, and allow greater insight and possibilities for approximate analytic solutions as well.

For comparison, two codes with six degrees of freedom (plus time) have been written to follow the exact behavior of test particles with a quite general specified electromagnetic wave, one for a dipole magnetic field and one for a slab approximation. Both codes use a Hamiltonian description to allow direct comparison with the theoretical treatment. Both use scalar functions to specify the vector potential of the magnetic fields, and so satisfy the Maxwell equation $\nabla \bullet \mathbf{B} = 0$ exactly. In the case of the dipole field, the canonical coordinates of the Hamiltonian are also dipole coordinates. The slab geometry code allows for arbitrary values of the inhomogeneity, including zero, which permits testing of theoretical ideas in a clear and simple way. We have also generated parameters for which the paradigm of Shklyar [Planet Space Sci. **34**, 1091, 1986] of many isolated ℓ resonances seems to be valid. It is not necessary to carefully tune the particle initial conditions to achieve resonance; the simulated particle "finds" resonances it encounters along its path.

We have seen very interesting behavior of the phase angle near resonance. Shklyar assumed that the value of this angle at exact resonance, which controls the sign and value of the jumps in action, would be randomly and uniformly distributed between 0 and 2π, and used this assumption to generate diffusion coefficients. We see instead that this angle takes on values only in a range of width π, and preferentially close to the angle of the x-point. This gives the jumps in action a systematic direction, determined by the resonance number and other parameters, which greatly affects the cumulative influence of many resonance crossings. Numerical results from both the resonance-averaged and exact numerical simulations support the following scenario: most of the time, the particle trajectory closely follows the contours of the instantaneous Hamiltonian (which would be exact streamlines in a homogeneous **B** field), while the separatrix between streaming and phase-trapped motion drifts slowly towards the particle. However, near the x-point of this separatrix, even slow drifting has a large effect because it allows the particle to cross the opposite side of the island enclosed by the separatrix, so that there is a net increase in the action variable of roughly the island width (which is proportional to $\epsilon^{1/2}$). Once the drifting has taken the island past the particle, the motion is again guided by H-contours.

These qualitative arguments, supported by estimates of the streaming and drifting rates as functions of distance from the island, explain much of the behavior observed: the localization and magnitude of the jumps in action (and therefore energy and pitch angle) near resonances, and also the systematic direction of these jumps. Jumps that tend to be in the same direction will have a much larger cumulative effect than jumps that occur in a random walk fashion. This work has been presented at the 1992 AGU Spring Meeting [EOS **73**, 253, 1992].

Work is also in progress on a three-dimensional particle-in-cell code for the Echo series of beam-in-space experiments. The design features cylindrical geometry and open radial boundary conditions. The electrostatic field solver is at a mature stage; the next issues are efficient charge-to-grid assignment (scatter of information) and grid-to-particle interpolation (gather) as w as time advancement. We are also considering incorporating the kernel of the field solver in a two-dimensional version of the code, which would be a relatively quick and useful took for exploring the qualitative dynamics.

B) *A study of nonadiabatic particle orbits and the electrodynamic structure of the coupled magnetosphere-ionosphere auroral arc system.*

In this area we have developed a model describing the structure of a prebreakup arc based on an ionospheric Cowling channel and its extension into the magnetosphere. A coupled two-circuit representation of the substorm current wedge is used which is locally superimposed on both westward and eastward electrojets. We find that brighter, more unstable prebreakup arcs are formed in the premidnight (southwest of the Harang Discontinuity) than in the postmidnight (northeast of the Harang Discontinuity) sector. This contributes to the observed prevalence of auroral activity in the premidnight sector. Also, our model predicts that the north-south dimensions of the current wedge in the ionosphere should vary from a few kilometers at an invariant latitude (Λ) of 62° to hundreds of kilometers above $\Lambda = 68°$. Comparison of the model results with the extensive observations of Marklund et al. (1983) for a specific arc observed just after onset shows good agreement, particularly for the magnitude of the polarization electric field and the arc size. We conclude that this agreement is further evidence that the substorm breakup arises from magnetosphere-ionosphere coupling in the near magnetosphere and that the steady state model developed here is descriptive of the breakup arc before inductive effects become dominant. A more detailed description of this work is given in the paper entitled, "*Prebreakup Arcs: A Comparison Between Theory and Experiment*". This work is reproduced in the next section.

The theory of auroral arcs has progressed along many lines of thought: electrostatic shocks, double layers, the Alfvén wave propagation, the formation of a small wedge, and viscous interaction of the magnetopause. In simple terms, the arc is analogous to a fountain that rises to some height at the center, spreads out at the top and then is returned over an extended area. The presence of a conductive ionosphere and the complex interaction of the associated fields and particles makes the problem very complex. A self-consistent model of an auroral arc should include a mechanism for generating the field-aligned potential drop associated with the arc and a description of how the associated currents are conserved, including ionospheric effects. In our research, we also address the additional complication that an auroral arc may not be self-contained. We find that it modifies the ion population that is EXB drifting through it. The drifting ions, on the other hand, affect the charge distribution inside the arc and, hence, the potential distribution itself. We have examined the effect of the arc on the ions in analogy with similar effects in the magnetotail.

We find that ions EXB drifting through an auroral arc can undergo transverse acceleration and stochastic heating. This result is very analogous to recent work regarding similar phenomena in the magnetotail. An analytic expression for the maximum arc width for which chaotic behavior is present is derived and numerically verified. We find, for example, that a 1.5 km thick arc at $\Lambda=65°$ requires a minimum potential drop of 3 Kv for transverse ion acceleration and heating to occur. Thicker arcs require higher potential drops for stochasticity to occur. This mechanism could be a partial cause for ion conics. A more detailed description of this work is reported in the paper, "*Acceleration and Stochastic Heating of Ions Drifting through an Auroral Arc*". The paper is included in the next section of this report.

C) *An experimental investigation of the wake signatures created by a solid body immersed in a flowing plasma.*

In this area we have experimentally studied the formation of the wake of a conducting body in a flowing plasma similar to that encountered in Low Earth Orbit. We developed a device that produced a well-behaved plasma stream. This device allows the laboratory simulation of plasmas over a wide range of conditions (including scalable to Low Earth Orbit) with the unique ability of allowing the study of the three-dimensional plasma phenomena.

We have developed a number of diagnostics for this device that allow us to measure ion and electron currents, densities and distribution functions, in addition to measuring the space and plasma potentials inside the device. Electron and ion currents are measured with the aid of collecting Langmuir probes while the particle distribution functions are ascertained with the aid of retarding potential analyzers. Space and plasma potentials are measured with a differential emissive probe operating in the limit of zero emission for a minimal perturbation of the plasma. All diagnostics were optimized for low density, fast time response measurements (frequency response = 1 MHz) and were designed to minimize the perturbation of the quantities being measured.

We have performed considerable work in studying the physics of wake and ram formation, current collection of biased objects in the wake of the objects, and the problem of secondary electron emission from biased objects in the plasma environment. Our experimental results have been used to verify the prediction of various computer models, including SIMION, MACH, and POLAR.

The study of wake and ram phenomena is important for a number of reasons. The ram and wake regions itself can be a source of noise due to instabilities being driven by the density and potential gradients at the wake-flowing plasma interface. Objects placed in the ion-free wake region can experience considerable charging problems due to the collection of electrons. Since there are no ions in the wake region to neutralize the charge collected from the electrons, the object may charge to a considerable voltage. This is especially true for an object in polar orbit, where high energy electrons precipitating down along magnetic field lines may induce charging of several thousand volts for large structures.

We have investigated the current collection of biased objects in the wake region of a conducting body. The experiments were performed in the JUMBO vacuum chamber (1.7 m long and 1.7 m diameter) at GL. For these experiments a 1 cm diameter biasable sphere was placed on axis 5 cm downstream from a 10 cm diameter grounded disk. The sphere was biasable to a potential of ± 5000 V and the current collected by the sphere was measured as a function of the voltage applied to the sphere. For positive bias voltages applied to the sphere current is collected as electrons are drawn into the sphere. It is observed that for low negative bias voltages there is no current collected by the object which is in the ion-free wake region. As the negative bias voltage is increased, there is a sharp turn-on of the current collected by the object as it draws ions into the wake region. The bias voltage at which this current turn-on occurs is dependent on a number of factors, e.g., the angular momentum of the flowing ions at a given sheath electric field. As the beam energy is increased the turn-on voltage also increases. This is to be expected since, for higher energies, it is more difficult to deflect the ions enough to be collected by the sphere.

We have also compared the measured current-voltage characteristics of a biased sphere in a wake with the predictions of a number of computer codes. For the simplest model we have used the particle trajectory code, SIMION. When the measured potential profiles are entered into SIMION and the particle trajectories are followed, the code predicts the dependence of the current turn-on voltage with beam energy, distance from the conducting body to the biased object, and the magnetic field. The code cannot, however, predict the magnitude of the current collected or solve for the potential profiles. In addition to the study of current collection, SIMION has been used to study the dynamics of wake formation. By entering the measured potential profiles this code is able to predict the size of the wake region and also predicts the important features of the mid-wake region, such as on-axis density enhancement. This code has been invaluable in the design of the advanced plasma detector. Since the detector operates at low plasma densities, the inability of the code to include space charge effects is not an issue. The code is in remarkable agreement with experimental data from laboratory tests of prototype detectors.

We have found that the MACH simulation results consistently give a wider contour for the ion sheath of the biased sphere in the wake than was measured in the experiment under almost identical conditions, although both simulation and laboratory data give a sheath dimension consistent with the Langmuir-Blodgett spherical sheath model. The difference may be due to a slight enhancement of scattering of ions into the wake region by charge exchange (although the charge exchange length is longer than the device) or some type of plasma oscillations. However, it is extremely time consuming to solve the current collection problem using computer simulations because MACH is a backwards tracking code where particles are launched from their collection point and tracked to their source. Due to this, the code has difficulty in converging.

Some Consequences of Intense Electromagnetic Wave Injection

into Space Plasmas

By

William J. Burke[1], Elena Villalon[2], Paul L. Rothwell[1],

and Michael Silevitch[2]

I Introduction

The past decade has been marked by an increasing interest in performing active experiments in space. These experiments involve the artificial injections of beams, chemicals, or waves into the space environment. Properly diagnosed, these experiments can be used to validate our understanding of plasma processes, in the absence of wall effects. Sometimes they even lead to practical results. For example, the plasma-beam device on SCATHA became the prototype of an automatic device now available for controlling spacecraft charging at geostationary orbit.

In this paper we discuss the future possibility of actively testing our current understanding of how energetic particles may be accelerated in space or dumped from the radiation belts using intense electromagnetic energy from ground based antennas. The ground source of radiation is merely a convenience. A space station source for radiation that does not have to pass through the atmosphere and lower ionosphere, is an attractive alternative. The text is divided into two main sections addressing the possibilities of (1) accelerating electrons to fill selected flux tubes above the Kennel-Petscheck limit for stably trapped fluxes and (2) using an Alfven maser to cause rapid depletion of energetic protons or electrons from the radiation belts. Particle acceleration by electrostatic waves have received a great deal of attention over the last few years (Wong et al., 1981; Katsouleas and Dawson, 1983). However, much less is known about acceleration using electromagnetic waves. The work described herein is still in evolution. We only justify its presentation at this symposium based on the novelty of the ideas in the context of space plasma physics and the excitement they have generated among several groups as major new directions for research in the remaining years of this century.

1. Air Force Geophysics Laboratory, Hanscom AFB, MA 01731

2. Center for Electromagnetic Research,
Northeastern University, Boston, MA 02115

II Electron Acceleration by Electromagnetic Waves

One of the first things we were mistaught in under graduate physics is that electromagnetic (em) waves can't accelerate charged particles. If the particle gains energy in the first half cycle, it loses it in the second half. Teachers are, of course, clever people who want graduate students. So they hold off discussing gyroresonance, in which case, all bets are off. The resonance condition is:

$$(1) \qquad \omega - k_z v_z - n\Omega_o/\gamma = 0$$

Here ω is the frequency of the driving wave, k_z the component of the wave vector along the zero order magnetic field $\underline{B_o} = B_o \hat{z}$, v_z the particle's component of velocity along $\underline{B_o}$ and n is an integer representing an harmonic of the gyrofrequency $\Omega_o = q B_o/m$, γ is the relativistic correction $(1 - v^2/c^2)^{-1/2}$, q is the charge, and m the rest mass of the electron.

Before going into a detailed mathematical analysis it is obvious that there are going to be problems accelerating cold ionospheric electrons to high energies. Higher than first gyroharmonics will have Bessel function multipliers where the argument of the Bessel function is the perpendicular component of the wave vector and the gyroradius. For cold electrons with small gyroradii, all but the zero index Bessel function terms will be small. The second concern can be understood by considering the motion of a charged particle in a circularly polarized wave. Roberts and Buchsbaum (1964) have shown that with an electron in gyroresonance according to eq.(1) and $\underline{v}_\perp$ initially antiparallel to the wave electric field $\underline{E}$ and perpendicular to the wave magnetic field $\underline{B}$, two effects combine to drive it away from resonance. As the electric field accelerates the electron, γ increases, changing the gyrofrequency. The magnetic component of the wave changes v_z and thus, the Doppler shift term. It is only in the case of the index of refraction $\eta = ck/\omega = 1$ that unrestricted acceleration occurs. In all other cases the electron goes through cycles gaining and losing kinetic energy.

Recently, the SAIC group (Menyuk et al. 1986) has devised a conceptually simple way to understand acceleration by em waves as a stochastic process. In terms of the relativistic momenta p_z and $p_\perp$, eq.(1) can be rewritten as

$$p_\perp^2 = (\eta^2 - 1)\, p_z^2 + 2\,\eta_z\, p_z mc\, (n\Omega_o/\omega) + \left((n\Omega_o/\omega)^2 - 1 \right) mc^2$$

Depending on the phase velocity of the waves, equation (2) represents a family of ellipses ($\eta_z = ck_z/\omega < 1$), hyperbolae ($\eta_z > 1$) and parabolae ($\eta_z = 1$) in a $p_\perp$, p_z phase space. The zero order Hamiltonian can also be written in the form

$$(2) \qquad H_o/mc^2 = \left[1 + (p_z/mc)^2 + (p_\perp/mc)^2 \right]^{1/2} - (p_z/mc)\,(\omega/ck_z)$$

Thus, in $p_{\perp}$, p_z space constant Hamiltonian surfaces represent families of hyperbolae ($n_z < 1$) ellipses ($n_z > 1$) and parabolae ($n_z = 1$). Hamiltonian surfaces have open topologies for indices of refraction $n_z < 1$. The case $n_z = 1$ in which resonance and Hamiltonian surfaces are overlying parabolae is that of unlimited acceleration studied by Roberts and Buschbaum (1964).*

In the case of small amplitude waves the intersections of resonance and Hamiltonian surfaces in $p_{\perp}$, p_z space are very sharp. As the amplitudes of the waves grow so too do the widths of resonance. For sufficiently large amplitudes, resonance widths may extend down to low kinetic energies allowing cold electrons to be stochastically accelerated to relativistic energies.

It should be pointed out that although this model heuristically explains the main conceptual reasons for stochastic acceleration to occur, its validity extends only to small angles θ between $\underline{k}$ and $\underline{B}_o$. At large angles, it is not clear that the zero-order Hamiltonian topologies described above will still hold.

Over the past several months we have developed a rigorous extension of the analytical model of Roberts and Buchsbaum by letting $\underline{k} = k_x \hat{x} + k_z \hat{z}$ assume an arbitrary angle to $\underline{B}_o$. We begin with the Lorentz equation.

$$(3) \qquad \frac{d\underline{p}}{dt} = q \left[\underline{E} + \underline{v} \times (\underline{B}_o + \underline{B}) \right]$$

The relativistic momentum and Hamiltonian are given by $\underline{p} = m \gamma \underline{v}$ and $H = mc^2 \gamma$, respectively. The magnetic field of the wave $\underline{B}$ is related to the electric $\underline{E}$ through Maxwell's equation $\underline{B} = (\underline{c}/\omega)\underline{k} \times \underline{E}$. The time rate of change of the Hamiltonian is

$$(4) \qquad \dot{H} = q\, \underline{E} \cdot \underline{v} = qc^2\, \underline{E} \cdot \underline{p}/H$$

If we define $E_x = E_1 \cos\phi$, $E_y = - E_2 \sin\phi$ and $E_z = - E_3 \cos\phi$, where $\phi = k_x x + k_z z - \omega t$ then equation (4) may be rewritten in the form

$$(5) \qquad \frac{H \dot{H}}{c^2 \omega} = \frac{qE_1}{\omega} p_x \cos\phi - \frac{qE_2}{\omega} p_y \sin\phi - \frac{qE_3}{\omega} p_z \cos\phi$$

The Lorentz force equation can also be rewritten as

(6) $\dot{p}_x + p_y \left[\Omega + \frac{qE_2}{m\gamma} \frac{k_x}{\omega} \sin\phi \right] = \frac{qE_1}{\omega} (\omega - K_z \dot{z}) \cos\phi$

(7) $\dot{p}_y - p_x \left[\Omega + \frac{qE_2}{m\gamma} \frac{k_x}{\omega} \sin\phi \right] = - \frac{qE_2}{\omega} (\omega - k_z \dot{z}) \sin\phi$

(8) $\dot{p}_z - \frac{K_z}{\omega} \dot{H} + \frac{E_3}{E_1} (\dot{p}_x + \Omega p_y) = 0$

where $K_z = k_z (1 + E_3 k_x / E_1 k_z)$. Equations (5-8) are exact. Our first simplification is to assume $E_2 k_x / \omega = B_z << B_o$, then eqs. (6-8) may be combined to give

(9)
$$\frac{4H\dot{H}}{c^2 \omega} = \frac{q}{\omega} (E_1 + E_2) \left[\int_o^t Q' \cos(\sigma + \phi - \sigma' + \phi')\, dt' + \right.$$
$$+ \left. \int_o^t R' \cos(\sigma + \phi - \sigma' - \phi')\, dt' - 2p_\perp \sin(\sigma + \phi + \alpha) \right]$$
$$+ \frac{q}{\omega} (E_1 - E_2) \left[\int_o^t Q' \cos(\phi - \sigma + \sigma' - \phi')\, dt' \right.$$
$$+ \left. \int_o^t R' \cos(\phi - \sigma + \phi' + \sigma')\, dt' + 2p_\perp \sin(\phi - \sigma - \alpha) \right]$$
$$- \frac{q}{\omega} E_3 \left\{ 4 \left(p_{zo} + \frac{K_z}{\omega} (H - H_o) \right) \cos\phi \right.$$
$$- \left. \frac{E_3}{E_1} \int_o^t (Q' + R') \left[\cos(\phi + \phi') + \cos(\phi - \phi') \right] dt' \right\}$$

where $\sigma(t) = \int_o^t \Omega(t')\, dt'$, $\tan\alpha = -(p_{xo}/p_{yo})$,

(the subscript o refers to the initial conditions at t = 0), and

$$Q = \frac{qE_1}{\omega} (\omega - K_z \dot{z}) - \frac{qE_2}{\omega} (\omega - k_z \dot{z})$$

$$R = \frac{qE_1}{\omega} (\omega - K_z \dot{z}) + \frac{qE_2}{\omega} (\omega - k_z \dot{z})$$

Primed and unprimed quantities are evaluated at times t' and t, respectively. We note that accelarations represented in Eq. (9) are related to terms multiplying electric fields in right-hand $(E_1 + E_2)$, left-hand $(E_1 - E_2)$ and parallel E_3 modes.

Our next simplification is to substitute for x and z in eq.(9) the zero order solutions (in the electric field amplitude) of eqs. (6-8). That is, we take $x = \rho \cos(\sigma + \alpha)$ where $\rho = v_\perp / \Omega$ is the electron gyroradius and

$$(10) \qquad p_z = \left[p_{zo} + \frac{K_z}{\omega} (H - H_o) \right] .$$

We note that eq.(10) reduces to eq.(2) by taking $K_z = k_z$, which is only valid for small angles between $\underline{k}$ and $\underline{B}_o$. In fact, Figure 1 shows that Hamiltonians with open (hyperbolic or parabolic) topologies in p_z, $p_\perp$ space at small angles between $\underline{k}$ and $\underline{B}_o$ become closed (elliptical) as the angle increases. The practical implication is that cases of potentially infinite accelaration with $k = k_z$ become restricted to finite values at other direction of wave propagation.

By taking $x = \rho \cos(\sigma + \alpha)$ and expanding terms with $\sin k_x x$ and $\cos k_x x$ in series of Bessel functions, eq. (9) becomes

$$(11) \qquad \frac{4H\dot{H}}{c^2 \omega} = \sum_n T_n$$

$$T_n = \frac{q}{\omega} (E_1 + E_2) J_{n-1} (k_x \rho) \Big\{ \sum_m \int_o^t \Big[Q'J'_{m+1} \cos(n\theta + m\theta' + \psi + \psi')$$

$$+ R'J'_{m-1} \cos(n\theta - m\theta' + \psi - \psi') \Big] dt' + 2p_\perp \cos(n\theta + \Psi) \Big\}$$

$$+ \frac{q}{\omega} (E_1 - E_2) J_{n+1} (k_x \rho) \Big\{ \sum_m \int_o^t \Big[Q'J'_{m+1} \cos(n\theta - m\theta' + \psi - \psi')$$

$$+ R'J'_{m-1} \cos(n\theta + m\theta' + \psi + \psi') \Big] dt' + 2p_\perp \cos(n\theta + \psi) \Big\}$$

$$- \frac{qE_3}{\omega} J_n (k_x \rho) \Big\{ 4 \Big(p_{zo} + \frac{K_z}{\omega} (H - H_o) \Big) \cos(n\theta + \psi)$$

$$- \frac{E_3}{E_1} \sum_m \int_o^t (Q' + R')J'_m \Big[\cos(n\theta + m\theta' + \psi + \psi')$$

$$+ \cos(n\theta - m\theta' + \psi - \psi') \Big] dt' \Big\}$$

where $\theta = \int_o^t \Omega(t') dt' + \alpha + \pi/2$, $J'_\nu \equiv J_\nu (k_x \rho')$, $(\nu = m, m \pm 1)$ and $\psi = k_z z - \omega t$.

After averaging over the fast (gyroperiod) time dependencies and a good deal of tedious algebra, we obtain that, for each n, the particle energy obeys the following differential equation:

$$(12) \qquad (U + 1)^2 \left(\frac{1}{\omega} \frac{dU}{dt} \right)^2 + V_n (U) = 0$$

where $U = (H-H_o)/H_o$ and

$$V_n(U) = \frac{d_1^2}{4} U^2 \left(U + 2\, r_n/d_1 \right)^2 - \psi(o)\sin\phi_n \; d_1 U \left(U + 2r_n/d_1 \right)$$

$$+ \frac{\Sigma_1 - \Sigma_2}{2} \left\{ \left(\Sigma_2 d_1 - \Sigma_1 h_1 \right) \left(G_{n+1}(U) + F_{n+1}(U) \right) + \left(\Sigma_2 d_2 - \Sigma_1 h_2 \right) F_{n+1}(U) \right\}$$

$$- \frac{\Sigma_1 + \Sigma_2}{2} \left\{ \left(\Sigma_1 h_1 + \Sigma_2 d_1 \right) \left(G_{n-1}(U) + F_{n-1}(U) \right) + \left(\Sigma_1 h_2 + \Sigma_2 d_2 \right) F_{n-1}(U) \right\}$$

$$- \Sigma_3^2 \left\{ h_1 \left(G_n(U) + F_n(U) \right) + h_2 F_n(U) \right\} - \left(\psi(0)\cos\phi_n \right)^2$$

where $\Sigma_i = -(q\, E_i/\omega)\, c/H_o \quad (i=1,2,3)$, $\quad d_1 = 1 - K_z k_z c^2/\omega^2$

$$d_2 = K_z k_z c^2/\omega^2 - k_z \dot{z}_o/\omega, \qquad h_1 = 1 + K_z/k_z\,(d_1 - 1)$$

$$r_n = 1 - k_z \dot{z}_o/\omega - n\,\Omega_o/\omega, \qquad h_2 = K_z/k_z\; d_2$$

$$\psi(0) = v_{\perp o}/2c \left[-(\Sigma_1 + \Sigma_2) J_{n-1}(k_x \rho_o) + (\Sigma_2 - \Sigma_1) J_{n+1}(k_x \rho_o) \right] + v_{zo}/c\; \Sigma_3 J_n(k_x \rho_o),$$

$$\phi_n = n\left(\alpha + \frac{\pi}{2} \right) + k_z z_o$$

and

$$G_\nu(U) = \int_0^U J_\nu^2 \left[k_x \rho(U') \right] U'\, dU'$$

$$F_\nu(U) = \int_0^U J_\nu^2 \left[k_x \rho(U') \right] dU', \quad (\nu = n,\ n \pm 1).$$

Eq.(12) is in the form of the equations of a harmonic oscillator. Under the limit $\theta = 0$, Eq. (12) becomes the equation derived by Robert and Buchsbaum (1964). The limits of the particles excursion in energy for a given resonance n and electric field E can be found by setting the potentials $V_n(U) = 0$. At wave amplitudes where the range of potentials for different harmonics overlap, we have the onset of stochasticity.

At the present time we have just begun to explore the numerical solutions of equation (12). In Figure 2, we show some of our preliminary results. We assume that $\omega_{pe}/\Omega_o = 0.3$, the electric field amplitude is such that $\Sigma 1 = 0.1$, and the wave frequency is $\omega = 1.8\,\Omega_o$. We consider only the second cyclotron harmonic since this is the closest to satisfying the resonance condition, eq.(1), for initially cold electrons. The components of the wave electric field and the refractive index n are calculated from the cold plasma dispersion relation for electromagnetic waves at any arbitrary angle θ to B_o. It turns out that n is always smaller than, but very close to 1 ($n \approx 0.97$). The maximum allowed

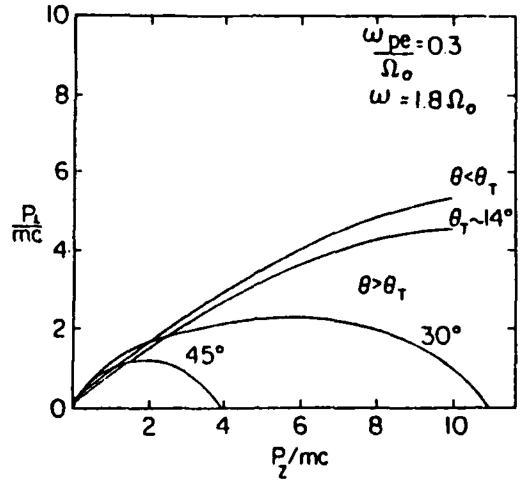

Fig. 1. Surfaces of zero order Hamiltonians with different propagation angles to magnetic field.

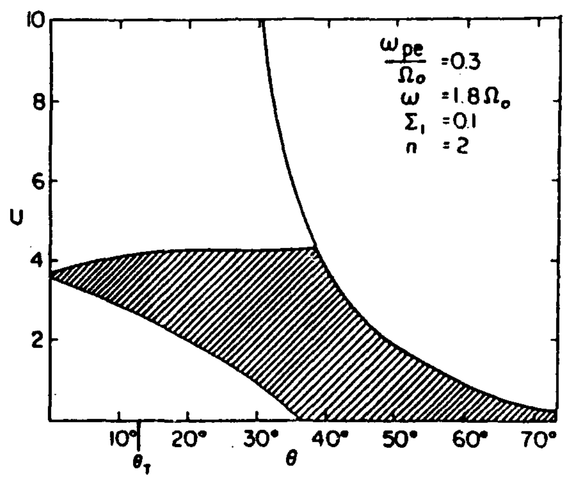

Fig. 2. Range of allowed electron energy gain (shaded) as a function of wave propagation angle to magnetic field. The solid line represents maximum energy excursion for elliptical topologies.

energy gain, as given by the zero order Hamiltonian topologies, is represented by the solid lines . The shaded region represents the actual energy gain as obtained by requiring $V_n(U) < 0$. We see that for $\theta = 35^o$, initially cold electrons can be accelerated to very high energies. In fact, for cold electrons we find that $U = \gamma - 1$ and that the particle can gain as much as 2.5 Mev. As θ decreases more initial kinetic energy is required for any acceleration to take place. For large θ , the elliptical hamiltonian topologies severely restrict the energy gain.

III The Alfven Maser

Active control of energetic particle fluxes in the radiation belts has maintained a continuing interest in both the United States and the Soviet Union. Electron dumping experiments concluded by the Stanford University and Lockheed groups using VLF transmissions are well known (Inan et al. 1982, Imhof et al. 1983). Perhaps less known is a theoretical paper by Trakthengerts (1983) entitled "Alfven Masers" in which he proposes a theoretical scheme for dumping both electrons and protons from the belts. The basic idea is to use RF energy to heat the ionosphere at the foot of a flux tube to raise the height integrated conductivity. The conductivity is then modulated at VLF or ELF frequencies which modulates the reflection of waves that cause pitch angle diffusion in the equatorial plane. The artifically enhanced conductivity of the ionosphere thus maintains high wave energy densities in the associated flux tube, thereby, producing a masing effect.

In addition to external ionospheric perturbations particle precipitation also raises ionospheric conductivity. The masing of the VLF waves causes further precipitation which, in principle, results in an explosive instability. The purpose of this section is to establish the basic equations and to present the results of a preliminary computer simulation.

The fundamental equations derived by Trakhtengerts (1983) are based on quasilinear theory and relate only to the weak diffusion regime. It is useful to use similar set of equations derived by Schulz (1974) based on phenomenological arguments that includes strong pitch angle diffusion. The key variables are N, the number of trapped particles per unit area on a flux tube and ε the wave intensity averaged over the flux tube. In this we assume that ε is directly proportioned to the pitch angle diffusion coefficient. The time rate of change for N is

$$(13) \quad \frac{dN}{dt} \quad \frac{-A\,\varepsilon\,N}{1+\varepsilon\,\tau} + S.$$

where the first term represent losses due to pitch angle scattering with A a constant and S accounts for represents particle source terms in the magnetospheric equatorial plane. τ is a parameter that characterizes lifetimes against strong pitch angle diffusion. The time rate of change of ε is given by

$$(14) \quad \frac{d\varepsilon}{dt} = \frac{\left(2\,\gamma\,{}^{*}N/N^{*}\right)}{1+\varepsilon\tau}\,\varepsilon + \frac{V_g\,\varepsilon}{LR_e}\ln R + W$$

The first term represents wave growth near the equatorial plane, the second term gives the wave losses in and through the ionosphere and the third accounts for any wave energy sources. The terms γ^* and N^* are used to denote the weak diffusion growth rate and column density of a flux tube at the Kennel and Petschek (1966) limit for stably trapped particles. In the second term, v_g/LR_e approximates bounce frequency of waves where v_g is the group velocity of the wave LR_e the approximate length of a flux tube; R is the reflection coefficient of the ionosphere. Since $R < 1$ the second term is always negative. The $(1 + \varepsilon \;\; \tau)$ term empirically lowers growth rate due to the pitch angle distribution becoming more isotropic under strong diffusion conditions.

In our present study we have examined numerical solutions of equations (13) and (14) using non-equilibrium initial conditions. The first case is represented by Figure 3 in which we started initial wave energy densities which are a factor of 3 (top panel) and 0.1 (bottom panel) above the Kennel-Petschek limit. In both cases we ignored associated enhancements in ionospheric coupling that lead to increased reflectivity. We see that the wave energy density quickly damps to the Kennel-Petschek equilibrium represented by the solid line.

In the second level of simulation the wave energy density is initially set at a factor of three above the Kennel-Petschek equilibrium value but includes a coupling factor to the ionosphere ζ. We find that for values of $\zeta \geq 10\%$ the oscillations become spike-like. The top panel of Figure 4 represents the normalized wave energy density for $\zeta = 10\%$ after the waves have evolved into periodic spikes. The middle and bottom panels of Figure 4 represent the normalized energetic particle density (cm^{-2}) contained on a flux tube and the normalized height integrated density of the ionosphere. Attention is directed to the phase relationship between the maxima of the three curves. The maximum, energetic particle flux leads the wave term and goes through the Kennel-Petschek value as the wave growth changes from positive to negative.

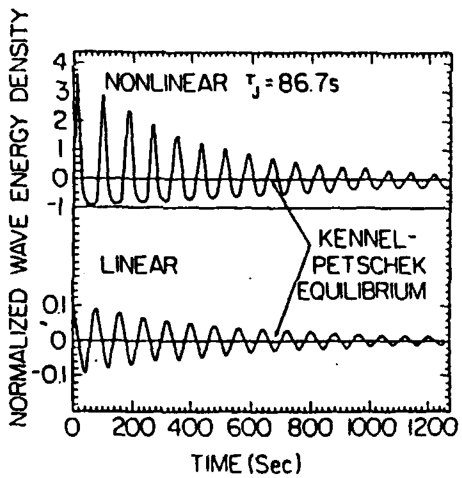

Fig. 3. Example of wave energy densities initially set at factors of 3.0 and 0.1 above Kennel Petschek equilibrium value.

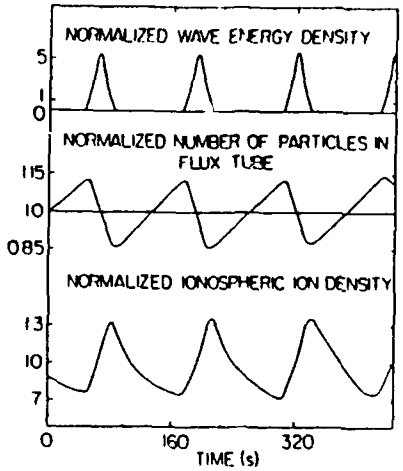

Fig. 4. Example of spike-like wave structures as well as energetic particle losses and ionospheric density changes with magnetosphere-ionosphere coupling.

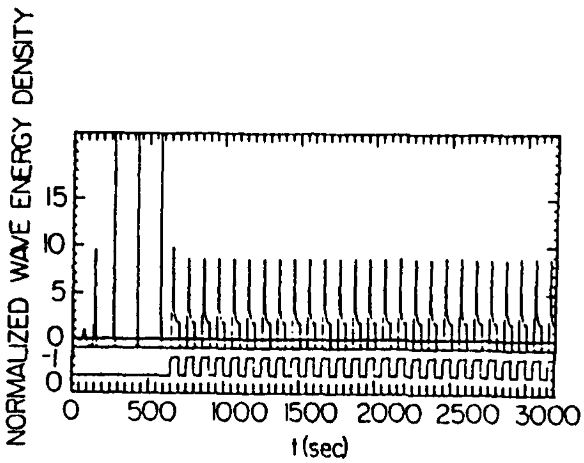

Fig. 5. Simulated, normalized wave energy density with magnetosphere-ionosphere coupling. A VLF source is turned on at t = 650s.

The maximum ionospheric effect occurs after the wave spike maximum. Our physical interpretation of Figure 4 is as follows. A spike in the wave energy density causes a depletion of electrons trapped in the belts to levels well below the Kennel-Petschek limit. The subsequent drop of precipitating electron flux allows the ionospheric conductivity to decrease. Thus, VLF waves are less strongly reflected back into the magnetosphere. This effectively raises the Kennel-Petschek limit as higher particle fluxes are necessary to offset increased ionospheric VLF absorbtion. In the presence of equatorial sources of particles, the simliations show flux levels building to 1.15 times the Kennel-Petschek limit. The enhanced fluxes in the magnetosphere, even with weak pitch angle diffusion, allows the ionospheric conductivity to rise, eventually leading to another masing spike.

Figure (5) shows the effect of an external VLF signal. The first few spikes result from the masing effect of the ionosphere due to particle precipitation. At t = 650 seconds a VLF square wave source is turned on with a 50 second duration. The spikes now are modulated at the driving frequency at a reduced amplitude. The amplitude is reduced since the fluxes are more frequently dumped with the VLF signal present than in its absence.

Iversen et al. (1984) using simultaneous ground and satellite measurements, have recently observed the modulation of precipitating electron at pulsation frequencies. In terms of our simulations these would be close to the situation shown in Figure 4 in which natural masing occurs in a flux tube. The observed frequencies are consistent with those expected from the linear theory. Detailed comparison with experimental data necessitates knowing the efficiency with which VLF waves reach the ionosphere.

IV Conclusion

Although the work presented in this paper is still in a very preliminary stage of development it appears that significant space effects can be produced by the injection of intense electromagnetic waves into ionospheric plasmas. In the coming months we expect that as calculations mature we will grow in the ability to translate mathematical representation into physical understanding. If the results of our analyses live up to early promise then a series of ground-based wave emission experiments will be developed to measure injection effects in space. The upcoming ECHO-7 experiment presents a well instrumented target of opportunity for electron acceleration experiments with the HIPAS system. After the launch of the CRRES satellite it will be possible to make simultaneous *in situ* measurements of wave and particle fluxes in artificially excited Alfven Masers. Looking forward to the 1990's it appears that WISP experiment planned for the Space Station will make an ideal source for both electron acceleration and radiation belt depletion experiments. Recently a Soviet experiment measured electrons accelerated to kilovolt energies using a low power telemetry system (Babaev et al., 1983). Just imagine what could be done with the specifically designed, high power WISP!

References

Babnev, A.P., S.B. Lyakhov, G.G. Managadze, A.A. Martinson and P.P. Timofeev, Plasma particle acceleration due to emission of ground-based and onboard transmitters, in Active Experiments in Space, ESA SP-195 61-65, 1983.

Imhof, W.L., J.B. Reagan, H.D. Voss, E.E. Gaines, D.W. Datlowe, J. Mobilia, R.A. Helliwell, U.S. Inan, J. Katsufrakis, and R.G. Joiner, Direct observation of radiation belt electrons precipitated by the controlled injection of VLF signals from a ground based transmitter, Geophys. Res. Lett., 4, 361 - 364, 1983.

Imhof, W.L., H.D. Voss, J.B. Reagan, D.W. Datlowe and D.S. Evans, Relativistic electron and energetic ion precipitation spikes near the plasmapause, J. Geophys. Res., 91, 3077 - 3088, 1986

Inan, U.S., T.F. Bell and H. C. Chang, Particle precipitation induced by short duration VLF waves in the magnetosphere, J. Geophys. Res., 87, 6243 - 6264, 1982.

Iversen, I.B., L.P. Block, K. Bronstad, R. Grad, G. Haerendel, H. Junginger, A Korth, G. Kremser M. Madsen, J. Niskanen, W. Riedler, P. Tanskanen, K.M. Torkar, and S. Ullaland, Simultaneous observations of a pulsation event from the ground with balloons and with a geostationary satellite on August 12, 1978, J. Geophys. Res., 89, 6775 - 6785, 1984.

Katsouleas, T., and J.M. Dawson, Unlimited electron acceleration in laser driven plasma waves, Phys. Rev. Lett., 51, 392 - 395, 1983.

Kennel, C.F., and H.E. Petschek, Limit on stably trapped particle fluxes, J. Geophys. Res., 71, 1 - 28, 1966.

Menyuk, C.R., A.T. Drobot, K. Papadopoulos and H. Karimabadi, Stochastic electron acceleration in obliquely propagating electromagnetic waves, SAIC Preprint, 1986

Roberts, C.S., and S.J. Buchsbaum, Motion of a charged particle in a constant magnetic field and a transverse electromagnetic field, Phys. Rev., 135, A381, 1964.

Schulz, M., Particle saturation of the outer zone: a nonlinear model, Astrophys. and Space Sci., 29, 232 - 242, 1974.

Trakhtengerts, V.Yu., Alfven masers, in Active Experiments in Space, ESA SP-195, 67 - 74, 1983.

Wong, A.Y., J. Santoru, and G.G. Sivjee, Active stimulation of the auroral plasma, J. Geophys. Res., 86, 7718 - 7732, 1981.

Relativistic particle acceleration by obliquely propagating electromagnetic fields

Elena Villalón
Center for Electromagnetics Research, Northeastern University, Boston, Massachusetts 02115
William J. Burke
Air Force Geophysics Laboratory, Hanscom Air Force Base, Massachusetts 01731

(Received 4 December 1986; accepted 24 July 1987)

The relativistic equations of motion are analyzed for charged particles in a magnetized plasma and externally imposed electromagnetic fields $(\omega,\mathbf{k})$, which have wave vectors $\mathbf{k}$ that are at arbitrary angles. The particle energy is obtained from a set of nonlinear differential equations, as a function of time, initial conditions, and cyclotron harmonic numbers. For a given cyclotron resonance, the energy oscillates in time within the limits of a potential well; stochastic acceleration occurs if the widths of different Hamiltonian potentials overlap. The net energy gain for a given harmonic increases with the angle of propagation, and decreases as the magnitude of the wave magnetic field increases. Applications of these results to the acceleration of ionospheric electrons are presented.

I. INTRODUCTION

The interaction of high-power rf fields with plasma particles is a subject of very active research because of its richness in basic plasma processes and practical applications. It can be used as a method to increase the plasma temperature[1] and to accelerate some particles to high energies.[2] Particle acceleration by electrostatic waves is a well-explored area of research because of its application in laboratory plasmas.[3] Although less is known about acceleration processes by electromagnetic waves,[4,5] they may have greater relevance in space plasma physics. Recently, there has been an increasing effort to understand the basic ionospheric plasma processes and the nature of particle motion under the influence of high-power rf fields.[6] A number of nonlinear phenomena have been observed such as the formation of cavitons (local plasma density depletion) and parametric instabilities. In addition, particle acceleration has also been observed near the critical layer where the wave frequency matches the local plasma frequency.[7] In this paper, we concentrate on single particle rather than collective plasma motion.

The motion of a relativistic particle of charge q and rest mass m, under the influence of an external electromagnetic field and a uniform magnetic field $\mathbf{B}_0$, is described by the Lorentz force equation

$$\frac{d\mathbf{p}}{dt} = q\left(\mathbf{E} + \frac{\mathbf{v}}{c}\times(\mathbf{B} + \mathbf{B}_0)\right), \tag{1}$$

where c is the speed of light. Gaussian units are used throughout the paper. The wave propagates at an arbitrary angle with respect to $\mathbf{B}_0$, which we assume to be along the z direction. Without loss of generality, the wave propagation vector is given by $\mathbf{k} = k_x\hat{\mathbf{x}} + k_z\hat{\mathbf{z}}$, and the electric field is

$$\mathbf{E} = \hat{\mathbf{x}}E_1\cos\Phi - \hat{\mathbf{y}}E_2\sin\Phi - \hat{\mathbf{z}}E_3\cos\Phi, \tag{2}$$

where $\hat{\mathbf{x}}$, $\hat{\mathbf{y}}$, and $\hat{\mathbf{z}}$ are unit vectors, $\Phi = k_x x + k_z\hat{\mathbf{x}} - \omega t$, and ω is the wave frequency. The wave magnetic field is given by the Maxwell equation: $\mathbf{B} = c/\omega(\mathbf{k}\times\mathbf{E})$. The relativistic momentum is $\mathbf{p} = m\gamma\mathbf{v}$, where $\gamma = (1 - v_\perp^2/c^2 - v_z^2/c^2)^{-1/2}$ is the Lorentz factor, $\mathbf{v}$ is the particle velocity, and $v_\perp$, v_z are the components perpendicular and parallel to $\mathbf{B}_0$, respectively. This interaction is resonant at multiple harmonics of the relativistic cyclotron frequency Ω. The resonance conditions are

$$\omega - k_z v_z - n\Omega = 0, \tag{3a}$$

$$\Omega = -qB_0/mc\gamma, \tag{3b}$$

where n is an integer; the nonrelativistic cyclotron frequency is denoted by Ω_c, where $\Omega = \Omega_c/\gamma$. The case of a circularly polarized wave (i.e., $E_1 = E_2$ and $E_3 = 0$) which propagates along $\mathbf{B}_0$ has been studied in Refs. 8–10. It has been shown[8] that to all orders in the field amplitudes, particles can be accelerated indefinitely provided that (1) the index of refraction $\eta = ck/\omega$ is equal to 1 and (2) the particle is initially at resonance with the $n = 1$ harmonic.

In this paper we extend the analytical results of Roberts and Buchsbaum[9] to waves of arbitrary polarizations, propagation angles, and refractive indices, by assuming that the field amplitudes become small compared to $|\mathbf{B}_0|$ as the propagation angle increases. Our analysis is also applicable to electrostatic modes, which appear as a particular application of our general results. We show that the net energy gain for any given harmonic resonance is always finite except in the case of circularly polarized waves with $\eta = 1$. To lowest order in field amplitudes, particles gain energy following certain trajectories in $(p_\perp, p_z)$ phase space. These trajectories may be opened or closed according to the magnitude of the wave magnetic field, the angle of propagation, and the value of refractive index η. We find that they are closed for electromagnetic fields that propagate at large angles, and hence the net energy gain is restricted to finite values. They can be opened for em waves that propagate at small angles, if η is small or equal to 1. For electrostatic waves (i.e., for small values of $|\mathbf{B}|$) the energy trajectories are always opened, and if resonances overlap, the net energy gain can be very large.

The total energy H is obtained from a set of nonlinear differential equations which depend on time, initial conditions, and the harmonic number n. In deriving these equations, we assume that the particle undergoes many cyclotron orbits before its energy changes appreciably. The slow time evolution of H is found by averaging over time scales associated with the motion of the wave and gyromotion, and satisfies equations of the form $(dH/dt)^2 + V_n(H) = 0$. For a given harmonic n, H oscillates in time within the Hamiltonian potential wells, and the maximum allowed energy gain is given by setting the potentials $V_n(H) = 0$. The widths of the potential wells are also given as functions of $|\mathbf{B}|$ and the angle of propagation. We find that the resonance widths increase with the angle and decrease as $|\mathbf{B}|$ increases. Besides, they are larger for particles that initially satisfy the resonance condition, Eq. (3). The particle motion becomes stochastic when the widths of potentials for different harmonics overlap, and then the mean net momentum transfer to the particles can be very large.

We apply our results to the acceleration of electrons in the ionosphere by considering an extraordinary mode propagating into a region of increasing plasma density. For the purpose of illustration, calculations are presented with a mode frequency $\omega = 1.8\Omega_e$; here Ω_e is evaluated in the Earth's magnetic field ($\Omega_e = 1.6$ MHz). We show that, at large angles of propagation, initially cold particles can be accelerated to large energies at power levels ($P \simeq 0.25$ W/cm^2). This happens near the critical density (cutoff) where the wave vector $\mathbf{k}$ and group velocity along $\mathbf{k}$ are zero and the wave amplitude is greatly enhanced.[7] In addition, we also find that the mode becomes purely circularly polarized near the cutoff layer, and its magnetic field amplitude is very small. Because the first and second cyclotron harmonic resonances overlap near the cutoff, initially cold particles which gain some energy interacting with the first harmonic can be picked up by the second and boosted to still higher energies. For small angles of propagation and at the power levels considered in our calculations, we find that resonances do not overlap so that initially cold particles only interact with the first harmonic. Because the resonance condition, Eq. (3), is far from being satisfied for $n = 1$, cold particles $v_z = 0$, and $\omega \simeq 2\Omega_e$, then the net energy gain for small angles of propagation is very small.

II. BASIC EQUATIONS

We start by considering that Eq. (1) admits the following three constants of motion[11]:

$$\frac{d}{dt}\left(\mathbf{p} - \frac{q}{c}\mathbf{r}\times\mathbf{B}_0 - \frac{\mathbf{k}}{\omega}H + \frac{q}{c}\mathbf{A}\right) = 0\,, \qquad (4)$$

where $\mathbf{r} = (x,y,z)$ is the vector position, $H = \gamma mc^2$ is the total particle energy including the rest energy, and $\mathbf{A}$, the vector potential, is

$$\mathbf{A} = \hat{\mathbf{x}}cE_1/\omega \sin\Phi + \hat{\mathbf{y}}cE_2/\omega\cos\Phi - \hat{\mathbf{z}}cE_3/\omega\sin\Phi\,.$$

After multiplying the x component of Eq. (4) by k_z and the z component by k_x, we easily obtain

$$\dot p_z - (K_z/\omega)H + (E_3/E_1)(\dot p_x + \Omega p_y) = 0\,, \qquad (5)$$

where $K_z = k_z(1 + E_3k_x/E_1k_z)$. Hereafter, dots signify differentiation with respect to time.

The equations of motion for the perpendicular components of the paticle momentum can also be written in the form

$$\dot p_x + p_y[\Omega + (qE_3/m\gamma)(k_x/\omega)\sin\Phi] = (qE_1/\omega)(\omega - K_z\dot z)\cos\Phi\,, \qquad (6)$$

$$\dot p_y - p_x[\Omega + (qE_3/m\gamma)(k_x/\omega)\sin\Phi] = -(qE_2/\omega)(\omega - k_z\dot z)\sin\Phi\,. \qquad (7)$$

In our calculations, we shall neglect the correction to the cyclotron frequency in Eqs. (6) and (7) by assuming $B_y = E_3ck_x/\omega \ll B_0$ (i.e., we assume that either $k_x \to 0$ or E_3/B_0 is very small).

The evolution in time of the particle energy is given by

$$\frac{H\dot H}{c^2\omega} = \frac{qE_1}{\omega}p_x\cos\Phi - \frac{qE_2}{\omega}p_y\sin\Phi - \frac{qE_3}{\omega}p_z\cos\Phi\,. \qquad (8)$$

Equations (5)–(8) are the foundations of our theoretical analysis.

Before going into a detailed mathematical derivation, it is useful to consider the lowest-order solutions in the electric field amplitudes to Eqs. (5)–(7). If the electric field amplitude is small we may approximate x by

$$x = \rho\cos(\sigma + \alpha), \qquad (9)$$

where $\sigma = \int_0^t \Omega(t')dt'$, $\tan\alpha = -p_{x0}/p_{y0}$, and $\rho = v_\perp/\Omega$ is the particle gyroradius. Hereafter, the subscript zero refers to the initial conditions at $t = 0$. To zeroth order in the electric field amplitudes, Eq. (5) yields

$$p_z = p_{z0} + (K_z/\omega)(H - H_0)\,. \qquad (10)$$

In terms of p_z and $p_\perp$, the components parallel and perpendicular to $\mathbf{B}_0$, respectively, Eq. (10) can also be written as

$$\left(\frac{p_\perp}{mc}\right)^2 = -1 + \gamma_0^2\left(1 - \frac{1}{\beta_z}\frac{v_{z0}}{c}\right)^2 + \frac{2}{\beta_z}\frac{p_z}{mc}\gamma_0\left(1 - \frac{v_{z0}}{c}\frac{1}{\beta_z}\right) + \left(\frac{p_z}{mc}\right)^2\left(\frac{1}{\beta_z^2} - 1\right), \qquad (11a)$$

$$\beta_z = \frac{ck_z}{\omega}\left(1 + \frac{E_3}{E_1}\frac{k_x}{k_z}\right), \qquad (11b)$$

where γ_0 is the Lorentz factor evaluated at $t = 0$, and v_{z0} is also evaluated at $t = 0$. Note that depending on the magnitude of β_z, Eq. (11) describes families of elliptical ($|\beta_z| > 1$), parabolic ($|\beta_z| = 1$), or hyperbolic ($|\beta_z| < 1$) trajectories in ($p_\perp, p_z$) phase space.

III. SOLUTION OF THE EQUATION OF MOTION

Equations (6) and (7) can be solved to all orders in the field amplitudes as functions of $\Phi = k_x x + k_z z - \omega t$ and

$$Q = (qE_1/\omega)(\omega - K_z\dot z) - (qE_2/\omega)(\omega - k_z\dot z)\,, \qquad (12a)$$

$$R = (qE_1/\omega)(\omega - K_z\dot z) + (qE_2/\omega)(\omega - k_z\dot z)\,. \qquad (12b)$$

We find

$$p_x = \frac{1}{2}\int_0^t [Q'\cos(\sigma - \sigma' + \Phi') + R'\cos(\sigma - \sigma' - \Phi')]dt' - p_1 \sin(\sigma + \alpha), \tag{13a}$$

$$p_y = \frac{1}{2}\int_0^t [Q'\sin(\sigma - \sigma' + \Phi') + R'\sin(\sigma - \sigma' - \Phi')]dt' + p_1 \cos(\sigma + \alpha). \tag{13b}$$

Primed and unprimed quantities are evaluated at times t and t', respectively. After substituting these equations into Eq. (5) and integrating, we obtain

$$p_z = p_{z0} + \frac{K_z}{\omega}(H - H_0) - \frac{1}{2}\frac{E_3}{E_1}\int_0^t (Q' + R')\cos\Phi' \, dt'. \tag{14}$$

Equations (13) and (14) together with Eq. (8) give the following expression for the rate of change of particle energy:

$$\begin{aligned}\frac{4H\dot{H}}{c^2\omega} &= \frac{q}{\omega}(E_1 + E_2)\Big(\int_0^t Q'\cos(\sigma + \Phi - \sigma' + \Phi')dt' + \int_0^t R'\cos(\sigma + \Phi - \sigma' - \Phi')dt' - 2p_1 \sin(\sigma + \Phi + \alpha)\Big)\\ &+ \frac{q}{\omega}(E_1 - E_2)\Big(\int_0^t Q'\cos(\Phi - \sigma + \sigma' - \Phi')dt' + \int_0^t R'\cos(\Phi - \sigma + \Phi' + \sigma')dt' + 2p_1 \sin(\Phi - \sigma - \alpha)\Big)\\ &- \frac{q}{\omega}E_3\Big[4\Big(p_{z0} + \frac{K_z}{\omega}(H - H_0)\Big)\cos\Phi - \frac{E_3}{E_1}\int_0^t (Q' + R')[\cos(\Phi + \Phi') + \cos(\Phi - \Phi')]dt'\Big].\end{aligned} \tag{15}$$

We note that polarizations represented in Eq. (15) are related to terms multiplying electric fields in right-hand $(E_1 + E_2)$, left-hand $(E_1 - E_2)$, and parallel E_3 modes.

Next, we substitute for x using Eq. (9) and define $\Upsilon = \sigma + \alpha + \pi/2$ and $\Psi = k_z z - \omega t$, so that $\Phi = \Psi + k_x \rho \sin \Upsilon$. After expanding the sine and cosine terms in Eq. (15) in the series of Bessel functions $J_\nu(\lambda)$, we obtain

$$\frac{4H\dot{H}}{c^2\omega} = \sum_n I_n, \tag{16a}$$

where

$$\begin{aligned}I_n &= \frac{q}{\omega}(E_1 + E_2)J_{n-1}(\lambda)\Big(\sum_m \int_0^t [Q'J_{m+1}(\lambda')\cos(n\Upsilon + m\Upsilon' + \Psi + \Psi')\\ &+ R'J_{m-1}(\lambda')\cos(n\Upsilon - m\Upsilon' + \Psi - \Psi')]dt' + 2p_1 \cos(n\Upsilon + \Psi)\Big) + \frac{q}{\omega}(E_1 - E_2)J_{n+1}(\lambda)\\ &\times\Big(\sum_m \int_0^t [Q'J_{m+1}(\lambda')\cos(n\Upsilon - m\Upsilon' + \Psi - \Psi') + R'J_{m-1}(\lambda')\cos(n\Upsilon + m\Upsilon' + \Psi + \Psi')]dt'\\ &+ 2p_1 \cos(n\Upsilon + \Psi)\Big) - \frac{qE_3}{\omega}J_n(\lambda)\Big[4\Big(p_{z0} + \frac{K_z}{\omega}(H - H_0)\Big)\cos(n\Upsilon + \Psi)\\ &- \frac{E_3}{E_1}\sum_m \int_0^t (Q' + R')J_m(\lambda')[\cos(n\Upsilon + m\Upsilon' + \Psi + \Psi') + \cos(n\Upsilon - m\Upsilon' + \Psi - \Psi')]dt'\Big],\end{aligned} \tag{16b}$$

where $\lambda = k_x \rho$, and the summations are over all integer values from $-\infty$ to $+\infty$. Note that H can be split into rapidly fluctuating parts, which depend on the time scales associated with the motion of the wave (through the function Ψ) and with the gyromotion (through the function Υ), and a slowly time-varying part H^S. If $f(H)$ is any given function of the total energy, the slow time variation of f is obtained as

$$f(H)^S = \int_0^{2\pi}\frac{d\Upsilon}{2\pi}\int_0^{\pi}\frac{d\Psi}{\pi}f(H).$$

Our next step is to approximate $v_z = (c^2/H)p_z$ in Q and R by the zeroth-order solution to Eq. (10). Here, every H function appearing in the definitions of v_z and p_z is given to lowest order by the slow time energy function H^S. The argument of the Bessel functions λ and the momentum p_1 are also given in terms of H^S and initial conditions by means of Eqs. (10) and (11),

$$\lambda = \frac{ck_x}{\Omega_0}\Big[1 - \frac{v_{z0}^2}{c^2} - \frac{1}{\gamma_0^2} + 2U\Big(1 - \beta_z \frac{v_{z0}}{c}\Big) + U^2(1 - \beta_z^2)\Big]^{1/2}, \tag{17}$$

where $\Omega_0 = -qB_0/mc\gamma_0$ is the relativistic cyclotron frequency evaluated at $t = 0$, and $U = (H^S - H_0^S)/H_0^S$ is the slow time evolution of the normalized particle energy. Differentiating Eq. (16b) with respect to time, we obtain the following:

$$\dot{I}_n = \frac{q}{\omega}(E_1+E_2)J_{n-1}(\lambda)\sum_m \{QJ_{m+1}(\lambda)\cos[(n+m)\Upsilon+2\Psi]+RJ_{m-1}(\lambda)\cos[(n-m)\Upsilon]\}$$

$$+\frac{q}{\omega}(E_1-E_2)J_{n+1}(\lambda)\sum_m \{QJ_{m+1}(\lambda)\cos[(n-m)\Upsilon]+RJ_{m-1}(\lambda)\cos[(n+m)\Upsilon+2\Psi]\}$$

$$+\frac{q}{\omega}\frac{E_3^2}{E_1}J_n(\lambda)\sum_m (Q+R)J_m(\lambda)\{\cos[(n+m)\Upsilon+2\Psi]+\cos[(n-m)\Upsilon]\}-(n\dot{\Upsilon}+\dot{\Psi})P_n\,. \tag{18}$$

where $n\dot{\Upsilon}+\dot{\Psi}=n\Omega+k_z v_z-\omega$. The function P_n is defined by

$$P_n=\frac{q}{\omega}(E_1+E_2)J_{n-1}(\lambda)\Big(\sum_m\int_0^t[Q'J_{m+1}(\lambda')\sin(n\Upsilon+m\Upsilon'+\Psi+\Psi')$$

$$+R'J_{m-1}(\lambda')\sin(n\Upsilon-m\Upsilon'+\Psi-\Psi')]dt'+2p_1\sin(n\Upsilon+\Psi)\Big)+\frac{q}{\omega}(E_1-E_2)J_{n+1}(\lambda)$$

$$\times\Big(\sum_m\int_0^t[Q'J_{m+1}(\lambda')\sin(n\Upsilon-m\Upsilon'+\Psi-\Psi')+R'J_{m-1}(\lambda')\sin(n\Upsilon+m\Upsilon'+\Psi+\Psi')]dt'$$

$$+2p_1\sin(n\Upsilon+\Psi)\Big)-\frac{qE_1}{\omega}J_n(\lambda)\Big[4\Big(p_{z0}+\frac{K_z}{\omega}(H^S-H_0^S)\Big)\sin(n\Upsilon+\Psi)$$

$$-\frac{E_3}{E_1}\sum_m\int_0^t(Q'+R')J_m(\lambda')[\sin(n\Upsilon+m\Upsilon'+\Psi+\Psi')+\sin(n\Upsilon-m\Upsilon'+\Psi-\Psi')]dt'\Big].$$

Differentiating P_n with respect to time, we obtain

$$\dot{P}_n=\frac{q}{\omega}(E_1+E_2)J_{n-1}(\lambda)\sum_m\{QJ_{m+1}(\lambda)\sin[(n+m)\Upsilon+2\Psi]+RJ_{m-1}(\lambda)\sin[(n-m)\Upsilon]\}$$

$$+\frac{q}{\omega}(E_1-E_2)J_{n+1}(\lambda)\sum_m\{QJ_{m+1}(\lambda)\sin[(n-m)\Upsilon]+RJ_{m-1}(\lambda)\sin[(n+m)\Upsilon+2\Psi]\}$$

$$+\frac{q}{\omega}\frac{E_3^2}{E_1}J_n(\lambda)\sum_m(Q+R)J_m(\lambda)\{\sin[(n+m)\Upsilon+2\Psi]+\sin[(n-m)\Upsilon]\}+(n\dot{\Upsilon}+\dot{\Psi})I_n\,. \tag{19}$$

Since we are only interested in the slow time evolution of the total particle energy, we can average Eqs. (18) and (19) over the fast time dependencies (i.e., over Υ and Ψ) to find that only terms with $n=m$ give a nonzero contribution.[12] *We also consider the contribution of a single (isolated) resonance*, and then for each harmonic n, we find that the particle energy ($4H\dot{H}/c^2\omega=I_n^S$) obeys the following coupled differential equations:

$$\dot{I}_n^S=\frac{q}{\omega}(E_1+E_2)RJ_{n-1}^2(\lambda)+\frac{q}{\omega}(E_1-E_2)QJ_{n+1}^2(\lambda)$$

$$+\frac{q}{\omega}\frac{E_3^2}{E_1}(Q+R)J_n^2(\lambda)-(n\dot{\Upsilon}+\dot{\Psi})P_n^S\,, \tag{20a}$$

$$\dot{P}_n^S=(n\dot{\Upsilon}+\dot{\Psi})I_n^S\,. \tag{20b}$$

The superscript S refers to the slow time contributions. Here, P_n^S is such that at $t=0$ one has $P_n^S(0)=4(H_0/c)^2\zeta_n(0)\sin\delta_n$, where

$$\zeta_n(0)=(v_{\perp0}/2c)[-(\Sigma_1+\Sigma_2)J_{n-1}(\lambda_0)+(\Sigma_2-\Sigma_1)J_{n+1}(\lambda_0)]+(v_{z0}/c)\Sigma_3J_n(\lambda_0)\,,$$

$$\delta_n=n(\alpha+\pi/2)+k_z z_0\,,$$

$$\Sigma_i=-(qE_i/\omega)(c/H_0)\,,\quad i=1,2,3.$$

and all quantities with the subscript 0 are evaluated at $t=0$. Combining Eqs. (10), (17), and (20) leads to a nonlinear equation for H as a function of time and initial conditions. Hereafter we shall drop the S on the function H, knowing that by H we always mean the slow time evolution of the particle energy. After multiplying by $H\dot{H}$, integrating once over time, and writing all expressions in terms of normalized quantities, we find (see the Appendix),

$$(U+1)^2\Big(\frac{1}{\omega}\frac{dU}{dt}\Big)^2+V_n(U)=0, \tag{21a}$$

$$V_n(U)=\frac{d_1^2}{4}U^2\Big(U+\frac{2r_n}{d_1}\Big)^2-\zeta_n(0)d_1U\Big(U+\frac{2r_n}{d_1}\Big)\sin\delta_n+\Big(\frac{\Sigma_2-\Sigma_1}{2}\Big)$$

$$\times\{-(\Sigma_2-\Sigma_1)[F_{n+1}(U)+G_{n+1}(U)]+(\Sigma_3\eta_z-\Sigma_1\beta_z)[(v_{z0}/c)F_{n+1}(U)+\beta_zG_{n+1}(U)]\}$$

$$
\begin{aligned}
&- [(\Sigma_1 + \Sigma_2)/2]\{(\Sigma_1 + \Sigma_2)[F_{n-1}(U) + G_{n-1}(U)] \\
&- (\beta_z\Sigma_1 + \Sigma_2\eta_z)[(v_{z0}/c)F_{n-1}(U) + \beta_z G_{n-1}(U)]\} \\
&- \Sigma_3^2\{G_n(U) + F_n(U) - \beta_z[(v_{z0}/c)F_n(U) + \beta_z G_n(U)]\} - [\zeta_n(0)\cos\delta_n]^2 .
\end{aligned}
\tag{21b}
$$

where $d_1 = 1 - \eta_z\beta_z$, $\eta_z = ck_z/\omega$, β_z is defined in Eq. (11b), $r_n = 1 - k_z v_{z0}/\omega - n\Omega_0/\omega$, and

$$G_\nu(U) = \int_0^U J_\nu^2[\lambda(U')]U'\,dU' ,$$

$$F_\nu(U) = \int_0^U J_\nu^2[\lambda(U')]dU' ,$$

with $\nu = n, n \pm 1$. This is just a differential equation describing the motion of trapped particles within the Hamiltonian potential well V_n. Under the limit $k_z \to 0$, Eqs. (21) reduce to the equations derived by Roberts and Buchsbaum[9] for the cases $n = \pm 1$. Note that in the limit $k_x \to 0$, Eqs. (21) and the Hamiltonian trajectories as defined in Eq. (10) are exact integrals to the equation of motion (i.e., they are valid to all orders in the field amplitudes).

IV. THE HAMILTONIAN POTENTIAL WELLS

We note that the first term of Eq. (21b) does not depend on the wave amplitude and is always positive for $d_1 \neq 0$. The case $d_1 = 0$ corresponds to a circularly polarized wave with a refractive index $\eta = 1$. If, in addition, $r_n = 0$, then this term is zero and we are in the case of unlimited acceleration. For $d_1 \neq 0$ and at large values of U, this first term dominates over all the others, and its contribution can be diminished by taking $r_n = 0$ (i.e., particles initially at resonance with the wave). Thus V_n can be regarded as a potential well within which H oscillates as a function of time. The maximum value that H can attain for a given resonance and field amplitude can be found by setting the potentials $V_n(U) = 0$. At wave amplitudes and propagation angles where the widths of potentials for different harmonics overlap, the particle motion becomes stochastic and at the net momentum transfer to the particle can be very large. Nevertheless, since λ (the argument of the Bessel functions) is given by the lower-order solution, Eq. (17), the amount of energy the particle can gain is limited according to the value of β_z. In fact, recall that the Hamiltonian trajectories as defined in Eqs. (11) are open hyperbolas for $|\beta_z| < 1$ in a $(p_\perp, p_z)$ phase space. For $|\beta_z| > 1$ they are closed ellipses and the range of accessible energy gain is restricted to finite values.

In order to better understand the physical meaning of β_z, let us consider the time average of the wave magnetic field

$$\langle \mathbf{B}^2 \rangle = (E_1^2/2)(\eta^2 E_3^2/E_1^2 + \beta_z^2) . \tag{22}$$

Electrostatic waves are characterized by small values of β_z and of the product $\eta E_2/E_1$. Thus, the zeroth-order trajectories associated with electrostatic fields are open in a $(p_\perp, p_z)$ phase space. For electromagnetic waves, β_z is large, in general. However, if the angle of propagation is small and if the refractive index is such that $\eta < 1$, then $\beta_z \sim \eta_z$ and the Hamiltonian trajectories can also be open as is the case for circularly polarized waves with $\eta < 1$. If the angle of propagation is large, the allowable energy gain is limited even for $\eta < 1$.

It is also instructive to study the behavior of V_n with respect to β_z. We consider only the case of particles which are initially at rest, i.e., $v_{z0} = v_{10} = 0$. Hence $U = \lambda - 1$ and the potential well becomes

$$
\begin{aligned}
V_n^c(U) = {}& (d_1^2 U^2/4)(U + 2r_n/d_1)^2 + [(\Sigma_2 - \Sigma_1)/2]\{ -(\Sigma_2 - \Sigma_1)[G_{n+1}(U) + F_{n+1}(U)] \\
&+ \beta_z(\Sigma_2\eta_z - \Sigma_1\beta_z)G_{n+1}(U)\} - [(\Sigma_1 + \Sigma_2)/2]\{(\Sigma_1 + \Sigma_2)[G_{n-1}(U) + F_{n-1}(U)] \\
&- \beta_z(\Sigma_1\beta_z + \Sigma_2\eta_z)G_{n-1}(U)\} - \Sigma_3^2[G_n(U) + F_n(U) - \beta_z^2 G_n(U)] .
\end{aligned}
\tag{23}
$$

Terms multiplying β_z in the right-hand and parallel polarization fields are always positive for any $\beta_z \neq 0$. Although the β_z term in the left-hand component may be negative, its contribution is small because the order of the Bessel function is higher. Therefore, we conclude that the larger β_z is, the smaller the widths of potential wells.

Finally, some comment should be made regarding the dependence of V_n on propagation angles. For initially cold particles with small gyroradii, all but the zeroth-order Bessel functions are very small. Since the argument of the Bessel functions is the perpendicular component of the wave vector k_x times the particle's gyroradius, increasing the propagation angle increases the value of the Bessel functions terms. Thus, for all but the first- and zeroth-order harmonics, the potential may not trap low-energy particles unless the propagation angle is large. The behavior of the potential for small values of k_x is as follows. For $k_x \to 0$ and $|n| > 2$, only the first term of Eq. (23) is nonzero, and therefore no particles can be trapped. For $k_x \to 0$ and $n = 1$, the right-hand polarization field may accelerate cold particles.

V. ELECTRON ACCELERATION IN THE IONOSPHERE

We consider an extraordinary mode propagating in a cold plasma at an angle θ with respect to $\mathbf{B}_0$. The dispersion relation is[11]

$$\eta^2 = 1 - X/D , \tag{24a}$$

$$
\begin{aligned}
D = {}& 1 - [Y^2/2(1 - X)]\sin^2\theta \\
&- \{[Y^2/2(1 - X)]^2 \sin^4\theta + Y^2\cos^2\theta\}^{1/2} ,
\end{aligned}
\tag{24b}
$$

where $X = \omega_{pe}^2/\omega^2$, ω_{pe} is the electron plasma frequency, $Y = \Omega_e/\omega$, and $\Omega_e = eB_0/cm$. The electric field component ratios are given by

$$\frac{E_2}{E_1} = \frac{XY}{(1-Y^2)(1-\eta^2)-X}, \tag{25a}$$

$$\frac{E_3}{E_1} = \frac{\eta_x \eta_z}{1-X-\eta_z^2}. \tag{25b}$$

Combining Eqs. (25b) and (11b) we find

$$\beta_z = \eta_x(1-X)/(1-X-\eta_z^2), \tag{26}$$

where η_x, η_z are the x and z components of the refractive index.

The magnitude of the electric field Σ_1 is given as a function of the power flow density P along $\mathbf{k}$ by solving for the following equation:

$$P = \frac{\omega^2 H_0^2}{q^2 c}\frac{v_g}{c}\frac{\Sigma_1^2}{16\pi}\left[\left(\frac{E_2}{E_1}\right)^2(1+\eta^2)+1+\left(\frac{E_3}{E_1}\right)^2+\beta_z^2\right], \tag{27a}$$

where v_g, the group velocity along $\mathbf{k}$, is given by

$$\frac{v_g}{c} = \frac{\eta}{1+\frac{1}{2}(D'\omega/D)(1-\eta^2)}, \tag{27b}$$

and $D' = dD/d\omega$.

In our numerical calculations we assume that $\omega = 1.8\Omega_e$, where $\Omega_e = 1.6$ MHz is the electron cyclotron frequency in the Earth's magnetic field. The wave propagates into a region of increasing plasma density until it reaches the cutoff point where $\mathbf{k}$ and v_g are zero. At the reflection point we find the following.

(i) The electron density is given by solving for $1 - X = Y$, which in our case is $n = 4.65 \times 10^4$ cm^{-3} and corresponds to $\omega_{pe}/\Omega_e = 1.22$.

(ii) The electromagnetic mode becomes circularly polarized, i.e., $\Sigma_1 = \Sigma_2$, and $\Sigma_3 = 0$.

(iii) The magnetic field is zero because $\mathbf{k}$, the propagation vector, is zero.

(iv) The electric field amplitude Σ_1 is very large because $v_g \simeq 0$.

(v) The resonance widths as obtained solving for $V_n(U) = 0$ are also large because β_z is zero.

We conclude that electron acceleration should be most effective near the turning point. In the following calculations we show that significant acceleration can indeed only take place near the cutoff layer.

Figure 1 shows the zeroth-order Hamiltonian trajectories for a low plasma density ($n = 3 \times 10^3$ cm^{-3}) *at different angles of propagation. These trajectories are open* (hyperbolic) for $\theta < \theta_T = 14°$ and closed (elliptical) for larger angles. In all cases the refractive index is smaller than, but close to, unity ($\eta \sim 0.95$). The ratio between the magnitudes of the wave magnetic and electric fields is also close to unity. For $\omega \simeq 2\Omega_e$ and for the power levels that are used in our calculations ($P \simeq 0.25$ W/cm^2), we find that the potentials are positive so that acceleration cannot take place. If the density is increased to 3.14×10^4 cm^{-3}, we find that electrons can gain about 12 keV through the interaction with the $n = 1$ harmonic.

In Figs. 2 and 3, the plasma density is 4.5×10^4 cm^{-3} which corresponds to $\omega_{pe}/\Omega_e = 1.2$, and the Hamiltonian

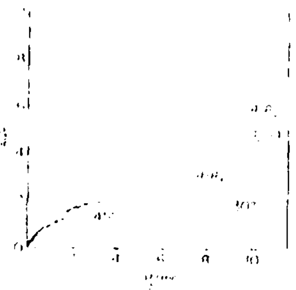

FIG. 1. Hamiltonian trajectories for different propagation angles to the magnetic field. The chosen parameters are $\omega_{pe}/\Omega_e = 0.3$ and $\omega = 1.8\Omega_e$. If $\theta = \theta_T$ the trajectory is a parabola, and it represents the transition angle between closed elliptical ($\theta > \theta_T$) and opened hyperbola ($\theta < \theta_T$) orbits.

trajectories are open for all angles of propagation. The net energy gain, as given by solving for the zeros of $V_n(U)$, is represented by the shaded regions as a function of θ. We consider the first two cyclotron harmonic resonances and assume that the particle is initially at rest. The first harmonic resonance interacts with cold particles through the contribution of the right-hand polarization field. The second harmonic does not interact with cold electrons even for the largest θ, because η, the refractive index, is very small ($\eta \simeq 0.25$). The energy that a particle can gain from the first harmonic is very limited because the resonance condition is far from being satisfied ($r_1 = 0.45$) for $v_{z0} = 0$ and $\omega \sim 2\Omega_e$. For the second harmonic $r_2 = -0.1$, and the net energy gain can be larger. In Fig. 2, $P = 0.15$ W/cm^2, and the first and second harmonics barely overlap. In Fig. 3 where $P = 0.25$ W/cm^2, they fully overlap (double shaded region) for angles greater than 40°. The second harmonic may trap those electrons that have already gained some energy interacting with the first harmonic, and boost them to still higher energies. In fact, since $U = \gamma - 1$, we see that the net energy gain can be as much as 150 keV.

In Fig. 4, we show the Hamiltonian potential wells as a function of the normalized particle energy U. We represent the inverse of the function W_n,

$$W_n(U) = -\operatorname{sgn}(V_n)\log[|V_n(U)|/(U+1)^2]. \tag{28}$$

The plasma parameters are those of Fig. 3, and we consider

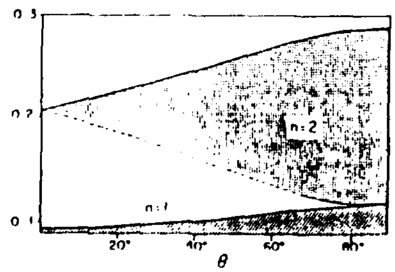

FIG. 2. Range of allowed energy gain (shaded regions) for the resonance harmonic numbers $n = 1, 2$, as a function of wave propagation angle to magnetic field. The plasma frequency is such that $\omega_{pe}/\Omega_e = 1.2$, $\omega = 1.8\Omega_e$, and the total power flux is $P = 0.15$ W/cm^2.

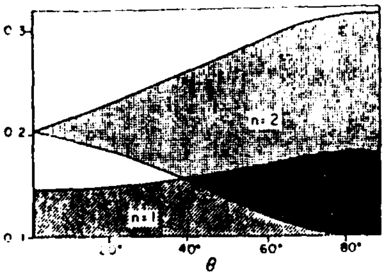

FIG. 3. The same as in Fig. 2 but with $P = 0.25$ W/cm^2.

two different angles of propagation: (a) $\theta = 80°$ and (b) $\theta = 20°$. The magnitudes of the potential wells, $|V_n(U)|$, are very small. For $\theta = 80°$ and $n = 2$ the maximum value of $|V_n|$ is of order 10^{-5}, and for $n = 1$ the maximum value is 2×10^{-3}. This is consistent with the assumption that the particle energy changes slowly over the gyro and wave periods. In fact, by normalizing time to Ω^{-1} in Eqs. (21) we see that $|V_n|(\omega/\Omega)^2$ must be much smaller than 1 if the changes in energy occur over many gyroperiods.

In the theory presented in Sec. III, we assume that the magnitude of the wave magnetic field is much smaller than that of the background magnetic field B_0 for increasing propagation angles. This allows us to use the zeroth-order solutions, Eqs. (9) and (10), in the perturbative analysis at large angles. In order to verify the validity of this approximation we have calculated the following dimensionless quantities:

$$B_z/B_0 = \eta_x(\omega/\Omega)\Sigma_2\gamma_0, \quad B_x/B_0 = \eta_z(\omega/\Omega)\Sigma_2\gamma_0,$$
$$B_y/B_0 = \beta_z(\omega/\Omega)\Sigma_1\gamma_0.$$

In the case of Fig. 4, we find that for $\theta = 80°$, $B_z/B_0 = 7\times 10^{-2}$, $B_x/B_0 = 9\times 10^{-4}$, and $B_y/B_0 = 1.3\times 10^{-2}$. For $\theta = 20°$ these values are 1.5×10^{-2}, 4×10^{-2}, and 4×10^{-2}, respectively. The magnitude of the wave electric field as given by Σ_1 (recall that near the cutoff we have $\Sigma_1 \simeq \Sigma_2$ and $\Sigma_3 \simeq 0$) is found to be closed to 0.14 for all cases of Fig. 4.

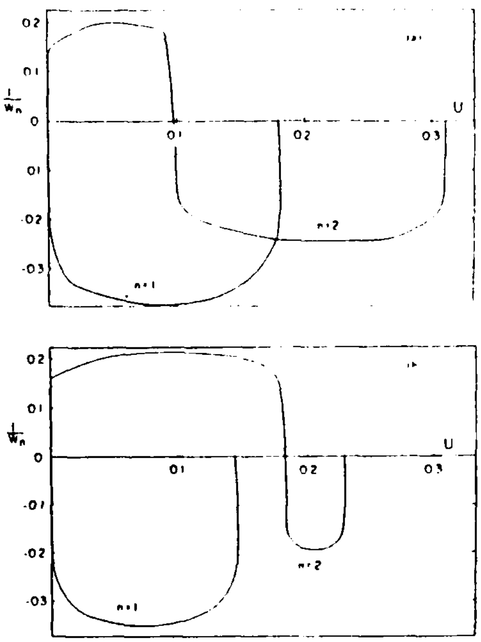

FIG. 4. Hamiltonian potential wells as represented by the functions $1/W_n$ [see Eq. (28)] as a function of particle energy for the plasma parameters of Fig. 3, and for two different angles of propagation: (a) $\theta = 80°$ and (b) $\theta = 20°$.

VI. CONCLUSION

In this paper, we have presented a theoretical analysis of the energy gained by relativistic charged particles in obliquely propagating electromagnetic waves. The main results of our analysis are as follows.

(1) To lower order in the field amplitudes, particles gain energy following certain trajectories in a $(p_\perp, p_z)$ phase space. Because these trajectories are closed for large values of the magnetic field amplitude $|\mathbf{B}|$ and the propagation angle θ, the net energy is restricted to finite values. They are, however, open for large values of $|\mathbf{B}|$ and small values of θ if the refractive index η is smaller or equal to 1. For sufficiently small values of $|\mathbf{B}|$ they are always open.

(2) For a given harmonic resonance, the range of the allowed particle energies is obtained by solving for the zeros of the Hamiltonian potentials V_n. The resonance widths are always finite except for the case of circularly polarized waves with $\eta = 1$ and for particles that are initially in resonance with the $n = 1$ harmonic.

(3) Resonance widths are larger for particles that initially most closely satisfy the resonance condition. They increase as θ increases and decrease as $|\mathbf{B}|$ increases.

(4) The onset of stochasticity occurs when the widths of potentials for different harmonics overlap.

This analysis is limited to small field amplitudes in comparison with the dc magnetic field $\mathbf{B}_0$ at large values of θ, which is a good approximation for the calculations we have presented on the acceleration of ionospheric electrons. It is valid to all orders in the field amplitudes for small values of θ. We have shown that electrons can be accelerated by extraordinary-mode waves which propagate into a plasma of increasing density. At moderate power levels, acceleration occurs near the cutoff point for large angles. This is because of the following results.

(5) The extraordinary mode becomes purely circularly polarized and its magnetic field is zero.

(6) The electric field amplitude is largest at the turning point.

(7) The resonance widths are also larger.

(8) The first and second cyclotron harmonic resonances overlap for large propagation angles.

Depending on the location in the plasma where one wishes to accelerate electrons, the wave frequency should be chosen so that the cutoff point falls within that region. For continuous acceleration over large regions of the plasma, a broad spectrum of waves should be considered. As the resonance widths overlap,[11] the electrons may gain considerable energy for different frequencies and harmonics. However, near the turning point the electric fields are so large that other nonlinear effects may also be important, and may affect both the acceleration and propagation processes. In addition, linear mode conversion into electrostatic waves[15] of large refractive indices can also be very relevant and may enhance the acceleration process by allowing initially cold particles to be picked up by the second- or higher-order harmonics. Questions related to the propagation of large-amplitude waves in the ionosphere and the consequent heating of plasma electrons deserve further attention.

ACKNOWLEDGMENTS

We are very grateful to Dr. A. Drobot and Dr. K. Papadopoulos for introducing us to this problem and for useful discussions. We also acknowledge helpful conversations with Dr. M. Silevitch.

This work was supported by the U.S. Air Force under Contract No. F19628-85-K-0053.

APPENDIX: DERIVATION OF EQS. (21)

From Eq. (10) we obtain

$$1 - k_z v_z/\omega = d_1 + (H_0/H) d_2, \tag{A1}$$

$$1 - K_z v_z/\omega = h_1 + (H_0/H) h_2, \tag{A2}$$

$$n\dot{\Upsilon} + \dot{\Psi} = -[d_1 + (H_0/H)(d_2 - n\Omega_0/\omega)], \tag{A3}$$

where $d_1 = 1 - \eta_z \beta_z$, $d_2 = \eta_z(\beta_z - v_{z0}/c)$, $h_1 = 1 - \beta_z^2$, and $h_2 = \beta_z(\beta_z - v_{z0}/c)$.

By using Eq. (A3), integrating Eq. (20b) over time from zero to t, and recalling that $I_n^S = 4H\dot{H}/c^2\omega$, we find that the function $\chi = (n\dot{\Upsilon} + \dot{\Psi}) P_n^S(t)/H$ is given by

$$\begin{aligned} \chi = & -(H_0\omega/H^2)\{r_n P_n^S(0) \\ & + [d_1 P_n^S(0) - 4r_n^2 H_0^2/c^2] U \\ & - 6r_n (H_0^2/c^2) d_1 U^2 - 2(H_0^2/c^2) d_1^2 U^3\}. \end{aligned} \tag{A4}$$

By substituting Eqs. (A1) and (A2) into Eqs. (12), we find Q and R as functions of H and initial conditions. Combining this with Eqs. (A4) and (20a), we obtain

$$\begin{aligned} H\dot{H} \frac{d}{dt}(H\dot{H}) = & -\frac{c^2\omega^2}{4} H\Big(\frac{q}{\omega}(E_1 + E_2)(b_1 H + H_0 b_2) J_{n+1}^2(\lambda) \\ & + \frac{q}{\omega}(E_1 - E_2)(a_1 H + H_0 a_2) J_{n-1}^2(\lambda) \\ & + 2\frac{q^2}{\omega^2} E_3^2 (h_1 H + H_0 h_2) J_n^2(\lambda)\Big) - \frac{c^2\omega}{4} H^2 \dot{H}_0, \end{aligned} \tag{A5}$$

where

$$a_1 = \frac{qE_1}{\omega} h_1 - \frac{qE_2}{\omega} d_1, \quad a_2 = \frac{qE_1}{\omega} h_2 - \frac{qE_2}{\omega} d_2,$$

$$b_1 = \frac{qE_1}{\omega} h_1 + \frac{qE_2}{\omega} d_1, \quad b_2 = \frac{qE_1}{\omega} h_2 + \frac{qE_2}{\omega} d_2.$$

Equation (A5) can be integrated once over time from 0 to t. The left-hand side becomes $\frac{1}{2}(H^2\dot{H}^2 - H_0^2\dot{H}_0^2)$. The contribution of the term $H_0\dot{H}_0$ can be calculated by means of Eq. (8). By considering that at $t = 0$, $\Phi_0 = k_x \rho_0 \cos\alpha + k_z z_0$ and that $p_{x0} = -p_{\perp 0}\sin\alpha$, $p_{y0} = p_{\perp 0}\cos\alpha$, and expanding in terms of Bessel functions, we obtain

$$\frac{\dot{H}_0}{\omega H_0} = \sum_n \zeta_n(0)\cos\delta_n, \tag{A6}$$

where $\zeta_n(0)$ and δ_n are defined after Eqs. (20). Using Eq. (A6) and after a good deal of tedious but straightforward algebra, we arrive at Eqs. (21).

[1] D. B. Batchelor and R. C. Goldfinger, Nucl. Fusion 20, 403 (1980).
[2] T. Katsouleas and J. M. Dawson, Phys. Rev. Lett. 51, 392 (1983).
[3] G. R. Smith and A. N. Kaufman, Phys. Rev. Lett. 34, 1613 (1975); P. J. Palmadesso, Phys. Fluids 15, 2006 (1972).
[4] P. C. Clemmow and R. D. Harding, J. Plasma Phys. 23, 71 (1980).
[5] A. B. Kitsenko, I. M. Pankratov, and K. N. Stepanov, Sov. Phys. Tech. Phys. 20, 575 (1976).
[6] A. Y. Wong, J. Santoru, C. Darrow, L. Wang, and J. G. Roederer, Radio Sci. 18, 815 (1983).
[7] A. Y. Wong, J. Santoru, and G. G. Sivjee, J. Geophys. Res. 86, 7718 (1981).
[8] V. Ya. Davydovskii, Zh. Eksp. Teor. Fiz. 43, 886 (1962) [Sov. Phys. JETP 16, 629 (1963)]; A. A. Kolomenskii and A. N. Lebedev, Sov. Phys. Dokl. 7, 745 (1963).
[9] C. S. Roberts and S. J. Buchsbaum, Phys. Rev. A 135, 381 (1964).
[10] H. Motz and C. J. H. Watson, Adv. Electron Phys. 23, 153 (1967).
[11] M. L. Woolley, Plasma Phys. 13, 1141 (1971).
[12] Similar calculations can be found in the theory of quasilinear diffusion of particles; see, for instance, C. F. Kennel and F. Engelmann, Phys. Fluids 12, 2377 (1966).
[13] P. C. Clemmow and J. P. Dougherty, *Electrodynamics of Particles and Plasmas* (Addison-Wesley, London, 1969).
[14] B. V. Chirikov, Phys. Rep. 52, 263 (1979).
[15] V. E. Golant and A. D. Piliya, Sov. Phys. Usp. 14, 413 (1972).

J. Geomag. Geoelectr., 40, 1147-1159, 1988

Electron Acceleration in the Ionosphere by Obliquely Propagating Electromagnetic Waves

William J. BURKE[1], Gregory P. GINET[1], Elena VILLALON[2], and Michael A. HEINEMANN[1]

[1]Air Force Geophys. Lab., Hanscom Air Force Base, MA 01731, U.S.A.
[2]Monsen Rd., Concord, MA 01742, U.S.A.

(Received January 14, 1988; Accepted April 20, 1988)

The relativistic equations of motion have been analyzed for electrons in magnetized plasmas and externally imposed electromagnetic fields that propagate at arbitrary angles to the background magnetic field. The electron energy is obtained from a set of non-linear differential equations as functions of time, initial conditions and cyclotron harmonic numbers. For a given cyclotron resonance the energy oscillates in time within the limits of a potential well. Stochastic acceleration occurs if the widths of hamiltonian potentials overlap. Numerical analyses suggest that, at wave energy fluxes in excess of 10^8 mW/m^2, initially cold electrons can be accelerated to energies of several MeV in less than a millisecond. Practical attempts to validate the theory with a series of planned rocket flights over the HIPAS facility in Alaska are discussed. The HIPAS antennas will be used to irradiate the magnetic mirror points of 10–40 keV electrons emitted from the ECHO 7 rocket in the early winter of 1988. Follow-on rocket experiments to exploit the wave amplification properties of the ionospheric "radio window" are described.

1. Introduction

Attempts to actively perturb space plasmas using HF emissions from ground based antennas have generally used O-mode radiation (STUBBE *et al.*, 1985; ROSE *et al.*, 1985; LEE *et al.*, 1988). The X-mode can only propagate to the altitude of cutoff. This is because the circularly polarized X-mode rotates in the same sense as electrons about the magnetic field, and thus interacts strongly with them. Recently scientists at the Air Force Geophysics Laboratory (AFGL) have become interested in using this characteristic for controlled, gyroresonant acceleration of electrons in space plasmas. Indeed, gyroresonant X-mode radiation has been used successfully to accelerate electrons to relativistic energies in the ELMO Bumpy Torus (BATCHELOR and GOLDFINGER, 1980). Although the driving mechanisms have not been established, JAMES (1983) has reported the presence of electrons accelerated up to several kilovolts in energy after sounder emissions from the ISIS satellites. BABAEV *et al.* (1983) have also reported the detection of electrons accelerated to kilovolt energies through interactions with a low power telemetry system.

The motion of an electron moving in the presence of a right circularly polarized wave propagating along the magnetic field has been treated by ROBERTS and

BUSCHBAUM (1964). They show that if the Doppler shifted frequency of the driver wave is at the electron gyrofrequency, and the phase speed of the wave is that of light in free space, test electrons stay in resonance and can be accelerated to arbitrarily high energy. For other wave phase speeds, electrons eventually lose resonance due either to the relativistic lowering of the gyrofrequency or to unbalanced Doppler shifts. In either case the electrons appear to move in pseudo-potential wells in which they alternately gain and lose kinetic energy. Recently the analysis of Roberts and Buschbaum has been extended to include the case of obliquely propagating waves using two different perturbation formalisms. MENYUK et al. (1987) utilized the canonical Hamiltonian while VILLALON and BURKE (1987) solved the Lorentz equation. While the first concentrated only on the stochastic regime, the second considered both stochastic and sub-stochastic acceleration.

This paper is divided into three sections in which we discuss: first, the relativistic Lorentz equation for a test electron moving under the influence of an electromagnetic wave in a cold magnetized plasma, second, wave propagation through the ionospheric "radio window," and third, a series of planned space flights to test the validity of our model.

2. Analytical and Numerical Solutions of the Lorentz Equation

We consider the motion of an electron gyrating in a constant magnetic field $B_0\hat{z}$ in the presence of an obliquely propagating electromagnetic wave with wave vector $\boldsymbol{k}=k_x\hat{x}+k_z\hat{z}$ and frequency ω. The wave's electric field is given by

$$\boldsymbol{E} = E_1\hat{x}\cos\phi - E_2\hat{y}\sin\phi - E_3\hat{z}\cos\phi,$$

where the phase angle $\phi=k_x x+k_z z-\omega t$. The Lorentz equation is

$$\dot{\boldsymbol{p}} = q[\boldsymbol{E} + \boldsymbol{V}\times(\boldsymbol{B}_0 + \boldsymbol{B}_w)],$$

where $\boldsymbol{p}$, $\boldsymbol{V}$ and q represent the momentum, velocity and charge of the electron; $\boldsymbol{B}_w$ is the wave magnetic field. This equation admits three constants of the motion derived from

$$\mathrm{d}/\mathrm{d}t[\boldsymbol{p} - q\boldsymbol{r}\times\boldsymbol{B}_0 - \boldsymbol{k}H/\omega + q\boldsymbol{A}] = 0,$$

where $\boldsymbol{A}$ is the vector potential of the wave and $H=mc^2\gamma$, is the relativistic energy. γ is the standard relativistic factor $1/\sqrt{1-v^2/c^2}$. The relativistic momentum and velocity are related by $\boldsymbol{p}=m\boldsymbol{V}\gamma$. The time rate of change of the electron's Hamiltonian is

$$\mathrm{d}H/\mathrm{d}t = qc^2(\boldsymbol{E}\cdot\boldsymbol{p})/H.$$

Substitution into the Lorentz equation gives

$$\dot{p}_x + p_y[\Omega + (qE_2k_x)/(m\gamma\omega)\sin\phi] = (qE_1/\omega)(\omega - K_z\dot{z})\cos\phi,$$

$$\dot{p}_y - p_x[\Omega + (qE_2k_x)/(m\gamma\omega)\sin\phi] = -(qE_2/\omega)(\omega - k_z\dot{z})\sin\phi,$$

$$\dot{p}_z - (K_z\dot{H}/\omega) + (E_3/E_1)(\dot{p}_x + \Omega p_y) = 0,$$

where $K_z = k_z[1 + E_3k_x/E_1k_z]$ and $\Omega = qB_0/m\gamma$ the relativistic electron cyclotron frequency. Dots over quantities indicate time derivatives. To this point the equations are exact.

Our first assumption is that terms containing the quantity $(E_2k_x/\omega) = B_z \ll B_0$ can be ignored in any reasonable geophysical situation. The second assumption is that to zero-order the x and y components of the momentum vector of any test electron follow Larmor trajectories.

$$p_x = -p\sin(\sigma + \alpha_0),$$

$$p_y = p\cos(\sigma + \alpha_0),$$

where

$$\sigma(t) = \int_0^t \Omega(t')\mathrm{d}t',$$

$$\alpha_0 = \tan^{-1}(p_{x0}/p_{y0}),$$

with the subscript 0 referring to initial momentum conditions.

After substituting into the Lorentz equation, expanding in a series of Bessel functions, averaging over fast time variation and filling many pages of algebra, whose main steps are indicated by VILLALON and BURKE (1987) we arrive at an equation in the form

$$[1 + U]^2[\mathrm{d}U/\mathrm{d}t]^2 + \omega^2 V_n(U) = 0.$$

This is very similar to the equation of a particle moving in a pseudo-potential field. The term $U = (H - H_0)/H_0$ represents the hamiltonian of the electron normalized to its initial value. The subscript n on the potential functions $V_n(U)$ represents the contribution of the n-th harmonic of the electron gyrofrequency. The actual form of the potential is given in Appendix 1. Here we note several features of the potential that provide immediate insight into this electron acceleration model. First, an electron can only access the regions of parameter space in which V_n is negative. The regions of access can be determined for each harmonic by solving for the zeros of the potential. Second, at large value of U the potential increases as U^4. Thus, in the asymptotic limit V_n is positive and the amount of energy that can be absorbed from the wave is finite. Third, the contributions of the right, left and parallel polarizations are distinct and depend on Bessel functions of order $n-1$, $n+1$ and n, respectively. Thus, right circularly polarized waves should interact most strongly. Since the arguments of the Bessel functions are products of k_x and the gyroradius, acceleration efficiency should be enhanced for test electrons with a substantial, initial kinetic energy.

To test the range of validity of the assumptions presented above, we have performed a series of numerical solutions of the Lorentz equation and compared the results with the predictions of our pseudo-potential model. In all cases we used electromagnetic waves propagating in the X-mode at a frequency twice that of the electron gyrofrequency. The ratio of the plasma frequency to the drive frequency is 0.58. These correspond the conditions of $B_0=0.55$ G and $n=10^4$/cc, typical of the bottomside of the ionosphere at auroral latitudes during periods of magnetic quiet. Note that under these conditions the waves are propagating below the right hand cutoff where VILLALON and BURKE (1987) predict the strongest electron/wave interactions. All cases presented here represent averages of 33 cases with random initial phases.

In Fig. 1 we present a summary of the numerical results. In log-log format we have plotted the maximum kinetic energy gained by initially cold test electrons normalized to their rest energy as a function of the wave Poynting flux in milli-Watts per square meter. Note that existing mega-Watt ionospheric heaters typically

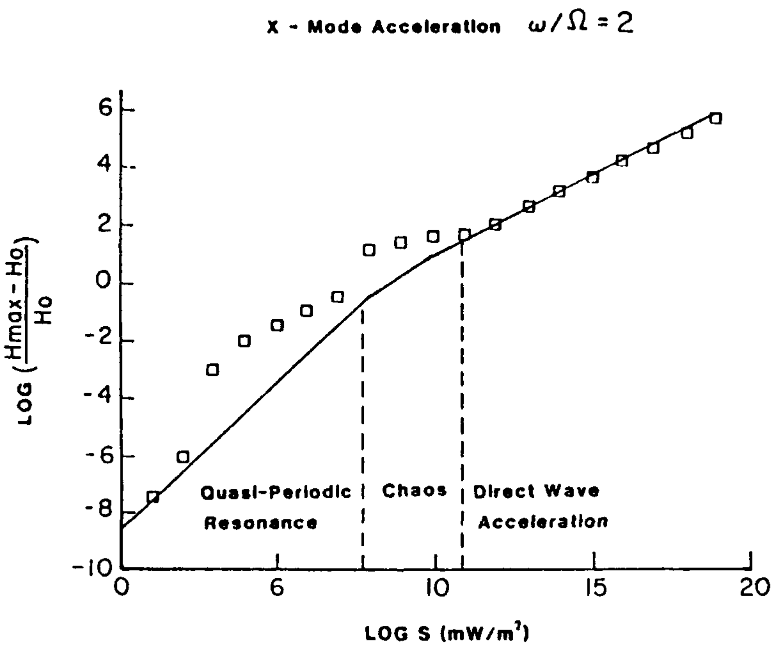

Fig. 1. Numerical solutions of Lorentz equation. The kinetic energy gain is plotted as a function of input wave energy flux. The straight line and triangles represent average energy gained by thirty three test electrons with random initial phase from gyroresonant waves propagating along and at 30° to magnetic field lines, respectively.

deliver 1-10 mW/m^2 to ionospheric altitudes of 200-300 km. The straight line and diamond symbols represent effects of radiation propagating along and at 30° to the magnetic field, respectively. Results for higher angles are similar to those at 30°. The characteristics of the acceleration divide into three categories which we call quasi-periodic resonance, chaotic and direct wave acceleration. The range of chaotic acceleration extends roughly from 10^7 to 10^{11} mW/m^2.

Figure 2 provides examples of each type of acceleration with the solutions followed for 0.7 ms. Wave intensities of 10^6 mW/m^2 accelerate initially cold electrons to 60 keV in 400 μs and then fall back to low energy. If the wave intensity is increased to 10^8 mW/m^2 electron are accelerated irregularly to 9 MeV. In the direct

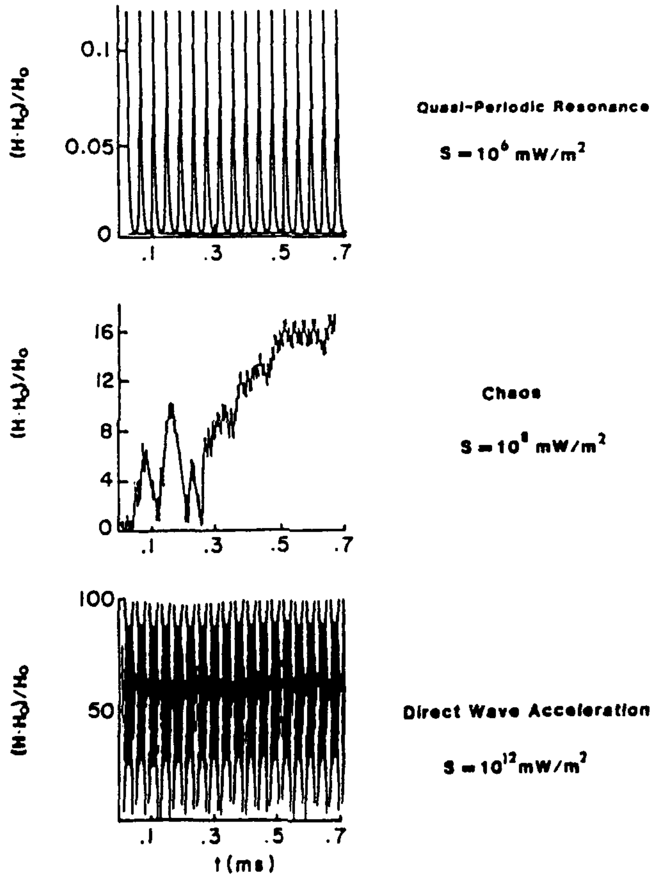

Fig. 2. Numerical solutions of the Lorentz equation for three wave energy flux levels followed for 0.7 ms.

acceleration regime wave magnetic fields are greater than B_0 and electrons undergo periodic accelerations up to 50 MeV.

Comparisons of the predictions of the pseudo-potential model of VILLALON and BURKE (1987) with the numerical solutions of the Lorentz equation are given in Fig. 3, represented by dashed lines and triangles, respectively. The first impression gained from this comparison is that predictions of these independent approaches to the problem are in remarkable agreement. At a propagation angle of 0° the V-B and numerical solutions agree exactly. At other angles V-B predicts less acceleration than was numerically calculated.

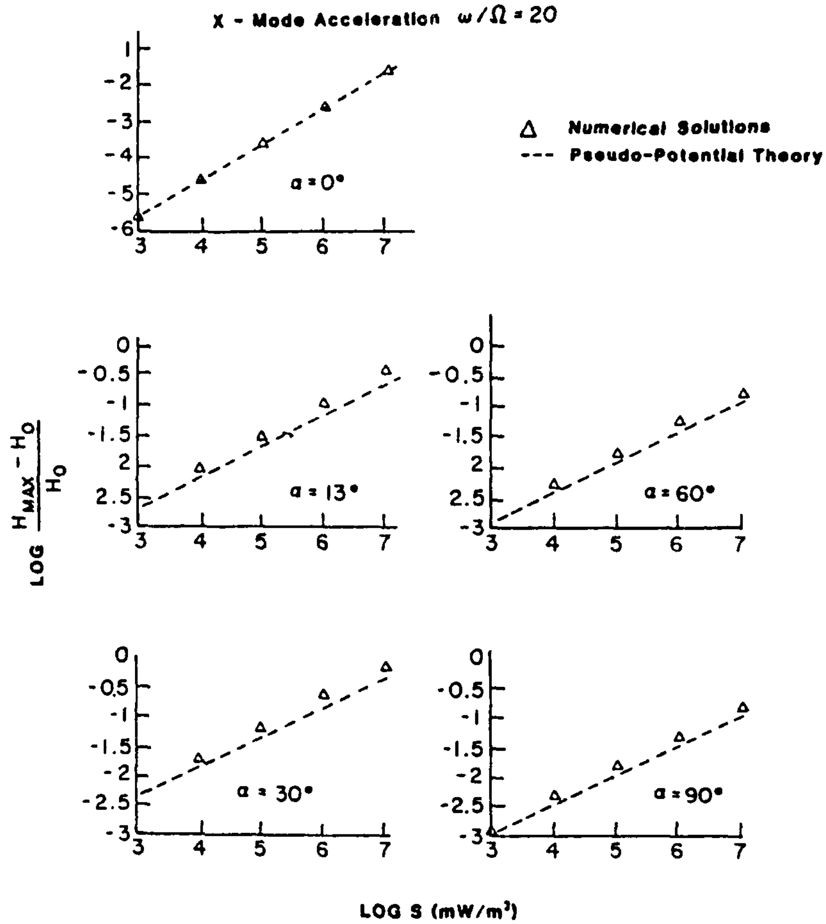

Fig. 3. Comparison of predictions of pseudo-potential models with exact numerical solutions of the Lorentz equation for different wave propagation angles.

Figure 4 plots the values of $V_n(U)$ for selected values of n. Again the wave frequency is at the second gyroharmonic, with a Poynting flux of 10^7 mW/m^2. The region of negative potentials extends down to $U=0$ for the first and second harmonics. We note however, that the slope of the potential for the first harmonic is steeper than the second at low energies. Thus, initial acceleration is by the first, rather than the second harmonic. Potentials of higher harmonics are initially positive and do not accelerate low energy electrons.

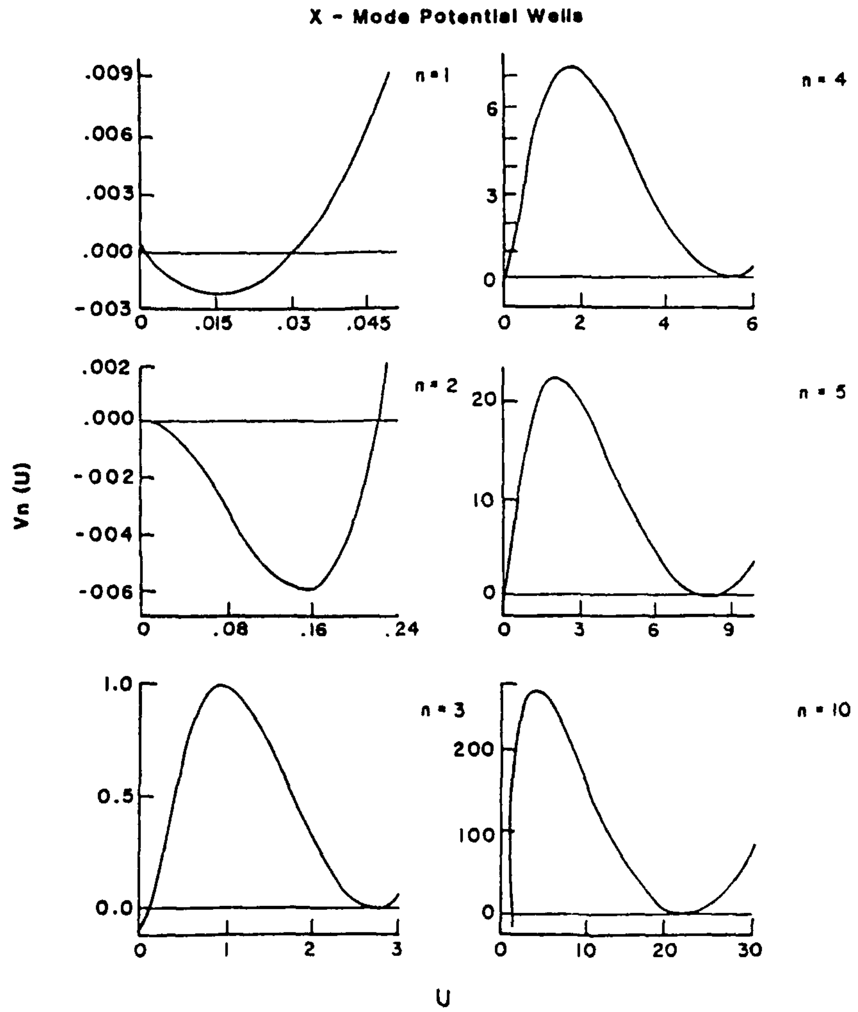

Fig. 4.

3. Radio Window Mode Conversion

It is obvious from the discussion presented above that serious acceleration of ionospheric electrons by ground antennas requires power enhancements that greatly exceed any capabilities that can be achieved within a reasonable time span. This is one time however, when nature appears to be working on our side. MJOLHUS and FLA (1984) have studied O-mode radiation propagating in the ionosphere where the vertical plasma density gradient is at an arbitrary angle to the earth's magnetic field. Consequent to obeying Snell's law the cold plasma dispersion relation reduces to the Booker quartic (BOOKER, 1938). Normally, O-mode radiation propagates to the altitude where the driver frequency is equal to the local plasma frequency and is reflected. It is possible however, for radiation transmitted from ground in the O-mode close to a critical angle Θ_c to convert linearly to the Z-mode, where

$$\sin\Theta_c = \sqrt{Y/(Y+1)}\sin\psi.$$

Here $Y=\Omega/\omega$. For the case we have been considering here $Y=2$. In Alaska where the magnetic dip angle is about 13°, $\Theta_c=7.5°$ towards the south of vertical.

O-mode rays in this "radio window" propagate in the slow extraordinary (Z) mode to the altitude of cutoff where they are reflected. As they approach the altitude where

$$X = (1 - Y^2)/(1 - Y^2\cos^2\psi),$$

with $X=(\omega_p/\omega)^2$, the Z-mode undergoes resonance. Here the group speed slows to zero. In this region the Z-mode turns into an electrostatic wave that propagates perpendicular to the $\boldsymbol{B}_0$. Cold plasma theory does not allow the possibility of electrostatic waves. VILLALON (1988) had included warm plasma effects as second order corrections to the Booker quartic. In the resonant region the group velocity (V_g) of the electrostatic waves is much less than the speed of light with which the radiation enters the ionosphere. The conservation of energy requires that the amplitude of the wave electric field steepens as $(c/V_g)^{1/2}$. Calculations by VILLALON (1988) show that in the resonant region electrons can be accelerated by several keV with modest input powers of 1 mW/m^2. The possibility of the wave energy being dissipated by other non-linear processes must next be given careful analysis.

4. Planned Space Experiments

Experiments to test in space the validity of the theoretical models outlined in the last two sections are planned for the next several years. To perform such experiments two major elements are necessary: (1) an HF ground source, and (2) properly instrumented space vehicles. We first consider the impact of these constraints for mission planning.

Suitable ground antennas exist at Tromso in Norway, Arecibo in Puerto Rico and HIPAS in Alaska. Although the Tromso and HIPAS antennas have access to nearby rocket ranges, Arecibo does not. From the closeness of the "radio window" to both the vertical and magnetic field directions at high latitudes, rocket trajectories must pass both overhead and close to the magnetic meridian. Rockets fired from the Andoya range are constrained to over-water trajectories at some distance from Tromso. It is possible to launch rockets toward magnetic north from mobile launchers located south of HIPAS.

To measure the characteristics of the waves transmitted from the ground as well as their effects on both the ionospheric plasma and the acceleration of electrons to kilovolt energies, in situ diagnostics are necessary. These instruments should measure: (1) the density and temperature of the ionospheric constituents to specify the cold plasma dielectric coefficient, (2) the spectral characteristics of waves in the ionosphere to provide information on alternate decay modes of the primary wave associated with parametric instabilities, and (3) energetic electron detectors that look both up and down magnetic field lines. The latter are useful for distinguishing wave-acceleration from natural auroral effects.

Some or all elements of this complement of passive detectors are available on present or planned American and Japanese polar orbiting satellites. Because of the repeatability of coordinated ground-satellite experiments these resources should be utilized to the fullest. There are however, significant drawbacks to satellite based experiments that cannot be ignored. First, satellites generally fly at altitudes far above the interactions discussed in the previous sections. At these heights it is very difficult to meet exacting magnetic conjunction conditions. Thus, only debris from wave-electron interactions can be detected. Second, because of the high speed of satellites and the relatively low sampling rates allowed to particle detectors, spatial resolution is probably insufficient. Limitations of the second kind are directly addressed by the joint US/Canadian satellite FOCUS I, scheduled for a Scout launch in the early 1990's. FOCUS will only operate in real time when in view of ground receiving stations. High spatial resolution will be achieved by using a broad band telemetry system normally associated with rocket experiments. Coordinated studies of wave-plasma interactions using ionospheric heaters is a prime scientific goal of this mission.

To understand the basic physics of wave particle interactions suborbital rocket flights have much to offer. First, they can be designed to pass close to or through critical volumes of space at relatively low speeds. Second, available telemetry rates allow important parameters to be measured with high resolution. Third, spatial-temporal ambiguities are easily resolved by simultaneous measurements with multiple payloads. Fourth, the environment can be actively varied to meet specific experimental goals. In the case at hand, an artificial auroral environment can be turned on and off by emitting charged particle beams from one of the rocket payloads. Fifth, rocket launches can be coordinated with satellite passes over heaters to gain maximum insight into the large-scale effects of localized plasma perturbation experiments.

An initial attempt to validate the electron acceleration concepts will be carried out during the flight of the ECHO 7 rocket. ECHO 7 represents a cooperative effort between NASA, the University of Minnesota and AFGL. Launch from Poker Flat toward magnetic east is scheduled for a moonless evening during a period of low magnetic activity in the early winter of 1988. There are four payloads, one to emit electrons with controlled injection energy between 10 and 40 keV and pitch angles between 15° and 180°; the other three measure plasma, energetic particle and electromagnetic field effects of the beam emissions. The primary mission of ECHO 7 is to study the long distance transmission properties of electron beams in space. It is also ideally instrumented to measure the effects of HF waves interacting with controlled plasma environments.

The ground track of the ECHO 7 trajectory along with the positions of the Poker Flat Range, the HIPAS facility and Eilson AFB are sketched in Fig. 5. The heavy part of the trajectory line represents the post-deployment segment of the flight. The hatched portion near the HIPAS magnetic meridian represents the "radio window." The dashed line to the north of the trajectory represents the

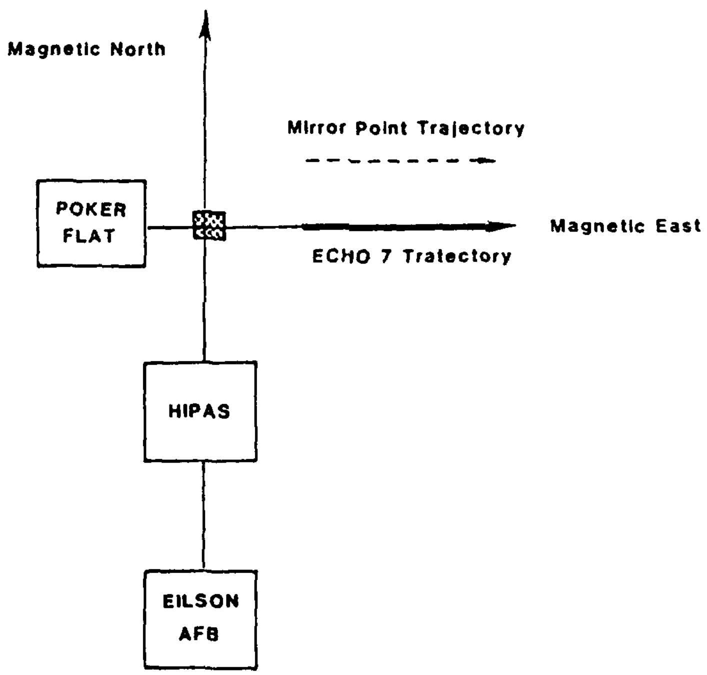

Fig. 5. Schematic representation of ECHO 7 trajectory relative to the position of the HIPAS facility. The heavy line represents the post deployments phase of the flight. The dashed line represents the mirror points of beam electrons emitted downward from ECHO. This region will be illuminated by X-mode radiation at the second harmonic of the electron gyro-frequency.

location of magnetic mirror points at 100 km for beam electrons injected down the field lines. We note that full deployment of the ECHO payloads occurs about thirty kilometers to the east of the HIPAS magnetic meridian. Experiments designed to verify the effects of transmission through the "radio window" are thus doomed to failure. For this reason we have decided that during the ECHO flight it is better to illuminate the region of the magnetic mirrors with radiation near the second harmonic of the electron gyrofrequency in the X-mode. This is the right hand polarization mode that does not propagate to very high altitudes in the ionosphere. However, the *V-B* model predicts efficient acceleration near the right-hand cutoff.

A series of follow-on rocket flights along the magnetic meridian over HIPAS is planned for the early 1990's as a joint effort with NASA and UCLA. The diagnostic packages to be flown during these experiments will be similar to those flown on ECHO 7. Photometers will be added to the complement to measure radiation from cavitons expected to form in the vicinity of the Z-mode resonance. Periodically during the mission, energetic electron beams will be injected into the resonance region. Thus, the relative efficiencies for cold/warm electron acceleration by Z-mode radiation can be determined.

Figure 6 is a sketch of the planned experimental geometry. The rocket trajectories will be in the HIPAS magnetic meridian. HIPAS will transmit at the

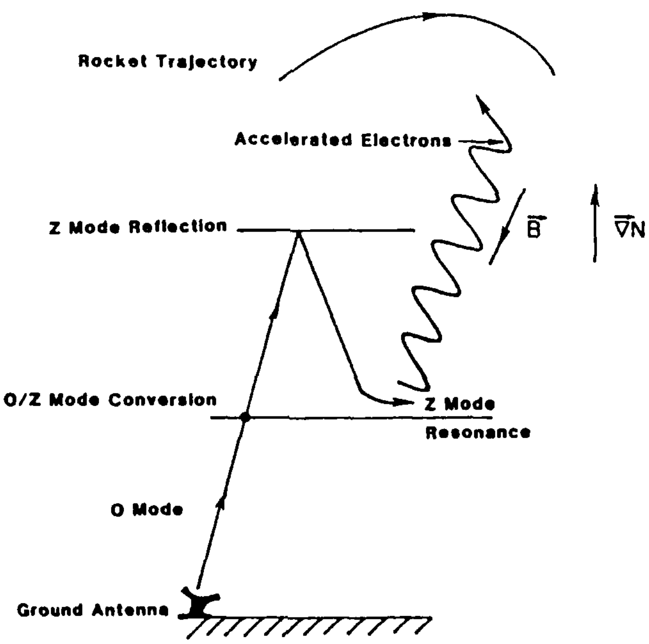

Fig. 6. Schematic representation of a ray propagating in the ionospheric "radio window." Near the Z-mode resonance it is expected that plasma density cavitons will form.

second gyroharmonic, in the O-mode. Rays outside the "radio window" are reflected to the ground with little effect on the ambient plasma. Inside the "radio window" radiation that converts to the Z-mode continue to propagate to the altitude of the left hand cutoff where they are reflected. As the Z-mode radiation approaches resonance the intensity of the wave vector turns normal to the magnetic field and the electric fields steepen. Ponderomotive forces generate plasma density cavitons (WONG and SANTORU, 1981; WONG et al., 1987). Electrons within the cavitons see intense electric field variations at the second gyroharmonic. When the rockets are near magnetic conjunction with HIPAS created cavitons, particle detectors should measure intense fluxes of accelerated electrons.

Appendix 1. Mathematical Form of Pseudo-Potentials

In the main text we argued that the equations of motion for a test electron in an obliquely propagating electromagnetic wave can be reduced to the form of motion in a potential well.

$$(\mathrm{d}U/\mathrm{d}t)^2 + \omega^2 V_n(U)/(U+1)^2,$$

where $U=(H-H_0)/H_0$ is the energy gained normalized to the initial relativistic Hamiltonian. The potential well associated with the n-th harmonic of the electron gyro-frequency is

$$\begin{aligned} V_n(U) = {} & (d_1 U/2)^2 (U + 2r_n/d_1)^2 - \psi(0)\sin\phi_n d_1 U(U + 2r_n/d_1) \\ & + (\Sigma_1 - \Sigma_2)/2\{(\Sigma_2 d_1 - \Sigma_1 h_1)(G_{n+1}(U) + F_{n+1}(U)) \\ & \qquad + (\Sigma_2 d_2 - \Sigma_1 h_1)F_{n+1}(U)\} \\ & - (\Sigma_1 - \Sigma_2)/2\{(\Sigma_1 h_1 + \Sigma_2 d_1)(G_{n-1}(U) + F_{n-1}(U)) \\ & \qquad + (\Sigma_1 h_2 + \Sigma_2 d_1)F_{n-1}(U)\} \\ & - \Sigma_3^2\{h_1(G_n(U) + F_n(U)) + h_2 F_n(U)\} - (\psi(0)\cos\phi_n)^2. \end{aligned}$$

Terms with $\Sigma_1+\Sigma_2$ and $\Sigma_1-\Sigma_2$ refer to the right and left hand polarization modes, respectively.

Here also

$$\begin{aligned} \Sigma_i &= -(qE_i/\omega)c/H_0 \qquad i = 1,2,3, \\ d_1 &= 1 - K_z k_z c^2/\omega^2, \\ d_2 &= (K_z k_z c^2/\omega^2) - k_z \dot{z}_0/\omega, \\ h_1 &= 1 + (K_z/k_z)(d_1 - 1), \\ h_2 &= (K_z/k_z)d_2, \end{aligned}$$

$$r_n = 1 - k_z\dot{z}_0/\omega - n\Omega_0/\omega,$$

$$\phi_n = k_z z_0 + n(\alpha_0 + \pi/2),$$

$$\psi(0) = V_0/2c[-(\Sigma_1 + \Sigma_2)J_{n-1}(k_x\rho_0) + (\Sigma_2 - \Sigma_1)J_{n+1}(k_x\rho_0)] + V_{z0}/c\Sigma_3 J_n(k_x\rho_0),$$

where J_n represents a standard Bessel function of order n. The functions $G_n(U)$ and $F_n(U)$ are defined by

$$G_n(U) = \int_0^U J_n^2[k_x\rho(U')]U'\mathrm{d}U',$$

$$F_n(U) = \int_0^U J_n^2[k_x\rho(U')]\mathrm{d}U'.$$

REFERENCES

Babaev, A. P., S. B. Lyakhov, G. G. Managadze, A. A. Martinson, and P. P. Timofeev, Plasma particle acceleration due to emission of ground-based and onboard transmitters, in *Active Experiments in Space*, ESA SP-195 61-65, 1983.

Batchelor, D. B. and R. C. Goldfinger, A theoretical study of electron-cyclotron absorbtion in ELMO bumpy torus, *Nuc. Fus.*, **20**, 403-417, 1980.

Booker, H. G., Propagation of wave-packets incident obliquely upon a stratified doubly refracting ionosphere, *Philos. Trans. R. Soc. London Ser. A*, **237**, 411, 1938.

James, H. G., Sounder-accelerated electrons observed on ISIS, *J. Geophys. Res.*, **88**, 4027-4040, 1983.

Lee, M. C., K. M. Groves, C. P. Liao, D. R. Rivas, and S. P. Kuo, Combined operation of two ground transmitters for enhanced ionospheric heating, *J. Geomag. Geoelectr.*, this issue, 1141-1145, 1988.

Menyuk, C. R., A. T. Drobot, K. Papadopoulos, and H. Karimabadi, Stochastic electron acceleration in obliquely propagating electromagnetic waves, *Phys. Rev. Lett.*, **58**, 2071-2074, 1987.

Mjolhus, E. and T. Fla, Direct access to plasma resonance in ionosphere radio experiments, *J. Geophys. Res.*, **89**, 3921-3928, 1984.

Roberts, C. S. and S. J. Buschbaum, Motion of a charged particle in a constant magnetic field and a transverse electromagnetic wave propagating along the field, *Phys. Ref.*, 135, A381-A389, 1964.

Rose, G., G. Grandal, E. Neske, W. Ott, K. Spencer, J. Holtet, K. Maseide, and J. Troim, Experimental results from the HERO project: in situ measurements of ionospheric modifications using sounding rockets, *J. Geophys. Res.*, **90**, 2851-2860, 1985.

Stubbe, P., H. Kapka, M. T. Rietveld, A. Frey, P. Hoeg, H. Kohl, E. Nielsen, G. Rose, C. LaHoz, R. Barr, H. Derblom, A. Hedberg, B. Thilde, T. B. Jones, T. Robinson, A. Brekke, T. Hansen, and O. Holt, Ionospheric modification experiments with the Tromso heating facility, *J. Atmos. Terr. Phys.*, **47**, 1151-1163, 1985.

Villalon, E., Ionospheric electron acceleration by electromagnetic waves near regions of plasma resonance, submitted to *Phys. Rev. Lett.*, 1988.

Villalon, E. and W. J. Burke, Particle acceleration by obliquely propagating electromagnetic fields, *Phys. of Fluids*, **30**, 3695-3702, 1987.

Wong, A. Y. and J. Santoru, Active stimulation of auroral plasma, *J. Geophys. Res.*, **86**, 7718-7732, 1981.

Wong, A. Y., T. Tanikawa, and A. Kauthi, Observation of ionospheric cavitons, *Phys. Rev. Lett.*, **58**, 1375-1378, 1987.

ACTIVE CONTROL AND NONLINEAR FEEDBACK INSTABILITIES IN THE EARTH'S RADIATION BELTS

H. B. Silevitch,* P. L. Rothwell,** and E. Villalon*

*Center for Electromagnetics Research, Northeastern University, Boston, MA 02115, U.S.A.,**Air Force Geophysics Laboratory, Hanscom Air Force Base, Bedford MA, 01731, U.S.A.

ABSTRACT

The stability of trapped particle fluxes are examined near the Kennel-Petschek limit. In the absence of coupling between the ionosphere and magnetosphere it is found that both the fluxes and the associated wave intensities are stable to external perturbations. However, if the ionosphere and magnetosphere are coupled through the ducting of the waves then a positive feedback may develop depending on the efficiency of the coupling. This results in a spiky, nonlinear precipitation pattern which for electrons has a period on the order of hundreds of seconds. Here we give a linear analysis that highlights the regions of instability together with a computer simulation of the nonlinear regimes.

INTRODUCTION

Active control of energetic particle fluxes in the radiation belts has been a topic of major interest in both the United States and the Soviet Union. Electron dumping experiments conducted by the Stanford University and Lockheed groups using VLF transmissions are well-known /1,2/. Perhaps less known is the theoretical work by Trakhtengerts /3/ entitled "Alfvén Masers" in which he proposes a theoretical scheme for dumping both electrons and protons from the radiation belts. The basic idea is to use RF energy to heat the ionosphere at the foot of a flux tube to raise the height integrated conductivity. The conductivity is then modulated at VLF or ELF frequencies which modulates the reflection of waves that cause pitch angle diffusion in the equatorial plane. The artificially enhanced conductivity of the ionosphere thus maintains high wave energy densities in the associated flux tube thereby producing a positive feedback.

In addition to external ionospheric perturbations particle precipitation also raises ionospheric conductivity. The trapping of VLF waves causes further precipitation which, in principle, results in an explosive instability. The purpose of this paper is to establish the basic equations.

The fundamental equations derived by /3/ are based on quasilinear plasma theory and relate only to the weak diffusion regime. We have plotted an example of the Trakhtengerts equations in Figure 1. Here we illustrate the importance of positive feedback from the ionosphere using a parameter ϵ_H which parameterizes the strength of the coupling. When the coupling is weak, perturbations near the Kennel-Petschek limit slowly damp away. However, as the coupling strength exceeds 5% highly nonlinear oscillations develop. It is important to note that the spiky behavior that results clearly violates the basic assumptions upon which quasilinear theory is based. We, therefore, need to set the Trakhtengerts analysis on firmer ground. In particular, one needs to take into account the change in pitch angle anisotropy as a function of the pitch angle diffusion coefficient.

It is useful to use a similar set of equations derived by Schulz /4/ which are based on phenomenological arguments that include strong pitch angle diffusion. The key variables are N, the number of trapped particles per unit area on a flux tube and D, the normalized pitch angle diffusion coefficient which is proportional to the inverse trapping lifetime. We note that D is averaged over the entire flux tube. In the Schulz formulation the time rate of change of N is given by

$$\frac{dN}{dt} = - \frac{ND}{(1 + Dt_s)} + S_o \qquad (1)$$

where the first term represents losses due to pitch angle scattering and S_o represents an equatorial particle source term for the particular flux tube. The parameter, τ_s, characterizes the expected trapped particle lifetimes due to strong pitch angle diffusion. For electrons this is on the order of a hundred seconds. Note that the denominator in (1) reflects the change in pitch angle anisotropy as a function of D which is necessary for consistency. The time rate of change of D is given by

$$\frac{dD}{dt} = D(2\gamma + \frac{V_g}{LR_E}\ln R) + W_o/\tau_s \qquad (2)$$

The first term represents wave growth near the equatorial plane, the second term gives the wave losses in and through the ionosphere and the third accounts for any wave energy sources.

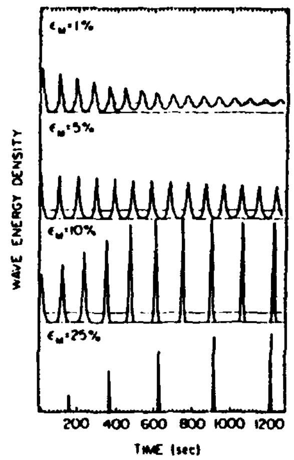

Fig. 1. The effect of ionospheric feedback on electron precipitation. Note the spiky behavior due to the nonlinear nature of the feedback process.

In the second term, the expression V_g/LR_E approximates the bounce frequency of waves where V_g is the group velocity of the wave, LR_E the approximate length of a flux tube; R is the reflection coefficient of the ionosphere. Since R < 1 the second term is always negative. The denominator in (1) reflects the decreased efficiency for pitch angle scattering through wave-particle interactions as the diffusion rate increases. This is due to the pitch angle distribution becoming more isotropic as described by Kennel and Petschek /5/.

The wave growth is of particular interest and requires further comment. It can be expressed as

$$\gamma = \frac{A_o N}{(1 + D\tau_s)} \qquad (3)$$

where A_o is defined by the value of the growth rate, γ_o, at the Kennel Petschek limit where $N = N_o$ and $D = D_o$. The source term in (1) can be defined in terms of these parameters by setting the LHS of (1) to zero.

$$S_o = -\frac{N_o D_o}{(1+D_o\tau_s)} \qquad (4)$$

We now include the coupling of the radiation belt waves and particles to the active ionosphere. This mechanism introduces a positive feedback effect which will structure the large amplitude nonlinear response of the system /3/. The key idea here is that the precipitating electrons modify the ionospheric plasma density which, in turn, modifies the ionospheric reflection of the waves causing the precipitation. The modification of the plasma density by the precipitation is given by

$$\frac{dn_i}{dt} = Q(\frac{DN}{2(1 + D\tau_s)}) - \sigma_r n_i^2 \qquad (5)$$

where n_i is the ionospheric plasma density. The RHS of (5) represents a balance of density increase due to the precipitating particle flux and a decrease due to electron-ion recombination effects. Q is the ionization efficiency (electrons/cm) and σ_r is the recombination coefficient.

Positive feedback arises when enhanced ionization causes enhanced wave reflection. The enhanced ionization as calculated from (5) increases R in (2) causing D to increase. Therefore, the trick is to relate changes in the reflection coefficient to changes in the ionospheric plasma density. This is particularly difficult for whistler waves because of the unknown nature of the ducting efficiency as well as uncertainties in the reflection process at the ionosphere. Therefore, we assume an empirical coupling relationship which is given by

$$\frac{\delta R}{R_o} = \frac{\epsilon \delta n_i}{n_{io}} \tag{6}$$

Here ϵ is an adjustable parameter whose strength indicates the degree of coupling between changes in the ionospheric density and changes in the wave reflection coefficient. Note that ϵ as used here is similar to but not exactly the same as ϵ_H used Figure 1. As seen below positive feedback is triggered when $\epsilon \geq O(D_o\tau_s)$ (i.e. on the order of 10^{-3} for the weak diffusion case).

We initially examine the stability of equations (1), (2) and (5) by performing a linear perturbation analysis. All first order quantities are considered to vary as $\exp(st/\tau_s)$. Zero order quantities are defined at the Kennel-Petschek limit and are denoted by the "o" subscript. A cubic equation (dispersion relation) is obtained for the nondimensional natural frequencies, s. This equation is given by

$$\begin{aligned}[s + W_o/D_o + 2\gamma_1 D_1][s + D_1][s+2\tau_s/\tau_r] \\ = 2\gamma_1(D_1 - 1)D_1[s+2\tau_s/\tau_r] \\ + (\epsilon\tau_s/\tau_r)(2\gamma_1 + W_o/D_o)s(1+D_o\tau_s)^{-1}\end{aligned} \tag{7}$$

where $\gamma_1 = \gamma_o\tau_s$ and $D_1 = D_o\tau_s/(1 + D_o\tau_s)$. Now in the "Schulz" /4/ limit where the ionosphere and magnetosphere are decoupled ($\epsilon = 0$) equation (7) can be reduced to a quadratic. It is found that damped oscillatory solutions exist in the weak diffusion limit ($D_o\tau_s \ll 1$) but there are no real frequencies that exist in the strong diffusion ($D_o\tau_s = 1$) limit for reasonable growth rates. Note that the factor $(1 + D_o\tau_s)$ in equations (1) and (3) must be retained in the linear analysis even in the weak diffusion limit.

The full cubic equation for the case when ϵ is nonzero yields the following three solutions in the weak diffusion limit. We choose $\gamma_1 = 100$ and $\tau_s/\tau_r = 2$ and find the following roots

$$s_1 = -4$$

$$s_{2,3} = \pm \frac{10i\sqrt{3}}{9} [\, 54\, D_1 - 35\, \epsilon]^{1/2} \tag{8}$$

Now when $\epsilon > 54D_1/35$ then we have a purely growing (unstable) mode. Alternatively when this condition is not satisfied we have oscillatory solutions. Evolution of the unstable mode will soon exceed the linear regime and the nonlinear dynamics must examined using other techniques. We, therefore, give a numerical example as shown in Figure 2 which highlights the nonlinear nature of the feedback mechanism. (See also Figure 1). The top panel of Figure 2 represents the normalized wave energy density for $\epsilon_H = 10\%$ in Figure 1. The middle and bottom panels of Figure 2 represent N and n_i. Attention is directed to the phase relationships between the three curves. The maximum particle flux leads the wave intensity and goes through the Kennel-Petschek limit as the wave growth changes from positive to negative. The maximum ionospheric effect occurs after the wave spike maximum. Our physical interpretation of Figure 2 is as follows. A spike in the wave energy density causes a depletion of electrons trapped in the belts to levels well below the Kennel-Petschek limit. The subsequent drop of precipitating electron flux allows n_i to decrease. Thus, VLF waves are less strongly reflected back into the magnetosphere. This effectively raises the Kennel-Petschek limit as higher particle fluxes are necessary to offset increased ionospheric VLF absorbtion. When the equatorial particle source causes the trapped electrons to exceed the new Kennel-Petschek limit an explosive burst of precipitation is produced due to the ionospheric feedback. The repetition rate or frequency of these bursts is on the order of hundreds of seconds and is governed by the global nonlinear dynamics of the radiation belt system.

DISCUSSION AND CONCLUSIONS

Davidson and Chiu /6/ assumed a passive ionosphere and obtained linear oscillatory solutions in the strong diffusion limit by having the growth rate be modulated by the filling and dumping of the loss cone. We have not yet incorporated this filling mechanism into the present approach. Instead our oscillations arise from the large amplitude nonlinear coupling between the precipitating particles and the reflected waves at the ionosphere. We are presently modifying our numerical approach by including a realistic estimation of the loss cone filling time in both weak and strong diffusion limits. Hopefully, this will more completely characterize those oscillatory (spiky !) regimes that have been observed in the data. For example, see the paper by Iversen et al. /7/.

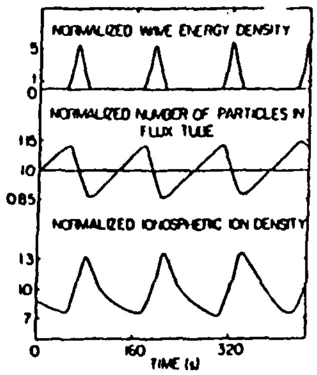

Fig. 2. Example of spike-like VLF wave structures as well as energetic particle losses and ionospheric density changes arising from the magnetosphere-ionosphere coupling described in text.

ACKNOWLEDGEMENTS

It is with pleasure that we acknowledge the helpful comments of Nelson Maynard, William Burke, Frederick Rich, Howard Singer and Michael Heinemann from the Air Force Geophysics Laboratory. One of the authors (MBS) would like to acknowledge the support of U.S. Air Force contract F19628-85-K-0053.

REFERENCES

1. U. S. Inan, T. F. Bell, and H. C. Chang, Particle precipitation induced by short duration VLF waves in the magnetosphere, J. Geophys. Res. 87, 6243-6264 (1982)
2. W. L. Imhof, H. D. Voss, J. B. Reagan, D. W. Datlowe, and D. S. Evans, Relativistic electron and energetic ion precipitation spikes near the plasmapause, J. Geophys. Res. 91, 3077-3088 (1986)
3. V. Yu. Trakhtengerts, Alfvén Masers, in: Active Experiments in Space, ESA-195, 1983, p 67.
4. M. Schulz, Particle saturation of the outer zone: a nonlinear model, Astrophys. and Space Sci. 29, 232-242 (1974)
5. C. F. Kennel and H. E. Petschek, Limit on stably trapped particle fluxes, J. Geophys. Res. 71, 1-28 (1966)
6. C. T. Davidson, and Y. T. Chiu, A closed nonlinear model of wave-particle interactions in the outer trapping and morningside auroral regions, J. Geophys. Res. 91, 13705-13710 (1986)
7. I. B. Iversen, L. P. Block, K. Bronstad, R. Grad, G. Haerendel, H. Junginger, A. Korth, G. Kremser, M. Madsen, J. Niskanen, W. Riedler, P. Tanskanen, K. M. Torkar, and S. Ullaland, Simultaneous observations of a pulsation event from the ground with balloons and with a geostationary satellite on August 12, 1978, J. Geophys. Res. 89, 6775-6785 (1984)

PHYSICS OF SPACE PLASMAS (1989)
SPI Conference Proceedings and Reprint Series, Number 9

GYRORESONANT INTERACTION OF ENERGETIC TRAPPED ELECTRONS AND PROTONS

Elena Villalón and Michael B. Silevitch
Center for Electromagnetics Research,
Northeastern University, Boston MA 02115

William J. Burke and Paul L. Rothwell
Geophysics Laboratory, Hanscom AFB, MA 01731

ABSTRACT

This paper studies the theory of gyroresonant interactions of energetic trapped electrons and protons in the Earth's radiation zones with ducted electromagnetic cyclotron waves. Substorm injected electrons in the mid-latitude regions interact with coherent VLF signals, such as whistler mode waves. Energetic protons may interact with narrow band hydromagnetic (Alfvén) waves. A set of equations is derived based on the Fokker–Planck theory of pitch–angle diffusion. They describe the evolution in time of the number of particles in the flux tube and the energy density of waves, for the interaction of Alfvén waves with protons and of whistler waves with electrons. The coupling coefficients are obtained based on a quasilinear analysis after averaging over the particle bounce motion. The reflection of the waves in the ionosphere is discussed. To dump the energetic particles from the radiation belts efficiently, the reflection coefficient must be very close to unity so waves amplitudes can grow to high values. Then, the precipitating particle fluxes may act as a positive feedback to raise the height integrated conductivity of the ionosphere which in turn, enhances the reflection of the waves. In addition, by heating the foot of the flux tube with high intensity, RF energy the mirroring properties of the ionosphere are also enhanced. The stability analysis around the equilibrium solutions for precipitating particle fluxes and wave intensity, show that an actively excited ionosphere can cause the development of exponentially growing instabilities.

I. INTRODUCTION

A theory of nonlinear interactions of radiation belts particles with cyclotron waves is developed here. We consider cases where the wave frequencies are small fractions of the equatorial cyclotron frequency and where the wave vectors are aligned with the geomagnetic field. Because of the latter we only consider resonant excitations due to the first harmonic of the cyclotron frequency. For high–temperature plasmas, the pitch–angle distributions of

Scientific Publishers, Inc., Cambridge, MA 02139

the particles are anisotropic, which provides the free energy for the cyclotron instability. As a distribution function relaxes toward equilibrium, it interacts with several types of electromagnetic waves. A number of observations of electron precipitation in middle latitudes ($L \leq 6$), have been attributed to highly coherent magnetospheric VLF waves [1 – 3]. Substorm–injected protons in the midlatitude regions, interact with ULF hydromagnetic pulsations of the Pc type, which are ducted along a given magnetic flux tube [4]. The amplitudes of the waves grow directly proportional to the number of resonant particles and the degree of the pitch angle anisotropy until they reach the equilibrium state. The generated waves, in turn, act upon the particles and change their velocity distributions. Some of these particles are scattered into the loss cone producing the well known particle precipitation fluxes investigated by Kennel and Petschek [5] and observed in the ionosphere.

The amplification of the electron (proton) cyclotron waves mainly occurs near the equatorial region where resonant wave–particle interactions are most efficient. As waves travel along the flux tube and enter the ionosphere they are partially reflected back into the flux tube, and partially transmitted toward the ground. An important concept developed by Bespalov and Trakhtengerts [6] and Trakhtengerts [7], considers the magnetosphere as a gigantic maser where whistler and Alfvén waves are trapped between ionospheric mirrors grow in amplitude as they cross back and forth across the equatorial region. They derive a set of equations based on quasilinear theory which gives the evolution in time of the trapped particles and the energy density of waves in the flux tube. The ray equations were also introduced in a phenomenological manner by Schulz [8]. Our paper is a detailed review of the theory developed by Bespalov and Trakhtengerts on the electron cyclotron wave instability. In addition, we extend this theory to the interaction of Alfvén waves with ions. For simplicity, we assume that the waves are ducted in the magnetosphere between the ionosphere and the equatorial plane. We also estimate the qualitative values of the ionospheric reflection coefficients for both whistler and Alfvén waves. The role that an actively excited ionosphere may play in modifying the wave reflection coefficients and hence, the maser efficiency within the Radiation Belts, is also discussed.

The paper is organized as follows. Sections II and III contain the basis of resonant interactions between waves and particles, and a description of the evolution in time of the particle distribution functions based on local, quasi-linear theory. We assume that the dielectric properties of wave propagation are given by a cold background of either electrons (for whistlers), or protons (for Alfvén waves). The population of hot plasma particles (*i.e.*, larger than 40 keV for the electrons and 100 keV for the ions), is represented by a particle source $\mathcal{J}(t)$. They interact with the electromagnetic waves near the equatorial regions. Because of resonant diffusion, the number of

trapped thermal particles in the flux tube changes in time and their distribution functions are studied in Sec. III. In Sec. IV we present the growth rates for the whistler and Alfvén instabilities, due to the resonant excitation by the thermal particles. After integrating along the flux tube, we obtain a set of coupled differential equations describing the evolution in time of the number of particles in the flux tube, and the energy density of waves. They are discussed in Sec. V. The equilibrium solutions for whistlers and Alfvén waves are given here. The nonlinear stability equation is also given in Sec. V. In Sec. VI we study the reflection of the waves at the foot of the flux tube for both whistlers, and Alfvén waves. In Sec. VII we also consider the effects that an actively excited ionosphere may have in the stability of the equilibrium solutions. Sec. VIII contains a summary and the conclusions.

II. RESONANT WAVE PARTICLE INTERACTION

A particle of mass m, charge q and velocity v, moving along the dipole field lines of the Earth's magnetic field, bounces from mirror points in the conjugate hemispheres in a time given by

$$\tau_B = 2\int_{-l_m/2}^{l_m/2} \frac{dz}{v_z} = \frac{4\pi a}{v}(1 - 0.23\sqrt{\mu}) \qquad (1)$$

where the coordinate z represents the distance along the magnetic field line. l_m is the length the particle travels along the field line, and a is a constant which is defined after Eq. (2). The particle's velocity along the magnetic field (z-direction), is $v_z = v(1 - \mu\Omega/\Omega_L)^{1/2}$, where $\Omega = qB/mc$ is the cyclotron frequency, and $\mu = \sin^2\theta_L$. Here θ_L is the particle's pitch angle at $z = 0$, *i.e.* the angle between the particle velocity vector and the geomagnetic field at the equator. We note that the bounce period is quite insensitive to variations in the equatorial pitch angles. Thus, we approximate τ_B by $4\pi a/v$ in the calculations that follow.

For analytical simplicity, we assume that in the equatorial region we may approximate the Earth's magnetic field by the parabolic profile

$$\frac{B}{B_L} = 1 + \left(\frac{z}{a}\right)^2 \qquad (2)$$

where the subscript L indicates the values at the central cross section of the flux tube. If we define ψ as the geomagnetic latitude in radian units, and expand the dipole magnetic field in powers of ψ, we find that $z \simeq R_E L\psi$ and $a = (\sqrt{2}/3)R_E L$. Here R_E is the Earth's radius and $R_E L$ measures the distance of the center cross section of the magnetic trap from the center of the Earth. Eq. (2) is a good approximation to the geomagnetic field lines for latitudes smaller than $\pm 20°$.

Ducted whistlers and Alfvén waves are such that their wave vector k is aligned with the geomagnetic field. These waves grow if the particle motion resonates at the first cyclotron harmonic and there is a sufficient number of electrons or protons which satisfy the resonant condition,

$$\omega - kv_z + \Omega = 0 \tag{3}$$

where ω is the wave frequency. The electromagnetic wave is assumed to be circularly polarized, with the electric and magnetic fields perpendicular to each other and both perpendicular to k. The refractive index is represented by η and it is given by the dispersion relation for either the whistler or the Alfvén waves (see Sec. IV). Eq. (3) defines a mapping between values of the cyclotron frequency Ω along the geomagnetic trap, and the resonant equatorial pitch angles μ, for given values of k and v, i.e. $(\Omega + \omega)/kv = (1 - \mu\Omega/\Omega_L)^{1/2}$. The range of resonant equatorial pitch angles, i.e. those that satisfy Eq. (3): $\mu_c \leq \mu \leq \mu_m$, is such that μ_c is given by the pitch angle at the boundary of the loss cone and μ_m is defined in terms of the equatorial cyclotron frequency. The resonant gyrofrequencies are such that $\Omega_L \leq \Omega \leq \Omega_M$. Here Ω_L is the equatorial gyrofrequency, and Ω_M is the maximum value of Ω which satisfies Eq. (3). The frequencies Ω_L, and Ω_M, are resonant with the values of the equatorial pitch angles corresponding to μ_m, and μ_c, respectively (see Fig. 1). We may also write that $\Omega_M/\Omega_L = 1 + (9/2)\psi_m^2$, where $\psi_m (\ll 1)$ is the maximum geomagnetic latitude for which resonant wave–particle interaction takes place. We find that ψ_m is related to the equatorial range of resonant pitch angles by the equation

$$\psi_m = \frac{1}{3}(\mu_m - \mu_c)^{1/2} \tag{4}$$

For given values of the particle's energy and wave vector, we obtain

$$\psi_m = \frac{\sqrt{2}}{3}(kv/\Omega_L - 1)^{1/2} \tag{5}$$

Then by equating Eqs. (4) and (5), we may obtain the equatorial range of resonant pitch angles in terms of the particle velocities and wave vectors. By realizing that the argument of the square root in Eq. (5) must be larger than zero we obtain that the wave frequency must be such that: $\omega/\Omega_L > c/(v\eta)$.

Next we evaluate the distribution functions of resonant particles over time scales which are much larger than the temporal changes in the magnetoplasma. We derive the equations for the evolution in time of the number of energetic particles in the flux tube as a function of the wave energy intensity.

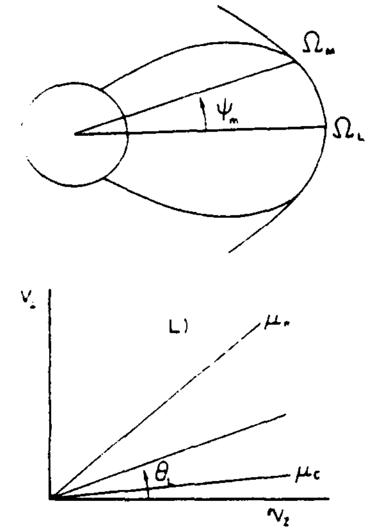

Figure 1. The Earth's dipole magnetic field and the parabolic profile are qualitatively depicted here. The gyrofrequencies Ω_L, Ω_M correspond to the equatorial and the maximum resonant geomagnetic fields, respectively. The angle ψ_m is the maximum geomagnetic latitude for which resonant wave-particle interaction takes place. The velocities $v_\perp, v_z$, represent the perpendicular and parallel components of the resonant particle's velocity as given in the equatorial cross section indicated by the index L). The equatorial pitch angle is denoted by θ_L, and $\mu = \sin^2\theta_L$. The values μ_c, μ_m, are evaluated for pitch angles at the equatorial loss cone and for the maximum value of θ_L which satisfied the resonant condition, respectively.

III. DISTRIBUTION FUNCTIONS OF RESONANT PARTICLES

The cold particle population gives the dielectric properties of wave propagation in the magnetosphere: their distribution function is isotropic in pitch angle. The total distribution functions for the energetic particles are anisotropic maxwellians. For a stable plasma, it is a function of μ and v and independent of the distance z along the flux tube for $|z| < l_m/2$. The energetic particle distribution functions are made up of two parts: those particles which are resonant with the waves and those which are not. In this paper f represents only the resonant portion of the distribution functions.

The cyclotron instability can modify the distribution functions of the resonant particles in such a way that it may become dependent on the distance z along the flux tube. However for the weak diffusion case we assume that f does not depend on z between the mirror points $|z| \leq l_m/2$, and that the anisotropy in pitch angle is independent on time; we may write

$$f = \frac{4}{\pi^{3/2}\sigma v_o^4} N(t) Z(\mu) \exp(-v^2/v_o^2) \tag{6}$$

where $Z(\mu)$ is the lowest order eigenfunction of the diffusion operator which is defined below, and $\sigma = 1/\mu_c$, is the mirror ratio. The number of resonant particles in the flux tube (particles per square cm) for given values of μ and v is denoted by $N(t)$. Here $N(t)$ depends on time over time scales such that $t \gg \tau_B$ and $t \gg \tau_g$, where τ_B, the particle's bounce time, is defined in Eq. (1). The time that the wave spends traveling between one conjugate hemisphere and the other is represented by τ_g.

The evolution in time of a plasma particle distribution function in the presence of a specified distribution of waves is described by quasilinear theory [3].

$$\frac{\partial f}{\partial t} = \frac{\pi\omega_p^2}{mn}\int_0^\infty dk \left(\hat{G} + \frac{\omega - kv_z}{\omega v_\perp}\right)\delta(-\omega + kv_z - \Omega)\frac{W_k}{\eta^2}\hat{G} f \tag{7}$$

$$\hat{G} + \frac{\omega - kv_z}{\omega v_\perp} = \frac{1}{p^2}\frac{\partial}{\partial p}p^2\frac{p_\perp}{p} - 2\frac{\Omega_L}{\omega}\frac{p_z}{p^2}\frac{\partial}{\partial \mu}\frac{p_\perp}{p_z} \tag{8}$$

$$\hat{G} = \frac{p_\perp}{p}\left(\frac{\partial}{\partial p} - 2\frac{\Omega_L}{\omega}\frac{1}{p}\frac{\partial}{\partial \mu}\right) \tag{9}$$

where $\eta = ck/\omega$ is the refractive index. The energy density of waves is $W_k = B_k^2/16\pi^2$, where B_k is the wave magnetic field. Here ω_p is the plasma frequency evaluated for the cold background of plasma particles of density n. We assume that $n \gg N/l$, where l is the length of the flux tube. We now integrate Eq (7) along the flux tube by applying the operator $(1/\tau_B)\int_{-l/2}^{l/2}(dz/v_z)$ to both the left and right sides of Eq. (7). We assume that the only spatial inhomogeneities are due to the magnetic field variations which is described by the parabolic profile in Eq. (2). We also assume that f does not depend on z and is given by Eq. (6). After some tedious algebra we arrive at the equation

$$\begin{aligned}\frac{\partial f}{\partial t} = {} & \frac{4\pi a k^2}{\tau_g n\Omega_L}\left(\frac{kv}{\Omega_L} - 1\right)^{-1/2}\frac{\Omega_L}{kv}W_k \times \\ & \left[\frac{2}{p}\frac{\Omega_L}{\omega}\frac{\partial}{\partial\mu}\mu\frac{\partial}{\partial\mu} - \frac{\partial}{\partial\mu}\mu\frac{\partial}{\partial p} - \frac{\mu}{p}\frac{\partial}{\partial p}p\frac{\partial}{\partial\mu} + \frac{1}{2}\frac{\omega}{\Omega_L}\frac{\mu}{p}\frac{\partial}{\partial p}p^2\frac{\partial}{\partial p}\right] f\end{aligned} \tag{10}$$

where we have assumed that $2\Omega_L/kv\mu \gg 1$, and a narrow spectrum of waves centered around a certain value of k. Hereafter we also assume that $\omega \ll \Omega_L$, which allows us to neglect the three energy diffusion terms in the square brackets of Eq. (8). Let us now consider the definitions,

$$\Upsilon = \frac{2\pi\Omega_L^2}{B_L^2 kv}, \tag{11}$$

and

$$F = \int_{\Omega_L/k}^\infty \pi\sigma v^3 f dv \tag{12}$$

In the weak diffusion case we have that $F(t,\xi) = N(t)Z(\xi)$. The eigenfunction $Z(\xi)$ satisfies

$$\frac{1}{\xi}\frac{d}{d\xi}\left(\xi\frac{dZ}{d\xi}\right) = -g^2(\xi_m^2 - \xi_c^2)Z(\xi) \tag{13}$$

where $\xi = \sqrt{\mu} = \sin\theta_L$, g is the lowest order eigenvalue of the diffusion operator, and the range of resonant pitch angles is now given by $\xi_c \leq \xi \leq \xi_m$. By defining $\hat{g} = g(\xi_m^2 - \xi_c^2)^{1/2}$ The general solution to Eq. (13) is

$$Z = C_1 J_o(\hat{g}\xi) + C_2 Y_o(\hat{g}\xi) \tag{14}$$

Here C_1 and C_2 are constants, and J_o and Y_o are Bessel functions of order zero. We also have

$$\int_{\xi_c}^{\xi_m}\xi Z(\xi)d\xi = \frac{2v}{\pi a g^2(\xi_m^2 - \xi_c^2)} \tag{15}$$

$$\left[\frac{dZ}{d\xi}\right]_{\xi=\xi_c,\xi_m} = 0 \tag{16}$$

By imposing the boundary conditions given in Eq. (16), we get the following equation which solves for the eigenvalues of the differential equation (13),

$$J_1(y_c)Y_1(y_m) - Y_1(y_c)J_1(y_m) = 0 \tag{17}$$

where $y_c = g\xi_c$, $y_m = g\xi_m$, and J_1, Y_1 are the Bessel functions of order one.

Let us call $\mathcal{J}$ the particle source which may depend on t and ξ, and write $\mathcal{J}(t, \xi) = \mathcal{J}(t) Z(\xi)$. By combining Eqs. (8) through (13), we obtain

$$\frac{dN}{dt} = -y^2[2(\mu_m - \mu_c)]^{1/2} \Upsilon W_k N + \mathcal{J}(t) \qquad (18)$$

We note that Eq. (18) can be applied to either the interaction of whistlers with electrons or Alfven waves with ions provided that the gyrofrequencies in Eq. (11) are evaluated for the resonant particles, i.e. electrons for whistlers and ions for Alfven waves.

IV. WAVE GROWTH RATES

The linear wave growth rates for resonant wave–particle interaction is given by [3]:

$$\frac{\gamma}{\omega} = \frac{2\pi^2\omega_p^2}{n\omega_g^2} \int_0^\infty v^2 dv \int_{\mu_c}^{\mu_m} \mu d\mu \frac{\Omega^2/\Omega_L}{(1 - \mu\Omega/\Omega_L)^{1/2}} \frac{1}{\eta^2} \delta(-\omega + kv_z - \Omega) \frac{\partial f}{\partial \mu} \quad (19)$$

where we have taken $\eta \gg c/v_z$. To obtain the spatial amplification factor we apply the operator $(1/\tau_g) \int_{-l/2}^{l/2} (dz/v_g)$ to both left and right sides of Eq. (19). Here v_g is the wave group velocity, and l is the total length of the field line. By assuming that the only spatial inhomogeneity is in the geomagnetic field, and using the parabolic profile in Eq. (2) we may write

$$\Gamma = \int_{\Omega_L}^{\Omega_M} \frac{a}{(\Omega/\Omega_L - 1)^{1/2}} \frac{\gamma}{v_g} \frac{d\Omega}{\Omega_L} \qquad (20)$$

The evolution in time of the energy density of waves W_k is given by

$$\frac{\partial W_k}{\partial t} + v_g \frac{\partial W_k}{\partial z} = \left(\gamma - \frac{r}{\tau_g}\right) W_k \qquad (21)$$

Here γ is given by Eq. (19) and $r = -2 \ln R$, where R is the reflection coefficient at both ends of the flux tube (i.e., the ionospheric reflection coefficient). By assuming that W_k depends weakly on z, and after integrating Eq. (21) along the flux tube we obtain

$$\frac{dW_k}{dt} = \frac{\Gamma}{\tau_g} W_k - \frac{r}{\tau_g} W_k \qquad (22)$$

We must now estimate the terms Γ/τ_g and r/τ_g for whistlers and Alfven waves.

A. Whistler waves

The dispersion relation is $\eta = \omega_p/(\Omega_L\omega)^{1/2}$ and the normalized group velocity is $v_g/c = 2/\eta$, where the plasma and cyclotron frequencies are evaluated for cold electrons. Combining Eqs. (19) and (20) and assuming that $2\Omega_L/kv\mu \gg 1$, we find

$$\Gamma = \frac{4\pi^3 k m_e a}{B_L^2} \int_0^\infty dv \int_{\mu_c}^{\mu_m} d\mu \frac{\mu v^4}{(kv/\Omega_L - 1)^{1/2}} \frac{\partial f}{\partial \mu} \qquad (23)$$

where m_e is the electron mass. Let us now consider the definition in Eq. (12), and that $F = N(t) Z(\xi)$ with $\xi = \sqrt{\mu}$. After some algebra we find

$$\frac{\Gamma}{\tau_g} = \Delta_e [2(\mu_m - \mu_c)]^{1/2} \frac{v}{\pi a} N(t) \qquad (24)$$

$$\Delta_e = \frac{2\pi^2 a m_e v \omega}{i \sigma B_L^2} \qquad (25)$$

where $\sigma = 1/\mu_c$, can be expressed in terms of the L-shell value as: $\sigma = L^3(4 - 3/L)^{1/2}$.

B. Alfvén waves

The dispersion relation is $\eta = \omega_p/\Omega$ and the group velocity is $v_g/c = 1/\eta$, where the plasma frequency, ω_p, is evaluated at the plasma density n of the ambient ions (e.g. cold protons), which support the Alfvén waves, and Ω is their gyrofrequency. Under the limit $2\Omega_L/kv\mu \gg 1$ we obtain

$$\Gamma = \frac{2\pi^2 k^3 a \omega_p}{\omega n \Omega_L^2 c} \int_0^\infty dv \int_{\mu_c}^{\mu_m} d\mu \frac{v^5 \mu}{(kv/\Omega_L - 1)^{1/2}} \frac{\partial f}{\partial \mu} \qquad (26)$$

By considering the definition of F given in Eq. (12), and the weak diffusion case (where f is given by Eq. (6)) we obtain

$$\frac{\Gamma}{\tau_g} = \Delta_i [2(\mu_m - \mu_c)]^{1/2} \frac{v}{\pi a} N(t) \qquad (27)$$

$$\Delta_i = \frac{v^4 \pi a \omega_p^3 \omega^2}{n \sigma i c^2 \Omega_L^4} \qquad (28)$$

We now combine Eqs. (24), (25) and (27), (28) with Eq. (22) to obtain the evolution in time of the energy density of whistlers and Alfvén waves respectively, as a function of the number of particles in the flux tube. These equations together with Eq. (18) are named the ray equations; they describe the self–consistent interaction of waves and particles in the magnetosphere. Next we study the conditions for equilibrium and stability of the ray equations.

V. THE RAY EQUATIONS

The equations describing the parametric coupling between the energy density of whistler (Alfvén) waves W_k, and the number of electrons (protons) in the flux tube are

$$\frac{dW_k}{dt} = \Delta_\alpha[2(\mu_m - \mu_c)]^{1/2}\frac{v}{\pi a}NW_k - \frac{r}{\tau_g}W_k \quad (29)$$

$$\frac{dN}{dt} = -g^2\Upsilon[2(\mu_m - \mu_c)]^{1/2}NW_k + \mathcal{J}(t) \quad (30)$$

where $\alpha = e,i$ depending on whether we study electrons or protons. Here Δ_α is given in Eqs. (25) and (28), Υ in Eq. (11), and g is the lowest order eigenvalue of the diffusion operator. Note that the growth of the instability is proportional to the range of resonant interaction, i.e. $(\mu_m - \mu_c)^{1/2}$, where $(\mu_m - \mu_c)^{1/2}$ is defined as a function of k, v, and Ω_L, by Eqs. (4) and (5).

Let us now assume that the system is in equilibrium, i.e. $dN/dt = dW_k/dt = 0$. We find that $W_k = W_o$ and $N = N_o$ where

$$W_o = \frac{\mathcal{J}\Delta_\alpha(v/a\pi)\tau_g}{rg^2\Upsilon} \quad (31)$$

$$N_o = \frac{r}{\tau_g\Delta_\alpha v/a\pi}[2(\mu_m - \mu_c)]^{-1/2} \quad (32)$$

For small deviation from equilibrium we may write: $N = N_o + \delta N\exp(\zeta\tau)$ and $W_k = W_o + \delta W\exp(\zeta\tau)$, where $\tau = t/\tau_g$. Upon substituting these expressions into Eqs. (29) and (30) and keeping only first order corrections, we find

$$\zeta^2 + (\zeta + r)\frac{\hat{\mathcal{J}}_o}{r} = 0 \quad (33)$$

where we define $\hat{\mathcal{J}}_o = \mathcal{J}\Delta_\alpha(v/\pi a)\tau_g^2[2(\mu_m - \mu_c)]^{1/2}$. By solving for Eq. (33) we obtain that $\zeta = -\nu \pm i(\rho^2 - \nu^2)^{1/2}$, where

$$\nu = \frac{\hat{\mathcal{J}}_o}{2r} \quad (34)$$

$$\rho = \hat{\mathcal{J}}_o^{1/2} \quad (35)$$

Because ν and $\rho > 0$, we see that the equilibrium solutions in Eqs. (34) and (35), are always stable.

As an application we consider the interaction of 40 keV electrons with a whistler wave with a frequency of 1 kHz and with a refractive index of 30. The interaction occurs at $L = 4.5$. Thus the mirror ratio σ is equal to 1.6×10^2, the square of the equatorial magnetic field is $B_L^2 = 1.16 \times 10^{-5}$

gaussian units, the length of the flux tube, l, is approximately of the order of ten times the Earth's radius, and τ_g of the order of a few seconds. The equatorial gyrofrequency is $\Omega_L = 10$ kHz, and ψ_m is about 12°. The range of resonant pitch angles is 40°. The coupling coefficient for the wave growth rate (see Eqs. (24) and (25)) is $\Delta_e(v/\pi a) \simeq 10^{-10}$ cm^2 s^{-1}. For a particle source, $\mathcal{J} = 10^3$ to 10^6 particles/(cm^{2}s), and by taking $R = 0.8$, we find that $\nu \sim \rho^2$ and their values range between 10^{-7} to 10^{-4} s$^{-2}\tau_g^2$.

We consider the interaction of 200 keV protons with Alfvén waves at $L = 4.5$. The wave frequency is taken equal to 1 Hz and the refractive index $\eta = 9$. Thus the plasma frequency is 10 Hz, the cyclotron frequency is 5.45 Hz, the maximum geomagnetic latitude ψ_m is about 10°, the range of resonant pitch angles is 34°, and $[2(\mu_m - \mu_c)]^{1/2}$ is 0.8. The group time delay for Alfvén waves may be of the order of minutes. We find that the growth rate is proportional to the coupling coefficient $\Delta_i(v/\pi a) \simeq 0.5 \times 10^{-9}$ cm^2 s^{-1}. By assuming that $\mathcal{J} = 10^3$ to 10^6 particles/(cm^2 s), and that $R = 0.8$, we show that $\nu \simeq \rho^2$ and their values range between 10^{-6} to 10^{-3} s$^{-2}\tau_g^2$

A. The stability equation

Let us now define

$$\hat{N} = \Delta_\alpha(\frac{v}{\pi a})\tau_g[2(\mu_m - \mu_c)]^{1/2}N \quad (36)$$

$$\hat{W} = g^2\tau_g\Upsilon[2(\mu_m - \mu_c)]^{1/2}W \quad (37)$$

where $\alpha = e,i$ depending on whether we are studying either electrons or protons. In terms of normalized quantities, the ray equations become

$$\frac{d\hat{N}}{d\tau} = -\hat{N}\hat{W}_k + \hat{\mathcal{J}}_o \quad (38)$$

$$\frac{d\hat{W}_k}{d\tau} = \hat{N}\hat{W}_k - r\hat{W}_k \quad (39)$$

The equilibrium solutions can now be written as $\hat{N}_o = r$ and $\hat{W}_o = \hat{\mathcal{J}}_o/r$.

We can further reduce Eqs. (38) and (39) to a single non-linear equation by defining

$$\hat{N} = \frac{d\phi}{d\tau} + r \quad (40)$$

$$\hat{W}_k = \hat{W}_o\exp(\phi) \quad (41)$$

we may write [6]

$$\frac{d^2\phi}{d\tau^2} + 2\nu\exp(\phi)\frac{d\phi}{d\tau} + \rho^2[\exp(\phi) - 1] = 0 \quad (42)$$

We note that as $\tau \to \infty$, $\dot{N}$ and $\dot{W}$ tend to the equilibrium solutions W_o and N_o, and then we must have that $\phi \to 0$.

In the linear approximation the deviation from equilibrium is small, *i.e.* we may assume that $\phi \ll 1$. In addition we may write $\phi = \exp(\zeta\tau)$ where $\zeta = -\nu \pm i(\rho^2 - \nu^2)^{1/2}$, and which for $\rho \gg \nu$ yields the oscillations around equilibrium given given in Eqs. (34) and (35).

VI. THE WAVES REFLECTION COEFFICIENTS

As a wave enters the ionosphere it is partially reflected back into the magnetic trap and partially penetrates the ionosphere and gets to the ground. We have already called R the reflection coefficient, where RW_k is the amount of the wave amplitude which gets reflected back, and W_k is the wave amplitude in the flux tube. The value of the reflection coefficient depends on several factors such as the ratio between the wave and collision frequencies with the enviromental particles (neutral). It also depends on the ratios of the size of the ionosphere d, the wavelength $\lambda = 2\pi/k$, and the scale of the density gradient $\mathcal{L}$, where

$$\frac{1}{\mathcal{L}} = \frac{1}{n}\frac{dn}{dz} \tag{43}$$

Typically, we have $\mathcal{L} \simeq 50$ km and $d \gg \mathcal{L}$ (*e.g.*, $d \simeq 300$ km). We represent by η_F, η_E, and η_o, the refractive indices in the F and E–layers, and in the flux tube, respectively. Next we discuss qualitatively the reflection of whistlers and Alfvén waves. We show that whistlers are mainly reflected from the E and D–layers of the ionosphere, while Alfvén waves are reflected from the F–layer. We assume perfect ducting for the reflection of ELF and VLF waves. In addition, for simplicity in the calculations, we assume that the inclination of the waves duct exit with respect to the vertical is small.

A. Reflection of whistlers

Here we consider the reflection of whistler waves with frequencies of the order of a few kHz, in the F, E and D regions of the ionosphere. In the F–layer the electron density is between values of 10^4 to 10^6 particles per cc, and the scale length of the density gradient is about $\mathcal{L} = 50$ km. The wavelengths of whistler modes are of the order of a few kilometers, and such that $\lambda \ll \mathcal{L}$. For example, for $\omega/2\pi \simeq 4$ kHz, and a density of 10^4 particles per cc, we find that $\lambda = 6$ km. Because the wave amplitude changes slowly as it penetrates the F–layer, a WKB analysis is a valid approximation. Thus one expects whistler waves which are ducted in the flux tube to penetrate the ionospheric F–layer without significant reflection. Whatever little reflection takes place is due to collisional effects. On the other hand in the E and D–layers the peak electron density ranges between values of 10^5 to 10^2 particles per cc, and the scale length is about $\mathcal{L} = 10$ km. For a wave of frequency equal to 4 kHz, we find that wavelengths are between values of a few to about 60 km depending on plasma density, and that $\lambda \geq \mathcal{L}$. In all cases we have $(\lambda/2\pi) \ll d$, where d is the size of the ionospheric layers. Because collisions between the neutral and electrons are more significant in the E– and D– layers, we expect whistler waves to be reflected there. We may distinguish between these cases depending on whether we consider reflection from a high or low density E– and D–layers. For a high density E–layer the reflection coefficient is obtained by assuming that the plasma density changes according to an exponential profile. For the weak density case, we treat the E–layer as a semiinfinite slab with a sharp boundary at the border with the F–layer.

Let us first study reflection from a high density collisional E–layer. The refractive index becomes complex: $\eta_E^* = \eta_E + i\kappa$. We define $\epsilon_c = \nu_c/\omega$ where ν_c is the collision frequency between the electrons and the neutral; it depends on the height z, and it is such that as $z \to \infty$, $\nu_c \to 0$. The origin of heights $z = 0$, is chosen at the bottom of the F–layer. Thus inside the E–layer $z \leq 0$. Here $Y = \Omega_e/\omega$, and $X = \omega_p^2/\omega^2$, where the plasma density ω_p depends on the density profile. We have [9]:

$$(\eta_E^*)^2 = 1 - \frac{X}{1 - i\epsilon_c \pm Y}, \tag{44}$$

The wave equation is

$$\frac{d^2\Sigma_\pm}{ds^2} + [1 - bX]\Sigma_\pm = 0 \tag{45}$$

where $\Sigma_\pm = E_x \pm iE_y$, E_x and E_y are the components of the electric field, and $s = z/\lambda$. The sign "+" corresponds to the right-hand polarization and "-" to the left-hand polarization. Here $b = [1 - i\epsilon_c \pm Y]^{-1}$ also depends on the wave polarization. Given some profiles for the plasma density and collision frequency, Eq. (45) may be studied by using the WKB approximation [10]. Here we solve Eq. (45) exactly when the the electron density profile is exponential. Thus we may write: $X = X_o + \exp(-\delta s)$, where X_o is an averaged value of X in the flux tube, and $\delta = \lambda/\mathcal{L}$. Eq. (45) can be solved in terms of Bessel functions. The absolute value of the reflection coefficient for $Y > 1$ is

$$R = \exp\Big[-\frac{2\pi}{\delta}\eta_o + \frac{2\eta_o}{\delta}\arctan(\frac{\epsilon_c}{1 - Y})\Big] \tag{46}$$

Eq. (46) generalizes the result obtained by Budden [10], by including the coupling to the flux tube. For a slowly varying medium we have that $\delta \to 0$ and the wave is totally transmitted and reaches the ground. Note that the larger the refractive index η_o the smaller the reflection coefficient. We now consider two cases: (a) if $\epsilon_c \ll Y$, very small collision frequency, we find that $R = \exp(-2\pi\eta_o/\delta)$, and (b) if $\epsilon_c \gg Y$, then $R = \exp(-\pi\eta_o/\delta)$. Thus collisions favor wave reflection back into the flux tube, as do large density gradients and large wavelengths.

Note that at normal nightime ionosphere, there is little ionization in the E−layer. These conditions and the fact that the collision frequency in the F−layer is so small, allow whistler waves to travel all the way down to the Earth through a collisionless media. We now treat the case of a weak E−layer, where the plasma density can be as low as 10^2 particles per cc. By taking the wave frequency equal to 4 kHz, we find that the refractive index η_E is very close to unity (*i.e.* $\eta_E = 1.3$). The wavelength $\lambda/2\pi$ is then equal to 9 km which is much smaller than the altitude of the ionospheric E−layer. The refractive index in the F−layer is $\eta_F \simeq 13$, which corresponds to an ionospheric density of approximately 10^4 particles per cc. Thus whistler waves which are passing through the F−layer encounter a sharp boundary at the low density night-time E−layer, and get almost totally reflected there.

B. Reflection of Alfvén waves

First let us look at the reflection of Alfvén waves in the F−layer. Because $(\lambda/2\pi)$ *is of the order of the altitude* d *of* the ionospheric F−layer, we can no longer assume that the dimensions of the ionosphere are infinite. The F−layer now has two boundaries. One is at $z = 0$, the border with the E−layer, and the other one is at $z = d$ somewhere inside the flux tube. Inside the E−layer ($z \leq 0$), we assume the wave propagates into a plasma medium with a refractive index equal to η_E. When the E−layer is equivalent to free space then $\eta_E = 1$. The F−layer ionospheric model with the two boundaries acts as a resonant cavity for the very large wavelength fields. A wave incident from the flux tube on the upper boundary ($z = d$) is partially reflected back into the flux tube, and partially transmitted into the ionospheric slab. The transmitted wave is partially reflected at the lower boundary $z = 0$ and partially transmitted below $z = 0$. By matching these waves at $z = 0$ and $z = d$, we find that the absolute value of the reflection coefficient is

$$|R|^2 = \frac{|r_1 + r_2(1 - \tan^2\vartheta)|^2 + 4r_2^2\tan^2\vartheta}{|d_1 + d_2(1 - \tan^2\vartheta)|^2 + 4d_2^2\tan^2\vartheta} \tag{47}$$

where $r_1 = (\eta_F + \eta_o)(\eta_E - \eta_F), r_2 = (\eta_F - \eta_o)(\eta_E + \eta_F), d_1 = (\eta_F - \eta_o)(\eta_E - \eta_F), d_2 = (\eta_F + \eta_o)(\eta_E - \eta_F)$, and $\vartheta = (2\pi/\lambda)d$. We recall that η_F and η_o are the refractive indices in the F−layer and flux tube, respectively. Eq. (47) reduces to the result derived by Budden [10] in the limit $\eta_o, \eta_E \to 1$. In addition, if we let the refractive index η_F have an infinitesimally small imaginary

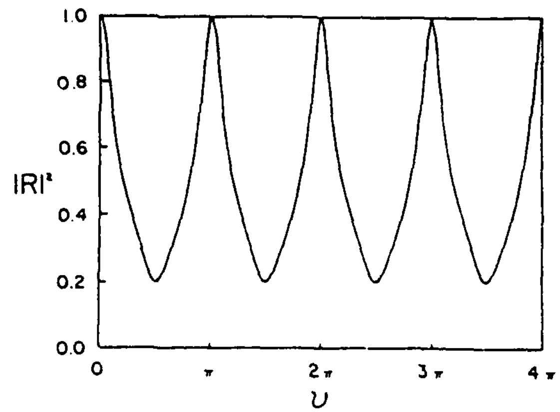

Figure 2. Square of the reflection coefficient as a function of ϑ (in radians) which is equal to $(2\pi/\lambda)d$, where λ is the wavelength and d the length of the ionospheric layer. We take n, the number of cold protons in the flux tube, to be equal to 100 per c.c. The density of O^+ ions in the ionosphere is taken equal to 10^6 per cc.

part and if $d \to \infty$, then we also recover the reflection coefficient for a semi-infinite slab. The reflection coefficient in the finite slab model of Eq. (47), is frequency dependent. In fact, it exhibits resonant behavior for certain values of the wave frequency. In particular for $\eta_F \simeq \eta_o$ and both much larger than η_E, we find that $d_2 \simeq -r_1 \simeq 2\eta_F^2$ and $d_1 \simeq r_2 \simeq 0$. The reflection coefficient now becomes $|R| = \cos^2\vartheta$, which is zero for $\vartheta = (\pi/2)(2n+1)$, where n is an integer, *i.e.* for $2d/\lambda = n + 1/2$.

Now let us illustrate the frequency dependency of the reflection coefficient in Eq. (47) with some examples. This should be contrasted with *the frequency independent nature of the semi−infinite slab model*. In the F−layer, Alfvén waves are mostly supported by O^+ ions. The ion cyclotron frequency is Ω_i =0.05 kHz. For an auroral ionospheric density of about 10^6 particles per cc, we find that the plasma frequency is 52.5 kHz. The collisionless dispersion relation for Alfvén waves yields a refractive index $\eta_F = 1027.5$. For wave frequencies of the order of 0.5 Hz, we have that $\lambda \sim$ 600 km. Hence we conclude that the reflection coefficient in the F−layer is given in Eq. (47). Let us now consider the flux tube as part of the same example. We assume that the particles supporting the Alfvén waves in the where $W_\omega = p^{\cdot}\tau_g \Upsilon[2(\mu_m - \mu_c)]^{1/2} W_o$, and W_o is the equilibrium energy density of waves which is defined in Eq. (31). The function ϕ_m satisfies the differential equation

$$\frac{d^2\phi_m}{d\tau^2} - 2\nu \exp(\phi_m)\frac{d\phi_m}{d\tau} + \rho^2[\exp(\phi_m) - 1] + \epsilon_m \frac{d\Lambda}{d\tau} + 2\nu\epsilon_m \Lambda \exp(\phi_m) = 0 \quad (50)$$

where τ and ρ are defined in Eqs. (31) and (35). Eq. (50) is comparable to Eq. (42), but here we have added the contribution of an actively excited ionosphere through the terms proportional to $\epsilon_m\Lambda$.

As an example we consider the coupling of the radiation belts waves and particles to the ionosphere [11]. This mechanism introduces a positive feedback effect which will structure the large amplitude non-linear response of the system. The precipitating electrons modify the ionospheric plasma density which, in turn, modifies the ionospheric reflection of the waves causing the precipitation. In the D- and E- layers, the modification of the plasma density by the precipitation is given by

$$\frac{dn_I}{dt} = \frac{Q}{2}\left(\mathcal{J} - \frac{dN}{dt}\right) - \sigma_r n_I^2 \quad (51)$$

where n_I is the ionospheric plasma density. The right-hand side of Eq. (51) represents the balance between the increasing density due to the precipiting particle flux and the decrease due to electron-ion recombination effects. Here Q is the ionization efficiency, and σ_r the recombination coefficient. Because the term proportional to the recombination coefficient is non-linear in n_I, we may neglect it in the linear calculations that follow.

We now assume that $\Lambda(\tau)$ is proportional to dn_I/dt, *i.e.* we have

$$\Lambda = -\frac{Q}{2}\left(\frac{d^2\phi_m}{d\tau^2}\right) \quad (52)$$

where we have redifined r as $r + \epsilon_m Q\dot{\mathcal{J}}_o/2$. After linearizing in ϕ_m, and taking $\phi_m \sim \exp(\zeta\tau)$, we find

$$\zeta^3 + 2(\nu - \frac{1}{Q\epsilon_m})\zeta^2 - \frac{4}{Q\epsilon_m}\nu\zeta - \frac{2}{Q\epsilon_m}\rho^2 = 0 \quad (53)$$

We may solve Eq. (53) approximately for $1/\nu \ll Q|\epsilon_m| \ll (\rho/\nu)^2$. We obtain the following unstable root ($\epsilon_m > 0$): $\zeta_1 = (2\rho^2/Q\epsilon_m)^{1/3}$.

In the numerical example presented in Sec. V, for the whistler instability, we found that $1/\nu$ varied between the values 10^7 to 10^4 times r (where $r = -2\ln R$). If the reflection coefficient, R, is very close to one, then r is very small (as small as 10^{-7} or 10^{-4}). Hence, when $R = 1$, we have that $1/\nu$ is a small number so the condition for the instability, $Q|\epsilon_m| > 1/\nu$, can be easily satisfied. Otherwise, *i. e.* for $R < 1$, it is very difficult to find unstable solutions to Eq. (53), since very large values for the particle source $\mathcal{J}$, are then required.

magnetosphere are protons, and that the wave-particle interaction occurs at $L = 4.5$. We also treat $z \leq 0$ as free space (*i.e.* we take $\eta_E = 1$). The equatorial cyclotron frequency is equal to 5.45 Hz. In Fig. 2, we have represented $|R|^2$ as function of ϑ for a plasma density of one hundred protons per c.c., the refractive index in the flux tube is now equal to 385. We can see the resonant behaviour of the reflection coefficient as function of ϑ. Because $\vartheta = (\eta_F d/c)\omega \sim (d/300)\omega$, we find that for $0 < \vartheta < 4\pi$ radians, the wave frequency varies roughly between zero and two Hertz .

VII. THE ACTIVELY EXCITED IONOSPHERE

The reflection of waves in the ionosphere is a very important factor in the growth of the whistler and Alfvén instabilities. An effectively operating cyclotron maser requires large wave amplitudes to pitch angle scatter trapped energetic particles into the loss cone. This is a diffusion process which is described by a Fokker-Planck type of equation. By changing the reflection coefficient at the ionospheric turning points of the waves, we may substantially modify the fields amplitudes and hence, the efficiency of the maser operation in the geomagnetic flux tube. In Sec. VI we presented a discussion on the qualitative values that the reflection coefficients take in an unperturbed (natural) ionosphere depending on the range of wave frequencies and wavelengths. We learned that wave reflection is increased by sharp density gradients and large values of the collision frequency. Thus we may want to modify the ionospheric properties with some external means, to improve wave reflection. One way of doing this is using a high power radio wave transmitter either from the ground or from space vehicles at the selected frequencies whose turning points fall at the height where the properties of the ionosphere are to be modified. Heating the ionosphere can produce energetic electrons which, by additional ionization, create a large population of thermal electrons and a substantial modification of the ionospheric impedance. In addition, by heating the D- and E- layers with a frequency close to Ω_e, the electron population can be increased by disassociation of some of the negative molecular and atomic ions that exist in the ionosphere. Here we assume that the reflection coefficient changes according to the expression, $r + \epsilon_m\Lambda(\tau)$. The unperturbed reflection coefficient is $r = -2\ln R$ and $\Lambda(\tau)$ is the modulation due to the presence of the HF-waves, where $\tau = t/\tau_g$ is the normalized time. We may now write that the number of particles in the flux tube $N(t)$, and the energy density of waves $W_k(t)$ are given by

$$\dot{N} = \frac{d\phi_m(\tau)}{d\tau} + r + \epsilon_m\Lambda(\tau) \quad (48)$$

$$W_k = W_o \exp(\phi_m) \quad (49)$$

VIII. SUMMARY AND CONCLUSIONS

We have presented a self-consistent theory on the interaction of magnetospheric particles with ducted electromagnetic cyclotron waves. Our theory is based on the following assumptions:

(1) The dielectric properties of wave propagation are given by a cold background of plasma particles, which can either be electrons (for the whistlers) or ions, *e.g.* protons, (for the Alfven instabilities). The density of the cold plasma population is taken constant along the flux tube, and the only spatial inhomogeneities are due to geomagnetic field variations.

(2) Near the equator the Earth's magnetic field is approximated by a parabolic profile. Because wave vectors are along the geomagnetic field we only consider the contribution of the first gyroharmonic.

(3) The maser instability is produced by the interaction of a hot plasma population (*e.g.* particles with energies larger than 40 keV for the electrons, and 100 keV for the ions), with the cyclotron waves near equatorial regions. The changes in the thermal distribution functions due to pitch-angle diffusion, are studied here.

The main results of our theory can be summarized as follows:

(1) The resonant part of the energetic particles' distribution functions are described within the framework of quasilinear theory. From the resonance condition, we establish relations between the range of equatorial pitch angles and the extent of geomagnetic latitudes for which interactions take place. After integrating along the flux tube, we arrive at equations describing the time evolution of the number of particles in the flux tube as functions of the energy density of waves.

(2) The spatial amplification factors are obtained for whistlers and Alfvén waves, after integrating the temporal growth rates over time scales which are comparable to the group time delays of the waves τ_g. The ray equations describing the evolution in time of the number of particles in the flux tube and the energy density of waves, are studied near equilibrium.

(3) The equatorially generated waves may be partially reflected back into the flux tube when they reach the ionosphere. Whistlers can penetrate the F-layer without significant reflection, and be reflected in the D- and E- layers. In contrast, Alfven waves are reflected in the F-layer which acts as a resonant cavity for these long wavelengths waves.

(4) We have also presented some calculations on the role that an actively excited ionosphere plays in the confinement of the cyclotron waves within the flux tube. The stability equation has been extended as to include time dependent reflection coefficients, which may be created

by either modulation of the ionosphere with high power microwave transmitters or by the particle precipitations due to the maser instabilities. Unstable modes are found for large external perturbations of the ionospheric conductivity.

ACKNOWLEDGEMENTS

Two of us (E.V. and M.B.S.) have been supported by the U.S. Air Force under contract F19628-89-K-0014.

REFERENCES

[1] J.M. Retterer, J.R. Jasperse and T.S. Chang, J. Geophys. Res. 88, 201 (1983).

[2] U.S. Inan, J. Geophys. Res. 92, 127 (1987).

[3] L.R. Lyons and D.J. Williams, *Quantitative aspects of magnetospheric physics* (D. Reidel Publishing Company, Boston, 1983), p. 133.

[4] W.L. Imhof, H.D. Voss, J.B. Reagan, D.W. Datlowe, E.E. Gaines, J. Mobilia and D.S. Evans, J. Geophys. Res. 91, 3077 (1986).

[5] C.F. Kennel and H.E. Petschek, J. Geophys. Res. 71, 1 (1966).

[6] P.A. Bespalov and V. Yu. Trakhtengerts, in *Rev. Plasma Phys., Vol.* 10 (1980), p. 88.

[7] V. Yu. Trakhtengerts, in *Active Experiments in Space, ESA SP-195*, Noordwijk, Netherlands (1983), p. 67.

[8] M. Schulz, Astrophys. and Space Sci. 29, 233 (1974).

[9] R.A. Helliwell, *Whistler and related ionospheric phenomena* (Stanford University press, Stanford, California, 1965).

[10] K.G. Budden, *Radio waves in the Ionosphere* (Cambridge University Press, England, 1961).

[11] G.T. Davidson and Y.T. Chiu, J. Geophys. Res. 91, 13705 (1986).

JOURNAL OF GEOPHYSICAL RESEARCH, VOL. 94, NO. A3, PAGES 2717–2720, MARCH 1, 1989

Ionospheric Electron Acceleration by Electromagnetic Waves Near Regions of Plasma Resonances

ELENA VILLALON[1]

Center for Electromagnetics Research, Northeastern University, Boston, Massachusetts

Electron acceleration by electromagnetic fields propagating in the inhomogeneous ionospheric plasma is investigated. It is found that high-amplitude short wavelength electrostatic waves are generated by the incident electromagnetic fields that penetrate the radio window. These waves can very efficiently transfer their energy to the electrons if the incident frequency is near the second harmonic of the cyclotron frequency.

1. INTRODUCTION

Acceleration of ionospheric electrons by electromagnetic (EM) fields via irradiation either from ground based microwave transmitters [*Wong et al.*, 1981; *Birkmayer et al.*, 1986], or from satellites or rockets [*James*, 1983], is a problem of very active research. This interest is motivated by observations of high-energy electrons by spacecraft in the ionosphere, and this fact can help to improve our understanding of basic properties of wave-particle plasma interactions [*Fejer*, 1979]. Artificially accelerated electrons can also be used as a probe of the potential coupling between the ionosphere and the magnetosphere. We consider an EM monochromatic plane wave of frequency ω and wave vector $\mathbf{k}$ and assume that the wave is launched near the ground at an arbitrary angle with respect to the constant, ambient magnetic field $\mathbf{B}_0$. We take $\mathbf{B}_0$ to be along the z direction, i.e., $\mathbf{B}_0 = B_0\mathbf{e}_z$, and $\mathbf{k} = k_x\mathbf{e}_x + k_z\mathbf{e}_z$. The wave electric field can be written as $\mathbf{E} = \mathbf{e}_x E_1 \cos\phi - \mathbf{e}_y E_2 \sin\phi - \mathbf{e}_z E_3 \cos\phi$, where $\phi = k_x x + k_z z - \omega t$, and E_i are real numbers. The motion of a relativistic electron of charge q and rest mass m is described by the Lorentz force equation

$$d\mathbf{p}/dt = q[\mathbf{E} + \mathbf{v}/c \times (\mathbf{B} + \mathbf{B}_0)] \tag{1}$$

where $\mathbf{B}$ is the wave magnetic field, $\mathbf{v}$ is the particle velocity, and $\mathbf{p} = m\gamma\mathbf{v}$ is the momentum. The relativistic factor is $\gamma = (1 + p_\perp^2/m^2c^2 + p_z^2/m^2c^2)^{1/2}$ where $p_\perp$ and p_z are the momentum components perpendicular and parallel to $\mathbf{B}_0$, respectively. The particle gains energy if the resonance conditions

$$\omega - k_z v_z - n\Omega/\gamma = 0 \tag{2}$$

are closely satisfied. Here n is an integer and $\Omega = -qB_0/mc$ is the electron cyclotron frequency.

Recently, *Villalón and Burke* [1987] have developed a theory in which EM supraluminous (i.e., the refractive index, η, is smaller than one) cold plasma waves accelerate the electrons via resonant stochastic acceleration. That is, by taking ω near 2Ω, they show that the cyclotron resonances overlap at high power levels. It was shown that wave intensities of 10^6 mW/m² accelerate the electrons up to energies of about 100 keV. Numerical integration of (1) shows that for the electrons to reach large energies (in the MeV range) the power levels that are required exceed a value of 10^7 mW/m² [*Burke et al.*, 1988]. Nevertheless, such power levels are at least a factor of 10^6 times greater than what is currently available in ionospheric heating experiments. Thus other more feasible approaches to accelerate cold ionospheric electrons should be investigated.

In this article, we propose a far more effective acceleration mechanism based upon propagation characteristics of EM waves in nonuniform plasmas. If the incident frequency ω is near 2Ω, and if the plasma density is such that ω is between the local upper hybrid, ω_{uh}, and electron plasma, ω_p, frequencies, $\omega_p \le \omega \le \omega_{uh}$, coupling to electrostatic (ES) plasma waves of short wavelength is possible. We show that these waves very efficiently transfer energy to the electrons. We also report calculations relevant to present RF heating experiments by considering a power flux $P = 1$ mW/m². The energy gained by the electrons is obtained by applying the Hamiltonian potential wells theory of *Villalón and Burke* [1987]. At low pump field amplitudes we find that particles gain energy following trajectories in p_z, $p_\perp$ phase space along the zero-order Hamiltonian H_0. For a relativistic particle we have

$$H_0 = mc^2\gamma - (c/\beta_z)p_z \tag{3}$$

where $\beta_z = \eta_z(1 + E_3k_x/E_1k_z)$ and η_z is the component of the refractive index, $\eta = ck/\omega$, along $\mathbf{B}_0$. For electrostatic waves we find that $\beta_z = 0$, and then that the zero-order trajectories are open and the particle gains energy in the direction perpendicular to the background magnetic field, i.e., p_z is constant.

2. ELECTROSTATIC WAVE GENERATION

We consider the propagation of EM waves in a nonuniform, ionospheric plasma. We assume that the density gradient is along the ζ (vertical) direction, that $\mathbf{B}_0$ forms an angle θ with respect to ζ, and that $\mathbf{k}$ is in the plane spanned by ζ and $\mathbf{B}_0$ (see Figure 1). The launching angle with respect to the vertical direction is denoted by ψ. The angle between $\mathbf{k}$ and $\mathbf{B}_0$ is called α and depends on the altitude. The refractive index η has a component Q along the vertical direction and a component S in the horizontal μ direction. We have the relation $\sin(\alpha + \pi/2 - \theta) = Q/\eta$. Because of the horizontally plane stratified ionospheric model considered here, the horizontal component of the refractive index S is a constant independent of the plasma density and then is given by $S = \sin\psi$. The vertical component Q depends on altitude (i.e., on the local plasma density) and can be obtained by solving for the Booker quartic dispersion relation [*Budden*, 1961]. We may choose the angle

[1] Also at Air Force Geophysics Laboratory, Hanscom Air Force Base, Massachusetts.

Paper number 88JA04089.
0148-0227/89/88JA-04089$02.00

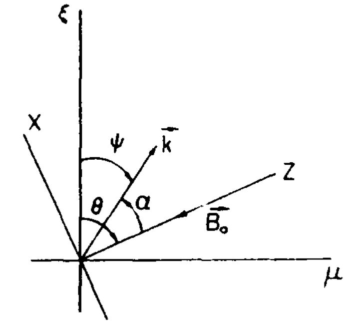

Fig. 1. Coordinate system as introduced in Section 2.

of incidence ψ such that

$$\sin\psi = Y^{1/2}(1+Y)^{-1/2}\sin\theta \qquad (4)$$

where $Y = \Omega/\omega$. If the ordinary (O) mode is launched near the ground at the critical angle given in (4), it will penetrate the radio window and will be transmitted near the coupling level where $\omega = \omega_p$ into the extraordinary mode (also called the Z mode). The transmission coefficient from O to Z modes has been obtained by *Mjølhus* [1984], and it is unity (total transmission) if $S = \sin\psi$ is given by (4). The Z mode propagates in the inhomogeneous plasma of the ionosphere until it falls into the region of high-frequency plasma resonances [*Mjølhus and Fla*, 1984]. Near the plasma resonance: (1) Q becomes very large ($Q \to \infty$), in fact, since $Q \gg S$ we find that $\alpha \to \theta$, (2) the wave becomes electrostatic, i.e., $E_1/E_3 = -\tan\theta$ and $E_2 = 0$, and (3) the vertical group velocity component becomes very small. The plasma density in the resonance region is given by solving for $X = X_r$ where, because $\alpha \to \theta$, we have

$$X_r = (1 - Y^2)(1 - Y^2\cos^2\theta)^{-1} \qquad (5)$$

and $X = \omega_p^2/\omega^2$. Near resonance, the vertical component of the refractive index Q must be calculated by considering a finite temperature plasma. In fact, by adding the lowest order thermal corrections to the coefficients of fourth and third degree of the Booker quartic, we find that Q is given by solving for the real root of the dispersion relation

$$(v_T/c)^2(\Lambda Q^3 + 2\kappa Q^2) - 2\Upsilon = 0 \qquad (6)$$

where

$$\Lambda = 3\cos^4\theta + \frac{3\sin^4\theta}{(1-Y^2)(1-4Y^2)} + \frac{(6-3Y^2+Y^4)}{(1-Y^2)^3}\cos^2\theta\sin^2\theta$$

$$\kappa = S\sin\theta\cos\theta\left\{\cos^2\theta\frac{(-15Y^2+17Y^4-6Y^6)}{(1-Y^2)^3} + \sin^2\theta\frac{(-15Y^2+7Y^4-4Y^6)}{(1-Y^2)^3(1-4Y^2)}\right\}$$

$$\Upsilon = S\sin\theta\cos\theta\frac{Y^2}{(1-Y^2)}$$

and v_T, the electron thermal speed, is such that $v_T/c \ll 1$. A brief sketch on the derivation of (6) is presented in the appendix. The term proportional to Λ was calculated by *Golant and Piliya* [1972], and its contribution is much larger than that proportional to κ if $\Lambda \neq 0$. The case $\Lambda = 0$ has not received any attention yet. Nevertheless, we find that it is of interest, since the refractive indices are larger than when $\Lambda \neq 0$ by a factor of $(c/v_T)^{1/3}$. For a given value of θ, Λ is equal to zero at a certain frequency which is greater than Ω and smaller than 2Ω. In fact, we find that for $\theta \leq 45°$, Λ becomes zero for ω very close to 2Ω. In Figure 2, we show the refractive indices as functions of the angle θ for two values of the incident frequency ω which are smaller than but close to 2Ω; we take $v_T/c = 0.25 \times 10^{-3}$. The largest Q are found near $\theta = \theta_c$, where θ_c is such that $\Lambda(\theta_c, \omega) = 0$. We have that for $\omega = 1.81\ \Omega$, $\theta_c = 43.6°$ and $Q = \pm 563$, and that for $\omega = 1.92\ \Omega$, $\theta_c = 32.7°$ and $Q = \pm 460$.

The Landau damping rate Γ due to the Doppler shifted frequency at the second harmonic is (see the appendix)

$$\Gamma/\omega = -(1/16)(\pi/2)^{1/2}(v_T/c)Q(\sin^4\theta/\cos\theta)(\sigma/Y^4) \cdot \exp\{-(\omega-2\Omega)^2/2(k_z v_T)^2\} \qquad (7)$$

where $\sigma = (1 - Y^2)/(X_r^{-1} - Y^2\cos^2\theta)$. We see that if $\Lambda \neq 0$, Γ/ω is of order $(v_T/c)^{1/3}$, but if $\Lambda = 0$, then $\Gamma/\omega \sim O(1)$.

The components of the group velocity along the vertical, $v_{g\xi}$, and horizontal, $v_{g\mu}$, directions are readily obtained from (6), we show

$$v_{g\xi}/c = \tfrac{1}{2}(v_T/c)^2(3\Lambda Q + 4\kappa)\sigma \qquad (8)$$

$$v_{g\mu}/c = -\tfrac{1}{2}(v_T/c)^2\Lambda Q^2\sigma S \qquad (9)$$

If $\Lambda \neq 0$, we find that $v_{g\xi}/v_{g\mu} \sim O(Q^{-1})$, and then that the wave propagates in the direction perpendicular to the density gradient, but if $\Lambda = 0$, then $v_{g\mu} = 0$. However, by adding to (6) a third thermal correction of the form $(v_T/c)^2 \nu Q$, where ν is a function of θ and Y, we show that $v_{g\mu}$ is proportional to $(v_T/c)^2\nu$, when $\Lambda = 0$. Thus $v_{g\xi}$ and $v_{g\mu}$ become of the same order of magnitude and much smaller than $v_{g\mu}$ for the case $\Lambda \neq 0$. The amplitude of the time-averaged electric field can be obtained solving for

$$P = (c/16\pi)(v_T/c)^2(3\Lambda Q + 4\kappa)X_r|E|^2 \qquad (10)$$

Here P is the vertical component of the energy flux density. The highest energy concentration occurs when the group velocity is the smallest.

3. ELECTRON ACCELERATION

Assuming that Γ is small, the energy that a single electron may gain interacting with a general EM plane wave of the

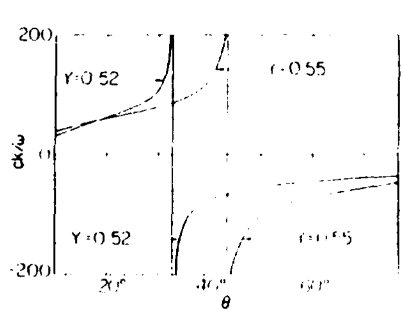

Fig. 2. Refractive indices in the plasma resonance regions as functions of the angle θ between the ambient magnetic field and the vertical for two values of $Y = \Omega/\omega$.

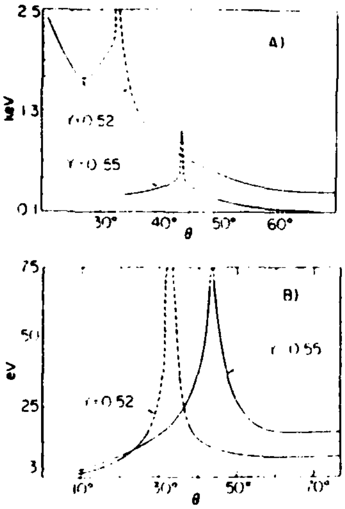

Fig. 3 Net energy gain as function of the angle θ between the ambient magnetic field and the vertical. We consider two values of $Y = \Omega/\omega$ and the interaction of cold electrons with (a) the $n = 2$, and (b) the $n = 1$ cyclotron resonances

form given before (1), has been obtained as a function of time in the article by *Villalón and Burke* [1987]. It was found that the normalized particle energy U is obtained solving for

$$(U + 1)^2(dU/d\tau)^2 + V_n(U) = 0 \tag{11}$$

where $U = \gamma - 1$, and time is normalized to number of wave-periods, $\tau = t\omega$. Here we consider the electron interaction with a single (isolated) cyclotron resonance of order n. For a particle initially ($\tau = 0$) at rest interacting with the ES waves ($E_1/E_3 = -\tan\theta$, and $E_2 = 0$) that are generated near resonance, the Hamiltonian potentials may be written as

$$V_n(U) = \tfrac{1}{4}U^2(U + 2r_n)^2 - \Sigma^2 \cos^2\theta K_n(U) - \Sigma^2\, 2\sin^2\theta[K_{n+1}(U) + K_{n-1}(U)] \tag{12}$$

with $r_n = 1 - nY$, $\Sigma = -q|\mathbf{E}|/mc\omega$, and

$$K_n(U) = \int_0^U J_n^2(k_\perp\rho')(U' + 1)\, dU'$$

Here $J_n(k_\perp\rho)$ are Bessel functions and ρ' is the Larmor radius evaluated at U'; we have $\rho = c/\Omega\,[2U + U^2]^{1/2}$. The allowable energies are restricted by the condition $V_n(U) \leq 0$. Note that the first term in (12) is always positive and dominates over all the others at large values of U. Thus $V_n(U)$ can be regarded as a potential well within which the particle's energy oscillates in time. The kinetic energy slowly increases over many cyclotron and wave periods, and the net energy gained by the particle has always a finite value. If $V_n(U) < 0$ when $U \to 0$, the potential can trap zero kinetic energy particles; these particles may increase their energy up to a value $U = U_0$ such that $V_n(U_0) = 0$. If $V_n(U) > 0$ when $U \to 0$, then the potential cannot trap zero kinetic energy particles.

4 Numerical Calculations

In Figure 3a, we represent the net energy gained by the electrons (in keV) due to the interaction with the $n = 2$ cyclotron resonance, as function of θ. These energies are calculated by solving for the zeros of the Hamiltonian potentials. We consider two values of ω and a power flux $P = 1$ mW/m². The amplitudes of the ES fields are obtained from (10). We see that the $n = 2$ resonance can only trap cold electrons for angles greater than 20° if $\omega = 1.92\ \Omega$ ($Y = 0.52$), and 34° if $\omega = 1.81\ \Omega$ ($Y = 0.55$). The broken lines near the $\theta = \theta_*$, which makes $\Lambda = 0$, indicate that $\zeta = |\omega - 2\Omega|/k_z v_t \leq 2$ and that $\Gamma/\omega \sim O(1)$. Thus the energy of the ES fields is strongly absorbed by the bulk distribution of plasma electrons. The kinetic energies reached by the electrons are very large due to the enhanced electric fields and large values of η near $\theta = \theta_*$. For larger values of ζ (solid lines), we find that Γ/ω is very small (i.e., $\Gamma/\omega < 2 \times 10^{-4}$), and hence that only a few electrons in the tail of the distribution function may interact with the waves. These electrons are accelerated in the direction perpendicular to the constant magnetic field up to energies of the order of hundreds of electron volts. Note that in the Earth's dipole magnetic field the mirroring force acting on the electrons will also accelerate them along geomagnetic field lines. The interaction of cold electrons with the $n = 1$ resonance takes place for all values of θ. The net energy gain (in eV) is represented in Figure 3b, and is quite small if $\theta \neq \theta_*$. This is because the resonance condition (2) is far from being satisfied for $\omega \gtrsim 2\Omega$, $n = 1$, and initially cold electrons.

The time it takes to reach these energies can be calculated with the help of (11) and (12). We start with the $n = 1$ cyclotron resonance and cold electrons until the potential becomes positive; then, if there is overlapping with the $n = 2$ resonance, the particles are accelerated to high energies. For example, for $\omega = 1.92\ \Omega$ and $\theta = 23°$, it takes 168 wave periods (WP) to gain 2 keV, where half of this time is spent reaching the first 100 eV. If $\theta = 43°$ the electrons gain 800 eV over 86 WP (see Figure 4a). As a second example, we consider $\omega = 1.81\ \Omega$; if $\theta = 37°$, it takes 35 WP to gain 350 eV, but if $\theta = 46°$, then it only takes 25 WP to reach the same energy (see Figure 4b). Although the first and second cyclotron resonances may overlap over a broad range in energies, we find that we can neglect the contribution of the $n = 2$ resonance in the overlapping region. In fact, if $\omega = 1.81\ \Omega$ and $\theta = 37°$ it takes 43 WP to reach the first 28 eV with the $n = 2$ resonance, but it only takes 7 WP with the $n = 1$. On average we find that, in Gaussian units, the amplitude of the electric fields are about 0.005 times the ambient magnetic field.

5 Concluding Remarks

In this article, we have investigated the possibility of accelerating ionospheric electrons in intense electromagnetic (EM) fields. We have presented a very efficient acceleration and heating mechanism which consists in the generation of short-wavelength, high-amplitude electrostatic (ES) fields by the incident EM waves that penetrate the radio window. By including thermal effects, we have derived the dispersion relation for these ES fields; analytical expressions are given for their group velocities and damping rates. Because of the very small group velocity components in both the vertical and horizontal directions, the electromagnetic energy is highly concentrated in a region of plasma resonance. The effectiveness of this mechanism depends on the value of the incident frequency ω and on the angle θ that the background magnetic field forms with the vertical direction. Calculations on single particle acceleration show that the electrons can gain 1 or 2 keV for moderate (1 mW/m²) power levels if, for small values of θ, ω is chosen slightly below the second gyroharmonic.

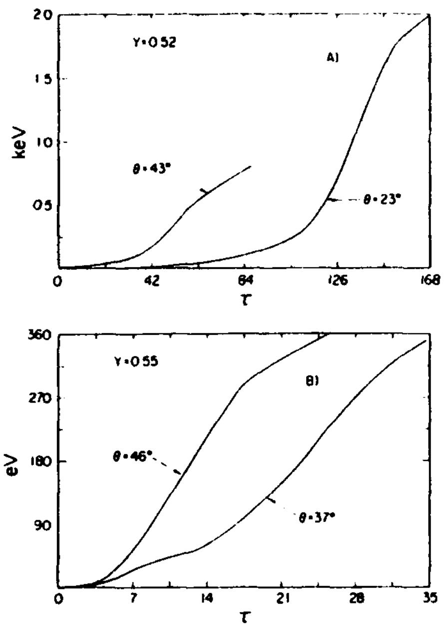

Fig. 4. Energy gain as function of time τ normalized to number of wave periods. Here θ is the angle between the ambient magnetic field and the vertical and $Y = \Omega/\omega$. The energy is given in (a) KeV, and (b) eV.

Appendix

For electrostatic waves the dielectric response function is

$$\mathscr{D} = \eta^4(\varepsilon_{11}\sin^2\alpha + \varepsilon_{33}\cos^2\alpha + 2\varepsilon_{13}\cos\alpha\sin\alpha) \tag{A1}$$

where ε_{ij} are components of the dielectric tensor (the row is indicated by the subscript i and the column by j) which can be found elsewhere [*Ichimaru*, 1973]. Next, we expand ε_{ij} in powers of the small quantities $(k_\perp v_T/\Omega)^2$ and $[(\omega - n\Omega)/k_z v_T]^{-1}$, where $n = 0, 1, 2$ and $k_\perp = k\sin\theta$, $k_z = k\cos\theta$ are the perpendicular and parallel components to $\mathbf{B}_0$ of the wave vector. By keeping only first-order terms in $(v_T/c)^2$, we find

$$\varepsilon_{11} = 1 - \frac{X}{(1 - Y^2)} - \eta^2\left(\frac{v_T}{c}\right)^2 X\left(\frac{3\sin^2\alpha}{(1 - Y^2)(1 - 4Y^2)}\right.$$

$$\left. + \cos^2\alpha\frac{(1 + 3Y^2)}{(1 - Y^2)^3} - \frac{i}{2}\frac{\sin^2\alpha}{Y^2(1 - 2Y)}W_i\right) \tag{A2}$$

$$\varepsilon_{33} = 1 - X - \eta^2\left(\frac{v_T}{c}\right)^2 X\left(\frac{\sin^2\alpha}{(1 - Y^2)} + 3\cos^2\alpha\right.$$

$$\left. - \frac{i}{8}\frac{\sin^4\alpha}{\cos^2\alpha}\frac{(1 - 2Y)}{Y^4}W_i\right) \tag{A3}$$

$$\varepsilon_{13} = \eta^2\left(\frac{v_T}{c}\right)^2 X\left(\frac{2\cos\alpha\sin\alpha}{(1 - Y^2)^2} + \frac{i}{4}\frac{\sin^3\alpha}{Y^3\cos\alpha}W_i\right) \tag{A4}$$

where

$$W_i = \sqrt{\frac{\pi}{2}}\frac{(1 - 2Y)}{|k_z|v_T\omega}\exp\left(-\left(\frac{\omega - 2\Omega}{2^{1/2}k_z v_T}\right)^2\right)$$

By considering that $\cos\alpha = (S\sin\theta + Q\cos\theta)/\eta$ with $Q \gg S$, and by keeping the higher-order powers in Q, we may write $\mathscr{D} = \mathscr{D}_R + i\mathscr{D}_I$, where

$$\mathscr{D}_R = Q^4\left[\varepsilon_{\zeta\zeta} - \left(\frac{v_T}{c}\right)^2(\Lambda Q^2 + 2\kappa Q)X + \frac{2\Upsilon X}{Q}\right] \tag{A5}$$

Here $\varepsilon_{\zeta\zeta} = 1 - X/X_r$, where X_r is given in (5) and Λ, κ, and Υ are given after (6). By taking $\varepsilon_{\zeta\zeta}$ very small and setting $\mathscr{D}_R = 0$, we obtain the dispersion relation (6). We also have

$$\mathscr{D}_I = -\frac{1}{8}\left(\frac{\pi}{2}\right)^{1/2}\left(\frac{v_T}{c}\right)Q^5\frac{\sin^4\theta}{|\cos\theta|}\frac{X}{Y^4}\exp\left[-\left(\frac{\omega - 2\Omega}{2^{1/2}k_z v_T}\right)^2\right] \tag{A6}$$

The components of the group velocity $v_{g\zeta}$, $v_{g\mu}$ in (8) and (9) are obtained by defining $\mathscr{K}_R = \mathscr{D}_R/Q^4$, and then

$$\mathbf{v}_g = -\frac{(\partial\mathscr{K}_R/\partial\mathbf{k})}{(\partial\mathscr{K}_R/\partial\omega)} \tag{A7}$$

where recall that $ck_\zeta/\omega = Q$ and $ck_\mu/\omega = S$. The Landau damping rate at the second cyclotron harmonic is also obtained by considering that $\mathscr{K}_I = \mathscr{D}_I/Q^4$ and then that $\Gamma = -\mathscr{K}_I/(\partial\mathscr{K}_R/\partial\omega)$. Here $\partial\mathscr{K}_R/\partial\omega \simeq \partial\varepsilon_{\zeta\zeta}/\partial\omega = 2X/\omega\sigma$, where σ is defined after (7).

Acknowledgments. The author is grateful to A. Y. Wong for drawing her attention to the problem of propagation through the radio window, and for very helpful discussions. We also acknowledge helpful conversations with W. J. Burke and E. Molhus. This work has been supported by the U.S. Air Force under contract F19628-85-K-0053.

The Editor thanks I. Kimura and another referee for their assistance in evaluating this paper.

References

Birkmayer, W., T. Hagfors, and W. Kofman, Small-scale plasma density depletions in Arecibo high-frequency modification experiments, *Phys. Rev. Lett.*, *57*, 1008, 1986.

Budden, K. G., *Radio Waves in the Ionosphere*, Cambridge University Press, New York, 1961.

Burke, W. J., G. Ginet, E. Villalón, and M. A. Heinemann, Electron acceleration in the ionosphere by obliquely propagating electromagnetic waves, *J. Geomagn. Geoelec.*, *40*, 1147, 1988.

Fejer, J. A., Ionospheric modification and parametric instabilities, *Rev. Geophys.*, *17*, 135, 1979.

Golant, V. E., and A. D. Piliya, Linear transformation and absorption of waves in a plasma, *Sov. Phys. Usp.*, Engl. Transl., *14*, 413, 1972.

Ichimaru, S., *Basic Principles of Plasma Physics: A Statistical Approach*, W. A. Benjamin, Reading, Mass., 1973.

James, H. G., Sounder-accelerated particles observed in ISIS, *J. Geophys. Res.*, *88*, 4027, 1983.

Mjølhus, E., Coupling to Z mode near critical angle, *J. Plasma Phys.*, *31*, part 1, 7, 1984.

Mjølhus, E., and T. Flå, Direct access to plasma resonance in ionospheric radio experiments, *J. Geophys. Res.*, *89*, 3921, 1984.

Villalón, E., and W. J. Burke, Relativistic particle acceleration by obliquely propagating electromagnetic fields, *Phys. Fluids*, *30*, 3695, 1987.

Wong, A. Y., J. Santoru, and G. G. Sivjee, Active simulation on the auroral plasma, *J. Geophys. Res.*, *86*, 7718, 1981.

E. Villalón, Center for Electromagnetic Research, Northeastern University, Boston, MA 02115.

(Received May 27, 1988;
revised November 14, 1988;
accepted November 14, 1988.)

JOURNAL OF GEOPHYSICAL RESEARCH, VOL. 95, NO. A5, PAGES 6451-6466, MAY 1, 1990

Electron Dispersion Events in the Morningside Auroral Zone and Their Relationship With VLF Emissions

David A. Hardy and William J. Burke

Space Physics Division, Air Force Geophysics Laboratory, Hanscom Air Force Base, Massachusetts

Elena Villalon

Center for Electromagnetics Research, Northeastern University, Boston, Massachusetts

Energy/time dispersion events have been observed in the precipitating electron data in the energy range from 630 eV to 20 keV recorded by the J sensor on the low-altitude, polar-orbiting HILAT satellite. The dispersions are such that the higher-energy electrons are observed earlier in time than the lower-energy electrons. The time interval for a single dispersion event is from 1 to 2 s. Within an auroral pass in which such energy/time dispersion events are observed, there are typically several such events, and they can be spaced within the pass in either a periodic or aperiodic manner. The events are typically observed within and toward the equatorward edge of the region of diffuse auroral electron precipitation. During a given pass the events can be observed over a wide range of L shells. The occurrence of these events maximizes in the interval 0600-1200 hours MLT. The energy/time dispersion is generally consistent with the electrons originating from a common source. The events are seen at L shells from 3.7 to greater than 15. The source distance for the electrons is inferred to be generally beyond the equator for events at L shells less than approximately 8 and before the equator for events at higher L shells. Because of the low energies at which the dispersions are observed, it is unlikely that their occurrence can be explained by resonant interaction with VLF waves. Based on circumstantial evidence from other reported observations common to the morning sector, an alternative theoretical explanation is presented. According to this model the dispersion events result from impulsive interactions of the electrons with intense, asymmetric packets of VLF waves via the nonlinear, ponderomotive force.

1. Introduction

The characteristics of VLF chorus emissions and the role such emissions play in electron pitch angle scattering and precipitation have long been a significant area of research. These emissions have been observed at both low altitudes over the auroral zone and high altitudes in the inner magnetosphere [*Dunkel and Helliwell*, 1969; *Russell et al.*, 1969; *Tsurutani and Smith*, 1974; *Burton and Holzer*, 1974; *Thorne et al.*, 1974, 1977; *Tsurutani and Smith*, 1977]. Chorus consists of many band-limited, randomly occurring, rising or falling tones each lasting a few tenths of a second. The frequency band for chorus lies above and/or below half the equatorial electron gyrofrequency. When both bands are present, there is usually a gap with no measurable waves near half the electron cyclotron frequency. The origin of this gap is still poorly understood [*Anderson and Maeda*, 1977].

Chorus emissions are confined primarily to the morningside of the magnetosphere over an L shell range from just outside the plasmapause to just inside the magnetopause. Within this region the occurrence frequency has two maxima, one slightly postmidnight and the other between 0600 and 1200 MLT. The emissions occur primarily at latitudes close to the magnetic equator. However, a second region of emissions at higher latitudes is observed in the 0600-1200 MLT sector for L shells near the magnetopause. Chorus is generated on field lines either directly populated with hot electrons injected into the inner magnetosphere during substorms or populated by hot electrons that have been transported to later local times after substorm injection.

A class of particle precipitation events called "microbursts" are associated with chorus emissions [*Venkatesan et al.*, 1968; *Oliven et al.*, 1968; *Oliven and Gurnett*, 1968]. They consist of spikes of energetic electron precipitation lasting a few tenths of a second and occurring over a small spatial extent. As with chorus emissions, the microbursts' occurrence frequency maximizes for L shells between 4 and 8.5 and MLTs between 0600 and 1200. The amplitudes of VLF waves measured in association with microbursts covered the entire 0.001- to 0.03-nT range of the INJUN 3 loop antenna [*Oliven and Gurnett*, 1968].

The most detailed work relating chorus emissions to microbursts has been done using data from the magnetically conjugate stations at Roberval, Canada, and Siple Station, Antarctica [*Rosenberg et al.*, 1971; *Foster and Rosenberg*, 1976; *Helliwell and Mende*, 1980; *Rosenberg et al.*, 1981]. These studies have established a clear relationship between discrete chorus elements and the precipitation of high-energy electrons inferred from either balloon-borne X ray detectors or ground-based optical systems. The measurements indicate a source region for the particles within 20° of the magnetic equator. In addition, *Rosenberg and Dudeney* [1986] have shown that the average level of high-energy electron precipitation at $L = 4.1$ during active times, deduced from riometer measurements, displays the same local time distribution as VLF emissions. In situ measurements near geosynchronous altitude have established good correlations between high-energy electron flux enhancements associated with substorm injections and the occurrence of chorus emissions [*Isenberg et al.*, 1982].

Paper number 89JA01235.
0148-0227/90/89JA-01235$05.00

Chorus emissions are thought to result from resonant interactions between energetic electrons and electromagnetic waves that are Doppler shifted to some harmonic of the electron gyrofrequency [*Kennel and Petschek*, 1966; *Kennel and Engelmann*, 1966; *Kennel et al.*, 1970]. Coherent emission may be produced by resonant, cyclotron emissions from phase-bunched electrons [*Helliwell*, 1967; *Helliwell and Crystal*, 1973]. These theoretical explanations predict that the wave-particle interactions take place near the magnetic equator for energies above a minimum resonant energy given by

$$E_{min} = B^2/[8\pi n A(A+1)]$$

where B is the equatorial field strength, n the plasma density, and A the anisotropy exponent whose typical value lies between 0.1 and 0.5 [*Davidson*, 1986*a*].

As pointed out by *Davidson* [1986*a*], these theoretical models successfully account for the precipitation of relatively high energy electrons ($E > 20$ keV) but not for precipitation in the low keV range. For the cases of microbursts seen at $L = 4.1$ [*Foster and Rosenberg*, 1976; *Helliwell and Mende*, 1980; *Rosenberg et al.*, 1981], plasma densities in the source region of the interaction are reported in the range from 10 to 50 cm^{-3}. For a density of 10 the minimum resonance energy varies from 560 to 82 keV for anisotropy exponents from 0.1 to 0.5. For densities of 50 cm^{-3} the resonance energy varies from 110 to 16.4 keV. Using data from the SCATHA satellite, *Isenberg et al.* [1982] estimated resonant energies in the range from 15 to 30 keV for radial distances between 5.5 and 6.3 R_E. At geosynchronous altitude, precipitation of electrons of 1 keV energy in the 0600 to 1200 MLT sector would require densities in excess of 10 cm^{-3} while the measured density is in the range from 0.1 to 8 cm^{-3} with typical values of a few per cubic centimeter [*Higel and Wu*, 1984].

In this paper we report on observations of electron precipitation bursts observed in the morningside auroral zone with the J sensor, an electron detector on the HILAT satellite. Although these bursts exhibit a distribution in MLT and L shell similar to microbursts and VLF chorus, they are typically observed for energies from the 20-keV upper energy limit of the HILAT detector down to a few keV and as low as 600 eV on occasion. The low energies of the electrons are shown to be difficult to reconcile with precipitation via resonant interactions with VLF waves. The fact that they occur preferentially in the region of enhanced VLF chorus suggests, however, that such waves may play a role in their precipitation. We first document the characteristics of these precipitation events and then present the outlines of a theoretical model that could account for their observed properties.

2. INSTRUMENTATION

Data used in this study are from the J sensor that was flown as part of the experiment complement on the HILAT satellite [*Hardy et al.*, 1984]. The J sensor consists of an array of six cylindrical curved-plate, electrostatic analyzers arranged into three pairs. In each pair there is a high-energy head measuring electrons from 630 eV to 20 keV and a low-energy head measuring from 20 eV to 630 eV. In both the high- and low-energy heads the energy range is covered in eight channels spaced at equal logarithmic intervals in energy. The channels are stepped simultaneously in the two heads such that a complete 16-point spectrum is returned at each voltage sweep. The peak geometric factors for the high- and low-energy heads are 8.50×10^{-4} and 2.25×10^{-4} cm^2 sr, respectively, with a $\Delta E/E$ of approximately 10%. The three pairs are oriented on the spacecraft with look directions toward the local zenith, 40° from the zenith, and toward the local nadir.

The J sensor has three operating modes. In mode 3 a full 16-point spectrum is returned by each pair of sensors four times per second. In mode 2 a full 16-point spectrum is returned from just the zenith-looking pair, 12 times per second. In mode 1 an eight-point spectrum is returned from the zenith-looking detector and in the energy range from 20 eV to 630 eV, 24 times per second. In this study, only the mode 2 and 3 data were used.

HILAT was launched in June 1983 into an 830 km, circular orbit at an inclination of 82.3°. The satellite is three axis gravity-gradient stabilized such that the look directions of the J sensors are reasonably fixed relative to the local zenith. The satellite precesses approximately 3° per day in local time such that all local times are samples every four months.

Because HILAT has no on-board tape recorder, data are acquired only when the satellite is within range of one of four ground stations. For this study the ground stations were located at Sondre Stromfjord, Greenland; Tromso, Norway; Fort Churchill, Canada; and Seattle, Washington. Approximately six HILAT overpasses per day are recorded at each station. The reported events occurred primarily within and toward the equatorward edge of diffuse auroral precipitation in the 0600–1200 MLT sector. Because of Tromso's location in latitude, the data recorded at this site most consistently covered the region of interest. Time versus energy dispersion events were seen, however, in data retrieved at all of the recording stations.

3. OBSERVATIONS

The observation section is divided into two parts. In the first part, J sensor data for several HILAT passes are presented to illustrate the detailed characteristics of the dispersion events. In the second part we summarize the observed distributions of events according to L shell, magnetic local time, and source distance.

3.1. *Detailed Event Analysis*

In this subsection we examine typical examples of the energy/time dispersion events recorded during three HILAT passes. These examples are used (1) to illustrate the range of event characteristics, (2) to examine event locations relative to identifiable auroral precipitation regions, and (3) to identify the roles these dispersions play in the dayside precipitation of diffuse auroral electrons.

The first pass occurred between 0435 and 0440 UT on Julian day 186, 1984, over the Tromso recording station. During this period the satellite moved equatorward, approximately along the 0800 MLT meridian from 78.5° to 6[illegible]° corrected geomagnetic latitude (CGL). Measurements from the mode 2 operation of the J sensor are shown in Plate 1 in color spectrogram format. (Plate 1 is shown here in black and white. The color version can be found in the special color section in this issue.) In the spectrogram each panel displays data from 600 spectra covering a 50 s interval

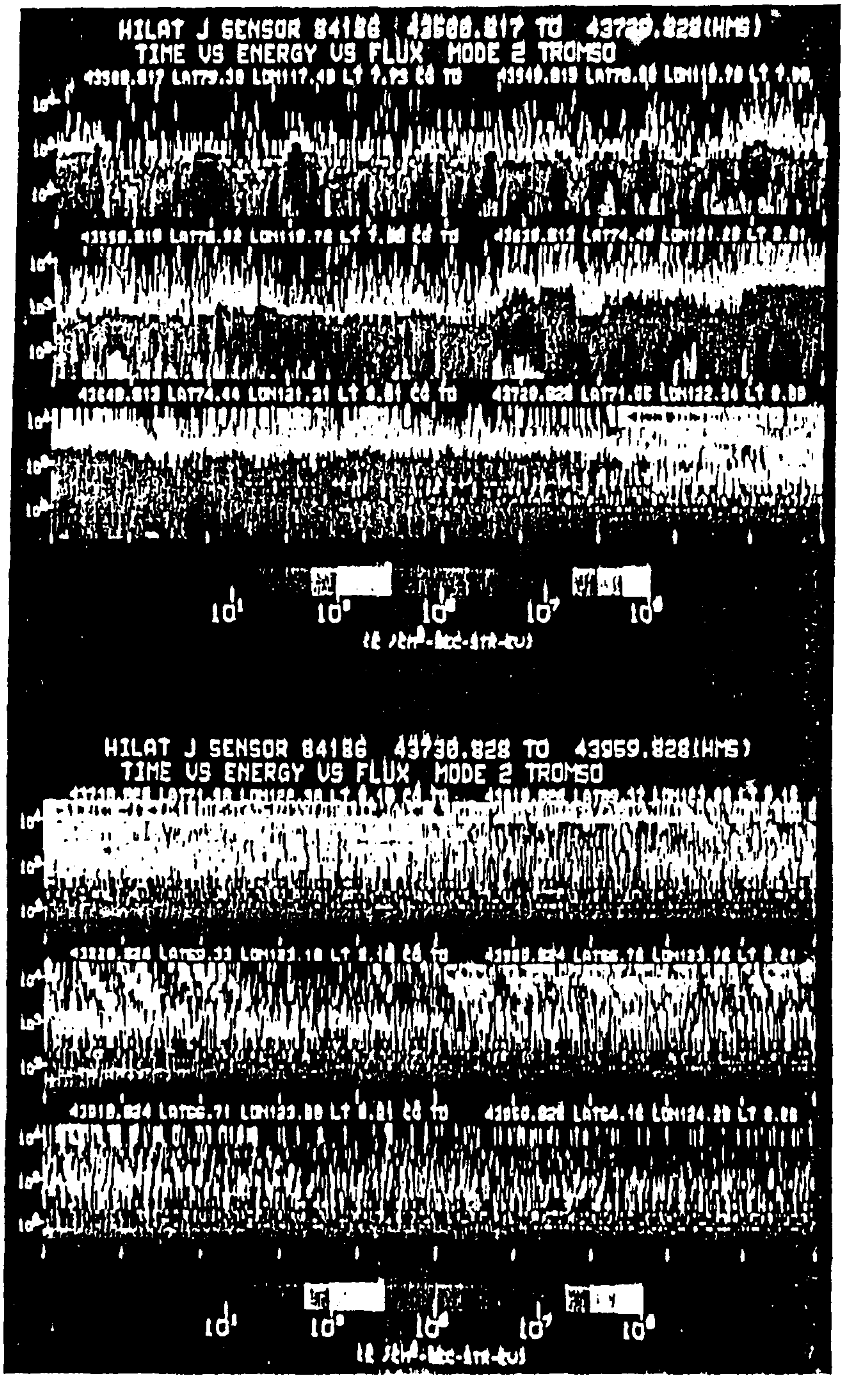

Plate 1. The differential number flux for electrons as measured by the J sensor for the Tromso pass occurring on Julian day 186, 1984, over the interval 0435–0440 UT. The J sensor was operating in mode 2. Each panel contains 50 s of data and is annotated with the universal time in hours, minutes, and seconds, and the geomagnetic latitude, longitude, and local time at the beginning and end of each 50 s interval. The color version of this figure can be found in the separate color section in this issue.

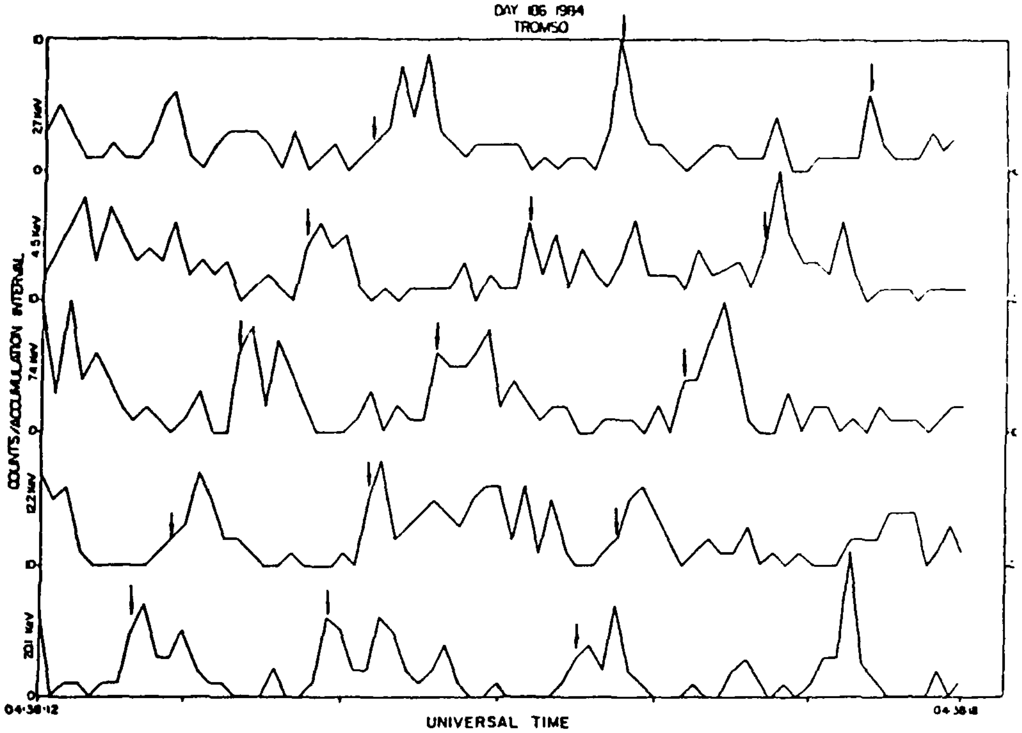

Fig. 1. The counts per accumulation interval plotted versus time for the five highest-energy channels of the J sensor for the time interval 0438:12–0438:18 UT.

Over the pass, significant variations in the electron spectra occurred. At the beginning of the interval, measurable fluxes of electrons were confined to energies generally below 1 keV and were temporarily and/or spatially highly variable in intensity. Such precipitation is characteristic of the cusp or cleft regions. At lower latitudes the spectra initially hardened, and the variability and intensity of fluxes below 1 keV decreased. Significant fluxes of electrons at energies above 1 keV were observed starting at approximately 0435:42 UT with a more continuous hardening of the spectrum beginning at 0436:20 UT. The spectral hardness reached a maximum at 0436:40 UT, after which the flux at energies below a few keV began to decrease. We interpret the spectral hardening and subsequent decrease in low-energy variability and intensity as the signature of the satellite passage from the cusp/cleft into the dayside diffuse auroral region.

In the interval after 0436:40 UT, patches of high-energy electron were detected. The occurrence and intensity of these patches appear unrelated to the overall decrease in intensity of the lower-energy electrons. This is particularly evident starting at 0437:20 UT when at low energies a weak, monotonically decreasing spectrum, produced primarily by photoelectrons, is observed along with a band of precipitation at energies above 10 keV.

It is within these regions of patchy, high-energy precipitation that energy/time dispersion events are observed. By energy/time dispersion events, we mean enhancements in the higher-energy electrons that are followed at later times by similar enhancements at lower energies. In the color spectrogram these appear as diagonal stripes. For this pass dispersion events occurred sporadically from approximately 0437:30 to 0439:10 UT and were particularly evident between 0438:20 and 0438:30 UT.

A detailed example of the dispersion events is shown in Figure 1, where the counts per accumulation interval are plotted for the five highest-energy channels for 6 s starting at 0438:12 UT. In this interval, three enhancements occurred in each channel and are marked by sequences of arrows. We define the onset of the enhancement in each channel as the point where the count rate exceeded 1 per accumulation interval. The data illustrate four points. First, enhancements occur in all five channels, with the time separations of the enhancements between consecutive channels increasing with decreasing energy. Second, the time separation between the enhancements in consecutive channels and the total time separation from the highest- to the lowest-energy channel are approximately the same for the three events. Third, the onset of enhancements occurs with an approximate periodicity of 1.5 s. Lastly, within each of the three events there are shorter time scale structures that are repeated in many or all of the energy channels. For example, during the first event there are two peaks with a time separation of approximately $\frac{1}{6}$ s in every channel except the one centered at 122 keV. Similarly, in the second event, three peaks are repeatein four of the five plotted channels. The temporal widths and repeat frequencies of these events are similar to those reported for microburst events [*Oliven et al.*, 1968; *Helliwell and Mende*, 1980].

There are two hypotheses that could explain such dispersions. The first hypothesis is that electrons of all energies were impulsively scattered simultaneously into the atmospheric loss cone at some point along the field lines of detection and that the dispersion resulted from the different transit times of the electrons along the field line from the source region to the point of observation. In this case the time delays in detecting electrons of different energies can be used to estimate the location at which the "impulses" originated. The second hypothesis is that electrons at higher energies are scattered into the loss cone near the equator before electrons at lower energies such that the dispersion results from a combination of the difference in time of injection and the difference of transit times along the field line for electrons at different energies. In the discussion section we show that the second hypothesis appears to be inconsistent with wave and/or cold plasma measurements in the magnetosphere. Here we only consider the first hypothesis.

These observed dispersion events are consistent with the first hypothesis discussed above. For this case the difference in arrival time, Δt, for electrons coming from a common source with parallel velocities v_1 and v_2, is related to the distance to the source, d, by the equation

$$d = \Delta t(1/v_1 - 1/v_2)^{-1}$$

In Figure 2 we show an example of the observed time delays. Here Δt is plotted as a function of the electron velocity for the third energy/time dispersion event of Figure 1. For this example, Δt was calculated as the time difference from the onset of the enhancement in the 20.1-keV channel, and the electron velocities were calculated for the central energy in each channel. The solid line is the best fit source distance d to the observed values of Δt. We find that a source distance of 92,000 km fits the data extremely well. A similar quality of fit is found for a majority of the other observed dispersion events.

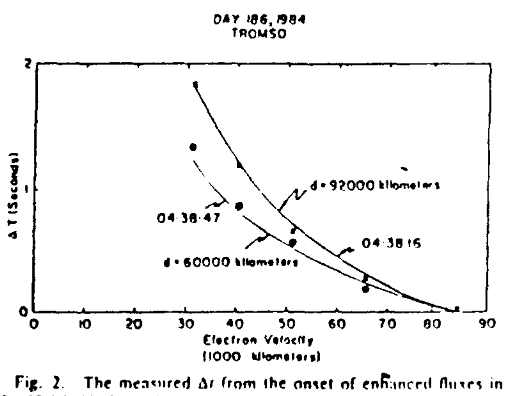

Fig. 2. The measured Δt from the onset of enhanced fluxes in the 20.1-keV channel plotted versus the electron velocity for two events for the day 186 pass. Crosses and circles give the measured values of Δt and the solid line gives the best fit to a single source distance, d.

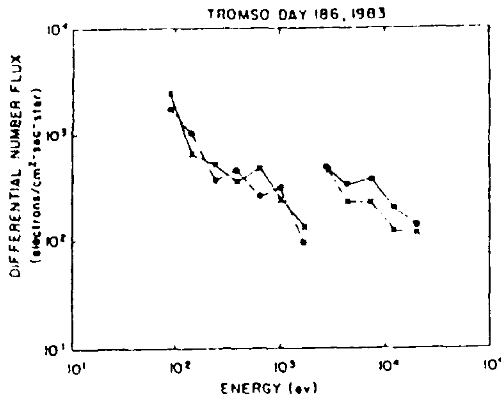

Fig. 3. The inferred differential number flux source spectrum for the two dispersion events starting at 0438:25 UT on day 186.

The energy/time dispersion event of Figure 1 occurred at 69.75° CGL and an L shell of 8.4. Using either the simple dipole or the Mead-Fairfield models gives a distance along the magnetic field line from HILAT to the equator of approximately 70,000 km. The fitted source distance of 92,000 km implies a source region about 22,000 km south of the magnetic equator. This is a general characteristic of the phenomenon.

For impulsive scattering of the electrons the widths of pulses observed at HILAT depend both on the extent of the scattering region along magnetic field lines and on the duration of the scattering interactions. The width of a pulse will vary with the interaction region length W as W/v, where v is the parallel velocity of the electron. Assuming that the interaction region is the same for electrons at all energies and that the source region is 10,000 km in extent, then the pulse widths should increase from approximately $\frac{1}{8}$ to $\frac{1}{2}$ s for electron energies from 20.1 to 1 keV. Width variations of this magnitude would be easily discernable for the J sensor operating in mode 2. The widths of pulses resulting only from the durations of the interactions would have no velocity dependence.

For the dispersion events shown in Figure 1 there is no width increase with decreasing energy. If anything, the width decreases with decreasing energy as is the general characteristic of the events. This suggests that the pulse shape is defined primarily by the duration of the scattering process and that the interaction region is at most a few thousand kilometers in extent.

Since the observed dispersions appear to be consistent with a common source for the particles, the low-altitude flux measurements can be used to reconstruct the source spectrum. Such reconstructed spectra are plotted in Figure 3 for the dispersion events starting at 0438:25 UT. At high energies the flux was calculated by averaging over the time the flux was enhanced in each channel. At energies lower than where dispersion was observed, the flux was averaged over the entire time interval.

For both spectra in Figure 3, at energies below the dispersion, the flux decreased, roughly monotonically, with increasing energy. For the lowest energy channel of the

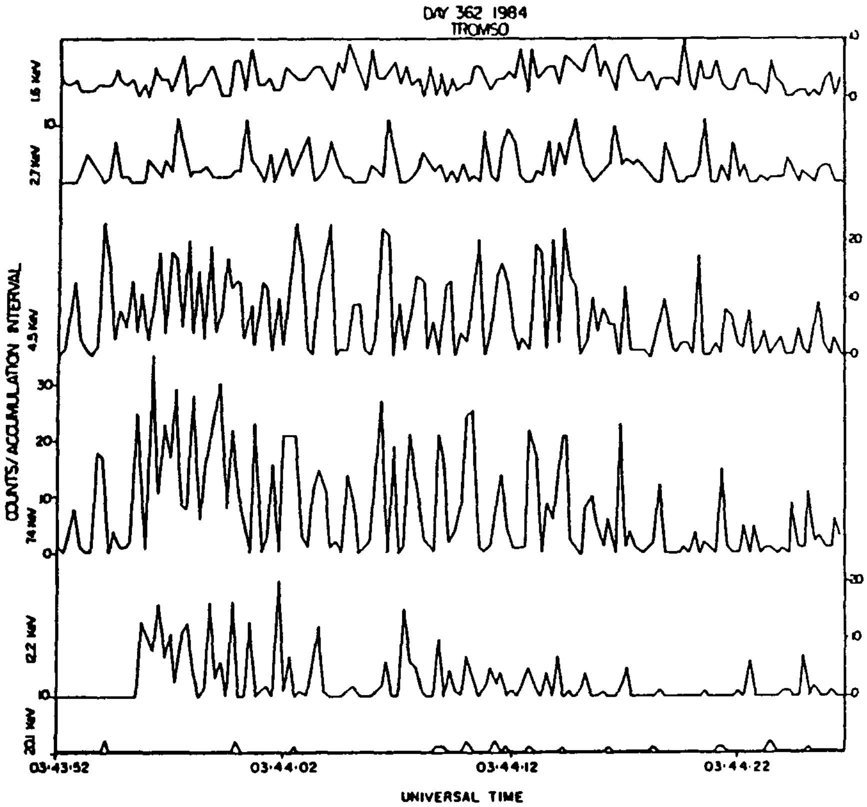

Fig. 4. A plot as in Figure 1 for the zenith-looking detector for the time interval 0342:22–0342:55 UT for the Tromso pass on Julian day 362, 1983.

dispersive part of the spectra, the flux increased by a factor of 4–5 and then decreased monotonically for increasing energy. Integrating over the portion of the spectrum above 2.73 keV and assuming the flux to be isotropic for pitch angles from 0° to 90° gives a total precipitating energy flux of 0.20–0.27 erg/(cm^2 s). If the measured portion of the spectrum is fit to a power law and extrapolated to higher energies, the energy flux values increase by about a factor of 2. Energy fluxes on the level of 0.5 erg/(cm^2 s) should be sufficient to produce visible optical emissions. Fluctuations in optical emissions attributed to particle precipitation have been observed in conjunction with VLF chorus [*Helliwell and Mende*, 1980].

In the spectrogram the slopes of the dispersion tracks increase with decreasing latitude, indicating a decrease in the source distance. This is illustrated in Figure 2, where the values of Δt are plotted for a dispersion event approximately 1.7° equatorward of the one previously discussed. One sees that for this case a source distance of approximately 60,000 km is inferred.

The second HILAT pass occurred from 0340 to 0345 UT on Julian day 362, 1983. The J sensor data recorded at the Tromso station are shown in color spectrogram format in Plate 2. (Plate 2 is shown here in black and white. The color version can be found in the special color section in this issue.) In this interval, HILAT moved from 75.6° to [illegible] CGL and from 0712 to 0755 MLT. The J sensor was operating in mode 3.

The measurements repeat the same basic morphology seen in the first example. At the beginning of the pass, the flux was observed primarily at energies below 1 keV. With decreasing latitude, the variability and intensity of the low-energy fluxes decreased, and the spectrum initially hardened. Coincident with the hardening of the spectrum, patches of high-energy electrons were detected. As in the previous case, the appearance and intensity of the high-energy patches were unrelated to variations with latitude in the spectrum at lower energies. After 0342:30 UT the spectra below 1 keV soften while patches continue to be observed at higher energies. A series of clear dispersion events appear during the 20-s period starting at 0343:53 UT.

The counts per accumulation interval for the six highest energy channels for the period of clear dispersion events are plotted in Figure 4. Measurable electron fluxes were observed up to the 12.1-keV channel. Clearly in every channel from 1.6 keV to 12.1 keV, there are a series of peaks that can be matched up to time offset peaks in one or more of the adjacent channels. The data for this period illustrate several

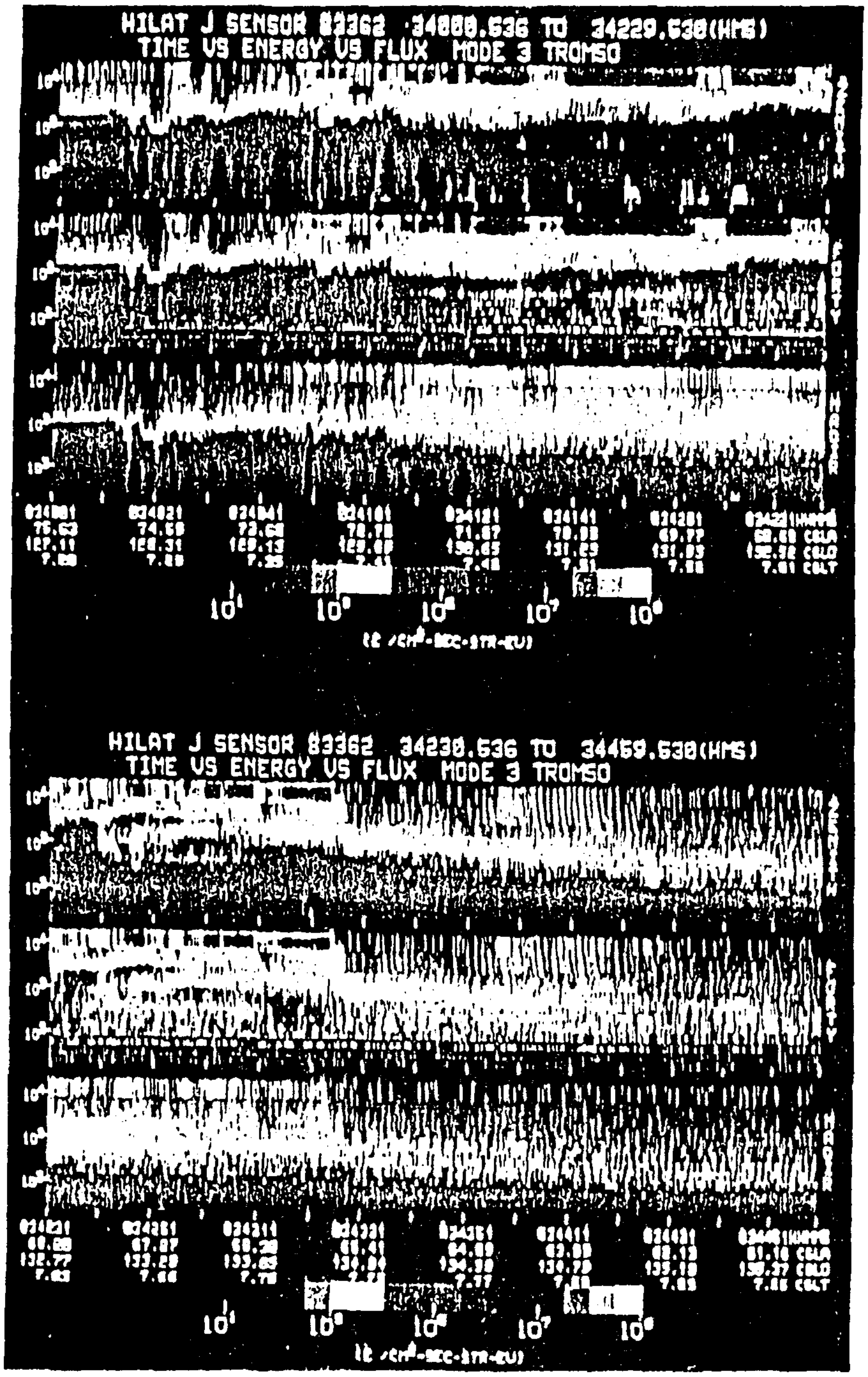

Plate 2. The differential number flux of electrons as measured by the HILAT J sensor for the Tromso pass on Julian day 362, 1983, from 0340:01 to 0345:01 UT. The J sensor is operating in mode 3. Each set of three panels displays the number flux as measured in the zenith, 40°, and nadir detectors. The bottom of each set is annotated with the universal time and the geomagnetic latitude, longitude, and local time of the satellite. The color version of this figure can be found in the separate color section in this issue.

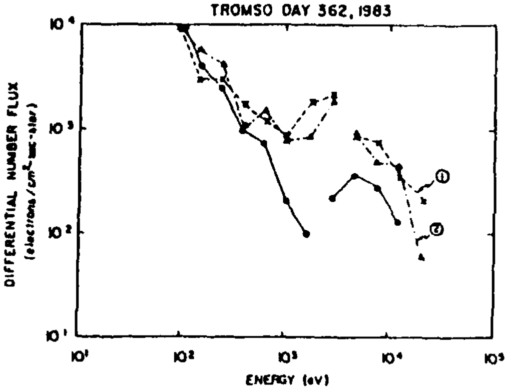

Fig. 5. The inferred source spectra for dispersion events observed in the Tromso pass on Julian day 362, 1983. The solid line gives the spectrum constructed from data in the interval 0342:22–0242:52 UT. The two spectra marked 1 and 2 are constructed from dispersion events 1 and 2 in Figure 6.

additional aspects of the phenomenon. First, the count rates at the peaks in any channel vary significantly. For example, in the 7.4-keV channel the counts per accumulation interval at peaks associated with dispersion events vary by a factor of 6. Second, the energy range over which the dispersion occurs also varies. Dispersion events can be observed over the entire range from 1.6 keV to 12.2 keV or in as few as two adjacent channels. Third, the intervals between consecutive peaks in a given channel vary. For example, in the 7.4-keV channel, near the beginning of the interval, consecutive peaks are separated by 0.5–0.75 s, while later they increase to 1.25 s or greater. Fourth, though the intervals between consecutive peaks vary, there is a significant interval over which peaks recur periodically. In both the 4.5-keV and 7.4-keV channels starting at approximately 0344:02 UT, there is a series of 12 peaks spaced periodically at 1.25-s intervals. In the same interval, additional peaks are occasionally observed between the periodically spaced peaks. Lastly, in most channels, the count rates drop to zero between peaks, implying that scattering has either stopped completely or decreased to low values below the instrument's flux sensitivity. This drop to a zero count level occurred in both the zenith and 40° detectors.

A source spectrum from this interval is plotted in Figure 5. The source spectrum was calculated as an average over the dispersion events in the period from 0344:00 to 0344:17 UT for which the peak counts per accumulation interval in the 12.2-keV channel exceeded 5. Averages were used because of low count rates in some of the channels. As in the day 186 examples, the spectrum monotonically decreases with increasing energy for the energies below the dispersion. In the dispersive energy range the spectrum peaks at 4.5 keV. Integrating over this portion of the spectrum gives a total energy flux of 0.28 erg/(cm^2 s) assuming isotropy over the downcoming hemisphere.

In Figure 6 the counts per accumulation interval are plotted for the six highest-energy channels for the period from 0342:20 to 0342:57 of this same pass. In this interval the spectrogram shows patches of high-energy fluxes with no clear indication of dispersion events. Figure 6 illustrates, however, that there were a number of dispersion events within this interval, typically extending over the four highest-energy channels. Several of these dispersion events are marked with arrows at the peak counts per accumulation interval for each event in each channel. The principal difference of this interval from the others is the greater disorder in the occurrence of the dispersion events. In this interval there are no consistent periodicities in the occurrence of the peaks, wide variations in the peak counts, and occasional peaks in individual channels with no matching peaks in adjacent channels.

Two source spectra from this interval are plotted in Figure 5. Unlike the previous examples, for these spectra the level in the dispersive portion is lower than that in the portion where no dispersions were observed. Integral energy fluxes of 0.47 and 0.35 erg/(cm^2 s) were calculated in the dispersive parts of the spectra.

The third pass occurred from 0544:30 to 0549:30 UT on day 365, 1983, with the J sensor operating in mode 3. For the pass, the satellite was traveling approximately along the 0830 MLT meridian from 78.7° to 61.9° CGL. The color spectrogram of the J sensor data (Plate 3) shows the same general spectral variations with latitude as the two previous examples. (Plate 3 is shown here in black and white. The color version can be found in the special color section in this issue.) At 0549:00 UT, dispersion events extending in energy from the 20.1-keV to the 630-eV channels were observed.

For this pass, we concentrate on the J sensor measurements from 0548:00 to 0548:50 UT. The color spectrogram in this interval shows a patch of enhanced high-energy electrons with dispersion events toward the end of the interval.

In Figure 7 the counts per accumulation interval for the four energy channels from 2.7 to 12.2 keV are plotted as a function of time for a 35-s period starting at 0548:00 UT. The figure illustrates that although dispersion events occurred toward the equatorward edge of this patch, no clear association of peaks in contiguous channels can be established in the poleward portion. The count rates did vary significantly in time. This can be seen in the 4.5-keV channel where the Poisson error bars have been plotted for several points in the interval. These illustrate that statistically significant variations occur on time scales down to the 0.25-s sampling frequency of the J sensor. In addition, the flux appears to have exhibited an occasional periodicity. For example, in the 4.5-keV channel at the beginning of the interval, there are four consecutive peaks with a 1.5-s spacing. Such periodicities were generally limited at any one time to a single channel.

The examples presented here suggest that the precipitation of keV, auroral electrons during these passes was produced by a common process. What varied between the examples is the clarity of the observability of the discrete events within the precipitation. The examples show a spectrum of observability that smoothly degrades from cases where the dispersion events are separate and periodic to those where the events become aperiodic and of more variable intensity, to finally, cases where the fluxes remain highly variable and no clear dispersion events can be identified. Such variability, we hypothesize, could result from either the intervals between dispersion events becoming short compared to the sampling period of the J sensor or the

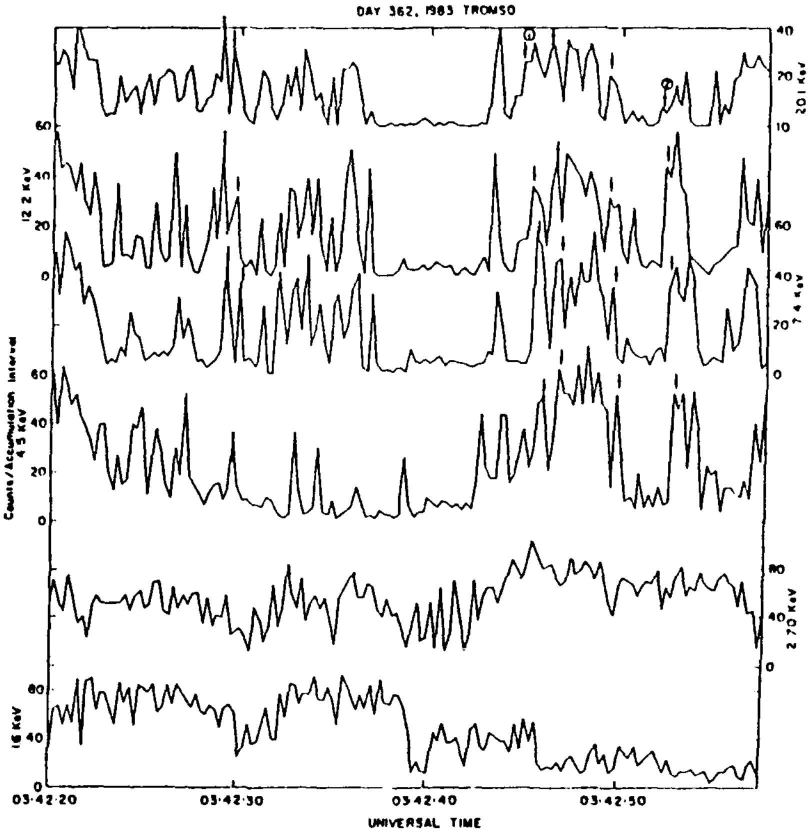

Fig. 6. A plot in the same format as Figure 1 for the time interval 0342:20–0343:00 UT for the Tromso pass on Julian day 362, 1983.

simultaneous presence of several trains of dispersion events with different periodicities and energy ranges.

In both the second and third examples the color spectrograms show approximately equal fluxes for electrons detected in the dispersion events in the zenith and 40° detectors. To check this degree of isotropy, the zenith and 40° detectors were first cross normalized using data from the middle of the midnight diffuse aurora where electron distributions are generally isotropic for pitch angles between 0° and 90°. The average ratio of the normalized fluxes in the zenith to 40° detectors was then calculated in each energy channel for the peaks in the dispersion events for passes on three days. A pass on day 176 was included since it contained a large number of dispersions over a wide range in energy. For the three events the zenith detector sampled pitch angles between 5° and 10°, and the 40° detector pitch angles between 38° and 43°. The results for the three days are listed in Table 1. In general, the values are within 10% of unity, implying that downcoming fluxes are reasonably isotropic over this angular range.

3.2. *Systematics of Locations, Source Distances, and Geomagnetic Activity*

We next consider the distributions of dispersion events in magnetic local times, the distribution of source distances along field lines as a function of *L* shell, and the distribution of events in geomagnetic activity. To determine the local time dependence, we divided MLT into 24 one-hour bins. All Tromso passes for the period from December 1983 to March 1984 were analyzed. Tromso was chosen since it consistently provided the best data coverage of the entire diffuse auroral region at all local times. Because of HILAT's orbital precession all MLTs are sampled in four months. A total of 743 separate passes were examined.

Color spectrograms of the J sensor data were examined to determine if, at any time during a given pass, time/energy dispersion events were observed. Each pass was assigned to a magnetic local time bin based upon the hour in MLT in which the majority of the data in the diffuse aurora were obtained. Due to the high inclination of the orbit, for most passes, all data in the diffuse aurora occurred within a single MLT bin. Typically, between 20 and 40 passes were examined in each local time bin, and the percentage of passes in which dispersion events occurred was calculated. The percentages are lower bounds since we did not count as dispersion events passes where only patchy precipitation at high energies was observed. As shown above, such patches may contain dispersion events not discernible in a color spectrogram.

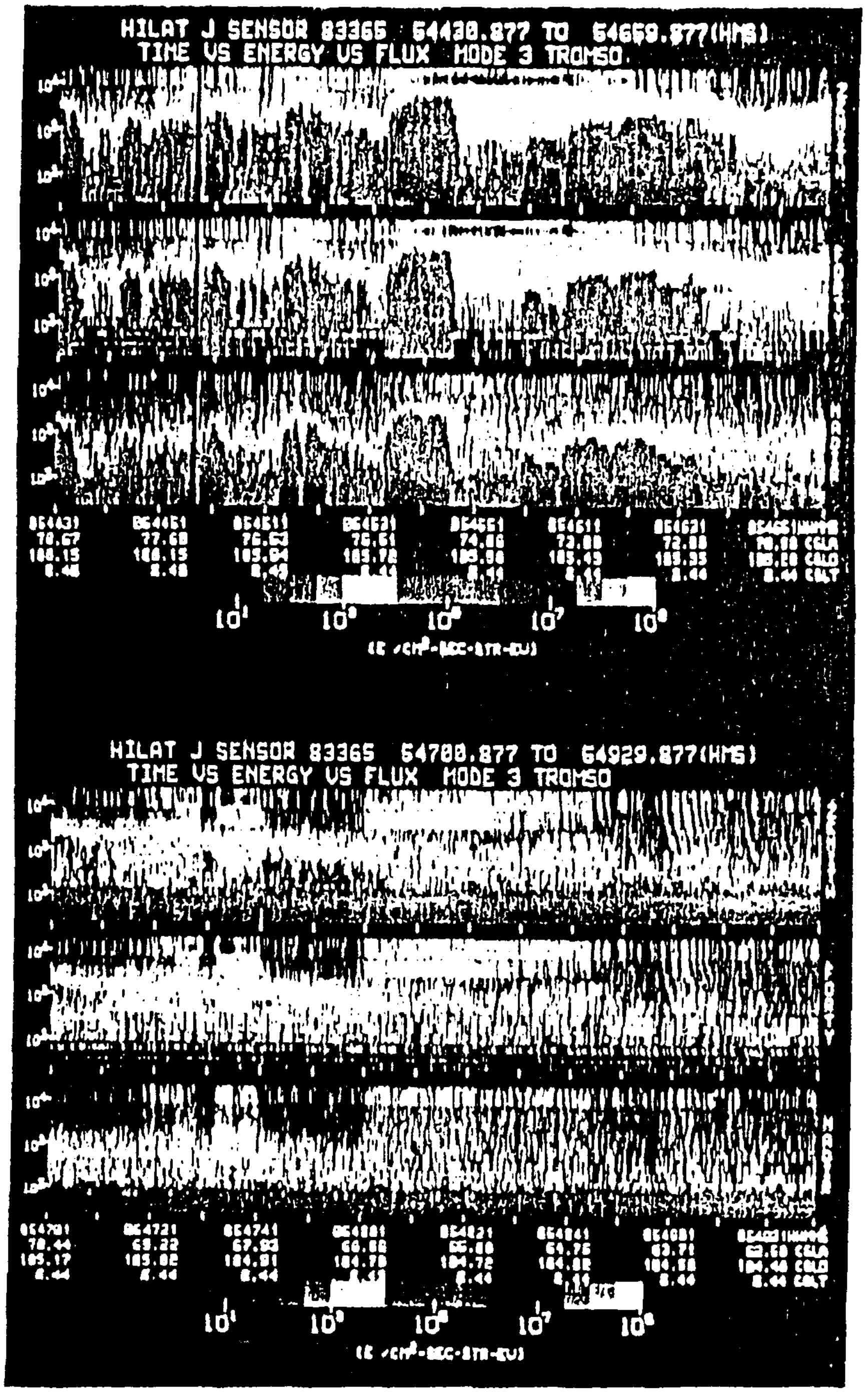

Plate 3. In the same format as Plate 2 for a Tromso pass on Julian day 365, 1983, for the interval 0544:31–0549:30 UT. The color version of this figure can be found in the separate color section in this issue.

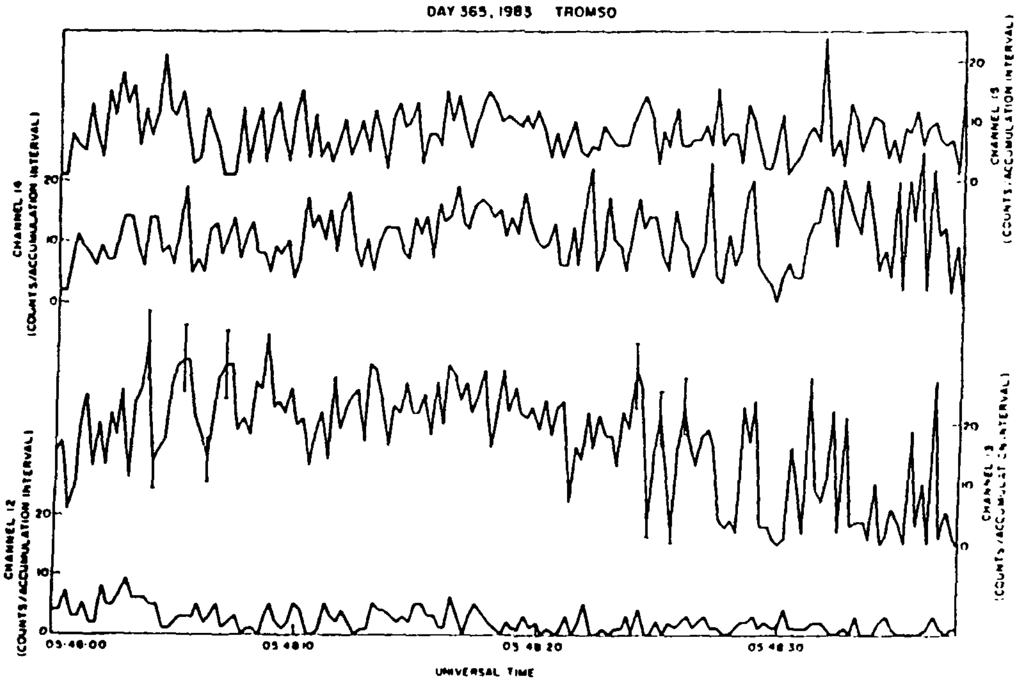

Fig. 7. A plot in the same format as Figure 1 for the time interval 0548:00–0548:35 for the Tromso pass on Julian day 365, 1983.

The results of this analysis are plotted as a histogram in Figure 8. The occurrence is strongly skewed to the morningside of the auroral oval; 80% of the passes exhibiting dispersions occurred between 0000 and 1200 MLT, and 66% occurred between 0600 and 1200 MLT. There is a clear peak in the 0800–1100 MLT bins at a level of approximately 50%. The occurrence percentage decreases after 1300 MLT with no cases seen from 1500 to 2300 MLT. In the midnight sector the occurrence rate is between 10 and 20%. The strong peaking of event occurrence in the 0600–1200 MLT sector is the same as for VLF emissions observed at both low and high altitudes and for microbursts [*Oliven et al.*, 1968; *Thorne et al.*, 1977; *Tsurutani and Smith*, 1977]. The distribution is also the same as that for substorm-associated, high-energy, microburst precipitation at subauroral latitudes [*Rosenberg and Dudeney*, 1986]. This point is considered in greater detail in the discussion section.

Second, we examined the relationship between the inferred source distances and the *L* shell on which the dispersion events were observed. For this analysis, events were chosen primarily from mode 2 operations of the *J* sensor when dispersion times could be determined most accurately. We also required that dispersion extend over at least three energy channels. In the few cases where data with the instrument in mode 3 were used, the dispersion was required to extend over at least four channels. For events occurring within a few seconds of one another the average source distance was calculated and assigned to the average *L* shell over which the events occurred. We considered events to be separate if there was a distance of more than 1° in latitude between them. *L* shells were assigned using a dipole magnetic field model. Comparisons between the dipole and Mead-Fairfield models showed negligible differences for $L < 10$.

The inferred source distances of 35 events are plotted versus *L* shell in Figure 9. These events occurred on 19 different days and for 21 different passes. Triangles and crosses denote events when the J sensor was in modes 2 and 3, respectively. Solid lines show the distance along the magnetic field line to the equatorial plane and to a point 10°, 20°, and 30° beyond the equatorial plane. Clearly, the inferred source distances increase with increasing *L* shell in the 3.5 to 10 range. For latitudes corresponding to $L > 10$ there is greater uncertainty in the assigned *L* value because of uncertainties in the mapping from low to high altitudes. The events are approximately evenly distributed over the *L* shell range from 4 to 9. Although the inferred source

TABLE 1. Average Ratios of Counts in the Zenith and 40° Detectors at Peaks of Dispersion Events

	Ratio of Zenith to 40° Detector Channels					Pitch Angle	
	12	13	14	15	16	Zenith	40°
Day 176	0.98	0.92	1.04	1.03	1.05	10.4	43.0
Day 362		0.98	1.21	1.08		3.4	38.2
Day 365		1.05	1.09	1.15	1.14	7.0	39.0

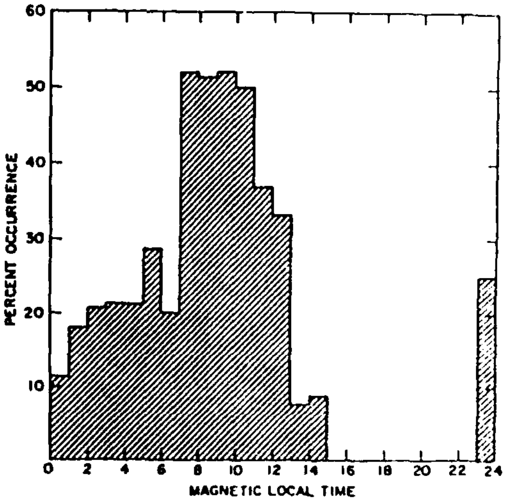

Fig. 8. *The percent occurrence as a function of magnetic local time of observation anywhere within a pass of energy/time dispersion events.*

distances of some events are closer than the equatorial plane, in the majority of cases they are significantly greater than the equatorial distance. On average, the sources are located 10°–20° from the equator.

We also did a preliminary analysis of the level of geomagnetic activity during the periods of dispersion event observation. For the 35 events included in Figure 9, only two were found to have occurred for *Kp* less than 2, and the average value of *Kp* over all 35 events was approximately 3. This indicates a preference for the occurrence of the events toward somewhat elevated levels of geomagnetic activity.

4. Discussion

In the previous section we presented observations of electron dispersion events in the morning sector of the auroral zone occurring over the energy range from 20 keV to a few keV or less. As noted, these events have occurrence distributions in MLT and *L* shell that closely mirror those of microbursts and VLF emissions [*Oliven et al.*, 1968; *Oliven and Gurnett*, 1968; *Russell et al.*, 1969; *Thorne et al.*, 1977; *Tsurutani and Smith*, 1977]. It is possible that the dispersion events are unconnected with VLF/microburst phenomenology. However, their similarities argue for an exploration of possible theories to explain such a relationship. Within this paper this involves some speculation about the nature of interactions between VLF waves and electrons with energies beyond the range of the HILAT sensors. Care has been taken to make quantitative estimates that can, in principle, in the future be verified by instrumentation flown on planned satellites.

This section is divided into two main subsections. In the first subsection we review the quasi-linear theory of pitch angle scattering and show that within the limits of experimental knowledge it cannot explain the dispersion events we have reported. In the second subsection we apply the nonlinear theory of pitch angle scattering originally developed by *Davidson* [1986*a*, *b*] to explain high energy microbursts. In our model the precipitation structures detected by HILAT represent debris from asymmetric wave pulses propagating though a trapped, warm plasma.

4.1. *Quasi-Linear Pitch Angle Scattering*

Pitch angle scattering of magnetospheric electrons by electromagnetic and electrostatic waves in the VLF frequency range has been analyzed by many investigators [*Kennel and Petschek*, 1966; *Kennel and Engelmann*, 1966; *Kennel et al.*, 1970; *Lyons*, 1974]. In these theoretical models the scattering is produced by waves that are Doppler shifted to some harmonic of the electron gyrofrequency.

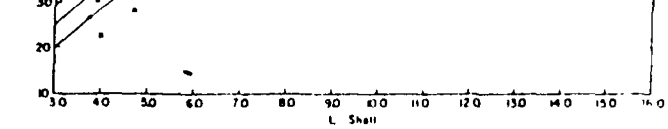

Fig. 9. The inferred source distances for energy/time dispersion events versus *L* shell. Solid lines give the distance to the equator and points 10°, 20°, and 30° off the equator in the opposite hemisphere.

$$\omega - \mathbf{k} \cdot \mathbf{v} + N\Omega = 0 \qquad (1)$$

where ω and Ω are the wave and electron gyrofrequencies, respectively; $\mathbf{k}$ is the wave vector, $\mathbf{v}$ is the electron's velocity, and N is an integer.

Using the cold plasma dispersion relationship for whistler waves, *Kennel and Petschek* [1966] showed that there is a range in energy where electrons resonate with waves at the $N = -1$ gyroharmonic. The minimum resonance energy E_r is given by

$$E_r = E_c(\Omega/\omega)(1 - \omega/\Omega)^3 \qquad (2)$$

where $E_c = B^2/8\pi n$ is the magnetic energy per particle; B is the magnetic field strength, and n the cold plasma density. For whistler waves to grow in amplitude the pitch angle anisotropy in the electron distribution function near the loss cone must be greater than $1/(\Omega/\omega - 1)$.

One can show that for such an interaction to pitch angle scatter electrons in the energy range of our observations requires cold plasma densities well in excess of those measured in the dayside, equatorial magnetosphere. On the dayside, for much of the L shell range over which the events are observed, the magnetic field is approximately dipolar. For a dipole field the equatorial field strength decreases from 248 to 60 nT as the radial distance from the center of the Earth increases from 5 to 8 R_E (1 R_E = 6370 km), the principal range over which we observed the dispersion events. This corresponds to a magnetic energy density from 155 to 10 keV/cm^3. For E_r to have a value of 1 keV, consistent with our observations, would require cold plasma densities from 155 to 10 cm^{-3} over this L shell range. *Higel and Wu* [1984], however, have reported that at geostationary orbit (L = 6.6) the cold plasma density generally increases from 1 cm^{-3} near the dawn meridian to 8 cm^{-3} near local noon, well below the required densities.

Lyons [1974] has proposed a model for the scattering and loss of plasma sheet electrons in the energy range 1–20 keV by electrostatic waves. This model applies to quasi-steady state electron precipitation and requires millivolt per meter electric field amplitudes. There are contradictory reports as to whether the average wave intensities reported are sufficiently large to support the proposed process [*Kennel et al.*, 1970; *Scarf et al.*, 1973; *Fredricks and Scarf*, 1973; *Belmont et al.*, 1983; *Roeder and Koons*, 1989]. In addition, there is nothing in the model that explains either the impulsive nature of the observed events, their off-equatorial origin, or their morningside occurrence.

An alternative explanation to the apparent off equatorial source for the HILAT dispersion events is that the warm electrons are resonantly scattered by rising chorus tones propagating near the equator. Rising tones occur because the phase velocities of whistler waves are inversely related to their frequencies. The process would therefore tend to pitch angle scatter 20-keV electrons before 1-keV electrons. The resulting dispersion combined with the dispersion produced by the difference in transit time could then mimic in the ionosphere an off-equatorial source.

To evaluate this explanation, let us consider the interaction of warm (1–20 keV) electrons with VLF rising tones near geostationary orbit where the range of cold plasma densities has been measured. For a cold plasma density of 5 cm^{-3}, typical of the postdawn sector and with B ~ 108 nT, the magnetic energy per electron is 6 keV. To pitch angle scatter electrons with energies between 20 and 1 keV, the rising tone would have to extend from $0.18\Omega_e$ to $0.58\Omega_e$. This covers the observed gap at half the cyclotron frequency. If we assume that the rising tone has frequencies above $0.52\Omega_e$ and scatters electrons with energies less than 20 keV, we estimate the required cold plasma density to be 0.3 cm^{-3}. This is much less than the observed, morningside, cold plasma density range. Conversely, if we assume that the rising tone has frequencies less than $0.48\Omega_e$ and scatters electrons with energies greater than 1 keV, the cold plasma density must be about 9 cm^{-3}. While this is comparable to densities found at geostationary orbit near noon, it cannot explain the many examples of near dawn dispersion events where the measurements of *Higel and Wu* [1984] indicate much lower densities.

On the basis of our observations and analysis of quasi-linear pitch angle scattering theory we conclude that any model explaining the dispersion events must invoke processes that (1) are specific to the morning sector and maximize between 0600 and 1200 MLT, (2) scatter electrons at locations away from the equator, generally in the opposite hemisphere to which the dispersion events are observed, (3) impulsively fill the loss cone with isotropic fluxes of electrons with energies between 0.6 and 20 keV, and (4) operate over a wide range of L shells.

4.2. *Nonlinear Pitch Angle Scattering*

Since neither the electromagnetic nor the electrostatic quasi-linear model can account for the HILAT observations, we have attempted a different approach that relies on previous work of *Davidson* [1986*a*, *b*]. Davidson has pointed out that free energy responsible for wave growth need not reside in the precipitating electrons. For the cases of hot (>20 keV) electron precipitation bursts in the morning magnetosphere, considered by Davidson, particle anisotropies are the free energy sources of wave growth. Thus Davidson was able to derive self-consistent relationships between the wave fields and the hot electron distribution functions.

Here we consider scattering of the 1- to 20-keV electrons by an interaction with VLF waves where these electrons do not act as the free energy source to drive the VLF waves. By the nature of this kind of interaction, without specific knowledge of the hot electron distribution, the initial value problem cannot be solved self-consistently.

Figure 10 is a flowchart of the suggested process. A source of trapped, hot electrons is required in the midnight sector. Whether these electrons originate from substorm injections or other processes is unimportant. We only require that a pitch angle anisotropy in their distribution function carries free energy that can be released when the appropriate conditions are met. The observations of *Higel and Wu* [1984] for GEOS 2 indicate that as these electrons drift eastward into the morning sector, they encounter azimuthal gradients in the cold plasma density. This reduced E_c, the magnetic energy per particle, allowing an increased portion of the trapped, hot electron distribution to resonate with whistler mode waves.

With both energy resonance and particle anisotropy conditions met, VLF waves can grow in the equatorial region. That this occurs is supported by the local time and L shell dependencies of VLF emissions and microburst occurrences

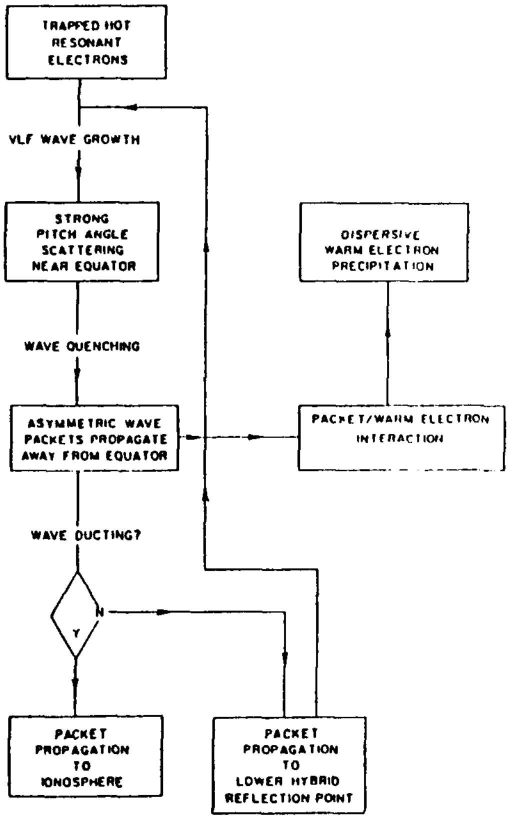

Fig. 10. Flowchart representing processes leading to impulsive scattering of auroral energy electrons into the loss cone.

cited above [*Isenberg et al.*, 1982; *Rosenberg and Dudeney*, 1986]. According to the model developed by Davidson, in the early stages of wave growth the pitch angle diffusion rate is weak. The waves grow in amplitude until strong pitch angle scattering is achieved, i.e., until in the equatorial region of wave particle resonance, electrons pitch angle scatter over half the width of the atmospheric loss cone on time scales less than the transit time across the interaction region. Once the electron flux in the loss cone is isotropic, the particle anisotropy in the equatorial region needed to support wave growth is no longer present, and the waves are quickly quenched. The wave growth should proceed more slowly than the quenching such that an asymmetric wave packet is produced with a much sharper gradient on the trailing edge of the packet than on its leading edge.

A schematic representation of this process is shown in Figure 11. Close to the equatorial resonance region, VLF waves propagate both toward and away from the equator. Under symmetric conditions between the northern and southern hemispheres, waves that have passed through the region of resonant interaction propagate away from the equator with larger amplitudes. The asymmetric amplitudes of wave trains produced during a cycle of wave growth and quenching are represented in the figure.

The distance from the equator at which such waves may be observed depends on whether or not they are ducted. Observations of ducted wave trains can, in principle, be made all the way down to the ionosphere. For the unducted case, waves only propagate to the locations where their frequencies match the lower hybrid frequency ω_{LH}. Here unducted waves reflect back toward the equator [*Kimura*, 1966; *Lyons and Thorne*, 1970]. The location of the reflection point is set by the condition that

$$\omega = F\Omega_0 = \omega_{LH} = \sqrt{m_e/m_i}\,\Omega(\Lambda) \qquad (3)$$

where ω is the frequency of the wave; Ω_0 is the electron gyrofrequency at the equator; F is a fraction of the order of 0.05-0.2; m_e and m_i are the electron and ion masses, respectively; and $\Omega(\Lambda)$ is the electron gyrofrequency at geomagnetic latitude Λ. In the dipole approximation this reduces to

$$\sqrt{m_e/m_i}/F = (1 + 3\sin^2\Lambda)^{1/2}/\cos^6\Lambda \qquad (4)$$

For the range in F given above, the latitude of reflection varies from 25° to 42°. We showed in Figure 9 that for $L > 8$ the warm electron bursts typically originated at magnetic latitudes between 10° and 20°. Thus both ducted and unducted wave trains coming from the equator propagate through the region where the impulsive scattering occurs.

We next consider the interaction of the warm electrons with wave trains of the general asymmetric shape shown in Figure 11. The warm electrons moving along the magnetic field lines toward and away from the equator can interact with the gradients in the wave train through the ponderomotive force [*Chen*, 1984], which is just the radiation pressure gradient. The force exerted on an individual electron via the nonlinear, ponderomotive force is

$$f_{NL} = -(e^2/4m\omega^2)\nabla|E|^2 \qquad (5)$$

where E is the amplitude of the wave electric field. The backside gradient of a wave train propagating away from the

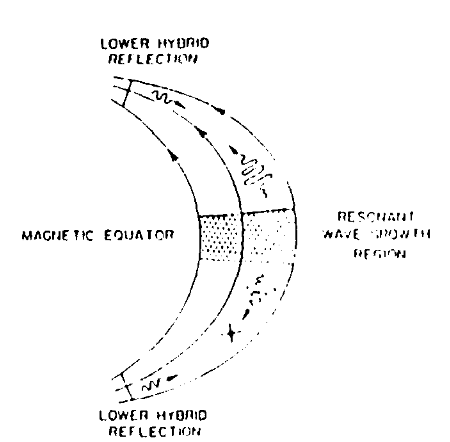

Fig. 11. A schematic representation of the generation and propagation of VLF wave packets in the magnetosphere.

equator exerts a field aligned force toward the equator. As a result, an electron moving toward (away from) the equator receive an impulse toward smaller (larger) pitch angles.

We can estimate the wave amplitude required to impulsively scatter warm electrons from just outside to just inside the loss cone. In the interaction the field-aligned component of the electron's momentum must increase by

$$\delta p_{\parallel} = p(1 - \cos \alpha) \approx p\alpha^2/2 \tag{6}$$

where α is the half width of the loss cone. This impulse is

$$\delta p_{\parallel} = \int_0^{\delta t} f_{NL}\, dt = -(e^2/4m\omega^2)\nabla|E|^2 \delta t \tag{7}$$

We approximate $\nabla|E|^2$ by E^2_{max}/D, where D is the scale length over which the wave amplitude decreases from its maximum value E_{max} to a low background level. The interaction time divided by the scale length $\delta t/D$ is $\sim 1/V_g$, where V_g is the group speed of the wave train. Combining the expressions for δ_p in equations (6) and (7), we get

$$E_{max} = \alpha(\omega/e)(2mV_g\, p)^{1/2} \tag{8}$$

In MKS units, electron momentum is related to kinetic energy K in convenient units as $p = 1.7 \times 10^{-23} K^{1/2}$(keV). We see that the electric field amplitude required for scattering by the ponderomotive force depends only weakly (fourth root) on the electron energy and thus is a viable candidate for impulsive scattering over the full 1- to 20-keV range. Note, too, that the maximum required electric field is directly proportional to α, the half width of the loss cone at the magnetic latitude λ of the impulse. For a dipole, α increases away from the equator roughly as $1/\cos^3\lambda$. Thus the ponderomotive force should be most effective for pushing trapped warm electrons into the loss cone immediately after a wave train emerges from the equatorial region of resonant interaction with the hot electrons.

We can estimate the electric field amplitude required for ponderomotive scattering at $\lambda = -15°$ along the $L = 6$ field line. At this position the half width of the loss cone is 3.3°. We assume a cold plasma density of 5 cm^{-3} and a VLF frequency of $0.1\Omega_0$. For a dipole field this corresponds to $E_c = 10$ and $E_r = 75$ keV. The group speed of the wave train is approximately 10^4 km/s. Substitution of these values into equation (8) gives $E_{max} = 10$ mV/m. Electrostatic waves of this magnitude have been observed near the equatorial plane [*Fredricks and Scarf*, 1973]. For the cited parameters the corresponding magnetic field amplitude for a whistler wave is 0.07 nT. This is consistent with the amplitudes of VLF waves measured by *Oliven and Gurnett* [1968] during microburst activity.

Other possible effects of intense wave trains propagating away from the equatorial plane can be considered. The wave train may be either ducted or unducted along the magnetic field flux tube. In the former case it would propagate down to the ionosphere. This appears to be true for the cases reported by *Rosenberg et al.* [1981]. In the unducted case the wave train is fully or partially reflected back toward the equator at the point where the drive frequency equals the lower hybrid frequency [*Kimura*, 1966]. If the distribution function of the hot electrons has again become anisotropic when the reflected wave returns to the equator, it can grow through the standard pitch angle scattering process. Such reflected waves could then interact with the warm electrons via the ponderomotive force, several times, to produce the multiple dispersion events observed.

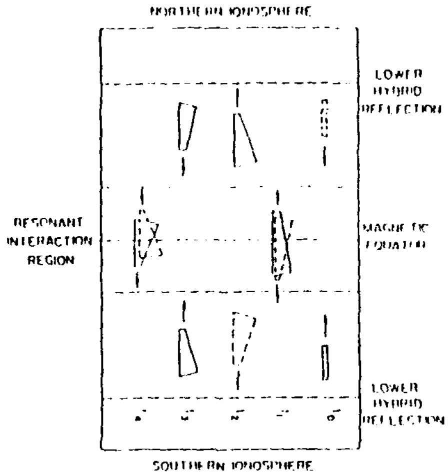

Fig. 12. Representation of oppositely directed VLF wave trains propagating between lower hybrid reflection points.

Figure 12 schematically represents the history of two oppositely traveling wave trains. At initial time t_0 the wave trains have small amplitudes as they approach the equator. During their passage through the equatorial layer (t_1) they grow and acquire asymmetric shapes and propagate away from the equator (t_2) toward the low hybrid point, where they are reflected (t_3) toward the equator to be again amplified (t_4). If the wave retains its shape and intensity on reflection at the lower hybrid point, one can explain the few examples of injections on the near (north) side of the equatorial plane. In this case the backside, ponderomotive force of the wave train moving toward the equator provides a direct impulse toward the ionosphere.

In conclusion, we have presented examples of energy/time dispersion events occurring over the energy range from 20 keV down to a few keV or less. The events occur either periodically or aperiodically with the fluxes isotropic for pitch angles between approximately 0° and 40°. The dispersion events are observed primarily in the morningside auroral zone over L shells from approximately 3.7 to 15. The events are consistent with a source distance along the field line 10°–20° beyond the magnetic equatorial plane. We argue that the occurrence of such events cannot be accounted for by a resonant interaction with VLF waves. Based on circumstantial evidence from similar morning sector VLF and microburst phenomenology, we propose that the warm electrons are impulsively scattered by ponderomotive forces exerted by asymmetric VLF wave packets.

Acknowledgments. The authors wish to express their thanks to Michael Heinemann and Gregory Ginet of AFGL for stimulating discussions on VLF wave propagation in inhomogeneous media. This work was supported in part by U.S. Air Force contract F19628-85-K0053 with Northeastern University.

The Editor thanks D. L. Matthews and another referee for their assistance in evaluating this paper.

REFERENCES

Anderson, R. R., and K. Maeda, VLF emissions associated with enhanced magnetospheric electrons, *J. Geophys. Res.*, *82*, 135, 1977.

Belmont, G., D. Fontaine, and P. Canu, Are equatorial electron cyclotron waves responsible for diffuse auroral electron precipitation? *J. Geophys. Res.*, *88*, 9163, 1983.

Burton, R. K., and R. E. Holzer, The origin and propagation of chorus in the outer magnetosphere, *J. Geophys. Res.*, *79*, 1014, 1974.

Chen, F. F., *Plasma Physics*, vol. 1, *Plasma Physics and Controlled Fusion*, 2nd ed., pp. 305–309, Plenum, New York, 1984.

Davidson, G. T., Pitch angle diffusion in the morningside aurorae, 2, The formation of repetitive auroral pulsations, *J. Geophys. Res.*, *91*, 4429, 1986*a*.

Davidson, G. T., Pitch angle diffusion in the morningside aurorae, 1, The role of the loss cone in the formation of impulsive bursts of precipitation, *J. Geophys. Res.*, *91*, 4413, 1986*b*.

Dunkel, N., and R. A. Helliwell, Whistler-mode emissions on the OGO 1 satellite, *J. Geophys. Res.*, *74*, 6371, 1969.

Foster, J. C., and T. J. Rosenberg, Electron precipitation and VLF emissions associated with cyclotron resonance interaction near the plasmapause, *J. Geophys. Res.*, *81*, 2183, 1976.

Fredricks, R. W., and F. L. Scarf, Recent studies of magnetospheric electric field emissions above the electron gyrofrequency, *J. Geophys. Res.*, *78*, 310, 1973.

Hardy, D. A., A. Huber, and J. Pantazis, The electron flux J-sensor for HILAT, *APL Tech. Dig.*, *5*, 125, 1984.

Helliwell, R. A., A theory of discrete VLF emissions from the magnetosphere, *J. Geophys. Res.*, *72*, 4773, 1967.

Helliwell, R. A., and T. L. Crystal, A feedback model of cyclotron interaction between whistler-mode waves and energetic electrons in the magnetosphere, *J. Geophys. Res.*, *78*, 31, 1973.

Helliwell, R. A., and S. B. Mende, Correlations between λ4278 optical emissions and VLF wave events observed at $L \sim 4$ in the Antarctic, *J. Geophys. Res.*, *85*, 3376, 1980.

Higel, B., and Wu Lei, Electron density and plasmapause characteristics at 6.6 R_E: A statistical study of the GEOS 2 relaxation sounder data, *J. Geophys. Res.*, *89*, 1583, 1984.

Isenberg, P. A., H. C. Koons, and J. T. Fennel, Simultaneous observations of energetic electrons and dayside chorus in geosynchronous orbit, *J. Geophys. Res.*, *87*, 1498, 1982.

Kennel, C. F., and F. Engelmann, Velocity space diffusion from weak plasma turbulence in a magnetic field, *Phys. Fluids*, *9*, 2377, 1966.

Kennel, C. F., and H. E. Petschek, Limit on stably trapped particle fluxes, *J. Geophys. Res.*, *71*, 1, 1966.

Kennel, C. F., F. L. Scarf, R. W. Fredricks, J. H. McGhee, and F. V. Coroniti, VLF electric field observations in the magnetosphere, *J. Geophys. Res.*, *75*, 6136, 1970.

Kimura, I., Effects of ions on whistler mode ray tracing, *Radio Sci.*, *1*, 269, 1966.

Lyons, L. R., Electron diffusion drive by magnetosphere electrostatic waves, *J. Geophys. Res.*, *79*, 575, 1974.

Lyons, L. R., and R. M. Thorne, The magnetospheric reflection of whistlers, *Planet. Space Sci.*, *18*, 1753, 1970.

Oliven, M. N., and D. A. Gurnett, Microburst phenomena, 3, An association between microbursts and VLF chorus, *J. Geophys. Res.*, *73*, 2355, 1968.

Oliven, M. N., D. Venkatesan, and K. G. McCracken, Microburst phenomena, 2, Auroral zone electrons, *J. Geophys. Res.*, *73*, 2345, 1968.

Roeder, J. L., and H. C. Koons, A survey of electron cyclotron waves in the magnetosphere and the diffuse auroral electron precipitation, *J. Geophys. Res.*, *94*, 2529, 1989.

Rosenberg, T. J., and J. R. Dudeney, The local time, substorm, and seasonal dependence of electron precipitation at $L \approx 4$ inferred from riometer measurements, *J. Geophys. Res.*, *91*, 12,032, 1986.

Rosenberg, T. J., R. A. Helliwell, and J. P. Katsufrakis, Electron precipitation associated with discrete very-low-frequency emissions, *J. Geophys. Res.*, *76*, 8445, 1971.

Rosenberg, T. J., J. C. Siren, D. L. Matthews, K. Marthinsen, J. A. Holtet, A. Egeland, D. L. Carpenter, and R. A. Helliwell, Conjugate of electron microbursts and VLF chorus, *J. Geophys. Res.*, *86*, 5819, 1981.

Russell, C. T., R. E. Holzer, and E. J. Smith, OGO 3 observations of ELF noise in the magnetosphere, 1, Spatial extent and frequency of occurrence, *J. Geophys. Res.*, *74*, 755, 1969.

Scarf, F. L., R. W. Fredricks, C. F. Kennel, and F. V. Coroniti, Satellite studies of magnetospheric substorms on August 15, 1968, OGO 5 plasma wave observations, *J. Geophys. Res.*, *78*, 3119, 1973.

Thorne, R. M., E. J. Smith, K. J. Fiske, and S. R. Church, Intensity variation of ELF hiss and chorus during isolated substorms, *Geophys. Res. Lett.*, *1*, 193, 1974.

Thorne, R. M., S. R. Church, W. J. Malloy, and B. T. Tsurutani, The local time variation of ELF emission during periods of substorm activity, *J. Geophys. Res.*, *82*, 1585, 1977.

Tsurutani, B. T., and E. J. Smith, Postmidnight chorus: A substorm phenomenon, *J. Geophys. Res.*, *79*, 118, 1974.

Tsurutani, B. T., and E. J. Smith, Two types of magnetospheric ELF chorus and their substorm dependence, *J. Geophys. Res.*, *82*, 5112, 1977.

Venkatesan, D., M. N. Oliven, P. J. Edwards, K. G. McCracken, and M. Steinbock, Microburst phenomena, 1, Auroral zone X rays, *J. Geophys. Res.*, *73*, 2333, 1968.

W. J. Burke and D. A. Hardy, AFGL/PHP, Hanscom Air Force Base, MA 01731.

E. Villalon, Center for Electromagnetics Research, Northeastern University, Boston, MA 02115.

(Received November 9, 1988;
revised May 1, 1989;
accepted June 13, 1989.)

JOURNAL OF GEOPHYSICAL RESEARCH, VOL. 94, NO. A11, PAGES 15,243–15,256, NOVEMBER 1, 1989

Quasi-Linear Wave-Particle Interactions in the Earth's Radiation Belts

ELENA VILLALÓN

Center for Electromagnetics Research, Northeastern University, Boston, Massachusetts

WILLIAM J. BURKE AND PAUL L. ROTHWELL

Air Force Geophysics Laboratory, Hanscom Air Force Base, Massachusetts

MICHAEL B. SILEVITCH

Center for Electromagnetic Research, Northeastern University, Boston, Massachusetts

This paper studies the theory of gyroresonant interactions of energetic trapped electrons and protons in the Earth's radiation zones with ducted electromagnetic cyclotron waves. Substorm injected electrons in the mid-latitude regions interact with coherent VLF signals, such as whistler mode waves. Energetic protons may interact with narrow-band hydromagnetic (Alfvén) waves. A set of equations is derived based on the Fokker-Planck theory of pitch angle diffusion. They describe the evolution in time of the number of particles in the flux tube and the energy density of waves, for the interaction of Alfvén waves with protons and of whistler waves with electrons. The coupling coefficients are obtained based on a quasi-linear analysis after averaging over the particle bounce motion. It is found that the equilibrium solutions for particle fluxes and wave amplitudes are stable under small local perturbations. The reflection of the waves in the ionosphere is discussed. To efficiently dump the energetic particles from the radiation belts, the reflection coefficient must be very close to unity so waves amplitudes can grow to high values. Then, the precipitating particle fluxes may act as a positive feedback to raise the height integrated conductivity of the ionosphere which in turn, enhances the reflection of the waves. In addition, by heating the foot of the flux tube with high intensity, RF energy the mirroring properties of the ionosphere are also enhanced. The stability analysis around the equilibrium solutions for precipitating particle fluxes and wave intensity show that an actively excited ionosphere can cause the development of explosive instabilities.

1. INTRODUCTION

A theory of nonlinear interactions of radiation belt particles with cyclotron waves is developed here. We consider cases where the wave frequencies are small fractions of the equatorial cyclotron frequency and where the wave vectors are aligned with the geomagnetic field. Because of the latter we only consider resonant excitations due to the first harmonic of the cyclotron frequency. For high-temperature plasmas, the pitch angle distributions of the particles are anisotropic, which provides the free energy for the cyclotron instability. As a distribution function relaxes toward equilibrium, it interacts with several types of electromagnetic waves. A number of observations of electron precipitation in middle latitudes ($L \le 6$), have been attributed to highly coherent magnetospheric VLF waves [*Dingle and Carpenter*, 1981; *Doolittle and Carpenter*, 1983]. This includes naturally occurring whistlers, triggered VLF emissions, chorus, signals that are injected into the magnetosphere by VLF ground transmitters and large-scale power grids signal from satellite-borne VLF transmitters. Substorms injected protons in the mid-latitude regions, interact with hydromagnetic ULF pulsations of the Pc type, which are ducted along a given magnetic flux tube. The amplitudes of the waves grow directly proportional to the number of resonant particles and to the degree of the pitch angle anisotropy until they reach the equilibrium state. The generated waves, in turn, act upon the particles and change their velocity distribution. Some of these particles are scattered into the loss cone producing the well-known particle precipitation fluxes investigated by *Kennel and Petschek* [1966] and observed in the magnetosphere. The electrons fluxes and associated wave activity in the radiation belts have been extensively studied over the years [*Hughes and Southwood*, 1976; *Retterer et al.*, 1983; *Tkalcevic et al.*, 1984; *Inan*, 1987; *Schulz and Davidson*, 1988] and provides a possible explanation for the presence of the electron slot around $L = 3, 4$ shells [*Lyons and Thorne*, 1973; *Lyons and Williams*, 1983]. In addition, pitch angle scattering of ring current ions by ion cyclotron waves, with a frequency in the range between 0.1 and 0.7 times the proton gyrofrequency, are believed to play a significant role in the plasma pause region [*Kozyra et al.*, 1984; *Imhof et al.*, 1986; *Gendrin*, 1968].

The amplification of the electron (proton) cyclotron waves mainly occurs near the equatorial region where the resonant wave particle interactions are more efficient. As waves travel along the flux tube and enter the ionosphere they are partially reflected back into the flux tube and partially transmitted toward the ground. An important concept developed by *Bespalov and Trakhtengerts* [1980] and *Trakhtengerts* [1983] considers the magnetosphere as a gigantic maser where whistler and Alfvén waves are trapped between the ionospheric mirror and grow in amplitude as they cross back and forth across the equatorial region. The maser will result if the path-integrated growth rate of the intensity of the wave packet exceeds the absolute value of the logarithm of the internal reflection coefficient at the magnetosphere-

Paper number 89JA01312.
0148-0227/89/89JA-01312$05.00

ionosphere interface. They derive a set of equations based on quasi-linear theory which gives the evolution in time of the trapped particles in the flux tube, and the energy density of waves. It is assumed that quasi-linear diffusion occurs over time scales which are longer than the particle bounce time between conjugate hemispheres and the time waves take to travel from one ionospheric mirror to its conjugate. The ray equations were also introduced in a phenomenological manner by *Schulz* [1974]; the time-dependent pitch angle anisotropies were also modeled as to include the strong pitch angle diffusion case. However, the coupling coefficients for the ray equations are not given in Schulz' phenomenological description.

Our paper is a detailed review of the theory developed by Bespalov, Trakhtengerts and their collaborators [*Bespalov et al.*, 1983; *Gaponov-Grekhov et al.*, 1981; *Trakhtengerts*, 1984] on the electron cyclotron wave instability. In addition, we extend this theory to the interaction of Alfvén waves with ions. The main contribution is to calculate the coupling coefficients for the ray equations describing the temporal evolution of the cyclotron instability. These are obtained within the framework of quasi-linear interaction of waves and particles. For simplicity, we assume that the waves are ducted in the magnetosphere between the ionosphere and the equatorial plane. We also give a detailed account of the qualitative values of the ionospheric reflection coefficients for both whistler and Alfvén waves. The role that an actively excited ionosphere may play modifying the wave reflection coefficients and hence the maser efficiency within the radiation belts is also discussed.

The paper is organized as follows. Sections 2 and 3 contain the basis of resonant interactions between waves and particles and a description of the evolution in time of the particle distribution functions based on local, quasi-linear theory [*Roberts*, 1969; *Schulz and Lanzerotti*, 1974]. We assume that the dielectric properties of wave propagation are given by a cold background of either electrons (for whistlers), or protons (for Alfvén waves). The hot population of plasma particles (e.g., larger than 40 keV for the electrons and 100 keV for the ions), is represented by the particle source $J(t)$, and they interact with the electromagnetic waves near the equatorial regions. The equatorial sources of particles in a given flux tube are due to gradient-curvature drifting on the same magnetic shell and inward radial diffusion that conserves the first two adiabatic invariants. The latter is greatly enhanced during magnetic substorms. Because of resonant diffusion, the number of trapped thermal particles in the flux tube changes in time, and their distribution functions are studied in section 3. We consider cases in which the pitch angle distribution function does not change in time, and also when it changes over time scales longer than the bounce time and the group time delay of the wave. The pitch angle distribution functions are eigenfunctions of the diffusion operator, and they are given in Appendix B. In section 4 we present the growth rates for the whistler and Alfvén instabilities, due to the resonant excitation by the thermal particles. We assume that the main spatial inhomogeneity that waves encounter as they move near the equator is due to the spatial variation of the geomagnetic field. After integrating along the flux tube (i.e., along the magnetic field variations), we obtain the spatial amplification factor as a function of the number of resonant particles in the magnetic trap. We arrive at a set of coupled differential equations describing the evolution in time of the number of particles in the flux tube, and the energy density of waves. These equations are valid over time scales longer than the bounce time of the particles and the group time delay of the waves and do not comprise the possibility of particles drifting away from the waves ducts. The ray equations are discussed in section 5. The equilibrium solutions for whistlers and Alfvén waves are given here. The nonlinear stability equation is also given in section 5. Section 6, and Appendix C contain a description on how a time-dependent, pitch angle anisotropy affects the ray equations and their equilibrium solutions. In section 7 we study the reflection of the waves at the foot of the flux tube for both whistlers [*Helliwell*, 1965], and Alfvén waves. We discuss the dependences of the reflection coefficients on the wavelength, size of the ionosphere, and the length of the density inhomogeneity. In section 7 we also consider the effects that an actively excited ionosphere may have in the stability of the equilibrium solutions. The ionospheric reflection coefficient may be changed in two different ways. First, by using high-power microwave transmitters, the dielectric properties of the ionosphere may be changed by creating a high population of thermal electrons. This modifies the reflection coefficients, and hence the condition for stability of the cyclotron wave modes. We also consider the effect on the height-integrated conductivity due to the filling of the loss cone and consequently, a large particle precipitation due to the maser instability. The conductivity is then modulated at VLF or ELF frequencies which modulates the reflection of waves that cause pitch angle diffusion in the equatorial plane and the growth of the waves themselves. This problem has been studied previously by *Davidson and Chiu* [1986]. Here we give a derivation of the stability equation starting from quasi-linear theory and incorporating the nonlinear feedback of the particle precipitation. This causes a third mode to appear which was not present in the stability analysis of a natural unperturbed ionosphere. The conditions under which this mode becomes unstable are given. Section 9 contains a summary and conclusions.

2. RESONANT WAVE-PARTICLE INTERACTION

A particle of mass m, charge q and velocity v, moving along the dipole field lines of the Earth's geomagnetic field, bounces from mirror point to its opposite hemisphere conjugate in a time given by [*Schulz and Lanzerotti*, 1974]

$$\tau_B = \int_{-l_m/2}^{l_m/2} \frac{dz}{v_z} = \frac{2\pi a}{v}\,(1 - 0.23\sqrt{\mu}) \qquad (1)$$

where the coordinate z represents the distance along the magnetic field line, l_m is the length the particle travels along the field line, and a is a constant which we shall define later on. The particle's velocity along the magnetic field (z direction), is $v_z = v(1 - \mu\Omega/\Omega_L)^{1/2}$, where $\Omega = qB/mc$ is the cyclotron frequency, and $\mu = \sin^2\theta_L$. Here θ_L is the particle's pitch angle at $z = 0$, i.e., the angle between the particle velocity vector and the geomagnetic field at the equator. We note that the bounce period is quite insensitive to variations in the equatorial pitch angles. Thus we will approximate τ_B by $2\pi a/v$ in the calculations that follows.

For the sake of analytical simplicity, we assume that near the equatorial region we may approximate the Earth's magnetic field by the parabolic profile

$$\frac{B}{B_L} = 1 + \left(\frac{z}{a}\right)^2 \qquad (2)$$

where the index L stands for the values at the central cross section of the flux tube. If we define ψ as the geomagnetic latitude in radian units, and by expanding the dipole magnetic field in powers of ψ, we find that $z = R_E L \psi$ and $a = (\sqrt{2}/3) R_E L$. Here R_E is the Earth's radius and $R_E L$ measures the distance of the center cross section of the magnetic trap from the center of the Earth. We show that (2) is a good approximation to the geomagnetic field lines for latitudes smaller than $\pm 20°$.

Ducted whistlers and Alfven waves are such that their wave vector **k** is aligned along the geomagnetic field. For these waves the particle motion resonates at the first cyclotron harmonic if there is a sufficient number of electrons or protons which satisfy the resonant condition

$$\omega - kv_\parallel + \Omega = 0 \qquad (3)$$

where ω is the wave frequency. The electromagnetic wave is assumed to be circularly polarized, with the electric and magnetic fields perpendicular to each other and both perpendicular to **k**. The refractive index is represented by η and it is given by the dispersion relation for either the whistler or the Alfvén waves (see section 4). Equation (3) defines a *mapping* between values of the cyclotron frequency Ω along the geomagnetic trap, and the resonant equatorial pitch angles μ, for given values of k and v, i.e., $(\Omega + \omega)/kv = (1 - \mu\Omega/\Omega_L)^{1/2}$. The range of resonant equatorial pitch angles, i.e., those that satisfy (3): $\mu_c \le \mu \le \mu_m$ is such that μ_c is given by the pitch angle at the boundary of the loss cone and μ_m is defined in terms of the equatorial cyclotron frequency. The resonant gyrofrequencies are such that $\Omega_L \le \Omega \le \Omega_M$. Here Ω_L is the equatorial gyrofrequency, and Ω_M is the maximum value of Ω which satisfies (3). The frequencies Ω_L, and Ω_M, are resonant with the values of the equatorial pitch angles corresponding to μ_m, and μ_c, respectively (see Figure 1). That is, the smallest value of Ω resonates with the largest possible value of μ, and vice versa. In fact, for $\omega \ll \Omega_L$ we have

$$\Omega_M = kv(1 - \mu_c \Omega_M/\Omega_L)^{1/2} \qquad (4)$$

$$\Omega_L = kv(1 - \mu_m)^{1/2} \qquad (5)$$

We may also write that $\Omega_M/\Omega_L = 1 + (9/2)\psi_m^2$, where $\psi_m (\ll 1)$ is *the maximum geomagnetic* latitude for which resonant wave-particle interaction takes place. We find that ψ_m is related to the equatorial range of resonant pitch angles by the equation

$$\psi_m = \frac{1}{3}(\mu_m - \mu_c)^{1/2} \qquad (6)$$

We also find that for given values of the particle's energy and wave vector, ψ_m is obtained from

$$\psi_m = \frac{\sqrt{2}}{3}(kv/\Omega_L - 1)^{1/2} \qquad (7)$$

Then by equating (6) and (7), we also find that in terms of the particle velocity and wave vector, the equatorial range of resonant pitch angles is

$$(\mu_m - \mu_c) = 2(kv/\Omega_L - 1) \qquad (8)$$

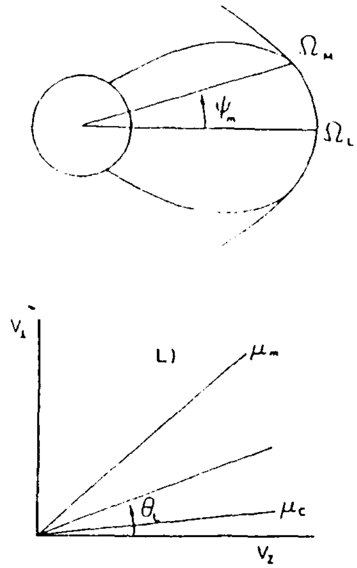

Fig. 1. The Earth's dipole magnetic field and the parabolic profile are qualitatively depicted here. The gyrofrequencies Ω_L, Ω_M correspond to the equatorial and the *maximum resonant geomagnetic* fields, respectively. The angle ψ_m is the maximum geomagnetic latitude for which resonant wave-particle interaction takes place. The velocities $v_\perp$, $v_\parallel$, represent the perpendicular and parallel components *of the resonant particle's* velocity *as given* in the equatorial cross section indicated by the index L). The equatorial pitch angle is denoted by θ_L, and $\mu = \sin^2 \theta_L$. The values μ_c, μ_m, are evaluated for pitch angles at the equatorial loss cone and for the *maximum* value of θ_L which satisfied the resonant condition, respectively.

By realizing that the argument of the square root in (7) has to be larger than zero, we obtain that the wave frequency *must* be such that

$$\frac{\omega}{\Omega_L} > \frac{c}{v}\frac{1}{\eta}$$

3. Distribution Function of Resonant Particles

The cold particle population gives the dielectric properties of wave propagation *in the magnetosphere*; their Maxwellian distribution function is isotropic in pitch angle. The total distribution function for the energetic particles is an anisotropic Maxwellian. For a stable plasma, it is a function of μ and v and independent of the distance z along the flux tube for $|z| < L_m/2$. The energetic particle distribution function is made up of two parts: those particles which are resonant with the waves and those which are not. In this paper f represents only the resonant portion of the distribution function.

The cyclotron *instability can modify the distribution function* of the resonant particles in such a way that it may become dependent on the distance z along the flux tube. *However, for the cases* of weak and moderate diffusion we assume that f does not depend on z between the mirror points $|z| < L_m/2$. For the weak diffusion case the anisotropy in pitch angle is independent on time, and we may write

$$f = \frac{4}{\pi^{3/2}\sigma v_0^4} N(t)Z(\mu) \exp(-v^2/v_0^2) \qquad (9)$$

where $Z(\mu)$ is the lowest order eigenfunction of the diffusion operator which is defined in Appendix B, and $\sigma = 1/\mu_c$ is the mirror ratio. The number of resonant particles in the flux tube (particles per square centimeter) for given values of μ and v is denoted by $N(t)$. Here $N(t)$ depends on time over times scales such that $t \gg \tau_B$ and $t \gg \tau_g$, where τ_B, the particle's bounce time, is defined in (1). The time that the wave spends traveling between one conjugate hemisphere and the other is represented by τ_g.

In the moderate diffusion case the particle anisotropy depends on time, but f is given for all values of z by the equatorial distribution function. Thus we have

$$f = \frac{4}{\pi^{3/2}\sigma v_0^4} \left(\sum_{\ell=1}^{\infty} N_\ell(t)Z_\ell(\mu) \right) \exp(-v^2/v_0^2) \qquad (10)$$

where $Z_\ell(\mu)$ are the eigenfunctions of the diffusion operator. The eigenvalues are represented by p_ℓ, with $\ell = 1, 2, \cdots$, and the summation extends to all possible eigenvalues. The *total number of resonant particles in the flux tube due to the contribution of all possible eigenvalues* is

$$N(t) = N_1(t) + \sum_{\ell,\ell \neq 1} \frac{p_1^2}{p_\ell^2} N_\ell(t) \qquad (11)$$

where N_1 corresponds to the lowest order eigenvalue which we denote by p_1^2, and N_ℓ corresponds to a higher order eigenvalue p_ℓ^2. In the limit $p_1^2 \ll p_\ell^2$, we find that $N \rightarrow N_1$, which is the value of N in the weak diffusion case. The strong diffusion case (i.e., when f depends on z) will not be treated in this article.

The evolution in time of the plasma particle distribution function in the presence of a specified distribution of waves is described by quasi-linear theory [*Lyons and Williams*, 1983]

$$\frac{\partial f}{\partial t} = \int_0^\infty dk \frac{4\pi^2 q^2}{m^2\eta^2} \left(\frac{k}{\omega} \dot{\Theta} + \frac{\omega - kv_z}{\omega v_\perp} \right)$$

$$\cdot\ \delta(-\omega + kv_z - \Omega) W_k \left(\frac{k}{\omega} \dot{\Theta} \right) f \qquad (12)$$

where $v_\perp$ is the *perpendicular* (*to* B) *component* of the particle's velocity, and $\eta = ck/\omega$, the refractive index, is such that $\eta \gg c/v_z$. The energy density of waves is $W_k = B_k^2/16\pi^2$, where B_k is the wave magnetic field. Since $\eta^2 \gg 1$, we need consider only pitch angle diffusion and neglect diffusion in energy. The operator $\dot{\Theta}$ is now given by

$$\dot{\Theta} = -2 \frac{\Omega_L}{\Omega} \frac{v_\perp v_z}{v^2} \frac{\partial}{\partial \mu} \qquad (13)$$

Upon substituting (13) into (12), we find

$$\frac{\partial f}{\partial t} = \frac{4\pi\omega_p^2\Omega_L^2}{v^2 mn\omega^2} \int_0^\infty dk (1 - \mu\Omega/\Omega_L)^{1/2} \frac{\partial}{\partial \mu}$$

$$\cdot \left(\frac{\Omega}{\Omega_L} \frac{W_k}{\eta^2} \frac{\mu}{(1 - \mu\Omega/\Omega_L)^{1/2}} \delta(-\omega + kv_z - \Omega) \frac{\partial f}{\partial \mu} \right) \qquad (14)$$

where ω_p is the *plasma frequency* evaluated for the cold background of plasma particles of density n. We assume that $n \gg N/l$, where l is the length of the flux tube. We now integrate (14) along the flux tube by applying the operator $(1/\tau_B)\int_{-l/2}^{l/2}(dz/v_z)$ to both left- and right-hand sides of (14). We assume that the only spatial inhomogeneities are due to the magnetic field variations, we also assume that f does not depend on z and is given by (9) or (10). By using the parabolic profile in (2) we may write

$$\frac{\partial f}{\partial t} = \frac{4\pi a\omega_p^2\Omega_L}{\tau_B v^3 mnc^2} \int_0^\infty \frac{dk}{k^2} W_k \int_{\Omega_L}^{\Omega_M} \frac{d\Omega}{(\Omega/\Omega_L - 1)^{1/2}}$$

$$\cdot \frac{\partial}{\partial \mu} \left(\frac{\Omega}{\Omega_L} \frac{\mu}{(1 - \mu\Omega/\Omega_L)^{1/2}} \delta(-\omega + kv_z - \Omega) \frac{\partial f}{\partial \mu} \right) \qquad (15)$$

To integrate this equation along the flux tube we make use of the delta function; for more details see Appendix A. After some tedious algebra we arrive at the equations [*Trakhtengerts*, 1984]

$$\frac{\partial f}{\partial t} = \frac{1}{\tau_B} \frac{\partial}{\partial \mu} \left(\mu H \frac{\partial f}{\partial \mu} \right) \qquad (16)$$

$$H = \frac{4\pi\Omega_L\omega_p^2 a}{v^3 mnc^2} \int_{k_0}^\infty \frac{dk}{k^2} \psi_1(k, \mu) W_k \qquad (17)$$

$$\psi_1 = 2 \frac{G - 1}{G} \left(2\mu(G - 1) - \left(\frac{2\Omega_L}{kv} \right)^2 \right)^{-1/2} \qquad (18)$$

Here $k_0 = \Omega_L/[v(1 - \mu)^{1/2}]$ and $G = [1 + (2\Omega_L/kv\mu)^2]^{1/2}$. The wave vector k should be evaluated at the magnetic equator. From (5), we see that $2\Omega_L/kv\mu \geq 2(1 - \mu_m)^{1/2}/\mu_m$. Thus for $\theta_L \leq 45°$, we may assume that $2\Omega_L/kv\mu \gg 1$. Equation (18) now becomes

$$\psi_1 = \frac{kv/\Omega_L}{(kv/\Omega_L - 1)^{1/2}} \qquad (19)$$

Let us now consider a narrow spectrum of waves centered around a certain value of k, and the definitions

$$\Upsilon = \frac{2\pi\Omega_L^2}{B_L^2 kv} \qquad (20)$$

and

$$F = \int_{\Omega_L/k}^\infty \pi\sigma v^3 f dv \qquad (21)$$

Combining (16) to (21) and (1), we find

$$\frac{\partial F}{\partial t} = \Upsilon W_k \frac{1}{\xi} \frac{d}{d\xi} \left(\frac{\xi}{(kv/\Omega_L - 1)^{1/2}} \frac{dF}{d\xi} \right) + J(t, \xi) \qquad (22)$$

where $\xi = \mu^{1/2} = \sin\theta_L$, and J is a particle source which may depend on t and ξ.

In the weak diffusion case we have that $F(t, \xi) = N(t)Z(\xi)$; we also assume that $J(t, \xi) = J(t)Z(\xi)$. The eigenfunction $Z(\xi)$ satisfies

$$\frac{1}{\xi}\frac{d}{d\xi}\left(\xi\frac{dZ}{d\xi}\right) = -p^2(\xi_m^2-\xi_c^2)Z(\xi) \qquad (23)$$

where p is the lowest order eigenvalue of the diffusion operator, and the range of resonant pitch angles is now given by $\xi_c \le \xi \le \xi_m$. We also have

$$\int_{\xi_c}^{\xi_m}\xi Z(\xi)\,d\xi = \frac{2v}{\pi a p^2(\xi_m^2-\xi_c^2)} \qquad (24)$$

$$\left[\frac{dZ}{d\xi}\right]_{\xi=\xi_c,\xi_m} = 0 \qquad (25)$$

For more details on the function $Z(\xi)$ see Appendix B. By using (23) we may rewrite (22) as

$$\frac{dN}{dt} = -p^2[2(\mu_m-\mu_c)]^{1/2}\Upsilon W_k N + J(t) \qquad (26)$$

We note that (26) can be applied to either the interaction of whistlers with electrons or Alfvén waves with ions provided that the gyrofrequencies in (20) are evaluated for the resonant particles, i.e., electrons for whistlers and ions for Alfvén waves.

4. Wave Growth Rates

The linear wave growth rates for resonant wave-particle interaction is given by [*Lyons and Williams*, 1983]

$$\frac{\gamma}{\omega} = \frac{\pi^2\omega_p^2}{\omega^2 n}\int_0^\infty v_\perp^2\,dv_\perp\int_{-\infty}^{\infty}dv_z\,\delta\left(\frac{-\omega}{k}+v_z-\frac{\Omega}{k}\right)\frac{1}{\eta^2}\hat{\Theta}f \qquad (27)$$

where $\hat{\Theta}$ is defined in (13). By using the constancy of the particle's magnetic moment we may write (27) as

$$\frac{\gamma}{\omega} = \frac{2\pi^2\omega_p^2}{n\omega^2}\int_0^\infty v^2dv\int_{\mu_c}^{\mu_m}\mu\,d\mu\,\frac{\Omega^2/\Omega_L}{(1-\mu\Omega/\Omega_L)^{1/2}}\cdot\frac{1}{\eta^2}\delta(-\omega+kv_z-\Omega)\frac{\partial f}{\partial\mu} \qquad (28)$$

The spatial amplification factor is given by integrating along the field line

$$\Gamma = \int_{-l/2}^{l/2}\frac{\gamma}{v_g}\,dz \qquad (29)$$

where v_g is the wave group velocity, and l is the total length of the field line. By assuming that the only spatial inhomogeneity is in the geomagnetic field and by using the parabolic profile in (2) we may write

$$\Gamma = \int_{\Omega_L}^{\Omega_M}\frac{a}{(\Omega/\Omega_L-1)^{1/2}}\frac{\gamma}{v_g}\frac{d\Omega}{\Omega_L} \qquad (30)$$

The evolution in time of the energy density of waves W_k is given by

$$\frac{\partial W_k}{\partial t}+v_g\frac{\partial W_k}{\partial z} = \left(\gamma-\frac{r}{\tau_g}\right)W_k \qquad (31)$$

Here γ is given by (28) and $r = -2\ln R$, where R is the reflection coefficient at both ends of the flux tube (i.e., the ionospheric reflection coefficient). By assuming that W_k depends weakly on z, and by applying the operator $1/\tau_g\int_{-l/2}^{l/2}(dz/v_g)$ to both left- and right-hand sides of (31), we find

$$\frac{dW_k}{dt} = \frac{\Gamma}{\tau_g}W_k - \frac{r}{\tau_g}W_k \qquad (32)$$

4.1. *Whistler Waves*

The dispersion relation is $\eta = \omega_p/(\Omega\omega)^{1/2}$ and the normalized group velocity is $v_g/c = 2/\eta$, where the plasma and cyclotron frequencies are evaluated for cold electrons. Combining (28) and (29) together with the equations in Appendix A, we find [*Bespalov et al.*, 1983]

$$\Gamma = \frac{4\pi^3 kam_e}{B_L^2}\int_0^\infty dv\int_{\mu_c}^{\mu_m}d\mu\,\frac{(G-1)^2}{G}\cdot\frac{(v^2\mu)^2}{[2\mu(G-1)-(2\Omega_L/kv)^2]^{1/2}}\frac{\partial f}{\partial\mu} \qquad (33)$$

where m_e is the electron mass. Under the limit $2\Omega_L/kv\mu \ll 1$, (33) becomes

$$\Gamma = \frac{4\pi^3 km_e a}{B_L^2}\int_0^\infty dv\int_{\mu_c}^{\mu_m}d\mu\,\frac{\mu v^4}{(kv/\Omega_L-1)^{1/2}}\frac{\partial f}{\partial\mu} \qquad (34)$$

Let us now consider the definition in (21) and that $F = N(t)Z(\xi)$ with $\xi = \mu^{1/2}$. We may now rewrite (34) as

$$\frac{\Gamma}{\tau_g} = \Delta_e\varphi(\omega)N(t) \qquad (35)$$

$$\Delta_e = \frac{2\pi^2 am_e v\omega}{l\sigma B_L^2} \qquad (36)$$

$$\varphi(\omega) = \int_{\xi_c}^{\xi_m}\frac{2\xi^2}{(kv/\Omega_L-1)^{1/2}}\frac{dZ}{d\xi}\,d\xi \qquad (37)$$

where $\sigma = 1/\mu_c$, can be expressed in terms of the L shell value as $\sigma = L^3(4-3/L)^{1/2}$. Equation (37) can be integrated approximately by assuming that ξ_m is very close to ξ_c (see Appendix B for details). We find

$$\frac{\Gamma}{\tau_g} = \Delta_e[2(\mu_m-\mu_c)]^{1/2}\frac{v}{\pi a}N(t) \qquad (38)$$

4.2. *Alfvén Waves*

The dispersion relation is $\eta = \omega_p/\Omega$ and the group velocity is $v_g/c = 1/\eta$, where the plasma frequency, ω_p, is evaluated at the plasma density n of the ambient ions (e.g., cold protons), which support the Alfvén waves, and Ω is their gyrofrequency. The spatial amplification factor Γ becomes

$$\Gamma = \frac{\pi^2 k^4 a\omega_p}{\omega n\Omega_L^3 c}\int_0^\infty dv \int_{\mu_*}^{\mu_m} d\mu$$

$$\cdot \frac{(G-1)^3}{G}\frac{(v^2\mu)^3}{[2\mu(G-1)-(2\Omega_L/kv)^2]^{1/2}}\frac{\partial f}{\partial\mu} \qquad (39)$$

Under the limit $2\Omega_L/kv\mu \gg 1$ we obtain

$$\Gamma = \frac{2\pi^2 k^3 a\omega_p}{\omega n\Omega_L^2 c}\int_0^\infty dv\int_{\mu_*}^{\mu_m} d\mu\,\frac{v^5\mu}{(kv/\Omega_L-1)^{1/2}}\frac{\partial f}{\partial\mu} \qquad (40)$$

By considering the definition of F given in (21) and the weak diffusion case (where f is given by (9)) we obtain

$$\frac{\Gamma}{\tau_g} = \Delta_i\varphi(\omega)N(t) \qquad (41)$$

$$\Delta_i = \frac{v^2\pi a\omega_p^3\omega^2}{nak^3\Omega_L^4} \qquad (42)$$

Substituting for $\varphi(\omega)$, we finally obtain for the growth of Alfvén waves

$$\frac{\Gamma}{\tau_g} = \Delta_i[2(\mu_m-\mu_c)]^{1/2}\frac{v}{\pi a}N(t) \qquad (43)$$

5. RAY EQUATIONS

5.1. *Whistler Waves*

The equations describing the parametric coupling between the energy density of waves W_k and the number of particles in the flux tube are

$$\frac{dW_k}{dt} = \Delta_e[2(\mu_m-\mu_c)]^{1/2}\frac{v}{\pi a}NW_k - \frac{r}{\tau_g}W_k \qquad (44)$$

$$\frac{dN}{dt} = -p^2\Upsilon[2(\mu_m-\mu_c)]^{1/2}NW_k + J(t) \qquad (45)$$

where Υ and Δ_e are given by (20) and (36), and p is the lowest order eigenvalue of the diffusion operator (see Appendix B). Note that the growth of the instability is proportional to the range of resonant interaction, i.e., $(\mu_m-\mu_c)^{1/2}$, where $(\mu_m-\mu_c)^{1/2}$ is defined as a function of k, v, and Ω_L, by (8).

Let us now assume that the system is in equilibrium, i.e., $dN/dt = dW_k/dt = 0$. We find that $W_k = W_o$ and $N = N_o$, where

$$W_o = \frac{J\Delta_e(v/a\pi)\tau_g}{rp^2\Upsilon} \qquad (46)$$

$$N_o = \frac{r}{\tau_g\Delta_e v/a\pi}[2(\mu_m-\mu_c)]^{-1/2} \qquad (47)$$

For small deviation from equilibrium we may write $N = N_o + \delta N\exp(\zeta\tau)$ and $W_k = W_o + \delta W\exp(\zeta\tau)$, where $\tau = t/\tau_g$. Upon substituting these expressions into (44) and (45) and keeping only first-order corrections, we find

$$\zeta^2 + (\zeta + r)\frac{j_e}{r} = 0 \qquad (48)$$

where we define $j_e = J\Delta_e(v/\pi a)\tau_g^2[2(\mu_m-\mu_c)]^{1/2}$. By solving for (48) we obtain that $\zeta = -\nu \pm i(\rho^2-\nu^2)^{1/2}$, where

$$\nu = \frac{j_e}{2r} \qquad (49)$$

$$\rho = j_e^{1/2} \qquad (50)$$

Because $\nu, \rho > 0$, we see that the equilibrium solutions in (46) and (47), are always stable.

As an application we consider the interaction of 40-keV electrons with a whistler wave with a frequency of 1 kHz and with a refractive index of 30. The interaction occurs at $L = 4.5$. Thus the mirror ratio σ is equal to 1.6×10^2, the square of the equatorial magnetic field is $B_i^2 = 1.16 \times 10^{-5}$ gaussian units, the length of the flux tube, l, is approximately of the order of 10 times the Earth's radii, and τ_g of the order of a few seconds. The equatorial gyrofrequency is $\Omega_L = 10$ kHz, and ψ_m is about 12°. The range of resonants pitch angles as obtained from (8), is 40°. We have estimated that $[2(\mu_m - \mu_c)]^{1/2} \simeq 0.9$. The coupling coefficient for the wave growth rate (see (35) and (36)) is $\Delta_e(v/\pi a) \simeq 10^{-10}$ cm^2 s^{-1}. For a particle source, $J = 10^3$ to 10^6 particles/(cm^2 s), and by taking $R = 0.8$, we find that $\nu \sim \rho^2$ and their values range between 10^{-7} to 10^{-4} s^{-2} τ_g^2.

5.2. *Alfvén Waves*

The evolution in time of the energy density of Alfvén waves and the number of resonant ions in the flux tube are given by the equations

$$\frac{dW_k}{dt} = \Delta_i\frac{v}{a\pi}[2(\mu_m-\mu_c)]^{1/2}NW_k - \frac{r}{\tau_g}W_k \qquad (51)$$

$$\frac{dN}{dt} = -p^2\Upsilon[2(\mu_m-\mu_c)]^{1/2}W_kN + J \qquad (52)$$

where Υ and Δ_i are given in (20) and (42), p^2 is the lowest order eigenvalue of (23), μ_m and μ_c are defined by (8), as a function of k, v, and Ω_L.

The equilibrium solution to the system of (51) and (52) is $W_k = W_o$ and $N = N_o$, where

$$W_o = \frac{J\Delta_i(v/a\pi)\tau_g}{rp^2\Upsilon} \qquad (53)$$

$$N_o = \frac{r}{\tau_g\Delta_i(v/a\pi)}[2(\mu_m-\mu_c)]^{-1/2} \qquad (54)$$

For small deviations from equilibrium (i.e., $N = N_o + \delta N\exp(\zeta\tau)$ and $W_k = W_o + \delta W_k\exp(\zeta\tau)$, where $\tau = t/\tau_g$), we also find $\zeta = -\nu \pm i(\rho^2-\nu^2)^{1/2}$. Here

$$\nu = \frac{j_i}{2r} \qquad (55)$$

$$\rho = j_i^{1/2} \qquad (56)$$

and $j_i = J\Delta_i(v/\pi a)\tau_g^2[2(\mu_m-\mu_c)]^{1/2}$

We consider the interaction of 200 keV protons with Alfvén waves at $L = 4.5$. The wave frequency is taken equal to 1 Hz and the refractive index $\eta = 9$. Thus the plasma frequency is 10 Hz, the cyclotron frequency is 5.45 Hz, the maximum geomagnetic latitude ϕ_m is about 10°, the range of resonant pitch angles is 34°, and $[2(\mu_m - \mu_c)]^{1/2}$ is 0.8. The group time delay for Alfvén waves may be of the order of minutes. We find that the growth rate is proportional to the coupling coefficient $\Delta_i(v/\pi a) \approx 0.5 \times 10^{-9}$ cm^2 s^{-1}. By assuming that $J \approx 10^3$ to 10^6 particles/(cm^2 s) and that $R = 0.8$, we show that $\nu \approx \rho^2$ and their values range between 10^{-6} to 10^{-3} s^{-2} τ_g^2.

5.3. *Stability Equation*

Let us now define

$$\dot N = \Delta_\alpha\left(\frac{v}{\pi a}\right)\tau_g[2(\mu_m - \mu_c)]^{1/2}N \tag{57}$$

$$\dot W = p^2\tau_g\Upsilon[2(\mu_m - \mu_c)]^{1/2}W \tag{58}$$

where $\alpha = e, i$ depending on whether we are studying either (44), (45) or (51), (52). In terms of normalized quantities, the ray equations become

$$\frac{d\dot N}{d\tau} = -\dot N\dot W_k + J_\alpha \tag{59}$$

$$\frac{d\dot W_k}{d\tau} = \dot N\dot W_k - r\dot W_k \tag{60}$$

The equilibrium solutions can now be written as $\dot N_o = r$ and $\dot W_o = J_\alpha/r$.

We can further reduce (59) and (60) to a single nonlinear equation by defining

$$\dot N = \frac{d\phi}{d\tau} + r \tag{61}$$

$$\dot W_k = \dot W_o \exp(\phi) \tag{62}$$

we may write [*Trakhtengerts*, 1984]

$$\frac{d^2\phi}{d\tau^2} + 2\nu\exp(\phi)\frac{d\phi}{d\tau} + \rho^2[\exp(\phi) - 1] = 0 \tag{63}$$

We note that as $\tau \to \infty$, $\dot N$ and $\dot W$ tend to the equilibrium solutions $\dot W_o$ and $\dot N_o$, and then we must have that $\phi \to 0$.

In the linear approximation the deviation from equilibrium is small, i.e., we may assume that $\phi \ll 1$, (63) now becomes

$$\frac{d^2\phi}{d\tau^2} + 2\nu\frac{d\phi}{d\tau} + \rho^2\phi = 0 \tag{64}$$

The solutions to this equation are $\exp(\zeta\tau)$ where $\zeta = -\nu \pm i(\rho^2 - \nu^2)^{1/2}$, and which for $\rho \gg \nu$ yields the oscillations around equilibrium given in (49), (50) and (55), (56).

6. CONTRIBUTION OF HIGHER-ORDER EIGENVALUES

In the moderate diffusion regime the pitch angle distribution of the resonant particles depend on time, the number of resonant particles in the flux tube, $N(t)$, is given in (11), and the distribution function in (10). Let us further write for the particle source

$$J(t,\xi) = \sum_{\ell=1}^{\infty} Z_\ell(\xi)J_\ell(t) \tag{65}$$

where the summation is extended to all possible eigenvalues and the eigenfunctions $Z_\ell(\xi)$ satisfy (23) by setting $p = p_\ell$. The eigenvalues and eigenfunctions are given in Appendix B.

The evolution in time of the functions $N_\ell(t)$ and the energy density of waves W_k are given by the system of equations

$$\frac{dN_\ell}{dt} = -p_\ell^2\Upsilon[2(\mu_m - \mu_c)]^{1/2}N_\ell W_k + J_\ell(t) \tag{66}$$

$$\frac{dW_k}{dt} = \left(\Delta_\alpha\frac{v}{a\pi}\right)[2(\mu_m - \mu_c)]^{1/2}W_k\left(\sum_{\ell=1}^{\infty}N_\ell\right) - \frac{r}{\tau_g}W_k \tag{67}$$

where $\alpha = e, i$ depending on whether we are considering the growth of whistler (e) or Alfvén (i) waves. By assuming that $p_\ell^2 \gg p_1^2$ for all $\ell \neq 1$ and keeping lowest order terms in the ratio $(p_1/p_\ell)^2$, we may approximately cast the system (66) and (67) into the set of two coupled equations (see Appendix C)

$$\frac{dN}{dt} = -p_1^2\Upsilon[2(\mu_m - \mu_c)]^{1/2}W_kN + J_1 \tag{68}$$

$$\frac{dW_k}{dt} = \left(\Delta_\alpha\frac{v}{a\pi}\right)[2(\mu_m - \mu_c)]^{1/2}W_kN + \left[\sum_{\ell,\ell\neq1}\frac{(\Delta_\alpha v/a\pi)}{\Upsilon}\frac{J_\ell}{(p_\ell^2 - p_1^2)}\right] - \frac{r}{\tau_k}W_k \tag{69}$$

These equations admit the equilibrium solution

$$W_o = \frac{J_1}{p_1^2}\frac{(\Delta_\alpha v/a\pi)\tau_g}{r\Upsilon}\left[1 + \sum_{\ell,\ell\neq1}\frac{J_\ell/J_1}{(p_\ell^2/p_1^2 - 1)}\right] \tag{70}$$

$$N_o = \frac{r}{(\Delta_\alpha v/a\pi)\tau_g}[2(\mu_m - \mu_c)]^{-1/2} \cdot \left[1 + \sum_{\ell,\ell\neq1}\frac{J_\ell/J_1}{(p_\ell^2/p_1^2 - 1)}\right]^{-1} \tag{71}$$

We see that the anisotropy of the particle source as defined in (65) is reflected in the equilibrium solutions. The predominant contribution is given by the component J_ℓ such that J_ℓ/p_ℓ^2 has the maximum value. In fact, an anisotropic source enhances the level of the energy density of waves and depletes a larger number of particles toward equilibrium. For small deviations from this solutions we have: $\zeta = -\nu \pm i(\rho^2 - \nu^2)^{1/2}$. Here $\nu = \dot W_o/2$, $\rho = (r\dot W_o)^{1/2}$ and $\dot W_o = p_1^2\tau_g\Upsilon[2(\mu_m - \mu_c)]^{1/2}W_o$.

7. WAVE REFLECTION COEFFICIENTS

As a wave enters the ionosphere it is partially reflected back into the magnetic trap and partially penetrates the ionosphere and gets to the ground [*Ginzburg*, 1970]. We have already called R the reflection coefficient, where RW_k

is the amount of the wave amplitude which gets reflected back, and W_k is the wave amplitude in the flux tube. The value of the reflection coefficient depends on several factors, such as the ratio between the wave and collision frequencies with the environmental particles (neutral). It also depends on the ratios of the size of the ionosphere d, the wavelength $\lambda = 2\pi/k$, and the scale of the density gradient $\mathcal{L}$, where

$$\frac{1}{\mathcal{L}} = \frac{1}{n}\frac{dn}{dz} \tag{72}$$

Typically, we have $\mathcal{L} \approx 50$ km and $d \gg \mathcal{L}$ (e.g., $d \approx 300$ km). We represent by η_F, η_E, and η_o, the refractive indices in the F and E layers, and in the flux tube, respectively. Next, we discuss qualitatively the reflection of whistlers and Alfven waves. We show that whistlers are mainly reflected from the E and D layers of the ionosphere, while Alfven waves are reflected from the F layer.

We assume perfect ducting for the reflection of ELF and VLF waves. Namely, the reflection coefficients are given for the ideal situation where the reflected wave reenters the same duct from which it originated. However, we note that, due to flux spreading, this may not be in general the case [*Thomson and Dowden*, 1977]. As a matter of fact, part of the energy can be directed outside the duct and be "lost" into the magnetosphere. On the other hand, adjacent ducts may be a source of wave energy for a given duct after the waves are reflected in the ionosphere and find their way into that duct. Nonducted whistler waves are reflected in the magnetosphere when their frequencies fall below the local lower hybrid frequency as they propagate into regions of increasing field strength away from the equator [*Lyons and Thorne*, 1970]. These waves are not studied here, and they may also be an important source of wave-particle interactions in the magnetosphere. In addition, for simplicity in the calculations, we assume that the inclination of the waves duct exit with respect to the vertical is small. A more realistic model of wave reflection should take into account all these complexities.

7.1. *Reflection of Whistlers*

Here we consider the reflection of whistler waves with frequencies of the order of a few kilohertz in the F, E, and D regions of the ionosphere. In the F layer the electron density is between values of 10^4 to 10^6 particles per cubic centimeter, and the scale length of the density gradient is about $\mathcal{L} \approx 50$ km. The wavelengths of whistler modes are of the order of a few kilometers, and such that $\lambda \ll \mathcal{L}$. For example, for $\omega/2\pi \approx 4$ kHz, and a density of 10^4 particles per cubic centimeter, we find that $\lambda \approx 6$ km. Because the wave amplitude changes slowly as it penetrates the F layer, a WKB analysis is a valid approximation. Thus one expects whistler waves which are ducted in the flux tube to penetrate the ionospheric F layer without significant reflection. Whatever little reflection takes place will be due to collisions with the neutral particles. On the other hand in the E and D layers the peak electron density ranges between values of 10^3 to 10^5 particles per cubic centimeter, and the scale length is about $\mathcal{L} \approx 10$ km. For a wave of frequency equal to 4 kHz, we find that wavelengths are between values of a few to about 60 km depending on plasma density, and that $\lambda \gtrsim \mathcal{L}$. In all cases we have $(\lambda/2\pi) \ll d$, where d is the size of the ionospheric layers. Because collisions with neutral particles are more significant in the E and D layers, we expect whistler waves to be reflected there. We may distinguish between these cases depending on whether we consider reflection from a high or low density E and D layers. For a high-density E layer the reflection coefficient is obtained by assuming that the plasma density changes according to an exponential profile. For the weak density case, we treat the E layer as a semiinfinite slab with a sharp boundary at the border with the F layer.

Let us first study reflection from a high density collisional E layer. The refractive index becomes complex $\eta_E^* = \eta_r + i\kappa$. We define $r_c = \nu_c/\omega$ where ν_c is the collision frequency which depends on the height z, and it is such that as $z \to \infty$, $\nu_c \to 0$. The origin of heights $z = 0$, is chosen at the bottom of the F layer. Thus inside the E layer $z \le 0$. Here $Y = \Omega_c/\omega$, and $X = \omega_p^2/\omega^2$, where the plasma density ω_p depends on the density profile. We have [*Helliwell*, 1965]

$$(\eta_E^*)^2 = 1 - \frac{X}{1 - ir_c \pm Y} \tag{73}$$

The wave equation is

$$\frac{d^2\Sigma_z}{ds^2} + [1 - bX]\Sigma_z = 0 \tag{74}$$

where $\Sigma_z = E_x \pm iE_y$, E_x and E_y are the components of the electric field, and $s = z/\lambda$. The sign plus corresponds to the right-hand polarization and minus to the left-hand polarization. Here $b = [1 - ir_c \pm Y]^{-1}$ also depends on the wave polarization. Given some profiles for the plasma density and collision frequency, (74) may be studied by using the WKB approximation [*Budden*, 1961]. Here we solve (74) exactly when the electron density profile is exponential. Note that for example, the exponential profile is of interest to describe auroral arcs in the night-time ionosphere. Thus we may write: $X = X_o + \exp(-\delta s)$, where X_o is an averaged value of X in the flux tube, and $\delta = \lambda/\mathcal{L}$. For $s \to \infty$, $X = X_o$; inside the E layer $s \le 0$. We also assume that the collision frequency is independent of height and given by an averaged value. Equation (74) can be reduced to the Bessel equation. For $\Re(b^{1/2}) > 0$, the solution to (74) which represents an upgoing wave at great heights is the Bessel function of the third kind,

$$\Sigma_z = H_\alpha^{(1)}(x) \tag{75}$$

where $x = -(2i/\delta)b^{1/2}\exp(-\delta s/2)$, and $\alpha = (-2i/\delta)(1 - X_o b)^{1/2}$. We use the asymptotic limits as $x \to 0, \infty$ (i.e., $s = \pm\infty$), where for $x \to 0$ we have only an upgoing wave. We also consider that the polarizations of the downcoming and upgoing waves are left-hand and right-hand, respectively. The absolute value of the reflection coefficient for $Y \gg 1$ is

$$R = \exp\left[-\frac{2\pi}{\delta}\eta_o + \frac{2\eta_o}{\delta}\arctan\left(\frac{r_c}{1 - Y}\right)\right] \tag{76}$$

Equation (76) generalizes the result obtained by *Budden* [1961], by including the coupling to the flux tube. For a slowly varying medium we have that $\delta \to 0$ and the wave is totally transmitted and reaches the ground. Note that the larger the refractive index η_o the smaller the reflection coefficient. We now consider two cases: (1) if $r_c \ll Y$ very small collision frequency, we find that $R = \exp(-2\pi\eta_w/\delta)$, and (2) if $\nu_e \gg Y$, then $R = \exp(-\pi\eta_w/\delta)$. Thus collisions favor wave reflection back into the flux tube, as do large density gradients and large wavelengths.

Note that at normal nighttime ionosphere, there is little ionization in the E layer. These conditions and the fact that the collision frequency in the F layer is so small, allow whistler waves to travel all the way down to the Earth through a collisionless media. We now treat the case of a weak E layer, where the plasma density can be as low as 10^2 particles per cubic centimeter. By taking the wave frequency equal to 4 kHz, we find that the refractive index η_E is very close to unity (i.e., $\eta_E = 1.3$). The wavelength $\lambda/2\pi$ is then equal to 9 km which is much smaller than the altitude of the ionospheric E layer. The refractive index in the F layer is $\eta_F \simeq 13$, which corresponds to an ionospheric density of approximately 10^4 particles per cubic centimeter. Thus whistler waves which are passing through the F layer encounter a sharp boundary at the low density nighttime E layer, and get reflected there. Under these conditions, the reflection coefficient can be obtained by assuming that the E layer is a semi-infinite slab of constant density. Here the upper boundary of the slab is the F layer. We find

$$R = \frac{\eta_F - \eta_E}{\eta_F + \eta_E} \tag{77}$$

For the example given above, R is equal to 0.8. In this paper we do not discuss the effect of the whistlers penetrating through the atmosphere and reflecting from the ground. For our applications this additional reflection process provides a secondary source of wave energy in the flux tube, which will only enhance the efficiency of the wave resonator.

7.2. *Reflection of Alfvén Waves*

First let us look at the reflection of Alfvén waves in the F layer. Because $(\lambda/2\pi)$ is of the order of the altitude d of the ionospheric F layer, we cannot any longer assume that the dimensions of the ionosphere are infinite. The F layer now has two boundaries. One is at $z = 0$, the border with the E layer, and the other one is at $z = d$ somewhere inside the flux tube. Inside the E layer ($z \le 0$), we assume the wave propagates into a plasma medium with a refractive index equal to η_E. When the E layer is equivalent to free space then $\eta_E = 1$. The F layer ionospheric model with the two boundaries acts as a resonant cavity for the very large wavelength fields. A wave incident from the flux tube on the upper boundary ($z = d$) is partially reflected back into the flux tube, and partially transmitted into the ionospheric slab. The transmitted wave is partially reflected at the lower boundary $z = 0$ and partially transmitted below $z = 0$. By matching these waves at $z = 0$ and $z = d$, we find that the absolute value of the reflection coefficient is (see Appendix D)

$$|R|^2 = \frac{[r_1 + r_2(1 - \tan^2\vartheta)]^2 + 4r_2^2\tan^2\vartheta}{[d_1 + d_2(1 - \tan^2\vartheta)]^2 + 4d_2^2\tan^2\vartheta} \tag{78}$$

where $r_1 = (\eta_F + \eta_w)(\eta_E - \eta_F)$, $r_2 = (\eta_F - \eta_w)(\eta_F + \eta_E)$, $d_1 = (\eta_F - \eta_w)(\eta_F - \eta_E)$, $d_2 = (\eta_F + \eta_w)(\eta_F + \eta_E)$, and $\vartheta = (2\pi/\lambda)d$. We recall that η_F and η_w are the refractive indices in the F layer and flux tube, respectively. Equation (78) reduces to the result derived by *Budden* [1961] in the limit $\eta_w, \eta_E \to 1$. In addition, if we let the refractive index η_F have an infinitesimally small imaginary part and if $d \to \infty$, then we also recover the reflection coefficient for a semi-infinite slab as treated above. Note that for nondispersive waves (such as Alfvén waves), the refractive indices do not depend on wave frequencies. Thus the semi-infinite slab model yields reflection coefficients independent on wave frequencies. Nevertheless, the reflection coefficient in the finite slab model of (78) is frequency dependent. In fact, it exhibits resonant behavior for certain values of the wave frequency. In particular for $\eta_F \simeq \eta_w$ and both much larger than η_E, we find that $d_2 \simeq -r_1 \simeq 2\eta_F^2$ and $d_1 \simeq r_2 \simeq 0$. The reflection coefficient now becomes $|R| = \cos^2\vartheta$, which is zero for $\vartheta = (\pi/2)(2n + 1)$, where n is an integer, i.e., for $2d/\lambda = n + 1/2$.

Now let us illustrate the frequency dependency of the reflection coefficient in (78) with some examples. This should be contrasted with the frequency independent nature of the semi-infinite slab model. In the F layer, Alfvén waves are mostly supported by O^+ ions. The ion cyclotron frequency is $\Omega_i = 0.05$ kHz. For an auroral ionospheric particle density of about 10^6 particles per cubic centimeter, we find that the plasma frequency is 52.5 kHz. The collisionless dispersion relation for Alfvén waves yields a refractive index $\eta_F \simeq 1027.5$. For wave frequencies of the order of 0.5 Hz, we have that $\lambda \sim 600$ km. Hence we conclude that wave reflection will mostly occur as described above, and that the reflection coefficient in the F layer is given in (78). Let us now consider the flux tube as part of the same example. We assume that the particles supporting the Alfvén waves in the magnetosphere are protons, and that the wave-particle interaction occurs at $L = 4.5$. We also treat $z \le 0$ as free space (i.e., we take $\eta_E = 1$). The equatorial cyclotron frequency is equal to 5.45 Hz. If the particle density in the flux tube is of one proton per cubic centimeter, we find that $\eta_w = 38.5$ which leads to a reflection coefficient equal to one. In Figure 2*a*, we have represented $|R|^2$ as function of ϑ for a plasma density of one hundred protons per cubic centimeter, the refractive index in the flux tube is now equal to 385. We can see the resonant behavior of the reflection coefficient as function of ϑ. Because $\vartheta = (\eta_F d/c)\omega \sim (d/300)\omega$, we find that for $0 < \vartheta < 4\pi$ radians, the wave frequency varies roughly between 0 and 2 Hz. Maximum reflection, $|R| = 1$, occurs for $\omega = 0, 0.5, 1, 1.5$, and 2 Hz. In Figure 2*b*, we take the number of protons in the flux tube to be equal to 400 particles per c.c., and show $|R|^2$ as a function of ϑ. Here we have that $\eta_w \sim 770$, and that ω varies between 0 and 2 Hz, where we have assumed that $d \sim 300$ km. From these examples we conclude that reflection of Alfvén waves in the F layer is very sensitive to the values of the wave frequency, and of the refractive index in the flux tube. If the waves penetrate the F layer, they then can be reflected in the highly collisional E and D layers. The reflection coefficient in these regions depends on the height integrated Pedersen conductivity [*Hostrom*, 1964], and can be found elsewhere [*Hughes*, 1982].

8. ACTIVELY EXCITED IONOSPHERE

The reflection of waves in the ionosphere is a very important factor in the growing of the whistler and Alfvén instabilities. An effectively operating cyclotron maser re

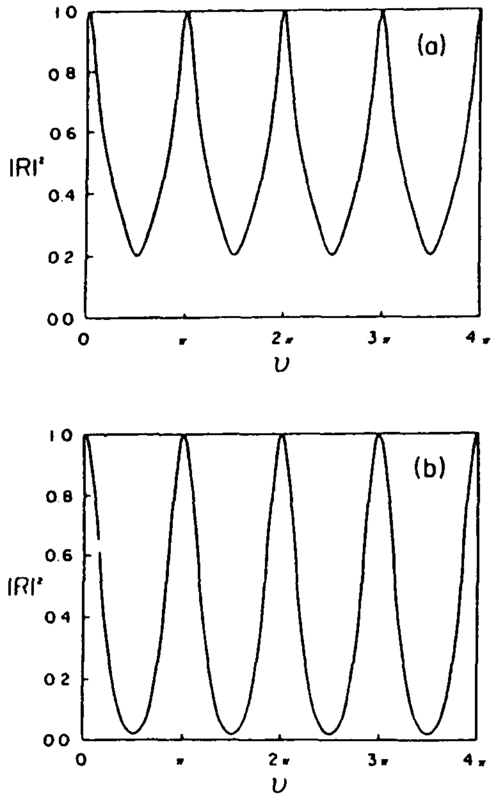

Fig. 2. *Square of the reflection coefficient as a function of* ϑ (in radians) which is equal to $(2\pi/\lambda)d$, where λ is the wavelength and d the length of the ionospheric layer. In case 2*a*, we take *n*, the number of protons in the flux tube, to be equal to 100 particles per cubic centimeter. In case 2*b*, *n* is equal to 400 protons per cubic centimeter. The density of O^+ ions in the ionosphere is taken equal to 10^6 particles per cubic centimeter.

quires large wave amplitudes to pitch angle scatter trapped energetic particles into the loss cone. This is a diffusion process which is described by a Fokker-Planck type of equation. By changing the reflection coefficient at the ionospheric turning points of the waves, we may substantially modify the fields amplitudes and hence, the efficiency of the maser operation in the geomagnetic flux tube. In section 7 we presented a discussion on the qualitative values that the reflection coefficients take in an unperturbed (natural) ionosphere depending on the range of wave frequencies and wavelengths. We learned that wave reflection is increased by sharp density gradients and large values of the collision frequency. Thus we may want to modify the ionospheric properties with some external means, to improve wave reflection. One way of doing this is using a high-power radio wave transmitter either from the ground or from space vehicles at the selected frequencies whose turning points fall at the height where the properties of the ionosphere are to be modified. Heating of the ionosphere at the turning points of the pump fields can produce energetic electrons which, by additional ionization, create a large population of thermal electrons and a substantial modification of the ionospheric impedance. Other physical phenomena can take place near the turning points of the transmitted radio waves such as parametric instabilities, and generation of large density cavities by the ponderomotive force of the radiated fields. They can also lead to electron acceleration and thus to modification of the dielectric properties of the ionosphere. In addition, by heating the D and E layers with a frequency close to Ω_e, the electron population can be increased by dissociation of some of the negative molecular and atomic ions that exist in the ionosphere [*Banks and Kockarts*, 1973]. This may also improved the collision rates, with relatively small values of the power radiated from the ground.

Here we assume that the reflection coefficient changes according to the expression, $r + \varepsilon_m \Lambda(\tau)$. The unperturbed reflection coefficient is $r = -2 \ln R$ and $\Lambda(\tau)$ is the modulation due to the presence of the HF waves, where $\tau = t/\tau_g$ is the normalized time. We may now write that the number of particles in the flux tube $N(t)$, and the energy density of waves $W_L(t)$ are given by

$$\dot{N} = \frac{d\phi_m(\tau)}{d\tau} + r + \varepsilon_m \Lambda(\tau) \qquad (79)$$

$$\dot{W}_L = \dot{W}_o \exp(\phi_m) \qquad (80)$$

where $\dot{W}_o = \rho^2 \tau_g \Lambda [2(\mu_m - \mu_c)]^{1/2} W_o$, and W_o is the equilibrium energy density of waves which is defined in (46) for whistlers, and (53) for Alfvén waves. The function ϕ_m satisfies the differential equation

$$\frac{d^2\phi_m}{d\tau^2} + 2\nu \exp(\phi_m) \frac{d\phi_m}{d\tau} + \rho^2 [\exp(\phi_m) - 1]$$

$$+ \varepsilon_m \frac{d\Lambda}{d\tau} + 2\nu\varepsilon_m \Lambda \exp(\phi_m) = 0 \qquad (81)$$

where ν and ρ are defined in (49) and (50) (for whistlers), and (55) and (56) (for Alfvén waves). Equation (81) is comparable to (63), but here we have added the contribution of an actively excited ionosphere through the terms proportional to $\varepsilon_m \Lambda$. We may further linearize (81) by assuming that $|\phi_m| \ll 1$. We find

$$\frac{d^2\phi_m}{d\tau^2} + 2\nu \frac{d\phi_m}{d\tau} + (\rho^2 + 2\nu\varepsilon_m\Lambda)\phi_m = -\varepsilon_m\left(\frac{d\Lambda}{d\tau} + 2\nu\Lambda\right) \qquad (82)$$

Let us study (82) after setting its right-hand side equal to zero. By further defining $\phi_m = V_m \exp(-\nu\tau)$, we find

$$\frac{d^2V_m}{d\tau^2} + Q_m(\tau)V_m = 0 \qquad (83)$$

where $Q_m = \rho^2 - \nu^2 + 2\nu\varepsilon_m\Lambda(\tau)$.

As an example we now assume that $\Lambda(\tau) = -\cos(2\omega_m\tau)$ [*Trakhtengerts*, 1983]. Here ω_m is the normalized (to τ_g) driver frequency, and define

$$a_m = \frac{\rho^2 - \nu^2}{\omega_m^2}$$

$$q_m = \frac{\varepsilon_m \nu}{\omega_m^2}$$

The WKB solution to (83) is

$$V_m \sim Q_m^{1/4} \cdot \exp\left(\pm \sqrt{2q_m - a_m} \int_0^{\tau_m} \sqrt{1 - k_m^2 \sin^2(\tau_m)}\, d\tau_m\right) \tag{84}$$

where $k_m^2 = 4q_m/(2q_m - a_m)$ and $\tau_m = \alpha_m \tau$.

Let us now write $V_m(\tau_m = \pi/2) = Q_m^{-1/4} \exp(\pm A_m)$. To find unstable modes we calculate the amplification, A_m, over one period of the driver frequency. The case $\epsilon_m = 0$ (i.e., the ionosphere is not externally perturbed) corresponds to $A_m = \pm i p \pi/2$, and the function $V_m(\pi/2)$ is purely oscillatory. If $\epsilon_m \neq 0$, we find that the equilibrium will be unstable only if $|\epsilon_m| \geq (\rho^2 - \nu^2)/2\nu$. In the case where $\rho^2 \gg \nu^2$, we find that in order to have unstability we need to require that $|\epsilon_m| \gg \nu/2$.

As a second example we consider the coupling of the radiation belts waves and particles to the ionosphere. This mechanism introduces a positive feedback effect which will structure the large-amplitude nonlinear response of the system. The precipitating electrons modify the ionospheric plasma density which, in turn, modifies the ionospheric reflection of the waves causing the precipitation. In the D and E layers, the modification of the plasma density by the precipitation is given by [*Silevitch et al.*, 1989]

$$\frac{dn_i}{dt} = \frac{Q}{2}\left(J - \frac{dN}{dt}\right) - \sigma_r n_i^2 \tag{85}$$

where n_i is the ionospheric plasma density. The right-hand side of (85) represents the balance between the increasing density due to the precipitating particle flux and the decrease due to electron-ion recombination effects. Here Q is the ionization efficiency, and σ_r the recombination coefficient. Because the term proportional to the recombination coefficient is nonlinear in n_i, we may neglect it in the linear calculations that follow.

We now assume that $\Lambda(\tau)$ is proportional to dn_i/dt, i.e., we have

$$\Lambda = -\frac{Q}{2}\left(\frac{d^2\phi_m}{d\tau^2}\right) \tag{86}$$

Where we have redefined r as $r + r_m Q J_n/2$. By combining (86) and (82), we find

$$r_m \frac{Q}{2}\frac{d^3\phi_m}{d\tau^3} + (\nu r_m Q - 1)\frac{d^2\phi_m}{d\tau^2} - 2\nu\frac{d\phi_m}{d\tau} - \rho^2\phi_m = 0 \tag{87}$$

Next we take $\phi_m \sim \exp(\zeta\tau)$, which yields

$$\zeta^3 + 2\left(\nu - \frac{1}{Qr_m}\right)\zeta^2 - \frac{4}{Qr_m}\nu\zeta - \frac{2}{Qr_m}\rho^2 = 0 \tag{88}$$

We may solve (88) approximately for $1/\nu \ll Q|\epsilon_m| \ll (\rho/\nu)^2$. We obtain the following three roots:

$$\zeta_1 = \left(\frac{2\rho^2}{Qr_m}\right)^{1/3}$$

$$\zeta_{2,3} = \left(\frac{2\rho^2}{Qr_m}\right)^{1/3}\left(-\frac{1}{2} \pm i\frac{\sqrt{3}}{2}\right)$$

We see that when $r_m \to 0$, the mode ζ_1 is unstable.

In the numerical example presented in section 5.1, for the whistler instability, we found that $1/\nu$ varied between the values 10^7 to 10^4 times r (where $r = -2 \ln R$). If the reflection coefficient, R, is very close to one, then r is very small (as small as 10^{-7} or 10^{-4}). Hence when $R \approx 1$, we have that $1/\nu$ is a small number so the condition for the instability, $Q|\epsilon_m| > 1/\nu$, can be easily satisfied. Otherwise, i.e., for $R < 1$, it is very difficult to find unstable solutions to (88), since very large values for the particle source J are then required.

9. Summary and Conclusions

We have presented a self-consistent theory on the interaction of magnetospheric particles with ducted electromagnetic cyclotron waves. Our theory is based on the following assumptions:

1. The dielectric properties of wave propagation are given by a cold background of plasma particles, which can either be electrons (for the whistlers) or ions, e.g., protons (for the Alfvén instabilities). Since the density of the cold plasma population is taken constant along the flux tube, the only spatial inhomogeneities are due to geomagnetic field variations.

2. Near the equator the Earth's magnetic field is approximated by a parabolic profile. This profile is shown to be a good approximation to the actual dipole geomagnetic field within latitudes smaller than approximately ±20° off the equator. Outside equatorial regions we use the dipole magnetic field to describe particles' orbits and bounce times.

3. The maser instability is produced by the interaction of a hot plasma population (e.g., particles with energies larger than 40 keV for the electrons, and 100 keV for the ions), with the cyclotron waves near equatorial regions. The changes in the thermal distribution functions due to pitch angle diffusion are studied here. We assume that diffusion occurs over times scales that are longer than particles' bounce times and the group time delays of the waves, and do not consider the possibility of particles drifting away from the waves ducts.

4. Because we assume that the wave vectors are field-aligned, resonant interactions can only take place at the first harmonic of the cyclotron frequency. We do not consider the contribution of larger harmonics to the diffusion processes, which becomes significant for highly energetic particles [*Lyons et al.*, 1971] and for non field-aligned (i.e., $k_\perp \neq 0$) waves [*Kimura*, 1966].

The main results of our theory can be summarized as follows:

1. The resonant part of the energetic particles' distribution functions are described within the framework of quasilinear theory. From the resonance condition, we establish relations between the range of equatorial pitch angles and the extent of geomagnetic latitudes for which interactions take place. After integrating along the flux tube, we arrive at equations describing the time evolution of the number of particles in the flux tube as functions of the energy density of waves.

2. The spatial amplification factors are obtained for whistlers and Alfvén waves, after integrating the temporal growth rates over time scales which are comparable to the group time delays of the waves τ_g. The ray equations describing the evolution in time of the number of particles in the flux tube and the energy density of waves are studied near equilibrium.

3. The equatorially generated waves may be partially reflected back into the flux tube when they reach the ionosphere. Whistlers can penetrate the F layer without significant reflection, and be reflected in the D and E layers. In contrast, Alfvén waves are reflected in the F layer which acts as a resonant cavity for these long wavelengths waves.

4. We have also presented some calculations on the role that an actively excited ionosphere plays in the confinement of the cyclotron waves within the flux tube. The stability equation has been extended as to include time dependent reflection coefficients, which may be created by either modulation of the ionosphere with high-power microwave transmitted or by the same particle precipitations due to the maser instabilities. Unstable modes are found for large external perturbations of the ionospheric conductivity.

The theory presented here provides a basis for additional research on the dynamics of nonlinear interactions of waves and particles in the magnetosphere. Some possible problems which deserve further attention are as follows:

1. Non field-aligned waves with wave vectors having components perpendicular to the geomagnetic field also interact with energetic particles. Since diffusion can now take place at higher harmonics of the gyrofrequency, their contribution to the diffusion processes and wave growth rates should be evaluated.

2. The strong diffusion problem where the energy density of waves, and the number of particles in the flux tube, may change over time scales which are comparable to the particles' bounce times and group time delays of the waves.

3. Changes in the ionospheric height integrated conductivity due to external perturbations such as heating with intense radio frequency waves. The effects that this has on the mirroring properties of the ionosphere has been introduced. Further research in this area is essential in order to effectively plan future active experiments.

Appendix A: Integration Along Field Lines

We consider

$$\int F(x)\delta(h(x))\,dx = \sum_{x_R} F(x_R)\left|\left(\frac{dh(x)}{dx}\right)_{x=x_R}\right|^{-1} \qquad \text{(A1)}$$

where x_R is such that $h(x_R) = 0$, and the summation is extended to all possible zeros of the function $h(x)$. Applying this formula to (15), we find that the resonance frequencies are [*Bespalov et al.*, 1983]

$$\Omega_R = \frac{k^2v^2\mu}{2\Omega_L}(G-1) \qquad \text{(A2)}$$

where G is defined after (18). We also find

$$\left(1-\mu\frac{\Omega_R}{\Omega_L}\right)^{1/2} = \frac{kv\mu}{2\Omega_L}(G-1) \qquad \text{(A3)}$$

$$\left(\frac{\Omega_R}{\Omega_L}-1\right)^{1/2} = \frac{2\Omega_L}{kv}\left[2\mu(G-1)-\left(\frac{2\Omega_L}{kv}\right)^2\right]^{1/2} \qquad \text{(A4)}$$

$$\left[\frac{d}{d\Omega}(\Omega-kv_\parallel)\right]_{\Omega=\Omega_R} = \frac{G}{G-1} \qquad \text{(A5)}$$

We next consider that the differential operator $(\partial/\partial\mu)$ on the right-hand side of (15) can be brought out the integral sign. Then by combining (A2)–(A5) together with (15), we can easily recover the results in (16)–(18).

Appendix B: Pitch Angle Eigenfunctions

By defining $\hat{p} = p(\xi_m^2 - \xi_c^2)^{1/2}$ and $y = \hat{p}\xi$, we may cast (23) into the Bessel equation [*Roberts*, 1969; *Bespalov et al.*, 1983]

$$y^2\frac{d^2Z}{dy^2} + y\frac{dZ}{dy} + y^2Z = 0 \qquad \text{(B1)}$$

whose general solution is

$$Z = C_1J_0(\hat{p}\xi) + C_2Y_0(\hat{p}\xi) \qquad \text{(B2)}$$

Here C_1 and C_2 are constants, and J_0 and Y_0 are Bessel functions of order zero. By imposing the boundary conditions given in (25), we get the following equation which solves for the eigenvalues of the differential equation (23)

$$J_1(y_c)Y_1(y_m) - Y_1(y_c)J_1(y_m) = 0 \qquad \text{(B3)}$$

where $y_c = \hat{p}\xi_c$, $y_m = \hat{p}\xi_m$, and J_1, Y_1 are the Bessel functions of order one. We also have

$$Z = C(-Y_1(y_c)J_0(y) + J_1(y_c)Y_0(y)) \qquad \text{(B4)}$$

Given that $\xi_c \ll 1$, *we have that* $Y_1(y_c) \sim 1/y_c$ *and* $J_1(y_c) \sim 0$. Thus (B3) approximately becomes

$$J_1(p(\mu_m-\mu_c)^{1/2}\mu_m^{1/2}) = 0$$

and hence that the eigenvalues are given in terms of the zeros of the first-order Bessel function. The normalization condition (24) yields

$$C\int_{y_c}^{y_m}(J_1(y_c)Y_0(y) - Y_1(y_c)J_0(y))y\,dy = \frac{2v_0}{\pi a} \qquad \text{(B5)}$$

We see that the function $Z(\mu)$ has the dimensions of velocity v, divided by length l, so that the dimensions of the distribution function as given in (9), (10) comes out to be $v^{-3}\times l^{-1}$.

In order to evaluate the function $\varphi(\omega)$ in (37), we first consider

$$\xi\frac{dZ}{d\xi} = \int_{\xi_m}^{\xi}\frac{d}{dx}\left(x\frac{dZ}{dx}\right)dx = -p^2(\mu_m-\mu_c)\int_{\xi_m}^{\xi}xZ(x)\,dx \qquad \text{(B6)}$$

By combining (8), (37) and (B6), we find

$$\varphi(\omega) = 4p^2(kv/\Omega_L - 1)^{1/2}\int_{\xi_c}^{\xi_m}x\,dx\int_x^{\xi_m}sZ(s)\,ds \qquad \text{(B7)}$$

Then by assuming that ξ_c is very close to ξ_m, we may further write

$$\varphi(\omega) \approx 2p^2(kv/\Omega_L - 1)^{1/2}\left(\int_{\xi_c}^{\xi_m}x\,dx\right)\left(\int_{\xi}^{\xi_m}xZ(x)\,dx\right) \qquad \text{(B8)}$$

After using the normalization condition in (24), we get

$$\varphi(\omega) \approx \frac{2v}{\pi a}\,(\omega/\Omega_L - 1)^{1/2} \qquad \text{(B9)}$$

This last equation easily leads to the results in (38) and (43).

APPENDIX C: TIME-DEPENDENT PITCH-ANGLE ANISOTROPIES

Let us write that all $\ell \neq 1$, $N_\ell(t) = N_1(t)\beta_\ell(t)$. Upon substituting this expression into (66) we find

$$\frac{d\beta_\ell}{dt} + K_\ell W_k \beta_\ell = \frac{J_\ell}{N_1} \qquad \text{(C1)}$$

Here $K_\ell = \dot{Y}_\ell + (J_1/N_1 W_k)$, and $\dot{Y}_\ell = (p_\ell^2 - p_1^2)Y[2(\mu_m - \mu_c)]^{1/2}$. We may also write the following integral equation

$$\beta_\ell(t) = \exp\left(-\int_0^t K_\ell W_k\, dx\right) \cdot \left[\int_0^t dx\,\frac{J_\ell}{N_1}\exp\left(\int_0^x K_\ell W_k\, dy\right)\right] \qquad \text{(C2)}$$

Integrating by parts we may approximate N_ℓ by

$$N_\ell = \frac{J_\ell N_1}{\dot{Y}_\ell N_1 W_k + J_1} \qquad \text{(C3)}$$

where we have imposed that at $t = 0$, we have $N_\ell = N_1 = W_k = 0$. We can further proceed by considering that $p_\ell^2 \gg p_1^2$, and by keeping the lowest order terms in the ratio $(p_1/p_\ell)^2$, we find

$$\frac{dN}{dt} = -p_1^2 Y[2(\mu_m - \mu_c)]^{1/2} W_k N \cdot \left[1 + \sum_{\ell,\ell \neq 1} \frac{J_\ell}{\dot{Y}_\ell W_k N + J_1}\right] + \sum_{\ell,\ell \neq 1}\left(\frac{p_1}{p_\ell}\right)^2 J_\ell \qquad \text{(C4)}$$

$$\frac{dW_k}{dt} = \Delta_a \frac{v}{\pi a}[2(\mu_m - \mu_c)]^{1/2} W_k N \cdot \left[1 + \sum_{\ell,\ell \neq 1} \frac{J_\ell}{\dot{Y}_\ell W_k N + J_1}\right] - \frac{r}{\tau_g} W_k \qquad \text{(C5)}$$

After assuming that

$$\dot{Y}_\ell W_k N \gg J_1 \qquad \text{(C6)}$$

and by combining this last equation with (C4) and (C5) we easily arrive at (68) and (69). We also consider that (70) and (71) lead to $W_a N_a = (J_1/p_1^2 Y)[2(\mu_m - \mu_c)]^{-1/2}$. Then by taking $N = N_a$ and $W_k = W_a$ in (C6), we obtain that it reduces to the condition $(p_1/p_\ell)^2 \ll 1$.

APPENDIX D: IONOSPHERIC SLAB MODEL

We model the ionosphere as a homogeneous slab with two horizontal boundaries. One boundary is located at $z = 0$. The second boundary is the flux tube, and it is located at $z = d$. A wave incident from above is partially reflected and partially transmitted. We assume that the wave vector is always along the z direction. The magnetic and electric fields, $\mathbf{B}(z)$ and $\mathbf{E}(z)$, are in the plane perpendicular to z, and they are perpendicular to each other. We call $\mathbf{B}^I$, $\mathbf{E}^I$, the incident wave from the flux tube, and $\mathbf{B}^R$, $\mathbf{E}^R$ the reflected wave, where

$$\mathbf{B}^I(z) = \hat{e}_x B^I \exp\left(i\frac{\omega}{c}\eta_a z\right) \qquad \text{(D1)}$$

$$\mathbf{E}^I(z) = -\frac{\hat{e}_y}{\eta_a} B^I \exp\left(i\frac{\omega}{c}\eta_a z\right) \qquad \text{(D2)}$$

$$\mathbf{B}^R(z) = \hat{e}_x B^R \exp\left(-i\frac{\omega}{c}\eta_a z\right) \qquad \text{(D3)}$$

$$\mathbf{E}^R(z) = \frac{\hat{e}_y}{\eta_a} B^R \exp\left(-i\frac{\omega}{c}\eta_a z\right) \qquad \text{(D4)}$$

Here $\hat{e}_x$ and $\hat{e}_y$ are unit vectors, and B^I, B^R, the wave amplitudes, are constant. The electric and magnetic fields of the transmitted wave into the E layer ($z \leq 0$) are

$$\mathbf{B}^T(z) = \hat{e}_x B^T \exp\left(i\frac{\omega}{c}\eta_I z\right) \qquad \text{(D5)}$$

$$\mathbf{E}^T(z) = -\frac{\hat{e}_y}{\eta_I} B^T \exp\left(i\frac{\omega}{c}\eta_I z\right) \qquad \text{(D6)}$$

In the F layer, $0 \leq z \leq d$, we have the upgoing, $\mathbf{B}^{(1)}$, $\mathbf{E}^{(1)}$, and downgoing, $\mathbf{B}^{(2)}$, $\mathbf{E}^{(2)}$, traveling waves, where

$$\mathbf{B}^{(1)}(z) = \hat{e}_x B^{(1)} \exp\left(-i\frac{\omega}{c}\eta_F z\right) \qquad \text{(D7)}$$

$$\mathbf{E}^{(1)}(z) = \frac{\hat{e}_y}{\eta_F} B^{(1)} \exp\left(-i\frac{\omega}{c}\eta_F z\right) \qquad \text{(D8)}$$

$$\mathbf{B}^{(2)}(z) = \hat{e}_x B^{(2)} \exp\left(i\frac{\omega}{c}\eta_F z\right) \qquad \text{(D9)}$$

$$\mathbf{E}^{(2)}(z) = -\frac{\hat{e}_y}{\eta_F} B^{(2)} \exp\left(i\frac{\omega}{c}\eta_F z\right) \qquad \text{(D10)}$$

By matching the electric and magnetic fields of the waves with superscripts (1) and (2), to those of the transmitted wave with superscript (T) at the boundary $z = 0$, we get

$$B^{(1)} + B^{(2)} = B^T \qquad \text{(D11)}$$

$$\frac{1}{\eta_F}(B^{(2)} - B^{(1)}) = \frac{1}{\eta_I} B^T \qquad \text{(D12)}$$

Hence we find that $B^{(1)}/B^{(2)} = (\eta_I - \eta_F)/(\eta_I + \eta_F)$.

By matching the waves (I) and (R), to the waves (1) and (2) at the boundary $z = d$ with the flux tube, we get

$$B^{(1)}\exp\left(-i\frac{\omega}{c}\eta_F d\right) + B^{(2)}\exp\left(i\frac{\omega}{c}\eta_F d\right) = B^R \exp\left(-i\frac{\omega}{c}\eta_a d\right) + B^I \exp\left(i\frac{\omega}{c}\eta_a d\right) \qquad \text{(D13)}$$

$$\frac{1}{\eta_I}\left(B^{(1)}\exp\left(-i\frac{\omega}{c}\eta_I d\right) - B^{(2)}\exp\left(i\frac{\omega}{c}\eta_I d\right)\right)$$
$$-\frac{1}{\eta_o}\left(B^R\exp\left(-i\frac{\omega}{c}\eta_o d\right)\right.$$
$$\left.- B^I\exp\left(i\frac{\omega}{c}\eta_o d\right)\right) \quad \text{(D14)}$$

After solving for the system of (D13) and (D14), the reflection coefficient which is defined as $R = B^R/B^I$, is given by

$$R = \exp\left(2i\frac{\omega}{c}\eta_o d\right)\frac{r_1 + r_2\exp(2i\vartheta)}{d_1 + d_2\exp(2i\vartheta)} \quad \text{(D15)}$$

where r_1, r_2, d_1, d_2 and ϑ are defined after (78). By taking the absolute value of R in (D15) we arrive at (78).

Acknowledgments. Two of us (E.V. and M.B.S.) have been supported by the U.S. Air Force under contracts F19628-85-K-0053 and F19628-89-K-0014.

The Editor thanks R. L. Dowden and D. Nunn for their assistance in evaluating this paper.

REFERENCES

Banks, P. M., and G. Kockarts, *Aeronomy*, Academic, San Diego, Calif., 1973.

Bespalov, P. A., and V. Yu. Trakhtengerts, Cyclotron instability of Earth radiation belts, *Rev. Plasma Phys.*, Engl. Transl., *10*, 88, 1980.

Bespalov, P. A., C. U. Wagner, A. Grafe, and V. Yu. Trakhtengerts, Gap formation in the electron belts, *Geomagn. Aeron.*, Engl. Transl., *23*, 52, 1983.

Bostrom, R., A model of the auroral electrojets, *J. Geophys. Res.*, *69*, 4983, 1964.

Budden, K. G., *Radio Waves in the Ionosphere*, Cambridge University Press, New York, 1961.

Davidson, G. T., and Y. T. Chiu, A closed nonlinear model of wave-particle interactions in the outer trapping and morningside auroral regions, *J. Geophys. Res.*, *91*, 13,705, 1986.

Dingle, B., and D. L. Carpenter, Electron precipitation induced by VLF noise bursts at the plasmapause and detected at conjugate ground stations, *J. Geophys. Res.*, *86*, 4597, 1981.

Doolittle, J. H., and D. L. Carpenter, Photometric evidence of electron precipitation induced by first hop whistlers, *Geophys. Res. Lett.*, *10*, 611, 1983.

Gaponov-Grekhov, A. V., V. M. Glagolev, and V. Yu. Trakhtengerts, Cyclotron resonance maser with background plasma, *Sov. Phys. JETP*, Engl. Transl., *53*, 1146, 1981.

Gendrin, R., Pitch angle diffusion of low energy protons due to gyroresonant interaction with hydromagnetic waves, *J. Atmos. Terr. Phys.*, *30*, 1313, 1968.

Ginzburg, V. L., *The Propagation of Electromagnetic Waves in Plasmas*, Pergamon, New York, 1970.

Helliwell, R. A., *Whistler and Related Ionospheric Phenomena*, Stanford University Press, Stanford, Calif., 1965.

Hughes, W. J., Hydromagnetic waves in the magnetosphere, in *Solar-Terrestrial Physics: Principles and Theoretical Foundations*, pp. 453–477, D. Reidel, Hingham, Mass., 1982.

Hughes, W. J., and D. J. Southwood, An illustration of modification of geomagnetic pulsation structure by the ionosphere, *J. Geophys. Res.*, *81*, 3241, 1976.

Imhof, W. L., H. D. Voss, J. B. Reagan, D. W. Datlowe, E. E. Gaines, J. Mobilia, and D. S. Evans, Relativistic electron and energetic ion precipitation spikes near the plasmapause, *J. Geophys. Res.*, *91*, 3077, 1986.

Inan, U. S., Gyroresonant pitch angle scattering by coherent and incoherent whistler mode waves in the magnetosphere, *J. Geophys. Res.*, *92*, 127, 1987.

Kennel, C. F., and H. E. Petschek, Limit on stably trapped particle fluxes, *J. Geophys. Res.*, *71*, 1, 1966.

Kimura, I., Effects of ions on whistler-mode ray tracing, *Radio Sci.*, *1*, 269, 1966.

Kozyra, J. U., T. E. Cravens, A. F. Nagy, and E. G. Fontheim, Effects of energetic heavy ions on electromagnetic ion cyclotron wave generation in the plasmapause region, *J. Geophys. Res.*, *89*, 2217, 1984.

Lyons, L. R., and R. M. Thorne, The magnetospheric reflection of whistlers, *Planet. Space Sci.*, *18*, 1753, 1970.

Lyons, L. R., and R. M. Thorne, Equilibrium structure of radiation belts electrons, *J. Geophys. Res.*, *78*, 2142, 1973.

Lyons, L. R., and D. J. Williams, *Quantitative Aspects of Magnetospheric Physics*, D. Reidel, Hingham, Mass., 1983.

Lyons, L. R., R. M. Thorne, and C. F. Kennel, Electron pitch-angle diffusion driven by oblique whistler-mode turbulence, *J. Plasma Phys.*, *6*, 589, 1971.

Retterer, J. M., J. R. Jasperse, and T. S. Chang, A new approach to pitch angle scattering in the magnetosphere, *J. Geophys. Res.*, *88*, 201, 1983.

Roberts, C. S., Pitch angle diffusion of electrons in the magnetosphere, *Rev. Geophys.*, *7*, 305, 1969.

Schulz, M., Particle saturation of the outer zone: A nonlinear model, *Astrophys. Space Sci.*, *29*, 233, 1974.

Schulz, M., and G. T. Davidson, Limiting energy spectrum of a saturated radiation belt, *J. Geophys. Res.*, *93*, 59, 1988.

Schulz, M., and L. J. Lanzerotti, *Particle Diffusion in the Radiation Belts*, Springer-Verlag, New York, 1974.

Silevitch, M. B., P. L. Rothwell, and E. Villalón, Active control and nonlinear feedback instabilities in the Earth's radiation belts, *Adv. Space Res.*, in press, 1989.

Thomson, R. J., and R. L. Dowden, Ionospheric whistler propagation, *J. Atmos. Terr. Phys.*, *40*, 215, 1977.

Tkalcevic, S., U. S. Inan, and R. A. Helliwell, Nonlinear pitch angle scattering and trapping of energetic particles during Landau resonance interactions with whistler mode waves, *J. Geophys. Res.*, *89*, 10,813, 1984.

Trakhtengerts, V. Yu., Alfvén masers in active experiments in space, *Eur. Space Agency Spec. Publ.*, *ESA SP-195*, 67, 1983.

Trakhtengerts, V. Yu., Relaxation of a plasma with anisotropic velocity distribution, in *Handbook of Plasma Physics*, vol. 2, *Basic Plasma Physics II*, edited by A. A. Galeev and R. N. Sudan, p. 519, Elsevier, New York, 1984.

W. J. Burke and P. L. Rothwell, Air Force Geophysics Laboratory, Hanscom Air Force Base, MA 01731.

M. B. Silevitch and E. Villalón, Center for Electromagnetics Research, Northeastern University, Boston, MA 02115.

(Received March 2, 1989;
revised May 26, 1989;
accepted June 20, 1989.)

AGARD

ADVISORY GROUP FOR AEROSPACE RESEARCH & DEVELOPMENT

7 RUE ANCELLE 92200 NEUILLY SUR SEINE FRANCE

Paper Reprinted from
Conference Proceedings No.485

Ionospheric Modification and its Potential to Enhance or Degrade the Performance of Military Systems

(La Modification de l'Ionosphère et son Potentiel d'Amélioration ou de Dégradation des Performances des Systèmes Militaires)

NORTH ATLANTIC TREATY ORGANIZATION

IONOSPHERIC HEATING FOR RADIATION BELT CONTROL*

William J. Burke
Geophysics Laboratory
Hanscom AFB, MA 01731

Elena Villalon
Northeastern University
Boston, MA 02115

SUMMARY

Pitch-angle scattering interactions of electromagnetic waves in the ELF/VLF bands with trapped electrons, as formulated by Kennel and Petschek [1], describe the dynamics of the freshly filled radiation belts flux tubes. The natural existence of a "slot" region with electron fluxes below the Kennel-Petschek limit requires non-local wave sources. We describe a set of planned, active experiments in which VLF radiation will be injected from ground and space based transmitters in conjunction with the CRRES satellite in the radiation belts. These experiments will measure the intensity of waves driving pitch-angle diffusion and the electron energies in gyroresonance with the waves. An ability to reduce the flux of energetic particles trapped in the radiation belts by artificial means could improve the reliability of microelectronic components on earth-observing satellites in middle-altitude orbits.

LIST OF SYMBOLS

B	Magnetic Field
c	Speed of Light
$E_{e,i}$	Resonant Energy for Electrons, Ions
E_A	Magnetic Energy per Particle
k	Wave Vector
L	Magnetic Shell Number
$m_{e,i}$	Mass of Electrons, Ions
n	Plasma Density
N	Harmonic Number
ϵ_o	Permittivity of Free Space
μ_o	Permeability of Free Space
ω	Wave Frequency
ω_{LH}	Lower Hybrid Frequency
ω_{pe}	Electron Plasma Frequency
$\Omega_{ce,i}$	Electron, Ion Cyclotron Frequency

INTRODUCTION

One of space physic's major success stories of the 1960's was the development of the theory of pitch-angle scattering of energetic electrons trapped in the earth's radiation belts by ELF/VLF radiation [1]. This theoretical model postulates that energetic electrons moving along magnetic field lines near the equatorial plane of the magnetosphere see low-frequency waves Doppler shifted to their local gyrofrequencies. In consequent, gyroresonant interactions particles diffuse in pitch angle along surfaces of constant phase velocity. Particles diffusing toward the loss cone give up small amounts of energy to wave growth. The model is self consistent in the sense that waves responsible for pitch-angle scattering grow from background fluctuation levels due to the free energy contained in the anisotropic pitch-angle distributions of trapped particles. If the anisotropy of the trapped distribution falls below a critical level growth ceases.

During magnetic storms the radiation belts fill up with trapped, energetic particles from about L = 8 to L = 1.5. In the weeks following storms the flux of trapped electrons in the slot between L = 2 to L = 3.5 fall to the thresholds of detector sensitivity, well below the stable trapping limit of Kennel and Petschek. Trapped protons do not show slot-like distributions. Lyons and coworkers [2] recognized that waves responsible for the pitch-angle scattering of slot electrons need not grow self consistently from background fluctuation levels. Rather, they can be injected from non-local sources and still pitch-angle scatter trapped electrons into the atmospheric loss cone.

The sources of ELF/VLF waves are multiple and their relative importance for magnetospheric particle distributions is the subject of an ongoing research. The waves envisaged by Kennel and Petschek arise naturally out of background fluctuations by selective amplification. Atmospheric lightning produces broad-band ELF/VLF emissions. Part of the radiation propagates in the earth-ionosphere waveguide and part accesses the magnetosphere in field-aligned ducts. Studies of lightning induced precipitation abound in the literature [3 - 6]. The Stanford group has pioneered techniques for monitoring lightning induced dumping of the radiation belts using the SUNY Albany network.

Another major source of VLF is man-made radiation. The Stanford group has made numerous studies of magnetospheric effects of ELF/VLF transmissions from the Siple station in Antarctica to magnetic conjugate points in Canada [7]. The intensities of waves emitted from Siple have been measured directly by the wave detector experiment on satellites near the equatorial plane of the magnetosphere [8]. A series of successful experiments were conducted in the early 1980's in which time-coded VLF emissions from US Navy transmitters were compared with electron precipitation events simultaneously detected by the SEEP satellite [9]. Vampola [10] investigated the effects of a powerful VLF transmitter at Gorky on radiation belt electrons and suggested that it maintains the inner reaches of the slot.

The purpose of this paper is to describe a group of active experiments that will be conducted by Geophysics Laboratory scientists after the launch of the CRRES satellite this summer. In these experiments, low-frequency waves will be injected into the magnetosphere by several different methods. Instrumentation on CRRES will monitor: (1) the intensity and interactions of the injected waves, and (2) the dynamics of electrons and protons near the loss cone. The object of these experiments is to establish the feasibility of using active techniques to control the fluxes of energetic particles in the slot. A human ability to accelerate or maintain slot depletion would allow earth observing satellites to fly in orbits now considered too hazardous [11]. Space Based Radar would profit from this capability [12]

In the following sections we first review criteria for pitch-angle scattering trapped particles. After summarizing the capabilities of CRRES instrumentation for measuring wave-particle interactions, we describe three methods of wave injection using ground-based VLF and HF transmitters, and VLF transmissions from the Soviet ACTIVE satellite.

WAVE-PARTICLE INTERACTIONS

To understand slot dynamics it is necessary to consider whistler mode propagation in the radiation belts and its interactions with energetic particles. The waves of interest are in the ELF-VLF (0.3-30 kHz) bands. Two empirical facts are used in our simple models: (a) The earth's magnetic field B is approximately dipolar, and at the magnetic equator is given by

(1) $$B(nT) = 3.1 * 10^4 * L^{-3}$$

where L is the standard magnetic shell number. (b) The background plasma is dominated by cold particles whose density is approximated [13]

(2) $$n(cm^{-3}) = 3 * 10^3 * [2 / L]^4$$

The high-energy particles have densities that are < 1 cm^{-3}. Thus, wave propagation is well described in the magnetized, cold plasma limit. The whistler wave is a right hand mode that propagates along the magnetic field if its frequency ω is less than the electron cyclotron Ω_{ce} and greater than the lower-hybrid ω_{LH} frequencies at all points.

As illustrated in Figure 1, whistler waves in the radiation belts in two distinct modes called ducted and unducted [14]. Ducted waves propagate along magnetic field-aligned plasma irregularities as in waveguides. Waves injected into a duct can propagate from one hemisphere to it conjugate and back many times [15]. Unducted waves observed in the magnetosphere never make it to the ground. Ray-tracing studies [16] show that as the waves propagate away from the equatorial region the contributions of ions to the dielectric coefficient grow in importance. As unducted waves propagate to locations along magnetic field lines where their frequencies approach ω_{LH} their wave vectors turn and reflect back toward the equator. The process is analogous to total internal reflection at optical frequencies. Not being confined to propagate in a single magnetic shell these waves suffuse throughout the plasmasphere as a broadband hiss.

For waves and particles to interact strongly they must satisfy a resonance condition

(3) $$\omega - k v + N \Omega_{ce,i} = 0$$

where N is an integer, v the component of particle motion along the magnetic field, ω and k are the wave frequency (in radians per second) and the wave vector. In the nonrelativistic limit the cyclotron frequency for electrons (e) and ions (i) is $\Omega_{ce,i} = |e B / m_{ce,i}|$ where e represents the elemental unit of charge, B the magnetic field and m the mass of an electron or ion. A particle must see the wave Doppler-shifted in to some harmonic of its gyrofrequency. Figure 2 depicts whistler interactions with electrons and protons. Electron interactions occur at the N = - 1, -2, ... harmonics and require that they travel in opposite directions to the waves. Protons interactions occur for positive values of N with the protons traveling in the same direction and overtaking the waves.

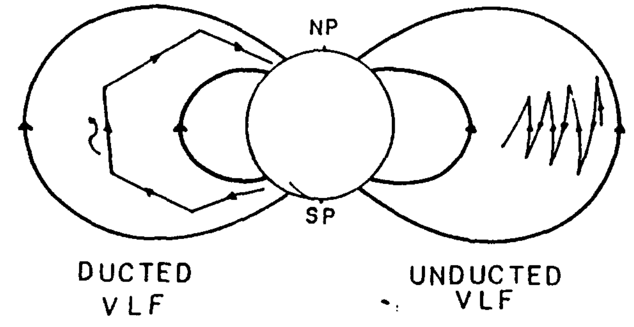

Fig. 1. Ducted and unducted whistler waves in the magnetosphere.

The dispersion relation for whistler waves propagating along the magnetic field near the equatorial plane is approximately

(4) $$\frac{c^2 k^2}{\omega^2} = \frac{\omega_{pe}^2}{\omega\,(\Omega_{ce} - \omega)}$$

where $\omega_{pe} = [n\, e^2/\, m_e\, \varepsilon_0]^{1/2}$ is the electron plasma frequency and ε_0 is the permittivity of free space. Combining equations (3) and (4) shows that the energy of resonant electrons is

(5) $$E_e = E_A N^2 \left[\frac{\Omega_{ce}}{\omega}\right] [1 - \frac{\omega}{\Omega_{ce}}]\, [1 + \frac{\omega}{N\Omega_{ce}}]^2$$

For protons the resonant energy is

(6) $$E_p = E_A N^2 \left[\frac{\Omega_{ci}}{\omega}\right] [1 - \frac{\omega}{\Omega_{ce}}]\, [1 + \frac{\omega}{N\Omega_{ci}}]^2$$

where $E_A = B^2/\, 2\, \mu_0\, n$ is the magnetic energy per particle and μ_0 is the permeability of free space. In planning active experiments in the radiation belts we estimate E_A using the dipolar magnetic fields and the cold plasma densities given in equations (1) and (2). To study pitch-angle scattering in a given energy range the only free parameters that remain are the wave frequency and the resonance harmonic number N.

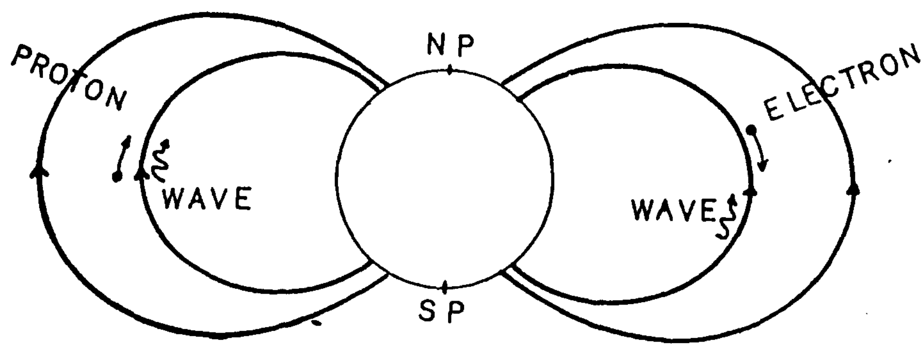

Fig. 2. Resonant interactions of whistlers with protons and electrons.

CRRES INSTRUMENTATION

CRRES (Combined Release Radiation Effects Satellite) is scheduled to be launched in June 1990 into a 17° inclination, geostationary transfer orbit. As its name suggests, CRRES has two mission objectives: to study the effects of chemical releases at high altitudes, and to understand the interactions of advanced microelectronics components with natural radiation environments. Detailed descriptions of the comprehensive scientific payload on CRRES have been compiled by Gussenhoven and coworkers [17]. For the studies discussed below three instruments are germane and are described briefly. These are the Low Energy Plasma Analyzer (LEPA), the Plasma Wave Experiment and a Langmuir Probe.

The LEPA experiment was designed to measure the three dimensional distribution function of ions and electrons with energies between 10 eV and 30 keV. The particle distribution functions are measured by two 260° spherical electrostatic analyzers. Each sensor consists of two concentric spherical plates. On one edge the space between the plates is closed off except for a 5.6° by 128° aperture. A microchannel plate is placed at the other edge. The energy analysis is achieved by changing the electrostatic potential between the plates. The instrument focusing is such that particle pitch angles are imaged on the microchannel plate to an accuracy of better than 1 degree. The particle positions are divided into sixteen 8o bin can be resolved into eight 1° zones. Because the limited telemetry does not allow the full data set to be transmitted to ground, a microprocessor has been programmed to select desired sampling patterns.

Particles that are in resonance with a given wave mode can be identified by means of a correlator device [18] that measures the time of arrival of electrons or ions in an 8° sector with a high-frequency clock. The microprocessor then preforms autocorrelations to identify bunching of the particles. During active experiments the microprocessor will select the bin closest to the direction of the local magnetic field to study the dynamics of particles in and near the atmospheric loss cone and identify the wave modes responsible for resonant pitch-angle scattering.

The Passive Wave Experiment was designed by the University of Iowa to measure electric and magnetic fluctuations over a dynamic range of 100 db using a 100 m tip-to-tip dipole and a search coil magnetometer. The instruments will operate in swept frequency and fixed-filter modes. The swept frequency analyzer covers the range from 100 Hz to 400 kHz in 128 steps. For wave frequencies in the VLF band both electric and magnetic spectra be complied every 16 s. The fixed filters will be used to compile a 14 point spectrum with center frequencies between 5.6 Hz and 10 kHz eight times per second.

The Langmuir probe experiment consists of a 100 m tip-to-tip dipole that uses spherical sensors each containing a preamplifier with a 1 MHz bandwidth. The instrument can be used in either a low-impedance mode to measure the plasma density or a high-impedance mode to measure electric fields. It contains two microprocessors, one controls ordinary operations and the other a "burst memory" device. The burst memory holds 192 kbytes and can be filled with data from the Plasma Wave and/or Langmuir Probe Experiments at rates up to 50 kHz. The measured parameters and collection rates are controlled by ground command. Data of the desired kind will be continually fed through the burst memory as a buffer. When the microprocessor recognizes some specified event, it will save a small amount of pre-event data and proceed to fill the burst memory. A rapid increase in the wave activity measured near the central frequency of a fixed-filter channels will probably be used to trigger burst memory data collections during the experiments described below. After the memory is filled, data will be slowly leaked to the main tape recorder for later transmission to ground.

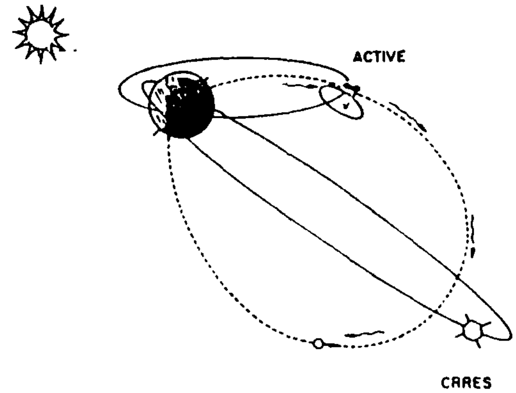

Fig. 3. Wave injection experiments from ACTIVE to CRRES.

VLF WAVE-INJECTION EXPERIMENTS

In this section we discuss a number of active techniques for injecting and diagnosing whistler waves in the radiation belts. The experiment concept is illustrated schematically in Figure 3. The antennas used to transmit energy into the radiation belts may operate in either the VLF or HF ranges and may be either ground or space based. For simplicity we first consider the case of transmissions from the polar orbiting ACTIVE satellite. This allows us to illustrate the principles that apply to experiment planning and easily extend to ground-based transmissions.

The ACTIVE satellite was launched on 28 September 1989, into polar orbit with an apogee, perigee and inclination of 2500 km, 500 km and 83o, respectively. The prime experiment is a VLF generator that powers a single turn loop antenna of 20 m diameter. The emitted frequency falls in the range from 9.0 to 10.5 kHZ and is controlled by ground command. There are eight preprogrammed on/off emission sequences that may be selected. Because the loop antenna failed to deploy properly the emitted power from ACTIVE is well below its planned 10 kW value.

The rates of orbital precession for the ACTIVE and CRRES satellites are - 1.65 and 0.67 degrees per day. This implies that within a few months of launch the orbital planes of the two spacecraft will overlap favorably for conducting experiments in which VLF radiation can be emitted from ACTIVE and received by CRRES. Since ACTIVE changes magnetic latitude quite rapidly relative to the near equatorial CRRES, it is necessary to determine the useful locations for conducting transmission and pitch-angle scattering experiments. Figure 4 plots the equatorial cyclotron and plasma frequencies derived for the magnetic field and plasma densities given in equations (1) and (2) as functions of L. We also indicate ACTIVE's emission band. The figure indicates that this radiation can only propagate to the equator for L shells less than 4. At greater distances ACTIVE's radiation cannot reach CRRES.

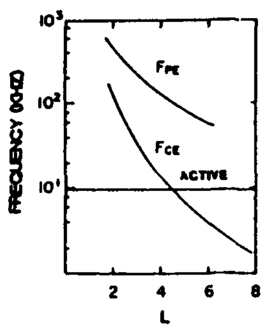

Fig. 4. Electron cyclotron and plasma frequencies at the magnetic equator.

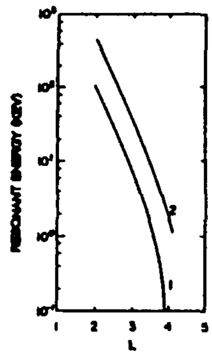

Fig. 5. Energies of electrons resonant with ACTIVE emissions for N = - 1 and - 2, at the magnetic equator as functions of L.

Using equations (1) and (2) we calculate that the magnetic energy per particle is 50 keV/ L^2. With an emission frequency from ACTIVE of 9.6 kHz, the ratios Ω_{ce}/ω and Ω_{ci}/ω are 90.4 $/L^3$ and $0.31/L^3$, respectively . In Figure 5 we have plotted the energies of electrons that are resonant with 9.6 kHz waves at the equator using equation (5) for the first two harmonics. At distances $L > 2.5$ (> 3) *the energy of resonant electrons is in range of LEPA's sensitivity for the N = -1 (- 2)* harmonic interaction. Higher harmonic interactions can be detected by high-energy detectors but with courser pitch-angle resolution than LEPA. At off equatorial latitudes the magnetic energy per particle increases leading to higher energies for resonant interactions. Note that CRRES can detect resonant interactions resulting from directly injected waves only if the two spacecraft are in opposite hemispheres. Resonant interactions can occur at the location of CRRES with the satellites in the same hemisphere if the waves undergo internal magnetospheric reflections. Protons interacting with whistler waves emitted by ACTIVE at the first harmonic must have energies > 1 MeV. Higher harmonic interactions take place at lower energies.

There are two methods for injecting VLF waves into the magnetosphere from the ground, directly from VLF transmitters or indirectly from HF ionospheric heaters. Many direct VLF injections have already been cited. The Siple transmitter had flexibility in its emitted frequencies. However, Siple was closed when Antarctic ice crushed the station. Imhof and coworkers carried out experiments using VLF transmitters at a number of fixed frequencies used by the U.S. Navy. These can be repeated with CRRES. Consistent with SEEP measurements [9], frequencies > 20 kHz will interact with electrons in LEPA's energy range at L > 2.

Indirect injections of VLF waves into the radiation belts can be accomplished by two methods. The first is through modulation of ionospheric currents and the second through beat waves. Ionospheric current modulations have been achieved by a modulated heating of the D region of the ionosphere [19-20]. The basic concept is that the HF waves heat the ionospheric electrons and thus increase the ionospheric conductivity. If the amplitude of the heater is modulated at VLF frequencies the ionospheric currents are also modulated, turning them into a virtual antenna in space. Trakhtengerts [21]

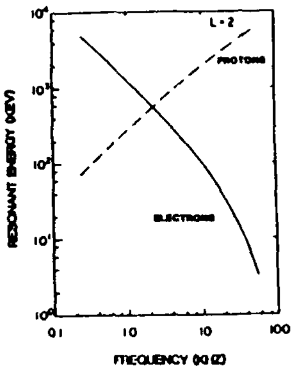

Fig. 6. Energies of electrons and protons resonant at the first harmonic with whistlers at L=2.

suggested that this technique can be adopted to turn whole flux tubes into a maser-like device in which injected waves grow to large amplitudes. Quantitative conditions required for growth with parallel wave propagation have been explored by Villalon and coworkers [22]. Ionospheric current modulation techniques have the advantage of flexibility over fixed frequency transmitters. However, while waves emitted from virtual ionospheric antennas have been detected at the ground, little is known about the efficiency with which they transmit across the ionosphere into deep space. The wave detectors on CRRES will reduce this uncertainty.

A second method for indirect VLF injection involves the use of beat waves. Different sectors of the Arecibo antenna can radiate at selected frequencies whose difference lies in the VLF range. This also provides flexibility for studying resonant interactions in LEPA's energy range near L = 2. The HF heater also provides a means for enhancing the efficiency of wave injections. If the ionosphere is heated for about ten minutes prior to VLF turn-on, it develops field-aligned thermal striations [23]. Induced irregularities can enhance VLF transmission through the ionosphere either along artificially created ducts or off strategically located scattering centers. Figure 6 plots the resonant energy of electrons and protons at the first harmonic at L = 2 as a function of frequency. Resonant electrons in LEPA's range of sensitivity require injected wave frequencies > 20 kHz.

REFERENCES

[1]. Kennel, C.F. and H.E. Petschek, Limit on stably trapped particle fluxes, J. Geophys. Res., 71, 1 - 28, 1966.

[2]. Lyons, L.R., R.M. Thorne and C.F. Kennel, Pitch-angle diffusion of radiation belt electrons within the plasmasphere., J. Geophys. Res., 77, 3455 - 3474, 1972.

[3]. Chang, H.C. and U.S. Inan, Lightning-induced electron precipitation from the magnetosphere, J. Geophys. Res., 90, 1531 - 1541, 1985.

[4]. Inan, U.S. and D.L. Carpenter, Lightning-induced electron precipitation events observed at L ~ 2.4 as phase and amplitude perturbations on subionospheric VLF signals, J. Geophys. Res., 92, 3293-3303, 1987.

[5]. Inan, U.S., W.C. Burgess, T.G. Wolf, D.C. Shater and R.E. Orville, Lightning-associated precipitation of MeV electrons from the inner radiation belt, Geophys. Res. Lett., 15, 172 - 175, 1988.

[6]. Rycroft, M.J., Strange new whistlers, Nature, 327, 368 - 369, 1987.

[7]. Helliwell, R.A., Controlled stimulation of VLF emissions from Siple Station, Antarctica, Radio Sci., 18, 801 - 814, 1983.

[8]. Inan, U.S., T.F. Bell, D.L. Carpenter and R.R. Anderson, Explorer 45 and Imp 6 observations in the magnetosphere of injected waves from the Siple VLF transmitter, J. Geophys. Res., 82, 1177 - 1187, 1977.

[9]. Imhof, W.L., J.B. Reagan, H.D. Voss, .E. Gaines, D.W. Datlowe, J. Mobilia, R.A. Helliwell, U.S. Inan, J. Katsufrakis and R.G. Joiner, The modulated precipitation of radiation belt electrons by controlled signals from VLF transmitters, Geophys. Res. Lett., 10, 615 - 618, 1983.

[10]. Vampola, A.L., Electron precipitation in the vicinity of a VLF transmitter, J. Geophys. Res., 92, 4525 - 4532, 1987.

[11]. Burke, W.J. and R.C. Sagalyn, Active space experiments and international treaty obligations, SIGNAL, (in press) 1990.

[12]. Tsandoulas, G.N., Space Based Radar, Science, 237, 257 - 262, 1987.

[13]. Chappell, C.R., K.K. Harris and G.W. Sharp, A study of the influence of magnetic activity on the location of the plasma pause as measured by OGO 5, J. Geophys. Res., 75, 50 - 56, 1970.

[14]. Smith, R.L. and J.J. Angerami, Magnetospheric properties deduced from OGO 1 observations of ducted and nonducted whistlers, J. Geophys. Res., 73, 1 - 20, 1968.

[15]. Helliwell, R.A., Whistlers and VLF emissions, in Physics of the Magnetosphere, ed. by R.L Carovillano, J.F. McClay and H.R. Radoski, D. Reidel Co., Dordrecht, 106 - 146, 1968.

[16]. Kimura, I., Effects of ions on whistler-mode ray tracing, Radio Sci., 1, 269 - 283, 1966.

[17]. Gussenhoven, M.S., E.G. Mullen and R.C. Sagalyn, CRRES-SPACERAD experiment descriptions, AFGL-TR-85-0017, 1985.

[18]. Gough, M.P. and A. Urban, Auroral beam/plasma interaction observed directly, Planet. Sp. Sci., 31, 875 - 883, 1983.

[19]. Lunnen, R.J., A.J. Ferraro, H.S. Lee, R. Allshouse, K. Carroll, D. Werner and T.W. Collins, Detection of local and long-path VLF/ELF radiation from modulated ionospheric current systems, Radio Sci., 20, 553 - 563, 1985.

[20]. Stubbe, P., H. Kopka, M.T. Rietveld, A. Frey, P. Hoeg, H. Kohl, E. Nielsen, G. Rose, C. LaHoz, R. Barr, H. Derblom, A. Hedberg, B. Thide, T.B. Jones, T. Robinson, A. Brekke, T. Hansen and O. Holt, Ionospheric modification experiments with the Tromso heating facility, J. Atmos. Terr. Phys., 47, 1151 - 1163, 1985.

[21]. Trakhtengerts, V. Yu., Alfven Masers, in Active Experiments in Space, ESA SP-195, 67 - 74, 1983.

[22]. Villalon, E., W.J. Burke, P.L. Rothwell and M.B. Silevitch, Quasi-linear wave-particle interactions in the earth radiation belts, J. Geophys. Res., 94, 15,243 - 15256, 1989.

[23]. Lee, M.C. and S.P. Kuo, Ionospheric irregularities and geomagnetic fluctuations due to ionospheric heating, in Active Experiments in Space, ESA SP-195, 81 -89, 1983.

ACKNOWLEDGEMENTS

This work was supported in part by USAF Contract No. F19628-89-K- 0014 with Northeastern University and by AFOSR Task 2311G6.

PAPER NO. 28

DISCUSSION

F. LEFEUVRE, FR

In a paper you co-authored with Dr. Villalen you suggested to heat the foot of the flux tube where the interaction takes place. Do you plan to do it in your CRRES experiment?

AUTHOR'S REPLY

The CRRES experiments are designed for single-hop whistlers. To heat the conjugate point for the Alfven maser would require a two-hop whistler. If it happens, CRRES could see it.

JOURNAL OF GEOPHYSICAL RESEARCH, VOL. 96, NO. A4, PAGES 5819-5824, APRIL 1, 1991

Cyclotron Resonance Absorption in Ionospheric Plasma

ELENA VILLALÓN[1]

Center for Electromagnetics Research, Northeastern University, Boston, Massachusetts

The mode conversion of ordinary polarized electromagnetic waves into electrostatic cyclotron waves in the inhomogeneous ionospheric plasma is investigated. Near resonance the warm plasma dispersion relation is a function of the angle θ between the geomagnetic field and the density gradient and of the wave frequency ω, where $\Omega \leq \omega \leq 2\Omega$ and Ω is the electron cyclotron frequency. The differential equations describing the electric field amplitudes near the plasma resonance are studied, including damping at the second gyroharmonic. For certain values of ω and θ (e.g., $\theta < 45°$, $\omega = 2\Omega$) the wave equations reduce to the parabolic cylinder equation. The energy transmission coefficients and power absorbed by the cyclotron waves are calculated. The vertical penetration of the plasma wave amplitudes is estimated using a WKB analysis of the wave equation.

1. INTRODUCTION

In ionospheric heating experiments the ordinary mode is launched from the ground at the critical angle of incidence that penetrates the radio window [*Wong et al.*, 1981; *Birkmayer et al.*, 1986; *Bernhardt et al.*, 1988]. After experiencing a rapid change in polarization it converts into an electrostatic wave which is rapidly absorbed by the plasma [*Mjølhus*, 1984; *Mjølhus and Flå*, 1984]. In a previous paper we studied the dispersion relation in an inhomogeneous plasma near resonance, considering thermal corrections and assuming an arbitrary angle θ between the geomagnetic field $\mathbf{B}_0$ and the density gradient [*Villalón*, 1989]. The wave frequency ω is such that $\Omega \leq \omega \leq 2\Omega$, where Ω is the electron gyrofrequency. The warm plasma dispersion relation contains third- and second-order power terms in the refractive index η. Our results extend previous work by *Golant and Piliya* [1972], which includes only the third-order power in η but not the second. We show that for certain values of θ and ω satisfying the equation $\Lambda(\theta, \omega) = 0$ (see the definition of Λ in equation (7)) the Golant and Piliya dispersion relation cannot be applied. As a matter of fact we found that for $\theta < 45°$, $\Lambda = 0$ if $\omega = 2\Omega$. In these cases, the refractive indices are very large, the group velocities are very slow, and wave energy should be absorbed efficiently by the electrons at the second gyroharmonic.

Here we further develop the theory of mode conversion by investigating the wave electric fields near the plasma resonance. We derive a differential equation for the variation of the wave amplitudes in the vertical coordinate along the density gradient. It contains third- and second-order spatial derivatives, and the contribution of the linear damping rates at the second gyroharmonic. Asymptotic expansions are given. The wave amplitudes are a combination of ordinary electromagnetic and warm plasma waves. We calculate the energy transmission coefficient [*Cairns and Lashmore-Davies*, 1982] and the power absorbed per unit area by the plasma wave [*Piliya and Fedorov*, 1970]. The amplification coefficient for the cyclotron waves depends on θ and ω/Ω and is very large for θ near 0° and ω very close to 2Ω. When θ and ω are such that $\Lambda = 0$, the wave equation reduces to the parabolic cylinder equation whose asymptotic solutions are well known. Note that the Weber's equation is the standard differential equation to describe a variety of mode conversion problems in plasma physics [*Piliya*, 1966; *Antonsen and Manheimer*, 1978; *Cairns and Lashmore-Davies*, 1983].

We apply a WKB analysis to investigate the roots of the wave equations. In the case $\Lambda(\theta, \omega) \neq 0$ we find three complex roots. One of them represents the O mode, and the other two are combinations of the O mode and plasma waves. By calculating the turning points we estimate the extent of vertical penetration of the wave fields. For typical ionospheric parameters this length is of the order of a few hundred meters. In the limit $\Lambda \to 0$ we find two roots, one the O mode and the second the plasma wave. The vertical penetration of the wave fields is now of the order of a few meters. Thus wave energy is efficiently absorbed by the electrons in very small regions of space.

2. WARM PLASMA DISPERSION RELATION

We consider the nonuniform plasma of the ionosphere, where the density changes slowly along the vertical direction ξ and is constant along the horizontal direction μ. The geomagnetic field $\mathbf{B}_0$ is taken at an angle θ with respect to the vertical ξ and is in the plane defined by the coordinates ξ and μ. The coordinates along and perpendicular to $\mathbf{B}_0$ are denoted by z and x, respectively (see Figure 1). An ordinary polarized electromagnetic wave (O mode), of frequency ω and wave vector $\mathbf{k}$, is launched from the ground at an angle ψ with respect to the vertical. The angle between $\mathbf{k}$ and $\mathbf{B}_0$ depends on the altitude and is represented by α (see Figure 1). The frequency ω is such that $\Omega \leq \omega \leq 2\Omega$, where $\Omega = eB_0/mc$ is the electron gyrofrequency (e is the electron charge and m its mass). The refractive index $\eta = ck/\omega$ has a component Q along the vertical direction and a component S in the horizontal direction. In terms of the angles θ and α we have the relation $\sin(\alpha + \pi/2 - \theta) = Q/\eta$. Because the plasma density does not change along μ, S is also a constant independent of altitude and given by $S = \sin\psi$. The vertical component Q depends on the plasma density (i.e., on the coordinate ξ); it can be obtained by solving for the Booker quartic cold plasma dispersion relation [*Budden*, 1961]

$$aQ^4 + bQ^3 + cQ^2 + dQ + e = 0 \qquad (1)$$

[1] Also at Air Force Geophysics Laboratory, Hanscom Air Force Base, Massachusetts.

Paper number 90JA02748.
0148-0227/91/90JA-02748$05.00

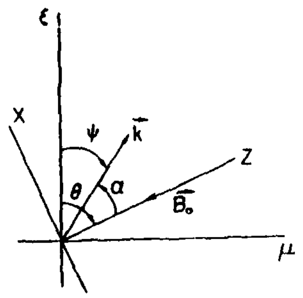

Fig. 1. The coordinates ξ and μ are along and perpendicular to the density gradient, respectively. The coordinates z and x are parallel and perpendicular to the geomagnetic field $\mathbf{B}_0$, respectively. The wave vector $\mathbf{k}$ is in the plane defined by $\mathbf{B}_0$ and ξ. The angles that $\mathbf{B}_0$ and $\mathbf{k}$ form with the vertical ξ are represented by θ and ψ, respectively.

where

$$\epsilon_{\xi\xi} = 1 - X/X_r, \qquad X_r = \frac{1 - Y^2}{1 - Y^2 \cos^2\theta} \tag{2}$$

Here $X = \omega_p^2/\omega^2$, where $\omega_p = (4\pi N e^2/m)^{1/2}$ is the electron plasma frequency, N is the plasma density, and $Y = \Omega/\omega$. The other coefficients in equation (1) may be found in the work by *Budden* [1961]. We assume that the angle of incidence ψ is such that

$$\sin\psi = \left(\frac{Y}{1+Y}\right)^{1/2} \sin\theta \tag{3}$$

If the ordinary mode is launched near the ground at the angle of incidence defined in (3), it penetrates the radio window and experiences a rapid change of polarization associated with a strong coupling between the ordinary and extraordinary waves [*Mjølhus*, 1984] (see Figure 2). The ordinary wave is totally transmitted near $X = X_r$ into the "slow extraordinary mode" (also called the Z mode), which becomes increasingly electrostatic as it propagates in the plasma [*Mjølhus and Flå*, 1984], i.e., the refractive index $Q \to \infty$ and $\alpha \to \theta$. The ratio between the z and x components of the electric field is such that $E_x/E_z = \tan\theta$ and $E_y = 0$.

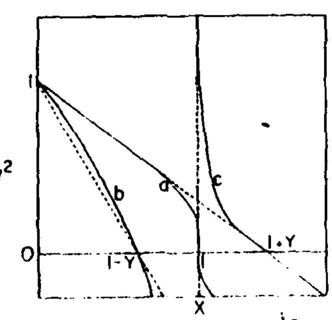

Fig. 2. Refractive index η versus $X = (\omega_p/\omega)^2$; here $Y = \Omega/\omega$. The curve a is an ordinary polarized mode, and b and c are extraordinary modes. The ordinary mode a propagates from free space ($\eta \to 1$) to its cutoff ($\eta = 0$) and may couple to the slow extraordinary mode branch c (also called the Z mode). The Z mode moves into the region of cyclotron plasma resonances ($\eta \to \infty$).

Near the plasma resonance where $\xi = \xi_0$, we assume that the density variation is

$$N = N_r\left(1 + \frac{\xi - \xi_0}{l}\right) \tag{4}$$

Here N_r is the plasma density at the resonance where $X = X_r$ as defined in (2), and l is the length of density variation (typically, in the F region of the ionosphere it is around 50 km). Near the mode conversion point, the O mode frequency satisfies the dispersion relation for the upper hybrid resonance in (2). Substituting (4) into the definition of $\epsilon_{\xi\xi}$ in (2), we find

$$\epsilon_{\xi\xi} = -\frac{(\xi - \xi_0)}{l} \tag{5}$$

The refractive index is near $\xi = \xi_0$, $Q \sim -b/\epsilon_{\xi\xi} \to \pm\infty$, and its actual value must be obtained by adding the lowest-order thermal corrections to the Booker quartic dispersion relation [*Budden*, 1961]. The complex dielectric response function, $\mathcal{H} = Q^3\mathcal{D}$, was derived by *Villalón* [1989], where $\mathcal{D}$ is

$$\mathcal{D} = Q\epsilon_{\xi\xi} - \frac{v_T^2}{c^2}(\Lambda Q^3 + 2\kappa Q^2)X + 2\Upsilon X + i2\frac{v_T}{c}\rho Q^2 X \tag{6}$$

Here v_T, the thermal velocity, is such that $v_T/c \sim 10^{-3}$, and

$$\Lambda = 3\cos^4\theta + \frac{3\sin^4\theta}{(1 - Y^2)(1 - 4Y^2)} + \frac{(6 - 3Y^2 + Y^4)}{(1 - Y^2)^3}\cos^2\theta \sin^2\theta \tag{7}$$

$$\kappa = S\sin\theta\cos\theta\left\{\cos^2\theta\,\frac{(-15Y^2 + 17Y^4 - 6Y^6)}{(1 - Y^2)^3} + \sin^2\theta\,\frac{(-15Y^2 + 7Y^4 - 4Y^6)}{(1 - Y^2)^3(1 - 4Y^2)}\right\} \tag{8}$$

$$\Upsilon = S\sin\theta\cos\theta\,\frac{Y^2}{(1 - Y^2)} \tag{9}$$

$$\rho = -\frac{1}{16}\left(\frac{\pi}{2}\right)^{1/2}\frac{\sin^4\theta}{|\cos\theta|}\frac{1}{Y^4}\exp\left[-\left(\frac{\omega - 2\Omega}{2^{1/2}k_z v_T}\right)^2\right] \tag{10}$$

where k_z is the component of $\mathbf{k}$ along $\mathbf{B}_0$. The refractive index Q may be obtained by setting the real part of (6) equal to zero. Refractive indices in the resonance regions have been studied in the papers by *Golant and Piliya* [1972] and *Villalón* [1989]. The Golant and Piliya paper does not include the term proportional to κ in the dispersion relation. As a matter of fact this term may be neglected provided that $\Lambda \neq 0$. In Figure 3 we represent θ versus ω/Ω as obtained by solving for the equation $\Lambda = 0$. We find that for $\theta \leq 45°$, Λ becomes zero for ω very close to 2Ω; in this case the term proportional to κ cannot be ignored. In Figure 4 we represent

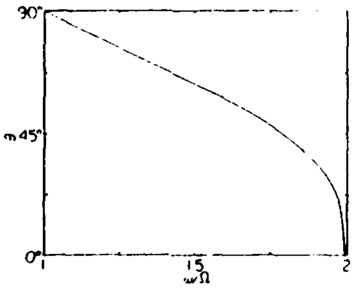

Fig. 3. We represent θ (the angle the geomagnetic field forms with the vertical) as a function of the ratio of wave to cyclotron frequencies ω/Ω, after solving for $\Lambda(\theta, \omega) = 0$ where Λ is defined in equation (7).

the refractive index Q as a function of θ by solving for the dispersion relation in (6). As shown in Figure 4, the refractive indices are much larger for $\Lambda = 0$ than for $\Lambda \neq 0$ by a factor of v_T/c. Thus if the angle θ between $\mathbf{B}_0$ and the density gradient is <45°, one expects plasma waves with frequencies $\omega \sim 2\Omega$ *to be absorbed more efficiently by the electrons than* waves with $\omega < 2\Omega$.

The components of the group velocity along the vertical $v_{g\xi}$ and horizontal $v_{g\mu}$ directions are

$$v_{g\xi}/c = \frac{1}{2}\left(\frac{v_T}{c}\right)^2 (3\Lambda Q + 4\kappa) f$$
$$v_{g\mu}/c = -\frac{1}{2}\left(\frac{v_T}{c}\right)^2 \Lambda Q^2 f/S \qquad (11)$$

where $f = (1 - Y^2)/(X_r^{-1} - Y^2 \cos^2 \theta)$. When $\Lambda \neq 0$, $v_{g\xi}/v_{g\mu} \ll 1$, and the wave propagates along the direction perpendicular to the density gradient. When $\Lambda \rightarrow 0$, $v_{g\mu}$ and $v_{g\xi}$ can be of the same order of magnitude and much smaller than $v_{g\mu}$ for the case $\Lambda \neq 0$. Because the group velocities are smaller when $\Lambda = 0$ than when $\Lambda \neq 0$, the waves interact with the electrons for longer times and then deliver their energy to the plasma more efficiently.

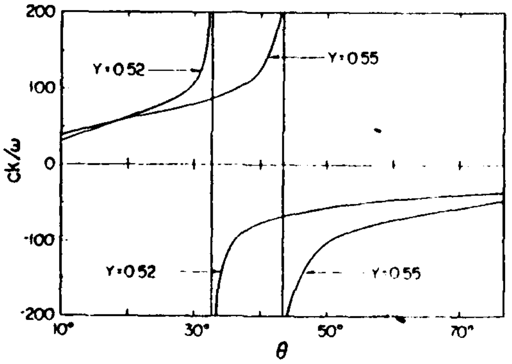

Fig. 4. Refractive indices near the plasma resonances as functions of θ and for two values of $Y = \Omega/\omega$. They are largest when θ and ω are such that $\Lambda = 0$ (equation (7)).

3. THE WAVE ELECTRIC FIELDS

The wave electric fields near resonance are polarized along the vertical, and their amplitudes vary as $\mathbf{E} = \mathbf{e}_\xi E(\xi) \exp[-i\omega t + i\omega/c(Q\xi + S\mu)]$. Here $\mathbf{e}_\xi$ is the unit vector along the ξ direction, and $E(\xi)$ is a slowly varying function of ξ. Next, to obtain the differential equation for the wave amplitude $E(\xi)$, we identify Q with the spatial derivative $Q = -(ic/\omega)\, d/d\xi$. When this is substituted into (6), $\mathcal{D}$ becomes a differential operator, and the equation for the electric field amplitude is then $\mathcal{D}\, E(\xi) = 0$. By defining $W = XE(\xi)$ and denoting with primes differentiation with respect to ξ, we show

$$\left[\epsilon'_{\xi\xi} - \epsilon_{\xi\xi}(\ln X)' + 2iYX\frac{\omega}{c}\right]W + \epsilon_{\xi\xi}W' + \left[2i\left(\frac{v_T}{c}\right)^2 \frac{c}{\omega} X\kappa + 2\frac{v_T}{c}\frac{c}{\omega}\rho X\right]W'' + \left(\frac{v_T}{c}\right)^2\left(\frac{c}{\omega}\right)^2 \Lambda X W''' = 0 \qquad (12)$$

Next, we define $u = 1 + (\xi - \xi_0)/l$ and $\delta = c/\omega l$ ($<10^{-1}$); (12) now becomes

$$\left[-\frac{\delta}{u^2} + 2iYX_r\right]W - \delta\frac{u-1}{u}\frac{dW}{du} + 2\frac{v_T}{c}\delta^2\left[i\frac{v_T}{c}\kappa + \rho\right]X_r\frac{d^2W}{du^2} + \left(\frac{v_T}{c}\right)^2 \delta^3 \Lambda X_r \frac{d^3W}{du^3} = 0 \qquad (13)$$

Near resonance we have that $u \simeq 1$; in addition, we define $\zeta = u - 1$ and

$$\sigma = 2YX_r\delta^{-1} \qquad (14)$$

$$\gamma = 2\frac{v_T}{c}\delta\left(\rho + i\frac{v_T}{c}\kappa\right)X_r \qquad (15)$$

$$\beta = \left(\frac{v_T}{c}\delta\right)^2 \Lambda X_r \qquad (16)$$

Equation (13) now becomes

$$\beta\frac{d^3W}{d\zeta^3} + \gamma\frac{d^2W}{d\zeta^2} - \zeta\frac{dW}{d\zeta} + (-1 + i\sigma)W = 0 \qquad (17)$$

By taking $\gamma = 0$ we recover the third-order differential equation as obtained by *Golant and Piliya* [1972]. As shown in section 4 when $\beta = 0$, (17) reduces to a second-order differential equation of the parabolic cylinder type.

The three solutions to (17) may be found by Laplace transform methods, as

$$W(\zeta) = \gamma^{(1-i\sigma)/2}\int_{c_k} dt\, t^{-i\sigma} \exp\left[\zeta t - \gamma\frac{t^2}{2} - \frac{\beta}{3}t^3\right] \qquad (18)$$

where the complex t plane has a cut taken from the origin at an angle $\arg t = \pi/3$. The contours of integration c_k ($k = 0$, 1, 2) are such that arg $t = 2k\pi/3$. *Golant and Piliya* [1972] studied (18) for $\beta \neq 0$ by neglecting the term $\gamma t^2/2$ in the exponential factor. The behavior of $W(\zeta)$ when $\zeta > 0$ and $\zeta \to \infty$ is given by W_c. Here

$$W_c = C\left(\frac{l}{\xi - \xi_0}\right)^{1-i\sigma} + B \qquad (19)$$

where C and B are arbitrary constants which have dimensions of electric fields. Note that (19), which is independent of v_T/c, represents the ordinary electromagnetic wave [*Dolgopolov*, 1966]. For $\zeta < 0$ the asymptotic form of W is a combination of the cold electromagnetic wave W_c and the warm plasma wave. In fact, *Golant and Piliya* [1972] show that

$$W \to W_c - \alpha_p \frac{i\pi^{1/2}}{\hat{\zeta}^{1/4}} \exp\left[-\frac{2}{3}\hat{\zeta}^{3/2} - \frac{i\sigma}{2}\ln\hat{\zeta}\right] \qquad (20)$$

where

$$\alpha_p = C\,\frac{\exp(-\pi\sigma)}{\Gamma(1-i\sigma)}\left(\frac{1}{\beta^{1/3}}\right)^{1-i\sigma}$$

and $\hat{\zeta} = \zeta\beta^{-1/3}$. The power absorbed at $\xi = \xi_0$ per unit area of surface, $\mathcal{P}$, was calculated by *Piliya and Fedorov* [1970]; it is determined completely by the cold solution W_c and given by

$$\mathcal{P} = \frac{c}{8\pi}|C^2|A \qquad (21)$$

where A is the amplification coefficient defined as

$$A = \frac{\omega l}{c}\,\frac{1 - \exp(-2\pi\sigma)}{2\sigma} \qquad (22)$$

Under the limit $\gamma \to 0$ we investigate the three roots of (17). By assuming that $W \sim \exp(\int Q\,d\zeta)$ one gets

$$Q_1 = s_1 + s_2$$
$$Q_{2,3} = -\frac{1}{2}(s_1 + s_2) \pm i\,\frac{3^{1/2}}{2}(s_1 - s_2) \qquad (23)$$

where

$$s_1 \pm s_2 = [E^{-1} - (E^{-2} - x^3)^{1/2}]^{1/3} \pm [E^{-1} + (E^{-2} - x^3)^{1/2}]^{1/3}.$$

$E = 2\beta/(1 - i\sigma)$ is such that $|E| \ll 1$, and $x = (\zeta/3\beta)$. By taking the limit $x^3 \gg E^{-2}$ we show

$$Q_1 \to \frac{2}{3}\exp\left(-i\frac{\pi}{3}\right)(Ex)^{-1}$$
$$Q_{2,3} \to \frac{-1}{3}\exp\left(-i\frac{\pi}{3}\right)(Ex)^{-1} \pm \exp\left(-i\frac{\pi}{3}\right)(3x)^{1/2} \qquad (24)$$

We see that Q_1 does not depend on v_T/c and represents the cold electromagnetic wave. The roots $Q_{2,3}$ are such that they tend to infinity as $v_T/c \to 0$; they represent the plasma waves. To estimate approximately how far along the vertical the plasma wave amplitude extends (i.e., is exponentially large), we calculate the turning points of the roots $Q_{2,3}$. The turning points are values of $\zeta = \zeta_0$ such that $s_1 - s_2 = 0$; we show that $\zeta_0 = 3[(1 - i\sigma)^2\beta/4]^{1/3}$. By taking $\omega = (2/3)\Omega$, $\theta \sim 20°$, and $v_T/c \sim \delta \sim 0.25 \times 10^{-3}$ one gets $|\zeta_0| = 3. \times 10^{-3}$. Hence, according to this simple calculation, the vertical penetration of the wave fields should be less than 150 m. If we take $\Omega/\omega \sim 1.8$, then $\xi - \xi_0$ is about 70 m.

4. SECOND HARMONIC RESONANCE ABSORPTION

Let us now consider the case $\Lambda \to 0$; here the term $\gamma t^2/2$ cannot be neglected. By taking $\Lambda \to 0$, we find that $|\beta| \ll 1$, and then we may expand $\exp(-\beta/3t^3)$ in powers of β [*Bender and Orszag*, 1978], which yields

$$W(\zeta) = \gamma^{(1-i\sigma)/2}\sum_{n=0}^{\infty}\frac{1}{n!}\left(\frac{-\beta}{3}\right)^n \cdot \int_c dt\, t^{(3n-i\sigma)}\exp\left(\zeta t - \frac{\gamma t^2}{2}\right) \qquad (25)$$

where the contour of integration c is taken from the origin at an angle arg $t = -1/2$ arg γ. The integrals in (25) represent parabolic cylinder functions [*Abramowitz and Stegun*, 1964]. Thus we write

$$W(\chi) = \exp(\chi^2/4)\sum_{n=0}^{\infty}\frac{1}{n!}\left(\frac{-\beta}{3\gamma^{3/2}}\right)^n \Gamma(-\nu)D_\nu(-\chi) \qquad (26)$$

where

$$\nu = i\sigma - 3n - 1 \qquad (27)$$

$$\chi = \gamma^{-1/2}\,\frac{\xi - \xi_0}{l} \qquad (28)$$

$\Gamma(-\nu)$ is the gamma (factorial) function, and $D_\nu(\chi)$ is the parabolic cylinder function. Note that the series expansion in (26) requires that $|\beta/\gamma^{3/2}| < 1$.

To study the behavior of $W(\chi)$ as $|\chi| \to \infty$, we must consider the asymptotic expansions of $D_\nu(-\chi)$ at large values of $|\chi|$. For $\pi/4 < \arg\chi < 7/4\,\pi$ one has

$$D_\nu(-\chi) \sim \chi^\nu \exp(i\nu\pi)\exp\left(-\frac{\chi^2}{4}\right) \qquad (29)$$

For $|\arg\chi| < 1/4\,\pi$, one gets

$$D_\nu(-\chi) \sim \chi^\nu \exp(i\nu\pi)\exp\left(-\frac{\chi^2}{4}\right) + \frac{(2\pi)^{1/2}}{\Gamma(-\nu)}\chi^{-\nu-1}\exp\left(\frac{\chi^2}{4}\right) \qquad (30)$$

Substituting (29) into (26) yields the asymptotic behavior of $W(\chi)$ for $\pi/4 < \arg\chi < 7\pi/4$.

$$W(\chi) \to -\frac{1}{\chi^{1-i\sigma}}\exp(-\sigma\pi)\Gamma(1-i\sigma) \qquad (31)$$

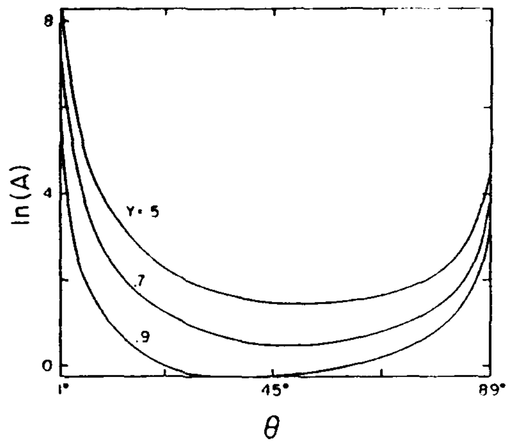

Fig. 5. Natural logarithm of the amplification coefficient (equation (22)) versus θ for three values of $Y = \Omega/\omega$. Maximum amplification is obtained for $\omega = 2\Omega$ and θ near 0°.

This equation contains only the contribution of the electromagnetic (O mode) wave. Combining (30) and (26), we obtain the asymptotic form of $W(\chi)$ for $|\arg \chi| < \pi/4$:

$$W(\chi) \sim -\frac{1}{\chi^{1-i\sigma}} \exp(-\sigma\pi)\Gamma(1-i\sigma) + \frac{(2\pi)^{1/2}}{\chi^{i\sigma}} \exp\left(\frac{\chi^2}{2}\right) \exp\left[-\frac{\beta}{3\gamma^{3/2}}\chi^3\right] \quad (32)$$

Equation (32) contains the contribution of the electromagnetic (first term in the right side of the equation) and plasma (second term) waves. Equation (32), valid if $|\beta/\gamma^{3/2}| < 1$, should be contrasted with (20), which was derived for the case $\beta \neq 0$ and $\gamma = 0$. The ratio of the O mode amplitude at $\xi - \xi_0 = r > 0$ to that at $\xi - \xi_0 = -r$ is obtained from (31) and (32); we show it is equal to $\exp(-\pi\sigma)$. The energy transmission coefficient $T = \exp(-2\pi\sigma)$. The quantity $1 - T$ is the fraction of the incident energy which is mode converted to the cyclotron harmonic wave. The power absorbed per unit area by the plasma wave at $\xi = \xi_0$ is

$$\mathcal{P} = (v/8\pi)\epsilon_{\xi\xi}|W_c|^2(1 - T)$$

where $v = c/Q \sim c\epsilon_{\xi\xi}/2YX$ and W_c is defined in (19). Note that this expression is identical to the power absorbed by the O mode as given in (21) and (22). In Figure 5 we have represented the natural logarithm of the amplification coefficient A defined in (22), as a function of θ for three values of $Y = \Omega/\omega$ (i.e., $Y = 0.5$, 0.7, and 0.9), and assuming that $\delta^{-1} = 1500/Y$. We show that maximum amplifications are obtained for $\omega = 2\Omega$ and θ very close to 0°. As a matter of fact the maximum value of A is calculated for $\theta \to 0°$ and 90°, where $A \to \delta^{-1}\pi$.

First, consider the limit where there is no damping, i.e., $(\omega - 2\Omega)/k_z v_T > 2^{1/2}$, $\rho = 0$, and then $\arg \gamma = \pi/2$. For $\xi > \xi_0$, $\arg \chi = -\pi/4$, and $3(\arg \chi - 1/2 \arg \gamma) = -(3/2)\pi$. For $\xi < \xi_0$, $\arg \chi = (3/4)\pi$, and then $3(\arg \chi - 1/2 \arg \gamma) = (3/2)\pi$. In both cases the plasma wave, as defined in (32), is an undamped plane wave propagating away from the resonant point $\xi = \xi_0$. Second, we assume that the wave is damped at the second cyclotron harmonic, i.e., $\omega \sim 2\Omega$ and $\rho \neq 0$. By taking $|\kappa v_T/\rho c| \ll 1$, we see that the plasma wave is generated for $\xi > \xi_0$ if $\beta > 0$ and for $\xi < \xi_0$ if $\beta < 0$. Its amplitude decays exponentially as $\mathrm{Re}\,[\chi^2/2 - \beta\chi^3/3\gamma^{3/2}]$, where Re denotes the real part of the expression in brackets. If $\beta > 0$ and $\xi < \xi_0$ or if $\beta < 0$ and $\xi > \xi_0$, then the asymptotic form of $W(\chi)$ is given by (31) containing only the electromagnetic wave.

The plasma wave which extends along a finite length in the ξ direction decays exponentially away from this region for large values of ξ. Next, we calculate the size of this region for the case $\beta = 0$, by applying a WKB analysis to (17). Let us define a new complex coordinate

$$\tau = \frac{i}{2}(a\gamma)^{-1/2}\frac{\xi - \xi_0}{l} \quad (33)$$

where $a = 1/2 - i\sigma$. With the introduction of $W(\tau) = \exp(-a\tau^2)V(\tau)$, equation (17) becomes a second-order equation of the Weber's type [*Abramowitz and Stegun*, 1964].

$$\frac{d^2V}{d\tau^2} + 4a^2(1 - \tau^2)V = 0 \quad (34)$$

where we have set $\beta = 0$. The WKB solutions to (34) are [*Nayfeh*, 1973]

$$W = \frac{1}{(1-\tau^2)^{1/4}}\exp(-a\tau^2) \cdot \left\{C \exp\left[-2ia\int_1^\tau (1-x^2)^{1/2}\,dx\right] + B \exp\left[2ia\int_1^\tau (1-x^2)^{1/2}\,dx\right]\right\} \quad (35)$$

where C and B are constants and the turning points are $\tau = \pm 1$. The solution with constant of proportionality C is the electromagnetic wave, and the one with constant of proportionality B is the plasma wave. This may be verified by taking $|x| \gg 1$, approximating $(1 - x^{-2})^{1/2} \sim 1 - x^{-2}/2$ and integrating (35), which leads to

$$W \to \frac{\exp(i\pi/4)}{\tau^{1/2}}\left\{C\frac{1}{\tau^a} + B\tau^a \exp(-2a\tau^2)\right\} \quad (36)$$

Comparing (36) and (32) yields the values of the constants of proportionality C and B.

$$\frac{C}{B} = \frac{\exp(-i\pi/2)}{(2\pi)^{1/2}}\frac{\Gamma(1-i\sigma)}{(4a)^a} \quad (37)$$

The amplitude of the plasma wave grows until τ is such that

$$\mathrm{Re}\left\{(2\sigma + i)\int^\tau [(1-x^2)^{1/2} + ix]\,dx\right\} = 0 \quad (38)$$

The length of wave growth is the maximum value of $\xi - \xi_m$ for which the plasma wave in (35) is exponentially large; it may be obtained by solving for (38). To give an estimate of this length, let us set $|\tau| = 1$, and then $\zeta = 2(a\gamma)^{1/2}$. We take

$\omega \sim 1.9\Omega$, $\theta = 20°$, $v_T/c = 0.25 \times 10^{-1}$, and $\delta = 0.3 \times 10^{-1}$. We also consider that there is no damping, i.e., take $\rho = 0$. Substituting these numbers in the definition of r, we show that $|\xi_m - \xi_0|$ is of the order of a few (<5) meters. Thus the power carried by the wave is delivered in small regions of space to the electrons through the second harmonic resonance absorption.

5. CONCLUSIONS

We have studied the mode conversion of ordinary electromagnetic waves into electrostatic plasma waves in inhomogeneous magnetized plasmas. The density gradient is along the vertical direction, and the geomagnetic field B_0 forms an angle θ with the vertical. The warm plasma dispersion relation for the plasma waves and the refractive indices are calculated as functions of θ and the ratio between the wave, ω, and cyclotron, Ω, frequencies. It is assumed that $\Omega \le \omega \le 2\Omega$. The differential equations for the electric fields describing the mode conversion processes near resonance are derived; the spatial derivatives are third order in the vertical coordinate. We investigate the wave equations using analytical techniques such as Laplace transform methods to obtain asymptotic behaviors. We also derive WKB solutions to calculate the penetration of the electric field amplitudes along the vertical. For certain values of θ and ω that satisfy the equation $\Lambda(\theta, \omega) = 0$ (see the definition of Λ in (7)) the wave equation reduces to the standard parabolic cylinder equation which describes a broad spectrum of mode conversion problems in plasma physics. The energy transmission coefficient and the power absorbed by the cyclotron waves are calculated. The amplification of the cyclotron waves is largest for $\omega = 2\Omega$ and $\theta \sim 0°$. For typical ionospheric parameters we estimate that the electric field amplitudes extend a few meters along the vertical coordinate. They should be absorbed by the electrons due to the second harmonic resonance damping.

Acknowledgments. This work has been supported by the U.S. Air Force under contract F19628-89-K-0014. The author thanks W. J. Burke for a careful reading of the manuscript.

The Editor thanks R. A. Cairns for his assistance in evaluating this paper.

REFERENCES

Abramowitz, M., and I. A. Stegun, *Handbook of Mathematical Functions, Appl. Math. Ser.*, vol. 55, p. 686, National Bureau of Standards, Washington, D. C., 1964.

Antonsen, T. M., Jr., and W. M. Manheimer, Electromagnetic wave propagation in inhomogeneous plasma, *Phys. Fluids*, *21*, 2295, 1978.

Bender, C. M., and S. A. Orszag, *Advanced Mathematical Methods for Scientist and Engineers*, p. 272, McGraw-Hill, New York, 1978.

Bernhardt, P. A., L. M. Duncan, and C. A. Tepley, Artificial airglow excited by high-power radio waves, *Science*, *242*, 1022, 1988.

Birkmayer, W., T. Hagfors, and W. Kofman, Small-scale plasma density depletions in Arecibo high frequency modification experiments, *Phys. Rev. Lett.*, *57*, 1008, 1986.

Budden, K. G., *Radio Waves in the Ionosphere*, p. 122, Cambridge University Press, New York, 1961.

Cairns, R. A., and C. N. Lashmore-Davies, The absorption mechanism of the ordinary mode propagation perpendicularly to the magnetic field at the electron cyclotron frequency, *Phys. Fluids*, *25*, 1605, 1982.

Cairns, R. A., and C. N. Lashmore-Davies, A unified theory of a class of mode conversion problems, *Phys. Fluids*, *26*, 1268, 1983.

Dolgopolov, V. V., Electromagnetic field singularities in an inhomogeneous magnetoactive plasma, *Sov. Phys. Tech. Phys.*, Engl. Transl., *11*, 198, 1966.

Golant, V. E., and A. D. Piliya, Linear transformation and absorption of waves in a plasma, *Sov. Phys. Usp.*, Engl. Transl., *14*, 413, 1972.

Mjølhus, E., Coupling to Z mode near critical angle, *J. Plasma Phys.*, *31*(1), 7, 1984.

Mjølhus, E., and T. Flå, Direct access to plasma resonance in ionospheric radio experiments, *J. Geophys. Res.*, *89*, 3921, 1984.

Nayfeh, A., *Perturbation Methods*, p. 48, Wiley-Interscience, New York, 1973.

Piliya, A. D., Wave conversion in an inhomogeneous plasma, *Sov. Phys. Tech. Phys.*, Engl. Transl., *11*, 609, 1966.

Piliya, A. D., and V. I. Fedorov, Linear wave conversion in an inhomogeneous magnetoactive plasma, *Sov. Phys. JETP*, Engl. Transl., *30*, 653, 1970.

Villalón, E., Ionospheric electron acceleration by electromagnetic waves near regions of plasma resonances, *J. Geophys. Res.*, *94*, 2717, 1989.

Wong, A. Y., J. Santoru, and G. G. Sivjee, Active simulation on the auroral plasma, *J. Geophys. Res.*, *86*, 7718, 1981.

E. Villalón, Center for Electromagnetics Research, Northeastern University, Boston, MA 02115.

(Received October 31, 1990;
accepted December 17, 1990.)

JOURNAL OF GEOPHYSICAL RESEARCH, VOL. 96, NO. A6, PAGES 9655-9667, JUNE 1, 1991

Near-Equatorial Pitch Angle Diffusion of Energetic Electrons by Oblique Whistler Waves

ELENA VILLALÓN

Center for Electromagnetics Research, Northeastern University, Boston, Massachusetts

WILLIAM J. BURKE

Geophysics Laboratory, Hanscom Air Force Base, Massachusetts

The pitch angle scattering of trapped, energetic electrons by obliquely propagating whistler waves in the equatorial regions of the plasmasphere is investigated. Storm-injected electrons moving along field lines near the equator interact with electromagnetic waves whose frequencies are Doppler-shifted to some harmonic of the cyclotron frequency. The wave normals are distributed almost parallel to the geomagnetic field. Waves grow from the combined contributions of a large reservoir of energetic electrons that are driven into the loss cone by the highest-harmonic interactions permitted to them. Relativistic, quasi-linear theory is applied to obtain self-consistent equations describing the temporal evolution of waves and particles over time scales which are longer than the particle bounce time and group time delay of the waves. The equilibrium solutions and their stability are studied, considering the reflection of the waves by the ionosphere and the coupling of multiple harmonic resonances. The contributions of nonlocal wave sources are also included in the theory. Numerical computations based on our theoretical analysis for regions inside the plasmasphere ($L < 2$) and near the plasmapause ($L \sim 4.5$) and for the first three harmonic resonances are presented.

1. INTRODUCTION

In this paper we investigate pitch angle scattering interactions of radiation belt electrons with obliquely propagating whistler waves. Trapped electrons in the radiation belts moving along field lines near the equatorial plane of the magnetosphere may see low-frequency electromagnetic waves Doppler-shifted to some harmonic of their local gyrofrequencies [*Roberts*, 1969; *Gendrin*, 1972; *Schulz and Lanzerotti*, 1974]. We assume that the waves are distributed over Gaussian profiles in frequencies ω and in angles φ between the wave vector **k** and the ambient geomagnetic field $\mathbf{B}_0$. The wave packet distributions are centered at values of ω well below the equatorial gyrofrequencies Ω_L and at the normal angle $\varphi = 0$. Since φ is small, the component of the group velocity parallel to $\mathbf{B}_0$ is much larger than the perpendicular component; thus the waves are almost field-aligned. Because $\omega \ll \Omega_L$, cyclotron resonant wave-particle interactions cause diffusion almost purely in pitch angle [*Kennel and Petschek*, 1966; *Lyons and Williams*, 1984; *Villalón et al.*, 1989*b*]. For high-temperature plasmas the pitch angle distributions of the particles are anisotropic and provide sources of free energy for cyclotron instabilities to occur. Consequently, particles diffuse in pitch angle along surfaces of constant phase velocity to reduce the anisotropy of their distribution functions [*Trakhtengerts*, 1984; *Sazhin*, 1989]. Particles scattered into the loss cone give up a small amount of energy to the waves, but many of these particles cause substantial wave growth [*Inan et al.*, 1978; *Imhof et al.*, 1986; *Huang et al.*, 1990]. *Kennel and Petschek* [1966] developed a model in which the waves responsible for pitch angle scattering are derived from the free energy contained in the anisotropic pitch angle distribution of the energetic trapped electrons. It predicts that when the particles' fluxes fall below a stable-trapping limit, the waves stop growing, and pitch angle scattering should cease.

During magnetic storms the radiation belts become filled with trapped, energetic particles from about $L = 8$ to $L = 1.5$ (L represents the magnetic shell). In the weeks following, the fluxes of trapped electrons in the range $L = 2$–3.5 diminish to levels below detector sensitivity and well below the trapping limits of *Kennel and Petschek* [1966]. *Lyons et al.* [1972] recognized that some of the waves responsible for pitch angle diffusion need not necessarily be generated locally from low, background fluctuation levels. Rather, they have been created elsewhere in the outer plasmasphere. They propagate along field lines to locations where their frequencies reach the local, lower-hybrid frequency and get reflected back across field lines toward equatorial regions, eventually filling the entire plasmasphere with waves [*Lyons and Thorne*, 1970; *Kimura*, 1966]. The waves responsible for diffusing particles in the slot regions may also be initiated in the atmosphere by, for example, lightning strokes [*Inan et al.*, 1988] or ground transmitters [*Luhmann and Vampola*, 1977]. We have phenomenologically incorporated the contribution of these sources of wave energy to electron pitch angle diffusion. Thus our theoretical model considers wave growth from background electromagnetic fluctuations as well as wave energy injected from nonlocal origin. Both sources of waves contribute to reducing the level of energetic plasmaspheric electrons by scattering them into either the atmosphere of the drift loss cones.

For wave propagation strictly along field lines (i.e., $\varphi = 0°$), quasi-linear diffusion reduces to the fundamental $l = 1$ harmonic resonance [*Bespalov and Trakhtengerts*, 1980; *Schulz and Davidson*, 1988]. However, much of the plasmaspheric, whistler wave turbulence propagates obliquely to the magnetic field. In addition, particle diffusion occurs over

Paper number 91JA00444
0148-0227/91/91JA-00444$05.00

a broad range of energies [*Swift*, 1981] which cannot be accounted for by strictly considering the fundamental resonance. As the particle's energy increases (say larger than 100 keV), resonant interactions near equatorial regions at the fundamental harmonic, for particles whose pitch angles are near the loss cone, are not permitted. By allowing the wave vectors to form small angles with respect to $\mathbf{B}_0$, higher-harmonic resonance interactions can take place. In fact, high-harmonic resonance resulting from oblique wave propagation together with high-latitude interactions is needed to explain the precipitation of many energetic electrons from the radiation belts.

Lyons et al. [1971] studied higher-harmonic, pitch angle diffusion at all geomagnetic latitudes. They showed that the diffusion into the loss cone of >100-keV electrons is controlled by harmonics with $l > 1$. In their work it was assumed that the wave intensity is given and does not grow from the anisotropy of the particles they are scattering toward the loss cone. Also, very energetic particles may interact with waves at the $l = 1$ harmonic away from the equator. However, the distance allowed for off-equatorial, resonant interaction is limited because of large gradients in the magnetic energy per particle with increasing latitude [*Bell*, 1986]. Efficient scattering of these particles requires that the waves have already grown to large amplitudes [*Rosenberg et al.*, 1981].

This paper extends previous work by *Villalón et al.* [1989*a*] on electron diffusion by parallel-propagating whistler waves to the case of oblique propagation. We assume that quasi-linear theory can be applied to study the temporal evolution of waves and particles which are resonantly coupled at some gyroharmonic. Our investigations are restricted to interactions that occur near the equator (i.e., for geomagnetic latitudes such that $\psi \leq 20°$). In the weak diffusion limit, interactions that significantly modify particle distributions occur on time scales much longer than either the wave travel times from one hemisphere to the other or the particle bounce periods. The diffusion coefficients are averaged over a bounce orbit. Energetic particles are driven into the loss cone by the highest-harmonic interactions permitted to them. We recognize that they may also be scattered at high latitudes by interactions at the first gyroharmonic with waves that are amplified near the equator [*Rosenberg et al.*, 1981]. For the sake of analytical simplicity we do not consider high-latitude scattering in our calculations. In the work by *Lyons et al.* [1972], high-latitude interactions are included numerically for a magnetic dipole profile. The more restrictive scope of our parabolic magnetic field model allows us to carry analytical studies further and to obtain transparent expressions for the diffusion coefficients. We also consider wave growth from the resonant interactions. The waves are growing from an extensive range of particle energies which depend on the harmonic with which they are in resonance. On the other hand, because we neglect high-latitude interactions, our results may not be realistic throughout the plasmasphere but may only apply to equatorial regions.

The paper is organized as follows: section 2 contains our basic model for the whistler wave spectral distributions. We assume that the dielectric properties of wave propagation are given by the cold plasmaspheric electrons whose densities are much larger than those of resonant, energetic electrons. Thus our model applies both inside the plasmasphere and in regions of cold plasma density enhancements beyond the plasmapause. We also assume that spatial inhomogeneities are aligned along geomagnetic field lines. Section 3 presents the theory of quasi-linear resonant diffusion of relativistic electrons by oblique, whistler waves. The energetic electrons are represented by the particle sources $S(E, L)$, which depends on the particle resonant energy E and on the magnetic shell L. The pitch angle eigenvalues and distribution functions are studied in Appendix A as functions of the harmonic resonances. Since we only investigate the weak diffusion limit, we consider the lowest-order pitch angle eigenvalues and eigenfunctions for each harmonic resonance. This should be contrasted with the moderate diffusion for parallel-propagating waves [*Villalón et al.*, 1989*a*], in which we treated many eigenvalues and eigenfunctions of the diffusion operator but only the fundamental resonance. Section 4 presents the growth rates for whistlers due to the contribution of several harmonics; this extends previous results by *Kennel and Petschek* [1966] on wave growth due to the fundamental resonance. Section 5 contains the equations which describe the evolution in time of the waves and the numbers of resonant particles in a flux tube. The waves which grow near the equator by selective amplification are partially reflected somewhere along the flux tube. Our theoretical model includes wave reflection as a parameter. The contributions of external wave sources which are not generated locally by the cyclotron instability are also included in the theory. We study the equilibrium solutions and the stability of the system, which is formally identical to the one obtained for parallel propagation in the moderate diffusion case. In Appendix B we solve the stability equations for the coupling of three harmonic resonances. We present some numerical applications of this theory in section 6, assuming that there are no external wave sources. We study three harmonic resonances at the shells $L \sim 2$ and $L \sim 4.5$, which corresponds to the slot portion of the radiation belt and to the plasmapause. The resonant energies and the equilibrium solutions for waves and particles are obtained. The times required for the first three harmonics to reach equilibrium are calculated. Section 7 contains a summary and conclusions.

2. WHISTLER ELECTRON RESONANT INTERACTIONS

Let us consider electromagnetic, whistler mode waves whose frequencies are small fractions of the equatorial, electron gyrofrequencies and that propagate at oblique angles to the geomagnetic field $\mathbf{B}_0$. The wave frequency is denoted by ω, and the wave vector by $\mathbf{k}$. The magnetic field $\mathbf{B}_0$ is taken along the z direction, and $\mathbf{k}$ propagates at an angle φ with respect to $\mathbf{B}_0$ (see Figure 1). The components of $\mathbf{k}$ parallel and perpendicular to $\mathbf{B}_0$ are represented by $k_\parallel$ and $k_\perp$, respectively. The refractive index $\eta = ck/\omega$ satisfies the dispersion relation

$$\eta^2 = \frac{\omega_p^2/\omega^2}{(\Omega/\omega)|\cos\varphi| - 1} \qquad (1)$$

where ω_p is the plasma frequency of plasmaspheric electrons, and Ω is the electron cyclotron frequency. Equation (1) is valid if $(\Omega/\omega)|\cos\varphi|$ and η are much larger than 1; thus φ is not too large. We also assume that $\Omega_p \ll \omega \ll \Omega$ where Ω_p is the proton gyrofrequency, and that $(\omega_p/\Omega)^2 \gg 1$ [*Helliwell*, 1965]

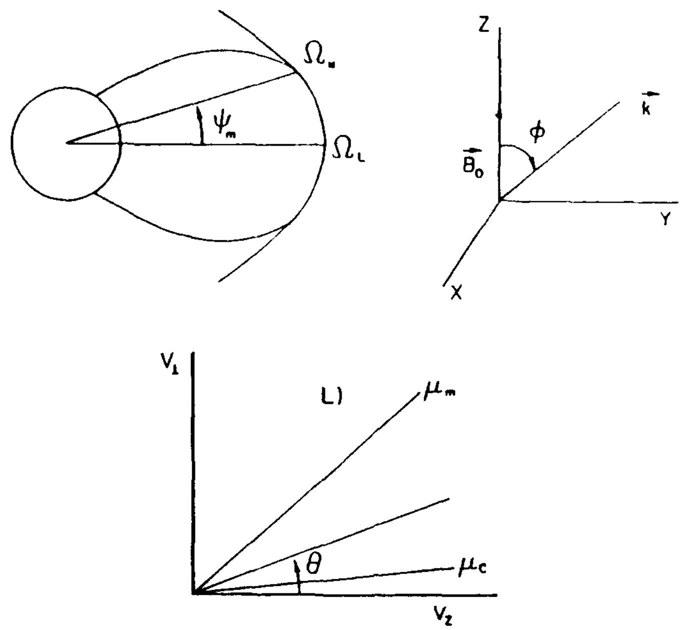

Fig. 1. The Earth's dipole magnetic field B_0 and the parabolic profile are qualitatively depicted here. The gyrofrequencies Ω_L and Ω_M correspond to the equatorial and the maximum resonant geomagnetic fields, respectively. The angle ψ_m is the maximum geomagnetic latitude for which resonant wave-particle interaction takes place. In a local coordinate system, $\mathbf{B}_0$ is along the z direction, and the wave vector $\mathbf{k}$ forms a small angle φ with respect to $\mathbf{B}_0$. The velocities v_z and $v_\perp$ represent the perpendicular and parallel components of the resonant particle's velocity as given in the equatorial cross section indicated by the index L. The equatorial pitch angle is denoted by θ, and $\mu = \sin^2\theta$. The values μ_c and μ_m are evaluated for pitch angles at the equatorial loss cone and for the maximum value of θ which satisfied the resonant condition, respectively.

Near the equator the Earth's magnetic field is approximated by the parabolic profile [*Villalón et al.*, 1989*a*, *b*]

$$\Omega/\Omega_L = 1 + (z/a)^2 \tag{2}$$

where $z \approx R_E L\psi$, $a = (\sqrt{2}/3)R_E L$, R_E is the Earth's radius, and LR_E measures the equatorial distance of the magnetic trap from the center of the Earth. Here ψ is the geomagnetic latitude in radian units. Equation (2) is obtained from a Taylor expansion of the dipole field and is an excellent representation of the magnetic geometry within ±20° of the equator.

2.1. *The Resonance Condition*

The electromagnetic waves interact with electrons whose energies are ≥10 keV. These electrons bounce between mirror points in a time equal to τ_B. We approximate τ_B by $4\pi a/v$, where v is the particle's velocity. The density of the hot electrons is much smaller than that of cold electrons, so they do not contribute to the dielectric properties of wave propagation. However, because their pitch angle distributions are very anisotropic, they provide sources of free energy for the growth of the cyclotron instability. The interaction with the waves occurs for those electrons which satisfy the Doppler-shifted resonance condition

$$\omega - k_\parallel v_\parallel - l(\Omega/\gamma) = 0 \tag{3}$$

where $\Omega = |qB_0/mc|$, q is the electron charge, m is its mass, and $l = 1, 2, 3, \cdots$ is the harmonic number. Here γ is the relativistic factor $\gamma = (1 - v^2/c^2)^{-1/2}$ which relates a particle's momentum p to its velocity $p = m\gamma v$. The components of the particle velocity and wave vector parallel to $\mathbf{B}_0$ are given by $v_\parallel$ and $k_\parallel = k\cos\varphi$. We call θ the particle's equatorial pitch angle, and $\mu = \sin^2\theta$. We assume that the *first adiabatic invariant* is almost conserved during the interactions. Therefore the particle's pitch angle θ_B at any point along the field line is related to its equatorial value by $\sin^2\theta_B = (\Omega/\Omega_L)\sin^2\theta$. The resonant condition is satisfied for values of μ such that $\mu_c \le \mu \le \mu_m$, where μ_c is defined in terms of the pitch angle at the boundary with the loss cone and $\mu_m = \sin^2\theta_m$ is an upper limit (see Figure 1). As function of the L shell, the mirror ratio $\sigma = 1/\mu_c$ is $\sigma = L^3(4 - 3/L)^{1/2}$. In terms of the equatorial pitch angle the parallel and perpendicular components of the particle velocity are $v_\parallel = -v(1 - \mu\Omega/\Omega_L)^{1/2}$ and $v_\perp = v(\mu\Omega/\Omega_L)^{1/2}$, respectively.

The resonant gyrofrequencies are such that $\Omega_L \le \Omega \le \Omega_M$, where Ω_L is the *equatorial cyclotron frequency* and Ω_M is the maximum value of Ω which satisfies (3). From now on the subscript L refers to values at the magnetic equator. The frequencies Ω_L and Ω_M are resonant with the values of the equatorial pitch angles corresponding to μ_m and μ_c, respectively (see Figure 1). The resonant geomagnetic latitudes are such that $0 \le \psi \le \psi_m$, where for $\psi = 0$, $\Omega = \Omega_L$, and for $\psi = \psi_m$, $\Omega = \Omega_M$. By writing the resonance condition (3) for $\Omega = \Omega_L$ and $\mu = \mu_m$, we find that the normalized relativistic momentum of the electron, p_l, is

$$\frac{p_l}{mc} = l\left(\frac{\Omega_L}{\omega}\right)^{1/2} \frac{\Omega_L}{\omega_p} \frac{1}{|\cos\varphi|} \left(\frac{|\cos\varphi| - \omega/\Omega_L}{1-\mu_m}\right)^{1/2} \quad (4)$$

where $\gamma\omega/l\Omega_L \ll 1$ and $\Omega_L/\omega_p < 1$. In our calculations we assume that the plasma density decreases within the plasmasphere as $1/L^4$ (see (53)); hence the value of Ω_L/ω_p decreases as $1/L$ with increasing L shell, and the resonant energies are larger for smaller L shells. The very low energy electrons (i.e., in the tens of electron volts) can interact with waves whose frequencies are such that $\omega/\Omega_L \sim |\cos\varphi|$. For $|\cos\varphi|$ close to 1 we must have $\omega \simeq \Omega_L$ for gyroresonant interactions with low-energy electrons. The energies increase well into the hundreds of keV as the harmonic number l increases. For a given value of l, as μ_m approaches unity, i.e., the equatorial pitch angles are near 90°, the energy also increases.

The refractive index along the field lines varies as $\eta/\eta_L = (\Omega_L/\Omega)^{1/2}$. Applying Snell's law yields the fact that $k_\perp$ does not change along a given field line; then the wave angle φ as related to its equatorial value φ_L is $\cos^2\varphi = 1 - (\Omega/\Omega_L)\sin^2\varphi_L$. The cyclotron frequency Ω is defined in (2). Since both ψ and φ_L are quite small, we may assume that $\varphi = \varphi_L$ [*Bell*, 1986]. If $\omega \ll \Omega_L$, the resonance condition at $\Omega = \Omega_M$ and $\mu = \mu_c$ yields

$$\frac{p_l}{mc} = l\left(\frac{\Omega_M}{\omega}\right)^{1/2} \frac{\Omega_M}{\omega_p} \frac{1}{|\cos\varphi|} \left(\frac{|\cos\varphi| - \omega/\Omega_L}{1-\mu_c\Omega_M/\Omega_L}\right)^{1/2} \quad (5)$$

where we have taken $v_\parallel$ as defined after (3). Combining (4) and (5) leads to

$$(\Omega_M/\Omega_L)^3(1-\mu_m) = 1 - \mu_c\,(\Omega_M/\Omega_L) \quad (6)$$

In deriving this equation, we have considered that the refractive index changes along the field lines as $\eta/\eta_L = (\Omega/\Omega_L)^{1/2}$. For a parabolic profile in the magnetic field we obtain

$$\psi_m = \frac{\sqrt{2}}{3}\left[\frac{\mu_m - \mu_c}{3(1-\mu_m) + \mu_c}\right]^{1/2} - \left(\frac{2}{3}\right)^{1/2} \frac{(\mu_m - \mu_c)^{1/2}}{3} \quad (7)$$

We find that

$$\psi_m = \frac{\sqrt{2}}{3}\left[\left(\frac{k_L v\gamma\cos\varphi}{l\Omega_L}\right)^{2/3} - 1\right]^{1/2} \quad (8)$$

The factor $(2/3)^{1/2}$ in (7) is due to the changes of the wave vector k along the field lines. Equations (7) and (8) should be contrasted with the same equations of *Villalón et al.* [1989*a*] where k was taken as a constant independent of z, and μ_m, $\mu_c \ll 1$.

We now summarize our investigations on the resonant wave particle coupling: (4) defines the electron's energy for a given harmonic number as a function of the L shell and pitch angles. Particles with this energy and with pitch angles at the equator such that $\mu_c \le \mu \le \mu_m$ satisfy the resonance condition somewhere along the near-equatorial portion of the field line. The geomagnetic latitudes for resonant interactions are such that $0 \le \psi \le \psi_m$, where ψ_m is given in (7).

Note that by increasing the maximum pitch angle θ_m, ψ_m also increases, and so does the electron energy. Thus high-latitude interactions at the first gyroharmonic can affect high-energy electrons. In addition, by increasing the harmonic number, we may also increase the electron resonance energies.

2.2. *Spectral Energy Distribution of Waves*

The magnetic field of the whistler mode $\mathbf{B}_k$ as a function of the wave vector $\mathbf{k}$, is related to the observable wave magnetic field at position $\mathbf{x}$, $\mathbf{B}_{wave}(\mathbf{x}, t)$, by

$$\mathbf{B}_{wave}(\mathbf{x}, t) = \frac{1}{(2\pi)^3} V^{1/2} \int \mathbf{B}_k \exp(i\mathbf{k}\mathbf{x})\, d^3\mathbf{k} \quad (9)$$

where V is the plasma volume. Note that in our representation $\mathbf{B}_k$ has units of the square root of energy. The wave energy as a function of $\mathbf{k}$ is represented by $W_k(\varphi, t)$, where $W_k = (1/8\pi)(\mathbf{B}_k/2\pi)^2$. We next assume that wave energy is distributed over Gaussian profiles in k^2 (i.e., in wave frequencies; see the dispersion relation in (1)) and in $\zeta = \cos\varphi$. These profiles are peaked at $k^2 = k_0^2$ and $\zeta^2 = 1$ with half widths Δk^2 and $\Delta\zeta^2$. We may write

$$W_k(\varphi, t) = \frac{C_\zeta}{C_k} W(t) \exp\left[-\left(\frac{k^2 - k_0^2}{\Delta k^2}\right)^2\right] \exp\left[-\left(\frac{\zeta^2 - 1}{\Delta\zeta^2}\right)^2\right] \quad (10)$$

where

$$C_k = \frac{k_0}{2}\int_0^\infty dk^2 \exp\left[-\left(\frac{k^2 - k_0^2}{\Delta k^2}\right)^2\right] \quad (11)$$

and

$$C_\zeta = \frac{2}{\sqrt{\pi}}\frac{1}{\Delta\zeta^2}. \quad (12)$$

The reasons for the representations of C_k and C_ζ in (11) and (12) are explained after (29). Here $W(t)$ is the equatorial energy density of waves.

The components of the group velocity parallel and perpendicular to $\mathbf{B}_0$ are

$$v_{g\parallel} \simeq \frac{c}{\eta}\frac{1 + \cos^2\varphi}{|\cos\varphi|}$$

$$v_{g\perp} \simeq \frac{c}{\eta}\sin\varphi\,\frac{\cos\varphi}{|\cos\varphi|} \quad (13)$$

Since the distribution profiles in (10) are centered around $\cos\varphi = 1$, $v_{g\parallel} \gg v_{g\perp}$, and we may consider the waves as field-aligned. The time it takes the waves to travel from a reflection point in one hemisphere to the conjugate reflection point is represented by τ_g. We approximate $\tau_g \simeq \eta_L a/c$, where η_L is the refractive index evaluated at the magnetic equator, i.e., for $\Omega = \Omega_L$, and $a = (\sqrt{2}/3)R_E L$. The electric field components are denoted by $\mathscr{E}_x = \mathscr{E}_1$, $\mathscr{E}_y = i\mathscr{E}_2$, and $\mathscr{E}_z = -\mathscr{E}_3$, where

$$\frac{\mathcal{E}_2}{\mathcal{E}_1} = |\cos\varphi| - \frac{\omega}{\Omega}$$

$$\frac{\mathcal{E}_3}{\mathcal{E}_1} = -\frac{\cos\varphi}{|\cos\varphi|}\sin\varphi\,\frac{\omega}{\Omega} \tag{14}$$

For the waves described in (10) we may neglect the component of the electric field, $\mathcal{E}_3$, along $\mathbf{B}_0$. These waves are preferentially right-hand circularly polarized, and their electric fields are $\mathcal{E}_R = (\mathcal{E}_1/\sqrt{2})(1 + |\cos\varphi|)$.

3. HIGHER-HARMONIC PITCH ANGLE DIFFUSION

In the limit of pure pitch angle diffusion we use relativistic quasi-linear theory to study the evolution in time of the electron whistler interactions. The electrons energies are given as a function of the harmonic numbers in (4). Because these energies usually do not overlap for different gyroharmonics, we treat each cyclotron resonance as independent of the others. Nevertheless, we assume that a broad energy range of electrons interact with the same waves. We also assume that their distribution functions are independent of the distance z along the flux tube. For the weak diffusion case we treat the pitch angle anisotropy to be independent of time and assume that for each resonance the distribution function is

$$f_l = \frac{4}{\pi^{1/2} a p_l^3} N_l(t) Z(\mu) \exp\left(-\frac{p^2}{p_l^2}\right) \tag{15}$$

where $Z(\mu)$ is the lowest-order eigenfunction of the diffusion operator defined below. The number of resonant electrons in the flux tube per square centimeter, $N_l(t)$, changes on time scales $t \gg \tau_B$, τ_g. We must find the equations for the temporal evolution of $N_l(t)$ and defining the eigenfunctions $Z(\mu)$. For an infinite homogeneous background plasma of cold particles immersed in the geomagnetic field $\mathbf{B}_0$ as in (2), the distribution function of resonant electrons is obtained for each cyclotron resonance solving for [*Lyons and Williams*, 1984]

$$\frac{\partial f_l}{\partial t} = \pi q^2 \int \frac{d^3k}{(2\pi)^3}\left[\frac{k_\parallel}{\omega}\hat{G} + \frac{\omega - k_\parallel v_\parallel}{\omega p_\perp}\right]$$

$$\cdot\,\delta\left(k_\parallel v_\parallel + \frac{l\Omega}{\gamma} - \omega\right)\Theta_{l,k}\left(\frac{k_\parallel}{\omega}\hat{G}\right) f_l \tag{16}$$

By assuming that $\omega \ll \Omega_L$, we may neglect diffusion in energy [*Kennel and Engelman*, 1966; *Villalón et al.*, 1989*b*] and write

$$\hat{G} = -2\frac{v}{p}\frac{\Omega_L}{\Omega}\frac{p_\perp p_\parallel}{p^2}\frac{\partial}{\partial\mu}$$

$$\left[\frac{k_\parallel}{\omega}\hat{G} + \frac{\omega - k_\parallel v_\parallel}{\omega p_\perp}\right] = -2\left(\frac{l\Omega}{\gamma\omega}\right)$$

$$\cdot\left(\frac{\Omega_L}{\Omega}\right)^{1/2}\frac{p_\parallel}{p^2}\frac{\partial}{\partial\mu}\frac{\mu^{1/2}}{(1 - \mu\Omega/\Omega_L)^{1/2}} \tag{17}$$

where $p_\perp$ and $p_\parallel$ represent the momentum components perpendicular and parallel to $\mathbf{B}_0$, respectively. The wave energy W_k appears in the function $\Theta_{l,k}$, where

$$\frac{\Theta_{l,k}}{(2\pi)^2} = \frac{4\pi}{\eta^2} W_k(\varphi, t)\frac{Q_l(\varphi, \lambda)}{(|\cos\varphi| - \omega/\Omega)}|\cos\varphi| \tag{18}$$

and $\lambda = k_\perp v_\perp/\Omega$. In terms of Bessel functions of the first kind we have

$$Q_l(\varphi, \lambda) = \frac{1}{4\cos^2\varphi}\Bigg[(1 + |\cos\varphi|)J_{l-1}(\lambda)$$

$$+ (1 - |\cos\varphi|)J_{l+1}(\lambda) \pm \frac{v_\parallel\omega}{v_\perp\Omega}\sin\varphi J_l(\lambda)\Bigg]^2 \tag{19}$$

where the plus or minus sign depends on the sign $\cos\varphi$. Because $\lambda \ll 1$ and $\cos\varphi \sim 1$, we may approximate

$$Q_l(\varphi, \lambda) \sim \left[\frac{(1 + |\cos\varphi|)}{2|\cos\varphi|}J_{l-1}(\lambda)\right]^2 \tag{20}$$

Combining (16)–(18) leads to

$$\frac{\partial f_l}{\partial t} = \frac{4\pi m\omega_p^2}{n_c p^2 c^2}\left(\frac{l\Omega_L}{\gamma}\right)^2\int_0^\infty dk\int_{-\pi/2}^{\pi/2} d\varphi\,\sin\varphi$$

$$\cdot\left(1 - \mu\frac{\Omega}{\Omega_L}\right)^{1/2}\frac{\partial}{\partial\mu}\left[\frac{\Omega}{\Omega_L}\frac{\mu}{(1 - \mu\Omega/\Omega_L)^{1/2}}\right.$$

$$\left.\cdot\,\delta\left(k_\parallel v_\parallel + \frac{l\Omega}{\gamma} - \omega\right)W_k(\varphi, t)Q_l(\varphi, \lambda)\frac{\partial f_l}{\partial\mu}\right] \tag{21}$$

where n_c, the density of the cold electrons, is such that $n_c \gg N_l/a$ and $\omega_p^2/c^2 \gg k^2$.

Because interactions take place near the equator, we first integrate (21) along the flux tube using the geomagnetic field profile in (2). The plasma density is taken as constant along z. We apply the operator $1/\tau_B \int dz/v_z$ to the left- and right-hand sides of (21) to average the distribution function over time scales comparable to the bounce time τ_B. The wave vector $\mathbf{k}$ as function of z is represented by $k/k_L = (\Omega_L/\Omega)^{1/2}$, where k_L is the value of k at the magnetic equator. In the weak diffusion case, f_l is a constant independent of z, and

$$\frac{\partial f_l}{\partial t} = \frac{8\pi m^2 a\omega_p^2}{\tau_B n_c p^3 c^2}\frac{(l\Omega_L)^2}{\gamma}\int_0^\infty dk_L\int_{-\pi/2}^{\pi/2} d\varphi\,\sin\varphi$$

$$\cdot\int_1^{\Omega_M/\Omega_L}\frac{d\Omega}{\Omega_L}\frac{1}{(1 - \Omega_L/\Omega)^{1/2}}\frac{\partial}{\partial\mu}$$

$$\cdot\left[\frac{\mu}{(1 - \mu\Omega/\Omega_L)^{1/2}}\delta\left(\omega - k_\parallel v_\parallel - \frac{l\Omega}{\gamma}\right)\right.$$

$$\left.\cdot\,W_k(\varphi, t)Q_l(\varphi, \lambda)\frac{\partial f_l}{\partial\mu}\right] \tag{22}$$

To integrate along Ω, we must consider the zeros of the delta function. For $\omega \ll \Omega_L$ and $k/k_L = (\Omega_L/\Omega)^{1/2}$ the resonance condition (3) becomes

$$\left(\frac{\Omega}{\Omega_L}\right)^3 + \left(\frac{k_L\gamma v\cos\varphi}{l\Omega_L}\right)^2\left[\mu\left(\frac{\Omega}{\Omega_L}\right) - 1\right] = 0 \tag{23}$$

The real root of (23) is represented by Ω_R. Under the limit $(k_L\gamma v/l\Omega_L)^{2/3} \ll 1/\mu$ we obtain

$$\frac{\Omega_R}{\Omega_L} \sim \left(\frac{k_L\gamma v\cos\varphi}{l\Omega_L}\right)^{2/3} \tag{24}$$

because of the resonance condition $k_L v\gamma\cos\varphi/l\Omega_L = (1-\mu_m)^{-1/2}$ independent of the wave vector. For resonant interactions near the equator $\mu_m \ll 1$, the particle's equatorial pitch angle must be near the loss cone. We call λ_R^2 the square of the argument of the Bessel function in (20), evaluated for $\Omega = \Omega_R$, where

$$\lambda_R^2 = \mu b_l \frac{1-\zeta^2}{\zeta^{4/3}}$$

$$b_l = \left(\frac{l}{\gamma}\right)^2\left(\frac{k_L\gamma v}{l\Omega_L}\right)^{2/3} \tag{25}$$

Since $\zeta^2 = \cos^2\varphi \sim 1$, $\lambda_R^2 \ll 1$.

Next, let us consider the definitions

$$F_l = \int_0^\infty \pi\sigma p^3 f_l(p, t)\, dp \tag{26}$$

$$Y = \frac{2\pi m\Omega_L^2}{pB_L^2k_0}\left[\left(\frac{2}{3}\right)^{1/2}\left(\frac{l\Omega_L}{\gamma v k_0}\right)^{2/3}\right] \tag{27}$$

Integrating along Ω leads to

$$\frac{\partial F_l}{\partial t} = Y\left(\frac{2}{3}\right)^{1/2}\left[\frac{1}{(k_0 v\gamma/l\Omega_L)^{2/3}-1}\right]^{1/2}\frac{\partial}{\partial\mu}\left(\mu^l\frac{\partial F_l}{\partial\mu}\right)$$
$$\cdot\frac{\sigma^{(l-1)}}{2^{l-1}\Gamma(l)}\left\{\int_0^1 d\zeta\,\zeta^{1/3}\left(\frac{\zeta+1}{\zeta}\right)^2 J_{l-1}\left(\frac{\lambda_R^2}{\sigma}\right)\right.$$
$$\left.\cdot\int_0^\infty k_L\, dk_L^2 W_k(\zeta, t)\right\} + \mathcal{S}_l(t, \mu) \tag{28}$$

where $\Gamma(l)$ is the standard gamma function. Combining (15) and (26) yields $F_l = N_l(t)Z(\mu)$. We assume that the particle flux is independent of time and $\mathcal{S}_l(t, \mu) = (\mathcal{S}_l/\tau_q)Z(\mu)$. The actual particle source $\mathcal{S}(E, L) = \mathcal{S}_l/\tau_q$ depends on the resonant particle energy E, which in turns depends on the lth harmonic number (see (4)) and the magnetic shell L; it is given in section 6. The pitch angle eigenfunctions $Z(\mu)$ satisfy the differential equation

$$\frac{d}{d\mu}\left(\mu^l\frac{dZ}{d\mu}\right) = -g_l^2(\mu_m - \mu_c)Z(\mu) \tag{29}$$

where g_l^2 refers to the lowest-order eigenvalues and is given in Appendix A. For $l = 2$ the solutions of (29) are trigonometric functions, and for $l \neq 2$ they are Bessel functions.

We next substitute the wave packet distributions $W_k(\zeta, t)$ given in (10)–(12) into (28). Since the main contribution to the integral in ζ comes from the neighborhood of $\zeta = 1$, we evaluate the integral approximately. The constants C_L and C_ζ are chosen so that by taking the limits $l = 1$ and $\Delta\zeta^2 = 0$ in (28), we recover the results of parallel propagation [*Villalón et al.*, 1989*a*, equation (22)]. The energy-dependent particle fluxes are represented by the constant source $\mathcal{S}_l$. After some algebra it can be shown that the evolution of $N_l(t)$ is given by

$$\frac{dN_l}{dt} = -Y4g_l^2[2(\mu_m - \mu_c)]^{1/2}\mathfrak{R}_l W(t)N_l(t) + \frac{\mathcal{S}_l}{\tau_q} \tag{30}$$

where

$$\mathfrak{R}_l = \frac{\Gamma(l/2)\Gamma(l/2+1/2)}{\Gamma(l)^2}\frac{\sigma^{(l-1)}}{\sqrt{\pi}}\exp\left(-\frac{\mathfrak{X}_l}{\sigma^2}\right)I_{(l-1)/2}\left(\frac{\mathfrak{X}_l}{\sigma^2}\right)$$

$$\mathfrak{X}_l = (b_l^2/2)(\Delta\zeta^2/2)^2 \tag{31}$$

and $I_{(l-1)/2}(\mathfrak{X}_l/\sigma^2)$ is the modified Bessel function. The factors 2/3 and $l\Omega_l/\gamma v k$ in the definition of Y, (27), are due to the variations of the wave vectors along the field lines. Because their contribution is of order unity, their variations may be ignored.

4. Temporal Growth of Whistlers

To describe the interaction of whistlers and energetic electrons at higher-harmonic resonances, we must derive an equation for the energy density of waves $W(t)$ as function of the numbers of resonant particles. In the limit of pure pitch angle diffusion the temporal wave growth rate γ_D is [*Lyons and Williams*, 1984]

$$\frac{\gamma_D}{\omega} = \frac{2\pi^2}{n_c}\sum_{l\geq 1}\int_0^\infty p^2\, dp\int_0^1 d\mu\,\frac{\mu}{(1-\mu\Omega/\Omega_L)^{1/2}}\frac{\Omega}{\Omega_L}$$
$$\cdot\left(\frac{l\Omega}{\gamma\omega}-1\right)\Omega\delta\left(\frac{l\Omega}{\gamma}-\omega+k_\parallel v_\parallel\right)|\cos\varphi|Q_l(\varphi, \lambda)\frac{\partial f_l}{\partial\mu} \tag{32}$$

where the summation extends over all possible harmonic numbers. Integrating along the flux tube yields the spatial amplification factor which is defined as $\Gamma_k(\varphi, t) = \int dz\, \gamma_D/v_g$. In doing this integral, we average over time scales comparable to the group time delay of the waves. After some tedious algebra we arrive at

$$\Gamma_k(\varphi, t) = \sum_{l>1}\frac{\pi\omega_p^2 a k_L p_l}{(l\Omega_L m)^2 n_c c^2\sigma}\left[\frac{2}{3}\left(\frac{l\Omega_L}{\gamma k_L v}\right)^{1/3}\right]$$
$$\cdot\int_{\mu_c}^{\mu_m} d\mu\,\cos^{8/3}\varphi\, Q_l(\varphi, \lambda_R)$$
$$\cdot\left[\frac{1}{(k_L v\gamma/l\Omega_L)^{2/3}-1}\right]^{1/2}\mu\frac{\partial F_l}{\partial\mu} \tag{33}$$

where $Q_l(\varphi, \lambda_R)$ is defined in (20). Recall that $F_l = N_l(t)Z(\mu)$, where N_l is the number of electrons in the flux tube interacting with the cyclotron resonance of order l. We must also consider that

$$\int_{\mu_c}^{\mu_m} d\mu\left[\frac{1}{(kv\gamma/l\Omega_L)^{2/3}-1}\right]^{1/2}\mu^l\frac{dZ}{d\mu}$$
$$\sim\left(\frac{3}{2}\right)^{1/2}\left(\frac{\mu_m-\mu_c}{2}\right)^{1/2}\frac{p_l}{\pi a} \tag{34}$$

The temporal evolution of the wave energy $W_k(\varphi, t)$ is obtained from

$$\frac{\partial W_k}{\partial t} = \left(\frac{\Gamma_k}{\tau_q} - \frac{r}{\tau_q}\right) W_k(\varphi, t) \tag{35}$$

Here $r = -2 \ln |R|$, where R is the amplitude, reflection coefficient. Wave reflection may occur either at both ends of the flux tube in the ionosphere or at the location along the field line at which the wave frequency matches the lower hybrid frequency [*Kimura*, 1966]. Next we substitute into $W_k(\varphi, t)$ the distributions in (10)–(12) and integrate both sides of (35) with respect to k and ζ, which after some algebra becomes

$$\frac{dW}{dt} = \left(\frac{\Gamma}{\tau_q} - \frac{r}{\tau_q}\right) W(t) + \frac{\mathcal{J}(t)}{\tau_q} \tag{36}$$

where $\mathcal{J}(t)$ is a external source of wave energy. Here

$$\frac{\Gamma}{\tau_q} = \sum_{l \geq 1} \Delta_e(l) \frac{v\gamma}{\pi a} [2(\mu_m - \mu_c)]^{1/2} \mathfrak{R}_l N_l(t)$$

$$\Delta_e(l) = \frac{2\pi^2 p_l \omega}{a(lB_l)^2} \left[\left(\frac{2}{3}\right)^{1/2} \left(\frac{l\Omega_L}{\gamma k v}\right)^{1/3}\right] \tag{37}$$

where $\mathfrak{R}_l$ has been defined in (31). If $l = 1$, then $\mathfrak{R}_l = 1$; for larger-harmonic resonances, $\mathfrak{R}_l$ is very small and the coupling between waves and particles is much weaker. The factor in the square brackets of the definition of $\Delta_e(l)$ in (37) is due to the variations in the wave vectors and is of order unity.

Equations (36) and (37) together with (30) and (31) are called the ray equations. They describe the self-consistent interactions of obliquely propagating whistlers and electrons in the magnetosphere. Because of the oblique propagation the waves grow from interactions with a wide energy range of electrons through higher cyclotron resonance coupling. The electrons are depleted from the magnetosphere because of pitch angle diffusion into the loss cone. The rate at which they are depleted is proportional to $\mathfrak{R}_l$, which is very small for $l > 1$. Because high-energy electrons interact with some $l > 1$ gyroharmonics, it takes longer for them to diffuse into the loss cone and for the waves to grow. We must now consider the conditions for equilibrium and stability of the ray equations.

5. EQUILIBRIUM AND STABILITY

We call

$$D_l = \Upsilon(4g_l^2)[2(\mu_m - \mu_c)]^{1/2} \mathfrak{R}_l \tau_q \tag{38}$$

$$K_l = \Delta_e(l) \frac{\gamma v}{\pi a} [2(\mu_m - \mu_c)]^{1/2} \mathfrak{R}_l \tau_q \tag{39}$$

By defining $\tau = t/\tau_q$, the ray equations (30) and (36) describing the interaction of waves and particles may be written as

$$\frac{dN_l}{d\tau} = -D_l N_l W + \mathcal{S}_l \tag{40}$$

$$\frac{dW}{d\tau} = \left(\sum_{l \geq 1} K_l N_l - r\right) W + \mathcal{J} \tag{41}$$

where the index l extends over all possible cyclotron resonances we may want to study (e.g., $l = 1, \cdots, M$, $M \geq 1$). This is a system of $M + 1$ equations whose equilibrium solutions are obtained by setting $dN_l/dt = dW/dt = 0$. We call $N_l^{(0)}$ and $W^{(0)}$ the solutions to the equilibrium where

$$N_l^{(0)} = (1/D_l)(\mathcal{S}_l/W^{(0)}) \tag{42}$$

$$W^{(0)} = \frac{1}{r}\left(\sum_{l=1}^{M} \frac{K_l}{D_l} \mathcal{S}_l + \mathcal{J}\right) \tag{43}$$

Next we introduce the functions Ψ_l and Λ_l such that the solutions to (40) and (41) can be written in terms of these functions as

$$N_l = N_l^{(0)} + \frac{1}{K_l}\left(\frac{d\Psi_l}{d\tau} + \Lambda_l\right) \tag{44}$$

$$W = W^{(0)} \exp(\Psi_T) \tag{45}$$

where

$$\Psi_T = \sum_{l=1}^{M} \Psi_l$$

$$\Lambda_l = \frac{\mathcal{J}}{W^{(0)}} \frac{\exp(\Psi_T) - 1}{\exp(\Psi_T)} \frac{\Psi_l}{\Psi_T} \tag{46}$$

After substituting (44)–(46) into (40) and (41), they reduce to a system of M equations for the functions Ψ_l,

$$\frac{d^2\Psi_l}{d\tau^2} + \frac{d\Lambda_l}{d\tau} = K_l \mathcal{S}_l [1 - \exp(\Psi_T)]$$

$$- D_l\left(\frac{d\Psi_l}{d\tau} + \Lambda_l\right) W^{(0)} \exp(\Psi_T) \tag{47}$$

for all $l \geq 1$ whose stability we may study by assuming small deviations from equilibrium. Thus we linearize (47) by taking $\Psi_l \ll 1$ and $\Lambda_l \sim (\mathcal{J}/W^{(0)})\Psi_l$, which leads to

$$\frac{d^2\Psi_l}{d\tau^2} + 2\nu_l \frac{d\Psi_l}{d\tau} + \Psi_l \rho_l^2 + K_l \mathcal{S}_l \sum_{j \geq 1, j \neq l} \Psi_j = 0 \tag{48}$$

where

$$2\nu_l = \left[\frac{\mathcal{J}}{W^{(0)}} + D_l W^{(0)}\right] \tag{49}$$

$$\rho_l^2 = [K_l \mathcal{S}_l + \mathcal{J} D_l] \tag{50}$$

Next take $\Psi_l \sim \beta_l \exp(\xi\tau)$ and substitute it into (48), which becomes a system of algebraic equations for ξ and β_l:

$$\beta_l(\xi^2 + 2\nu_l \xi + \rho_l^2) + K_l \mathcal{S}_l \sum_{j \neq l} \beta_j = 0 \tag{51}$$

There are $2M$ solutions to this system of equations. Then the solution to (48) will be

$$\Psi_l = \sum_{m=1}^{2M} \beta_{lm} \exp(\xi_m \tau) \quad (52)$$

In Appendix B we have solved (51) assuming no wave source ($\mathcal{S} = 0$) for the case of three $l = 1$, 2, and 3 resonances.

For the case $\mathcal{S} = 0$ we define $\xi_m = -\xi_m^R + i\xi_m^I (m = 1, \cdots, M + 1)$, where ξ_m^R and ξ_m^I are real numbers. We arrange the eigenvalues so the time scales associated with them, $\tau_m = 1/\xi_m^R$, are such that $\tau_1 \sim \tau_2 \ll \tau_3 \ll \cdots \tau_{M+1}$. The eigenvalues $\xi_{1,2}$ are driven by the fundamental harmonic and have the shorter, associated time scales (see Appendix B). The evolution of the waves over times of the order of $\tau_{1,2}$ are dominated by the $l = 1$ harmonic, and the equilibrium solutions contain only the contribution of $l = 1$. By increasing time so that $\tau \sim \tau_3$, we must include the second resonance $l = 2$ in the equilibrium solutions. There appears to be a third eigenvalue ξ_3 which results from contributions of the fundamental and second resonances. This is because *the waves which have already grown to a certain level because of the interaction at the fundamental act as sources to drive the second harmonic. By increasing time to* $\tau \sim \tau_4$, we need to consider the first three ($l = 1, 2, 3$) resonances in the equilibrium solutions for waves and particles. The new eigenvalue ξ_4, which is driven by the third harmonic, contains contributions of the $l = 1$ and 2 resonances. This is due to the fact that the waves which have grown from the interaction with the $l = 1$ and 2 resonances act as sources to drive the eigenmode ξ_4. All these ideas have been detailed with the calculations presented in the Appendix B.

The modes ξ_m given in Appendix B should be contrasted with the eigenvalues we would obtain by assuming that the resonances can be treated separately and independent of each other. That is, let us assume that for each value of l we have $\xi_l^2 + \xi_l 2\nu_l + \rho_l^2 = 0$, whose solution is $\xi_l = -\nu_l \pm i(\rho_l^2 - \nu_l^2)^{1/2}$. In our numerical computations we show that except for the fundamental harmonic, ν_l is smaller (by a factor of 2–4) than ξ_m^R. Thus the equilibrium times τ_m may sometimes be a factor of 4 smaller than $1/\nu_l$.

6. NUMERICAL CALCULATIONS

The density of cold, plasmaspheric electrons is approximated by a function of the distance R from the center of the Earth to the equatorial field line as [*Chappell et al.*, 1970]

$$n_c = 3 \times 10^3 (2R_E/R)^4 \quad (53)$$

Recall that the dipole geomagnetic field is proportional to R^{-3}. In our numerical examples we study the shells $L \sim 2$ and 4.5, which corresponds to the slot region of the radiation belts and to near the plasmapause in the outer radiation belt, respectively. *The differential fluxes of energetic electrons* (i.e., el/(cm^2 s sr keV)) are represented as a function of energy in Figure 2 for the values $L \sim 2$ and 4.5 [*Spjeldvik and Rothwell*, 1985].

The resonant energies are represented in Figure 3 as obtained from (4). We calculate three harmonic resonances for each of the shells at $L = 2$ and 4.5. At $L = 2$ the *equatorial loss cone is* $\theta_c = 16.5°$, and at $L = 4.5$ it is $\theta_c = 4.5°$. As an example, we assume that θ_m (the maximum equatorial pitch angle for resonant interactions) is 25° at $L = 2$, and $\theta_m = 15°$ at $L = 4.5$. From (7) the maximum

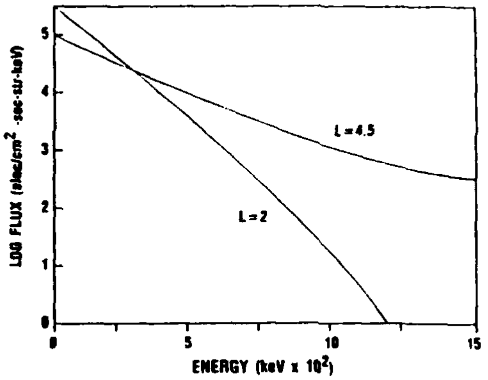

Fig. 2. Radiation belt electron fluxes in logarithmic units versus energy in keV at $L = 2$ and 4.5. The energy axis must be multiplied by 10^2 to obtain the actual electron energies.

geomagnetic latitudes are $\psi_m = 5.34°$ at $L \sim 2$ and $\psi_m = 4°$ at $L \sim 4.5$. Figure 3 shows that resonant energies are smaller at $L = 4.5$ than at $L = 2$ because of the decreasing values of $(\Omega_L/\omega_p)^2$ (the magnetic energy per particle). For a *given L shell the energies increase with l and with increasing* Ω_L/ω. Note that the particle's energy as given by (4) increases with θ_m. If we were taking $\theta_m = 55°$, then $\psi_m = 20°$ at $L = 2$ and $\psi_m = 22°$ at $L = 4.5$, and the resonant energies will be larger than in the examples in Figure 3. The parabolic profile in (2) is a good approximation to the geomagnetic field only if $\psi < 20°$. This means that our model applies to particles whose equatorial pitch angles are such $\theta < 55°$. Here we present only examples with θ within 10° off *the loss cone. This is because for θ near the loss cone*, the

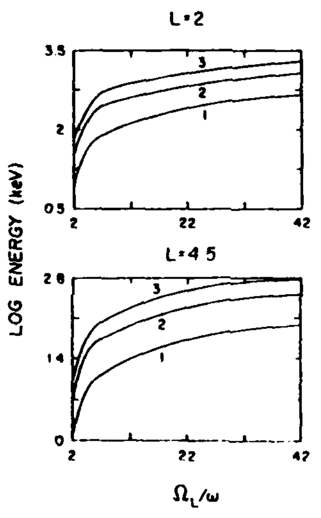

Fig. 3. Logarithm of the electron energies in keV versus Ω_L/ω (equatorial gyrofrequencies/wave frequencies) at (top) $L = 2$ and maximum pitch angle $\theta_m = 25°$ and (bottom) $L = 4.5$ and $\theta_m = 15°$ for wave normal angle $\cos\psi = 1$. The numbers by the curves indicate the harmonic resonances $l = 1$, 2, and 3.

particles' energies are smaller than if $\theta = 55°$. In addition, the time it takes to establish equilibrium is shorter.

We have calculated the lower hybrid frequencies ω_{LH} at geomagnetic latitudes $\psi_m \sim 5°$ and found that $\Omega_L/\omega_{LH} \sim 43$. For unducted waves [*Kimura*, 1966] the wave frequency is larger than ω_{LH} at any point in the interaction region and smaller than the equatorial gyrofrequency, and the frequency range may be defined as $6 < \Omega_L/\omega < 42$. Hence the frequency range at $L = 2$ is 2.6 kHz $\leq \omega \leq$ 18 kHz, which corresponds to the VLF band. At $L = 4.5$, 227 Hz $< \omega <$ 1.6 kHz, which is in the ELF band of frequencies. The fluxes of resonant electrons $\mathcal{F}_l/\tau_g = \mathcal{F}(E, L)$ are functions of the particles' energies E and the magnetic shell L. They can be obtained by multiplying the differential fluxes in Figure 2 by the energy widths ΔE. If v is the velocity of a resonant electron, we take $\Delta E = mc^2[1 - (\Delta v/c)^2]^{-1/2}$ where $\Delta v/v = 0.01$. For the cases represented in Figure 2, ΔE ranges from 0.001 up to 0.025 keV, corresponding to the smallest (10 keV) and to the largest (~1 MeV) energies, respectively. The contributions of the particles' fluxes to the equilibrium equations (42) and (43) are proportional to an effective flux, which is defined as $\hat{\mathcal{F}}(E, L) = \mathcal{F}(E, L)/4q_l^2$. The eigenvalues $4q_l^2$ are given in Appendix A. Because $4q_l^2$ decreases with increasing l, the effective fluxes are larger for larger energies than those depicted in Figure 2. That is, there is an enhancement of the particles' fluxes at large energies due to a decrease in the eigenvalues $4q_l^2$ as l increases.

We have carried out calculations for the equilibrium solutions of waves and particles considering three harmonic resonances at the L shell values of 2 (Figure 4) and 4.5 (Figure 5). The magnetic field of the wave normalized to the equatorial geomagnetic field (B_L) is represented by B_W; it can be obtained for each value of l from (43):

$$B_W = \frac{1}{B_L}\left[8\pi \frac{\tau_g}{r}\frac{K_l}{D_l}\mathcal{F}(E, L)\right]^{1/2} \tag{54}$$

where we shall assume that $r = 1$. We note that B_W does not depend on $\mathcal{R}_l$ (equation (31)). Because of this, B_W can also be very large for larger harmonics (i.e., $l > 1$). The number of resonant particles in the flux tube normalized to $\dot{N}_l = \omega\tau_g^2\mathcal{F}(E, L)/4q_l^2$ is obtained for each value of l as

$$\dot{N}_l = \frac{1}{\omega\tau_g}\frac{4q_l^2}{D_l}\frac{1}{W_l^{(0)}} \tag{55}$$

where

$$W_l^{(0)} = \frac{\tau_g}{r}\sum_{n=1}^{l}\frac{K_n}{D_n}\mathcal{F}(E_n, L) \tag{56}$$

and E_n is the resonant energy. Here we include in the wave amplitude $W_l^{(0)}$ the contributions of harmonic numbers such that $n \leq l$. This is because when $n < l$, resonances contribute to wave growth in much shorter times than when $n = l$. Thus the harmonics $n < l$ act as sources for wave growth which, in turn, help to deplete the electrons in resonance with the $n = l$ harmonic. In Figure 4 we represent B_W and $\dot{N}_l$ at $L = 2$ for $l = 1$, 2, and 3. As an example, we take $r = 1$, $\Delta\zeta^2 = 0.5$, and $\theta_m = 25°$. The whistler magnetic field can grow to large values independent of l. The maximum of B_W is shifted toward smaller Ω_L/ω as l increases. Note that wave growth is limited to a narrower range in Ω_L/ω as l increases. The number of resonant

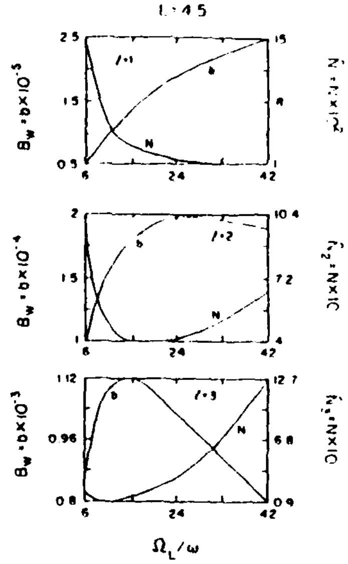

Fig. 5. Same as Figure 4 but at $L = 4.5$ and $\theta_m = 15°$.

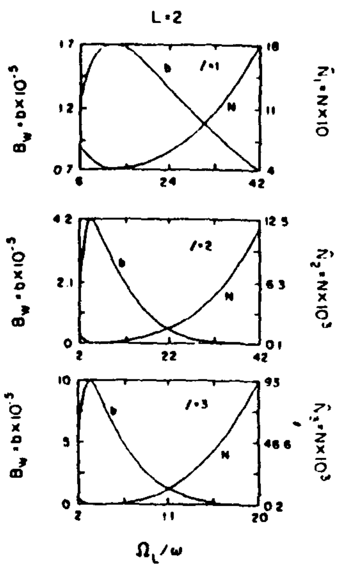

Fig. 4. The magnetic field of whistlers (B_W) normalized to the equatorial geomagnetic field versus Ω_L/ω (equatorial gyrofrequencies/wave frequencies), and the number of resonant electrons in the flux tube ($\dot{N}_l$) normalized to the radiation belt fluxes versus Ω_L/ω. Each of the panels represents the case at $L = 2$, and for $r = 1$, $\theta_m = 25°$, and $\Delta\zeta^2 = 0.5$, the harmonic resonances $l = 1$, 2, and 3 are indicated inside the panels. The curves labeled b and N must be multiplied by the factors indicated in the left- and right-hand sides of the panels to obtain B_W and $\dot{N}_l$, respectively.

electrons in the flux tube $\dot{N}_l$ is a minimum when B_W is a maximum. Since $\dot{N}_l \sim 1/\mathfrak{R}_l$ (where $\mathfrak{R}_l \ll 1$ for $l > 1$ and $\mathfrak{R}_1 = 1$), particles are more easily depleted from the radiation belts by the fundamental harmonic than for larger ones. The fundamental $l = 1$ harmonic is not sensitive to the value of $\Delta\zeta^2$. However, larger harmonics are affected by the values of $\Delta\zeta^2$. In fact, if $\Delta\zeta^2 < 0.5$, the number of resonant electrons in the flux tube becomes larger than for the cases represented in Figure 4. The refractive index η is larger than 10, $0.5 < \tau_\eta < 2$, and $0.25 < 2\tau_B < 0.6$ s. In our theoretical derivations the number of resonant electrons in the flux tube must be much smaller than that of cold particles (N_c). To find N_c we integrate (53) along a dipole field line from $\psi = 0$ to $\psi = \psi_M$, where ψ is the geomagnetic latitude and ψ_M is such that $\cos^2 \psi_M = 1/L$. We find that the ratio between the number of resonant electrons to cold particles along a field line for $l = 1$ is smaller than 10^{-4}, for $l = 2$ is smaller than 10^{-3}, and for $l = 3$ is smaller than 10^{-2}.

Figure 5 represents B_W and $\dot{N}_l$ for $l = 1, 2$, and 3 and $L = 4.5$. As an example, we take $r = 1$, $\Delta\zeta^2 = 0.5$, and $\theta_m = 15°$. Because B_W is smaller for $l = 1$ than for $l = 2$ and 3 and B_W is also smaller for $l = 2$ than for $l = 3$, electrons are now more easily depleted by the larger resonances. Note that B_W is proportional to $\mathcal{G}(E, L)/4g_l^2$, which is quite large for larger harmonics since energies are comparatively small (i.e., $10 \leq E \leq 600$ keV) and $4g_l^2$ decreases with increasing l. The maximum of B_W and minimum of $\dot{N}_l$ are shifted toward larger Ω_L/ω in comparison with the $L = 2$ case, because energies are now smaller. They move toward smaller Ω_L/ω as l increases. By comparing the cases $L = 2$ and 4.5, we find that the resonant energies for the fundamental harmonic and $L = 2$ (i.e., $50 \leq E \leq 500$ keV) overlap with energies in resonance with the $l = 2$ and 3 harmonics in the $L = 4.5$ case. However, as we show next, the fundamental resonance is in all cases the fastest to reach equilibrium, that is, to achieve wave growth and particle depletion. This is why low-energy electrons, with $E \sim 10$ keV, are first depleted by the fundamental harmonic in the outer edge of the plasmasphere. As the energy increases, electrons are trapped for longer times in the outer plasmasphere and are more easily scattered into the loss cone when L decreases. The refractive index η is greater than 20, and $3 < \tau_\eta < 9$ and $1 < 2\tau_B < 3$ s. We have also compared the numbers of resonant and cold (N_c) electrons in the field line, where N_c is obtained by integrating (53) from $\psi = 0$ to ψ_M (where $\cos^2 \psi_M = 1/L$). In all cases we found that the ratio of resonant to cold electrons is much smaller than 1.

The linear theory of the evolution of the wave-particle interactions is described in section 5 and in Appendix B. The stability of the equilibrium solutions is given as function of $2\nu_l = D_l W_l^{(0)}$ and $\rho_l^2 = K_l \Gamma_l$. In Figure 6 we represent $1/\nu_l$ and ρ_l for $L = 2$ and the first three resonances, where $r = 1$, $\Delta\zeta^2 = 0.5$, and $\theta_m = 25°$. For the fundamental harmonic the time it takes to establish equilibrium (in units of τ_g) is $1/\nu_1$, and ρ_1 is the oscillating frequency (see the definition of the eigenvalues $\xi_{1,2}$ in Appendix B). Note that $1/\nu_l$ is much smaller for the $l = 1$ harmonic than for larger ones; thus the equilibrium time is shorter for the fundamental resonance. In fact, for the harmonics $l = 2$ and 3 the time it takes to reach equilibrium (in units of τ_g) is equal to $1/\xi_3$ and $1/\xi_4$, respectively (see the definitions of $\xi_{3,4}$ in Appendix B). In our numerical calculations we find that $2\nu_2 \leq |\xi_3| \leq 4\nu_2$ and that $2\nu_3 \leq |\xi_4| \leq 3\nu_3$. Thus the equilibrium times τ for the second and third resonances are such that $1/4\nu \leq \tau \leq 1/2\nu$ (where $\nu = \nu_{2,3}$), but still they are much larger than for the case $l = 1$. Recall that the resonant energies for $l = 1$ are $50 \leq E \leq 500$ keV, and for $l = 2$ and 3 they are $200 \leq E \leq 2 \times 10^3$ keV.

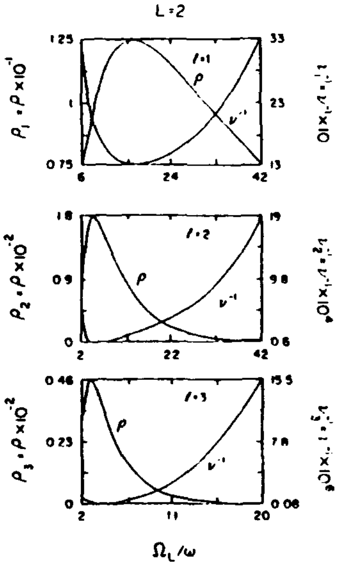

Fig. 6. Eigenvalues of the stability equation (51), ρ_l and $1/\nu_l$, versus Ω_L/ω (equatorial gyrofrequencies/wave frequencies) at $L = 2$ and for $r = 1$, $\theta_m = 25°$, and $\Delta\zeta^2 = 0.5$. Each of the panels represents the harmonic resonances $l = 1, 2$, and 3, as indicated inside the panels. The curves labeled ρ and ν^{-1} must be multiplied by the factors in the left- and right-hand sides of the panels to obtain ρ_l and $1/\nu_l$, respectively. The equilibrium times for the three harmonic resonances are proportional to $1/\nu_l$.

In Figure 7 we represent ρ_l and $1/\nu_l$ for $l = 1, 2$, and 3 and the shell $L = 4.5$. Here $r = 1$, $\Delta\zeta^2 = 0.5$, and $\theta_m = 15°$. Again, we show that equilibrium times, which are proportional to $1/\nu_l$, are longer the larger the harmonic numbers are. In our numerical calculations we find that $\xi_3 \approx -4\nu_2$ and $\xi_4 \approx -3\nu_3$. The resonant energies for the fundamental $l = 1$ resonance are such that $10 \leq E \leq 100$ keV. For the second and third resonances, $40 \leq E \leq 600$ keV. By comparing the cases $L = 2$ and 4.5, we conclude that the electrons whose energies are larger than or of the order of 50 keV are more easily depleted at smaller L shells since the equilibrium times are shorter then.

7. Summary and Conclusions

We have modeled the pitch angle scattering of energetic electrons by obliquely propagating whistler waves. The waves grow near the equator in the plasmasphere because of the pitch angle anisotropies of the energetic electrons. The wave vectors form small angles with respect to the geomagnetic field, and the frequencies are small fractions of the gyrofrequencies. Relativistic, quasi-linear theory is applied to study the temporal evolution of waves and particles in the weak diffusion limit, by assuming that the only spatial

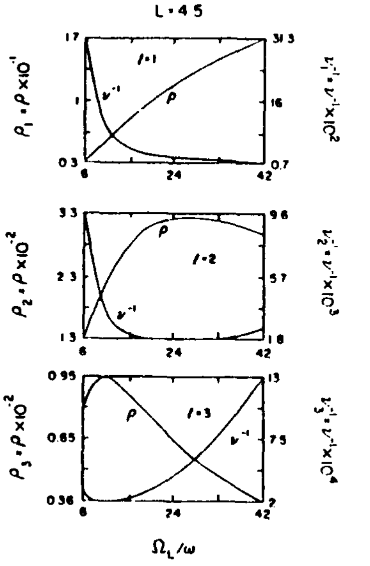

Fig. 7. Same as Figure 6 but at $L = 4.5$ and $\theta_m = 15°$.

inhomogeneities are along the geomagnetic field. The main results of our investigations are as follows.

1. We have derived equations which describe the temporal evolution of wave-particle interactions. The diffusion coefficients are obtained for all gyroharmonics and for interactions that take place near the equator after averaging over electron bounce orbits. The pitch angle distributions of the electrons are proportional to linear combinations of Bessel functions. The growth rates of the waves are calculated in terms of the distribution functions of the resonant electrons for all gyroharmonics. Our results complement previous results by *Lyons et al.* [1972] for high-latitude interactions in a dipole field and by *Kennel and Petschek* [1966] for wave growth due to the fundamental harmonic.

2. The equilibrium and stability of the system of nonlinear equations describing the wave-particle instabilities are investigated. By including an external wave source which is not generated from local background fluctuations, we reduce the limit of stably trapped particles to a level below the equilibrium solutions of the self-consistent problem. The time it takes to reach equilibrium is defined in terms of the eigenmodes of the stability equation.

3. Numerical calculations are carried out for the slot region and near the plasmapause in the outer radiation belt for three harmonic resonances and assuming no external wave source. They indicate that wave amplitudes may grow as much from the fundamental harmonic as from larger ones, but particles are more efficiently depleted from the radiation belts by the fundamental resonance. The wave frequencies are in the ELF band (227 Hz $\leq \omega \leq$ 1.6 kHz) at $L = 4.5$; they are in the VLF band of frequencies (2.6 kHz $\leq \omega \leq$ 18 kHz) at $L = 2$.

4. Equilibrium is established in much shorter times for the fundamental harmonic than for larger harmonic numbers. Wave-particle interactions for the highest harmonics are enhanced by contributions of lower harmonics, which act as a feedback to supply wave energy.

5. High-energy particles, >50 keV, are depleted at low L shells. Electrons with lower energies, ~10 keV, are scattered into the loss cone at the outer edge of the plasmasphere.

APPENDIX A: PITCH ANGLE EIGENFUNCTIONS

For a given harmonic number l the pitch angle eigenfunctions $Z(\mu)$ satisfy the differential equation (29) and the boundary conditions

$$[dZ/d\mu]_{\mu=\mu_c,\mu_m} = 0 \qquad (57)$$

The normalization equation is

$$\int_{\mu_c}^{\mu_m} Z(\mu)\, d\mu = \frac{p}{\pi a q_l^2(\mu_m - \mu_c)} \qquad (58)$$

where $\mu_c \leq \mu \leq \mu_m$ is the range of resonant interactions in equatorial pitch angles, q_l^2 are the eigenvalues, p is the particle momentum, and a is a distance defined after (2).

First, we study the case $l = 2$. By defining $\hat{q}_l = q_l(\mu_m - \mu_c)^{1/2}$, the solution to (29) is

$$Z(\mu) = \frac{i}{(\mu)^{1/2}} \{A \cos [(\hat{q}_l^2 - \tfrac{1}{4})^{1/2} \ln \mu] + B \sin [(\hat{q}_l^2 - \tfrac{1}{4})^{1/2} \ln \mu]\} \qquad (59)$$

where A and B are arbitrary functions whose ratio is given solving for the normalization condition in (58). Imposing the boundary conditions in (57) yields the eigenvalues of the diffusion operator, which are such that $\hat{q}_l^2 > \frac{1}{4}$ and which are obtained from

$$\sin [(\hat{q}_l^2 - \tfrac{1}{4})^{1/2} \ln (\mu_m/\mu_c)] = 0 \qquad (60)$$

Next, let us study the case $l \neq 2$ (i.e., $l = 1$ and $l > 3$). We define $\alpha = 1 - l/2$, $\beta = (1 - l)/(2 - l)$, and $\delta = 2\hat{q}_l/|2 - l|$. The solutions to (29) are Bessel functions of the first and second kind [*Bespalov et al.*, 1984]:

$$Z(\mu) = A\mu^{\alpha - 1/2} J_\beta(\delta\mu^\alpha) + B\mu^{\alpha - 1/2} Y_\beta(\delta\mu^\alpha) \qquad (61)$$

where A and B are constants which according to (58) have dimensions of momentum divided by length. After imposing the boundary conditions, the eigenvalues of the diffusion operator satisfy the following equation

$$J_{\beta-1}(\delta\mu_c^\alpha) Y_{\beta-1}(\delta\mu_m^\alpha) = Y_{\beta-1}(\delta\mu_c^\alpha) J_{\beta-1}(\delta\mu_m^\alpha) \qquad (62)$$

For the case $l = 1$ we have $\alpha = \frac{1}{2}$, $\beta = 0$, and $\delta = 2\hat{q}_l$. When $l = 3$, $\alpha = -\frac{1}{2}$, $\beta = 2$, and $\delta = 2\hat{q}_l$. We have solved (60) and (62) numerically at $L = 2(\theta_c = 16.3°)$ and $\theta_m = 25°$. We find that the minimum eigenvalues are $4q_1^2 = 5 \times 10^3$, $4q_2^2 = 607.$, and $4q_3^2 = 70$. If we increase θ_m, the eigenvalues decrease; for example, if $\theta_m = 35°$, then $4q_1^2 = 480.$, $4q_2^2 = 81.7$, and $4q_3^2 = 12.5$. The calculations were also done at $L = 4.5\,(\theta_c = 4.5°)$. By taking $\theta_m = 15°$, the minimum eigenvalues are $4q_1^2 = 5.4 \times 10^3$, $4q_2^2 = 127.8$, and $4q_3^2 = 2$. If we increase θ_m to 35°, then $4q_1^2 = 152.$, $4q_2^2 = 10.73$, and $4q_3^2 = 0.31$.

APPENDIX B: THREE MODES COUPLING

For the case of three resonances (l = 1, 2, 3) and no wave source, $\mathcal{S}$ = 0, (51) becomes

$$\beta_1(\xi^2 + 2\nu_1\xi) + \rho_1^2\beta_T = 0 \tag{63}$$

$$\beta_2(\xi^2 + 2\nu_2\xi) + \rho_2^2\beta_T = 0 \tag{64}$$

$$\beta_3(\xi^2 + 2\nu_3\xi) + \rho_3^2\beta_T = 0 \tag{65}$$

where $\beta_T = \beta_1 + \beta_2 + \beta_3$, and equilibrium is given by (42) and (43) after setting l = 1, 2, and 3. This system of equations yields the fourth-order equation for the eigenvalues ξ,

$$\xi^4+\xi^3 2\nu_T+\xi^2[\rho_T^2+4\nu_1(\nu_2+\nu_3)+4\nu_2\nu_3]$$
$$+\xi[2\nu_1(\rho_2^2+\rho_3^2)+2\nu_2(\rho_1^2+\rho_3^2)+2\nu_3(\rho_1^2+\rho_2^2)+8\nu_1\nu_2\nu_3]$$
$$+4\nu_1(\nu_2\rho_3^2+\nu_3\rho_2^2)+4\rho_1^2\nu_2\nu_3=0 \tag{66}$$

where $\nu_T = \nu_1 + \nu_2 + \nu_3$ and $\rho_T^2 = \rho_1^2 + \rho_2^2 + \rho_3^2$. Next we shall find these eigenvalues by assuming that $\nu_l \sim O(\epsilon^l) \ll 1 (\epsilon \to 0$ and l = 1, 2, and 3) and $1 \gg \rho_1^2 \gg \rho_2^2 \gg \rho_3^2$ (where $\rho_l^2 \sim \nu_l$), which are supported by the numerical calculations in section 6. These assumptions will allow us to solve approximately (63)–(65) for the eigenvalues and eigenvectors.

First, consider the solutions $\xi_{1,2}$ driven by the fundamental l = 1 harmonic. Now we have that $\beta_2 < \beta_1$, $\beta_3 < \beta_1$, and $\beta_3 < \beta_2$. From (64) and (65) we get

$$\beta_2/\beta_1 = -\rho_2^2/\xi^2 \sim -\rho_2^2/\rho_1^2$$

$$\beta_3/\beta_1 = -\rho_3^2/\xi^2 \sim -\rho_3^2/\rho_1^2 \tag{67}$$

The eigenvalues derived from (63) are

$$\xi_{1,2} = -\nu_1 \pm i(\rho_1^2 - \nu_1^2)^{1/2} \tag{68}$$

The time it takes to reach equilibrium for the fundamental harmonic is $\tau \sim 1/\nu_1$.

The third eigenmode $\xi_3 \sim O(\epsilon^2)$ is driven by the second harmonic. We must now have $\beta_3 < \beta_1$ and $\beta_1 \sim \beta_2$. From (63) and (65) we get

$$\beta_2/\beta_1 = -1 - (2\nu_1/\rho_1^2)\xi$$

$$\beta_3/\beta_1 = (2\nu_1/\rho_1^2)(\rho_3^2/\xi) \tag{69}$$

By combining these equations with (64), we show

$$\xi_3 = -2[\nu_2 + \rho_2^2(\nu_1/\rho_1^2)] \tag{70}$$

The time it takes to establish equilibrium for the second resonance is $\tau \sim 1/\xi_3$.

The fourth eigenmode $\xi_4 \sim O(\epsilon^3)$ is driven by the third harmonic resonance (l = 3) and is such that $\beta_3 \sim \beta_1$ and $\beta_2 \sim \beta_1$. Equations (63) and (64) become approximately

$$\beta_T/\beta_3 = -(2\nu_1/\rho_1^2)\xi(\beta_1/\beta_3)$$

$$\beta_T/\beta_3 = -(2\nu_2/\rho_2^2)\xi(\beta_2/\beta_3) \tag{71}$$

Then we obtain

$$\beta_1/\beta_2 = (\nu_2/\rho_2^2)(\rho_1^2/\nu_1)$$

$$\beta_1/\beta_3 = \frac{-\rho_1^2/\nu_1}{\rho_1^2/\nu_1 + \rho_2^2/\nu_2} \tag{72}$$

Combining (65), (71), and (72) yields the eigenvalue of the third resonance:

$$\xi_4 = -2\left[\nu_3 + \frac{\rho_3^2}{\rho_1^2/\nu_1 + \rho_2^2/\nu_2}\right] \tag{73}$$

The time it takes to reach equilibrium is proportional to $1/\xi_4$.

The eigenmodes $\xi_{1,2}$ may also be obtained from (66) by taking

$$\xi^4 + \xi^3 2\nu_T + \xi^2\rho_T^2 = 0$$

and recalling that $\rho_T^2 \sim \rho_1^2$ and $\nu_T \sim \nu_1$. To find the eigenvalue ξ_3, we need to consider the terms in ξ^2 and ξ in (66), that is,

$$\xi^2\rho_T^2 + \xi(2\nu_1\rho_2^2 + 2\nu_2\rho_1^2) = 0$$

Finally, the eigenvalue ξ_4 may be obtained from (66) by considering only the terms in first and zero order in ξ:

$$\xi(2\nu_1\rho_2^2 + 2\nu_2\rho_1^2) + 4\nu_1\nu_2\rho_3^2 + 4\nu_1\nu_3\rho_2^2 + 4\nu_2\nu_3\rho_1^2 \sim 0$$

NOTATION

$\mathbf{B}_0$ geomagnetic field.
$\mathbf{B}_l$ equatorial geomagnetic field.
$\mathbf{B}_L$, B_W wave magnetic field.
c speed of light.
E particle's energy.
$\mathcal{E}$ wave electric field
f_l distribution function of resonant electrons.
g_l pitch angle eigenvalues.
$\mathcal{S}$ external wave source.
$\mathbf{k}$ wave vector.
l harmonic number.
L magnetic shell number.
m electron mass.
n_c density of cold electrons.
N_l number of resonant electrons in a flux tube.
p particle's momentum.
q particle's charge.
R_E Earth radius.
$\mathcal{F}_l$ particle flux.
t time.
v particle's velocity.
v_g wave group velocity.
W_k equatorial wave energy.
W equatorial energy density of waves.
z distance along flux tube from magnetic equator
$Z(\mu)$ pitch angle eigenfunctions.
γ relativistic factor.
γ_0 temporal growth rate.
Γ wave spatial amplification factor.
$\zeta = \cos \varphi$.
η refractive index.
θ equatorial pitch angle.
θ_c pitch angle at the loss cone boundary
θ_m maximum pitch angle for which electrons are in resonance.
$\mu = \sin^2 \theta$.

$\mu_e = \sin^2 \theta_e$.
$\mu_m = \sin^2 \theta_m$.
ρ_l, ν_l stability eigenvalues.
σ mirror ratio.
τ normalized time.
τ_B electron bounce time.
τ_g wave group traveling time.
φ angle between wave vector and magnetic field.
ψ magnetic latitude.
ψ_m an upper magnetic latitude limit for resonant interactions.
ω wave frequency.
ω_p plasma frequency.
ω_{LH} lower hybrid frequency.
Ω electron gyrofrequency.
Ω_E equatorial, electron gyrofrequency.
Ω_M maximum gyrofrequency with which electrons are in resonance.

Acknowledgments. This work has been supported by the U.S. Air Force under contract F19628-89-K-0014.

The Editor thanks G. Davidson and L. Lyons for their assistance in evaluating this paper.

REFERENCES

Bell, T. F., The wave magnetic field amplitude threshold for nonlinear trapping of energetic gyroresonant and Landau resonant electrons by nonducted VLF waves in the magnetosphere, *J. Geophys. Res.*, *91*, 4365, 1986.

Bespalov, P. A., and V. Yu. Trakhtengerts, Cyclotron instability of Earth radiation belts, *Rev. Plasma Phys.*, *10*, 88, 1980.

Bespalov, P. A., C. U. Wagner, A. Grafe, and V. Yu. Trakhtengerts, Gap formation in the electron belts, *Geomagn. Aeron.*, *23*, 52, 1984.

Burke, W. J., and E. Villalón, Ionospheric heating for radiation belt control, *AGARD Conf. Proc.*, *485*, 28-1, 1990.

Chappell, C. R., K. K. Harris, and G. W. Sharp, A study of the influence of magnetic activity on the location of the plasmapause as measured by OGO 5, *J. Geophys. Res.*, *75*, 50, 1970.

Gendrin, R., Gyroresonant wave particle interactions, in *Solar Terrestrial Physics*, part III, *Astrophys. Space Sci. Libr.*, vol. 29, edited by E. R. Dyer, p. 236, Kluwer Academic, Boston, Mass., 1972.

Helliwell, R. A., *Whistlers and Related Ionospheric Phenomena*, p. 27, Stanford University Press, Stanford, Calif., 1965.

Huang, L., J. G. Hawkins, and L. C. Lee, On the generation of the pulsating aurora by the loss cone driven whistler instability in the equatorial region, *J. Geophys. Res.*, *95*, 3893, 1990.

Imhof, W. L., H. D. Voss, J. B. Reagan, D. W. Datlowe, E. E. Gaines, J. Mobilia, and D. S. Evans, Relativistic electron and energetic ion precipitations spikes near the plasmapause, *J. Geophys. Res.*, *91*, 3077, 1986.

Inan, U. S., T. F. Bell, and R. A. Heliwell, Nonlinear pitch angle scattering of energetic electrons by coherent ELF waves in the magnetosphere, *J. Geophys. Res.*, *83*, 3235, 1978.

Inan, U. S., W. C. Burgess, T. G. Wolf, D. C. Shater, and R. E. Orville, Lightning associated precipitation of MeV electrons from the inner radiation belt, *Geophys. Res. Lett.*, *15*, 172, 1988.

Kennel, C. F., and F. Engelman, Velocity space diffusion from weak plasma turbulence in a magnetic field, *Phys. Fluids*, *9*, 2377, 1966.

Kennel, C. F., and H. E. Petschek, Limit on stably trapped particle fluxes, *J. Geophys. Res.*, *71*, 1, 1966.

Kimura, I., Effects of ions on whistler mode ray tracing, *Radio Sci.*, *1*, 269, 1966.

Luhmann, J. G., and A. L. Vampola, Effects of localized sources on quiet time plasmasphere electron precipitation, *J. Geophys. Res.*, *82*, 2671, 1977.

Lyons, L. R., and R. M. Thorne, The magnetospheric reflection of whistlers, *Planet. Space Sci.*, *18*, 1753, 1970.

Lyons, L. R., and D. J. Williams, *Quantitative Aspects of Magnetospheric Physics*, D. Reidel, Hingham, Mass., 1984.

Lyons, L. R., R. M. Thorne, and C. F. Kennel, Electron pitch-angle diffusion driven by oblique whistler-mode turbulence, *J. Plasma Phys.*, *6*, 589, 1971.

Lyons, L. R., R. M. Thorne, and C. F. Kennel, Pitch angle diffusion of radiation belt electrons within the plasmasphere, *J. Geophys. Res.*, *77*, 3455, 1972.

Roberts, C. S., Pitch angle diffusion of electrons in the magnetosphere, *Rev. Geophys.*, *7*, 305, 1969.

Rosenberg, T. J., J. C. Sinen, D. L. Matthews, K. Marthinsen, J. A. Holtet, A. Egeland, D. L. Carpenter, and R. A. Helliwell, Conjugate of electron microburst and VLF chorus, *J. Geophys. Res.*, *86*, 5819, 1981.

Sazhin, S. S., Improved quasilinear models of parallel whistler-mode instability, *Planet. Space Sci.*, *37*, 633, 1989.

Schulz, M., and G. T. Davidson, Limiting energy spectrum of a saturated radiation belt, *J. Geophys. Res.*, *93*, 59, 1988.

Schulz, M., and L. J. Lanzerotti, *Particle Diffusion in the Radiation Belts*, Springer-Verlag, New York, 1974.

Spjeldvik, W. N., and P. L. Rothwell, The radiation belts, in *Handbook of Geophysics and the Space Environment*, edited by A. S. Jursa, p. 5-1, National Technical Information Service, Springfield, Va., 1985.

Swift, D. W., Mechanisms for auroral precipitation: A review, *Rev. Geophys.*, *19*, 185, 1981.

Trakhtengerts, V. Yu., Relaxation of a plasma with anisotropic velocity distribution, in *Handbook of Plasma Physics*, vol. 2, *Basic Plasma Physics II*, p. 519, Elsevier Scientific, New York, 1984.

Villalón, E., W. J. Burke, P. L. Rothwell, and M. B. Silevitch, Quasi-linear wave particle interactions in the Earth's radiation belts, *J. Geophys. Res.*, *94*, 15,243, 1989*a*.

Villalón, E., M. B. Silevitch, W. J. Burke, and P. L. Rothwell, Gyroresonant interaction of energetic trapped electrons and protons, in *Physics of Space Plasmas (1989)*, *SPI Conf. Proc. Reprint Ser.*, vol. 9, edited by T. Chang, G. B. Crew, and J. R. Jasperse, p. 365, Scientific, Cambridge, Mass., 1989*b*.

W. J. Burke, Geophysics Laboratory, Hanscom Air Force Base, MA 01731.

E. Villalón, Center for Electromagnetic Research, Northeastern University, Boston, MA 01742.

(Received June 20, 1990;
revised January 17, 1991;
accepted February 4, 1991.)

Proton-Whistler Interactions in the Radiation Belts

Elena Villalón
Center for Electromagnetics Research
Northeastern University
Boston MA 02115
and
William J. Burke
Geophysics Directorate, PL/OL-AA,
Hanscom AFB, MA 01731

ABSTRACT

The interactions of whistlers with radiation belt protons is investigated. In the inhomogeneous geomagnetic field, near the equator, the spacing between cyclotron resonances is very small. After crossing multiple harmonic resonances, a significant change of particle energy takes place, and the protons pitch-angle scatter toward the atmospheric loss cone. A test-particle hamiltonian formalism is investigated for first and second order resonant protons. Quasilinear theory is applied for first-order resonant particles to obtain bounce-averaged, diffusion coefficients. The Fokker Planck equation, containing pitch-angle, energy and the cross energy/ pitch-angle diffusion terms, is investigated to calculate diffusion life times.

I. INTRODUCTION

We consider the interaction of plasmaspheric electrons and protons with whistler waves. The particles are trapped within the earth's radiation belts moving back and forth along field lines between magnetic mirror points. We call τ_B the bounce period, the time required for a particle to go from one mirror point to the other and return. In the region of interest, the geomagnetic field, $\mathbf{B}_o$, is described as a dipole. The interaction region is limited to the plasmasphere, $L < 4$, where L is the equatorial distance of the field line measures in Earth radii (R_E). The plasmashere is made up of cold particles of ionospheric origin

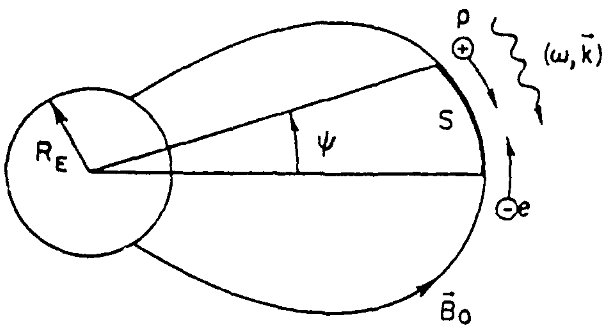

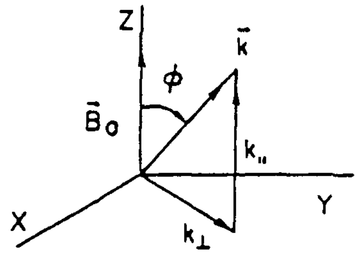

Figure 1. Schematic representation of whistler (ω, k), interacting with electrons and protons near the equator. The coordinate system used in this paper is depicted here.

whose distribution is isotropic and Maxwellian. During magnetic storms the radiation belts fill with energetic, trapped particles whose density is much smaller than that of the cold plasma. Whistlers are right-hand polarized electromagnetic waves whose magnetic field, $|B_k| \ll B_o$. Often they propagate in field-aligned ducts due to density depletions in local flux tubes. They can either be launched from ground sources or be generated in the plasmasphere. The dielectric properties for wave propagation are determined by the magnetized cold plasma distribution. These waves interact with the energetic particles, if the Doppler-shifted frequency of the waves is some harmonic of the gyrofrequency. For electron-whistler interactions the waves and particles travel in opposite directions. For protons they travel in the same direction and the wave phase velocity is very close to the proton parallel velocity. The situation is depicted in the Figure 1.

Whistler-electron interactions has been extensively study over the years [1,2,3]. The electrons typically have energies between 10 to 50 keV. The interaction occurs mainly at the first gyroharmonic of the electron gyrofrequency, although higher gyroharmonics may also be important[4]. The electron energies change very little during these interactions. The electron pitch angle is θ, where $\tan\theta = v_\perp/v_\parallel$, the ratio between the parallel and perpendicular components of the particle velocity. The pitch angle can be significantly changed and, as a result, the particle is scattered into the loss cone and precipitate into the ionosphere. Because large numbers of electrons interact with the waves, they grow in amplitude to values whose limits depend on the degree of anisotropy of the electron distribution function[2]. Detailed analyses are given in the papers by Villalón and coworkers[4,5]. These investigations where based on relativistic, quasilinear theory that simultaneously considers wave growth and particle depletion from the radiation belts.

Proton-whistler interactions have not received as much attention. Recents experiments have shown[6,7] that protons whose energies are in the hundreds of keV range, can be scattered from the radiation belts by analogous interactions. The frequency of the wave must be close to the equatorial electron gyrofrequency. The particle energy changes significantly during the interactions[8]. Thus, the changes in pitch angle is due to both direct pitch angle and energy diffusion. Because of the small population of high-energy protons we neglect their effects on the amplitudes of the waves. We present a study of proton whistler interactions by using a test particle formalism and a statistical approach based on the Fokker-Planck equation. In Sec. II, we present the main dielectric properties of whistler waves; because the whistler protons interactions require large refractive indices, we limit ourselves to the pararesonance mode[9]. Sec. III presents the resonance condition for multiple harmonics of the gyrofrequency. The geomagnetic latitudes of high harmonic resonances are obtained based in a parabolic approximation for the near equatorial geomagnetic field. We show that the distance between subsequence resonances is very small. The crossing of multiple resonances near the equator makes the interactions very effective[10]. Sec IV contains the equations for the test particle in a varying geomagnetic field using hamiltonian formalism. Sec V studies the evolution of the action (I) angle (ξ_ℓ) variables as function of the distance (s) along the flux tube using Taylor expansions around isolated resonances. Let us expand ξ_ℓ around the equator: $\xi_\ell(s) = \xi_\ell(0) + \xi_\ell^{(1)}s + \xi_\ell^{(2)}s^2$. First-order resonant particles are such that $\xi_\ell^{(1)} = 0$ (i. e., at the equator $d\xi_\ell/ds = 0$). This is the resonance condition as given in Eq. (5). The second-order term $\xi_\ell^{(2)} \sim dB_o/ds + O(B_k)$.

For large wave amplitudes $O(B_k)$ is larger than the contribution of the inhomogeneous geomagnetic field dB_o/ds. In this case, we say that protons which are in gyroresonance (i. e. $\xi_\ell^{(1)} = 0$), satisfy the second-order resonance condition. This is because to zero order in the electric field amplitudes $d\xi_\ell/ds = d^2\xi_\ell/ds^2 \simeq 0$. For first-order resonant particles, the change in action is proportional to the electric field amplitude. For second-order resonant protons the change in action is proportional to the square root of the electric field amplitude. The second-order resonance condition is met when the field amplitude is large[11,12], the threshold is calculated in this paper. Sec. VI contains a quasilinear formulation for the distribution function of first order resonant protons. We assume that the protons are unmagnetized in time scales of the order of $2\pi/\omega$, where ω is the frequency of the whistler wave. They are magnetized in times comparable to the bounce period. Because diffusion occurs over many bounce periods, we average the diffusion equation along the flux tube. The bounce averaged, Fokker-Planck equation contains the diffusion coefficients for the pitch angle, energy, and the cross energy/ pitch angle terms. These coefficients are shown to have the same orders of magnitude. We reduce the equation to a one-dimensional diffusion equation to be solved for the energy part of the distribution function. This eigenvalue equation gives the diffusion life-times of protons in the radiation belts.

II. QUASI-ELECTROSTATIC WHISTLER WAVES

We consider a whistler wave of frequency ω and wave vector $\mathbf{k}$, propagating in a field aligned duct. The geomagnetic field $\mathbf{B_o}$ is along the z direction and ϕ is the angle between $\mathbf{k}$ and $\mathbf{B_o}$. The dispersion relation for the refractve index $\eta = ck/\omega$ is

$$\eta^2 = 1 + \frac{(\omega_p/\omega)^2}{(\Omega_e/\omega)\,|\cos\phi| - 1} \tag{1}$$

where ω_p and Ω_e are the electron plasma and gyro frequencies, respectively.

The electric fields components are denoted by $\mathcal{E}_x = \mathcal{E}_1$, $\mathcal{E}_y = i\mathcal{E}_2$, and $\mathcal{E}_z = -\mathcal{E}_3$, where

$$\frac{\mathcal{E}_2}{\mathcal{E}_1} = \frac{1}{\eta^2 - 1}\;\frac{(\omega_p/\omega)^2}{(\Omega_e/\omega) - |\cos\phi|} \tag{2}$$

$$\frac{\mathcal{E}_1}{\mathcal{E}_3} = \frac{1 - (\omega_p/\omega)^2 - (\eta\,\sin\phi)^2}{\eta^2\,\sin\phi\,\cos\phi} \tag{3}$$

For the case where $\omega \sim \Omega_e(L)|\cos\phi|$, the equatorial refractive index $\eta^2(L) \gg 1$, then $\mathcal{E}_2/\mathcal{E}_1 \ll 1$, and $\mathcal{E}_1/\mathcal{E}_3 \sim -\sin\phi/\cos\phi$. The wave becomes quasi-electrostatic, i.e. E is in the direction of $\mathbf{k}$, and the group velocities $v_g \sim 1/\eta$ are very small. These waves can interact with protons which energies are in the hundreds of keV.

Near the equator, the Earth's magnetic field approximates a parabolic profile

$$\frac{\Omega}{\Omega(L)} = 1 + (\frac{s}{r_L})^2 \tag{4}$$

where $s \simeq R_E L\psi$, R_E is the Earth's radius, L is the magnetic shell and ψ is the geomagnetic latitude (see the figure), and $r_L = (\sqrt{2}/3)R_E L$. The equatorial gyrofrequency is $\Omega(L)$; Ω stands for the gyrofrequencies either for electrons or protons, along the field line.

III. RESONANT PROTON-WHISTLER INTERACTIONS

For whistler waves to interact strongly with protons near equatorial regions, they must satisfy the resonance condition

$$\omega - k_{\|}v_{\|} - \ell\Omega_p = 0 \tag{5}$$

where, $\ell = 0, 1, 2...$; Ω_p is the proton gyrofrequency, and $k_{\|}$ and $v_{\|}$ are the parallel components of the wave vector and particle's velocity, respectively. We call $\mu = \sin^2\theta_L$, where θ_L is the equatorial pitch angle. Here $\theta_L > \theta_c(L)$, where $\theta_c(L)$ is the pitch angle at the boundary of the loss cone, and μ_c the corresponding value of μ. As function of the L shell, the mirror ratio is $\sigma = 1/\mu_c = L^3(4-3/L)^{1/2}$. To zero order in electric field amplitudes, the first adiabatic invariant is conserved. Then we may write for the parallel and perpendicular components of the particle velocity v: $v_{\|} = v[1 - \mu\Omega/\Omega(L)]^{1/2}$, $v_{\perp} = v[\mu\Omega/\Omega(L)]^{1/2}$.

If we assume that at the equator the protons interact with the harmonic $\ell = 1$, the energy of resonant particles is found solving for the equation: $\omega - k_{\|}\, v_{\|} - \Omega_p(L) = 0$. We show

$$\frac{v}{c} = \frac{1}{\eta(L)\,\cos\phi}\,\frac{1}{(1-\mu)^{1/2}}\,(1 - \frac{m_e}{m_p}\,f_e) \tag{6}$$

where L denotes equatorial values, $m_{e,p}$ are the electron, proton masses, and $f_e = \Omega_e(L)/\omega$.

By solving for Eq. (5), using the parabolic profile in Eq. (4) , we find the geomagnetic latitude ψ_ℓ of higher order resonances (i.e., $\ell \geq 1$),

$$\psi_\ell^2 = \frac{4}{9}\,\frac{m_e}{m_p}\,(\ell - 1)\,(f_e\,|\cos\phi| - 1)\,\frac{1}{g(\mu)} \tag{7}$$

where

$$g(\mu) = \frac{\mu}{1-\mu}\left(|\cos\phi| - \frac{1}{f_e}\right) + |\cos\phi|. \tag{8}$$

The distance along the flux tube where resonant interactions take place is given by, $s_\ell = R_E L \psi_\ell$. The distance between sequential resonances is $\Delta s_\ell = R_E L(\psi_{\ell+1} - \psi_\ell)$.

For example, we take $L = 3.5$, $\omega_p/\Omega_e(L) = 7.9$, $\omega/\Omega_e(L) = 0.75$, and $\theta_L = 10°$. For $\phi = 37°$, we show that $\eta(L) = 41.4$ and the energy of the resonant protons is 437 keV. The location along the geomagnetic field of the gyroresonances are: $\psi_2 = 0.25°, \psi_3 = 0.35°, ..., \psi_{17} = 1.°$. As another example we take $\phi = 40°$, then $\eta(L) = 72$ and the proton energy is 158.6 keV. The location of the gyroresonances are: $\psi_2 = 0.15°, \psi_3 = 0.21°, ..., \psi_{47} = 1.°$. Thus there are multiple resonances crossings (17 for the first and 47 for the second examples) within one degree of the magnetic equator, which makes the proton whistler interactions very efficient.

IV. THE HAMILTONIAN EQUATIONS

We normalize time t to $\Omega_p(L)$, velocity v to c^{-1}, and length s to r_L^{-1}, and from now on we always refer to these normalized variables. Let us define

$$\xi_\ell = \ell\lambda + \int_0^s ds'\, r_L\, k_\parallel(s') - \frac{\omega}{\Omega_p(L)}\, t \tag{9}$$

where $\tan\lambda = v_y/v_x$, and $v_{x,y}$ are the components of the particle velocity in the x and y directions, respectively. The dimensionless electric field amplitudes are

$$\varepsilon_i = \frac{q\mathcal{E}_i}{m_p c\omega} \tag{10}$$

for $i = 1, 2, 3$, and where q is the proton charge. The action-angle variables are (I, λ), where

$$I = \frac{v_\perp^2}{2}\,\frac{\Omega_p(L)}{\Omega_p} \tag{11}$$

To first order in the electric field amplitudes ε_i, the normalize, time-dependent hamiltonian, as function of the canonical pairs, $(v_\parallel, s)$, and action-angle variables, is

$$\mathcal{H} = \frac{v_\parallel^2}{2} + I\,\frac{\Omega}{\Omega(L)} + \sum_{\ell=-\infty}^{\infty} \sin\xi_\ell \left\{\varepsilon_3\, v_\parallel\, J_\ell(k_\perp\rho) - \left[\frac{I\Omega}{2\Omega(L)}\right]^{1/2}\Gamma_\ell\right\} \tag{12}$$

Here

$$\Gamma_\ell = (\varepsilon_1 - \varepsilon_2)\, J_{\ell+1}(k_\perp\rho) + (\varepsilon_1 + \varepsilon_2)\, J_{\ell-1}(k_\perp\rho) \tag{13}$$

where J_ℓ are Bessel functions whose arguments are $k_\perp \rho = (ck_\perp/\Omega_p)\,[2I\Omega/\Omega(L)]^{1/2}$. If, in addition to the electromagnetic wave, there is an electrostatic potential ϕ_o, then we replace in Eq. (12), ϵ_3 by $\epsilon_3 + \epsilon_o/v_\parallel$, where $\epsilon_o = q\phi_o/m_p c^2$.

For particles crossing a single isolated cyclotron resonance, we consider only one term ℓ in the summation in Eq. (12). In this case, we find the following constant of motion

$$C_\ell = \ell \mathcal{H} - \frac{\omega}{\Omega_p(L)}\, I \tag{14}$$

By calling $\chi = (\omega/\Omega_p)\,\sin^2\theta(s)$, where $\theta(s)$ is the local pitch angle, we find

$$\chi = \frac{\ell\omega}{\Omega_p(L)}\;\frac{I}{C_\ell + [\omega/\Omega_p(L)]\, I} \tag{15}$$

This defines the evolution of the pitch angle as a function of the action I.

By defining v_o so that $\mathcal{H} = v_o^2/2 + I\Omega/\Omega(L)$, we obtain

$$v_o = \left\{\frac{2}{\ell}\,[C_\ell + I\,(\frac{\omega}{\Omega_p(L)} - \ell\frac{\Omega}{\Omega(L)})]\right\}^{1/2} \tag{16}$$

We can now reduce the problem to one-dimension, in which case we find

$$\begin{aligned} v_\parallel &= v_o + \sin\xi_\ell \left\{-\epsilon_3\, J_\ell(k_\perp\rho) + \frac{1}{v_o}\,[\frac{I\Omega}{2\Omega(L)}]^{1/2}\,\Gamma_\ell\right\} \\ \frac{ds}{dt} &= v_o + \frac{1}{v_o}\,[\frac{I\Omega}{2\Omega(L)}]^{1/2}\,\Gamma_\ell\,\sin\xi_\ell \end{aligned} \tag{17}$$

To zero order in ϵ_i, the dimensionless length $s = t\, v_o$. The equation of motion for I as a function of s is

$$\frac{dI}{ds} = \ell\cos\xi_\ell\,\Upsilon_\ell(I, v_o) \tag{18}$$

$$\Upsilon_\ell(I, v_o) = -\epsilon_3\, J_\ell(k_\perp\rho) + \frac{1}{v_o}\,[\frac{I\Omega}{2\Omega(L)}]^{1/2}\,\Gamma_\ell \tag{19}$$

As $\epsilon_i \rightarrow 0$, then

$$\frac{d\xi_\ell}{ds} \rightarrow k_\parallel r_L + \frac{\ell\Omega_p - \omega}{\Omega_p(L) v_o} \tag{20}$$

The gyroresonance condition is obtained by setting Eq. (20) equal to zero. When this is satisfied $s = s_\ell$ (the resonance length) which is defined as $s_\ell = 3/\sqrt{2}\,\psi_\ell$ and ψ_ℓ is given in Eq. (7).

By assuming that the protons are in gyroresonance, we show that ξ_ℓ satisfies the second order differential equation

$$\frac{d^2\xi_\ell}{ds^2} = \alpha_\ell + \frac{(k_\parallel r_L)^2}{v_o}\,\frac{1}{\ell}\,\frac{dI}{ds} \tag{21}$$

The change in χ after crossing a resonance is

$$\Delta\chi = \chi(R)\left[\frac{1}{I(R)} - \frac{1/f_p}{C_\ell + I(R)/f_p}\right]\left(\frac{dI}{ds}\right)_{(R)}\,\delta s_\ell \tag{30}$$

where $\chi(R)$ is given by Eq. (15) setting $I = I(R)$.

The resonance length δs_ℓ is defined as

$$\delta s_\ell = \int_{-\infty}^{+\infty} ds \cos\xi_\ell \tag{31}$$

By combining Eqs. (26), (28), and integrating along s we show

$$\delta s_\ell = \Gamma(1/2)\,\cos(\pi/4)\left[\frac{2}{|\xi_\ell^{(2)}|}\right]^{1/2} \tag{32}$$

The condition of isolated resonances is $\delta s_\ell < \Delta s_\ell$, where $\Delta s_\ell = 3/\sqrt{2}\,(\psi_{\ell+1} - \psi_\ell)$ and ψ_ℓ is given in Eq. (7).

In the case where the inhomogeneity of the magnetic field is larger than the contribution of the resonance, we may neglect the term proportional to $(dI/ds)_{(R)}$ in Eq. (28), we get

$$\Delta I = \left(\frac{dI}{ds}\right)_{(R)}\Gamma(1/2)\,\cos(\pi/4)\left[\left|\frac{1}{\beta_\ell(R)\,s_\ell}\right|\right]^{1/2} \tag{33}$$

where $\beta_\ell(R)$ is given by Eq. (23) and must be evaluated at resonance. From the definition of Γ_ℓ in Eq. (13), the change in the action is proportional to the electric field amplitudes.

For interactions such that the contribution of $\alpha_\ell(R)$ in Eq. (28) is smaller than the contribution of $(dI/ds)_R$, we get

$$\Delta I = \pm\left[\left|\ell\left(\frac{dI}{ds}\right)_{(R)}\right|\right]^{1/2}\Gamma(1/2)\,\frac{[2|v_o(R)|]^{1/2}}{k_\parallel r_L}\cos(\pi/4) \tag{34}$$

where the $\pm$ sign depends on the sign of $(dI/ds)_R$. We see that the change in particle momentum I is now proportional to the square root of the electric field amplitudes, i.e. $\sqrt{\varepsilon_i}$. We call this the second order resonance condition because to zero order in the electric field amplitudes $d^2\xi_\ell/ds^2 \simeq 0$. For the case of equatorial interactions ($s_\ell = 0$), the condition for the validity of this approximation is

$$\left[\frac{k_\parallel r_L}{\sqrt{2v_o}}\left(\frac{1}{\ell}\left|\left(\frac{dI}{ds}\right)_{(R)}\right|\right)^{1/2}\right]^3 \gg \beta_\ell(R)\,\Gamma(1/2)\,\cos\pi/4 \tag{35}$$

Note that for a fix value of ω the second order resonance condition is most likely satisfied for equatorial interactions, because then the inhomogeneity of the magnetic field is small.

Thus the first harmonic will dominate the second-order interactions. If we allow ω to be a function of s, then

$$\alpha_\ell = \beta_\ell \frac{1}{\Omega(L)} \frac{d\Omega}{ds} + r_L \frac{dk_\parallel}{d\omega} \frac{d\omega}{ds} \tag{36}$$

By changing ω so that $\alpha_\ell(R) = 0$ for $s_\ell > 0$, the second-order resonance condition is satisfied for other harmonics, and the change in the particle velocity is proportional to $\sqrt{\epsilon_i}$. This should be contrasted with the result in Eq. (33) where the change in action is linear with the electric fields and thus smaller than when the condition for second order resonance is satisfied.

VI. QUASILINEAR THEORY

The distribution function of protons which satisfy the first order resonance condition is given by solving for the quasilinear equation Lyons and Williams (1984):

$$\left(\frac{1}{\tau_{atm}} + \frac{\partial}{\partial t}\right) f = \pi q^2 \sum_{\ell=-\infty}^{+\infty} \int \frac{d^3\mathrm{k}}{(2\pi)^3} \left[\hat{G} + \frac{\omega - k_\parallel v_\parallel}{\omega p_\perp}\right] \delta(k_\parallel v_\parallel - \ell\Omega_p - \omega)\, \Theta_\ell(\mathrm{k})\, \hat{G}\, f \tag{37}$$

where p is momentum and τ_{atm}, the atmospheric loss time is defined in[1]. By assuming that $\omega/\Omega p \ll \sin^2\theta_c$ (where θ_c is the local pitch angle at the loss cone boundary) we may approximate

$$\hat{G} = -\frac{2}{p} \frac{\Omega_e(L)}{\Omega_e} \left(\frac{p_\perp}{p}\right)^3 \frac{\partial}{\partial\mu} + \frac{p_\perp}{p} \frac{\partial}{\partial p} \tag{38}$$

$$\hat{G} + \frac{\omega - k_\parallel v_\parallel}{\omega p_\perp} = \frac{1}{p^2} \frac{\partial}{\partial p} p^2 \sin\theta - \frac{2}{p} \frac{\Omega_e(L)}{\Omega_e} \frac{p_\parallel}{p} \frac{\partial}{\partial\mu} \left(\frac{p_\perp}{p}\right)^3 \frac{p}{p_\parallel} \tag{39}$$

$$\sum_{\ell=-\infty}^{+\infty} \delta(k_\parallel v_\parallel + \ell\Omega_p - \omega)\, \Theta_\ell(\mathrm{k}) \simeq (2\pi)^3\, \delta(k_\parallel v_\parallel - \omega) \frac{\omega\Omega_e}{\omega_p^2} \frac{W_k(\phi, t)}{|\cos\phi|} b(\phi) \tag{40}$$

where

$$b(\phi) = 1 + \cos^2\phi + \frac{1}{2}\left|\frac{p_\parallel}{p_\perp} \frac{\omega}{\Omega_e} \sin\phi\right|^2 \tag{41}$$

If B_k is the wave magnetic field ($B_k \ll B_o$, the geomagnetic field), then the energy density of waves is

$$W_k(\phi, t) = \frac{1}{8\pi} \left(\frac{B_k}{2\pi}\right)^2 \tag{42}$$

We assume that diffusion occurs on time scales such $t \gg \tau_B$, where τ_B is the proton bounce time between ionospheric conjugates. We integrate the diffusion equation along the flux tube by applying the operator $1/\tau_B \int dz/v_\parallel$ to both sides of Eq. (37). The bounce-averaged diffusion equation, in terms of equatorial pitch-angles θ_L and particle momentum, is

$$\left(\frac{1}{\tau_{atm}} + \frac{\partial}{\partial t}\right) f = \frac{1}{p \sin\theta_L \cos\theta_L} \frac{\partial}{\partial \theta_L} \sin\theta_L \cos\theta_L \left[D_{\theta,\theta} \frac{1}{p} \frac{\partial f}{\partial \theta_L} + D_{\theta,p} \frac{\partial f}{\partial p} \right] + \frac{1}{p^2} \frac{\partial}{\partial p} \left\{ p \left[p\, D_{p,p} \frac{\partial f}{\partial p} + D_{p,\theta} \frac{\partial f}{\partial \theta_L} \right] \right\} \tag{43}$$

The bounce-averaged diffusion coefficients are

$$D_{\theta,\theta} = \tan^2\theta_L \; D_{p,p} \tag{44}$$

$$D_{\theta,p} = D_{p,\theta} = -\tan\theta_L \; D_{p,p} \tag{45}$$

The energy-diffusion coefficient is

$$D_{p,p} = \frac{\pi q^2}{v \tau_B} \int_0^\infty k^2\, dk \int_{-\pi/2}^{+\pi/2} \sin\phi\, \Lambda(k,\phi)\, d\phi \tag{46}$$

where

$$\Lambda(k,\phi) = \frac{4\pi \Omega_e(L)^3}{\omega_p^2} \frac{W_k(\phi,t)}{|\cos\phi|} \left(\frac{ds}{d\Omega}\right)_{(R)} \left[\frac{\Omega(R)}{\Omega(L)}\right]^2 \frac{p_\parallel}{p}\, b(\phi) \tag{47}$$

Here R denotes values at the resonance where $v_\parallel \sim v$, and $\omega - k_\parallel v \simeq 0$. Note that for small values of ϕ, we can neglect the contribution of the parallel component of the wave field in $b(\phi)$ (see Eq. (41)), then $D_{p,p}$ is approximately independent of μ, the equatorial pitch angle, and we write

$$f = F(t)\, \mu^\sigma\, K(p) \tag{48}$$

where $\sigma > 0$ is a free parameter. We define the precipitation lifetime as

$$\tau_p = -\left[\frac{1}{F} \frac{dF}{dt}\right]^{-1} \tag{49}$$

By combining Eqs. (43) through (45) and Eq. (48), we show

$$\left[\frac{2\kappa_c}{\tau_B} - \frac{1}{\tau_p}\right] K(p) = \frac{4\sigma(\sigma+1)}{p^2} D_{p,p} K + \frac{d}{dp}\left[D_{p,p} \frac{dK}{dp}\right] - \frac{4\sigma}{p} D_{p,p} \frac{dK}{dp} - \frac{2\sigma}{p^2} K \frac{d}{dp}\left[p\, D_{p,p}\right] \tag{50}$$

where $\kappa_c = \mu_c^{(\sigma+1)}$. This is an eigenvalue equation for τ_p as a function of the free parameter σ. The eigenfunction $K(p)$ is such that must be regular as $p \to 0$, and well behaved for large p, i. e. as $p \to \infty$ then $K \ll p^{-2}$.

VII. SUMMARY AND CONCLUSIONS

We have presented a theoretical analysis of proton-whistler interactions near the equator in the plasmasphere. Whistler waves which are near the pararesonance mode[9], can interact with protons whose energies are in the hundreds of keV. In an inhomogeneous geomagnetic field, we show that the spacing between subsequence cyclotron resonances is very small. Because of that, protons are scattered into the atmospheric loss cone after crossing multiple resonances. A test-particle hamiltonian formalism is given in terms of the action (I), angle (ξ_l), variables as function of the distance (s) along the flux tube. We show that for second-order resonant protons, $d\xi_l/ds = d^2\xi_l/ds^2 = 0$, and the change in the particle's momentum is proportional to the square root of the electric field amplitudes. The thresholds in electric fields for second-order resonance conditions are calculated. A quasi-linear formulation for the distribution function of first-order resonant protons is presented. The bounce-averaged diffusion equation contains diffusion coefficients for the pitch angle, energy, and cross energy/ pitch angle terms. They are shown to be of the same orders of magnitude. We reduce the diffussion equation to a one-dimensional energy dependent equation to be solved for the precipitation life times of protons in the Radiation Belts.

Acknowledgements. This work has been supported in part by the U. S. Air Force contract F19628-89-K-0014 with Northeastern University.

VIII. REFERENCES

1. L. R. Lyons and D. J. Williams, Quantitative Aspects of Magnetospheric Physics, D. Reidel Publising Company, The Netherlands, 1984.

2. C. F. Kennel and H. E. Petschek, J. Geophys. Res., 1966, 71, 1.

3. P. A. Bespalov and V. Yu. Trakhtengerts, Rev. Plasma Phys., 1980, 10, 88.

4. E. Villalón and W. J. Burke, J. Geophys. Res., 1991, 96, 9655.

5. E. Villalón, W. J. Burke, P. L. Rothwell, M. B. Silevitch, J. Geophys. Res., 1989, 94, 15243.

6. H. C. Koons, Geophys. Res. Lett., 1975, 2, 281.

7. R. A. Kovrazhkin, M. M. Mogilevskii, O. A. Molchanov, Yu. I. Gal'perin, N. V. Dzhordzhio, Zh. M. Bosbe, and A. Rem, JETP Lett., 1984, 39, 228.

8. R. Gendrin, J. Atmospheric Terrest. Phys., 1968, 30, 1313.

9. M. G. Morgan, J. Geophys. Res., 1980, 85, 130.

10. D. R. Shklyar, Planet. Space Phys., 1986, 34, 1091.

11. R. A. Helliwell, J. Geophys. Res., 1967, 72, 4773.

12. K. B. Dysthe, J. Geophys. Res., 1971, 76, 6915.

WHISTLER INTERACTIONS WITH ENERGETIC PROTONS

Elena Villalón
Center for Electromagnetics Research,
Northeastern University, Boston MA 02115

William J. Burke
Geophysics Directorate, PL/OL-AA, Hanscom AFB, MA 01731

ABSTRACT

Whistler waves, near the electrostatic limit, can interact with trapped, energetic protons close to the equator in the Earth's Radiation Belts. In an inhomogeneous geomagnetic field, the spacing between cyclotron resonances is very small due to large ion Larmor radii. After crossing multiple resonances, the pitch angles change significantly and the protons are scattered toward the atmospheric loss cone. A test-particle, Hamiltonian formalism is investigated. For second-order resonant protons, the change in particle momentum is proportional to the square root of the wave electric field amplitudes. The thresholds in electric fields for second-order resonance conditions are calculated. Quasilinear theory is studied to describe the distribution functions and calculate the diffusion life times of first-order resonant protons. The diffusion coefficients for the energy, pitch angle, and the cross energy/ pitch angle terms are shown to be of the same orders of magnitude.

I. INTRODUCTION

Interactions between whistler waves and energetic electrons in the magnetosphere have been the subject of intensive research during the past two decades [1 – 3]. The wave-electron, resonant interactions are believed to account for many phenomena such as growth of signals [2], emissions of varying frequencies [4] and electron precipitation into the ionosphere [5]. Most of the theoretical work is based on resonant interactions at the first harmonic of the electron gyrofrequency, although higher harmonics interactions may also be important [1]. Detailed theoretical analyses taking into account wave growth and particle depletion, is given in the papers by Villalón and coworkers (see Refs. [6, 7] and references therein).

The interactions of plasmaspheric protons and whistler waves have not received as much attention. This is because the energies required are very large and the population of protons with energies larger than 500 keV, is small. Since the proton gyrofrequency Ω_p, is much lower than the wave frequency ω, the resonant velocity $v_{||}$ is of the order of the wave phase velocity $\omega/k_{||}$

(where $k_{\|}$ is the parallel component of the wave vector). However recent experiments [8, 9] have demonstrated that *protons precipitate* by interactions with VLF waves launched into the magnetosphere from ground sources. The wave frequencies are close to the equatorial electron gyrofrequency. Thus, near the equator, $k_{\|}$ is very large and the resonant energies of protons relatively low. We limit our studies to regions near the magnetic equator of the plasmasphere $L < 4$ (where L is the equatorial crossing distance of the field line measured in Earth radii R_E).

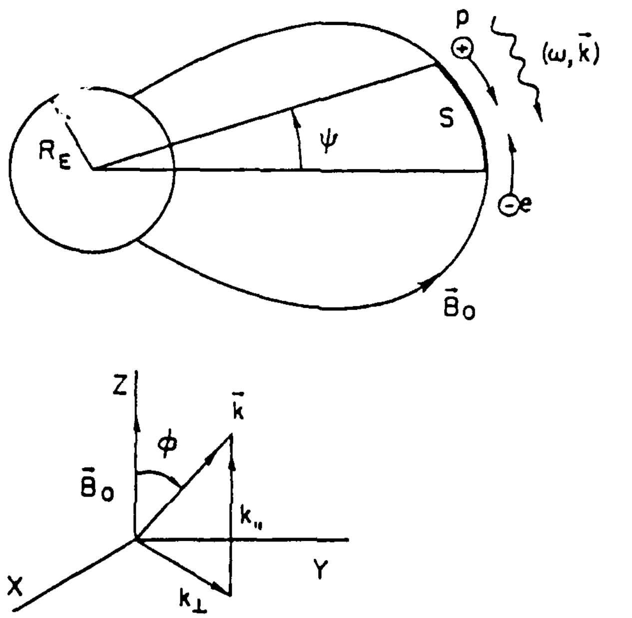

Figure 1. Schematic representation of whistler (ω, k), interacting with electrons and protons near the equator. The coordinate system used in this paper is depicted here.

The plasmasphere contains a relatively dense population of cold particles of ionospheric origin whose distribution function is isotropic in pitch angle. The energetic particles originate from stationary sources (convective transfer accross L shells) and pulsed sources (sudden impulses during magnetic storms and substorms). They are trapped within the radiation belts traveling back and forth along field lines between magnetic mirror points, and interacting with the quasi-electrostatic whistler waves near the magnetic equator. The predominant feature of the resonant interactions is the crossing of multiple harmonics of the proton gyrofrequency. The proton pitch angle is θ, where $\tan\theta = v_\perp/v_\parallel$ (the ratio between the perpendicular and parallel components of the velocity). The pitch angles can change due to direct pitch-angle scattering or to energy diffusion [10]. This should be contrasted with the analogous whistler-electron interactions, where the predominant harmonic is the first. Also, electron energies do not change during the interactions. For proton-whistler interactions, the waves and particles travel in the same direction, with the waves slightly overtaking the protons. For electron-whistler interactions the waves and particles travel in opposite directions. The situation is depicted in the Figure 1.

The paper is organized as follows: Sec. II describes the propagation of whistler waves in a cold plasma, near the electrostatic limit [11]. Sec. III studies the resonance conditions for multiple harmonics of the proton gyrofrequency. The inhomogeneous, near-equatorial geomagnetic field is described by a parabolic profile. Due to the large ion Larmor radii, we show that the distance between resonances is very small. Because of the inclusion of multiple harmonics, these interactions are very effective [12]. The test-particle Hamiltonian formalism for each isolated cyclotron resonance, is given in Sec. IV. Sec V studies the evolution of the action (I) and angle (ξ_ℓ) variables as function of the distance (s) along the flux tube using Taylor expansions around isolated resonance points. Let us expand ξ_ℓ around the equator: $\xi_\ell(s) = \xi_\ell(0) + \xi_\ell^{(1)}\, s + 1/2\, \xi_\ell^{(2)}\, s^2$. First-order resonant particles are such that $\xi_\ell^{(1)} = 0$. That is, at the equator $d\xi_\ell/ds = 0$, which is the resonance condition as given in Eq. (5). The second-order term $\xi_\ell^{(2)} \sim dB_o/ds + O(B_k)$. For large wave amplitudes $O(B_k)$ is larger than the contribution of the inhomogeneous geomagnetic field dB_o/ds. In this case, we say that protons which are in gyroresonance (i. e. $\xi_\ell^{(1)} = 0$), satisfy the second-order resonance condition. This is because to zero order in the electric field amplitude. $d\xi_\ell/ds = d^2\xi_\ell/ds^2 \simeq 0$. For first-order resonant particles, the change in action is proportional to the electric field amplitude. For second-order resonant protons, the change in action is proportional to the square root of the electric field amplitude. The second-order resonance condition is met when the field amplitude is large [13, 14]. The thresholds in electric fields, are then calculated. Sec. VI contains a quasilinear formulation for the distribution function of first order resonant protons. We assume that the protons are unmagnetized in time scales of the order of $2\pi/\omega$, where ω is the frequency of the whistler wave. They are however magnetized in times comparable to the bounce period. Because diffusion occurs over many bounce periods, we average the diffusion equation along the flux tube. The bounce averaged, Fokker-Planck equation contains the diffusion coefficients for the pitch angle, energy, and the cross energy/ pitch angle terms. These coefficients are shown to have the same orders of magnitude. We reduce the equation to a one-dimensional diffusion equation to be solved for the energy part of the distribution function. This eigenvalue equation estimates the VLF diffusion life times of protons in the radiation belts.

II. QUASI-ELECTROSTATIC WHISTLER WAVES

We consider a whistler wave of frequency ω and wave vector $\mathbf{k}$, propagating in a field-aligned duct. The geomagnetic field $\mathbf{B_o}$ is along the z direction and ϕ is the angle between k and $\mathbf{B_o}$. The dispersion relation for the refractve index $\eta = ck/\omega$ is

$$\eta^2 = 1 + \frac{(\omega_p/\omega)^2}{(\Omega_e/\omega)\,|\cos\phi| - 1} \tag{1}$$

where ω_p and Ω_e are the electron plasma and gyro frequencies, respectively.

The electric field is [15]

$$\mathbf{E} = \hat{\mathbf{x}}\,\mathcal{E}_1\,\cos\Psi - \hat{\mathbf{y}}\,\mathcal{E}_2\,\sin\Psi - \hat{\mathbf{z}}\,\mathcal{E}_3\,\cos\Psi \tag{2}$$

where $\hat{\mathbf{x}}, \hat{\mathbf{y}}$ and $\hat{\mathbf{z}}$ are unit vectors; $\Psi = k_\perp\,x + k_\parallel\,z - \omega\,t$, and $k_\parallel, k_\perp$ are the components along and perpendicular to $\mathbf{B_o}$ of the wave vector. The ratios of electric field components are

$$\frac{\mathcal{E}_2}{\mathcal{E}_1} = \frac{1}{\eta^2 - 1}\,\frac{(\omega_p/\omega)^2}{(\Omega_e/\omega) - |\cos\phi|} \tag{3}$$

$$\frac{\mathcal{E}_1}{\mathcal{E}_3} = \frac{1 - (\omega_p/\omega)^2 - (\eta\,\sin\phi)^2}{\eta^2\,\sin\phi\,\cos\phi} \tag{4}$$

For the case where $\omega \sim \Omega_e(L)|\cos\phi|$, the equatorial refractive index $\eta^2(L) \gg 1$, then $\mathcal{E}_2/\mathcal{E}_1 \ll 1$, and $\mathcal{E}_1/\mathcal{E}_3 \sim -\sin\phi/\cos\phi$. The wave becomes quasi-electrostatic,*i.e.* $\mathbf{E}$ has a significant component in the direction of $\mathbf{k}$, and the group velocity $v_g \sim 1/\eta$. This wave can interact with protons which energies are in the hundreds of keV.

Near the equator, the Earth's magnetic field may be approximated as having a parabolic profile

$$\frac{\Omega}{\Omega(L)} = 1 + (\frac{s}{r_L})^2 \tag{5}$$

where $s \simeq R_E L\psi$ and ψ is the geomagnetic latitude (see the figure), and $r_L = (\sqrt{2}/3)R_E L$. The equatorial gyrofrequency is denoted by $\Omega(L)$, and Ω stands for the gyrofrequencies either for electrons or protons at a location s away from the equator along the field line.

III. RESONANCE PROTON WHISTLER INTERACTIONS

For whistler waves to interact strongly with protons near equatorial regions, they must satisfy the resonance condition

$$\omega - k_{\parallel} v_{\parallel} - \ell \Omega_p = 0 \tag{6}$$

where, $\ell = 0, 1, 2...$; Ω_p is the proton gyrofrequency, and $v_{\parallel}$ is the parallel component of the particle's velocity. We call $\mu = \sin^2 \theta_L$, where θ_L is the equatorial pitch angle. Here $\theta_L > \theta_c(L)$, where $\theta_c(L)$ is the pitch angle at the boundary of the loss cone, and μ_c the corresponding value of μ. As function of the L shell, the mirror ratio is $\sigma = 1/\mu_c = L^3 (4 - 3/L)^{1/2}$. To zero order in electric field amplitudes, the first adiabatic invariant is conserved. Then we may write for the parallel and perpendicular components of the particle velocity v: $v_{\parallel} = v[1 - \mu\Omega/\Omega(L)]^{1/2}$, $v_{\perp} = v[\mu\Omega/\Omega(L)]^{1/2}$.

At the equator the protons interact with the harmonic $\ell = 0$, and then the energy of resonant particles is found solving for the equation: $\omega - k_{\parallel} v_{\parallel} = 0$. We show

$$\frac{v}{c} = \frac{1}{\eta(L) \cos\phi} \frac{1}{(1-\mu)^{1/2}} \tag{7}$$

where $\eta(L)$ denotes equatorial values of the refractive index, and $f_e = \Omega_e(L)/\omega$.

By solving for Eq. (6), using the parabolic profile in Eq. (5) , we find the geomagnetic latitude ψ_ℓ of higher order resonances (i.e., $\ell \geq 0$),

$$\psi_\ell^2 = \frac{4}{9} \frac{m_e}{m_p} \ell \left(f_e \, |\cos\phi| - 1\right) \frac{1}{g(\mu)} \tag{8}$$

where

$$g(\mu) = \frac{\mu}{1-\mu} \left(|\cos\phi| - \frac{1}{f_e}\right) + |\cos\phi|. \tag{9}$$

where $m_{e,p}$ are the electron, proton masses. The distance along the flux tube where resonant interactions take place is given by, $s_\ell = R_E L \psi_\ell$. The distance between two subsequent resonances is obtained from $\Delta s_\ell = R_E L(\psi_{\ell+1} - \psi_\ell)$.

For example, we take $L = 3.5$, $\omega_p/\Omega_e(L) = 7.9$, $\omega/\Omega_e(L) = 0.75$, and $\theta_L = 10°$. For $\phi = 37°$, we find that $\eta(L) = 41.4$ and the energy of the resonant protons is 437 keV. The location along the geomagnetic field of the gyroresonances are: $\psi_2 = 0.25°, \psi_3 = 0.35°, ..., \psi_{17} = 1.°$. As another example we take $\phi = 40°$, then $\eta(L) = 72$ and the proton energy is 158.6 keV. The location of the gyroresonances are: $\psi_2 = 0.15°, \psi_3 = 0.21°, ..., \psi_{47} = 1.°$. We also show that ψ_ℓ is very weakly dependent upon pitch angle μ. Thus there are multiple resonances crossings (17 for the first and 47 for the second examples) within one degree of the magnetic equator, which makes the proton whistler interactions very efficient.

IV. THE HAMILTONIAN EQUATIONS

We normalize time t to $\Omega_p(L)$, velocity v to c^{-1}, and length s to r_L^{-1}, and from now on we always refer to these normalized variables. Let us define

$$\xi_\ell = \ell\lambda + \int_0^s ds' \, r_L \, k_\parallel(s') - \frac{\omega}{\Omega_p(L)} t \tag{10}$$

where $\tan\lambda = v_y/v_x$, and $v_{x,y}$ are the components of the particle velocity in the x and y directions, respectively. The dimensionless electric field amplitudes are

$$\varepsilon_i = \frac{q\mathcal{E}_i}{m_p c\omega} \tag{11}$$

for $i = 1, 2, 3$, and where q is the proton charge. The action-angle variables are (I, λ), where

$$I = \frac{v_\perp^2}{2} \frac{\Omega_p(L)}{\Omega_p} \tag{12}$$

To first order in the electric field amplitudes ε_i, the normalize, time-dependent hamiltonian, as function of the canonical pairs, $(v_\parallel, s)$, and action-angle variables, is

$$\mathcal{H} = \frac{v_\parallel^2}{2} + I\frac{\Omega}{\Omega(L)} + \sum_{\ell=-\infty}^{\infty} \sin\xi_\ell \left\{ \varepsilon_3 \, v_\parallel \, \mathcal{J}_\ell(k_\perp\rho) - [\frac{I\Omega}{2\Omega(L)}]^{1/2} \, \Gamma_\ell \right\} \tag{13}$$

Here Γ_ℓ is a linear combination of Bessel functions $\mathcal{J}_\ell$,

$$\Gamma_\ell = (\varepsilon_1 - \varepsilon_2)\, \mathcal{J}_{\ell+1}(k_\perp\rho) + (\varepsilon_1 + \varepsilon_2)\, \mathcal{J}_{\ell-1}(k_\perp\rho) \tag{14}$$

whose arguments are $k_\perp\,\rho = (ck_\perp/\Omega_p)\,[2I\Omega/\Omega(L)]^{1/2}$. If, in addition to the electromagnetic wave, there is an electrostatic potential ϕ_o, then we replace in Eq. (13), ε_3 by $\varepsilon_3 + \varepsilon_o/v_\parallel$, where $\varepsilon_o = q\phi_o/m_p c^2$.

For particles crossing a single isolated cyclotron resonance, we consider only one term ℓ in the summation in Eq. (13). In this case, we find the following constant of motion

$$C_\ell = \ell\mathcal{H} - \frac{\omega}{\Omega_p(L)} I \tag{15}$$

The criterion for overlapping of resonances is given later on in Eq. (37).

By defining v_o so that $\mathcal{H} = v_o^2/2 + I\Omega/\Omega(L)$, we obtain

$$v_o = \left\{ \frac{2}{\ell} \, [C_\ell + I\,(\frac{\omega}{\Omega_p(L)} - \ell\frac{\Omega}{\Omega(L)})] \right\}^{1/2} \tag{16}$$

We can now reduce the problem to one-dimension, in which case we find

$$
\begin{aligned}
v_{\parallel} &= v_o + \sin\xi_\ell \, \Upsilon_\ell(I, v_o) \\
\frac{ds}{dt} &= v_o + \frac{1}{v_o}\,[\frac{I\Omega}{2\Omega(L)}]^{1/2}\,\Gamma_\ell \, \sin\xi_\ell
\end{aligned}
\tag{17}
$$

where $\Upsilon_\ell(I, v_o)$ is defined in Eq. (19).

To zero order in ε_i, the dimensionless length $s = t\,v_o$. The equation of motion for I as a function of s is

$$\frac{dI}{ds} = \ell \, \cos\xi_\ell \, \Upsilon_\ell(I, v_o) \tag{18}$$

$$\Upsilon_\ell(I, v_o) = -\varepsilon_3 \, \mathcal{J}_\ell(k_\perp \rho) + \frac{1}{v_o}\,[\frac{I\Omega}{2\Omega(L)}]^{1/2}\,\Gamma_\ell \tag{19}$$

As $\varepsilon_i \to 0$, then

$$\frac{d\xi_\ell}{ds} \to k_{\parallel} r_L + \frac{\ell\Omega_p - \omega}{\Omega_p(L) v_o} \tag{20}$$

The gyroresonance condition is obtained by setting Eq. (20) equal to zero. When this is satisfied $s = s_\ell$ (the resonance length) which is defined as $s_\ell = 3/\sqrt{2}\,\psi_\ell$ and ψ_ℓ is given in Eq. (8).

By assuming that the protons are in gyroresonance, we show that ξ_ℓ satisfies the second order differential equation

$$\frac{d^2\xi_\ell}{ds^2} = \alpha_\ell + \frac{(k_{\parallel} r_L)^2}{v_o}\,\frac{1}{\ell}\,\frac{dI}{ds} \tag{21}$$

Here

$$\alpha_\ell = \frac{\beta_\ell}{\Omega(L)}\,\frac{d\Omega}{ds} \tag{22}$$

$$\beta_\ell = \Omega_p(L)\, r_L \,\frac{m_p}{m_e}\,\frac{dk_{\parallel}}{d\Omega_e} + \frac{1}{v_o}\,[\frac{\ell}{2} + \frac{C_\ell}{v_o^2}] \tag{23}$$

where $d\Omega/ds = 2s\,\Omega(L)$.

V. SECOND ORDER RESONANCE

We next solve the pair of coupled Eqs. (18) and (21) under the assumption that s is very close to the resonance length s_ℓ. The parallel velocity v_o is given by setting Eq. (20) equal to zero, *i.e.*

$$v_o(R) = \frac{\omega}{ck_{\parallel}}\,\frac{c}{\Omega_p(L)\, r_L}\,(1 - \ell\,\frac{\Omega_p}{\omega}) \tag{24}$$

In this case we may use a Taylor expansion around s_ℓ, then

$$I \simeq I_\ell(R) + (\frac{dI}{ds})_{(R)}\ (s - s_\ell) \tag{25}$$

$$\xi_\ell \simeq \xi_\ell(R) + \xi_\ell^{(1)}\,(s - s_\ell) + \frac{\xi_\ell^{(2)}}{2}\,(s - s_\ell)^2 \tag{26}$$

where $I_\ell(R), \xi_\ell(R)$ are constants, and R denotes values at the resonance ($s = s_\ell$). Here $(dI/ds)_{(R)}$ is given by Eqs. (18) and (19), with $\xi_\ell = \xi_\ell(R), I = I(R)$, and $v_o = v_o(R)$, evaluated for resonant values. For protons satisfying the resonance condition, $\xi_\ell^{(1)} = 0$. For convenience we choose $\cos[\xi_\ell(R)] = 1$.

The constant of motion C_ℓ is obtained evaluating Eq. (15) at the equator, we show

$$C_\ell = \left(\frac{1}{\sqrt{2}\,\eta(L)\,\cos\phi}\,\frac{c}{\Omega_p(L)\,r_L}\right)^2 \frac{1}{1-\mu}\,[\frac{-\mu}{f_p} + \ell] \tag{27}$$

where $f_p = \Omega_p(L)/\omega \ll 1$. Using Eq. (16) and setting $v_o = v_o(R)$, we find

$$I_\ell(R) = \frac{f_p}{[1 - \ell f_p\,\Omega(R)/\Omega(L)]}\ \left\{-C_\ell + \frac{\ell}{2}\,v_o^2(R)\right\} \tag{28}$$

where $\Omega(R)/\Omega(L) = 1 + s_\ell^2$. By substituting Eq. (26) into Eq. (21) we show

$$\xi_\ell^{(2)} = \alpha_\ell(R) + \frac{(k_\| r_L)^2}{v_o(R)}\ \frac{1}{\ell}\ (\frac{dI}{ds})_{(R)} \tag{29}$$

where $\alpha_\ell(R)$ is evaluated at the resonance.

The change of the action I after crossing the ℓ'th resonance, ΔI, obtained by integrating Eq. (18), is approximately

$$\Delta I = (\frac{dI}{ds})_{(R)}\ \delta s_\ell \tag{30}$$

The resonance length δs_ℓ is defined as

$$\delta s_\ell = \int_{-\infty}^{+\infty} ds \cos\xi_\ell \tag{31}$$

By combining Eqs. (26), (29), and integrating along s we show

$$\delta s_\ell = \Gamma(1/2)\ \cos(\pi/4)\ \left[\frac{2}{|\xi_\ell^{(2)}|}\right]^{1/2} \tag{32}$$

Resonances are isolated in space if $\delta s_\ell < \Delta s_\ell$, where $\Delta s_\ell = 3/\sqrt{2}\,(\psi_{\ell+1} - \psi_\ell)$ and ψ_ℓ is given in Eq. (8).

In the case where the inhomogeneity of the magnetic field is larger than the contribution of the resonance, we may neglect the term proportional to $(dI/ds)_{(R)}$ in Eq. (29), we get

$$\Delta I = (\frac{dI}{ds})_{(R)}\ \Gamma(1/2)\ \cos(\pi/4)\ \left[|\frac{1}{\beta_\ell(R)\, s_\ell}|\right]^{1/2} \tag{33}$$

where $\beta_\ell(R)$ is given by Eq. (23) and must be evaluated at resonance. From the definition of Γ_ℓ in Eq. (14), the change in the action is proportional to the electric field amplitudes.

For interactions such that the contribution of $\alpha_\ell(R)$ in Eq. (29) is smaller than the contribution of $(dI/ds)_R$, we get

$$\Delta I = \pm\left[|\ell\,(\frac{dI}{ds})_{(R)}|\right]^{1/2}\ \Gamma(1/2)\ \frac{[2|v_o(R)|]^{1/2}}{k_\| r_L}\ \cos(\pi/4) \tag{34}$$

where the $\pm$ sign depends on the sign of $(dI/ds)_R$. We see that the change in particle momentum I is now proportional to the square root of the electric field amplitudes, i.e. $\sqrt{\epsilon_i}$. We call this the second order resonance condition because to zero order in the electric field amplitudes $d^2\xi_\ell/ds^2 \simeq 0$. For the case of equatorial interactions ($s_\ell = 0$), the condition for the validity of this approximation is

$$\left[\frac{k_\| r_L}{\sqrt{2 v_o}}\left(\frac{1}{\ell}\,|(\frac{dI}{ds})_{(R)}|\right)^{1/2}\right]^3 \gg \beta_\ell(R)\,\Gamma(1/2)\ \cos\pi/4 \tag{35}$$

Note that for a fix value of ω the second order resonance condition is most likely satisfied for equatorial interactions, because then the inhomogeneity of the magnetic field is small. Thus the first harmonic will dominate the second-order interactions. If we allow ω to be a function of s, then

$$\alpha_\ell = \beta_\ell\,\frac{1}{\Omega(L)}\,\frac{d\Omega}{ds} + r_L\,\frac{dk_\|}{d\omega}\,\frac{d\omega}{ds} \tag{36}$$

By changing ω so that $\alpha_\ell(R) = 0$ for $s_\ell > 0$, the second-order resonance condition is satisfied for other harmonics, and the change in the particle velocity is proportional to $\sqrt{\epsilon_i}$. This should be contrasted with the result in Eq. (33) where the change in action is linear with the electric fields and thus smaller than when the condition for second order resonance is satisfied.

We have carried out some preliminary calculations applying the theory presented in this section; for waves such that $0.5 \le \omega/\Omega_\ell \le 1$, and $\cos\phi \ge \omega/\Omega_\ell$, and for electric field amplitudes which are in the range 10^{-6} to 10^{-4} Volt/cm. They show the contribution of large harmonic resonances, *i.e.* $\ell \ge 50$ in the change of the action ΔI as defined in Eq. (30). As a matter of fact of fact the largest contributions to ΔI come from values of ℓ which are close to the argument of the Bessel functions $k_\perp \rho$. For equatorial pitch angles between 7.5 and 20 degrees, at the L shell 3.5, the values of ℓ which give maximum change in the action are larger than 50 and smaller than 150. Overlapping of resonances occur when

$$\frac{\Delta I}{I_{\ell-1}(R) - I_\ell(R)} \geq 1 \tag{37}$$

For electric fields greater than 10^{-4} Volt/cm all resonances ($150 \geq \ell \geq 1$) overlap, but for smaller electric fields only some of them do for particles which equatorial pitch angles are near the loss cone. Note that even if resonances overlap in space (see comments after Eq. (32)), we must still treat them as independent of each other if the criterion in Eq. (37) is not met.

VI. QUASILINEAR THEORY

The distribution function of protons which satisfy the first order resonance condition is given by solving for the quasilinear equation Lyons and Williams (1984):

$$\left(\frac{1}{\tau_{atm}} + \frac{\partial}{\partial t}\right) f = \pi q^2 \sum_{\ell=-\infty}^{+\infty} \int \frac{d^3\mathrm{k}}{(2\pi)^3} \left[\hat{G} + \frac{\omega - k_\parallel v_\parallel}{\omega p_\perp}\right] \delta(k_\parallel v_\parallel - \ell\Omega_p - \omega)\, \Theta_\ell(\mathrm{k})\, \hat{G} f \tag{38}$$

where p is momentum and τ_{atm}, the atmospheric loss time is defined in [1]. By assuming that $\omega/\Omega p \ll \sin^2\theta_c$ (where θ_c is the local pitch angle at the loss cone boundary) we may approximate

$$\hat{G} + \frac{\omega - k_\parallel v_\parallel}{\omega p_\perp} = \frac{1}{p^2}\frac{\partial}{\partial p} p^2 \sin\theta - \frac{2}{p}\frac{\Omega_e(L)}{\Omega_e}\frac{p_\parallel}{p}\frac{\partial}{\partial \mu}\left(\frac{p_\perp}{p}\right)^3 \frac{p}{p_\parallel} \tag{39}$$

$$\hat{G} = -\frac{2}{p}\frac{\Omega_e(L)}{\Omega_e}\left(\frac{p_\perp}{p}\right)^3 \frac{\partial}{\partial \mu} + \frac{p_\perp}{p}\frac{\partial}{\partial p} \tag{40}$$

$$\sum_{\ell=-\infty}^{+\infty} \delta(k_\parallel v_\parallel + \ell\Omega_p - \omega)\,\Theta_\ell(\mathrm{k}) \simeq (2\pi)^3\, \delta(k_\parallel v_\parallel - \omega)\,\frac{\omega\Omega_e}{\omega_p^2}\,\frac{W_k(\phi,t)}{|\cos\phi|}\, b(\phi) \tag{41}$$

where

$$b(\phi) = 1 + \cos^2\phi + \frac{1}{2}\left[\frac{p_\parallel}{p_\perp}\frac{\omega}{\Omega_e}\sin\phi\right]^2 \tag{42}$$

If B_k is the wave magnetic field ($B_k \ll B_o$, the geomagnetic field), then the energy density of waves is

$$W_k(\phi,t) = \frac{1}{8\pi}\left(\frac{B_k}{2\pi}\right)^2 \tag{43}$$

We assume that diffusion occurs on time scales such $t \gg \tau_B$, where τ_B is the proton bounce time between ionospheric conjugates. We integrate the diffusion equation along the flux tube by applying the operator $1/\tau_B \int dz/v_{\|}$ to both sides of Eq. (38). The bounce-averaged diffusion equation, in terms of equatorial pitch-angles θ_L and particle momentum, is

$$\begin{aligned}(\frac{1}{\tau_{atm}} + \frac{\partial}{\partial t}) f &= \frac{1}{p \sin\theta_L \cos\theta_L} \frac{\partial}{\partial \theta_L} \sin\theta_L \cos\theta_L \\ & \left[\mathcal{D}_{\theta,\theta} \frac{1}{p} \frac{\partial f}{\partial \theta_L} + \mathcal{D}_{\theta,p} \frac{\partial f}{\partial p}\right] + \\ & \frac{1}{p^2} \frac{\partial}{\partial p} \left\{ p \left[p\, \mathcal{D}_{p,p} \frac{\partial f}{\partial p} + \mathcal{D}_{p,\theta} \frac{\partial f}{\partial \theta_L}\right]\right\} \end{aligned} \tag{44}$$

The bounce-averaged diffusion coefficients are

$$\mathcal{D}_{\theta,\theta} = \tan^2\theta_L\ \mathcal{D}_{p,p} \tag{45}$$

$$\mathcal{D}_{\theta,p} = \mathcal{D}_{p,\theta} = -\tan\theta_L\ \mathcal{D}_{p,p} \tag{46}$$

The energy-diffusion coefficient is

$$\mathcal{D}_{p,p} = \frac{\pi q^2}{v \tau_B} \int_0^\infty k^2\, dk \int_{-\pi/2}^{+\pi/2} \sin\phi\, \Lambda(k,\phi)\, d\phi \tag{47}$$

where

$$\Lambda(k,\phi) = \frac{4\pi \Omega_e(L)^3}{\omega_p^2} \frac{W_k(\phi,t)}{|\cos\phi|} \left(\frac{ds}{d\Omega}\right)_{(R)} \left[\frac{\Omega(R)}{\Omega(L)}\right]^2 \frac{p_{\|}}{p}\, b(\phi) \tag{48}$$

Here R denotes values at the resonance where $v_{\|} \sim v$, and $\omega - k_{\|} v \simeq 0$. Note that for small values of ϕ, we can neglect the contribution of the parallel component of the wave field in $b(\phi)$ (see Eq. (42)), then $\mathcal{D}_{p,p}$ is approximately independent of μ, the equatorial pitch angle, and we write

$$f = F(t)\, \mu^\sigma\, K(p) \tag{49}$$

where $\sigma > 0$ is a free parameter. We define the precipitation lifetime as

$$\tau_p = -\left[\frac{1}{F} \frac{dF}{dt}\right]^{-1} \tag{50}$$

By combining Eqs. (44) through (46) and Eq. (49), we show

$$\begin{aligned}\left[\frac{2\kappa_c}{\tau_B} - \frac{1}{\tau_p}\right] K(p) &= \frac{4\sigma(\sigma+1)}{p^2} \mathcal{D}_{p,p} K + \frac{d}{dp}\left[\mathcal{D}_{p,p} \frac{dK}{dp}\right] - \\ & \frac{4\sigma}{p} \mathcal{D}_{p,p} \frac{dK}{dp} - \frac{2\sigma}{p^2} K \frac{d}{dp}[p\, \mathcal{D}_{p,p}] \end{aligned} \tag{51}$$

where $\kappa_c = \mu_c^{(\sigma+1)}$. This is an eigenvalue equation for τ_p as a function of the free parameter σ. The eigenfunction $K(p)$ is such that must be regular as $p \to 0$, and well behaved for large p, *i. e.* as $p \to \infty$ then $K \ll p^{-2}$.

ACKNOWLEDGEMENTS

We are grateful to J. M. Albert and J. U. Kozyra for helpful conversations. This work has been supported in part by the U. S. Air Force contract F19628-89-K-0014 with Northeastern University.

REFERENCES

[1] L. R. Lyons and D. J. Williams, *Quantitative Aspects of Magnetospheric Physics* (D. Reidel Publising Company, The Netherlands, (1984).
[2] C. F. Kennel and H. E. Petschek, J. Geophys. Res. **71**, 1 (1966).
[3] P. A. Bespalov and V. Yu. Trakhtengerts, Rev. Plasma Phys. **10**, 88 (1980).
[4] R. A. Helliwell, J. Geophys. Res. **72**, 4773 (1967).
[5] W.L. Imhof, H.D. Voss, J.B. Reagan, D.W. Datlowe, E.E. Gaines, J. Mobilia and D.S. Evans, J. Geophys. Res. **91**, 3077 (1986).
[6] E. Villalón, W. J. Burke, P. L. Rothwell, M. B. Silevitch, J. Geophys. Res. **94**, 152 (1989).
[7] E. Villalón and W. J. Burke, J. Geophys. Res. **96**, 9655 (1991).
[8] H. C. Koons, Geophys. Res. Lett. **2**, 281 (1975).
[9] R. A. Kovrazhkin, M. M. Mogilevskii, O. A. Molchanov, Yu. I. Gal'perin, N. V. Dzhordzhio, Zh. M. Bosbe, and A. Rem, JETP Lett. **39**, 228 (1984).
[10] R. Gendrin, J. Atmospheric Terrest. Phys. **30**, 1313 (1968).
[11] M. G. Morgan, J. Geophys. Res., **85**, 130 (1980).
[12] D. R. Shklyar, Planet. Space Phys. **34**, 1091 (1986).
[13] K. B. Dysthe, J. Geophys. Res. **76**, 6915 (1971).
[14] D. Nunn, Planet. Space Sci. **19**, 1141 (1971).
[15] E. Villalón and W. J. Burke, Phys. Fluids, **30**, 3695 (1987).

Test particle motion in the cyclotron resonance regime

Gregory P. Ginet and Jay M. Albert
Geophysics Directorate, Phillips Laboratory, Hanscom Air Force Base, Massachusetts 01731

(Received 20 March 1991; accepted 12 July 1991)

Test particles moving in the field of an electromagnetic wave propagating in a background magnetic field can gain significant energy when the wave parameters and particle energy are such that the cyclotron resonance condition is satisfied. Central to the acceleration process and long time scale periodic behavior is the coherent accumulation over many cyclotron orbits of a small change in energy during each orbit, a result of the circularly polarized component of the wave electric field. Also important is the small change in the relative wave phase during each orbit resulting from relativistic variations of the cyclotron frequency and wave-induced streaming along the background magnetic field. The physical mechanisms underlying cyclotron resonance acceleration are explored using a set of heuristic mapping equations (the PMAP) describing changes in the particle momentum and relative wave phase. More accurate (but less transparent) descriptions of the particle motion are pursued in the context of orbit-averaged Hamiltonian theory. A discrete set of mapping equations for the slowly varying canonical action and angle are derived (the QMAP) but are found to generate inaccurate solutions in certain regions of phase space when the resonance number l is such that $|l| \sim 1$ and the particles are initially cold. These difficulties are avoided by constructing a continuous time orbit-averaged Hamiltonian and solving the resultant canonical equations of motion. Assuming the momentum is small relative to mc (where m is the particle mass and c is the speed of light), details of the distribution of particle trajectories in the action-angle phase space for $|l| = 1$ and $|l| = 2$ are presented and criteria for the existence of orbits oscillatory in angle are derived.

I. INTRODUCTION

When constructing a kinetic–theoretic description of the interaction between an electromagnetic wave and a magnetized plasma, it is important to know the trajectory of test particles in the presence of the electromagnetic wave and background magnetic field. A particularly interesting regime of wave–test particle interaction occurs when the wave frequency ω and the particle momentum satisfy the cyclotron resonance condition,

$$\omega - k_z v_z - |l|\Omega \simeq 0, \tag{1}$$

where Ω is the cyclotron frequency, l is the resonance number, and k_z and v_z are the wave vector and particle velocity, respectively, in the direction of the background magnetic field $\mathbf{B}_0 = B_0\mathbf{e}_z$. In the cyclotron resonance regime, it is possible for test particles to achieve kinetic energies far in excess of the "quiver energy" on time scales of many wave periods, even for relatively small wave amplitudes.[1-7] We define the quiver energy as the maximum energy achieved by a test particle in an electromagnetic wave without a background magnetic field.

In the work of Ginet and Heinemann[8] (hereafter Paper I), a Hamiltonian pseudopotential (HPP) theory was developed and used to predict the maximum kinetic energy U_{max} (normalized to the rest mass energy) and acceleration time τ_p (normalized to the wave period) resulting from the cyclotron resonance acceleration process in the limit of small wave amplitude. Although the HPP theory proves to be a useful predictive tool, as demonstrated by the extensive comparison of HPP predictions with those obtained from numerical solutions of the full equations of motion given in Paper I, there are limitations. The HPP theory does not predict any details of the particle trajectory other than the temporal dependence of the kinetic energy and does not provide much physical insight into how the acceleration process actually works.

This paper addresses the details of the cyclotron resonance interaction process that are not covered by the HPP theory. As in Paper I, we restrict ourselves to the regime of small wave amplitude so that particles are not trapped in the troughs of a wave and chaotic motion resulting from overlapping resonances does not occur. In Sec. II, we discuss the physical mechanism underlying the acceleration process in the context of a set of pedagogical mapping equations that describes the change in particle momentum and wave phase from one cyclotron orbit to the next. More accurate (but less transparent) methods for computing details of the cyclotron orbit-averaged particle trajectory based on Hamiltonian theory are presented in Sec. III. At the end of Sec. III, we study in some detail the distribution of particle trajectories in phase space when the momentum is small $(|\mathbf{p}|/(mc) \ll 1)$. A summary of the entire paper is contained in Sec. IV.

II. THE PHYSICAL MECHANISM

To better understand the physical mechanism responsible for the resonance acceleration process, we develop in this section a mapping of particle momentum and phase from one cyclotron orbit to another. The pedagogical map (PMAP) will be derived from the equations of motion by using estimates of the particle trajectory that are characteristic of the true trajectory yet simple enough to allow us to piece together the details of the acceleration mechanism. Focusing on the small momentum regime, a reduced version of the PMAP will be obtained that depends only on the perpendicular momentum and relative wave phase. This reduced map will then guide our extended discussion of the acceleration mechanism. For notational convenience, we assume a negatively charged particle in our discussion, though all of the analysis applies equally well to positively charged particles given appropriate sign changes in the trajectory and wave polarizations.

A. Derivation of the pedagogical map

The equations of motion for the momentum $\mathbf{p}$ and position $\mathbf{x}$ of a particle of charge q and mass m in a Cartesian coordinate system (x,y,z) can be written as

$$\frac{d\mathbf{p}}{dt} = q\left(\mathbf{E}_w + \frac{\mathbf{v}}{c}\times(\mathbf{B}_0 + \mathbf{B}_w)\right), \tag{2}$$

$$\frac{d\mathbf{x}}{dt} = \mathbf{v}, \tag{3}$$

where $\mathbf{p} = \gamma m\mathbf{v}$, $\gamma = \sqrt{1 + |\mathbf{p}|^2/(mc)^2}$, and $\mathbf{B}_0$ is the background magnetic field $\mathbf{B}_0 = B_0\mathbf{e}_z$. The plane wave electric and magnetic fields are taken to be

$$\mathbf{E}_w = E_1\cos(\mathbf{k}\cdot\mathbf{x} - \omega t)\mathbf{e}_x - E_2\sin(\mathbf{k}\cdot\mathbf{x} - \omega t)\mathbf{e}_y + E_3\cos(\mathbf{k}\cdot\mathbf{x} - \omega t)\mathbf{e}_z, \tag{4}$$

$$\mathbf{B}_w = B_1\sin(\mathbf{k}\cdot\mathbf{x} - \omega t)\mathbf{e}_x + B_2\cos(\mathbf{k}\cdot\mathbf{x} - \omega t)\mathbf{e}_y - B_3\sin(\mathbf{k}\cdot\mathbf{x} - \omega t)\mathbf{e}_z, \tag{5}$$

where ω is the wave frequency and $\mathbf{k} = k_x\mathbf{e}_x + k_z\mathbf{e}_z$ is the wave vector in a coordinate system where $k_y = 0$ with no loss of generality. The sign convention has been chosen so that if all the wave components are positive then the wave is right-hand circularly polarized. Using the plane wave solution to Faraday's law,

$$\mathbf{B}_w = (c/\omega)\mathbf{k}\times\mathbf{E}_w, \tag{6}$$

the components of the wave magnetic field can be written in terms of the components of the wave electric field,

$$B_1 = \eta_z E_2, \tag{7}$$

$$B_2 = \eta_x E_3 + \eta_z E_1, \tag{8}$$

$$B_3 = \eta_x E_2, \tag{9}$$

where $\eta_x = ck_x/\omega$, $\eta_z = ck_z/\omega$, and the index of refraction η is defined as $\eta = c|\mathbf{k}|/\omega$.

The wave electric field amplitudes can be expressed as dimensionless quantities ϵ_i, where

$$\epsilon_i = |q|E_i/mc\omega, \quad i = 1,2,3,\ldots . \tag{10}$$

The assumption that $\epsilon \ll 1$, where $\epsilon = \max(\epsilon_1,\epsilon_2,\epsilon_3)$, defines the small wave amplitude approximation. In this limit, the quiver energy is proportional to ϵ^2 (cf. Appendix A of Paper I).

Numerical solutions of the full equations of motion in the small wave amplitude limit show that the particle motion in the plane perpendicular to $\mathbf{B}_0$ can be viewed as cyclotron motion with a slowly varying cyclotron radius ρ and perpendicular momentum $p_\perp = \sqrt{p_x^2 + p_y^2}$ (e.g., Fig. 2 of Paper I). Thus we are motivated to model the system as a sequence of discrete cyclotron orbits in the perpendicular plane with streaming parallel to the field (i.e., v_z is a constant) during each orbit. The dynamics can then be reduced to a map that gives the momentum and position of the particle at a particular phase of the cyclotron orbit in terms of the momentum and position exactly one orbit earlier. We outline the derivation of this pedagogical map (PMAP) below.

Assume that a particle undergoes cyclotron motion in the perpendicular plane and streaming motion parallel to $\mathbf{B}_0$ with a constant perpendicular and parallel momentum $(p_{\perp n}, p_{zn})$ between times t_n and $t_{n+1} = t_n + 2\pi/\Omega_n$, $n = 0,1,2,\ldots$. For $t_n < t < t_{n+1}$, the orbits for a negatively charged particle can be written as

$$\mathbf{p}_\perp = p_{\perp n}\{\sin[\Omega_n(t - t_n)]\mathbf{e}_x - \cos[\Omega_n(t - t_n)]\mathbf{e}_y\}, \tag{11}$$

$$p_z = p_{zn}, \tag{12}$$

$$x = -\rho_n\cos[\Omega(t - t_n)], \tag{13}$$

$$y = Y - \rho_n\sin[\Omega(t - t_n)], \tag{14}$$

$$z = z_n + v_{zn}(t - t_n), \tag{15}$$

where $\rho_n = v_{\perp n}/\Omega_n$, $v_{\perp n} = p_{\perp n}/(\gamma_n m)$, $v_{zn} = p_{zn}/(\gamma_n m)$, and the relativistic cyclotron frequency is defined as

$$\Omega_n = |q|B_0/\gamma_n mc = \omega_c/\gamma_n, \tag{16}$$

with ω_c the nonrelativistic cyclotron frequency. In Fig. 1, these orbits are plotted in various slices of $(\mathbf{x},\mathbf{p})$ phase space. Since the guiding center in x is a constant of the motion (Paper I), we have set it equal to zero without any loss of generality. We have also arbitrarily set the y guiding center Y equal to zero for illustrative purposes in Fig. 1. The value of Y, although not constant, is irrelevant since there is no y dependence in the problem.

At time t_{n+1}, the particle momentum, z position, and cyclotron radius are jumped (Fig. 1) by an amount that can be computed by integrating the equations of motion between t_n and t_{n+1}, assuming that the wave field is small enough that the particle motion can be reasonably approximated by a cyclotron orbit with streaming parallel to the background field. The z position variable can be replaced by the relative wave phase variable ψ, which we define to be

$$\psi = k_z z - \omega t. \tag{17}$$

Noting that the jump in the x position can be computed from the jump in $p_\perp$ using the definition of the cyclotron radius ρ, the equations of motion necessary to compute the jump values can be reduced to three,

$$\frac{dp_\perp}{dt'} = \frac{|q|}{2}\sum_{m=-\infty}^{\infty}\cos\left((m\Omega_n + \omega - k_z v_{zn})t' + \frac{m\pi}{2} - \psi_n\right)$$
$$\times\left[\left(E_1 + E_2 - \frac{v_{zn}}{c}(B_1 + B_2)\right)J_{m+1}(k_x\rho_n) + \left(E_1 - E_2 - \frac{v_{zn}}{c}(B_2 - B_1)\right)J_{m-1}(k_x\rho_n)\right]. \tag{18}$$

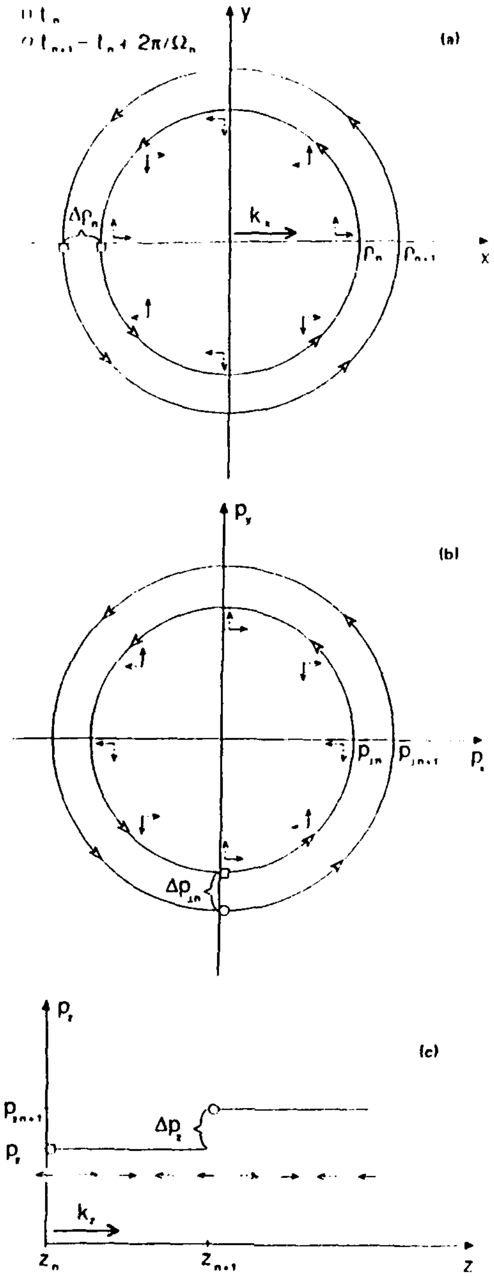

FIG. 1. Phase space trajectories in (a) the x-y plane, (b) the p_x-p_y plane, and (c) the z-p_z plane, which are used for computing the PMAP. The particle begins at t_n (labeled with a box), completes one orbit, and then is jumped as indicated to begin another orbit at t_{n+1} (labeled with a circle). Also shown in (a) and (b) are the components of the corotating wave electric field (solid arrows) and magnetic field (dotted arrows) at various points in the orbit for a wave with $\omega = 2\omega_c$, $\psi_n (\mathrm{mod}\ 2\pi) = 0$, and $|E_x| = |B_x|$. Orientations of the parallel wave electric field (solid arrow) and magnetic field (dashed arrow) at points along the trajectory are shown in (c). Bold face arrows correspond to components of the wave vector k.

$$\frac{dp_z}{dt'} = \frac{|q|}{2} \sum_{m=-\infty}^{\infty} \cos\left((m\Omega_n + \omega - k_z v_{zn}) t' + \frac{m\pi}{2} - \psi_n \right)$$

$$\times \left(2E_z J_m(k_\perp \rho_n) + \frac{v_{\perp n}}{c} [(B_1 + B_2) J_{m+1}(k_\perp \rho_n)$$

$$- (B_2 - B_1) J_{m-1}(k_\perp \rho_n)] \right), \tag{19}$$

$$\frac{d\psi}{dt'} = k_z v_{zn} - \omega, \tag{20}$$

where $t' = t - t_n$ and J_m represents a Bessel function of integer order m. These modified equations have been derived from the Cartesian equations of motion [Eqs. (2) and (3)] using the definition of $p_\perp$, the explicit form for the wave fields [Eqs. (4) and (5)], and the approximate trajectories [Eqs. (11)–(15)] with the appropriate Bessel function expansion.[8] Making the cyclotron resonance approximation [Eq. (1)] with $l < 0$ for negatively charged particles, the modified equations of motion [Eqs. (18)–(20)] can be integrated over the interval $t' = [0, 2\pi/\Omega_n]$ to yield

$$\Delta p_{\perp n} = \frac{(-1)^{|l|+1} |q| \pi}{\Omega_n} \cos\left(\psi_n + \frac{|l|\pi}{2} \right)$$

$$\times \left[\left(E_1 + E_2 - \frac{p_{\perp n}}{\gamma_n mc} (B_1 + B_2) \right) J_{|l|-1}(k_\perp \rho_n) \right.$$

$$\left. + \left(E_1 - E_2 - \frac{p_{\perp n}}{\gamma_n mc} (B_2 - B_1) \right) J_{|l|+1}(k_\perp \rho_n) \right]. \tag{21}$$

$$\Delta p_{zn} = \frac{(-1)^{|l|+1} |q| \pi}{\Omega_n}$$

$$\times \cos\left(\psi_n + \frac{|l|\pi}{2} \right) \left(-2E_z J_{|l|}(k_\perp \rho_n) \right.$$

$$+ \frac{p_{\perp n}}{\gamma_n mc} [(B_1 + B_2) J_{|l|-1}(k_\perp \rho_n)$$

$$\left. + (B_2 - B_1) J_{|l|+1}(k_\perp \rho_n)] \right) \tag{22}$$

$$\Delta \psi_n = 2\pi (k_z p_{zn}/m\omega_c - \omega/\Omega_n). \tag{23}$$

The PMAP is now completely specified: given $(p_{\perp n}, p_{zn}, \psi_n)$ at time t_n, the corresponding quantities at t_{n+1} are given by

$$p_{\perp n+1} = p_{\perp n} + \Delta p_{\perp n}, \tag{24}$$

$$p_{zn+1} = p_{zn} + \Delta p_{zn}, \tag{25}$$

$$\psi_{n+1} = \psi_n + \Delta \psi_n, \tag{26}$$

using Eqs. (21)–(23) for the jump values.

The PMAP will prove to be a useful pedagogical tool for understanding the resonance acceleration process. However, it is not a good computational tool for accurately predicting a particle trajectory over any long period of time. This is largely because the map is not area-preserving in phase space and hence not time-reversal invariant, though the true equations of motion are derivable from a Hamiltonian. After many iterations, the phase space trajectories of the PMAP solutions will drift away from the trajectories of the true solutions.

The PMAP also has difficulties in predicting the initial phase and initial momentum dependence of the motion, at least when the initial energy is less than or equal to the quiver energy. Our assumption in deriving the PMAP that the particle orbit differs only slightly from a cyclotron orbit could break down when the momentum is at the quiver energy level $[p/(mc) \lesssim O(\epsilon)]$. If the particle does not complete a reasonable approximation to a cyclotron orbit in the time interval of an unperturbed cyclotron period, then the change in both p_{1n} and p_{zn} will not necessarily be as dictated by the PMAP and could be of $O(\epsilon)$. This will certainly be the case for the first cyclotron period when starting from cold initial conditions.

In light of these problems, the reader might wonder how we can be confident that the PMAP will be at all useful in understanding the acceleration process. We acquired our confidence from analysis with the PMAP, which yielded the kinetic energy and oscillation period scaling laws for the $\eta_z \neq 1$ regime derived in Paper I to within a constant factor of order unity. Furthermore, analysis in the limit of parallel propagation $(\mathbf{k} = k\mathbf{e}_z)$ with the PMAP can reproduce precisely the asymptotic scaling of energy as a function of time derived from the exact solution of Roberts and Buchsbaum. The derivations of the $\eta_z \neq 1$ scaling laws from the PMAP are given in the Appendix.

B. The small momentum limit of the PMAP

The PMAP can be made simpler by assuming that the momentum will be relatively small $[|\mathbf{p}_n|/(mc) \ll 1, n = 1,2,3,...]$, though perhaps much larger than $O(\epsilon)$. Having the advantage of knowing what maximum energies are possible (Paper I) we can expect this to be a reasonable approximation in all parameter regimes excepting the case when $\eta_z \simeq 1$. Even when $\eta_z \simeq 1$, the small momentum limit of the PMAP will be useful in illustrating how cold initial particles are accelerated through the small momentum regime to eventually achieve energies where $|\mathbf{p}|/(mc) \sim O(1)$.

Recalling that $k_x\rho_n = k_x p_{1n}/(m\omega_c)$, the Bessel functions in the full PMAP [Eqs. (21)-(23)] can be approximated as[2]

$$J_{|l|}(k_x\rho_n) \simeq \frac{1}{2^{|l|}\Gamma(|l|+1)}\left(\eta_x \frac{\omega}{\omega_c}\frac{p_{1n}}{mc}\right)^{|l|} \tag{27}$$

when $|l| \geq 1$. If $|l| = 0$, then $J_{|l|} \simeq 1$. Expanding the relativistic gamma factor and the cyclotron frequency we obtain

$$\gamma_n \simeq 1 + p_{1n}^2/2m^2c^2 + p_{zn}^2/2m^2c^2, \tag{28}$$

$$\Omega_n \simeq \omega_c(1 - p_{1n}^2/2m^2c^2 - p_{zn}^2/2m^2c^2), \tag{29}$$

and, after some manipulation, we find that to lowest order in $|\mathbf{p}|/(mc)$ the jump values for the PMAP become

$$\Delta p_{1n} = d_{|l|}(E_1 + E_2)\cos(\psi_n + |l|\pi/2)(p_{1n}/mc)^{|l|-1}, \tag{30}$$

$$\Delta p_{zn} = d_{|l|}(-\eta_x E_3 + B_1 + B_2) \times \cos(\psi_n + |l|\pi/2)(p_{1n}/mc)^{|l|}, \tag{31}$$

$$\Delta\psi_n = -2\pi|l|\left(1 + \frac{p_{1n}^2}{2m^2c^2} + \frac{p_{zn}^2}{2m^2c^2} - \eta_z\frac{p_{zn}}{mc}\right), \tag{32}$$

where $d_1 = |q|\pi/\omega_c$ and

$$d_{|l|} = [(|l|-1)!\,2^{|l|-1}]^{-1}|q|\pi/\omega_c \times [\eta_x(\omega/\omega_c)]^{|l|-1}, \tag{33}$$

for $|l| > 1$.

Further simplification is possible by noting a convenient relation that follows from the plane wave solution of Faraday's law [Eqs. (7)-(9)],

$$-\eta_x E_3 + B_1 + B_2 = \eta_z(E_1 + E_2). \tag{34}$$

Using this polarization relation, the equation for Δp_{zn} [Eq. (31)] can be rewritten as

$$\Delta p_{zn} = d_{|l|}\eta_z(E_1 + E_2)\cos(\psi_n + |l|\pi/2)(p_{1n}/mc)^{|l|}. \tag{35}$$

Comparing this expression for Δp_{zn} with the mapping equation for Δp_{1n} [Eq. (30)], we find

$$\eta_z \frac{p_{1n}}{mc}\frac{\Delta p_{1n}}{mc} = \frac{\Delta p_{zn}}{mc}. \tag{36}$$

Considering a sequence of orbits, we can sum Eq. (36), beginning at $n = 0$, to obtain

$$\eta_z\left(\frac{p_{1n}^2}{2m^2c^2} - \frac{p_{10}^2}{2m^2c^2}\right) = \frac{p_{zn}}{mc} - \frac{p_{z0}}{mc}, \tag{37}$$

where we have assumed $p_{1n}\Delta p_{1n} \simeq \Delta p_{1n}^2/2$. This relation is the small wave amplitude, small momentum approximation to an exact constant of the motion [cf. Eq. (15) of Paper I].

Using the reduced constant of the motion [Eq. (37)] to replace p_{zn} in the phase jump equation, we discover to lowest order

$$\Delta\psi_n = -2\pi|l|\left(1 + (1 - \eta_z^2)\frac{p_{1n}^2}{2m^2c^2} - \eta_z\frac{p_{z0}}{mc} + \eta_z^2\frac{p_{10}^2}{2m^2c^2}\right), \tag{38}$$

where the quadratic term in p_{z0} has been dropped since it is much smaller than the term linear in p_{z0}. The normalized kinetic energy $U_n = \gamma_n - 1$ can also be approximated using the small momentum expansion [Eq. (28)] and the reduced constant of the motion [Eq. (37)]. We obtain to lowest order in ϵ,

$$U_n = p_{1n}^2/2m^2c^2 + p_{z0}^2/2m^2c^2. \tag{39}$$

Note that the change in kinetic energy is proportional to the change in perpendicular momentum $\Delta U_n \simeq p_{1n}\Delta p_{1n}$. Thus a discussion of the physical mechanism responsible for the change in momentum will be equally applicable to the change in kinetic energy.

To summarize, the PMAP reduces to two jump equations in the small momentum limit: one for $\Delta\psi_n$ [Eq. (38)] and another for Δp_{1n} [Eq. (30)]. Values of p_{zn} are obtained from the reduced constant of the motion [Eq. (37)]. The approximation of small momentum will be valid for small wave amplitudes except when $\eta_z \simeq 1$, where, after acceleration has taken place, $p_{1n}/(mc) \sim O(1)$. We remark that when $k_x = 0$, the full version of the PMAP [Eqs. (21)-(23)] is identical to that given in Eqs. (30) and (32) regardless of the value of $|\mathbf{p}|/(mc)$.

C. Discussion of the physical mechanism

Test particles can achieve kinetic energies far in excess of the quiver energy, on times scales of many cyclotron orbits, by coherently accumulating the relatively small changes in kinetic energy that occur during each orbit. The degree to which a particle will gain or lose energy each orbit depends on the value of the relative wave phase, which will vary from orbit to orbit as a function of the energy. In this section, using the PMAP as a guide, we probe the physical effects underlying the change in energy and phase during each cyclotron orbit and how these effects act in concert to produce the long time scale acceleration mechanism. Our discussion will focus on the regime of small momentum describable by the version of the PMAP given in Eqs. (30) and (38).

1. The change in energy

The normalized kinetic energy U of a particle changes in an electromagnetic field according to the relation

$$\frac{dU}{dt} = \frac{q\mathbf{v}\cdot\mathbf{E}}{mc^2}. \tag{40}$$

Our study of the variation of kinetic energy becomes a study of how the particle velocity "lines up with" the wave electric field during the course of a cyclotron orbit. Since the change in kinetic energy ΔU_n is proportional to the change in perpendicular momentum $\Delta p_{\perp n}$ [Eq. (39)] in the small momentum limit, we can use the PMAP expression for $\Delta p_{\perp n}$ to illustrate the processes responsible for ΔU_n.

Examining the expression for $\Delta p_{\perp n}$ [Eq. (30)], we see that a necessary condition for acceleration is $E_1 + E_2 \neq 0$. The reason for this becomes more clear when the wave electric field [Eq. (4)] is written in the following manner:

$$\begin{aligned}\mathbf{E}_w = {} & [(E_1 + E_2)/2][\cos(\mathbf{k}\cdot\mathbf{x} - \omega t)\mathbf{e}_x \\ & - \sin(\mathbf{k}\cdot\mathbf{x} - \omega t)\mathbf{e}_y] \\ & + [(E_1 - E_2)/2][\cos(\mathbf{k}\cdot\mathbf{x} - \omega t)\mathbf{e}_x \\ & + \sin(\mathbf{k}\cdot\mathbf{x} - \omega t)\mathbf{e}_y] \\ & - E_3\cos(\mathbf{k}\cdot\mathbf{x} - \omega t)\mathbf{e}_z.\end{aligned} \tag{41}$$

The term proportional to $E_1 + E_2$ represents the electric field component in the plane perpendicular to $\mathbf{B}_0$ that rotates about B_0 in the same sense as the particle cyclotron motion. Not surprisingly, it is this component of the electric field (which we term the "corotating component" and denote as $\mathbf{E}_c$) that dictates the energy transfer between the wave and particle via the change in $p_{\perp n}$. The corotating wave magnetic field $\mathbf{B}_c$ can be defined in a similar manner with an amplitude

$$(B_1 + B_2)/2 = [\eta_2(E_1 + E_2) + \eta_1 E_3]/2$$

[Eq. (34)].

The nonzero $\Delta p_{\perp n}$ arising from the corotating component of the electric field is a result of either of two effects: the corotation effect or the Doppler effect. If $\omega \simeq \omega_c$, so that $|l| = 1$ satisfies the resonance condition [Eq. (1)], it is the corotation effect that dominates as follows. When the wave frequency is within $O(\epsilon)$ of the cyclotron frequency the corotation angle θ, defined as the angle between $\mathbf{p}_\perp$ and $\mathbf{E}_c$,

$$\theta = \arccos\left(\frac{\mathbf{p}_\perp\cdot\mathbf{E}_c}{|\mathbf{p}_\perp||\mathbf{E}_c|}\right) \tag{42}$$

remains relatively constant during the entire orbit. If the corotating electric field component $\mathbf{E}_c$ is nonzero, then the integral of $\mathbf{p}_\perp\cdot\mathbf{E}_c$ will be nonzero and the particle will interact with the wave either gaining or losing energy depending on the value of the corotation angle. Though relatively constant during one orbit, θ will vary slightly from orbit to orbit and this slow variation will prove to be a major factor in the acceleration process. We will demonstrate below that θ is related to the PMAP phase variable ψ_n in a simple manner.

If $\omega \simeq |l|\omega_c$ such that $|l| > 1$ satisfies the cold particle resonance condition, it is the Doppler effect that determines $\Delta p_{\perp n}$. The corotating component of the electric field does not maintain a relatively constant angle with respect to $\mathbf{p}_\perp$ but rotates through an angle of roughly $2\pi(|l| - 1)$ during the course of an orbit. We illustrate this in the phase space plots of Fig. 1 by showing the directions of the wave electric field vector (solid arrows) and magnetic field vector (dotted arrows) for various points in the PMAP cyclotron orbit for $|l| = 2$. Unlike the situation when the corotation effect dominates, the x dependence of the wave phase (i.e., $k_x \neq 0$) is essential to the energy gain process. The integral of $\mathbf{p}_\perp\cdot\mathbf{E}_w$ is dominated by the corotating component of the electric field $\mathbf{E}_c$ evaluated during that part of the orbit where $\mathbf{p}_\perp$ is parallel to $\mathbf{k}$ (the point where $p_x > 0$, $p_y = 0$ in Fig. 1). At this point, which we term the "Doppler point," the change of the wave phase with respect to the particle position is slower than at any other point in the orbit. The sign and magnitude of $\Delta p_{\perp n}$ will depend on the value of the corotation angle at the Doppler point. We denote this angle as θ_{DP}. As with the corotation effect scenario, the value of the θ_{DP} (mod 2π) will change slightly from orbit to orbit according to the change of ψ_n.

Whether it is the corotation effect or the Doppler effect that is responsible for altering $p_{\perp n}$, the sign and magnitude of $\Delta p_{\perp n}$ will depend on θ_{DP} (in the case of the corotation effect, θ_{DP} is characteristic of the value of θ over the entire orbit). To deduce the relation between θ_{DP} and the PMAP phase variable ψ_n, we first note that the Doppler point is the point one-quarter of the way around the PMAP cyclotron orbit (Fig. 1), which will be reached at the time $t_{n+1/4} = t_n + \pi/(2\Omega_n)$. Evaluating the expression for the corotation angle [Eq. (42)] at $t = t_{n+1/4}$ using the PMAP trajectories [Eqs. (11)–(15)] and the wave field definitions [Eq. (4)], we discover

$$\theta_{DP} = \mathbf{k}\cdot\mathbf{x}_{n+1/4} - \omega t_{n+1/4}. \tag{43}$$

Since $x_{n+1/4} = 0$, this reduces to $\theta_{DP} = k_z z_{n+1/4} - \omega t_{n+1/4}$. Setting $\Delta\psi_{n+1/4} = \psi_n + \Delta\psi_n/4$, we can substitute into the PMAP expression for $\Delta\psi_n$ [Eq. (38)] to arrive at the relation

$$\theta_{DP} = \psi_n - |l|\pi/2, \tag{44}$$

where we have ignored the small momentum terms. We see that the change in θ_{DP} from one orbit to the next orbit is equivalent to $\Delta\psi_n$ (mod 2π).

The phase dependence of $\Delta p_{\perp n}$, as dictated by the PMAP [Eq. (30)], is contained in the factor

$\cos(\psi_n + |l|\pi/2)$. Substituting in the expression for the corotation angle at the Doppler point [Eq. (44)], we find

$$\Delta p_{\perp n} \propto (-1)^{n} \cos \theta_{\mathrm{DP}}. \tag{45}$$

Taking into account the sign of the factor $a_{l/|l|}$, $\Delta p_{\perp n}$ is indeed maximized as a function of ψ_n at exactly the value of ψ_n that maximizes $q\mathbf{p}_{\perp} \cdot \mathbf{E}_c / (|\mathbf{p}_{\perp} \mathbf{E}_c|)$ at the Doppler point.

It is clear that only the perpendicular component of the particle momentum $p_{\perp n}$ and the wave electric field component $\mathbf{E}_w$ are needed to alter the kinetic energy of each cyclotron orbit. If $|l| > 1$, there must also exist a nonzero oblique component to the wave vector $(k_x \neq 0)$. The parallel momentum p_{zn} and the wave magnetic field $\mathbf{B}_w$ cannot be neglected, however, as they play an important role in altering the phase.

2. The change in phase

Having established the importance of the Doppler point corotation angle θ_{DP} in determining the kinetic energy gain, we consider now the physical mechanisms responsible for the slow variation of θ_{DP}, or, equivalently, ψ_n [Eq. (44)]. The jump in ψ_n predicted by the PMAP [Eq. (38)] is approximately $-2\pi|l|$, indicating that the wave propagates past the particle approximately $|l|$ phases in a single cyclotron orbit. The small, but essential $O(\epsilon)$ deviations from an exact $-2\pi|l|$ phase change are a result of the energy dependence of the cyclotron frequency and the particle's streaming motion along the background magnetic field. These effects are clearly evident in the unapproximated PMAP expression for $\Delta\psi_n$ [Eq. (23)].

The $\Delta\psi_n$ equation in the small momentum version of the PMAP [Eq. (38)] contains the energy dependence of the cyclotron frequency in the negative semidefinite term $-\pi|l|[p_{\perp n}/(mc)]^2$. As the particle gains energy, the cyclotron frequency decreases and, with a fixed phase velocity ω/k, the wave will propagate further past the particle during the increased cyclotron period. Consequently, ψ_n will decrease slightly more than the nominal value of $-2\pi|l|$. Interestingly, the energy dependence of the cyclotron frequency is a relativistic effect and plays a major role in the resonance acceleration process in the apparently nonrelativistic regime of $|\mathbf{p}|/(mc) \ll 1$.

The phase ψ_n (mod 2π) can also be altered by the particle motion along the background magnetic field during the course of the orbit. The streaming component of $\Delta\psi_n$, originally proportional to p_{zn} in the full PMAP [Eq. (23)], reduces to the term

$$2\pi|l|\left(\eta_z^2 \frac{p_{1n}}{2m^2c^2} - \eta_z \frac{p_{z0}}{mc} - \eta_z^2 \frac{p_{10}^2}{2m^2c^2}\right) \tag{46}$$

in the small momentum version of $\Delta\psi_n$. Besides the initial streaming terms proportional to p_{z0} and p_{10}, there is an energy-dependent streaming term resulting from the wave interaction. This term is positive semidefinite because the wave interaction always produces a p_{zn} greater than p_{z0}, i.e., $p_{zn} - p_{z0} > 0$ [Eq. (37)]. Assuming for a moment that $p_{z0} = 0$, then $p_{zn} > 0$ so that the particle moves in the same direction as the wave along $\mathbf{B}_0$. Consequently, the wave does not move quite so far past the particle during the course of a cyclotron orbit as would be the case if $p_{zn} = 0$ and ψ_n will be increased slightly from the nominal value of $-2\pi|l|$. If $p_{z0} > 0$, the wave-induced streaming is enhanced by the initial streaming. If $p_{z0} < 0$, the initial streaming opposes the wave-induced streaming and thus the total streaming part of $\Delta\psi_n$ will be negative unless the particle energy becomes high enough that the wave-induced streaming dominates.

It is through the non-negligible streaming contribution *to $\Delta\psi_n$ that the motion of the particle in the direction of $\mathbf{B}_0$* plays a role in the acceleration process. The variation of this motion is determined by the PMAP equation for Δp_{zn} [Eq. (31)] and perhaps a little surprisingly Δp_{zn} is proportional to the corotating component of the wave electric field. A closer examination of the relation between the wave electric and magnetic field polarizations [Eq. (34)] that leads to the simplified form of Δp_{zn} reveals the following picture. If the wave is electrostatic $(\mathbf{k}\|\mathbf{E}_w)$, then wave magnetic field is zero and the components of the electric field can be written as $E_2 = 0$, $\eta_x E_3 + \eta_z E_1 = 0$. The component of the force in the z direction being proportional only to E_3 can then be expressed in terms of E_1 and hence the corotating component of the wave electric field [Eq. (41)].

If the wave has an electromagnetic component, then Δp_{zn} is determined entirely by the $(\mathbf{v}\times\mathbf{B}_c)/c$ magnetic force. When averaged over a cyclotron period, the z component of the electric force is canceled out by the $(v_x \mathbf{e}_x \times \mathbf{B}_c)/c$ component of the magnetic force leaving the other components of the magnetic force (proportional to $E_1 + E_2$) to push the particle in z. The one exception would be the case of a wave where $\eta_x E_3 + \eta_z E_1 = 0$ but $E_2 \neq 0$ (linearly polarized in the y direction). In this case, the z component of the electric force is not canceled out and it is both the electric *and magnetic forces that push the particle in z*. We conclude that, for waves that are not purely electrostatic, the magnetic field of the wave cannot be ignored since it determines, to a large extent (if not completely), the motion of the particle parallel to $\mathbf{B}_0$ and, as we have seen, this is important in determining the variation of ψ_n (mod 2π) and hence $p_{\perp n}$.

3. The acceleration scenario for $p_{10} = p_{z0} = 0$

Our discussion of the cyclotron resonance acceleration process will not be complete until we explain how it is that the momentum and phase changing mechanisms work together to produce large energy gains over many cyclotron orbits. The acceleration scenario will be presented in two parts. First, we consider the case where $p_{10} = 0$ (this section). Second, we consider initial momentum such that $p_{10} \sim p_{z0} \sim O(\epsilon)$ (Sec. II C 4). We reiterate our earlier comments (Sec. II A) that the PMAP initial momentum will only be within $O(\epsilon)$ of the true initial momentum. For example, $p_{z0} = 0$ in the PMAP might correspond to a finite p_{z0} in reality and vice versa.

The change in phase [Eq. (38)] in the $p_{10} = p_{z0} = 0$ limit takes the simple form

$$\Delta\psi_n = -2\pi|l|\,[1 + (1 - \eta_z^2)(p_{1n}^2/2m^2c^2)]. \quad (47)$$

Though the magnitude of $\Delta\psi_n$ (mod 2π) depends upon energy, the behavior of ψ_n (mod 2π) will be monotonic; either monotonic decreasing if $\eta_z < 1$, monotonic increasing if $\eta_z > 1$, or constant if $\eta_z = 1$. When $\eta_z < 1$, the phase velocity in the direction of $\mathbf{B}_0$ is greater than the speed of light and the relativistic cyclotron frequency effect dominates the phase change. Conversely, when $\eta_z > 1$, the phase velocity along $\mathbf{B}_0$ is less than the speed of light and the streaming effect dominates. The phase change effects cancel each other out when $\eta_z = 1$ leaving ψ_n (mod 2π) a constant and, as we shall see, this causes singular behavior.

Let us first examine in detail the acceleration scenario for $|l| = 1$ and then generalize for the scenario for other resonance numbers. When $|l| = 1$, the wave frequency is within $O(\epsilon)$ of the cyclotron frequency and the PMAP equation for the change in perpendicular momentum [Eq. (30)] reduces to

$$\Delta p_{1n} = d_1(E_1 + E_2)\cos(\psi_n + \pi/2), \quad (48)$$

where d_1 is positive definite. Assume that $\eta_z > 1$ and $\psi_0 = \pi + \delta$, where δ is a small number greater than zero ($\delta/\pi \ll 1$). The scenario is illustrated schematically in Fig. 2, where we plot Δp_{1n} as a function of ψ_n (solid curve). A dot-dashed line below the curve indicates the time history of ψ_n with a circle denoting the initial and final state of one period within $O(\epsilon)$.

Initially, $\Delta p_{1n} > 0$ causing p_{1n} to grow and ψ_n (mod 2π) to increase. The growth of p_{1n} will continue as long as ψ_n is in the range $\pi < \psi_n < 2\pi$ (the "acceleration range") corresponding to the range of corotation angles where $q\mathbf{p}_1 \cdot \mathbf{E}_r > 0$. After a finite number of orbits, say N, ψ_n (mod 2π) will reach the value of $2\pi[\psi_N$ (mod $2\pi) = 0]$ and p_{1n} will be a maximum, having accumulated over the N orbits where $\Delta p_{1n} > 0$. Continuing the monotonic increase, ψ_n will traverse the range $0 < \psi_n < \pi$ (the "deceleration range") where $\Delta p_{1n} < 0$ because of the corotation angle being such that $q\mathbf{p}_1 \cdot \mathbf{E}_r < 0$. The inverse symmetry of Δp_{1n} about ψ_N ensures that p_{1n} will decrease for N orbits until the initial condition of $p_{12N} = 0$ is reached at $\psi_{2N} = \pi + \delta$. At this point, one cycle of a periodic process has been completed (give or take the small factor of δ) with a maximum energy from the accumulation process exceeding the quiver energy and a period much longer than a cyclotron period.

If, instead, we were to consider the acceleration scenario for the case where $\eta_z < 1$, then ψ_n (mod 2π) would be monotonically decreasing. The scenario described above would apply given the appropriate choice of initial phase ($\psi_0 = 2\pi - \delta$) and the sign changes for $\Delta\psi_n$. Likewise, if we consider different resonance frequencies ($|l| > 1$), the above described scenario will apply given the appropriate choice of ψ_0 and sign of $\Delta\psi_n$. The major difference between the acceleration processes at $|l| = 1$ and $|l| > 1$ is the relative inefficiency of the Doppler effect in changing the energy compared to the corotation effect. This inefficiency is manifested in the PMAP through the factor of $(p_{1n}/mc)^{|l|-1}$ in Δp_{1n} [Eq. (30)]. As a result of the less efficient energy gain per orbit p_{1n} will remain small for a larger number of orbits and ψ_n will take a larger number of orbits to cover the acceleration and deceleration ranges yielding a longer period for the cyclic process. For $|l| > 3$, the Doppler effect becomes sufficiently inefficient that maximum energies exceeding the quiver energy are no longer possible.

A less complicated, but more dramatic acceleration scenario exists when $\eta_z = 1$. According to the small momentum version of the PMAP, $\Delta\psi_n = 0$ when $\eta_z = 1$ [Eq. (38)]. Choosing ψ_0 so that $\Delta p_{10} > 0$ implies that Δp_{1n} will be greater than zero for all n, and the particle will accelerate indefinitely. This will be true for arbitrarily large p_{1n} in the limit $k_x = 0$, where the small momentum version of the PMAP becomes equivalent to the full PMAP. If $k_x \neq 0$, then the rising p_{1n} will saturate when $p_{1n} \sim O(mc)$ because of the effects of higher-order terms not included in the expansions of the relativistic cyclotron frequency and the constant of the motion that were used in deriving the small momentum version of $\Delta\psi_n$. Thus, when $p_{1n} \sim O(mc)$, the relativistic cyclotron frequency effect no longer cancels out the streaming effect and the phase begins to slip. Such a higher-order effect

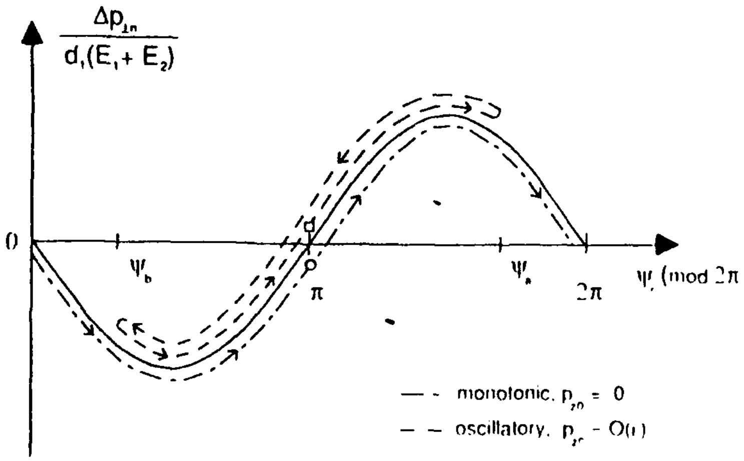

FIG. 2. The change in perpendicular momentum Δp_{1n} as a function of phase ψ_n (mod 2π) according to the PMAP when $|l| = 1$ (solid curve). Schematic representations of the time history of ψ_n are shown for a specific case of $p_{z0} \sim 0$ (dot dashed curve) and $p_{z0} \sim O(\epsilon)$ (dashed curve). See the text for a detailed description.

would explain why the maximum energies observed when $\eta_z = 1$ and $k_\perp \neq 0$ are independent of wave amplitude and resonance frequency (Paper I).

The reader may have noted that the descriptions of the acceleration scenarios all depend upon a judicious choice of the initial phase ψ_0. If ψ_0 is not chosen properly, the PMAP can predict negative values of p_{1n}, an unphysical situation. As we have emphasized, this failure of the PMAP to elucidate the initial phase dependence is a consequence of the cyclotron orbit sometimes failing to be a good approximation to the particle trajectory when $p_{10} \lesssim O(\epsilon)$.

4. The acceleration scenario for $p_{10} \sim p_{z0} \sim O(\epsilon)$

Let us consider briefly how the acceleration mechanism works when the initial particle energy is of the order of the quiver energy. When formulated in terms of the PMAP, the predominant changes in the acceleration scenario with respect to the $p_{10} = p_{z0} = 0$ case will be due to the effect of the p_{z0} term in the $\Delta\psi_n$ relation [Eq. (38)]. This term provides a constant streaming phase change in addition to the phase changes stemming from the energy-dependent streaming and relativistic cyclotron frequency terms. The behavior of ψ_n, and hence p_{1n}, depends on the relative sign of the p_{z0} term with respect to the energy-dependent terms that are proportional to $(1 - \eta_z^2)$.

If the sign of p_{z0} is opposite that of $(1 - \eta_z^2)$, the acceleration process is little changed from the $p_{z0} = 0$ scenario. The behavior of ψ_n is monotonic increasing or decreasing (depending on the value of η_z), with the background streaming effect simply increasing the rate of change. An increased rate of change means that ψ_n passes through the acceleration range in fewer orbits. This decreases the sum of Δp_{1n} over the acceleration range and, consequently, lowers the maximum energy.

If p_{z0} has the same sign as $(1 - \eta_z^2)$, then the background streaming term contributes to $\Delta\psi_n$ with a sign opposite to that of the energy-dependent effects. To illustrate how this alters the acceleration scenario, we consider the case where $|l| = 1$, $\eta_z < 1$, and $p_{z0} > 0$, i.e., a regime where the relativistic cyclotron frequency effect dominates the energy-dependent contribution to $\Delta\psi_n$. These parameters lead to the simplified Δp_{1n} relation given in Eq. (48). To help guide the reader through the scenario, we display in Fig. 2 a schematic of the time history of ψ_n on the Δp_{1n} vs ψ_n plot (dashed line above the solid curve) with the square denoting the initial and final states of a long period to within $O(\epsilon)$.

Initially, the background streaming dominates the phase change since $|p_{z0}/mc| \gg |p_{10}^2/m^2c^2|$ and ψ_n will increase. Given the appropriate choice of initial phase ($\psi_0 = \pi + \delta$), Δp_{1n} will initially be positive and remains positive as long as $\pi < \psi_n < 2\pi$. If p_{z0} is not too large, then the rate of change of ψ_n will be slow enough to allow p_{1n} to build up to a level that allows the energy-dependent term in $\Delta\psi_n$ to cancel out and then exceed the background streaming term. Assume that the cancellation of the two terms $[\Delta\psi_n (\mathrm{mod}\ 2\pi) = 0]$ occurs at $\psi_n = \psi_a$, where $\pi < \psi_a < 2\pi$. The phase will begin to decrease but Δp_{1n} remains positive until $\psi_n = \pi$, at which point p_{1n} has reached a maximum. Continuing to decrease, ψ_n enters the deceleration range $(0 < \psi_n < \pi)$, where $\Delta p_{1n} < 0$. The perpendicular momentum decreases and at the point $\psi_n = \pi - \psi_a$, the background streaming term will begin again to dominate $\Delta\psi_n$. The phase begins to increase while Δp_{1n} remains negative until $\psi_n = \pi - \delta$ and the cycle is complete.

This acceleration scenario applies equally well to the $\eta_z > 1$ and $p_{z0} < 0$ case, provided the appropriate changes in initial phase, acceleration–deceleration ranges, and sign of $\Delta\psi_n (\mathrm{mod}\ 2\pi)$ are made. The scenario is similar to the $p_{z0} = 0$ scenario in that maximum energies much larger than the quiver energy occur with periods of variation much larger than a cyclotron period. In contrast with the $p_{z0} = 0$ scenario, ψ_n exhibits oscillatory behavior instead of monotonic behavior. Maximum kinetic energies with an oscillatory ψ_n can often exceed maximum kinetic energies with a monotonic ψ_n because an oscillating ψ_n spends more cyclotron orbits in the acceleration range.

Oscillatory ψ_n behavior disappears when p_{z0} exceeds some critical value, say p_{zc}, and the background streaming propels ψ_n through the acceleration range before the energy-dependent contributions to $\Delta\psi_n$ can "shut off" the background streaming. For $p_{z0} > p_{zc}$, the phase monotonically changes and the maximum p_{1n} decreases as p_{z0} increases. Numerical solutions of the full equations of motion have verified that this type of phase behavior occurs with values of p_{zc} within order unity of those estimated by the PMAP.

As was the case when $p_{z0} = 0$, it is not wise to press the PMAP too far since problems with the initial phase and momentum dependence thwart the PMAP predictive power. This becomes obvious when we ask what happens when $p_{z0} \to 0$. Sticking to the oscillatory scenario described in this section for $p_{z0} \sim O(\epsilon)$, we would expect that the oscillation period and maximum energy would decrease to zero. But this is not what happens; the initial phase changes to different values so that, when $p_{z0} \to 0$, we have the $p_{z0} = 0$ acceleration scenario as discussed in Sec. II C 3 with large maximum energies. Let us appreciate the physical intuition that the PMAP has given us and move on to a more complex Hamiltonian analysis that will satisfy our quantitative needs.

III. REDUCED HAMILTONIAN EQUATIONS OF MOTION

To probe the details of the cyclotron resonance acceleration process that fell through the cracks of the PMAP we turn to a Hamiltonian formulation of the test particle problem. Hamiltonian methods were used in Paper I to derive a pseudopotential function that was able to describe the behavior of the kinetic energy on time scales longer than a cyclotron period. In this section, we extend the Hamiltonian formulation of Paper I to produce reduced equations of motion capable of predicting cyclotron orbit-averaged details of the particle trajectory either analytically or in far less computational time than it would take to compute solutions of the full equations of motion.

In Cartesian coordinates, the Hamiltonian for a test particle in the electromagnetic wave fields described in Sec. II [Eqs. (4) and (5)], is

$$\mathcal{H}(\mathbf{x},\mathbf{p};t) = [m^2c^4 + (\mathbf{P}c - q\mathbf{A})^2]^{1/2}. \tag{49}$$

-147-

where the canonical momenta are defined in terms of the physical momenta as $\mathbf{P} = \mathbf{p} + q\mathbf{A}/c$. The components of the vector potential can be reduced to

$$A_x = (mc^2/|q|)[-(\omega_c/\omega)y + \epsilon_1 \sin\beta], \tag{50}$$

$$A_y = (mc^2\epsilon_2/|q|)\cos\beta, \tag{51}$$

$$A_z = -(mc^2\epsilon_1/|q|)\sin\beta, \tag{52}$$

where ϵ_i is given by Eq. (10) and we have introduced the phase variable

$$\beta(x,z,t) = k_x x + k_z z - \omega t. \tag{53}$$

A number of canonical transformations of the Cartesian Hamiltonian must be performed before a sufficiently useful time-independent Hamiltonian and corresponding set of canonical coordinates is produced. We refer the reader to Paper I for details on the sequence of transformations that we employ and will only present here the resultant Hamiltonian and the definitions of the corresponding canonical coordinates in terms of physical coordinates.

The Hamiltonian of interest [Eq. (24) of Paper I] can be written to $O(\epsilon)$ as

$$H(\xi,\bar{\phi},P_\xi,\bar{I},P_\mu) = H_0(P_\xi,\bar{I},P_\mu) + H_1(\xi,\bar{\phi},P_\xi,\bar{I},P_\mu), \tag{54}$$

where

$$H_0(P_\xi,\bar{I},P_\mu) = \Upsilon - P_\xi, \tag{55}$$

$$H_1(\xi,\bar{\phi},P_\xi,\bar{I},P_\mu) = \frac{1}{2\Upsilon}\sum_{n=-\infty}^{\infty} a_n \sin[\xi + s(n-l)\bar{\phi}], \tag{56}$$

with $H_0 \sim O(1)$ and $H_1 \sim O(\epsilon)$. We have introduced the following quantities into the H representation:

$$\Upsilon(P_\xi,\bar{I},P_\mu) = [1 + (2\omega_c/\omega)(\bar{I} + slP_\xi) + (\eta_z P_\xi - \eta_x P_\mu)^2]^{1/2}, \tag{57}$$

$$a_n(P_\xi,\bar{I},P_\mu) = -(\omega_c/\omega)\bar{\rho}\{(\epsilon_1+\epsilon_2)J_{n+1}(\eta_x\bar{\rho}) + (\epsilon_1-\epsilon_2)J_{n-1}(\eta_x\bar{\rho})\} + 2s\epsilon_3(\eta_z P_\xi - \eta_x P_\mu)J_n(\eta_x\bar{\rho}), \tag{58}$$

where

$$\bar{\rho}(P_\xi,\bar{I}) = [(2\omega/\omega_c)(\bar{I} + slP_\xi)]^{1/2} \tag{59}$$

and s is the sign of the charge. Unlike the Paper I representation of H, we have chosen to use dimensionless canonical variables. In particular, the canonical momenta $(P_\xi,\bar{I},P_\mu)$ are in units normalized to ω/mc^2 and the Hamiltonian H is normalized to mc^2. To maintain the canonical properties of the Hamiltonian system it is necessary to introduce the normalized time variable $\bar{t} = \omega t$. In our set of dimensionless variables, derivatives with respect to time are expressed with the independent variable $\bar{t}$.

The canonical variables $(\xi,\bar{\phi},P_\xi,\bar{I},P_\mu)$ are defined in terms of the physical variables by the relations,

$$\xi = \beta + (\omega/\omega_c)s\eta_x(p_y/mc + s\epsilon_2\cos\beta) + sl\bar{\phi}, \tag{60}$$

$$\bar{\phi} = \arctan\left(\frac{-(p_y/mc + s\epsilon_2\cos\beta)}{s(p_x/mc + s\epsilon_1\sin\beta)}\right), \tag{61}$$

$$\mu = k_z x - k_x z - (\omega/\omega_c)s\eta_z(p_y/mc + s\epsilon_2\cos\beta), \tag{62}$$

$$P_\xi = \frac{1}{\eta^2}\left(\eta_x\frac{p_x}{mc} + \eta_z\frac{p_z}{mc} - \frac{\omega_c}{c}s\eta_x y + s(\eta_x\epsilon_1 - \eta_z\epsilon_3)\sin\beta\right), \tag{63}$$

$$\bar{I} = \frac{\omega}{2\omega_c}\left[\left(\frac{p_x}{mc} + s\epsilon_1\sin\beta\right)^2 + \left(\frac{p_y}{mc} + s\epsilon_2\cos\beta\right)^2\right] - slP_\xi, \tag{64}$$

$$P_\mu = \frac{1}{\eta^2}\left(\eta_z\frac{p_x}{mc} - \eta_x\frac{p_z}{mc} - \frac{\omega_c}{c}s\eta_z y + s(\eta_z\epsilon_1 + \eta_x\epsilon_3)\sin\beta\right), \tag{65}$$

with $\beta(x,z,t)$ given by Eq. (53). Inverting these definitions, we obtain the following expressions for the physical variables as functions of the canonical variables:

$$x = (c/\omega\eta^2)(\eta_z\mu + \eta_x\xi - sl\eta_x\bar{\phi} + \eta_x\bar{t} + s\eta^2\bar{\rho}\sin\bar{\phi}), \tag{66}$$

$$y = (c/\omega)[-s(\omega/\omega_c)(\eta_x P_\xi + \eta_z P_\mu) + \bar{\rho}\cos\bar{\phi}], \tag{67}$$

$$z = (c/\omega\eta^2)(\eta_z\xi - \eta_x\mu - sl\eta_z\bar{\phi} + \eta_z\bar{t}), \tag{68}$$

$$p_x/mc = (s\omega_c/\omega)\bar{\rho}\cos\bar{\phi} - s\epsilon_1\sin(\xi - sl\bar{\phi} + s\eta_x\bar{\rho}\sin\bar{\phi}), \tag{69}$$

$$p_y/mc = -(\omega_c/\omega)\bar{\rho}\sin\bar{\phi} - s\epsilon_2\cos(\xi - sl\bar{\phi} + s\eta_x\bar{\rho}\sin\bar{\phi}), \tag{70}$$

$$p_z/mc = \eta_z P_\xi - \eta_x P_\mu + s\epsilon_3\sin(\xi - sl\bar{\phi} + s\eta_x\bar{\rho}\sin\bar{\phi}), \tag{71}$$

with $\bar{\rho}(P_\xi,\bar{I})$ given by Eq. (60). In Paper I, the relation between the canonical coordinates $(\xi,\bar{\phi},\mu,P_\xi,\bar{I},P_\mu)$ and conventional action-angle guiding center canonical variables is discussed. The Hamiltonian H and corresponding canonical variables differ from Hamiltonian formulations used in previous studies of wave-particle interactions[5-10] in that there is no singular behavior in the canonical coordinates as $\eta_z \to 0$.

The cyclotron resonance approximation used in Paper I and in the construction of the PMAP (Sec. II) is founded on the assumption that there are two widely varying dynamical time scales, with the faster time scale being on the order of the nonrelativistic cyclotron period. In the Hamiltonian formulation, this separation of time scales is determined by the relative magnitude of the two frequencies $\omega_1 = d\xi/d\bar{t}$ and $\omega_2 = d\bar{\phi}/d\bar{t}$. These nondimensional frequencies can be computed from H and are found to be

$$\omega_1 = (1/\Upsilon)[(sl\omega_c/\omega) + \eta_z(\eta_z P_\xi - \eta_x P_\mu)] - 1 + O(\epsilon), \tag{72}$$

$$\omega_2 = \omega_c/\Upsilon\omega + O(\epsilon) \tag{73}$$

Defining the winding number r to be the ratio of the slow to fast frequency, we see

$$r = sl + (\omega/\omega_c)\eta_z(\eta_z P_\xi - \eta_x P_\mu) - (\omega/\omega_c)\Upsilon + O(\epsilon) \tag{74}$$

The cyclotron resonance approximation assumes $r \sim O(\epsilon)$ with l chosen to satisfy this as well as possible. When expressed in terms of the physical variables, the assumption of small winding number is equivalent to the resonance condition [Eq. (1)] normalized to the relativistic cyclotron frequency Ω. In the above analysis, it has been implicitly assumed that $\partial H_1/\partial P_\xi \sim O(\epsilon)$, which seems reasonable given $H_1 \sim O(\epsilon)$. We shall discover later (Sec. III C 2) that this is not always the case.

Reduction of the Hamiltonian H in the cyclotron resonance approximation can be carried out either discretely or continuously. Though the discrete mapping approach presented in Sec. III A is often the method of choice (since the time averaging process is explicit), there are difficulties with accuracy in certain regions of phase space. We are thus led to construct equations of motion with a continuous time variable in Sec. III B from an orbit-averaged reduced Hamiltonian. Details of the particle trajectories in the small momentum limit are studied in Sec. III C.

A. Orbit-averaged mapping equations

Our goal in this section is to construct a set of area-preserving mapping equations that will approximate the particle trajectory in the canonical variable phase space. The mapping equations will determine the slowly varying variables P_ξ and ξ on the phase space surface of constant $\tilde{\phi}(\mathrm{mod}\ 2\pi)$ with successive iterations of the map (denoted by the subscript n) indicating an increase of $\tilde{\phi}$ by 2π, i.e., $\tilde{\phi}_{n+1} = \tilde{\phi}_n + 2\pi$. The map construction outlined below employees standard methods of Hamiltonian analysis that are discussed in detail elsewhere.[11]

We seek a mapping of the form

$$P_{\xi_{n+1}} = P_{\xi_n} + \Delta P_{\xi_n}(P_{\xi_{n+1}}, \xi_n), \tag{75}$$

$$\xi_{n+1} = \xi_n + 2\pi r(P_{\xi_{n+1}}) + g(P_{\xi_{n+1}}, \xi_n), \tag{76}$$

where r is the winding number given by Eq. (74) without the "$O(\epsilon)$" term. When $\epsilon = 0$, then $\Delta P_{\xi_n} = g = 0$ and P_{ξ_n} is a constant of the motion. In this limit, ξ_n will advance by an amount equal to the slow frequency ω_1 times the fast period $T = 2\pi/\omega_2$, with ω_2 given by Eq. (73) without the "$O(\epsilon)$" term.

The first-order correction ΔP_{ξ_n} to the trivial zeroth-order behavior of P_{ξ_n} is computed by integrating the equation of motion for $dP_\xi/d\hat{t}$ from time $\hat{t}_n$ to $\hat{t}_n + T$,

$$\begin{aligned} \Delta P_{\xi_n} &= \int_{\hat{t}_n}^{\hat{t}_n + T} d\hat{t}\, \frac{dP_\xi}{d\hat{t}} \\ &= -\int_0^T d\hat{t}\, \frac{\partial H_1}{\partial \xi}(\xi_n + \omega_1 \hat{t}, \tilde{\phi}_0 + \omega_2 \hat{t}, P_{\xi_{n+1}}, \tilde{I}), \end{aligned} \tag{77}$$

where the zeroth-order trajectories are substituted in for the canonical variables in the integrand. For purposes of area preservation, the value $P_{\xi_{n+1}}$ is used instead of P_{ξ_n}. Also, $\tilde{I}$ is a constant to $O(\epsilon^2)$ independent of n. This can be deduced by integrating the expression $d\tilde{I}/d\hat{t} = -\partial H_1/\partial\tilde{\phi}$ to lowest order between $\hat{t}_n$ and $\hat{t}_n + T$.

Evaluating the ΔP_{ξ_n} integral [Eq. (77)] using the first-order Hamiltonian [Eq. (56)] and keeping in mind the resonance approximation, we find

$$\Delta P_{\xi_n} = -(\pi\omega/\omega_r)a_l \cos\xi_n, \tag{78}$$

where $a_l(P_{\xi_n})$ is given by Eq. (58) with $P_{\xi_{n+1}}$ substituted in for P_ξ.

The first-order correction g to the zeroth-order rotation of ξ_n is determined by demanding that the map be area-preserving in (P_ξ, ξ) phase space. A consideration of the Jacobian of the map transformation defined by Eqs. (75) and (76) yields the following condition for area preservation:

$$\frac{\partial(\Delta P_{\xi_n})}{\partial P_{\xi_{n+1}}} + \frac{\partial g}{\partial \xi_n} = 0. \tag{79}$$

This differential equation can be easily integrated upon substitution of the ΔP_{ξ_n} expression [Eq. (78)] to yield

$$g = (\pi\omega/\omega_r)a_l' \sin\xi_n, \tag{80}$$

where

$$\begin{aligned} a_l' = &-(sl^2/\bar{\rho})[(\epsilon_1 - \epsilon_2)J_{l-1}(\eta_\perp\bar{\rho}) \\ &-(\epsilon_1 + \epsilon_2)J_{l+1}(\eta_\perp\bar{\rho})] - 2sl\eta_\parallel\epsilon_3 J_l(\eta_\perp\bar{\rho}) \\ &+ 2s\epsilon_3\{\eta_\parallel J_l(\eta_\perp\bar{\rho}) + (sl\omega/\bar{\rho}^2\omega_r)(\eta_\parallel P_{\xi_{n+1}} - \eta_\parallel P_\parallel) \\ &\times[\eta_\perp\bar{\rho}J_{l-1}(\eta_\perp\bar{\rho}) - lJ_l(\eta_\perp\bar{\rho})]\}. \end{aligned} \tag{81}$$

The map is now complete. Starting with values for (ξ_n, P_{ξ_n}), the value of $P_{\xi_{n+1}}$ is obtained by solving the P_ξ map equation [Eq. (75)] for $P_{\xi_{n+1}}$ given the function $\Delta P_{\xi_n}(P_{\xi_{n+1}}, \xi_n)$ [Eq. (78)]. Direct substitution of $P_{\xi_{n+1}}$ and ξ_n into the ξ map equation (76) with $r(P_{\xi_{n+1}})$ given by Eq. (75) and $g(P_{\xi_{n+1}}, \xi_n)$ given by Eq. (80) yields ξ_{n+1}. Initial conditions fix the value of $\tilde{\phi}(\mathrm{mod}\ 2\pi)$ and the constants of the motion $\tilde{I}$ and $P_\parallel$. We denote the map constructed above as the "QMAP" since it is more quantitatively accurate than the PMAP constructed in Sec. II.

The QMAP can be simplified by assuming small momenta. In physical variables, the small momentum limit demands $|\mathbf{p}/mc| \ll 1$, which, when translated to canonical variables, is equivalent to the conditions $\tilde{I} + slP_\xi \ll 1$ and $\eta_\parallel P_{\xi_n} - \eta_\parallel P_\parallel \ll 1$. Expanding the ΔP_{ξ_n}, ω_r, and g functions of the QMAP in the small arguments [making use of Eq. (27)] we arrive at the following set of mapping equations for negatively charged particles:

$$P_{\xi_{n+1}} = P_{\xi_n} - (\pi\omega/\omega_r)b_{|l|}\bar{\rho}^{|l|}\cos\xi_n, \tag{82}$$

$$\begin{aligned} \xi_{n+1} = \xi_n &+ 2\pi\Big(|l| - \frac{\omega}{\omega_r} - (\tilde{I} + |l|P_{\xi_{n+1}}) \\ &+ \frac{\eta_\parallel\omega}{\omega_r}(\eta_\parallel P_{\xi_{n+1}} - \eta_\parallel P_\parallel)\Big) \\ &+ \frac{\pi\omega}{\omega_r}c_{|l|}\bar{\rho}^{|l|-2}\sin\xi_n, \end{aligned} \tag{83}$$

where

$$b_{|l|} = -(-\eta_\perp)^{|l|-1}\omega_r(\epsilon_1 + \epsilon_2)/2^{|l|-1}\Gamma(|l|)\omega, \tag{84}$$

$$c_{|l|} = (|l|^2\omega/\omega_r)b_{|l|}. \tag{85}$$

and $\bar{p}(P_{\xi_{n+1}})$ is given by Eq (59) with $P_\xi \to P_{\xi_{n+1}}$. In the small momentum approximation $\bar{p} \ll 1$.

To see if the QMAP provided a reasonably accurate estimate of the true phase space trajectories, we compared QMAP solutions with numerical solutions of the full equations of motion [Eqs. (2) and (3)] over a range of the free parameters ($|l|$, ω/ω_c, η, α, ϵ, $\mathbf{k}\cdot\mathbf{x}_0$) for cold initial conditions ($\mathbf{p}_0 = 0$). We found good agreement when $|l| > 2$, albeit we did not do as complete a survey as will be discussed in Sec. III B. There is a problem, however, when $|l| = 1$ and the true behavior of ξ in certain regions of phase space is not well modeled by the QMAP.

This difficulty can be understood as follows. When $|l| = 1$, the ξ QMAP equation [Eq. (83)] contains a term proportional to $(\sin \xi_n)/\bar{p}(P_{\xi_{n+1}})$. For cold initial particles, there are portions of the phase space orbits (where the momenta are very small) that pass very close to those values of P_ξ that make $\bar{p} = 0$. Fortunately, the true phase trajectory is also in a region near $\xi = 0$ or π so that the value of $\sin \xi_n$ also approaches 0. The behavior of the ratio $(\sin \xi / \bar{p}(P_\xi))$ is extremely sensitive to the exact values of (ξ, P_ξ) to the extent that a slight deviation from the true trajectory as $\xi \to 0$ or π results in a value much greater than unity. Unfortunately, as a consequence of the fixed time-step size of the QMAP and the implicit nature in which the quantities are advanced, the discrete jump in P_ξ is computed *before* the corresponding jump in ξ, and the quantity $(\xi_n, P_{\xi_{n+1}})$ deviates enough from the true trajectory that QMAP ratio $\sin \xi_n / \bar{p}(P_{\xi_{n+1}})$ becomes extremely large. The deviation is enough, in fact, to cause large inaccuracies in the values of $\xi_{n+1} - \xi_n$. More will be said about these regions of singular behavior in Sec. III C.

In trying to circumvent this problem, we are immediately led to consider the possibility of decreasing the time step of the jump so that the quantity $(\xi_n, P_{\xi_{n+1}})$ more closely approximates the desired quantity $[\xi(t), P_\xi(t)]$. This can be done most effectively by abandoning the discrete jumps of a map altogether and constructing orbit-averaged equations of motion with a continuous time variable.

B. Orbit-averaged continuum equations

With the aid of adiabatic canonical perturbation theory,[12] it is possible to transform the Hamiltonian H to a new Hamiltonian $\bar{H}$ that will depend only on slowly varying variables to $O(\epsilon)$, provided the resonance approximation is satisfied. This transformation was used in the course of deriving the HPP theory in Appendix B of Paper I. We outline the transformation below in the context of the dimensionless canonical variables that have been introduced in this paper.

The generating function S for the transformation can be written as a function of the old coordinates and new momentum as

$$S(\xi,\phi,\mu,\bar{P}_\xi,\bar{I},\bar{P}_\mu) = \xi\bar{P}_\xi + \phi\bar{I} + \mu\bar{P}_\mu + S_1(\xi,\phi,\bar{P}_\xi,\bar{I},\bar{P}_\mu), \tag{86}$$

where

$$S_1(\xi,\phi,\bar{P}_\xi,\bar{I},\bar{P}_\mu) = \frac{\omega}{2\omega_c} \sum_{\substack{n=-\infty \\ n \neq l}}^{\infty} \frac{a_n}{s(n-l)} \cos[\xi + s(n-l)\phi] \tag{87}$$

and $a_n(\bar{P}_\xi,\bar{I},\bar{P}_\mu)$ is given by Eq (58) with $(P_\xi,I,P_\mu) \to (\bar{P}_\xi,\bar{I},\bar{P}_\mu)$. To $O(\epsilon)$, the new canonical variables $(\bar{\xi},\bar{\phi},\bar{P}_\xi,\bar{I})$ are defined in terms of the old variables according to the relations

$$\bar{\xi} = \xi + \frac{\partial S_1}{\partial P_\xi}, \tag{88}$$

$$\bar{\phi} = \phi + \frac{\partial S_1}{\partial I}, \tag{89}$$

$$\bar{\mu} = \mu + \frac{\partial S_1}{\partial P_\mu}, \tag{90}$$

$$\bar{P}_\xi = P_\xi - \frac{\partial S_1}{\partial \xi}, \tag{91}$$

$$\bar{I} = I - \frac{\partial S_1}{\partial \phi}, \tag{92}$$

$$\bar{P}_\mu = P_\mu, \tag{93}$$

where (P_ξ,I,P_μ) have been substituted in for $(\bar{P}_\xi,\bar{I},\bar{P}_\mu)$ in the S_1 definition [Eq. (87)]. The Hamiltonian H [Eq. (54)] transforms to $\bar{H}$, where

$$\bar{H} = \Upsilon - \bar{P}_\xi + (a_l/2\Upsilon)\sin\bar{\xi} \tag{94}$$

and $\Upsilon(\bar{P}_\xi,\bar{I},\bar{P}_\mu)$ is given by Eq (57) with $(P_\xi,I,P_\mu) \to (\bar{P}_\xi,\bar{I},\bar{P}_\mu)$. By choosing S_1 properly, the last varying terms have been displaced to $O(\epsilon^2)$ in transforming from H to $\bar{H}$. What remains in $\bar{H}$ is essentially H averaged over one period in ϕ while the other variables are held constant. Thus, like the QMAP, dynamic details occurring on time scales less than $2\pi/\omega_c$ (roughly the cyclotron period) are absent.

From the orbit-averaged Hamiltonian $\bar{H}$, we can compute the orbit-averaged equations of motion for the canonical variables $\bar{\xi}$ and $\bar{P}_\xi$:

$$\frac{d\bar{\xi}}{dt} = \Upsilon' - 1 + \frac{1}{2\Upsilon}\left(a_l' - a_l\frac{\Upsilon'}{\Upsilon}\right)\sin\bar{\xi}, \tag{95}$$

$$\frac{d\bar{P}_\xi}{dt} = -\frac{a_l}{2\Upsilon}\cos\bar{\xi}, \tag{96}$$

where

$$\Upsilon' = sl\omega_c/\omega\Upsilon + (\eta_x/\Upsilon)(\eta_x\bar{P}_\xi - \eta_z\bar{P}_\mu) \tag{97}$$

and a_l' is given by Eq (81) with $P_\xi \to \bar{P}_\xi$ and $I \to \bar{I}$. The canonical momenta $\bar{I}$ and $\bar{P}_\mu$ are constants of the motion and the linear time variation of the corresponding angles can be written as

$$\bar{\phi} = \bar{\phi}_0 + \frac{\partial\bar{H}}{\partial\bar{I}}\,t, \tag{98}$$

$$\bar{\mu} = \bar{\mu}_0 + \frac{\partial\bar{H}}{\partial\bar{P}_\mu}\,t \tag{99}$$

In the small momentum limit, the orbit-averaged equations of motion can be reduced to the simpler form [cf. the QMAP reduction, Eqs. (82) and (83)]

$$\frac{d\bar{P}_z}{dt} = -\frac{b_l}{2}\left[\left(\frac{2\omega}{\omega_c}\right)(\bar{I} + |l|\bar{P}_z)\right]^{|l|/2} \cos\bar{\xi}, \quad (100)$$

$$\frac{d\bar{\xi}}{dt} = \frac{|l|\omega_c}{\omega} - \left(\frac{\omega_c}{\omega}\right)(\bar{I} + |l|\bar{P}_z) + \eta_z(\eta_z\bar{P}_z - \eta_x\bar{P}_{\parallel}) - 1 + \frac{c_l}{2}\left[\left(\frac{2\omega}{\omega_c}\right)(\bar{I} + |l|\bar{P}_z)\right]^{|l|/2-1} \sin\bar{\xi}, \quad (101)$$

where b_l and c_l are given by Eqs. (84) and (85), respectively, and we have assumed negatively charged particles. We also make use of the fact that, in the small momenta limit, the resonance condition is satisfied when $\omega = |l|\omega_c + O(\epsilon)$.

To complete the orbit-averaged continuum description, we need a prescription that gives the canonical variables $(\bar{\xi},\bar{\phi},\bar{P}_z,\bar{I},\bar{\mu},\bar{P}_{\parallel})$ in terms of the physical variables and vice versa. In theory, this is straightforward, given the definitions of these variables in terms of $(\xi,\phi,P_z,I,\mu,P_{\parallel})$ [Eqs. (88)–(93)] and the explicit relations between $(\xi,\phi,P_z,I,\mu,P_{\parallel})$ and the physical variables [Eqs. (60)–(71)]. In practice, we have chosen to simply set $(\bar{\xi},\bar{\phi},\bar{P}_z,\bar{I},\bar{\mu},\bar{P}_{\parallel}) = (\xi,\phi,P_z,I,\mu,P_{\parallel})$ and ignore the S_i corrections. Equating the angles $(\bar{\xi},\bar{\phi},\bar{\mu}) = (\xi,\phi,\mu)$ is undoubtedly a reasonable approximation since the angular variations are $O(2\pi)$ and the corrections are $O(\epsilon)$. Equating the actions $(\bar{P}_z,\bar{I}) = (P_z,I)$ is reasonable if we interpret (P_z,I) as representing quantities time-averaged over the fast period $2\pi/\omega$. We must then assume that the physical initial conditions represent the initial time-averaged values of (P_z,I) through Eqs. (60)–(65). Conversely, the physical variables derived from Eqs. (66)–(71), assuming $(P_z,I) = (\bar{P}_z,\bar{I})$, will be characteristic of the time average.

With $(\bar{\xi},\bar{\phi},\bar{P}_z,\bar{I},\bar{\mu},\bar{P}_{\parallel}) = (\xi,\phi,P_z,I,\mu,P_{\parallel})$, the orbit-averaged continuum equations are identical to the continuous limit of the QMAP [Eqs. (75) and (76)] in the sense that

$$\frac{d\bar{P}_z}{dt} = \frac{\Delta P_{z,n+1}}{T}, \quad (102)$$

$$\frac{d\bar{\xi}}{dt} = \frac{2\pi r + g}{T}, \quad (103)$$

when $P_{z_{n+1}} \to \bar{P}_z$ and $\xi_n \to \bar{\xi}$.

Being ordinary differential equations in a continuous time variable, the orbit-averaged equations of motion can be solved numerically with arbitrary time steps (i.e., as small as needed for stability) and hence avoid the difficulties that were imposed on the QMAP by a fixed time step interval. The freedom to impose an arbitrary time step should be viewed solely as a mathematical convenience since short time-scale physical effects have been averaged out.

To numerically solve the equations of motion, we use a standard fourth-order accurate Runge-Kutta[11] algorithm. As a demonstration of the validity of the orbit-averaged continuum approach, we compare numerical solutions of the orbit-averaged equations to numerical solutions of the full equations of motion [Eqs. (2) and (3)], which were also solved with a Runge-Kutta algorithm. In particular, we compare predictions of the maximum kinetic energy U_{max} and the oscillation period τ_r characteristic of solutions in the cyclotron resonance regime, over a broad range of the parameters $|l|$, ω/ω_c, η_z, $\mathbf{k}\cdot\mathbf{x}_0$, α, and ϵ for circularly polarized waves and cold initial conditions. The size of the parameter space surveyed is somewhat greater than that surveyed in the extensive comparison of predictions of the HPP theory to solutions of the full equations of motion that was presented in Sec. IV of Paper I.

Referring to the "deviation" as the difference between the orbit-averaged prediction and the full equation prediction normalized to the full equation prediction, we find that, on the average, when $|l| = 1$, the deviation in U_{max} is typically 1% with a maximum around 11%. The deviation in τ_r is typically 3% with a maximum of around 17%. When $|l| = 2$, typical deviations in U_{max} and τ_r are 5% and 17%, respectively, with maximums around 39% (U_{max}) and 50% (τ_r). For $|l| = 3$, we compared only solutions with $\eta_z \simeq 1$ and found typical deviations of U_{max} to be 4% with a maximum of 13%. Typical deviations of τ_r were 40% with a maximum of 56%. In short, the U_{max} and τ_r estimates from the orbit-averaged equations are accurate to the same order as those from the HPP theory.

Examination of the particle trajectories generated from the full equations of motion reveals that when the larger than typical deviations occurred, it was often for the following reasons. First, solutions that have large values of τ_r (e.g., when $|l| = 3$) require extremely large numbers of time steps and the numerical solutions of the full equations can become inaccurate. Second, some parameter values (for example, $\beta_0 = \pi$ when $|l| = 2$) place the particle trajectories uncomfortably close to separatrices, i.e., boundaries in phase space defined by the orbit-averaged Hamiltonian theory that separate regimes of qualitatively different behavior. Higher-order effects not included in the orbit-averaged theory will cause the actual particle trajectory to jump between regions of phase space both inside and outside the separatrix, whereas the trajectory generated from the orbit-averaged theory will remain smoothly on one side or the other. We have more to say about the detailed phase space structure in the next subsection.

C. Phase space structure in the small momentum limit

The orbit-averaged continuum equations can be readily employed to predict details of the particle trajectories beyond the scope of both the Hamiltonian pseudopotential theory (Paper I) and the PMAP (Sec. II). In what follows we explore the character of the trajectories for negatively charged particles in the $\bar{P}_z$-$\bar{\xi}$ canonical phase space as determined by the orbit-averaged equations of motion in the small momentum limit [Eqs. (100) and (101)]. To keep within this realm of parameter space, we will only consider parameter sets where $\eta_z \neq 1$. We limit our analysis to $|l| = 1$ and $|l| = 2$, since they are the only values of $|l|$ that lead to energies above the quiver energy when $\eta_z \neq 1$.

Of primary importance in determining the properties of the particle trajectories in phase space is the location and nature of the fixed points, i.e., those points where $d\bar{\xi}/d\hat{t} = d\bar{P}_\xi/d\hat{t} = 0$. Setting $dP_\xi/d\hat{t} = 0$ [Eq. (101)], we find that any fixed points must satisfy one of two possible conditions:

$$A: \cos\bar{\xi}_A = 0, \tag{104}$$

$$B: a_{|l|}(\bar{P}_{\xi_B}) = 0, \tag{105}$$

where we denote the candidate fixed points that satisfy condition A or condition B as $(\bar{\xi}_A, \bar{P}_{\xi_A})$ and $(\bar{\xi}_B, \bar{P}_{\xi_B})$, respectively.

Before pursuing the fixed point solutions, we pause to introduce some new notation. Consideration of the canonical cyclotron radius $\bar{\rho}$ [Eq. (59)] indicates that, for physically realizable problems (where $\bar{\rho}$ is a real number), the values permissible for $\bar{P}_\xi$ are bounded from below by $\bar{P}_{\xi_{min}}$, where $\bar{P}_{\xi_{min}} = -\bar{l}/|l|$. It is convenient to introduce the dimensionless variable $\bar{P}'_\xi$ defined as

$$\bar{P}'_\xi = \bar{P}_\xi - \bar{P}_{\xi_{min}}. \tag{106}$$

When expressed in terms of the physical variables [Eqs. (60)-(65)], $\bar{P}'_\xi$ reduces to an expression involving only the perpendicular momentum and the phase:

$$\bar{P}'_\xi = \frac{\omega}{2|l|\omega_c}\left[\left(\frac{p_x}{mc} + s\epsilon_1 \sin\beta\right)^2 + \left(\frac{p_y}{mc} + s\epsilon_2\cos\beta\right)^2\right]. \tag{107}$$

Another useful quantity is a constant of the motion $P'_{z\,min}$, where

$$P'_{z\,min} = \eta_z\bar{P}_{\xi_{min}} - \eta_x\bar{P}_\mu. \tag{108}$$

Written in terms of the initial values of the physical variables, $P'_{z\,min}$ becomes

$$P'_{z\,min} = p_{z0}/mc - s\epsilon_3\sin\beta_0 - \eta_z\bar{P}'_{\xi_0}. \tag{109}$$

The assumption of small momenta is equivalent to the assumption that $\bar{P}'_\xi \ll 1$ and $P'_{z\,min} \ll 1$.

The existence of fixed points is established by solving the equation $d\bar{\xi}/d\hat{t} = 0$ [Eq. (100)] for either $\bar{P}'_{\xi_A}$ (case A) or $\bar{\xi}_B$ (case B). The nature of the particle motion near the fixed point is then investigated via linear stability analysis. Using the case A fixed point as an example, we assume solutions of the form

$$\bar{P}'_\xi(\hat{t}) = \bar{P}'_{\xi_A} + \delta\bar{P}'_{\xi_0}\exp(\lambda\hat{t}), \tag{110}$$

$$\bar{\xi}(\hat{t}) = \bar{\xi}_A + \delta\bar{\xi}_0\exp(\lambda\hat{t}), \tag{111}$$

where $\delta\bar{P}'_\xi$ and $\delta\bar{\xi}$ are perturbations sufficiently small so that the equations of motion can be linearized about $(\bar{\xi}_A, \bar{P}'_{\xi_A})$. Solving the resultant set of linear equations for the eigenvalues λ, the fixed point can be classed as the stable type if both eigenvalues are imaginary, or of the unstable type if both eigenvalues are real. When the eigenvalues are real, there will be both a positive and negative branch, in which case the fixed point is of the hyperbolic type.

The remaining discussion is broken up into separate sections, the first describing phase space properties for $|l| = 2$ and the second for $|l| = 1$. In addition to the fixed point structure, we will examine the behavior of the phase angle $\bar{\xi}$ and determine under what physical initial conditions $\bar{\xi}$ becomes an oscillatory (as opposed to monotonic) function of time. An oscillatory $\bar{\xi}$ implies that the particles are "phase trapped," which is an important process, for example, in interactions of whistler waves with charged particles in the Earth's magnetosphere.[14,15]

1. The $|l|=2$ resonance

We consider first the $|l| = 2$ resonance since the candidate fixed points are of a more standard variety than what we will find for $|l| = 1$. In Fig. 3(a), we show curves of constant $\bar{H}$ (denoting possible particle orbits) in $(\bar{\xi}, \bar{P}_\xi)$ phase space. Fixed points corresponding to cases A and B are labeled with an "A" and "B," respectively.

The fixed points for case A must clearly have $\bar{\xi}_A = \pi/2$ or $3\pi/2$. Solving the $d\bar{\xi}/d\hat{t} = 0$ equation for $\bar{P}'_{\xi_A}$, we find

$$\bar{P}'_{\xi_A} = [1/(1-\eta_z^2)] \times [2\omega_c/\omega - 1 + \eta_z P'_{z\,min} + \eta_x(\epsilon_1 + \epsilon_2)\sin\bar{\xi}_A]. \tag{112}$$

Performing the stability analysis we find that the eigenvalues satisfy the equation

$$\lambda^2 = -(1-\eta_z^2)\eta_x(\epsilon_1+\epsilon_2)\bar{P}'_{\xi_A}\sin\bar{\xi}_A, \tag{113}$$

indicating that $(\bar{\xi}_A, \bar{P}'_{\xi_A})$ is a stable fixed point for $\bar{\xi}_A = \pi/2(3\pi/2)$ when $\eta_z < 1(>1)$. A flipping of the stable point from $\bar{\xi}_A = \pi/2$ to $\bar{\xi}_A = 3\pi/2$ as η_z increases through the value of 1 does occur and has been observed in numerical solutions of the full equations of motion.

The oscillation period about the stable fixed point provides a crude estimate of the oscillation period τ_p characteristic of the cyclotron resonance acceleration process. Assuming $\omega = 2\omega_c$ and cold initial particles, the eigenvalue relation [Eq. (113)] and definition of $\bar{P}'_{\xi_A}$ yield the estimate

$$\tau_p = [\eta_x^2(\epsilon_1+\epsilon_2)^2 + \eta_z P'_{z\,min}\sin\bar{\xi}_A]^{-1/2}, \tag{114}$$

where τ_p is in units of the wave period $(2\pi/\omega)$. Comparing this estimate to those obtained in Paper I, we find that Eq. (114) predicts a significantly lower value than that found from either the HPP theory [Eq. (44) of Paper I] or the numerical solutions of the equations of motion [Sec. IV of Paper I]. The reason for this is that all trajectories for cold initial particles lie close to the separatrix (a point discussed later in this section) and will therefore have a longer oscillation period than those near the stable fixed point.

Turning to the case B fixed points, a solution to the equation $a_{|l|}(\bar{P}_{\xi_B}) = 0$ is $\bar{P}_{\xi_B} = P_{\xi_{min}}$, or $\bar{P}'_{\xi_B} = 0$. Other solutions might exist, but they will have $\bar{P}'_{\xi_B} \sim O(1)$ and are therefore beyond the scope of this study. The solutions $\bar{\xi}_B$ to $d\bar{\xi}/d\hat{t} = 0$ must satisfy the relation

$$\sin\bar{\xi}_B = -[1/\eta_x(\epsilon_1+\epsilon_2)](2\omega/\omega_c - 1 + \eta_z P'_{z\,min}). \tag{115}$$

There will be two solutions for $\bar{\xi}_B$ if the right-hand side of Eq. (115) is less than one, and no solutions otherwise. Assuming that solutions exist, the stability analysis yields the eigenvalues

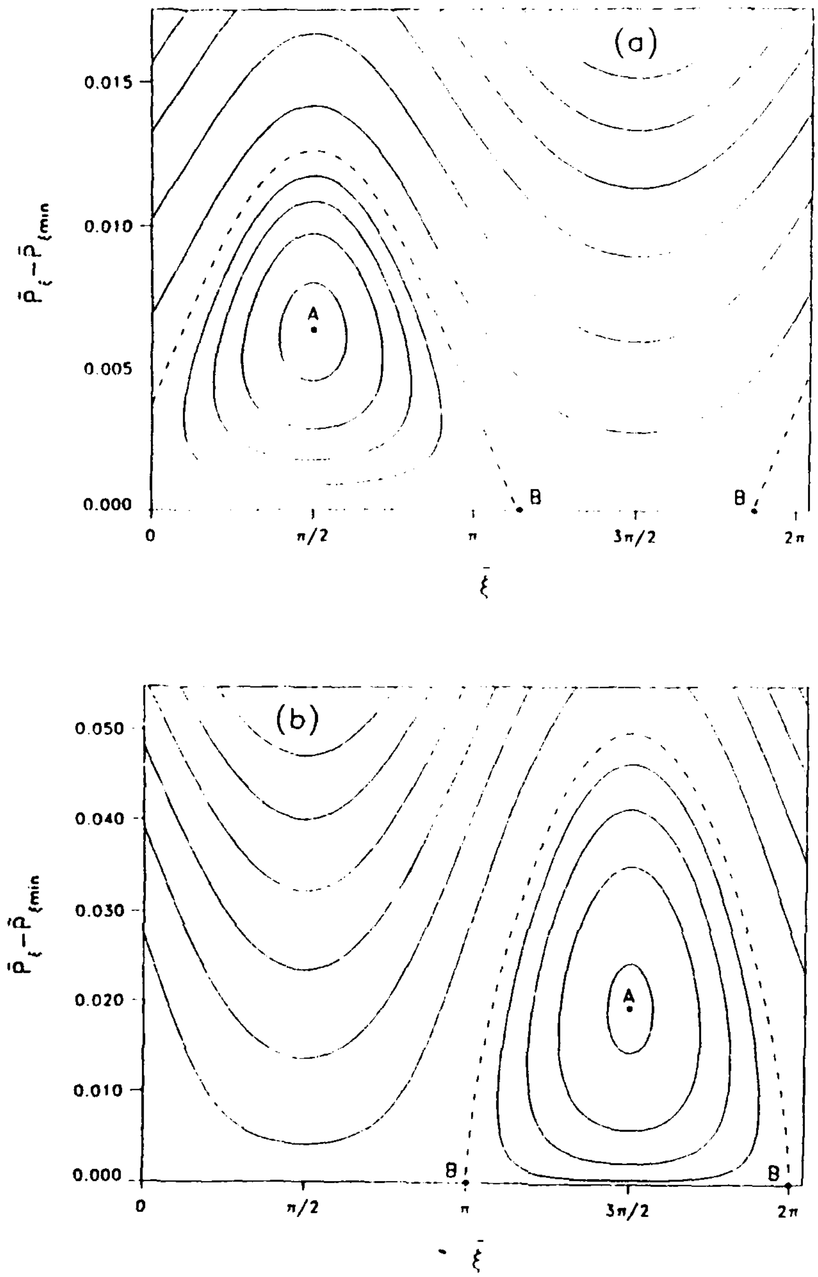

FIG. 3. Contours of constant $\bar{H}$ in the $(\bar{\xi}, \bar{P}_\xi)$ phase plane representing the possible trajectories when $|l| = 2$ (a) and $|l| = 1$ (b). Throughout the small momentum regime, the distribution of trajectories resembles that shown here. Separatrices are indicated with a dashed line and the stable fixed points are labeled "A." The label "B" corresponds to unstable fixed points in (a) and unstable singular points in (b). The particular parameters used to generate this figure were $\eta = 0.8$, $\alpha = 45°$, $\epsilon = 3.16 \times 10$[illegible], $\omega/\omega_c = |l|$, and $\beta_0 = \pi/2$ ($\beta_0 = 0.0$) for $|l| = 2$ ($|l| = 1$) with right-hand circularly polarized waves.

$$\lambda = \pm \eta_z (\epsilon_1 + \epsilon_2) \cos \bar{\xi}_B. \tag{116}$$

The points $(\bar{\xi}_B, \bar{P}'_{\xi_B})$ are thus fixed points of the unstable hyperbolic variety.

The structure of the orbits in $(\bar{\xi}, \bar{P}_\xi)$ phase space [Fig. 3(a)] is not unlike that for a classic nonlinear oscillator, i.e., a stable fixed point flanked by two unstable fixed points. There exists a separatrix connecting the two unstable fixed points that separates the orbits that are oscillatory in $\bar{\xi}$ from those that are monotonic [dashed line in Fig. 3(a)]. Qualitatively, the phase space structure throughout the small momentum regime resembles Fig. 3(a) when fixed-point solutions for $\bar{\xi}$ exist, though the locations of the fixed points vary depending on parameter values and initial conditions.

Whether ξ is monotonic or oscillatory in time depends on which side of the separatrix the initial conditions place the trajectory. This can be determined in the following manner. When $\eta_z < 1$ we consider the functional dependence of $\overline{H}$ on $\overline{\xi}$ as we move along line of constant $\overline{P}'_{\xi}$ when $\overline{P}'_{\xi} = \overline{P}'_{\xi_A}$. Starting at the stable fixed point $\overline{\xi}_A = \pi/2$ and moving in the direction of increasing $\overline{\xi}$, we see that $\overline{H}$ is monotonically decreasing in the interval $\overline{\xi} = [\pi/2, 3\pi/2]$. Thus, if the value of $\overline{H}$ corresponding to a given set of initial conditions is greater than the value of $\overline{H}$ evaluated on the separatrix, $\overline{H}_B = \overline{H}(\overline{\xi}_B, \overline{P}'_{\xi_B})$, the orbit will be oscillatory in $\overline{\xi}$. Evaluating $\overline{H}$ and $\overline{H}_B$ [Eq. (54)] in terms of the initial conditions using the estimates for $(\overline{\xi}_B, \overline{P}'_{\xi_B})$ and assuming $\omega = 2\omega_c$, the oscillatory condition $\overline{H} - \overline{H}_B > 0$ can be written

$$\sin \overline{\xi}_0 + \eta_z P'_{z\,\min}/\eta_x(\epsilon_1 + \epsilon_2) > 0. \tag{117}$$

When $\eta_z > 1$, the stable fixed point shifts to $\overline{\xi}_A = 3\pi/2$ and $\overline{H}(\overline{\xi}, \overline{P}'_{\xi_A})$ is monotonically increasing as $\overline{\xi}$ decreases from $3\pi/2$ to $\pi/2$. In this case, the condition for oscillatory $\overline{\xi}$ behavior $\overline{H} - \overline{H}_B < 0$ and the direction of the inequality in Eq. (117) must be reversed.

As an example, we investigate the condition for oscillatory $\overline{\xi}$ when $\eta_z < 1$ and the particles are initially cold. We first note that whether the orbits are oscillatory or not, they will all be close to the separatrix in the sense that the initial conditions place $\overline{H}$ much closer to the value of $\overline{H}_B$ then to the value of $\overline{H}$ at the stable fixed point. This claim follows from the fact that $\overline{P}'_{\xi_0}/\overline{P}'_{\xi_A} \sim \theta(\epsilon) 1$ for the initially cold particles. Recalling the definitions of the canonical variables in terms of the physical variables [Eqs. (60)–(65)], the oscillatory condition can be written to lowest order as

$$G_2(\beta_0) > 0, \tag{118}$$

where

$$G_2 = \sin \beta_0 \left(\frac{\epsilon_1^2 \sin^2 \beta_0 - \epsilon_2^2 \cos^2 \beta_0 + 2\epsilon_1 \epsilon_2 \cos^2 \beta_0}{\epsilon_1^2 \sin^2 \beta_0 + \epsilon_2^2 \cos^2 \beta_0} + \frac{\eta_z \epsilon_3}{\eta_x (\epsilon_1 + \epsilon_2)} \right). \tag{119}$$

Figure 4(a) contains plots of G_2 for circularly polarized waves as a function of the initial phase β_0. Several different curves are shown, each with a unique value of the propagation angle α. The condition for oscillatory $\overline{\xi}$ behavior is satisfied for a variety of initial conditions and exhibits a nontrivial dependence on angle. These predictions of the onset of oscillatory behavior agree with numerical solutions of the orbit-averaged equations of motion. Comparing to the solutions of the full equations motion, we find good agreement for $\alpha = 5°$ and $45°$. When $\alpha = 85°$, the full equation solutions have a tendency to jump between the oscillatory and monotonic branches if β_0 is not close to $\pi/2$ or $3\pi/2$.

2. The $|l| = 1$ resonance

In Fig. 3(b), curves of constant $\overline{H}$ are plotted in $(\overline{\xi}, \overline{P}'_{\xi})$ phase space for the $|l| = 1$ resonance. The curves look qualitatively similar to the $|l| = 2$ curves and in many ways they are. Both resonances have stable fixed points (labeled by "A") and have a clear separation between the orbits that oscillate in $\overline{\xi}$ and those that do not. The primary difference between the two resonances is that for $|l| = 1$, there are no fixed points that satisfy condition B [Eq. (106)]. Rather, "singular points" satisfying condition B exist and they behave like fixed points in certain respects.

Before considering the details of case B, we examine case A. For angles $\overline{\xi}_A = \pi/2, 3\pi/2$ the $d\overline{\xi}/dt = 0$ equation dictates that $\overline{P}'_{\xi_A}$ satisfies the relation

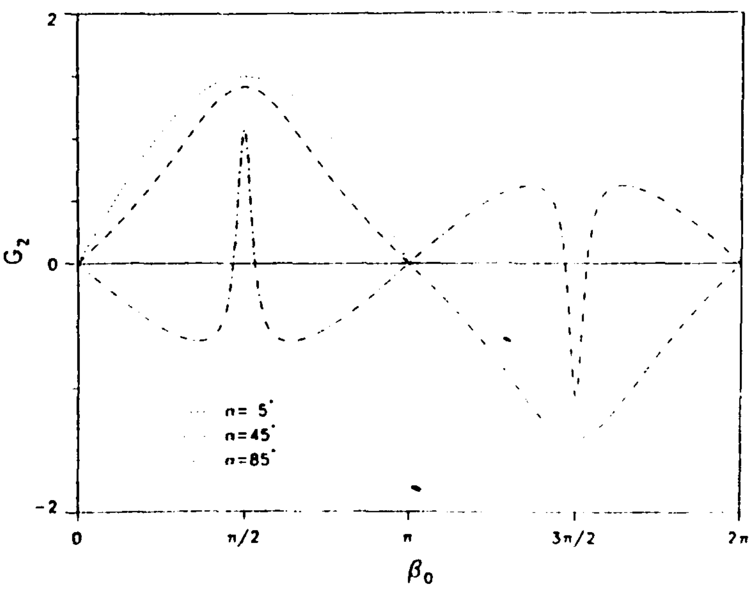

FIG. 4. The function G_2 versus initial phase β_0 when $|l| = 2$ for various angles of propagation α when $\eta = 0.8$, $\epsilon = 3.16 \times 10^{-3}$, and $\omega = 2\omega_c$ for cold initial particles and right-hand circularly polarized waves. When $G_2 > 0$, the behavior of $\overline{\xi}$ is oscillatory.

$$\bar{P}'_{\xi_4}\left[\bar{P}'_{\xi_4}\left(\frac{\omega_c}{\omega}-\eta_z^2\right)+1-\frac{\omega_c}{\omega}-\eta_z P'_{z\,\min}\right]^2$$
$$=\frac{\omega_c}{8\omega}(\epsilon_1+\epsilon_2)^2. \qquad (120)$$

The stability analysis yields the eigenvalue equation

$$\lambda^2=\frac{(\epsilon_1+\epsilon_2)^2}{\bar{P}'_{\xi_4}}\left(\frac{\omega_c}{\omega}\right)^{1/2}$$
$$\times\left[(1-\eta_z^2)\frac{\bar{P}'^{1/2}_{\xi_4}}{\sin\bar{\xi}_4}-\frac{(\epsilon_1+\epsilon_2)}{4}\left(\frac{\omega_c}{\omega}\right)^{1/2}\right]. \qquad (121)$$

Thus $\bar{\xi}_4=3\pi/2(\pi/2)$ corresponds to a stable fixed point when $\eta_z<1(>1)$. The shifting of the fixed point as η_z passes through 1 has been verified with numerical solutions of the full equations of motion. In Fig. 3(b), we show the stable fixed point (A) for $\eta_z<1$.

Considering cold initial particles and setting $\omega=\omega_c$, we obtain from Eq. (120) the following expression for $\bar{P}'_{\xi_4}$:

$$\bar{P}'_{\xi_4}=\tfrac{1}{2}\left|(\epsilon_1+\epsilon_2)/(1-\eta_z^2)\right|^{2/3}, \qquad (122)$$

when we assume $P'_{z\,\min}\ll\bar{P}'_{\xi_4}$ (justified *a posteriori*). As was done for $|l|=2$, we can estimate the resonance oscillation period τ_r using the stable fixed point eigenvalues [Eq. (121)] and the $\bar{P}'_{\xi_4}$ relation [Eq. (12)]. Normalizing τ_r to the wave period, we find

$$\tau_r=\frac{2/\sqrt{3}}{|1-\eta_z^2|^{1/3}|\epsilon_1+\epsilon_2|^{2/3}}. \qquad (123)$$

Contrary to what was found for $|l|=2$, the τ_r estimate resulting from the stable fixed point eigenvalue analysis is remarkably close to the τ_r estimate from the HPP theory [Eq. (41) of Paper I] and the predictions of numerical solutions to the full equations of motion [Sec. IV of Paper I]. Like the $|l|=2$ case, the orbits of cold initial particles lie near the separatrix. However, unlike the $|l|=2$ case, the oscillation periods for orbits near the separatrix are approximately equivalent to the oscillation periods of orbits near the stable fixed point. Anticipating our upcoming analysis, we conjecture that the fast periods near the separatrix are a manifestation of the particle behavior in the vicinity of the case B singular points, where changes in $\bar{\xi}$ become quite rapid.

Moving on to the analysis of case B, the solution of interest to the equation $a_{l|l|}(\bar{P}_{\xi_B})=0$ is $\bar{P}_{\xi_B}=\bar{P}_{\xi_{\min}}$, the same as we found for $|l|=2$. Consequently, any candidate fixed points must have angles $\bar{\xi}_B$ that solve the equation

$$0=\frac{\omega_c}{\omega}-1+\eta_z P'_{z\,\min}-(\epsilon_1+\epsilon_2)\left(\frac{\omega_c}{8\omega}\right)^{1/2}$$
$$\times\lim_{(\bar{\xi},\bar{P}_\xi)\to(\bar{\xi}_B,\bar{P}_{\xi_B})}\left(\frac{\sin\bar{\xi}}{(\bar{P}_\xi-\bar{P}_{\xi_B})^{1/2}}\right). \qquad (124)$$

The only hope for a solution is $\bar{\xi}_B=0$ or π so that the limit as $\bar{\xi}\to\bar{\xi}_B$ and $\bar{P}_\xi\to\bar{P}_{\xi_B}$ has a chance of remaining finite. Even so, the limit in Eq. (124) is not uniquely determined so we will have to content ourselves with examining the trajectories in the vicinity of the candidate fixed points.

Letting $\bar{\xi}$ and $\bar{P}_\xi$ take the form $\bar{\xi}=\bar{\xi}_B+\delta\bar{\xi}(\hat{t})$ and $\bar{P}_\xi=\bar{P}_{\xi_B}+\delta\bar{P}_{\xi_B}(\hat{t})$, where $\delta\bar{\xi}$ and $\delta\bar{P}_\xi$ are infinitesimal perturbations, the orbit-averaged equations of motion [Eqs. (100) and (101)] to lowest order become

$$\frac{d\,\delta\bar{P}_\xi}{d\hat{t}}=(\epsilon_1+\epsilon_2)\cos\bar{\xi}_B\left(\frac{\omega_c}{2\omega}\right)^{1/2}\delta\bar{P}_\xi^{1/2}, \qquad (125)$$

$$\frac{d\,\delta\bar{\xi}}{d\hat{t}}=\frac{\omega_c}{\omega}-1+\eta_z P'_{z\,\min}$$
$$-(\epsilon_1+\epsilon_2)\cos\bar{\xi}_B\left(\frac{\omega_c}{8\omega}\right)^{1/2}\frac{\delta\bar{\xi}}{\delta\bar{P}_\xi^{1/2}}. \qquad (126)$$

Analytic solutions to these time-differential equations are found to be

$$\delta\bar{P}_\xi=\delta\bar{P}_{\xi_0}(1+\hat{t}/C_1)^2, \qquad (127)$$

$$\delta\bar{\xi}=(\omega_c/\omega-1+\eta_z P'_{z\,\min})$$
$$\times[(\hat{t}+C_1)^2-C_1^2+2C_2]/2(\hat{t}+C_1), \qquad (128)$$

where

$$C_1=\left[\delta\bar{P}_{\xi_0}^{1/2}/(\epsilon_1+\epsilon_2)\cos\bar{\xi}_B\right](8\omega/\omega_c)^{1/2}, \qquad (129)$$

$$C_2=\frac{C_1\delta\bar{\xi}_0}{\omega_c/\omega-1+\eta_z P'_{z\,\min}}, \qquad (130)$$

and $(\delta\bar{\xi}_0,\delta\bar{P}_{\xi_0})$ are the initial values at time $\hat{t}=0$. If we make the assumption that $\delta\bar{P}_{\xi_0}$ is small enough so that

$$\delta\bar{\xi}_0\gg C_1(\omega_c/\omega-1+\eta_z P'_{z\,\min}), \qquad (131)$$

then the $\delta\bar{\xi}$ solution takes the relatively simple form

$$\delta\bar{\xi}=\delta\bar{\xi}_0(1-\hat{t}/C_1) \qquad (132)$$

when $\hat{t}/C_1\ll 1$. In the discussion to follow, we will use the full $\delta\bar{P}_\xi$ solution and the approximate $\delta\bar{\xi}$ solution [Eq. (132)], though we realize the approximation might not encompass all physically possible trajectories.

Caveats notwithstanding, the local $\delta\bar{P}_\xi$ and $\delta\bar{\xi}$ solutions indicate the following general behavior. If $\bar{\xi}_B=0$, then trajectories approaching $(\bar{\xi}_B,\bar{P}_{\xi_B})$ will have $|\delta\bar{\xi}|$ decreasing with $\delta\bar{P}_\xi$ increasing. Conversely, trajectories approaching $\bar{\xi}_B=\pi$ will have $|\delta\bar{\xi}|$ increasing with $\delta\bar{P}_\xi$ decreasing. This behavior in the vicinity of the singular points is consistent with the many numerical solutions of the equations of motion we have examined, and is similar to that found near the unstable hyperbolic fixed points at $(\bar{\xi}_B,\bar{P}_{\xi_B})$ when $|l|=2$. We cannot, however, deduce that $(\bar{\xi}_B,\bar{P}_{\xi_B})$ is a fixed point for $|l|=1$ using the local analytic solutions because the same problems exist in taking the limit $\delta\bar{\xi}_0\to 0$, $\delta\bar{P}_{\xi_0}\to 0$ as did in evaluating Eq. (124). In fact, numerical solutions of the full equations of motion indicate that, as trajectories approach the point $(0,\bar{P}_{\xi_B})$, values of $d\bar{\xi}/d\hat{t}$ can become very large. The rate of change of the fast angle $\bar{\phi}$ becomes large also and the ratio of the fast angle to slow angle variation becomes of $O(1)$, stretching the validity of the resonance approximation. It is this rapid evolution of $\bar{\xi}$ near the singular points that causes the convergence problems for the QMAP (Sec. III A).

We will sidestep the issue of the precise characterization of the $(\bar{\xi}_B,\bar{P}_\xi)$ points when $|l|=1$ and assert that these "unstable singular points" [labeled with a "B" in Fig. 3(b)] behave in a manner similar to hyperbolic fixed points. The contour connecting the two singular points separates trajectories monotonic in $\bar{\xi}$ from those oscillatory in $\bar{\xi}$ and is therefore a separatrix [dashed line in Fig. 3(b)]. Full numerical solutions of the equation of motion have verified that the phase space structure throughout the small momentum regime resembles Fig. 3(b) and the locations of the points $(\bar{\xi}_A, \bar{P}'_{\xi_A})$ and $(\bar{\xi}_B, \bar{P}_{\xi_B})$ are in good agreement with the locations predicted by the preceding analysis.

The range of parameters and initial conditions that produce oscillatory $\bar{\xi}$ behavior can be deduced by the method that was used in the $|l| = 2$ analysis. When $|l| = 1$, the Hamiltonian $\bar{H}$ is monotonically decreasing (increasing) away from the stable fixed point when $\eta_z < 1$ ($\eta_z > 1$) so that the condition for oscillatory $\bar{\xi}$ is $\bar{H} - \bar{H}_B > 0$ ($\bar{H} - \bar{H}_B < 0$). Assuming $\omega = \omega_c$, this condition simplifies to

$$\sin \bar{\xi}_0 < 0 \tag{133}$$

when $\eta_z < 1$ with a reversal of the inequality for $\eta_z > 1$. Expanding $\bar{\xi}_0$ in terms of the physical variables, the condition for oscillatory $\bar{\xi}$ can be written to lowest order as

$$G_1(\beta_0, \mathbf{p}_0) < 0, \tag{134}$$

where

$$G_1 = -\left(\frac{p_{x0}}{mc} - \epsilon_1 \sin \beta_0\right)\sin\left(\beta_0 + \eta_x \frac{p_{y0}}{mc}\right)$$
$$-\left(\frac{p_{y0}}{mc} - \epsilon_2 \cos \beta_0\right)\cos\left(\beta_0 + \eta_x \frac{p_{y0}}{mc}\right). \tag{135}$$

Addressing the specific case of cold initial conditions, it can be shown that, like the $|l| = 2$ situation, all physically realizable orbits are very close to the separatrix, i.e., $\bar{P}'_{\xi_0}/\bar{P}'_{\xi_A} \sim O(\epsilon^{4/3})$. Unlike the situation when $|l| = 2$, all cold particle orbits will be monotonic for $|l| = 1$ when the angle of propagation $\alpha < 90°$ [Eq. (134)]. Oscillatory behavior can be found for some combination of parameters if $\alpha > 90°$ or if the initial perpendicular momentum is nonzero. Figure 5 illustrates this point with plots of G_1 versus initial phase β_0 for several different values of p_{x0} when $p_{y0} = p_{z0} = 0$ and the wave is circularly polarized. Numerical solutions of both the orbit-averaged equations of motion and the full equations of motion have verified that the sign of G_1 is an accurate predictor of the $\bar{\xi}$ behavior.

IV. SUMMARY

The objectives of this paper have been twofold: first, to understand the physical mechanisms responsible for generating large kinetic energy gains in the cyclotron resonance acceleration process; and second, to obtain a set of reduced equations of motion that still allow the accurate determination of details of the particle orbits in the cyclotron resonance regime.

The phenomenology of the acceleration mechanism is addressed with the PMAP, a set of mapping equations jumping the momentum and phase of the test particle from one cyclotron orbit to the next. For each orbit, the change in kinetic energy is proportional to the corotating component of the wave electric field and is of the order of the quiver energy or less. This small change in kinetic energy is the result of either the corotation effect ($|l| = 1$) or the Doppler effect ($|l| > 1$) with the sign and magnitude of the change depending on the relative phase of the wave at certain points during the orbit. For the Doppler effect to be operative, there must be a nonzero k_x. Large changes in the kinetic energy arise from the accumulation of the small changes over many orbits.

Crucial to the energy accumulation process and the long time scale periodic behavior is a small shifting in the wave

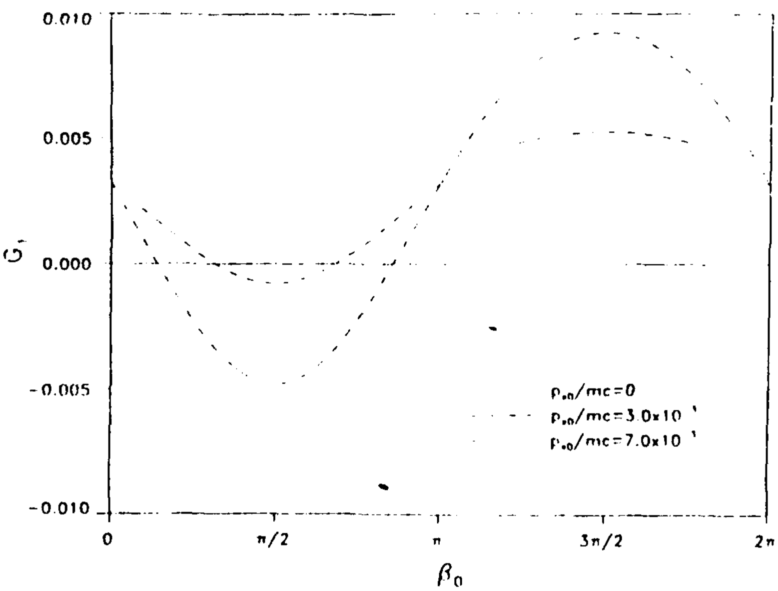

FIG. 5. The function G_1 versus initial phase β_0 when $|l| = 1$ for various values of initial momenta p_{x0}/mc when $\eta = 0.8$, $\epsilon = 3.16 \times 10$ [illegible], $\alpha = 45°$, and $\omega = \omega_c$ for right hand circularly polarized waves. When $G_1 < 0$ the behavior of $\bar{\xi}$ is oscillatory.

phase ψ (mod 2π) of each cyclotron orbit. The shift in phase has two energy-dependent contributions arising from the wave interaction; one is a result of streaming along the background magnetic field caused by the acceleration of the particle parallel to $\mathbf{B}_0$, and the other is a result of an increase in the cyclotron period arising from relativistic effects. There is also a constant parallel streaming contribution due to the initial conditions. We find that, when $\eta_z \neq 1$, the behavior of the ψ(mod 2π) can be either monotonic or oscillatory, depending on the value of the initial streaming term. It is a limitation of the PMAP that we can only predict the existence of both monotonic and oscillatory phase behavior for initial momenta $\mathbf{p}_0/mc < O(\epsilon)$ and not the exact functional dependence. When $\eta_z = 1$, the energy-dependent terms cancel each other out and, at least for some ranges of initial phase and momentum, the phase remains constant in the small momentum limit. This allows for kinetic energy gains of order of the rest mass energy.

It can be concluded from the PMAP analysis that the magnetic field of the wave plays a significant, if not dominant role in altering the relative phase of the wave of each cyclotron orbit. Furthermore, the energy-dependent cyclotron frequency plays a large role in altering the phase even when the particle energies are far below the rest mass energy. Clearly, it is not reasonable to ignore the wave magnetic field or relativistic cyclotron frequency effects in studies of resonance acceleration no matter what the particle energy.

Reduced equations of motion more accurate than the PMAP are obtained by turning to a Hamiltonian formulation of the problem. A set of mapping equations (QMAP) is derived that jump the slowly varying canonical action P_ξ and angle ξ over a 2π period of variation in the fast angle $\bar{\phi}$. The QMAP performs well when $|l| > 1$ but runs into accuracy problems for cold initial conditions when $|l| = 1$. Difficulties arise because the particle orbits in phase space pass close to singular points where the rate of change of the slow angle apparently diverges.

The QMAP difficulties are avoided by working with a set of orbit-averaged equations of motion obtained from a Hamiltonian that was derived using adiabatic perturbation theory. In terms of the physical processes being modeled, the orbit-averaged continuum equations and the QMAP are of identical scope. However, with a continuous time variable the orbit-averaged equations of motion can be numerically solved with an arbitrary time step and therefore avoid convergence difficulties near the $|l| = 1$ singular points. An extensive comparison of numerical solutions of the full equations of motion to solutions of the orbit-averaged equations demonstrates the viability of the orbit-averaged approach.

Details of the orbit distribution in the phase space defined by the orbit-averaged continuum variables $(\bar{\xi}, \bar{P}_\xi)$ [which have been equated to the QMAP variables (ξ, P_ξ)] are examined for $|l| = 1$ and $|l| = 2$ in the limit of small momentum. When $|l| = 2$, the structure is similar to that of a one-dimensional nonlinear oscillator, i.e., a stable fixed point between two unstable fixed points that define a separatrix. A general criterion for oscillatory $\bar{\xi}$ behavior is derived, which is a function of the wave parameters and particle initial conditions. For initially cold particles and $\omega = 2\omega_c$, we find that all particle orbits will be close to the separatrix and that the existence of oscillatory behavior depends strongly on the values of the initial phase, wave polarization, and index of refraction [Eq. (119)].

The phase space structure when $|l| = 1$ differs from the $|l| = 2$ structure in that there are no unstable fixed points. Instead, there are unstable singular points where fixed points might be expected. Though the time rate of change of $\bar{\xi}$ is not uniquely determined at these singular points, analysis of the behavior of nearby orbits suggests divergence. Numerical solutions of the full equations of motion also show divergent behavior in the vicinity of the singular points and indicate that $\bar{\xi}$ ceases to be a slowly varying variable. Despite the singular nature of these points, they play much the same role as unstable hyperbolic fixed points; they can attract and repel orbits along different axes, and they define a separatrix between orbits oscillatory and monotonic in $\bar{\xi}$. Like the $|l| = 2$ case, a general criterion for oscillatory behavior can be derived. When $\omega = \omega_c$ and the particles are initially cold all the orbits are near the separatrix and all are monotonic in $\bar{\xi}$ for angles of propagation $0° < \alpha < 90°$. Only when the initial perpendicular momentum is nonzero or $\alpha > 90°$ can oscillatory motion occur, and then only for certain values of the initial phase that depend on the wave polarization and index of refraction [Eq. (134)].

ACKNOWLEDGMENTS

One of us (G.P.G.) wishes to thank Gareth Guest and Michael Heinemann for useful discussions.

This work was partially sponsored by AF Contract No. F 19628-86-C-0224 while one of us (J.M.A.) was an Air Force Geophysics Laboratory Geophysics Scholar. The United States Government is authorized to reproduce and distribute reprints for governmental purposes notwithstanding any copyright notation hereon.

APPENDIX: SCALING LAWS FROM THE PMAP WHEN $\eta_z \neq 1$

In this appendix, we use the PMAP to derive scaling relations for the kinetic energy U_{max} and oscillation period τ_p associated with the resonance acceleration process. The small momentum approximation to the PMAP is employed and we assume cold initial particles with $\omega = |l|\omega_c$. Having the benefit of the Paper I results, we know this to be a reasonable approximation when $\eta_z \neq 1$.

We will work with the small momentum version of the PMAP [Eqs. (30)-(32)] in the following form:

$$\frac{\Delta p_{\perp n}}{mc} = \bar{d}_{|l|}(\epsilon_1 + \epsilon_2)\left(\frac{p_{\perp n}}{mc}\right)^{|l|-1}\cos\left(\psi'_n + \frac{|l|\pi}{2}\right), \tag{A1}$$

$$\frac{\Delta p_{zn}}{mc} = \bar{d}_{|l|}\eta_z(\epsilon_1 + \epsilon_2)\left(\frac{p_{\perp n}}{mc}\right)^{|l|}\cos\left(\psi'_n + \frac{|l|\pi}{2}\right), \tag{A2}$$

$$\Delta\psi'_n = -\pi|l|(1 - \eta_z^2)(p_{\perp n}/mc)^2, \tag{A3}$$

where

$$\bar{d}_l = (-\eta_z/2)^{|l|-1}[\pi|l|^{|l|}/\Gamma(|l|)] \tag{A4}$$

and the truncated phase has been defined to be $\psi_n' = \psi_n \pmod{2\pi}$. The quantities ϵ_i, $i = 1,2$ are defined in Eq. (10).

Consider the ratio of Δp_{1n} to $\Delta\psi_n'$ arising from the mapping equations (A1) and (A3),

$$\frac{\Delta(p_{1n}/mc)}{\Delta\psi_n'} = -\frac{\bar{d}_{|l|}\eta_x^{|l|-1}(\epsilon_1+\epsilon_2)}{\pi|l|(1-\eta_z^2)}\left(\frac{p_{1n}}{mc}\right)^{|l|-3} \times\cos\left(\psi_n' + \frac{|l|\pi}{2}\right). \quad (A5)$$

Approximating the finite differences as continuous differentials, we obtain the following differential equation:

$$\frac{d}{d\psi_n'}\left(\frac{p_{1n}}{mc}\right)^{4-|l|} = -(4-|l|)\frac{\bar{d}_{|l|}\eta_x^{|l|-1}(\epsilon_1+\epsilon_2)}{\pi|l|(1-\eta_z^2)} \times\cos\left(\psi_n' + \frac{|l|\pi}{2}\right). \quad (A6)$$

Integrating this differential equation assuming $p_{10} = 0$, we find with the appropriate choice of initial phase,

$$\frac{p_{1\max}}{mc} = \left|2\frac{(4-|l|)\bar{d}_{|l|}\eta_x^{|l|-1}(\epsilon_1+\epsilon_2)}{\pi|l|(1-\eta_z^2)}\right|^{2/(4-|l|)} \quad (A7)$$

For $|l| = 1$, the maximum kinetic energy computed from $p_{1\max}$ is

$$U_{\max} = 1.65|(\epsilon_1+\epsilon_2)/(1-\eta_z^2)|^{2/3} \quad (A8)$$

and for $|l| = 2$, we find

$$U_{\max} = 2\eta_x|(\epsilon_1+\epsilon_2)/(1-\eta_z^2)|. \quad (A9)$$

For $|l| = 3$, $U_{\max} \sim O(\epsilon^2)$, the same order as the quiver energy. The scaling of $U_{\max}$ in ϵ, η, and α given by Eqs. (A8) and (A9) is identical to that obtained from the HPP theory (Paper I). Even the constants of proportionality are fairly close to those obtained from the HPP theory (1.26 for $|l| = 1$ and 2 for $|l| = 2$).

To probe the scaling of the long time oscillation period τ_r, we consider the change in phase $\Delta\psi_n'$, which can be either positive definite ($\eta_z > 1$) or negative definite ($\eta_z < 1$) if we ignore the unstable fixed point at $p_{1n} = 0$. The phase ψ_n' will then be either monotonically increasing or decreasing leading to alternating periods of acceleration and deceleration, as we discussed in Sec. II C. Letting N be the number of orbits that $\Delta p_{1n} > 0$ (which is equivalent to the number of orbits that $\Delta p_{1n} < 0$ by the symmetry of the map), we deduce from the Δp_{1n} mapping equation (41)

$$\pi = \sum_{n=1}^{N}|\Delta\psi_n'|. \quad (A10)$$

Substituting in the $\Delta\psi_n'$ mapping equation (A3) we find the sum relation

$$1 = |l|\,|1-\eta_z^2|\sum_{n=1}^{N}\left(\frac{p_{1n}}{mc}\right)^2. \quad (A11)$$

Defining $\langle p_{1n}^2\rangle$ to be the average value of p_{1n}^2 over the acceleration range of ψ_n', we can further reduce the sum relation to

$$1 = |l|\,|1-\eta_z^2|N(\langle p_{1n}^2\rangle/m^2c^2) \quad (A12)$$

Since the acceleration process is cyclic, we can express the average of p_{1n}^2 as a function of the maximum of p_{1n}^2:

$$p_{1\max}^2 = C\langle p_{1n}^2\rangle, \quad (A13)$$

where C is of order unity and, we hypothesize, weakly dependent on ϵ, η, and α. Noting that τ_r is the long time scale oscillation period normalized to the wave period, i.e., $\tau_r = 2|l|N$, we manipu te the reduced sum relation (A12) to find

$$U_{\max}\tau_r = C/|1-\eta_z^2|. \quad (A14)$$

Using the previously derived expressions for $U_{\max}$ [Eqs (A8) and (A9)], the expression for τ_r when $|l| = 1$ is found to be

$$\tau_r \propto 1/|1-\eta_z^2|^{1/3}|\epsilon_1+\epsilon_2|^{2/3} \quad (A15)$$

and, when $|l| = 2$, the scaling relation becomes

$$\tau_r \propto 1/\eta_x|\epsilon_1+\epsilon_2|. \quad (A16)$$

By depicting only a proportionality, we have neglected constants of order unity and the C factor in the above τ_r estimate. The scaling of τ_r with ϵ, η, and α are the same as that derived from the HPP theory except for a logarithmic factor that appears in the HPP expressions when $|l| = 2$.

The agreement of the PMAP and HPP scaling laws, at least to order unity when $\eta_z \neq 1$, demonstrates that the PMAP does reasonably represent the main features of the physical processes that underlie the resonance acceleration mechanism when the momenta are small compared to mc. We reiterate, however, that the PMAP is limited and does not explain very well the initial phase and momentum dependence (Sec. II A).

[1] Y. Ya. Davydovski, Zh. Eksp. Teor. Fiz. 43, 886 (1962) [Sov. Phys. JETP 16, 629 (1963)]

[2] C. S. Roberts and S. J. Buchsbaum, Phys. Rev. 135, A 381 (1964)

[3] P. J. Palmedesso, Phys. Fluids 15, 2006 (1972)

[4] H. Karimabadi, C. R. Menyuk, P. Sprangle, and L. Vlahos, Astrophys. J. 316, 462 (1987)

[5] H. Karimabadi, K. Akimoto, N. Omidi, and C. R. Menyuk, Phys. Fluids B 2, 606 (1990)

[6] G. Ginet and M. Heinemann, Phys. Fluids B 2, 700 (1990)

[7] G. E. Guest, M. E. Fetzer, and R. A. Dandl, Phys. Fluids B 2, 1210 (1990)

[8] M. Abramowitz and I. A. Stegun, *Handbook of Mathematical Functions* (U.S. Government Printing Office, Washington, DC, 1972), p. 361

[9] See Ref. 8, p. 360.

[10] C. R. Menyuk, A. T. Drobot, D. Papadopoulos, and H. Karimabadi, Phys. Fluids 31, 2071 (1988); K. Akimoto and H. Karimabadi, Phys. Fluids 31, 1505 (1988).

[11] A. J. Lichtenberg and M. A. Lieberman, *Regular and Stochastic Motion* (Springer-Verlag, New York, 1983), p. 157

[12] See Ref. 11, p. 88

[13] W. H. Press, B. P. Flannery, S. A. Teukolsky, and W. T. Vetterling, *Numerical Recipes* (Cambridge U. P., Cambridge, 1986), p. 550

[14] T. F. Bell, Phys. Fluids 8, 1829 (1965)

[15] K. B. Dysthe, J. Geophys. Res. 76, 6915 (1971)

THE SUBSTORM ONSET AND MAGNETOSPHERE-IONOSPHERE COUPLING

P. L. Rothwell
Geophysics Laboratory, Hanscom AFB, Bedford, MA 01731

M. B. Silevitch
Center for Electromagnetics Research,
Northeastern University, Boston , MA 02115

L. P. Block and C.- G. Fälthammar
The Royal Institute of Technology, S 100 44, Stockholm 70, Sweden

ABSTRACT

We have developed a model describing the structure of a pre-breakup arc based on an ionospheric Cowling channel and its extension into the magnetosphere. A coupled two-circuit representation of the substorm current wedge is used which is locally superimposed on both westward and eastward electrojets. We find that brighter, more unstable pre-breakup arcs are formed in the premidnight (southwest of the Harang Discontinuity) than in the post-midnight (northeast of the Harang Discontinuity) sector. This contributes to the observed prevalence of auroral activity in the premidnight sector. Also, our model predicts that the north-south dimensions of the current wedge in the ionosphere should vary from a few kilometers at an invariant latitude (Λ) of 62° to hundreds of kilometers above $\Lambda = 68°$. Comparison of the model results with the extensive observations of Marklund *et al.* [1] for a specific pre-breakup arc shows good agreement, particularly for the magnitude of the polarization electric field and the arc size.

I. INTRODUCTION

Substorm breakup, as theoretically defined, marks the onset of a substorm's expansion phase. According to Rostoker *et al.* [2] there must be a minumurn of one auroral breakup before an event can qualify as a substorm. Substorm breakup, as observationally defined, is the sudden brightening of a previously quiescent auroral arc near local midnight. Once it is "triggered" the arc dynamics is characterized by a rapid poleward and east-west expansion (Akasofu [3]; Tanskanen *et al.* [4]; and Hallinan [5]; Shepherd *et al.* [6]). Other key features of auroral breakup are: (1) Breakup occurs predominantly west of the Harang Discontinuity (HD) in the pre-midnight sector (Heppner [7], Akasofu [3], Craven and Frank, [8]. where it can occur at L-values as low as 5.2 (Kremser *et al.* [9]; Kremser *et al.* [10]; Tanskanen *et al.* [4] ; Hallinan [5] ; Galperin and Feldstein [11]). (2) Breakup also occurs in a limited longitudinal sector near local midnight (Lezniak and Winckler [12], Nagai *et al.* [13]). (3) During the growth phase there is an enhancement of the polar-cap potential. Therefore, the likehood of breakup must increase as the cross-tail electric field is increased.

We assume that many of the above features are determined by the con

Scientific Publishers, Inc., Cambridge, MA 02139

ditions underwhich the pre-breakup arc is formed. That is the electrical configuration of the pre-breakup arc sets the stage for the breakup mechanism. In this paper the pre-breakup arc is treated as a local substorm current wedge [14]. As such, the east-west and north-south circuits that form the current wedge are strongly coupled both in the ionosphere and in the magnetosphere. An important complication arises from the embedding of these local wedge structures in the large-scale electrojets. It is found that the formation of a local current wedge is enhanced west of the HD and impaired east of the HD by the large-scale electrojets. It is strongly emphasized that the present model is static in nature and does not pretend to describe the full time-dependent coupling between the fields and particles that must occur when breakup is occurring.

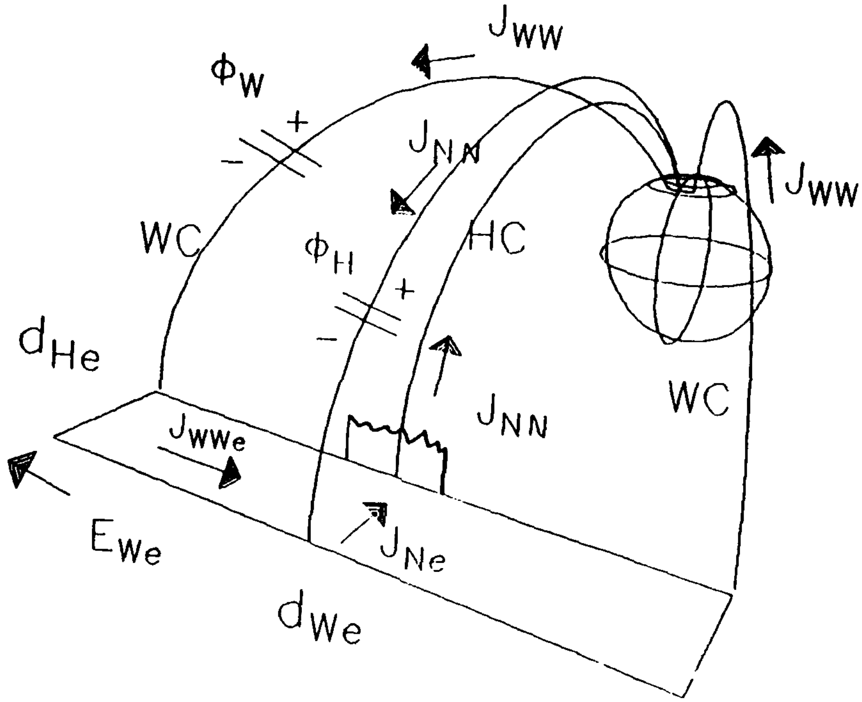

Figure 1. A three-dimensional view from the equatorial plane of the coupled circuits discussed in the text. J_{NN} is a current sheet downward on the equatorward side of the current wedge and upward on the poleward side. Note that it is closed by an earthward current in the equatorial plane. The other symbols shown in the figure are defined in the text.

Other model features are the coupling of magnetospheric plasma flows to the north-south circuit and the use of the work of Fridman and Lemaire [15] to relate the field-aligned current density to the field-aligned potential drops. If the HD as mapped to the equatorial plane bifurcates eastward and westward plasma flows (G. Erickson [16]) then the resulting asymmetry will also enhance wedge formation west of the HD.

The independent parameters in the model are the field aligned potential drop $\Phi_{//}$ in the north-south circuit (see Fig. 1) and the total east-west electric field in the equatorial plane, E_{W_e}. The field-aligned potential drop $\Phi_{//}$ can be related in a one-to-one manner to the diverted east-west current, J_{WW}. We believe that these magnetospheric parameters play a key role in determining the properties of the pre-breakup arc. In our model breakup occurs when the field-aligned potential drop along the poleward boundary is suddenly enhanced which causes an unstable poleward expansion of the wedge.

From our model we have found that (1) auroral arcs created through the formation of a wedge current system fall into either a "generator" or "load" class. The definition of generator and load arises from how the magnetospheric portion of the north-south circuit closes in the equatorial plane. Westward plasma flows produce a tailward equatorial electric field which, as seen from Fig. 1, creates a generator in the north-south circuit. Eastward plasma flows produce an earthward equatorial electric field which acts as a load on the north-south circuit. In this paper we will only treat generator-type arcs west of the HD. (2) the imposition of reasonable physical constraints on the wedge formation implies that only a restricted range of arc thicknesses are allowed at a given latitude. (See Fig. 2.) This ranges from a few kilometers at $\Lambda = 62°$ to hundreds of kilometers for latitudes greater than $\sim \Lambda = 69°$. (3) Higher values of the cross-tail electric field shifts our results to lower latitudes and allows the formation of steady-state arc structures that correspond to a DC diversion of the cross-tail current through the ionosphere. In these cases the field-aligned potential drop along the poleward boundary may exceed 30 kV consistent with the results of Kremser *et al.* [10] and Tanskanen *et al.* [4]. (4) We also found that the thickness of the pre-breakup arc is dependent on the O^+ concentration in the plasma sheet which connects our work with the results of Lennartsson and Sharp [17], Cladis [18], Chappell [19] and Burch [20] that indicate that the ionosphere seeds the inner edge of the plasma sheet with energetic O^+ during times of high magnetic activity. See Fig. 4 and Rothwell *et al.* [21] and Rothwell *et al.* [22] for details. We now refer to these earlier papers as Paper 1 and Paper 2.

The ionospheric location where breakup is observed often maps to an equatorial location substantially earthward of the expected location of a near-earth neutral line. This point has been emphasized by Block *et al.* [23] and more recently by Galperin and Feldstein [11]. In our model, therefore, breakup does not explicitly depend on the existence of a near-earth neutral line, although breakup may cause the outward propagation of an Alfvén wave which results in the formation of a near-earth neutral line. Recently, Lui *et al.* [24] have observed current interruption at L~8 without the usual signatures associated with magnetic reconnection. Lopez *et al.* [25] used two satellites to conclude that disruption of the current sheet sometimes begins near geosynchronous, and rapidly expands outward in the near-earth magnetotail. One key feature, therefore, of the present model is that it does not require the formation of a near-earth neutral line and it places the location of substorm breakup where it has been observed. See Baumjohann [26] for a recent critique of the boundary layer and neutral-line substorm models. The major difference between our breakup model and that of Kan *et al.* [27] and Kan and Akasofu [28] is that we treat the stability of a single arc structure while they examine the global effects of enhanced earthward convection.

The substorm current wedges are imbedded in the electrojets on each side of the HD. Current continuity requires the current inside the wedge to be a superposition of the diverted magnetospheric currents and the electrojets.

$$J_W = J_{W_o} + K_W \Phi_W \tag{1a}$$

$$J_N = J_{N_o} + K_H \Phi_H \tag{1b}$$

where K_W and K_H are integrated field-aligned conductances along the western and poleward boundaries, respectively. Note that Φ_W and Φ_H are the field-aligned potential drops at the westward and poleward boundaries of the current wedge. We treat Φ_H and Φ_W as spatially constant at the boundaries and zero elsewhere. Inside the wedge, however, we scale the enhanced conductivity with Φ_H using the model of Robinson *et al.* [32]. In Section II we show that this is a reasonable approximation for at least one arc and we also include the effect of the background electrojets on the electrical properties of the current wedge.

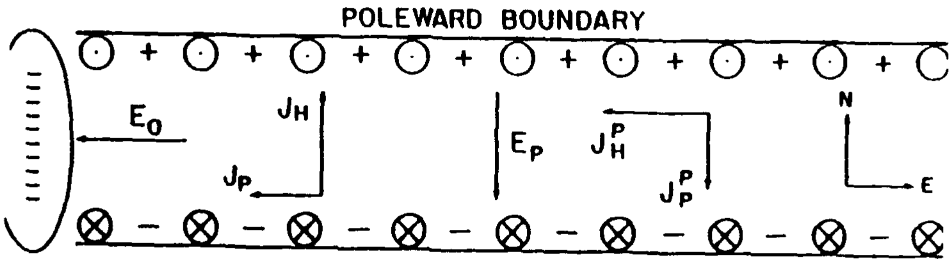

Figure 2. The substorm current wedge as seen in the ionosphere. This has been referred to as the Inhester–Baujohann model in our earlier work [21], [22]. E_o is the east-west field that drives a westward Pedersen current J_p and a poleward Hall current J_H. The polarization electric field E_p, which results from the nonequal continuation of J_H into the magnetosphere, also drives a westward Hall current and a southward Pedersen current as shown.

On the other hand, northeast of the Harang Discontinuity where the convection electric field points equatorward the reverse effect occurs which tends to inhibit the formation of the substorm current wedge. Therefore, it is easier for a current wedge to form and breakup to occur southwest rather than northeast of the Harang Discontinuity as observed by Heppner [7], Nagai [13] and others.

II. THE TWO-CIRCUIT MODEL

Let us now assume that enhanced electron precipitation has created a localized region of enhanced conductivity in the ionosphere. We now want to electrically couple this region with the magnetosphere. The extended east-west orientation of the observed breakup arc motivates an approach which models the system as two coupled circuits, one north-south and the other east-west. (Parts of this section are also in Papers 1 and 2). In our model these circuits close in the magnetosphere via magnetic-field aligned currents. The field-aligned currents, in turn, are the continuation of magnetospheric currents in the equatorial plane and are dependent on the plasma characteristics there. It is the compatibility of this earthward convection with the field-aligned currents and with the ionospheric configuration that determines where quiescent current systems can be established between the ionosphere and the magnetosphere. The associated auroral arcs are the sites of auroral breakup.

Looking at Fig. 1 we see a three-dimensional projection of the substorm current wedge circuits as seen from the magnetotail. A diverted current density J_{WW} is observed in the ionosphere in the east-west direction. This current closes in the magnetosphere through a field-aligned potential drop (Φ_W) at the western boundary of the current wedge. J_{WW_e} closes the equatorial loop in this east-west circuit which we now label WC. The diverted current is driven by the potential produced by the cross-tail electric field, E_{W_e}.

This field is mapped with corrections for field-aligned potential drops in the east-west circuit to the ionosphere as E_o in Fig. 2, which shows the ionospheric elements of the two circuits. Briefly, the westward-directed electric field, E_o, drives both a westward Pedersen current and a poleward Hall current in a highly conducting slab which is embedded in the electrojets. The lack of full continuation of the Hall current into the magnetosphere is associated with positive charges along the poleward boundary. The net poleward current density that closes in the magetosphere is labelled J_N in Fig. 1. In our model there are current sheets along the poleward and equatorward boundaries of the wedge region. Along the poleward boundary there is also a field-aligned potential drop, Φ_H. In our model the magnitude of this potential drop is critical in determining the stability of the pre-breakup arcs. We label the north-south circuit as HC. Partial closure also generates a southward pointing polarization field, E_p. This field drives a southward Pedersen current and a westward Hall current thereby creating a Cowling channel. Note that the poleward current and the southward polarization field acts as a generator for the north-south (HC) circuit. We believe that the establishment of this Cowling channel is an essential element of the breakup mechanism. The H circuit (HC) is closed by an earthward current, J_{N_e}, in the equatorial plane between the upward and downward current sheets.

One of the key elements of our model is how the HC current is closed in the magnetosphere. The north-south extent, d_H, of the ionospheric current system shown in Fig. 2 is mapped to the equatorial plane as $d_{H_e} = d_H/F_r$ where F_r is a scaling factor equal to $\Delta\Lambda/\Delta L$ where L is the McIlwain L-shell parameter. F_a is the azimuthal ionosphere-magnetosphere scaling factor which, in a dipole field, is equal to $L^{-3/2}$ [29]. F_r and F_a can easily be extended for nondipolar magnetic field models such as that of Tsyga nenko [30]. We choose a coordinate system in the equatorial plane such that x points earthward, y westward and z northward. Over the interval, d_{He}, the earthward-flowing magnetospheric closure current, J_{Ne}, causes the bulk plasma to be accelerated in the -y direction. Following the approach of Weimer *et al.* [31] we have for J_{Ne}.

$$J_{Ne} = \frac{\rho d_{\|}}{B_e{}^3}[E_{We}\frac{\partial E_{pe}}{\partial x} - E_{pe}\frac{\partial E_{pe}}{\partial y}] \tag{2}$$

where ρ is the mass density in the plasma sheet, B_e is the equatorial value of the magnetic field, $d_{\|} \sim R_{eq}/3$ is the assumed field line segment over which J_{Ne} is nonzero, and E_{pe} is the radial component of the magnetospheric electric field. For simplicity we assume that the arc is uniform in longitude so that the second term does not contribute. However, the remaining term depends on the radial gradient of E_{pe}, not on its magnitude. On the other hand, the load or generator character of the magnetospheric circuit depends on the average value and direction of E_{pe}. The exact relationship between these two quantities depends on a self-consistent solution for the arc structure. We resolve the problem here by assuming that the electric field gradient is constant. That is, the average electric field across d_{He} is some fraction of the ramp height of the gradient. In this way we can examine the coupling of the equatorial plasma flow with the wedge circuit.

III. THE EQUATIONS

In this section we give the relevant equations and a brief description of how they are solved. There are eight equations and eight unknowns.

A. Ionospheric Equations

(1)*Inside the current wedge*

$$J_W = E_o\Sigma_p + E_p\Sigma_H \tag{3}$$

$$J_N = E_o\Sigma_H - E_p\Sigma_p \tag{4}$$

(2)*Outside the current wedge*

$$J_{Wo} = E_o\Sigma_{po} + E_{po}\Sigma_{Ho} \tag{5}$$

$$J_{No} = E_o\Sigma_{Ho} - E_{po}\Sigma_{po} \tag{6}$$

The subscript "o" refers to the background values of the electric fields and conductivities just outside the current wedge. The use of E_o in both sets of equations ensures a solution consistent with a curl free electric field.

B. Current Continuity at the wedge boundaries

$$J_{WW} = J_W - J_{Wo} = K_W\Phi_W \tag{7}$$

$$J_{NN} = J_N - J_{No} = K_H\Phi_H \tag{8}$$

C. Kirchhoff's Law in the East-West Circuit

$$\frac{\Phi_W}{d_W} = [\frac{E_{We}}{F_n} - E_o] \tag{9}$$

where Φ_W is the field-aligned potential drop along the western boundary and E_{We} is the cross-tail electric field ~ 1 mv/m. $d_W \sim 1000km$.

Define: $\delta\Sigma_H = \Sigma_H - \Sigma_{Ho}, \delta\Sigma_p = \Sigma_p - \Sigma_{po}, R \equiv \Sigma_H/\Sigma_p, \Sigma_H = \Sigma_H(\Phi_H), \Sigma_p = \Sigma_p(\Phi_H)$ Robinson *et al.*[32]. ($\delta\Sigma_H$ and $\delta\Sigma_p$ are finite here.) The above equations can be solved for E_o as a function of Φ_H

$$E_o = \frac{K_W d_W E_{We}/F_a + RK_H\Phi_H - E_{po}[R\Sigma_{po} - \Sigma_{Ho}]}{[\delta\Sigma_p + R\delta\Sigma_H + K_W d_W]} \quad (10)$$

D. Inputs: $\Phi_H, E_{We}, E_{po}, \Sigma_{Ho}, \Sigma_{po}$

E. Fixed parameters: $L_H, L_W, T_{e\perp}, T_{e\parallel}, n_e$. The first two parameters are the spatial extent of the current closure along the poleward and western wedge boundaries, respectively. The next three parameters are the electron temperature and density. These are inputs to the Fridman and Lemaire [15] relation that relates the field-aligned potential drop to the field-aligned current density. The ratio of these latter two quantities gives the field-aligned conductivity k_H. Note that $K_H = k_H L_H$. k_W is fixed at 3×10^{-9} S/m^2. The last three parameters are the electron temperature and density. These are inputs to Fridman and Lemaire [15] relation that relates the field-aligned potential drop to the field-aligned current.

F. Outputs: $E_o, E_p, J_{NN} \equiv K_H\Phi_H, J_{WW}, \Phi_W$

G. Magnetospheric Equations.

(1) *North-South Circuit*

Kirchhoff's Law

$$< \Delta E_{pe} > = F_r[\Delta E_p - \frac{\Phi_H}{d_H}] \quad (11)$$

where

$$\Delta E_p = E_p - E_{po} \quad (12)$$

and $< \Delta E_{pe} >$ is the average value of the perturbed radial magnetospheric electric field across the arc. The earthward radial current in the magnetosphere is approximated from the results of [31] as discussed above.

$$J_{Ne} = K_m \frac{\partial E_{pe}}{\partial x} \sim K_m \frac{\delta E_{pe}}{d_{He}} \quad (13)$$

where

$$K_m = \frac{\rho d_\parallel E_{We}}{B_e^3} \quad (14)$$

Note that we have approximated the magnetospheric electric field by a ramp-like behavior which corresponds to a spatially constant polarization current, J_{Ne}. The value of $< \Delta E_{pe} >$ is assumed proportional to the height of the ramp δE_{pe} by some constant γ where $0 \leq |\gamma| \leq 0.5$. As mentioned above, the precise value of γ can be ascertained only by understanding the spatial structure of the auroral arc and the details of its coupling to the background plasma flows in the equatorial plane.

Current continuitv requires

$$J_{Ne} = F_a K_H \Phi_H \quad (15)$$

Combining equations(11), (13) and (15) we find a quadratic expression for d_H.

$$a_2 d_H^2 + a_1 d_H + a_o = 0 \quad (16)$$

373

where

$$a_o = -F_r{}^2 K_m \Phi_H \tag{17}$$

$$a_1 = F_r{}^2 K_m \Delta E_p$$

$$a_2 = F_a K_H \Phi_H \gamma$$

We find that a positive root for d_H only exists when γ is negative. We choose γ = -0.5. This corresponds to a tailward directed ΔE_{pe} since δE_{pe} is always positive for an earthward closure current, J_{Ne}. This is a generator configuration and kinetic energy is being converted from the background plasma flows.

(1) ***Inputs:*** $\Phi_H, \Delta E_p, E_{We}$

(2) ***Fixed parameters:*** $F_r, F_a, K_H, \gamma, \rho, B_e, d_{\parallel}$

(3) ***Outputs:*** $d_H, < \Delta E_{pe} >, J_{Ne}$

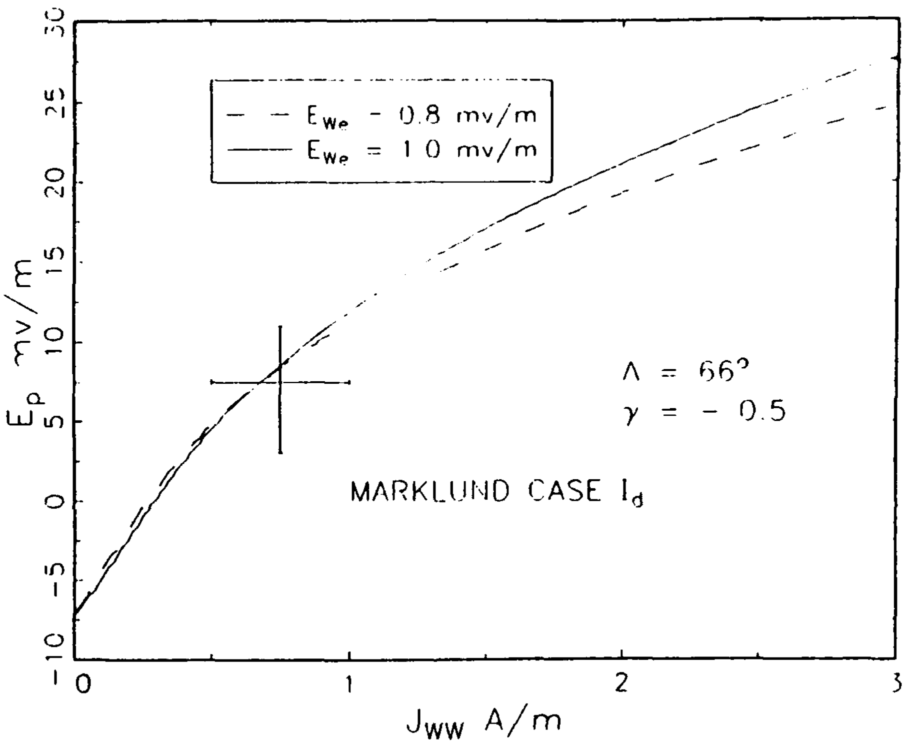

Figure 3. Comparison of the present model with the observations of Marklund *et al.* [1]. E_p refers to the polarization field shown in Fig. 2. There are two values of the cross-tail electric field as this quantity is difficult to estimate from the data [1].

IV. RESULTS

We will now compare our model with a specific pre-breakup arc as measured by Marklund *et al.* [1] and is classified as I_d in the nomenclature defined in [33]. The Substorm-GEOS rocket was launched at 21.01.59 UT on 27 January, 1979 from ESRANGE, Kiruna, Sweden ($\Lambda = 66°$) near local midnight on January 27, 1979 shortly after the onset of an intense magnetospheric substorm over northern Scandinavia. The obtained data represents a comprehensive data set of the arc's electric field profile in both the east-west and north-south directions as well as the spectra and flux of the precipitating electrons. Although this data is for an arc presumably undergoing breakup we compare the experimental results with the static model developed here and find good agreement. Model inputs are $E_{We} = 0.8, 1.0$ mv/m , $E_{pe} = -5$ mv/m, $\Sigma_{He} = 16$ S, $\Sigma_{pe} = 10$ S as taken from Marklund *et al.* [1]. The mapping factors are calculated using the 1987 model of Tsyganenko [30]. B_e and $d_\parallel$ are fixed by

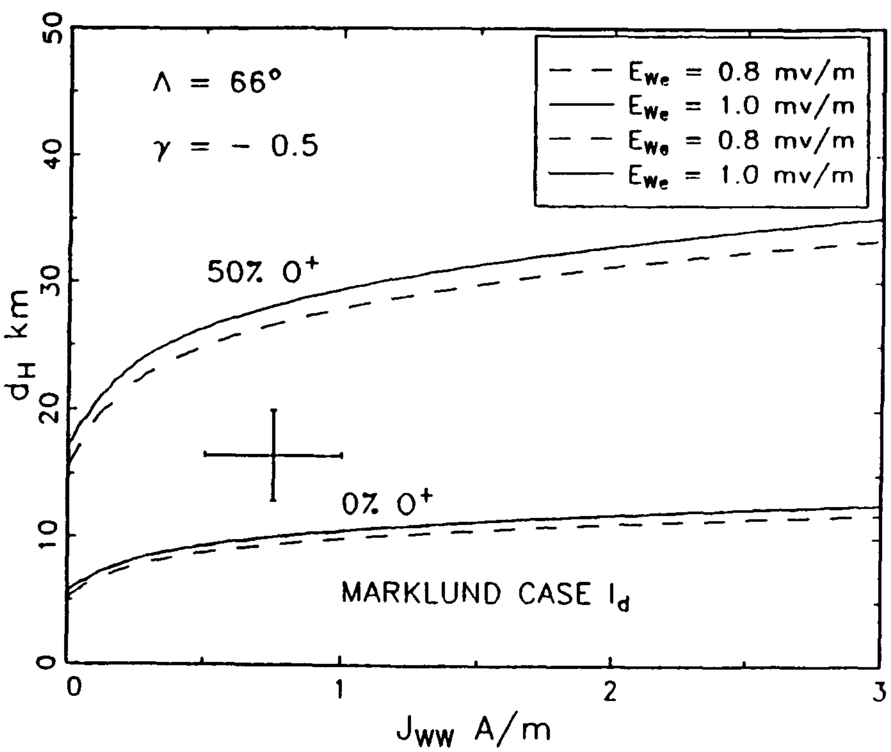

Figure 4. One of the more interesting features of our model is the capability to calculate the arc thickness. Four calculations were made for various cross-tail electric fields and ion mass densities. (The number density is maintained at 1 ion per cc.). It is seen that the Marklund *et al.*'s [1] data is well bracketed by an assumption of 0 and 50 per cent for the O^+ concentration. A potential utilization of such a model is to estimate magnetospheric quantities using ionospheric measurements.

the choice of Λ and the discussion above. $K_H = L_H k_H$ is determined setting L_H, the size of the conductivity gradient along the poleward boundary, to 20 km and by using the results of Fridman and Lemaire [15] to determine the field-aligned conductivity. γ = -0.5. Fig. 3 shows excellent agreement for the polarization electric field inside the arc. Fig. 4 shows the model results for d_H, the north-south extent of the arc in the ionosphere as determined from equation (16). The The error bars are taken from Fig. 8 of Marklund *et al.* 's [1] data. The number density in the plasma sheet is taken as 1 ion (electron) per cc. The uncertainty in E_{W_e}, the cross-tail electric field, is due to the spatial variations in E_y as shown in the same work [1]. It is seen that the experimental results are well bracketed by a plasma sheet mass density that

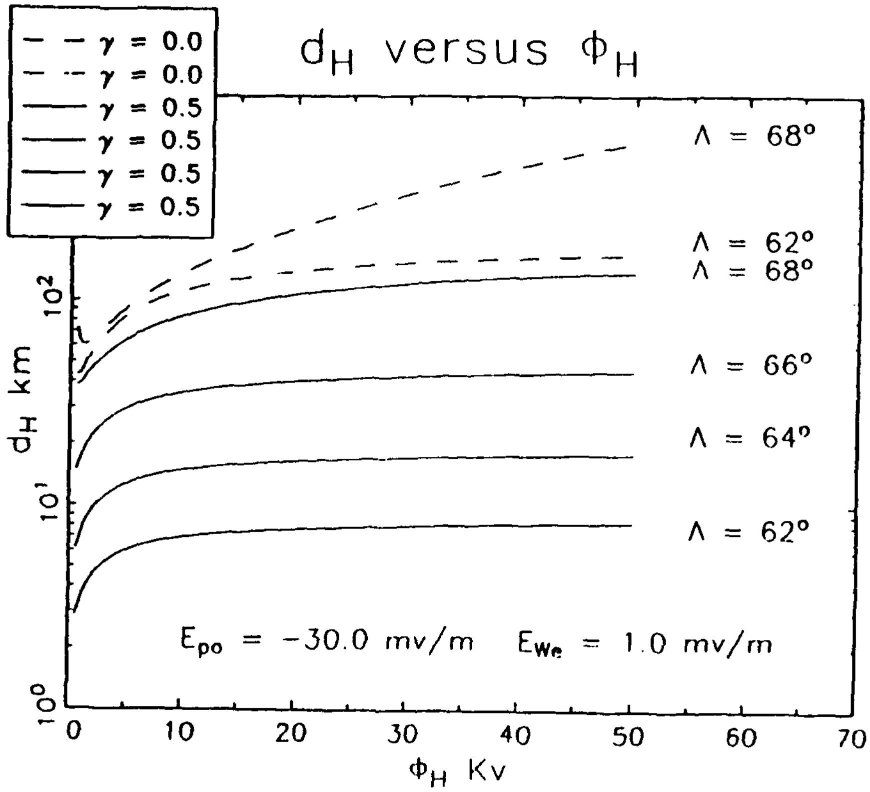

Figure 5. The wedge thickness as a function of the field-aligned potential drop along the poleward boundary for several magnetic latitudes. Note that in the steady-state model as presented here d_H has an upper limit at a given magnetic latitude. These calculations were made for a background electric field consistent with being west of the HD. The γ = 0 solutions correspond to no coupling between the background plasma flows and the north-south circuit. γ = -0.5 corresponds to maximum coupling. See text.

is between 0 and 50 per cent in O^+ concentration. Fig. 5 shows a graph of d_H versus Φ_H for several values of Λ . Note that if there is no coupling with the plasma flows in the equatorial plane (*i.e.* $\gamma = 0$) then thinner arc structures cannot form. It is only when such a coupling exists that thin arcs can form . Note that there is an upper limit to d_H for each value of Λ which indicates that thinner wedges tend to form at lower latitudes.

V. CONCLUSIONS

We have shown that pre-breakup arcs can be represented by two coupled circuits between the ionosphere and the magnetosphere similar to the current wedge configuration proposed by [14]. The formation of such a current system is strongly influenced by the presence of background electrojets in the ionosphere and directed plasma flows in the magnetosphere. A comparison with the measurements of Marklund *et al.* [1] for a specific pre-breakup arc shows excellent agreement. The present model highlights the interdependence between ionospheric and magnetospheric quantities and suggests that by measuring one set that one could inply values for the other. For example, the above application of the the model to Marklund *et al.*'s observations imply a tailward magnetospheric electric field of -0.9-(-1.6) mv/m which is in excellent agreement with the in situ measurement of [4] during another breakup event.

REFERENCES

[1] G. Marklund , W. Baumjohann, and I. Sandahl, Planet. Spac. Sci. **31**, 207 (1983).

[2] G. Rostoker, S.-I. Akasofu, W. Baumjohann, Y. Kamide, and R. L. McPherron, Space Sci. Revs. **46**, 93 (1987).

[3] S. - I. Akasofu, Space Sci. Rev. **16**, 617 (1974).

[4] P. Tanskanen, J. Kangas, L. Block, G. Kremser, A. Korth, J. Woch, I.B. Iversen, K. M. Torkar, W. Riedler, S. Ullaland, J. Stadsnes, K.-H. Glassmeir, J. Geophys. Res. **92**, 7443 (1987).

[5] Thomas J. Hallinan, EOS, **68**, 1420 (1987).

[6] G. G. Shepherd, C. D. Anger, J. S. Murphee, and A. Vallance Jones, Geophys. Res. Lett. **14**, 395 (1987).

[7] James P. Heppner, (Ph. D. thesis), Defence Research Board of Canada report No. DR 135 (1958).

[8] J. D. Craven, L. A. Frank, and S.-I. Akasofu, J. Geophys. Res. **94**, 6961 (1989).

[9] G. Kremser, J. Bjordal, L. Block, K. Bronstad, M. Håvåg, I. B.Iversen, J. Kangas, A. Korth, M. M. Madsen, J. Niskanen, W. Riedler, J. Stadsnes, P. Tanskanen, K. M. Torkar, and S. L. Ullaland, J. Geophys. Res. **87**, 4445, (1982).

[10] G. Kremser, A. Korth, S. Ullaland, J. Stadnes, W. Baumjohann, L. Block, K. M. Torkar, W. Riedler, B. Aparicio, P. Tanskanen, I. B. Iversen, N. Corncilleau-Wehrlin, J. Solomon, and E. Amata, J. Geophys. Res. **91**, 5711 (1986).

[11] Yu. Galperin, and Ya. Feldstein, in *Proceedings, Auroral Physics Conference, St. Johns College, Cambridge, England , July 11-15, 1988* in press.

[12] T. W. Lezniak, and J. R. Winckler, J. Geophys. Res. **75**, 7075 (1970).
[13] T. Nagai, D. N. Baker, and P. R. Higbie, J. Geophys. Res. **88**, 6994 (1983).
[14] R. L. McPherron, C. T. Russell, and M. P. Aubrey, J. Geophys. Res. **78**, 3131, (1973).
[15] M. Fridman, and J. Lemaire, J. Geophys. Res. **85**, 664 (1980).
[16] Gary Erickson, private communicationm, 1990.
[17] W. Lennartsson, and R. D. Sharp, Adv. Spac. Res. **5**, 411 (1985).
[18] J. B. Cladis, Geophys. Res. Ltrs. **13**, 893 (1986).
[19] Charles L. Chappell, Revs. of Geophys. **26**, 229 (1988).
[20] J. L. Burch, J. of Geophys. **26**, 215 (1988).
[21] P. L. Rothwell, L. P. Block, M. B. Silevitch, and C.-G. Fälthammar, Geophys. Res. Lett. **15**, 1279 (1988).
[22] Paul L. Rothwell, Lars P. Block, Michael B. Silevitch, and Carl-Gunne Fälthammar, *IEEE Trans. on Plasma Science***17**, (1989).
[23] Lars P. Block, Paul L. Rothwell, and Michael B. Silevitch, EOS **67** , 1178 (1986).
[24] A. T. Y. Lui, R. E. Lopez, S. M. Krimigis, R. W. McEntire, L. J. Zanetti, and T. A. Potemra, Geophys. Res. Lett. **15**, 721 (1988).
[25] R. E. Lopez, D. G. Sibeck, R. W. McIntire, and S. M. Krimigis, J. Geophys. Res. **95**, 109 (1990).
[26] Wolfgang Baumjohann, J. Geomag. Geoelectr. **40**, 157 (1988).
[27] J. R. Kan, L. Zhu, and S.-I. Akasofu, J. Geophys. Res. **93** , 5624 (1988).
[28] J. R. Kan, and Syun-Ichi Akasofu, *IEEE Trans. on Plasma Science* **17**, 83 (1989).
[29] W. Lotko, B. U. Ö. Sonnerup, and R. L. Lysak, J. Geophys. Res. **92**, 8635 (1987).
[30] N. A. Tsyganenko, Global quantitative models of the geomagnetic field in the Planet. and Space Sci. **35**, 1347 (1987).
[31] D. R. Weimer, N. C. Maynard, W. J. Burke, and M. Sugiura, J. Geophys. Res. **93**, 11436 (1988).
[32] R. M. Robinson, R. R. Vondrak, K. Miller, T. Dabbs and D. Hardy, J. Geophys. Res. **92**, 2565 (1987).
[33] Göran Marklund, Planet. Space Sci **32**, 193 (1984).

JOURNAL OF GEOPHYSICAL RESEARCH, VOL. 96, NO. A8, PAGES 13,967-13,975, AUGUST 1, 1991

Prebreakup Arcs: A Comparison Between Theory and Experiment

P. L. ROTHWELL

Geophysics Directorate, Phillips Laboratory, Hanscom Air Force Base, Bedford, Massachusetts

M. B. SILEVITCH

Center for Electromagnetics Research, Northeastern University, Boston, Massachusetts

L. P. BLOCK AND C.-G. FÄLTHAMMAR

The Royal Institute of Technology, Stockholm, Sweden

We have developed a model describing the structure of a prebreakup arc based on an ionospheric Cowling channel and its extension into the magnetosphere. A coupled two-circuit representation of the substorm current wedge is used which is locally superimposed on both westward and eastward electrojets. We find that brighter, more unstable prebreakup arcs are formed in the premidnight (southwest of the Harang Discontinuity) than in the postmidnight (northeast of the Harang Discontinuity) sector. This contributes to the observed prevalence of auroral activity in the premidnight sector. Also, our model predicts that the north-south dimensions of the current wedge in the ionosphere should vary from a few kilometers at an invariant latitude (Λ) of 62° to hundreds of kilometers above Λ = 68°. Comparison of the model results with the extensive observations of Marklund et al. (1983) for a specific arc observed just after onset shows good agreement, particularly for the magnitude of the polarization electric field and the arc size. We conclude that this agreement is further evidence that the substorm breakup arises from magnetosphere-ionosphere coupling in the near magnetosphere and that the steady state model developed here is descriptive of the breakup arc before inductive effects become dominant.

1. INTRODUCTION

Substorm breakup, as theoretically defined, marks the onset of a substorm's expansion phase. According to *Rostoker et al.* [1987] there must be a minimum of one auroral breakup before an event can qualify as a substorm. Substorm breakup, as observationally defined, is the sudden brightening of a previously quiescent auroral arc near local midnight. Once it is "triggered", the arc dynamics is characterized by a rapid poleward and east-west expansion [*Akasofu*, 1974; *Tanskanen et al.*, 1987; *Hallinan*, 1987; *Shepherd et al.*, 1987]. Other key features of auroral breakup are as follows: (1) Breakup occurs predominantly west of the Harang Discontinuity (HD) in the premidnight sector [*Heppner*, 1958; *Akasofu*, 1974; *Craven et al.*, 1989], where it can occur at L values as low as 5.2 [*Kremser et al.* 1982, 1986; *Tanskanen et al.*, 1987; *Hallinan*, 1987; *Galperin and Feldstein*, 1991]. (2) Breakup also occurs in a limited longitudinal sector near local midnight [*Lezniak and Winckler*, 1970; *Nagai et al.*, 1983]. (3) During the growth phase there is an enhancement of the polar cap potential. Therefore the likelihood of breakup must increase as the cross-tail electric field is increased.

We assume that many of the above features are determined by the conditions under which the prebreakup arc is formed; That is, the electrical configuration of the prebreakup arc sets the stage for the breakup mechanism. In this paper the prebreakup arc is treated as a local substorm current wedge [*McPherron et al.*, 1973]. As such, the east-west and north-south circuits that form the current wedge are strongly coupled both in the ionosphere and in the magnetosphere. An important complication arises from the embedding of these local wedge structures in the large-scale electrojets. It is found that the formation of a local current wedge is more favorable west of the HD due to the presence of the large-scale electrojets. It is strongly emphasized that the present model is static in nature and does not pretend to describe the full time-dependent coupling between the fields and particles that must occur when breakup is occurring.

Other model features are the coupling of magnetospheric plasma flows to the north-south circuit and the use of the *Fridman and Lemaire* [1980] formula to relate the field-aligned current density to the field-aligned potential drops. If the HD as mapped to the equatorial plane delineates a region of enhanced westward plasma flows [*Erickson et al.*, 1991], then the resulting asymmetry will also enhance wedge formation west of the HD.

The independent parameters in the model are the field-aligned potential drop Φ_c in the north-south circuit (see Figure 1) and the total east-west electric field in the equatorial plane, E_{ye}. The field-aligned potential drop Φ_c can be related in a one-to-one manner to the diverted east-west current J_y. We believe that these magnetospheric parameters play a key role in determining the properties of the prebreakup arc. In our model, breakup occurs when the field-aligned potential drop along the poleward boundary is suddenly enhanced; this causes an unstable poleward expansion of the wedge. From our model we have found that (1) auroral arcs created through the formation of a wedge current system fall into either a "generator" or "load" class. The definition of generator and load arises from how

Paper number 91JA01268.
0148-0227/91/91JA-01268$05.00

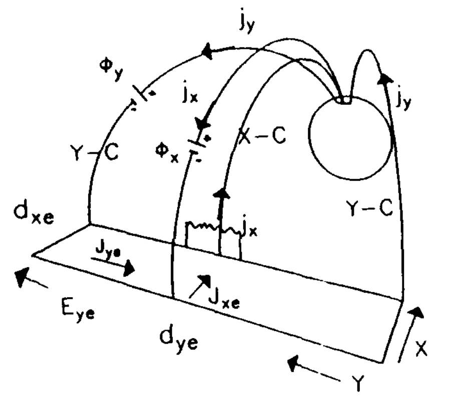

Fig. 1. A three-dimensional view from the equatorial plane of the coupled circuits discussed in the text. J_y is downward current on the eastern edge and an upward current on the western edge. J_x is a current sheet downward on the equatorward side of the current wedge and upward on the poleward side. Note that it is closed by an earthward current in the equatorial plane. Φ_y and Φ_x represent field-aligned potential drops along the western and poleward boundaries, respectively. The other symbols shown in the figure are defined in the text. The coordinate system is such that x is toward the Earth and y points duskward (westward).

the magnetospheric portion of the north-south circuit closes in the equatorial plane. Westward plasma flows produce a tailward equatorial electric field which, as seen from Figure 1, creates a generator in the north-south circuit. Eastward plasma flows produce an earthward equatorial electric field which acts as a load on the north-south circuit. In this paper we will treat only generator-type arcs west of the HD. (2) The imposition of reasonable physical constraints on the wedge formation implies that only a restricted range of arc thicknesses are allowed at a given latitude (see Figure 12). This ranges from a few kilometers at $\Lambda = 62°$ to hundreds of kilometers for latitudes greater than $\sim\Lambda = 69°$. (3) Higher values of the cross-tail electric field allows the formation at lower latitudes of steady state arc structures that correspond to a DC diversion of the cross-tail current through the ionosphere. In these cases the field-aligned potential drop along the poleward boundary may exceed 30 kV which is consistent with the values observed in the preonset precipitation front by *Kremser et al.* [1986] and *Tanskanen et al.* [1987]. (4) We also found that the thickness of the prebreakup arc is dependent on the O^+ concentration in the plasma sheet which connects our work with the results of *Lennartsson and Sharp* [1985], *Cladis* [1986], *Chappell* [1988] and *Burch* [1988] that indicate that the ionosphere seeds the inner edge of the plasma sheet with energetic O^+ during times of high magnetic activity. See Figure 9 and *Rothwell et al.* [1988, 1989] for details. We now refer to these earlier papers as paper 1 and paper 2.

The ionospheric location where breakup is observed often maps to an equatorial location substantially earthward of the expected location of a near-Earth neutral line. This point has been emphasized by *Block et al.* [1986] and more recently by *Galperin and Feldstein* [1991]. In our model therefore breakup does not explicitly depend on the existence of a near Earth neutral line, although breakup may cause the outward propagation of an Alfven wave which results in the formation of a near-Earth neutral line. Recently, *Lui et al.* [1988] have observed current interruption at $L \sim 8$ without the usual signatures associated with magnetic reconnection. *Lopez et al.* [1990] used two satellites to conclude that disruption of the current sheet sometimes begins near geosynchronous and rapidly expands outward in the near-Earth magnetotail. One key feature therefore of the present model is that it does not require the formation of a near-Earth neutral line and it places the location of substorm breakup where it has been observed. See *Baumjohann* [1988] for a recent critique of the boundary layer and neutral-line substorm models. The major difference between our breakup model and that of *Kan et al.* [1988] and *Kan and Akasofu* [1989] is that we treat a single arc structure while they examine the global effects of enhanced earthward convection.

The substorm current wedges are modeled as being imbedded in the electrojets on each side of the HD. Current continuity requires the current inside the wedge to be a superposition of the diverted magnetospheric currents and the electrojets.

$$J_{yi} = J_{yo} + K_y \Phi_y \qquad (1a)$$

$$J_{xi} = J_{xo} + K_x \Phi_x \qquad (1b)$$

where K_y and K_x are integrated field-aligned conductances along the western and poleward boundaries, respectively. Note that Φ_y and Φ_x are the field-aligned potential drops at the westward and poleward boundaries of the current wedge. We treat Φ_x and Φ_y as spatially constant at the boundaries and zero elsewhere. Inside the wedge, however, we scale the enhanced conductivity with Φ_x using the model of *Robinson et al.* [1987]. In section 4 we show that this is a reasonable approximation for at least one arc.

2. Two-Circuit Model

Let us now assume that enhanced electron precipitation has created a localized region of enhanced conductivity in the ionosphere. We now want to electrically couple this region with the magnetosphere. The extended east-west orientation of the observed breakup arc motivates an approach that models the system as two coupled circuits, one north-south and the other east-west. (Parts of this section are also in papers 1 and 2.) In our model these circuits close in the magnetosphere via magnetic-field-aligned currents. The field-aligned currents in turn are the continuation of magnetospheric currents in the equatorial plane and are dependent on the plasma characteristics there. It is the compatibility of this earthward convection with the field-aligned currents and with the ionospheric configuration that determines where quiescent current systems can be established between the ionosphere and the magnetosphere. We believe that the associated auroral arcs are the sites of auroral breakup.

Looking at Figure 1 we see a three-dimensional projection of the substorm current wedge circuits as seen from the magnetotail. A diverted current density J_y is observed flowing through the ionosphere in the east-west direction. This current closes in the magnetosphere through a field-aligned potential drop Φ_y at the western boundary of the current wedge. J_{yi} closes the equatorial loop in this east

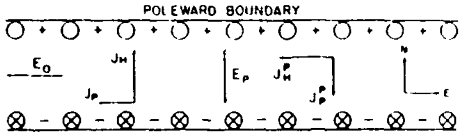

Fig. 2. The substorm current wedge of Figure 1 as seen in the ionosphere. This has been referred to as the Inhester-Baumjohann model by *Rothwell et al.* [1988, 1989]. Basically, the current density J_y shown in Figure 1 consists of a Pedersen component J_P and a Hall component J_H^P from the polarization electric field $E_p(E_x)$. The current density J_x shown in Figure 1 also consists of a Pedersen J_P^P component and a Hall component J_H. E_o is equivalent to E_y in the text.

west circuit which we now label Y-C. The diverted current is consistent with the potential produced by the cross-tail electric field E_{ye}. (We choose a coordinate system in the equatorial plane such that x points earthward, y points westward, and z is parallel to B. In the ionosphere the corresponding x coordinate points equatorward. An additional "e" subscript denotes a magnetospheric quantity.)

This field is mapped with corrections for field-aligned potential drops in the east-west circuit to the ionosphere as $E_o(E_y)$ in Figure 2. This figure shows the ionospheric elements of the two circuits. Briefly, the westward directed electric field E_y drives both a westward Pedersen current J_p and a poleward Hall current J_H in a highly conducting slab which is embedded in the electrojets. The lack of full continuation of the Hall current into the magnetosphere is associated with positive charges along the poleward boundary. The net poleward current density that closes in the magnetosphere is labeled J_x in Figure 1. In our model there are current sheets along the poleward and equatorward boundaries of the wedge region. Along the poleward boundary there is also a field-aligned potential drop, Φ_x. The magnitude of this potential drop is critical in determining the stability of the prebreakup arcs. We label the north-south circuit as X-C. Partial closure also generates a southward pointing polarization field, $E_x(E_p)$ in the ionosphere. This electric field drives a southward Pedersen current (J_P^P) and a westward Hall current (J_H^P) thereby creating a Cowling channel as shown in Figure 2. Note that the poleward current and the southward polarization field act as a generator for the north-south (X-C) circuit. We believe that the establishment of this Cowling channel is an essential element of the breakup mechanism. The north-south circuit (X-C) is closed by an earthward current J_{xe} in the equatorial plane between the upward and downward current sheets. We assume here that J_{xe} is purely an inertia current while the total westward magnetospheric current is consistent with an earthward pressure gradient. The first assumption may be modified as the present model is incorporated into more global models. The second assumption follows from our treatment of a quasi-stationary structure.

One of the key elements of our model is how the X-C current is closed in the magnetosphere. The north-south extent, d_x, of the ionospheric current system shown in Figure 2 is mapped to the equatorial plane as $d_{xe} = d_x/F_x$, where F_x is a scaling factor equal to $\Delta\Lambda/\Delta L$ (L is the McIlwain L shell parameter and Λ is the corresponding invariant latitude). F_y is the azimuthal ionosphere-magnetosphere scaling factor which, in a dipole field, is equal to $L^{-3/2}$ [*Lotko et al.*, 1987]. F_x and F_y can easily be extended for nondipolar magnetic field models such as that of *Tsyganenko* [1987]. We use the *Tsyganenko* [1987] model in section 4. Over the interval d_{xe} the earthward flowing magnetospheric closure current J_{xe} causes the bulk plasma to be accelerated in the $-y$ direction. This means that westward flowing plasma will be decelerated while eastward flowing plasma will be accelerated. Therefore in a region of westward flowing plasma we expect a generator-type circuit, while in the region of eastward flowing plasma we expect a load-type circuit.

The magnetospheric inertia current [*Weimer et al.*, 1988] is given by

$$J_{xe} = \frac{\rho d_\parallel}{B_e^3}\left(E_{ye}\frac{\partial E_{xe}}{\partial x} - E_{xe}\frac{\partial E_{ye}}{\partial y}\right) \tag{2}$$

where ρ is the mass density in the plasma sheet, B_e is the equatorial value of the magnetic field, $d_\parallel$ $R_{eq}/3$ is the assumed field line segment over which J_{xe} is nonzero, and E_{xe} is the radial component of the magnetospheric electric field. For simplicity we assume that the arc is uniform in longitude so that the second term does not contribute. However, the remaining term depends on the radial gradient of E_{xe}, not on its magnitude. On the other hand, the load or generator character of the magnetospheric circuit depends on the average value and direction of E_{ye}. We must look therefore outside our present model for the appropriate electric field gradient. This term could arise, for example, from a more detailed self-consistent solution for auroral arc structure. We resolve the problem below by assuming that the electric field gradient is constant; that is, the average perturbed electric field across d_{xe} is taken as some fraction of the ramp height of the gradient. In this way we approximate the coupling of the equatorial plasma flow with the wedge circuit which can be compared with experimental data. Note that one cannot approximate (2) with an ohmic relation. The reason is that there must be current across d_{xe} even when E_{xe} is zero. That is the case when $\Phi_x = E_x d_x$.

3. EQUATIONS

In this section we give the relevant equations and a brief description of how they are solved.

Ionospheric Equations

Inside the current wedge

$$J_{xt} = E_x\Sigma_p + E_y\Sigma_H \tag{3}$$

$$J_{yt} = E_y\Sigma_H - E_x\Sigma_p \tag{4}$$

Outside the current wedge

$$J_{yo} = E_y\Sigma_{po} + E_{po}\Sigma_{Ho} \tag{5}$$

$$J_{xo} = E_y\Sigma_{Ho} - E_{po}\Sigma_{po} \tag{6}$$

The subscript "o" refers to background quantities outside the current wedge, and the subscript "t" denotes the total ionospheric currents inside the wedge. The use of E_y in both sets of equations is consistent with a curl free electric field. Note that E_y does not equal the mapped value of E_{ye} to the ionosphere except in the limit that the Φ_y vanishes. We make the not very radical assumption that nature finds a way to configure the electric fields so that Faraday's Law is obeyed. A full treatment of this problem which entails negative charge buildup at the western boundary of the wedge is beyond the scope of this paper.

Current continuity at the wedge boundaries.

$$J_y = J_{yi} - J_{yo} = K_y \Phi_y \qquad (7)$$

$$J_x = J_{xi} - J_{xo} = K_x \Phi_x \qquad (8)$$

Kirchhoff's Law in the east-west circuit.

$$\frac{\Phi_y}{d_y} = \left(\frac{E_{ye}}{F_y} - E_y\right) \qquad (9)$$

where Φ_y is the field-aligned potential drop along the western boundary and E_{ye} is the cross-tail electric field, ~ 1-2 mv/m [*Fälthammar*, 1989*a*, *b*]; d_y ~ 1000 km.

Definitions. We define $\delta\Sigma_H = \Sigma_H - \Sigma_{Ho}$, $\delta\Sigma_P = \Sigma_P - \Sigma_{Po}$, $R \equiv \Sigma_H/\Sigma_P$, $\Sigma_H = \Sigma_H(\Phi_x)$, and $\Sigma_P = \Sigma_P(\Phi_x)$ using the model of *Robinson et al.* [1987]. Note that these are finite differences. The above equations can be solved for E_y and E_x as a function of Φ_x, where

$$E_y = \frac{K_y d_y E_{ye}/F_y + R K_x \Phi_x - E_{po}(R\Sigma_{po} - \Sigma_{Ho})}{(\delta\Sigma_P + R\delta\Sigma_H + K_y d_y)} \qquad (10)$$

and E_x is easily obtained by substitution.

Inputs. The inputs for the ionospheric equations are Φ_x, the field-aligned potential drop along the poleward boundary; E_{ye}, the cross-tail electric field; E_{po}, the north-south electric field component outside the current wedge; and Σ_{Ho} and Σ_{Po}, the Hall and Pedersen conductivities outside the current wedge.

Fixed parameters. The fixed parameters are L_x, L_y, $T_{e\perp}$, $T_{e\parallel}$, n_e, d_y, and F_y. The first two parameters are the spatial extent of the current closure along the poleward and western wedge boundaries, respectively. The next three parameters are the plasma sheet electron temperature and density. These are inputs to *Fridman and Lemaire* [1980] relation that relates the field-aligned potential drop to the field-aligned current density. The ratio of these latter two quantities gives the field-aligned conductivity k_e. Note that $K_x = k_x L_x$ and $K_y = k_y L_y$ are the integrated field-aligned conductivities (siemens per meter). k_y is fixed at 3×10^{-9} S/m^2. The *Fridman and Lemaire* [1980] relation allows one to estimate the energy flux of the precipitation which is then inputted into the *Robinson et al.* [1987] model for the ionospheric conductivities. Figure 3 shows a sample calculation and a comparison with experimental data.

Outputs. The outputs are E_y, the ionospheric east-west electric field component inside the wedge; E_x, the ionospheric north-south polarization electric field inside the wedge; $J_x \equiv K_x \Phi_x$, the net poleward current density inside the wedge; J_y, the net westward current density (in amperes per meter) inside the wedge; and Φ_y, the field-aligned potential drop along the western boundary of the current wedge.

Magnetospheric Equations

North-south circuit. Kirchhoff's Law is

$$\langle \Delta E_{xe} \rangle = F_x\left[\Delta E_x - \frac{\Phi_x}{d_x}\right] \qquad (11)$$

where

$$\Delta E_x = E_x - E_{po} \qquad (12)$$

and $\langle \Delta E_{xe} \rangle$ is the average value of the perturbed radial magnetospheric electric field across the arc. The earthward radial current in the magnetosphere is approximated from (2) as discussed above.

$$J_{xe} = K_m \frac{\partial E_{xe}}{\partial x} \sim K_m \frac{\delta E_{xe}}{d_{xe}} \qquad (13)$$

where

$$K_m = \frac{\rho d_\parallel E_{xe}}{B_e^3} \qquad (14)$$

Note that we have approximated the magnetospheric electric field by a ramplike behavior which corresponds to a spatially constant inertia current J_{xe}. The value of $\langle \Delta E_{xe} \rangle$ is assumed proportional to the height of the ramp δE_{xe} by some constant γ where $0 \le |\gamma| \le 0.5$. As was mentioned above, the precise value of γ can be ascertained only by understanding the spatial structure of the auroral arc and the details of its coupling to the background plasma flows in the equatorial plane. Here we assume $|\gamma| = 0.5$ which is consistent with the assumption of a ramplike behavior for E_{xe}.

Current continuity requires

$$J_{xe} = F_x K_x \Phi_x \qquad (15)$$

Combining equations (11), (13), and (15) we find a quadratic expression for d_x.

$$a_2 d_x^2 + a_1 d_x + a_o = 0 \qquad (16)$$

where

$$a_o = F_x^2 K_m \Phi_x$$

$$a_1 = -F_x^2 K_m \Delta E_x \qquad (17)$$

$$a_2 = F_x K_x \Phi_x \gamma$$

The requirement that (16) has only real roots implies

$$\Phi_x^2 \gamma \le \frac{F_x^2 K_m (\Delta E_x)^2}{4 F_x K_x} \equiv \Gamma_t \qquad (18)$$

Using the *Tsyganenko* [1987] model at $\Lambda = 66°$ we find that $\Gamma_t \sim 10^4$. For positive values of γ, which correspond to a "load-type" perturbation, Φ_x can take on only small values (<<1 kV at $\Lambda = 66°$). Values a kilovolt or higher can only be obtained at higher latitudes ($\Lambda \ge 70°$). In order to obtain the higher values of Φ_x that are observed at lower latitudes, γ must be negative. This corresponds to a tailward directed ΔE_{xe} since δE_{xe} is always positive for the earthward closure current J_{xe}. This is a generator configuration, and kinetic energy is being converted from the background plasma flows. The background convection electric field enhances the "generator-type" properties of the arc west of the HD and the "load-type" properties east of the HD. Figure 12 shows a model calculation of d_x versus Φ_x at different invariant latitudes west of the HD. Note that only generator type values of γ allow the formation of narrow wedge structures at lower latitudes. This is where breakup is often observed.

West of the HD the ambient tailward electric field adds to the tailward perturbation. This enhances the generator nature of the X-C in the equatorial plane. East of the HD the opposite is true. There the ambient earthward electric field tends to negate the tailward perturbation and the equatorial "generator" either is weakened or becomes a "load". Therefore, since we believe that the explosive nature of the breakup arc arises from the X-C generator in the equatorial plane, breakup is more likely west of the HD.

Inputs. The inputs for the magnetospheric equations are the field-aligned potential drop along the poleward boundary; ΔE_x, the enhancement of the north-south component of the electric field above background (E_{x0}); and E_{yc}, the cross-tail electric field.

Fixed parameters. The fixed parameters are F_x, F_y, mapping factors between the ionosphere and the magnetosphere in the north-south and east-west directions, respectively; K, (in siemens per meter), the field-aligned conductivity integrated over the poleward boundary; γ, the parameter that couples the north-south circuit to equatorial plasma flows; ρ, the mass density in the plasma sheet; B_e, equatorial value of the magnetic field; and $d_\parallel$, the distance over which the cross-tail current is integrated.

Outputs. The outputs are d_x, the north-south extent of the current wedge in the ionosphere; (ΔE_{xe}), the perturbation of the radial component of the equatorial electric field inside the wedge region; and J_{xe}, the equatorial earthward current that closes the north-south circuit.

Summary of model assumptions. The model is summarized as follows:

1. A prebreakup auroral arc may be reasonably represented by a current wedge. A two-dimensional rectangular shape in the ionosphere is adequate for a first approximation.

2. The radial electric field in the magnetosphere must be nonconstant (equation (2)) in order to properly close the current in the north-south circuit. A linear ramp is assumed adequate for a first approximation. See (13) and subsequent discussion.

3. Reasonable estimates may be made of the fixed parameters labeled above.

4. RESULTS

We will now compare our model with a specific prebreakup arc as measured by *Marklund et al.* [1983] and classified as I_a in the nomenclature defined by *Marklund* [1984]. The Substorm-GEOS rocket was launched at 2101:59 UT on January 27, 1979, from ESRANGE, Kiruna, Sweden (Λ = 66°), near local midnight on January 27, 1979, shortly after the onset of an intense magnetospheric substorm over northern Scandinavia. The obtained data represent a comprehensive data set of the arc's electric field profile in both the east-west and north-south directions as well as the spectra and flux of the precipitating electrons. Although these data are for an arc presumably undergoing breakup, we compare the experimental results with the static model developed above and find good agreement. This implies that inductive effects inside this specific arc were small at the time of the rocket flight. Model inputs are F_x = 0.8, 1.0 mV/m, E_{x0} = 5 mV/m, Σ_{H0} = 16 S, and Σ_{P0} = 10 S as taken from *Marklund et al.* [1983]. The mapping factors are calculated using the 1987 model of *Tsyganenko* [1987]. B_e and $d_\parallel$ are fixed by the choice of Λ and the discussion above. K_x = $L_x k_x$ is determined setting L_x, the size of the conductivity gradient along the poleward boundary, to 20 km and by using the results of *Fridman and Lemaire* [1980] to determine the field-aligned conductivity. The electron number density in the plasma sheet is taken at 1 electron/cm^3 and the parallel and perpendicular electron temperatures as 5 keV. Note that we set γ = −0.5 in light of the above discussion after (17).

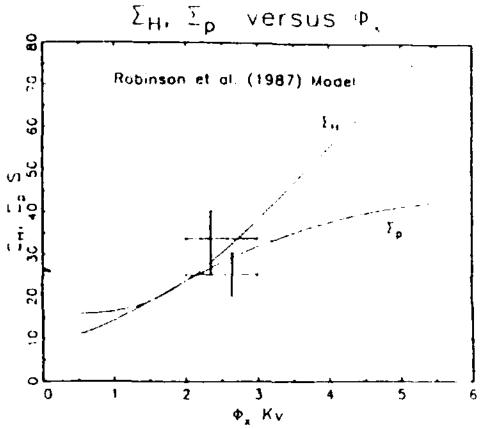

Fig. 3. Comparison of the Hall (upper curve) and Pedersen (lower curve) conductivities as estimated by *Marklund et al.* [1983] inside the arc with that predicted by the model of *Robinson et al.* [1987]. The inputs to the Robinson et al. model were attained using the results of *Fridman and Lemaire* [1980]. A field-aligned potential drop of 2.5 kV was used.

One of the assumptions in the present model is that the ionospheric conductivities inside the wedge region are a function of the field-aligned potential drop along the poleward boundary. This assumption is somewhat artificial because the conductivity inside the wedge region may also be affected by other precipitation mechanisms such as wave-particle interactions. However, the assumption tends to give results in agreement with data as is seen from Figure 3. Here we plot Σ_H and Σ_P as a function of Φ_x using the *Robinson et al.* [1987] conductivity model and estimating the precipitation current from the model of *Fridman and Lemaire* [1980]. The top curve and cross hair is for Σ_H, and the bottom curve and cross hair is for Σ_P. The conductivities are determined as the square root of the sum of squares of the ambient conductivity as determined by *Marklund et al.* [1983] and the enhanced conductivity as determined from the model of *Robinson et al.* [1987]. Note that the agreement between experiment and theory is excellent. We will now compare each of the output variables in our model with the results of *Marklund et al.* [1983].

Figure 4 relates the field-aligned potential drop Φ_x with the east-west current J_y. Presently, we are treating E_{yc} as a fixed parameter. We use two values for the magnetospheric east-west electric field E_{yc} because of the uncertainty in the background electric field as estimated from the experimental data. Figure 5 shows the ionospheric east-west electric field as a function of J_y. This figure can be understood more clearly if one envisions the east-west circuit as a voltage

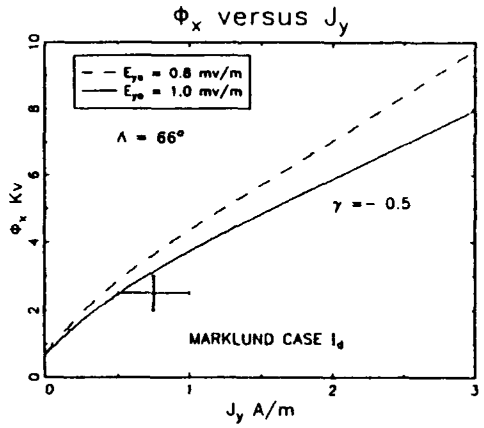

Fig. 4. Comparison of the field-aligned potential drop along the poleward boundary Φ_x as a function of the diverted current J_y. It is seen that a 1.0 mv/m cross-tail electric field E_{ye} gives better agreement.

divider. The potential drop across the magnetospheric portion of the circuit is divided between the field-aligned potential drop Φ_y along the western boundary and the east-west extent of the wedge in the ionosphere. The field-aligned potential drop is directly proportional to J_y as long as the area over which the associated upward current exists remains constant as is assumed here. In that case E_y must decrease as J_y increases in order to satisfy Kirchhoff's Law. The y intercepts are consistent with the direct mapping of the assumed values of E_{ye} to the ionosphere using a mapping factor of $F_y = 0.055$ as calculated from the model of *Tsyganenko* [1987] ($Kp = 3$). *Pedersen et al.* [1985] and *Fälthammar* [1989*a, b*] report the preonset east-west electric field to be 1-2 mv/m which is consistent with the values used here. Figure 6 shows excellent agreement for the polarization electric field inside the arc. Although no measured data

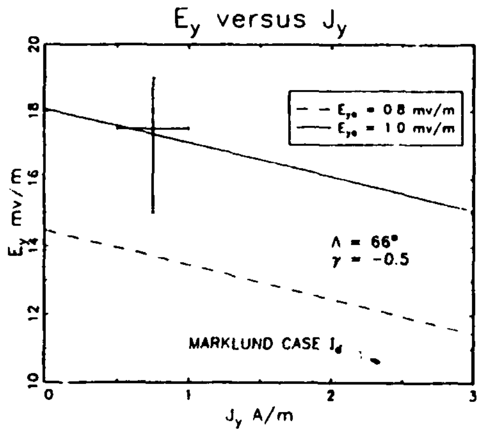

Fig. 5. The east west electric field E_y inside the auroral arc as predicted by the model. Note that the 1.0 mv/m value for E_{ye} gives better agreement as is the case in Figure 4.

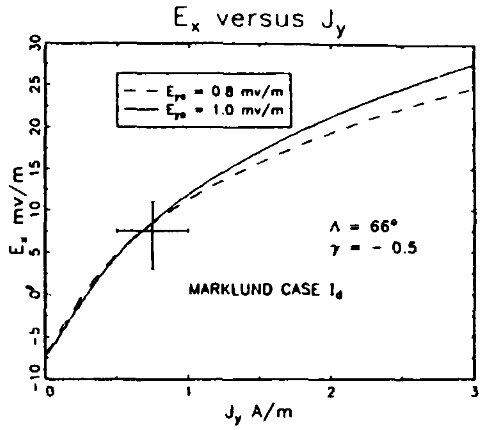

Fig. 6. Comparison of the measured value of the polarization field E_x inside the arc as shown in Figure 6 of *Marklund et al.* [1983] with that predicted by the current model. Note that we assume E_x to be positive in the equatorward direction, while *Marklund et al.* [1983] assume the opposite convention. The error bars presented here are estimated from Figure 6 of *Marklund et al.* [1983].

exist for Φ_y, we show it, for completeness, as as function of J_y in Figure 7. For the western boundary we fix k_y, the field-aligned conductivity, at 3×10^{-9} S/m^2. The east-west extent of the wedge is d_y, and the fractional distance over which the upward current exists is η_y. Clearly, η_y affects the slope of the curve shown. That is, if the upward current is confined to a smaller area, Φ_y will be higher for constant J_y, i.e., the smaller spots should be brighter for the same value of diverted current. The net poleward current inside the wedge ($J_x = K_x\Phi_x$) as a function of J_y is shown in Figure 8. The discrepancy is consistent with the large error bars and the uncertainty in estimating the extent of the conductivity

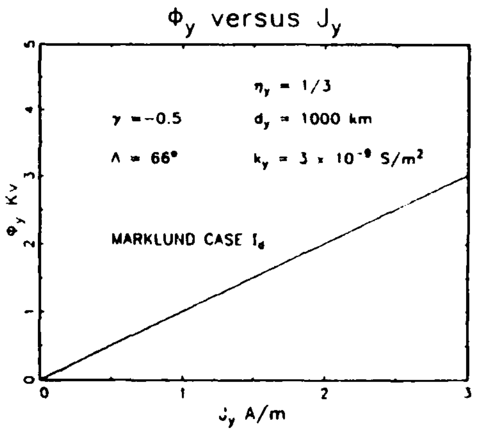

Fig. 7. The modeled field-aligned potential drop Φ_y along the western boundary of the wedge region (i.e., the "hot spot"). d_y is the east-west extent of the current wedge. The east-west spatial extent of the upward closure current along the wedge is assumed to be 333 km. The parameter k_y is the field aligned conductivity at the western boundary.

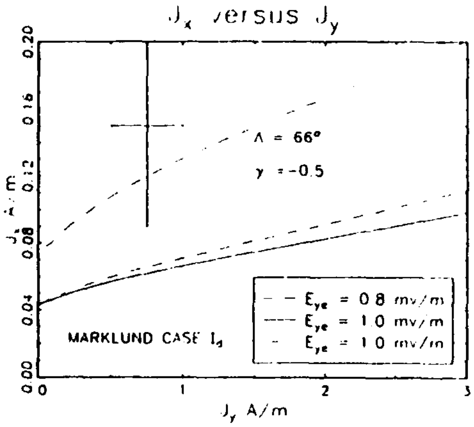

Fig. 8. Net poleward current density J_x inside the current wedge (arc) as a function of the diverted east-west current. Although the model results are not inconsistent with the error bars shown, agreement can be improved by lowering the plasma sheet electron temperature from 5 to 2.5 keV and increasing the plasma sheet particle density from 1 to 2 particles/cm³. This result is shown by the dashed-dotted line. No significant modifications in the other parameters that have been plotted were observed.

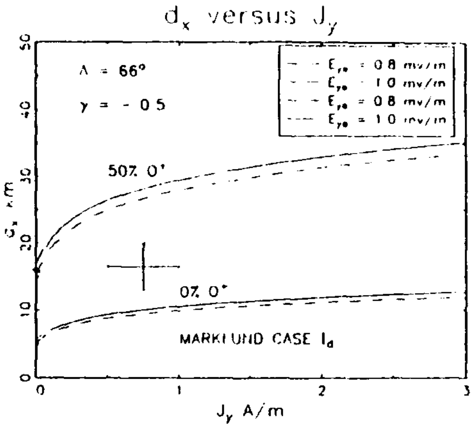

Fig. 9. One of the more interesting features of our model is the capability to calculate the arc thickness d_x. Four calculations were made for various cross-tail electric fields and ion mass densities. (The number density is maintained at 1 ion per cubic centimeter.) It is seen that the *Marklund et al.* [1983] data are well bracketed by an assumption of 0 and 50% for the O⁺ concentration. A potential utilization of such a model is to estimate magnetospheric quantities using ionospheric measurements.

gradient along the poleward boundary and the electron temperature and number density in the plasma sheet. The dashed-dotted curve shows how the agreement can be improved by a lower plasma sheet electron temperature (from 5 keV to 2.5 keV) and a higher plasma sheet electron number density (from 1 e^-/cm³ to 2 e^-/cm³). Figure 9 shows the model results for d_x, the north-south extent of the arc in the ionosphere as determined from (16). The error bars are taken from Figure 8 of *Marklund et al.* [1983]. The number density in the plasma sheet is taken as 1 ion (electron)/cm³. The variation in E_{ye}, the cross-tail electric field, is due to the observed fluctuations in E_y as shown in Figure 6 of *Marklund et al.* [1983]. It is seen that the experimental results are well bracketed by a plasma sheet mass density that contains between 0 and 50% of O⁺.

Figure 10 shows the predicted value of the magnetospheric electric field fluctuation arising from the wedge presence. This fluctuation points tailward and lies between −1.6 and −0.8 mV/m, which is very consistent with the value of −1.2 to −0.6 mV/m as reported by *Tanskanen et al.* [1987] for another magnetic storm. Finally, Figure 11 shows a plot of the magnetospheric closure current in the equatorial plane. We estimate this to be about 3 mA/m in magnitude for the present example. Therefore it is seen that our model gives a rather complete picture of the wedge structure in both the ionosphere and the magnetosphere. Figure 12 shows a graph of d_x versus Φ_x for several values of Λ. Note that if the averaged perturbed electric field is zero in the equatorial plane (i.e., $\gamma = 0$), then thinner arc structures cannot form. It is only when there is a finite tailward electric field perturbation in the equatorial plane that thin arcs can form. Also note that there is an upper limit to d_x for each value of Λ, which indicates that thinner current wedges tend to form at lower latitudes.

5. CONCLUSIONS

We have shown that prebreakup arcs can be represented by two coupled circuits between the ionosphere and the magnetosphere similar to the current wedge configuration proposed by *McPherron et al.* [1973]. The formation of such a current system is strongly influenced by the presence of background electrojets in the ionosphere and directed plasma flows in the magnetosphere. A detailed comparison with the measurements of *Marklund et al.* [1983] for a specific breakup arc shows good agreement. The present model highlights the interdependence between ionospheric

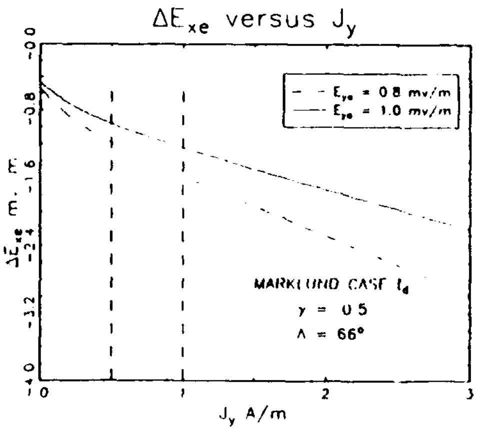

Fig. 10. The range of values predicted by our model for the radial component of the perturbed equatorial electric field ΔE_{xe}. The E_{xe} values are consistent with another example presented by *Tanskanen et al.* [1987].

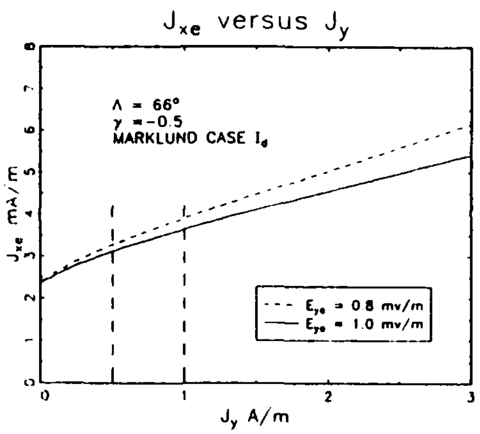

Fig. 11. J_{xe} is the earthward closure current in the equatorial plane that is required to close the north-south (X-C) circuit in our model. See Figure 1. For the Marklund case I_d we find a value of about 3 mA/m.

and magnetospheric quantities and suggests that, by measuring one set, one could imply values for the other. For example, the above application of the model to Marklund et al.'s observations imply a tailward magnetospheric electric field of −0.8 to −1.6 mv/m which is comparable with the in situ measurements of *Tanskanen et al.* [1987] during another breakup event.

We consider the agreement of our model with experimental data as strong evidence that substorm breakup originates in the near-Earth magnetosphere as proposed by *Block et al.* [1986]; *Kaufmann* [1987]; papers 1 and 2, *Galperin and Feldstein* [1991]; *Baker et al.* [1990] and others. Moreover, we have shown (see Figure 12) that in order for the current wedge to have similar dimensions as the observed arcs, the plasma flows in the equatorial plane must be decelerated by the equivalent circuit. That is, the equatorial portion of the X-C must act as a generator ($\gamma < 0$). This is more likely to occur in regions of enhanced westward convection in the equatorial plane which is in the premidnight sector.

Briefly summarizing, we have assumed that at least part of an auroral arc may be represented by a two-circuit current wedge between the ionosphere and magnetosphere. A quasi-stationary situation is assumed which implies that the duskward current in the magnetosphere is consistent with an earthward pressure gradient while the earthward magnetospheric current is inertial. Our model is not complete as this inertia current requires specification of a radial electric field gradient in the equatorial plane. This might be determined by a more complete model of auroral arc structure or by incorporating a global model of plasma convection. The good agreement of our static model with an auroral arc already undergoing breakup [*Marklund et al.*, 1983] implies that inductive effects were still weak even some minutes after breakup.

We need to make a few final points. We have ignored a current-voltage relation in the east-west circuit in the equatorial plane for the simple reason we do not presently know how to quantify it. Overall consistency in this circuit is maintained by adjusting L_y, the distance over which the westward current closes into the magnetosphere. Knowledge of the equatorial current-voltage relation would fix L_y rather than arbitrarily setting it at one third the east-west extent of the arc as is done here. It is interesting to note that L_y scales the size of the expected hot spot at the western wedge boundary. Increasing L_y could give the appearance of eastward propagation. We speculate that the prebreakup arc forms near the inner edge of the plasma sheet where radial, more intense electric field gradients are expected. Another speculation is that the earthward convection of electrons may cause them to exceed their whistler self-excitation limit. The resulting precipitation causes a local conductivity enhancement in the ionosphere that favors the diversion of the cross-tail current. If the cross-tail electric field is sufficiently strong, a quasi steady state current wedge can form as shown by our model. The picture is that of an azimuthal slice of field lines that are displaced earthward due to the current diversion. Breakup probably commences when the associated equatorial ions, which must also be depleted to maintain charge neutrality, cause a pressure imbalance and the magnetic field lines move inward. We do not yet understand the time evolution of this process, but we can with the present model estimate the initial properties of the breakup arc from magnetospheric and ionospheric conditions.

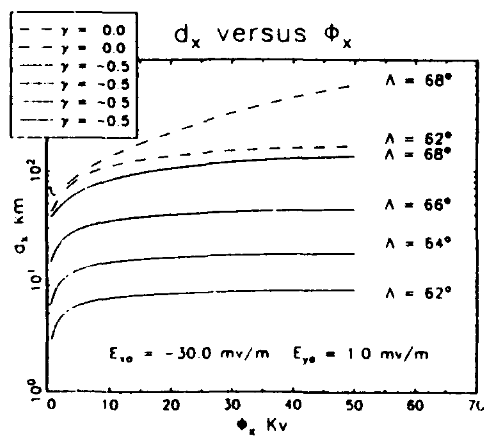

Fig. 12. The predicted wedge thickness d_x as a function of the field aligned potential drop along the poleward boundary for several magnetic latitudes. Note that in the steady state model as presented here d_x has an upper limit at a given magnetic latitude. These calculations were made for a background electric field consistent with being west of the Harang Discontinuity. The $\gamma = 0$ solutions correspond to no coupling between the background plasma flows and the north-south circuit. The case where $\gamma = -0.5$ corresponds to maximum coupling. See text.

Acknowledgments. We would like to acknowledge helpful discussions with W. J. Burke, N. Maynard, M. Heinemann, G. Siscoe, and G. Rostoker. One of us (M. B. S.) would like to acknowledge support from the Air Force contract F19628-85-K-0051. The referees were also helpful in making the manuscript more readable.

The Editor thanks R. L. Kaufmann and another referee for their assistance in evaluating this paper.

REFERENCES

Akasofu, S.-I., A study of auroral displays photographed from the DMSP 2 satellite and from the Alaska meridian chain of stations, *Space Sci. Rev.*, *16*, 617-725, 1974

Baker, D. N., Extreme energetic particle decreases near geostationary orbit: A manifestation of current diversion within the inner plasma sheet, *J. Geophys. Res.*, 95, 6591–6599, 1990

Baumjohann, W., The plasma sheet boundary layer and magnetospheric substorms, *J. Geomagn. Geoelectr.*, *40*, 157–175, 1988

Block, L. P., P. L. Rothwell, and M. B. Silevitch, A new model for substorm breakup (abstract), *Eos Trans. AGU*, *67*, 1178, 1986

Burch, J. L., Energetic particles and currents: Results from Dynamic Explorer, *Rev. Geophys.*, *26*, 215–228, 1988

Chappell, C. L., The terrestrial plasma source: A new perspective in solar-terrestrial processes from Dynamic Explorer, *Rev. Geophys.*, *26*, 229–248, 1988.

Cladis, J. B., Parallel acceleration and transport of ions from polar ionosphere to the plasma sheet, *Geophys. Res. Lett.*, *13*, 893-896, 1986.

Craven, J. D., L. A. Frank, and S.-I. Akasofu, Propagation of a westward traveling surge and the development of persistent auroral features, *J. Geophys. Res.*, *94*, 6961–6967, 1989

Erickson, G. M., R. W. Spiro, and R. A. Wolf, The physics of the Harang Discontinuity, *J. Geophys. Res.*, 96, 1633–1645, 1991

Fälthammar, C.-G., Electric fields in the magnetosphere—the evidence from ISEE, GEOS, and Viking, *IEEE Trans. Plasma Sci.*, *17*, 174–185, 1989*a*.

Falthammar, C.-G., Electric fields in the magnetosphere—A review, *Planet. Space Sci.*, *37*, 899-914, 1989*b*

Fridman, M., and J. Lemaire, Relationships between auroral electron fluxes and field-aligned potential differences, *J. Geophys. Res.*, *85*, 664–670, 1980

Galperin, Yu. I., and Ya. I. Feldstein, Auroral luminosity and its relationship to magnetospheric plasma domains, in *Auroral Physics*, edited by C.-I. Meng et al., Cambridge University Press, New York, 1991.

Hallinan, T. J., The dynamics of substorm onset (abstract), *Eos Trans. AGU*, *68*, 1420, 1987.

Heppner, J. P., A study of the relationships between the aurora borealis and the geomagnetic disturbances caused by electric currents in the ionosphere, *Rep. DR 135*, Def. Res. Board of Can., Ottawa, 1958.

Kan, J. R., and S. I. Akasofu, Electrodynamics of solar wind-magnetosphere-ionosphere interactions, *IEEE Trans. Plasma Sci.*, *17*, 83–108, 1989

Kan, J. R., L. Zhu, and S.-I. Akasofu, A theory of substorms: Onset and subsidence, *J. Geophys. Res.*, *93*, 5624–5640, 1988.

Kaufmann, R. L., Substorm currents: Growth phase and onset, *J. Geophys. Res.*, 92, 7471-7486, 1987.

Kremser, G., et al., Coordinated balloon satellite observations of energetic particles at the onset of magnetospheric substorms, *J. Geophys. Res.*, *87*, 4445–4453, 1982.

Kremser, G., et. al., Energetic electron precipitation during a magnetospheric substorm and its relation to wave-particle interaction, *J. Geophys. Res.*, *91*, 5711–5718, 1986

Lennartsson, W., and R. D. Sharp, Relative contribution of terrestrial and solar wind ions in the plasma sheet, *Adv. Space Res.*, *5*, 411–414, 1985

Lezniak, T. W., and J. R. Winckler, Experimental study of magnetospheric motions and the acceleration of energetic electrons during substorms, *J. Geophys. Res.*, *75*, 7075-7098, 1970

Lopez, R. E., D. G. Sibeck, R. W. McIntire, and S. M. Krimigis, *J. Geophys. Res.*, 95, 109-117, 1990

Lotko, W., B. U. O. Sonnerup, and R. L. Lysak, Nonsteady boundary layer flow including ionospheric drag and parallel electric fields, *J. Geophys. Res.*, 92, 8635-8648, 1987

Lui, A. T. Y., R. E. Lopez, S. M. Krimigis, R. W. McEntire, L. J. Zanetti, and T. A. Potemra, A case study of magnetotail current sheet disruption and diversion, *Geophys. Res. Lett.*, *15*, 721-724, 1988

Marklund, G., Auroral arc classification scheme based on the observed arc-associated electric field patterns, *Planet. Space Sci.*, *32*, 193–211, 1984.

Marklund, G., W. Bamjohann, and I. Sandahl, Rocket and ground-based study of an auroral breakup event, *Planet. Space Sci.*, *31*, 207–220, 1983.

McPherron, R. L., C. T. Russell, and M. P. Aubrey, Satellite studies of magnetospheric substorms on August 15, 1968, 9. Phenological model for substorm, *J. Geophys. Res.*, *78*, 3131-3149, 1973.

Nagai, T., D. N. Baker, and P. R. Higbie, Development of substorm activity in multiple onset substorms at synchronous orbit, *J. Geophys. Res.*, *88*, 6994-7004, 1983.

Pedersen, A., C. A. Cattell, C.-G. Falthammar, K. Knott, P. A. Lindqvist, R. H. Manka, and F. S. Mozer, Electric fields in the plasma sheet and plasma sheet boundary layer, *J. Geophys. Res.*, *90*, 1231–1242, 1985.

Robinson, R. M., R. R. Vondrak, K. Miller, T. Dabbs, and D. Hardy, On calculating ionospheric conductances from the flux and energy of precipitating electrons, *J. Geophys. Res.*, 92, 2565–2569, 1987.

Rostoker, G., S.-I. Akasofu, W. Bamjohann, Y. Kamide, and R. L. McPherron, The roles of direct energy input of energy from the solar wind and unloading of stored magnetotail energy in driving magnetospheric substorms, *Space Sci. Rev.*, *46*, 93-111, 1987

Rothwell, P. L., L. P. Block, M. B. Silevitch, and C.-G. Falthammar, A new model for substorm onsets: The pre-breakup and triggering regimes, *Geophys. Res. Lett.*, *15*, 1279–1282, 1988

Rothwell, P. L., L. P. Block, B. Silevitch, and C. G. Fälthammar, A new model for auroral breakup during substorms, *IEEE Trans. Plasma Sci.*, *17*, 150–157, 1989.

Shepherd, G. G., C. D. Anger, J. S. Murphee, and A. Vallance Jones, Auroral intensification in the evening sector observed by the Viking ultra violet imager, *Geophys. Res. Lett.*, *14*, 395–398, 1987.

Tanskanen, P., J. Kangas, L. Block, G. Kremser, A. Korth, J. Woch, I. B. Iversen, K. M. Torkar, W. Riedler, S. Ullaland, J. Stadsnes, K.-H. Glassmeir, Different phases of a magnetospheric substorm on June 23, 1979, *J. Geophys. Res.*, 92, 7443-7457, 1987

Tsyganenko, N. A., Global quantitative models of the geomagnetic field in the cislunar magnetosphere for different disturbance levels, *Planet. Space Sci.*, *35*, 1347-1358, 1987

Weimer, D. R., N. C. Maynard, W. J. Burke, and M. Sugiura, Stationary auroral current oscillations resulting from the magnetospheric generator, *J. Geophys. Res.*, *93*, 11,436–11,444, 1988.

L. P. Block and C.-G. Fälthammar, The Royal Institute of Technology, S 100 44, Stockholm 70, Sweden.

P. L. Rothwell, Geophysics Directorate/PHG, Phillips Laboratory, Hanscom Air Force Base, Bedford, MA 01731.

M. B. Silevitch, Center for Electromagnetics Research, Northwestern University, Boston, MA 02115

(Received November 28, 1990;
revised March 27, 1991;
accepted April 29, 1991.)

ACCELERATION AND STOCHASTIC HEATING OF IONS DRIFTING THROUGH AN AURORAL ARC

P. L. Rothwell

Geophysics Laboratory, Hanscom AFB, Bedford, MA 01731

M. B. Silevitch

Center for Electromagnetics Research, Northeastern University, Boston , MA 02115

L. P. Block and C.- G. Fälthammar

The Royal Institute of Technology, S 100 44, Stockholm 70, Sweden

June 25, 1992

ABSTRACT

We find that ions EXB drifting through an auroral arc can undergo transverse acceleration and stochastic heating. This result is very analogous to recent work regarding similar phenomena in the magnetotail (Büchner and Zelenyi (1990), Chen and Palmadesso (1986) and Brittnacher and Whipple (1991)). An analytic expression for the maximum arc width for which chaotic behavior is present is derived and numerically verified. We find, for example, that a 1.5 km thick arc at $\Lambda = 65°$ requires a minimum potential drop of 3 Kv for transverse ion acceleration and heating to occur. Thicker arcs require higher potential drops for stochasticity to occur. This mechanism could be a partial cause for ion conics.

I. INTRODUCTION

The theory of auroral arcs has progressed along many lines of thought: electrostatic shocks (Swift 1979,1988; Kan 1975); double layers (Block, 1972; Borovsky, 1983; Singh et al., 1987); Alfvén wave propagation (Lysak 1990; Seyler 1990) ; the formation of a small current wedge (Rothwell et al., 1991) and viscuous interaction at the magnetopause (Lotko et al., 1987). In simple terms the arc is analogous to a fountain that rises to some height at the center, spreads out at the top and then is returned over an extended area. The presence of a conductive ionosphere and the complex interaction of the associated fields and particles makes the problem very complex. A self-consistent model of an auroral arc should include a mechanism for generating the field-aligned potential drop associated with the arc and a description of how the associated currents are conserved, including ionspheric effects. In this paper we address the additional complication that an auroral arc may not be self-contained. We find that it modifies the ion population that is EXB drifting through it. The drifting ions, on the other hand, affect the charge distribution inside the arc and, hence, the potential distribution itself. We will examine the effect of the arc on the ions in analogy with similar effects in the magnetotail.

Recent studies of Speiser type orbits in the magnetotail have been shown to exhibit chaotic type behavior (Büchner and Zelenyì (1990), Chen and Palmadesso(1986)). This occurs when an ion makes a transition from gyrating solely on one side of the neutral sheet to gyrating on both sides of the neutral sheet (Speiser orbit). This transition is extremely sharp as is seen from Figure 1 of Rothwell and Yates (1984) and, in fact, corresponds to a point in direct analogy with the unstable equilibrium of a simple harmonic oscillator. It is well known that in the latter case if one places a pendulum so that its weight is directly above the pivot point then upon release the pendulum may either oscillate back and forth or rotate about the pivot point. Which mode is taken is so sensitive to the initial conditions that it is impossible to predict. The boundary in phase space that separates the two types of motion is called the separatrix. In mathematical terms placing a pendulum above its pivot point is equivalent to starting it at a hyperbolic fixed point in phase space. Lichtenberg and Lieberman (1983) give an extensive treatment on the stochastic nature of nonlinear harmonic oscillators near hyperbolic fixed points. From a different point of view Brittnacher and Whipple (1991) examine the discontinuity in the invariants of motion as a particle crosses a separatrix. Their work was based on earlier work by Kruskal (1962) and with specific application to the magnetotail problem. The discontinuity of the particle motion as it crossed the separatrix was found to be analogous to scattering.

Here we apply these concepts to an auroral arc. Visualize ions EXB drifting from the magnetotail towards the earth. In their path lies an auroral arc which is elongated in the east-west direction. In the earth-tail direction the arc is assumed to have a U-shaped (gaussian) potential structure (see Figure 1). The subject of this paper is to determine response of the ions to the arc as they pass through. For simplicity, it also assumed that the ions pass through the arc in a time short compared to a bounce period. This allows us to treat a two dimensional problem. The coordinates are chosen such that x is earthward, y points west and z is parallel to the magnetic field. As the ion enters the potential structure an earthward electric field accelerates it and at the same time imparts an eastward drift. See Figure 8a. The E_y electric field causes the ion to continue drifting through the arc. When the ion encounters the tailward electric field it drifts westward and eventually escapes the potential. While inside the well the ion may be trapped. In that case when the ion exits the well it must cross a separatrix and scatter (Brittnacher and Whipple (1991)). The cross-tail electric field E_y accelerates the ion westward while it is undergoing nonadiabatic motion (scattering). If we now consider an ensemble of ions entering the potential well and recall that in the vicinity of a hyperbolic fixed point motion is stochastic then we can understand how a net westward ion acceleration and the associated heating arise. In section II an upper limit is found for the scale size of the potential. Below this limit acceleration and stochastic heating take place, but of above this limit the motion is adiabatic. In Section III a base set of inputs are chosen and appropriately varied to show that this upper limit is a good approximation. In this section we also show that below the limit a hyperbolic fixed point exists and that it causes the drifting ions to scatter as in the manner of Brittnacher and Whipple (1991). In Section IV we give our conclusions.

II. EQUATIONS

The equations of motion in component form are

$$M\dot{V}_x = e[E_x + V_y B] \tag{1a}$$

$$M\dot{V}_y = e[E_y - V_x B] \tag{1b}$$

where e and M are the ion's charge and mass. B denotes the magnetic field in the postitive z-direction. $V=(V_x^2 + V_y^2)^{1/2}$ is the ion velocity. $E_x = -\nabla\phi(x)$ where

$$\phi(x) = \phi_o \exp[-(\frac{x}{L_x})^2] \tag{2}$$

and E_y in equation (1b) is considered constant. A finite E_y within an auroral arc has been observed by Marklund (1984) and others. Since x(t) denotes the ion's position and, therefore, $E_x(x) \equiv E_x(x(t))$ we may combine equations (1a) and (1b).

$$M\ddot{V}_x + [\omega^2 - \frac{e}{M}\frac{dE}{dx}]V_x = \frac{\omega^2}{B}E_y \tag{3}$$

$$\omega = \frac{eB}{M}$$

We gain some insight into the physics represented by equation (3) by momentarily assuming dE/dx = const. Cole (1976). In that case the homogeneous solutions to equation (3) are either oscillatory or exponential depending on whether the coefficient of V_x is positive or negative. More explicitly, if (Cole, 1976)

$$\omega^2 < \frac{e}{M}\frac{dE}{dx} \tag{4}$$

then the electric potential has a dominating effect on the ion motion. From equation (2) and Figure 1 we see that in our problem the ions initially encounter a positive ramp in E_x. Therefore, equation (4) is an approximation to the value of this dE/dx above which we expect to see nonadiabatic effects.

We appoximate dE/dx by

$$\frac{dE}{dx} \sim \frac{|\phi_o|}{L_x{}^2} \tag{5}$$

using equation (2). Therefore, equation (4) is satisfied if

$$L_x \leq L_t = \frac{1.0}{\omega}\left(\frac{e}{M}\phi_o\right)^{1/2} \tag{6}$$

Below we verify equation (6) by varying B,M, and ϕ_o and show that it is a reasonable indicator between the adiabatic and nonadiabatic regimes.

L_t can also be found by linearizing the potential given in equation (2). This leads to simple harmonic motion near x=0 which can be in resonance with the gyromotion. By equating the electric oscillator frequency with the gyrofrequency we find that the condition for resonance is the same condition as given by equation (6) to within a numerical factor. A similar bound will also result if we compare the maximum amplitude of the trochoidal ion motion in the electric field to the scale L_x i.e. when $((E_{xmax}/B) \cdot (M/eB) \sim L_x)$. For shallow gradients the ions follow an adiabatic trajectory through the potential well and no net energy exchange takes place. It is only when equation (4) is sufficiently satisfied that significant entrapment in the potential well takes place and stochastic heating and acceleration occur as the ions pass through the vicinity of the hyperbolic fixed point as discussed above.

III. RESULTS

Mathematical Preliminaries The equations of motion were numerically integrated using a step-wise adaptive technique with a fourth order Runge Kutta method as described by Press et al. (1986). At each step of the integration procedure the total energy

$$E_T = \frac{1}{2}MV^2 + e\phi(x) - eE_y y \tag{7}$$

was calculated and compared to the initial total energy. The accuracy of the integration procedure was adjusted to keep the maximum error in the total energy below 2 parts in a thousand. With this criterion it took between 30s and one minute to trace one ion using an IBM Compatible 386 personal computer.

The Hyperbolic Fixed Point We now wish to illustrate the presence of the hyperbolic fixed point. Figure 2a shows the results in coordinate space for two 200 ev O+ ions that start 100 meters (0.002 L_x) apart 500 kilometers (-10 L_x) downstream of the potential well. (L_x = 50 km). They then EXB drift towards the potential well. (B=144 nT). After scattering through the separatrix the ions are separated in the y-direction by 387 km. Figures 2b and 2c show phase space plots of the two ion trajectories. Note that the ion with the smaller y-displacement (Figure 2c) bearly escaped the potential well while the ion with the larger y-displacement (Figure 2b) remained narrowly trapped and oscillated in the well structure one more time before exiting. During this one bounce it, of course, was gaining additional energy from E_y (1 mv/m). By superimposing both ion trajectories in an exploded view near where the quasi-discontinous motion appears the hyperbolic nature of the two trajectories is readily apparent (Figure 2d). This is the hyperbolic fixed point. The analogy to scattering as proposed by Brittnacher and Whipple (1991) is clearly apparent.

Acceleration and Stochastic Heating There are six variables that affect the ion trajectory : L_x, the size of the potential well; E_y, the east-west electric field; ϕ_o, the depth of the potential well; ϵ_i , the initial kinetic energy of the ion before it enters the potential well; M, the ion mass; and B, the local magnetic field strength. An initial base result is established and then tested for sensitivity to changes in each of the parameters. The initially chosen values are ϕ_o = 3 Kv, ϵ_i= 200 ev, E_y = 1 mv/m, B = 144 nT, and M = 16 (O^+). We then scanned in L_x to determine the region of nonadiabatic behavior. For each value of L_x we followed 100 ions randomly chosen over an interval of $2R_c$ (R_c = ion gyroradius). This interval is centered < · $6L_x$ from the well center. Each ion is started with its velocity pointing along the x-axis and with y=0. Figure 3 shows the results for the base run. The circles denote the mean values of the exit energy ϵ_f and the triangles and squares denote the one standard deviation limits. Note that the energy distribution will generally not be Maxwellian so that these limits may not correspond to true temperatures. However, they do indicate the relative importance of heating. We see that there is a maximum heating and acceleration at about L_x = 140 km. L_t is the threshold value of L_x as given by equation (6). L_a corresponds to the ion gyroradius (56 km). The upper limit L_t, which has an actual value of 155 km, does not exactly correspond to the break between adiabatic and nonadiabatic motion at ~ 200 km. We, therefore, rescale L_t to agree with the base case (Figure 3) and test this agreement by changing the values of B, M, and ϕ_o as shown in equation (6). For example, if we change ϕ_o and B as shown in Figures 4 and 5 then we see that L_t scales as expected. However, for the M= 1 (protons) case shown in Figure 6 L_t is ~20 % too high which indicates a mass dependence in L_t more complex than that shown in equation (6). We, therefore, conclude that the upper limit given by equation (6) is a reasonable estimate of the threshold between adiabatic and nonadiabatic motion. Having established this we can then use equation (6) to estimate the maximum arc thickness underwhich ion acceleration and heating will occur. This will be done in Section V.

Single Ion Trajectories Now we take three single ion trajectories for the base case shown in Figure 3 ; L_x = 10 km, L_x = 140 km and L_x = 400 km. These three cases allow a comparison between the acceleration/heating regime and the non-acceleration/heating regimes. For the $L_x = 10$ km case shown in Figures 7a and 7b we see that although there is significant trapping by the potential well (Figure 7b) there is little drift in the -y-direction (Figure 7a). Therefore, E_y does not significantly interact with the ions in contrast to the next case. The x-coordinate tic marks in Figures 7a and 7b are in units of R_c. Note $L_x \sim 0.2\ R_c$ so that the ion executes only a small part of its gyromotion while being trapped in the well. In other words, the potential well introduces a relatively small perturbation on the gyromotion although there is still some scattering as the ion crosses the separatrix. This is seen as residual heating at low values of L_x as seen in the base plot (Figure 3).

The second case ($L_x > 2.5\ R_c$) results are shown in Figures 8a and 8b . The tic marks shown here are units of $L_x = 140$ km. Note from Figure 8b how the gyromotion is dominated by the electric potential. As the ion EXB drifts in the -y-direction it becomes more entrapped by the potential well (Figure 8a). Note that the -y-drift distance is more than $9L_x$. The drift in y as previously stated is controlled by the reverse electric fields inside the well. It is the beating of the gyromotion with the trapping inside the potential well that makes the ion trajectories so phase sensitive subject to stochastic behavior.

The third case ($L_x = 8\ R_c$) results are shown in Figures 9a and 9b . Again the units are in multiples of L_x. Here it is apparent that the gyromotion dominates even in the regions of positive dE/dx. The ions are never decoupled from the magnetic field as they were in the second case. Here they simply adiabatically drift back and forth in y following an equipotential contour.

IV. CONCLUSIONS

Here we have applied the chaotic properties of the nonlinear harmonic oscillator to an auroral arc. The associated hyperbolic fixed point was explicitly determined and the resonance type behavior of the ion acceleration and heating demonstrated and explained. Although equation (6) was approximate, it was shown to scale properly in the exact case. Therefore, we use it as a measure for the onset of chaos in an auroral arc. For example, if we assume the field-aligned potential drop is located at approximately 2.5 R_E at $\Lambda = 65°$. The B-field value is 3.7×10^{-6}T. From equation (6) we obtain $L_b = 111(\phi_o)^{1/2}$ m. The scale factor is about a factor of four for a dipole field so at the ionosphere we have

$$L_{bi} = 27.7(\phi_o)^{1/2} m \tag{8}$$

If $\phi_o = 3$Kv then $L_{bi} = 1.5$ km. Mapping this up to 2.5 R_E we have $L_b = 6$ km which is 2.7 R_c for an O^+ (200 ev) ion. This is consistent with Figure 3. Therefore, moderate field-aligned potential drops are adequate to cause drifting ions to be transversely accelerated and heated. Thicker arcs require a higher value of ϕ_o in accordance with equation (8). Whether this could be related to substorm onsets is an open, but interesting question. Also low altitude ion acceleration and stochastic heating could be an important source for ion conics (Lysak, 1981; Yang and Kan, 1983; Borovsky, 1984). Mozer et al. (1980) notes the experimental observation of electric field gradients that satisfy equation (4). Finally, we note that the expected presence of turbulence inside the arc should add to the stochastic heating determined here. Also from Figures 2b and 2c it is apparent that trapped ions will modify the charge distribution inside the arc and, hence, the potential structure.

ACKNOWLEDGEMENTS

We would like to express our thanks to J. Albert and M. MacLeod for their interest and comments. One of us (MBS) would like to acknowledge support from Air Force Contracts F19628-85-K-0053, F19628-92-K-0071.

FIGURE CAPTIONS

FIGURE 1. The auroral arc potential structure and the associated electric field. The abscissas denote the x-coordinate in units of L_x while the ordinates are in units of ϕ_o and ϕ_o/L_x, respectively. Note the reversed electric field profile that imposes a nonlinear harmonic component on the ion motion.

FIGURE 2. Explicit representation of the hyperbolic fixed point associated with the nonlinear harmonic motion produced by the potential structure shown in Figure 1. (a) Highlights the sudden bifurcation in the trajectories of two ions that are started 0.002 L_x units apart 10 L_x units (L_x = 50km) upstream of the potential. A net displacement in the y-direction implies a net gain or loss of particle energy due to E_y. (b) Phase space plot for the ion that exited the potential with the largest y-displacement in (2a). Note that the ion just barely missed escaping the potential and executed one more oscillation in comparison with the other ion shown in (2c). This allowed the ion shown in (2b) to gain additional energy from E_y. V_s is the thermal energy. (c) Phase space plot for the ion that exited the potential well with the lower kinetic energy. (d) By superimposing these two trajectories in an exploded view the hyperbolic fixed point is clearly evident.

FIGURE 3. Base plot for the ion (O^+) exit energy as a function of L_x (meters). For each value of L_x 100 ions were drifted through the potential structure shown in Figure 1. The circles denote mean values while the triangles and squares represent a one standard deviation from the mean. L_s denotes the ion gyroradius. L_t denotes an upper threshold to nonadiabatic motion as described in the text. The inputs for this base run were M = 16, E_y = 1 mv/m, B = 1.44 X 10^{-7}T, ϕ_o = 3kV. These input values were also used for the results shown in Figure 2.

FIGURE 4. The effect seen in Figure 3 is clearly enhanced if the depth of the potential well is increased from 3 kV to 6 kV. Note that L_t is shifted consistent with the square root

dependence found in the text.

FIGURE 5. This figure is the same as Figure 3 except that the B-field value has been doubled. Note that L_t follows the transition between nonadiabatic and adiabatic motion consistent with an inverse B-dependence as found in the text.

FIGURE 6. Same as Figure 3 except now $M = 1$. Again note the scaling of L_t. L_t is at 50km instead at $\sim$ 42km. This is an error of about 20 % which is, no doubt, reflects the simplicity of our assumptions in deriving L_t.

FIGURE 7. (a) A coordinate space plot of an ion trajectory for which $L_x = 10$ km and for the parameter values as given in Figure 3. (b) The corresponding phase space plot. Note that although the potential traps the ion it only causes a minor perturbation in its gyromotion. The resulting limited excursion in y accounts for the diminished acceleration and heating observed at lower values of L_x in Figure 3.

FIGURE 8. Coordinate (a) and phase space plots (b) of an ion trajectory such that $L_x = 140$ km which corresponds to the region of maximum acceleration and heating as seen in Figure 3. Note the large displacement in the -y (eastward) direction with significant oscillation in the x-component. The key point here is that as the ion enters the potential the electric field has a much greater effect on the ion trajectory than the magnetic field. This is seen in both (a) and (b).

FIGURE 9. Coordinate (a) and phase space plots (b) of an ion trajectory where $L_x = 400$ km. This corresponds to the adiabatic region shown in Figure 3. Note in (a) the ion is executing almost pure EXB drift in the y-direction with only a limited extent of x being traversed during each gyroperiod. Therefore, the ion is simply following an equipotential contour.

REFERENCES

Block, L. P., Potential double layers in the ionosphere, *Cosmic Electrodyn.*, *3*, 349, 1972.

Borovsky, Joseph E., and Glenn Joyce, Numerically simulated two-dimensional auroral double layers, *J. Geophys. Res.*, 3116, 1983.

Brittnacher, M. J., and E. C. Whipple, Chaotic jumps in the generalized first adiabatic invariants in current sheets, *J. Geophys. Res.*, *18*, 1599, 1991.

Borovsky, J. E., The production of ion conics by oblique double layers, *J. Geophys. Res.*, *89*,2251,1984.

Büchner, J., and L. M. Zelenyi, Deterministic Chaos in the dynamics of charged particles near a magnetic reversal, *Phys. Rev. Lett. A*, *118*, 395, 1986.

Chen, J., and P. J. Palmadesso, Chaos and nonlinear dynamics of single-particle orbits in a magnetotail-like magnetic field, *J. Geophys. Res.*, *91*,1499, 1986.

Cole, K. D., Effects of crossed magnetic and (spatially dependent) electric fields on particle motion, *Planet. Space Sci.*, *24*,515, 1976.

Kan, J. R., Energization of auroral electrons by electrostatic shock waves, *J. Geophys. Res.*, 80, 2089, 1975.

Kruskal, Martin, Asymptotic theory of Hamiltonian and other systems with all solutions nearly periodic, *J. Math. Phys.*, 3, 806, 1962.

Lichtenberg, A. J., and M. A. Lieberman, *Regular and Stochastic Motion*, Springer-Verlag, New York, 1983.

Lotko, W., B. U. Ö. Sonnerup, and R. L. Lysak, Nonsteady boundary layer flow including ionospheric drag and parallel electric fields, *J. Geophys. Res.*, 92, 8635, 1987.

Lysak, R. L., Electric and ion acceleration by strong electrostatic turbulence, in *Physics of Auroral Arc Formation*, (S.-I. Akasofu and J. R. Kan, eds.), AGU Monograph 25, American Geophysical Union, Washington, D. C., 144, 1981.

Lysak, R. L., Electromagnetic coupling of the magnetosphere and the ionosphere, *Space Sci. Rev., 52,* 33, 1990.

Marklund, G., Auroral arc classification scheme based on the observed arc-associated electric field patterns , *Planet. Space Sci., 32,*193, 1984.

Mozer, F. S., C. A. Cattell, M. K. Hudson, R. L. Lysak, M. Temerin, and R. B. Torbert, Satellite measurements and theories of auroral particle acceleration, *Space Sci. Rev., 27,*155, 1980.

Press, William H., Brian P. Flannery, Saul A. Teukolsky, and William T. Vettering, *Numerical Recipes,*University of Cambridge Press, New York, 1986.

Rothwell, Paul L., and G. Kenneth Yates, Global single ion effects within the earth's plasma sheet, in *Magnetic reconnection in space and laboratory plasmas* , Edward J. Hones, Jr., Ed., AGU Monograph No. 30, 51, 1984.

Seyler, C. E., A mathematical model of the structure and evolution of small-scale discrete arcs, *J. Geophys. Res., 95* 17, 199, 1990.

Singh, Nagendra, H. Thiemann, and R. W. Schunk, Simulations of auroral plasma processes: electric fields, waves and particles, *Planet. Spac. Sci.,*35, 353, 1987.

Swift, D. W., An equipotential model for auroral arcs: The theory of two-dimensional laminar electrostatic shocks, *J. Geophys. Res., 84,* 6427, 1979.

Swift, D. W., A numerical model for auroral acceleration, *J. Geophys. Res. , 93,* 9815, 1988.

Yang, W. H., and J. R. Kan, Generation of conic ions by auroral electric fields, *J. Geophys. Res.*, *88*,465, 1983.

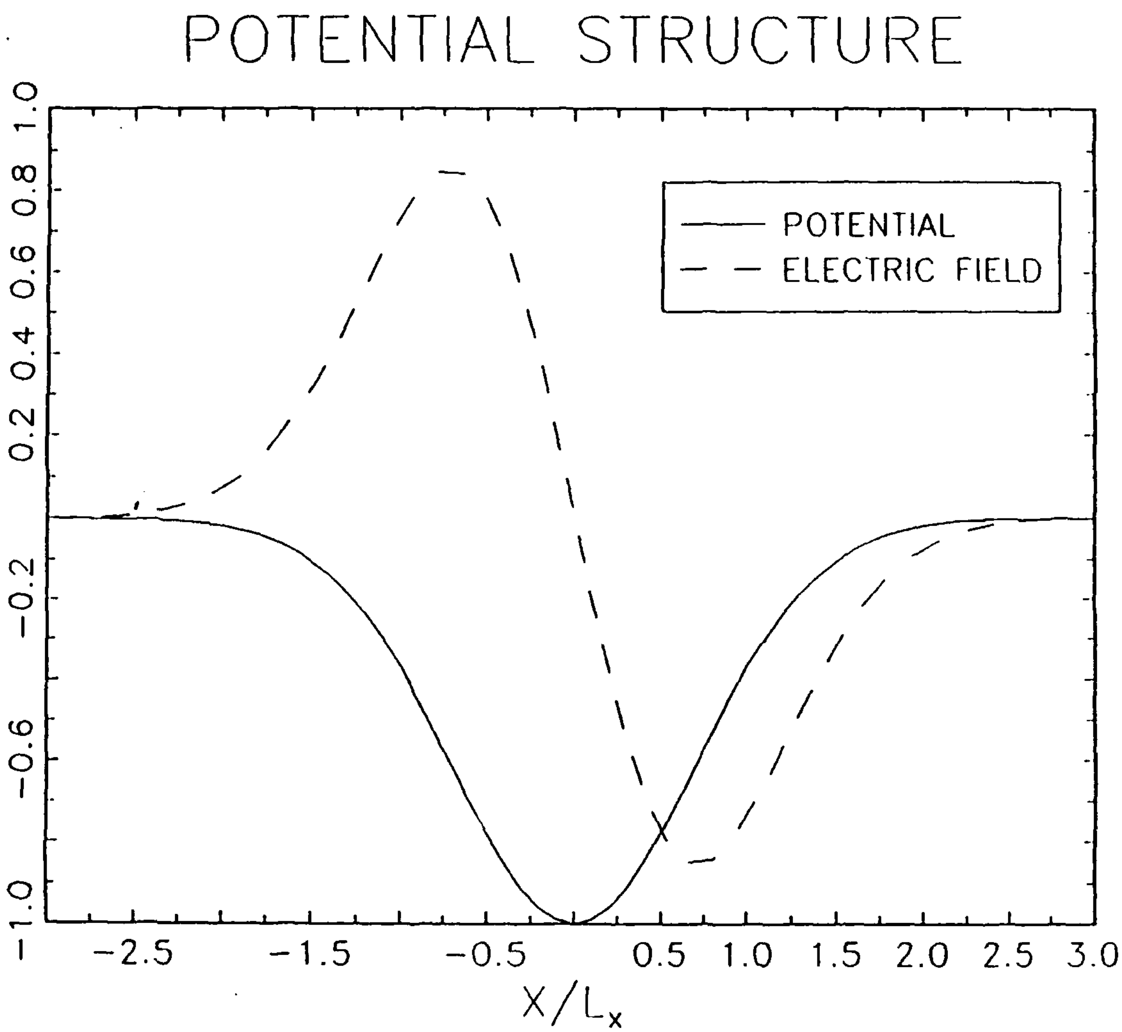
POTENTIAL STRUCTURE
POTENTIAL
ELECTRIC FIELD
1.0
0.8
0.6
0.4
0.2
-0.2
-0.6
-1.0
-2.5
-1.5
-0.5
0.5
1.0
1.5
2.0
2.5
3.0
X/L
x

Fig. 1.

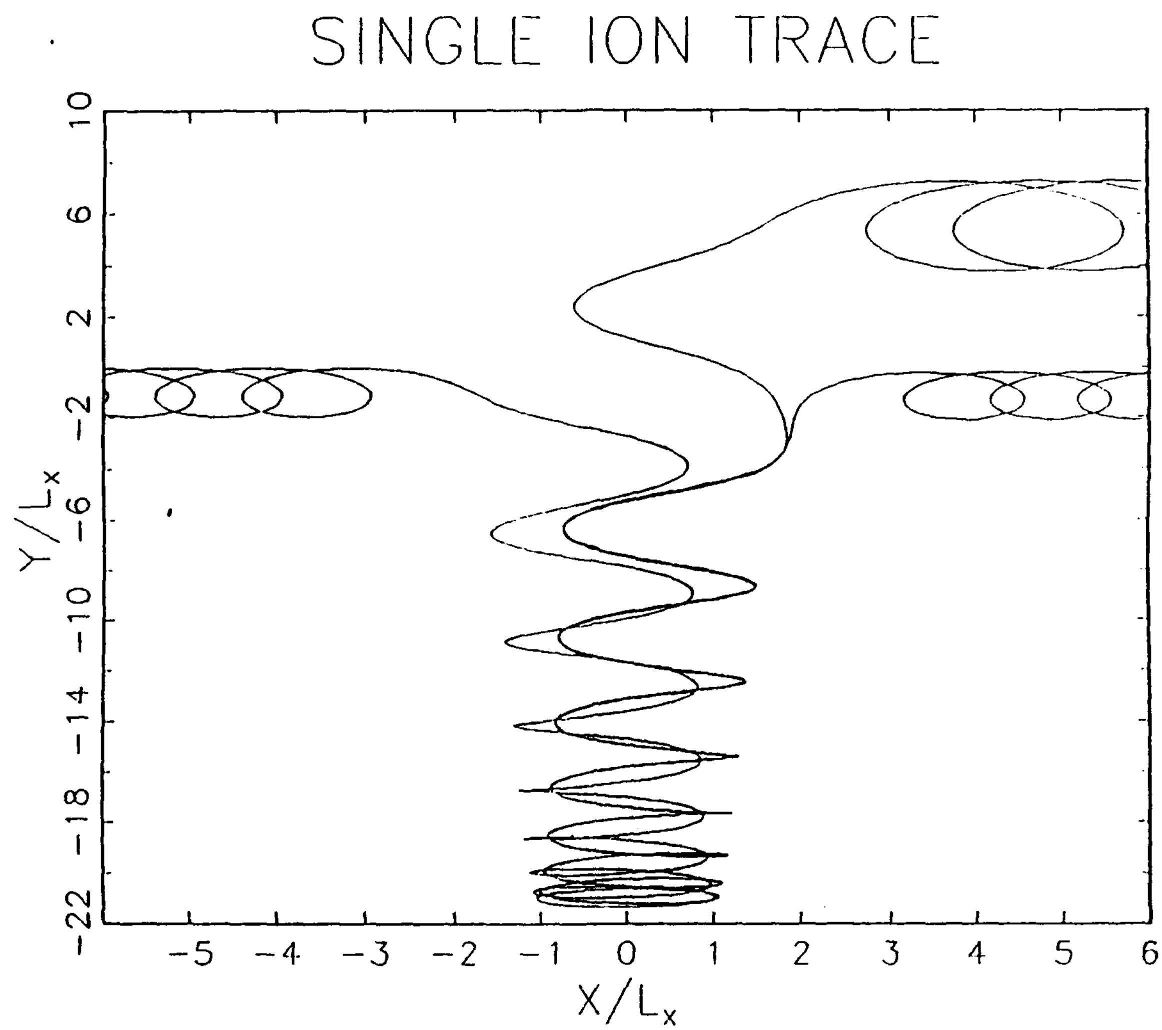

Fig. 2a

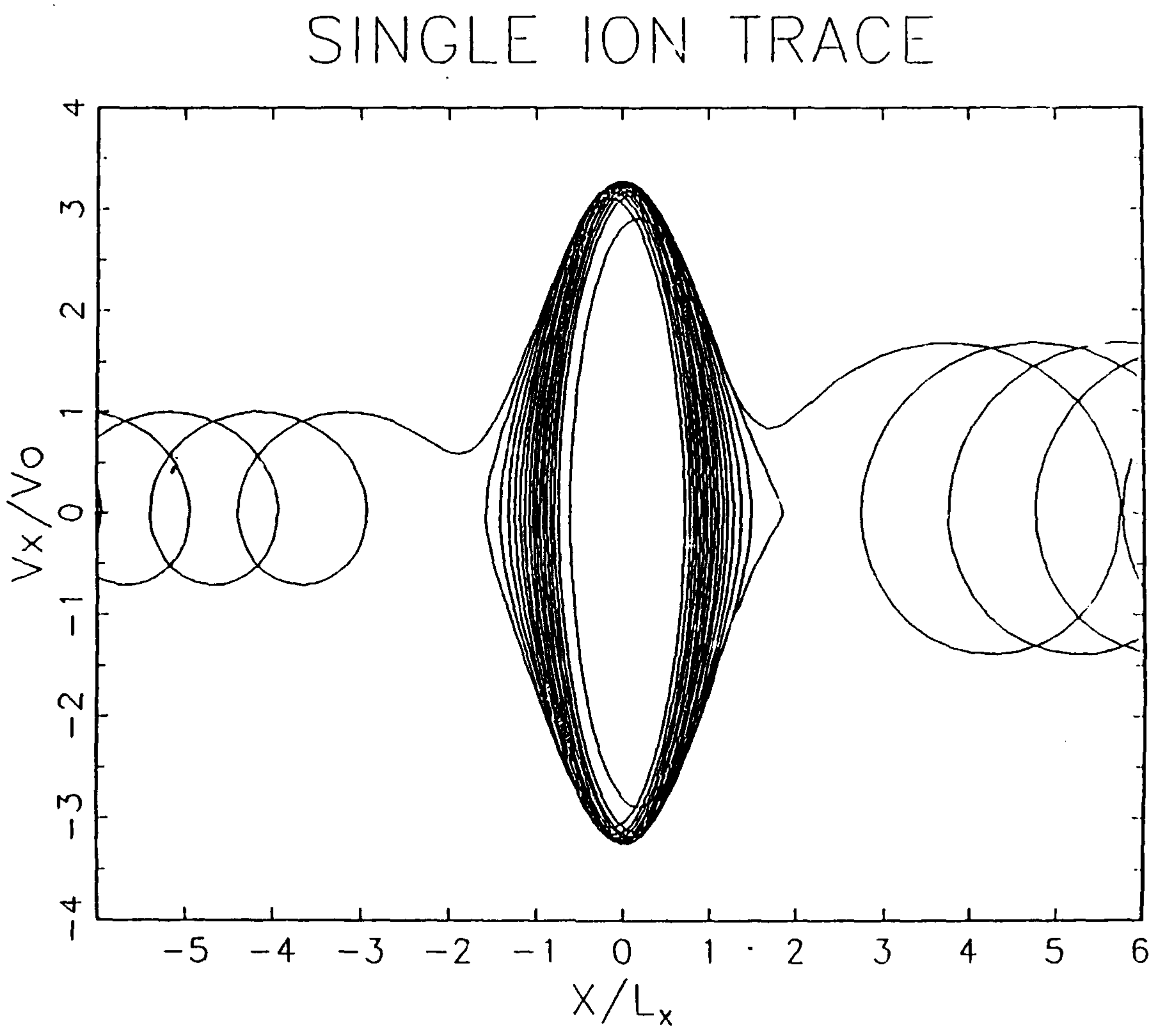

Fig. 2b

SINGLE ION TRACE

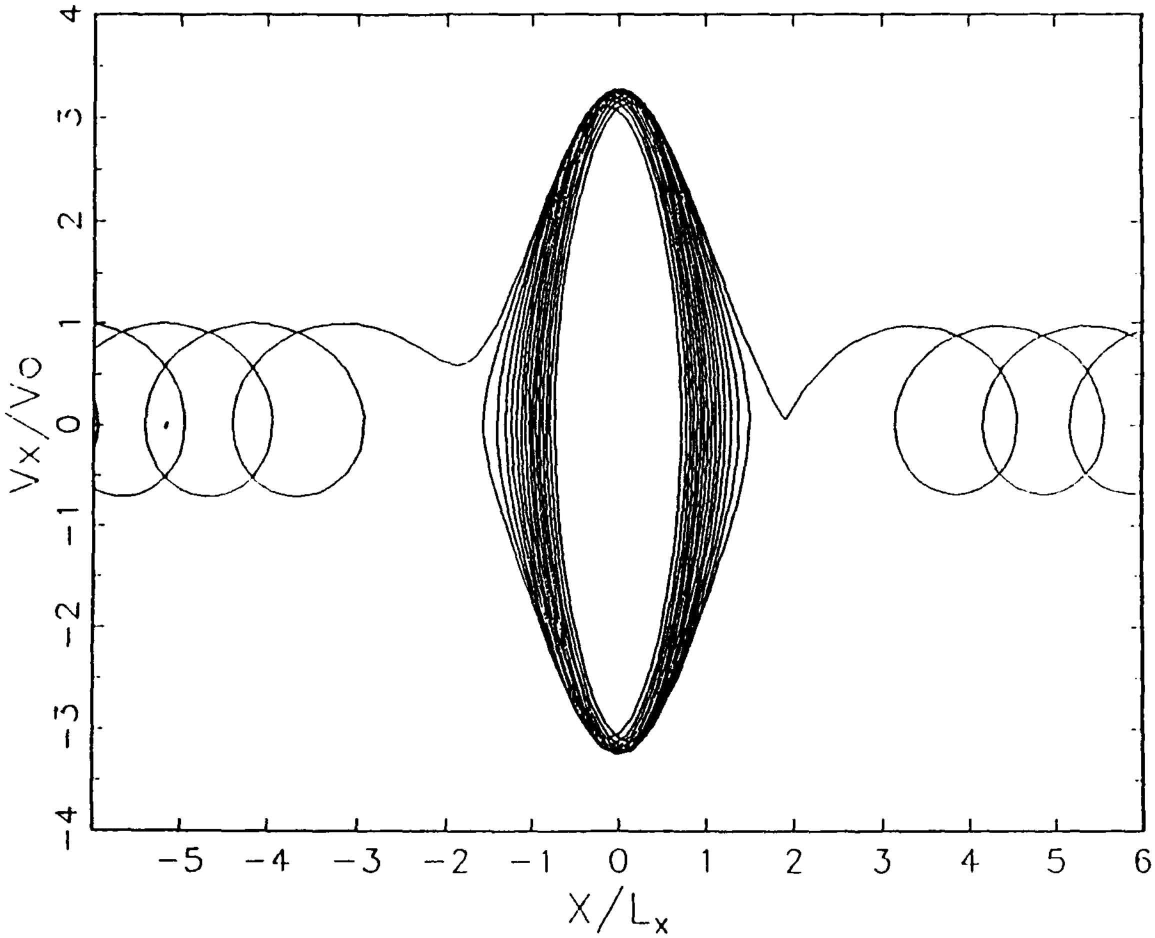

Fig. 2c

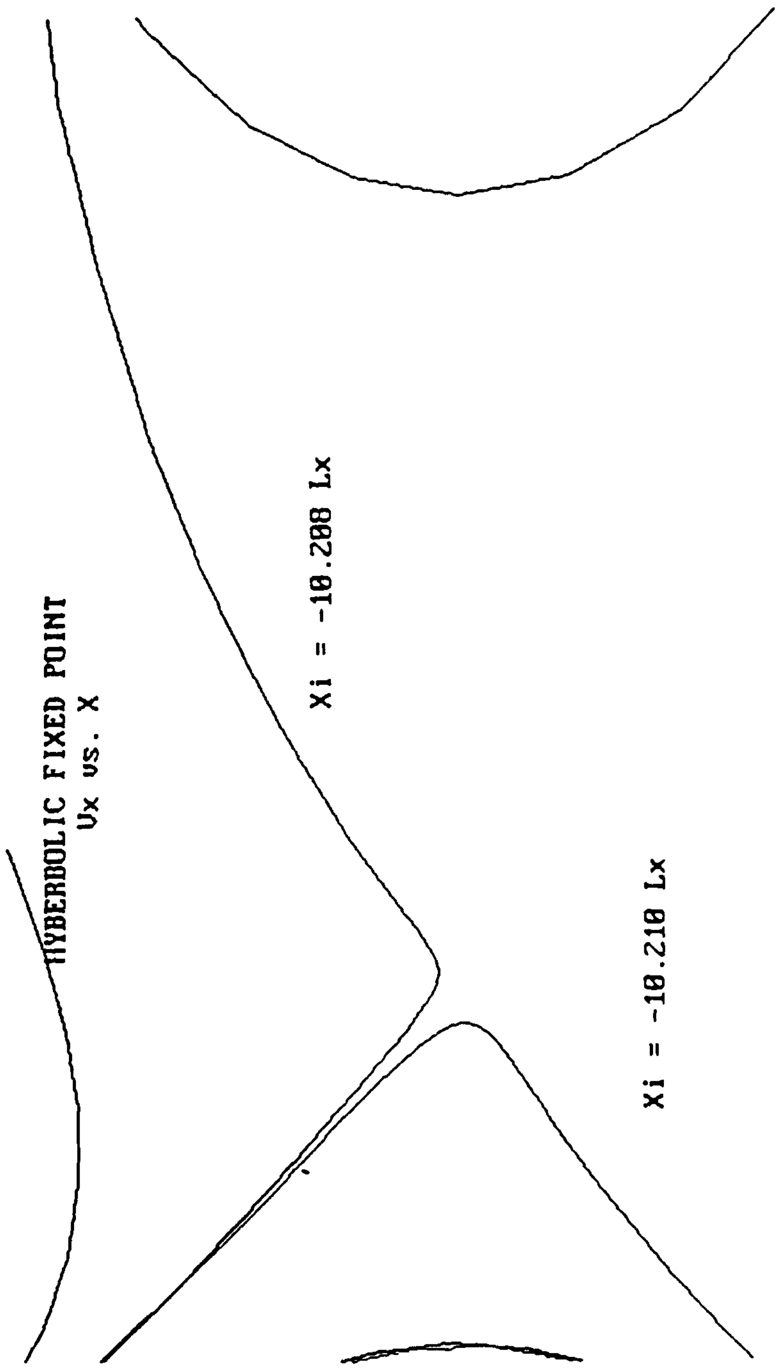

Fig. 2d

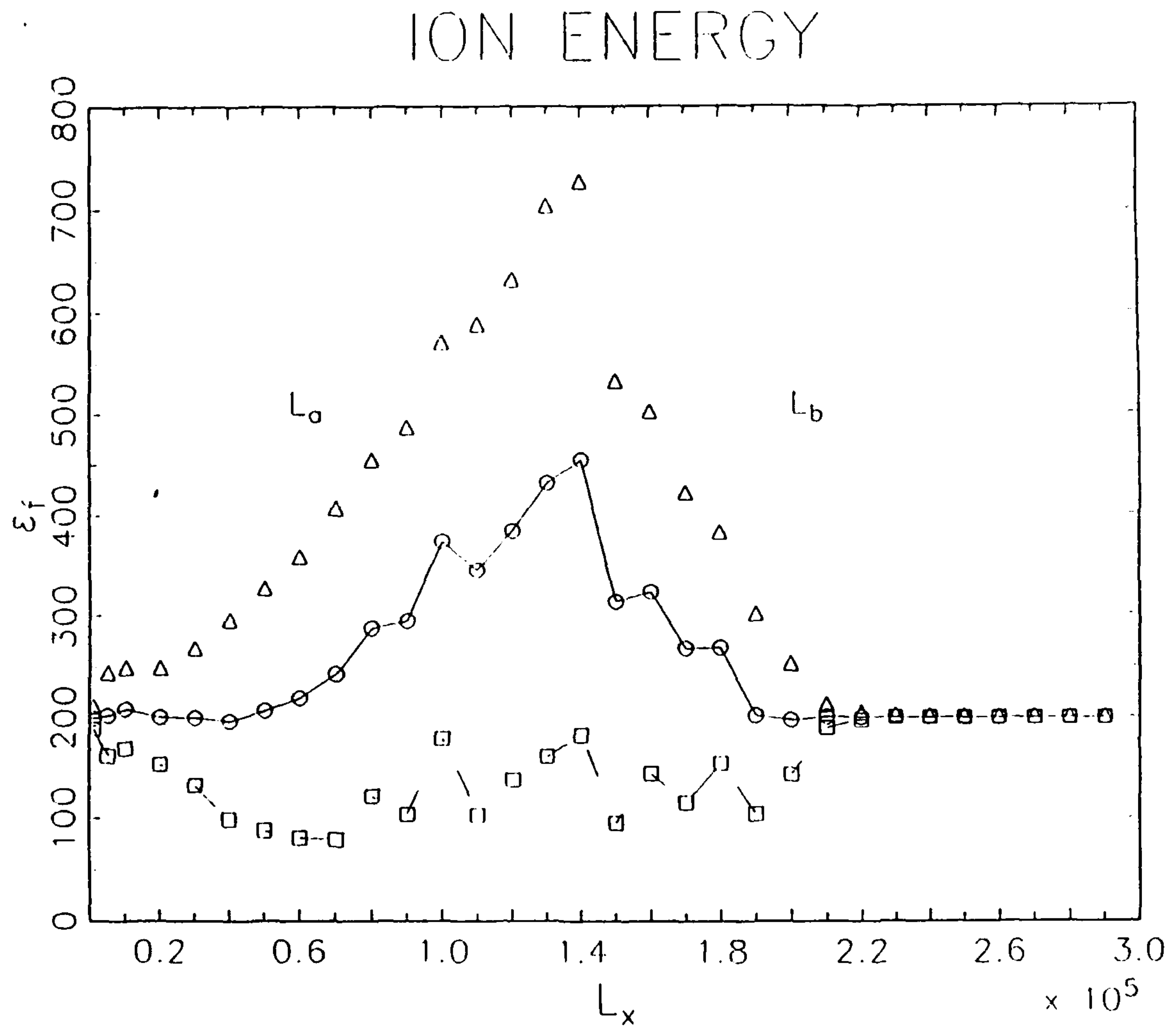

ION ENERGY
ε_i
0
100
200
300
400
500
600
700
800
L_a
L_b
0.2
0.6
1.0
1.4
1.8
2.2
2.6
3.0
L_x
$\times 10^5$

Fig. 3

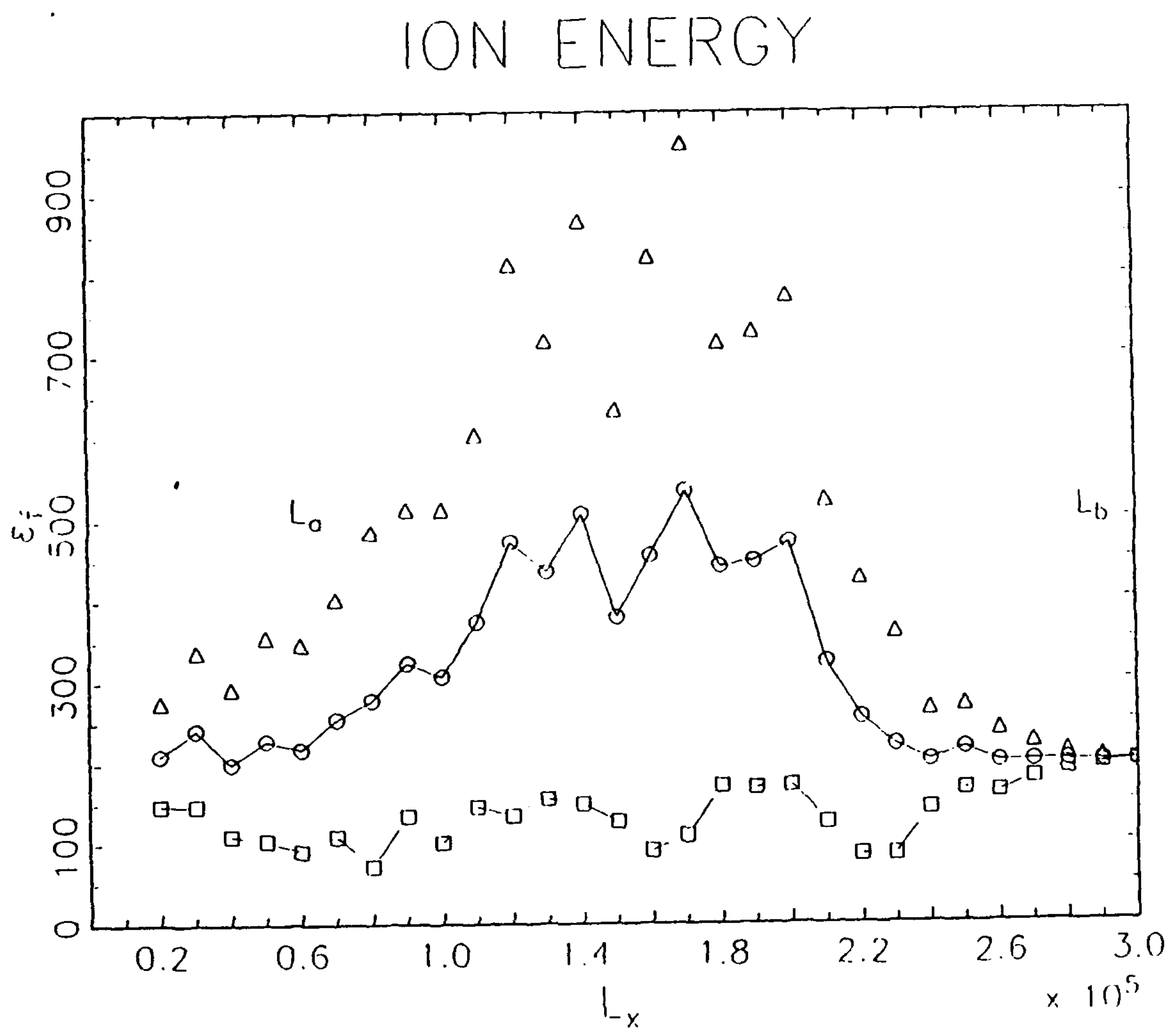
ION ENERGY
900
700
500
300
100
0
ε_i
L_a
L_b
0.2
0.6
1.0
1.4
1.8
2.2
2.6
3.0
$\times 10^5$
L_x

Fig. 4

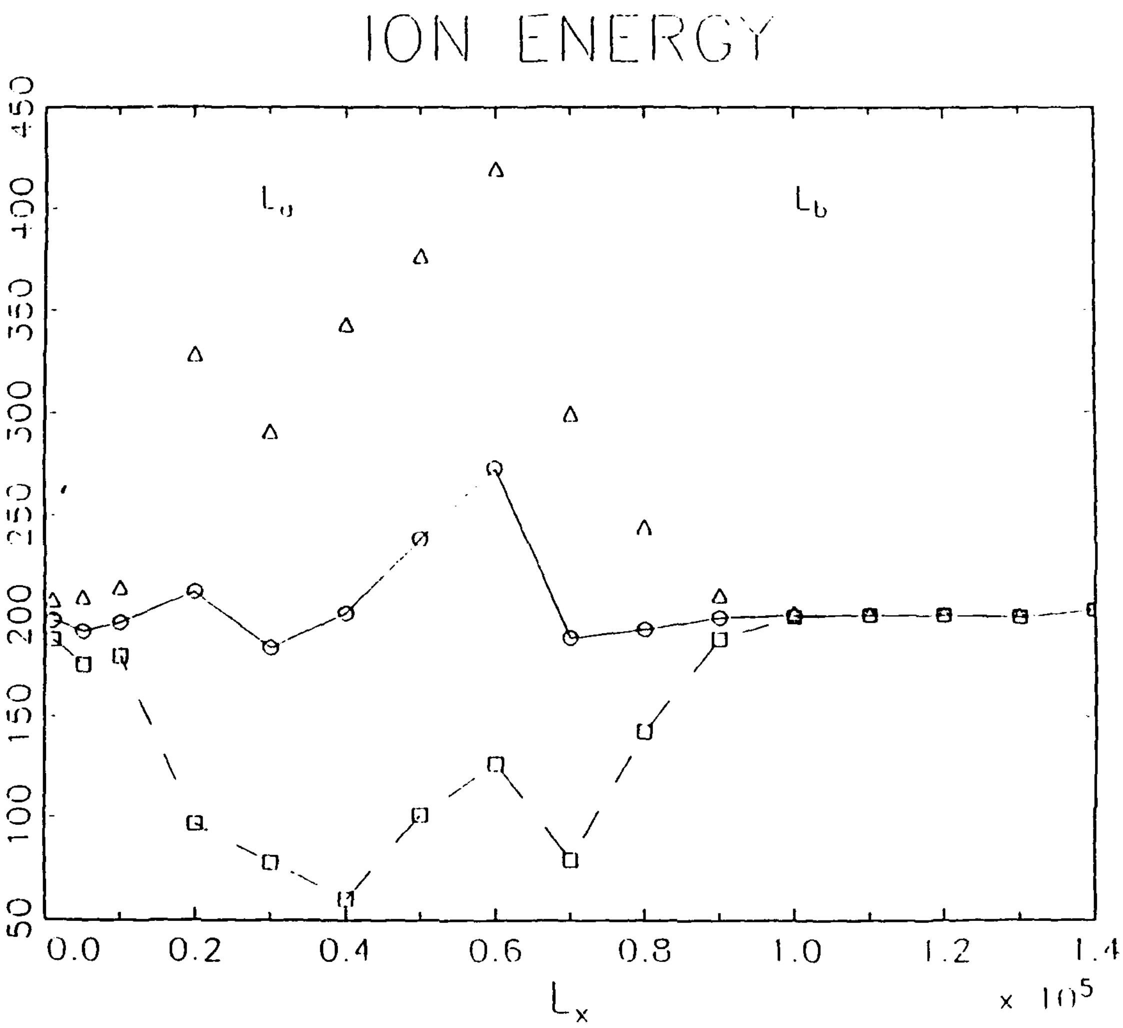

ION ENERGY
L_a
L_b
450
400
350
300
250
200
150
100
50
0.0
0.2
0.4
0.6
0.8
1.0
1.2
1.4
L_x
x 10^5

Fig. 5

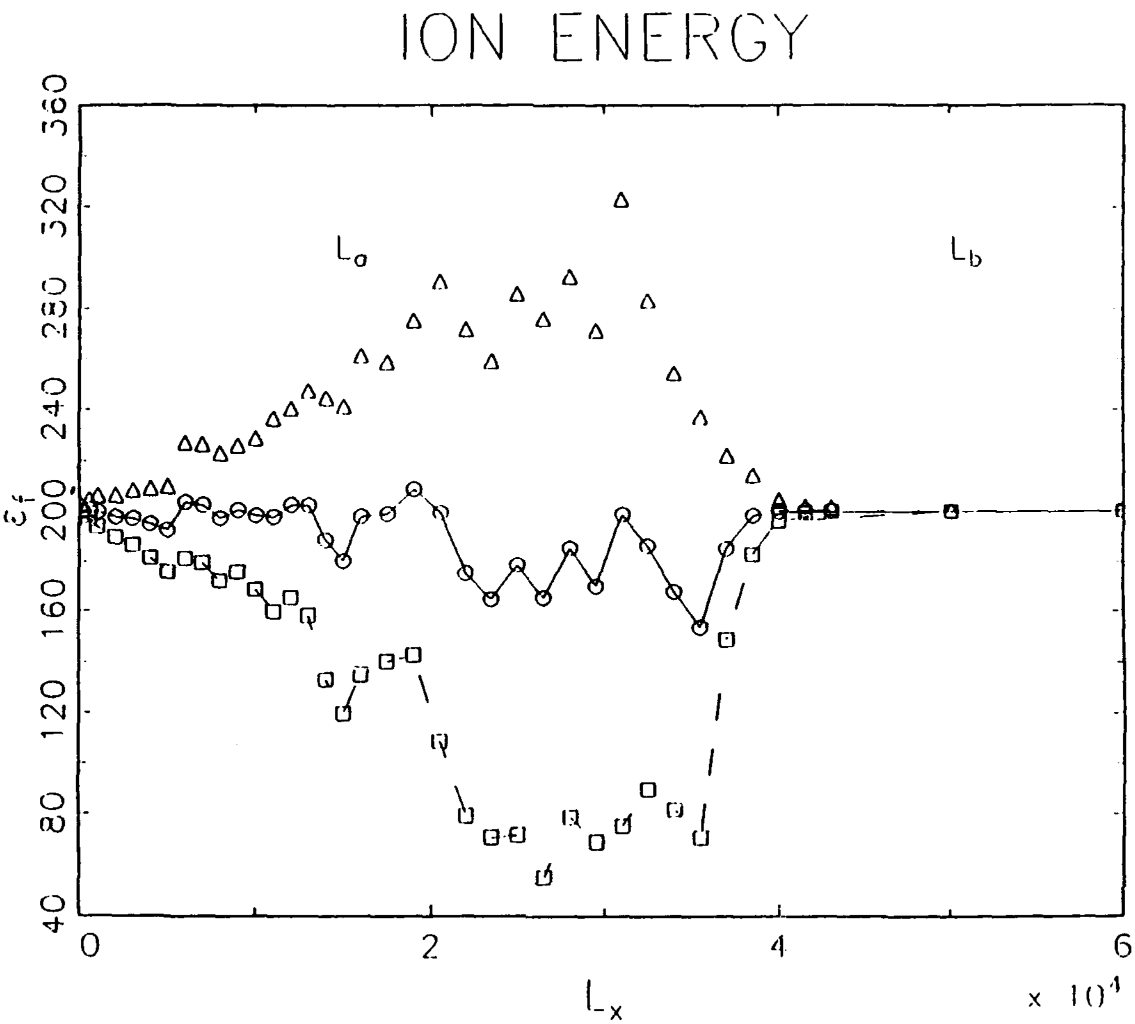

ION ENERGY
L_a
L_b
ε_f
40
80
120
160
200
240
280
320
360
0
2
4
6
L_x
x 10^4

Fig. 6

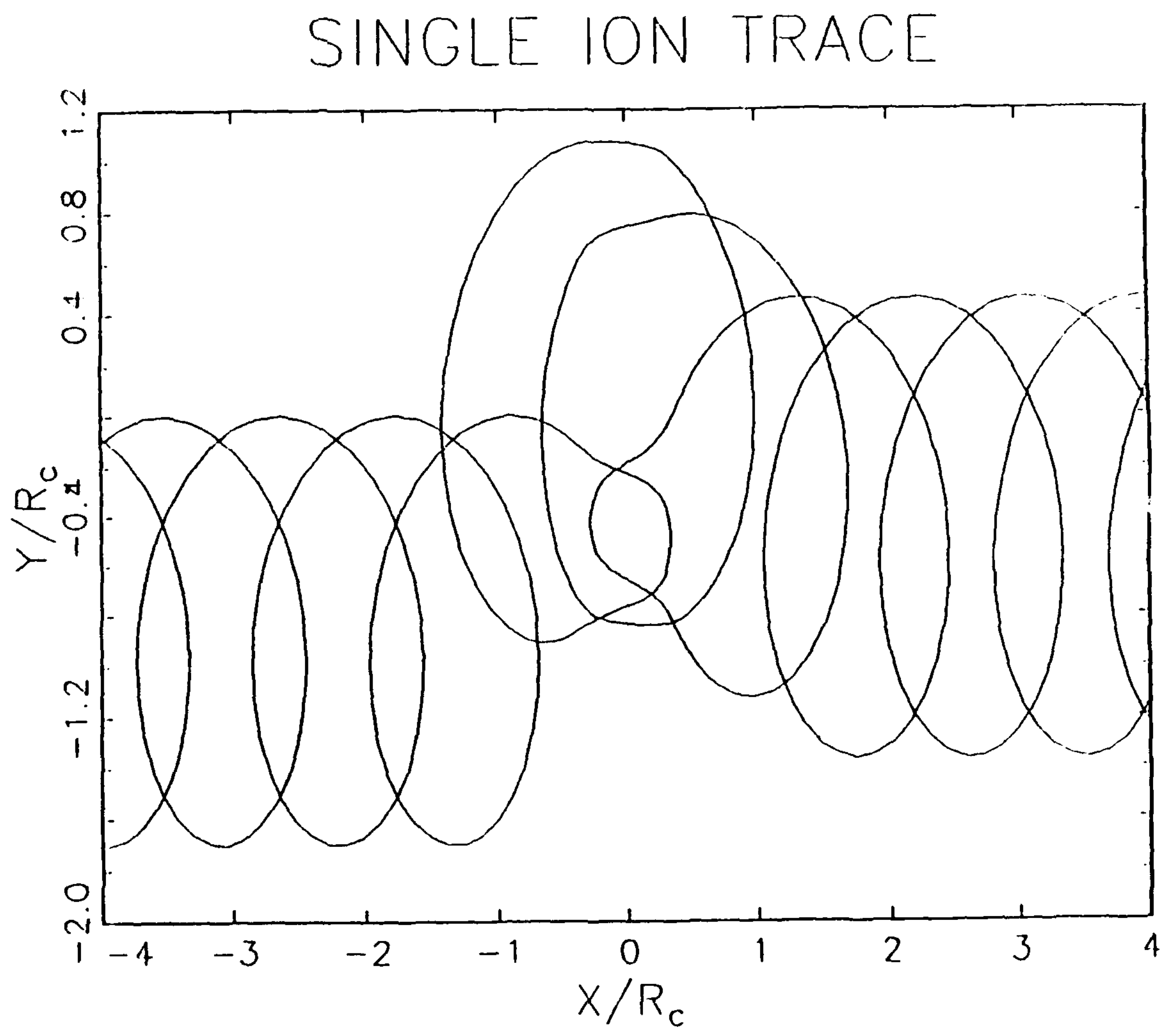

Fig. 7a

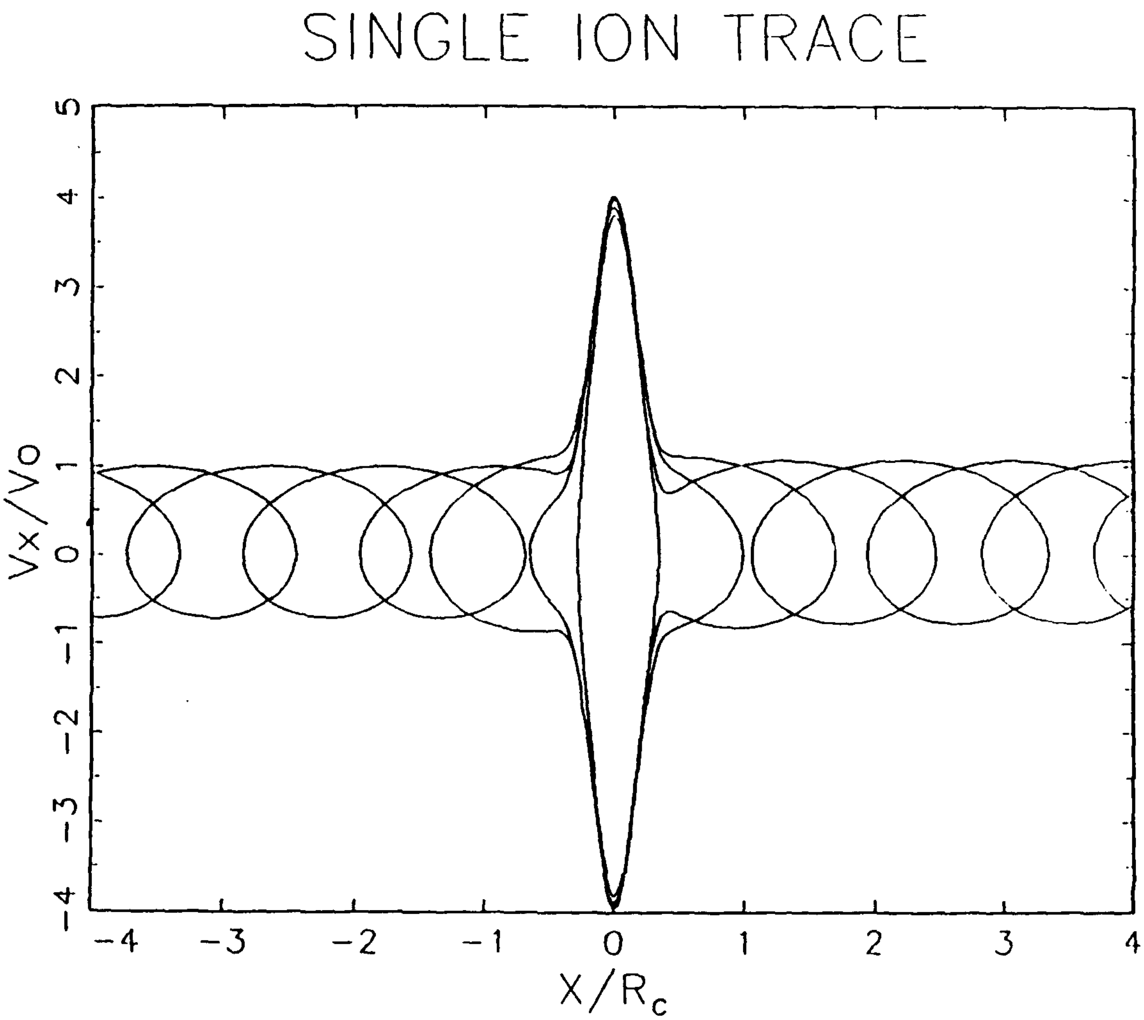

Fig. 7b

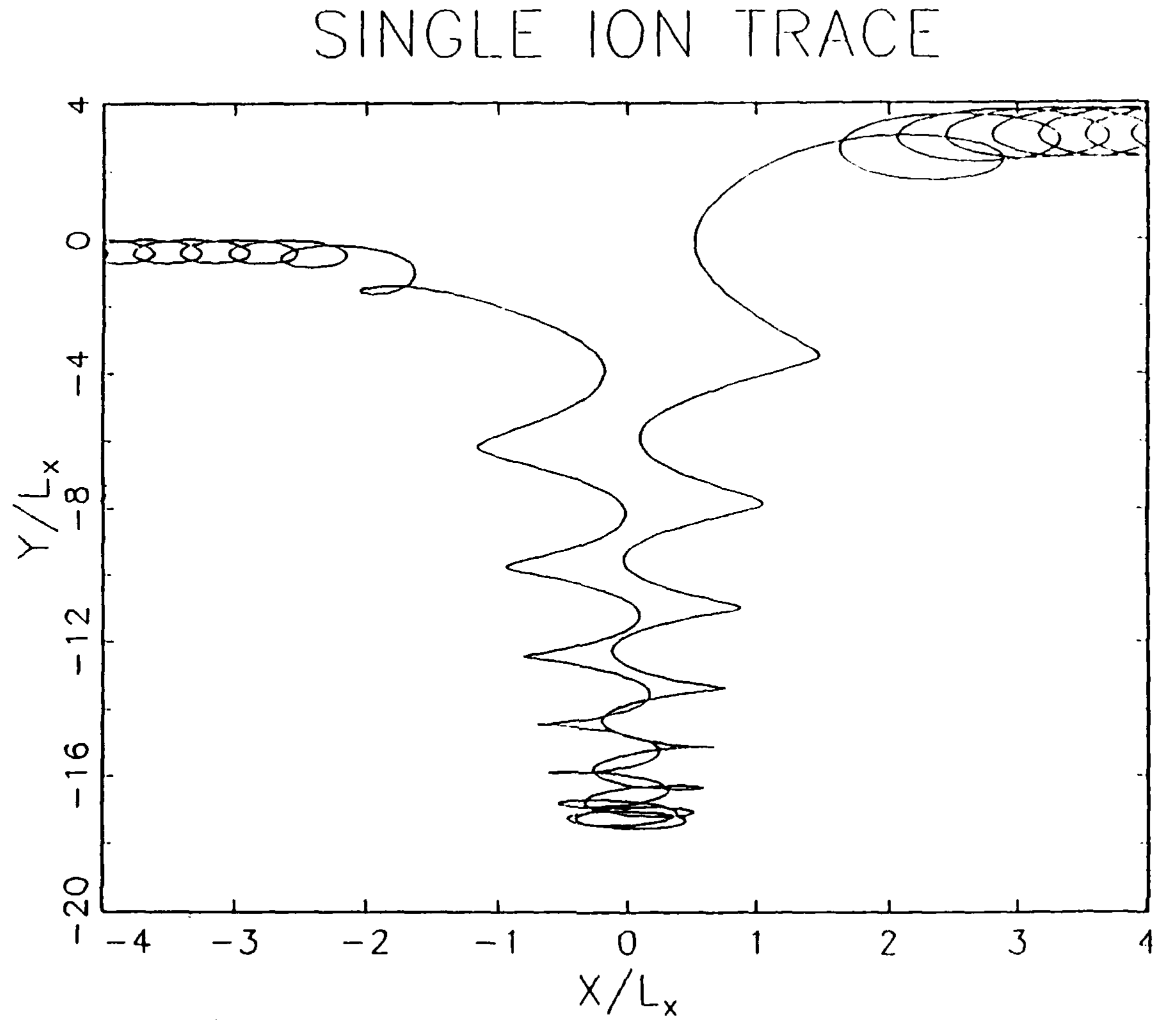

Fig. 8a

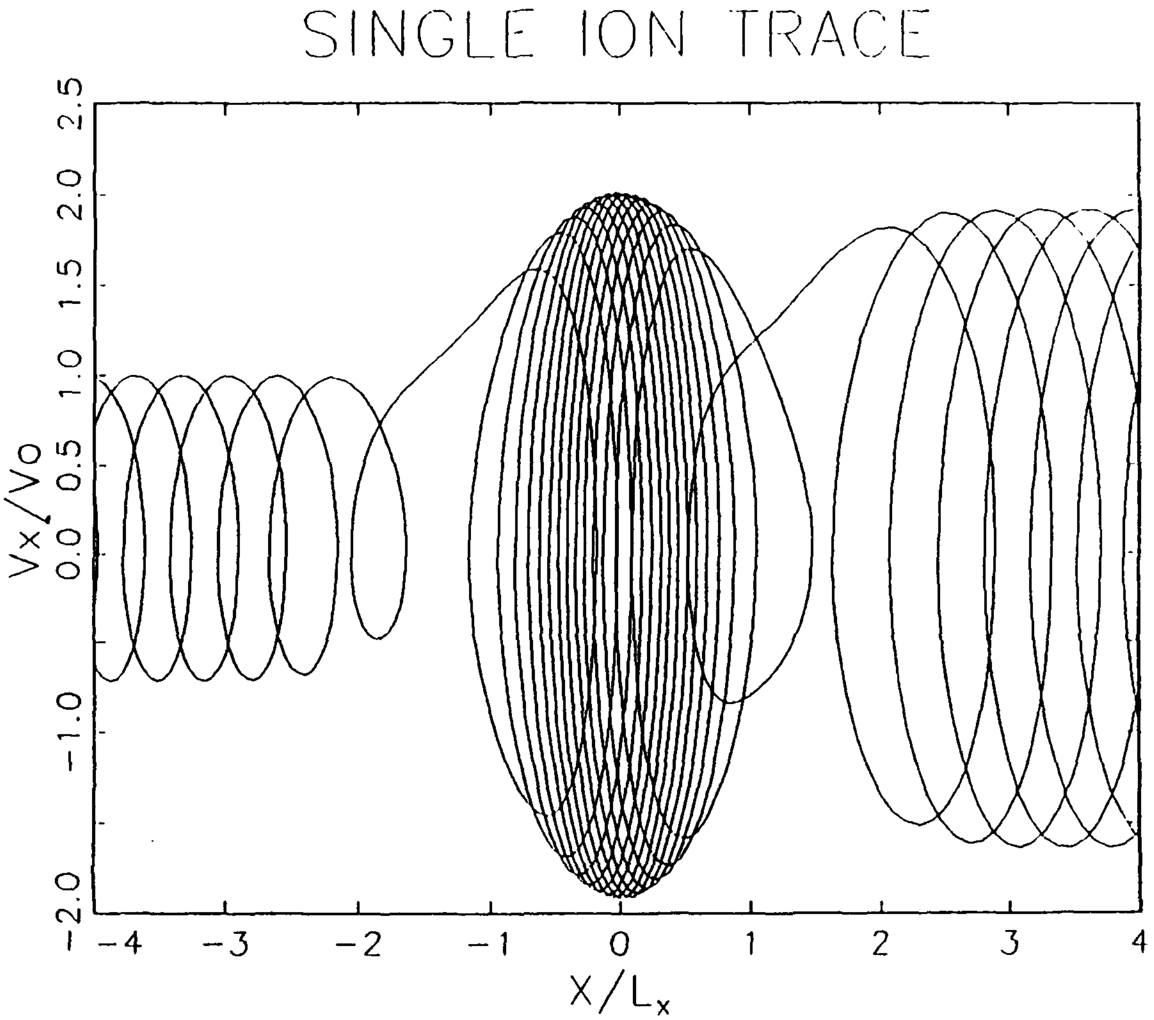

Fig. 8b

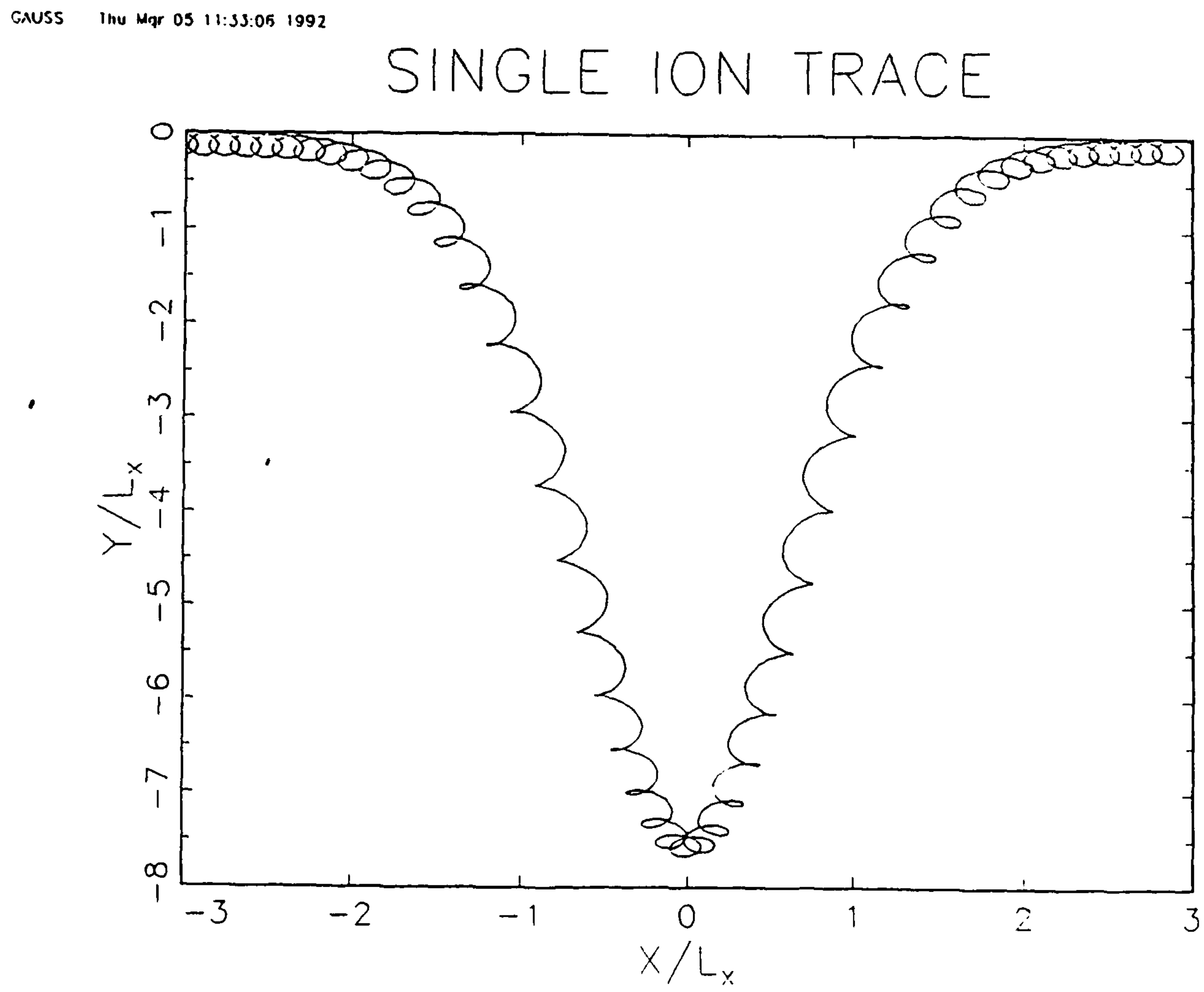
GAUSS Thu Mar 05 11:33:06 1992
SINGLE ION TRACE
0
-1
-2
-3
-4
-5
-6
-7
-8
Y/Lx
-3
-2
-1
0
1
2
3
X/Lx

FIGURE 9a

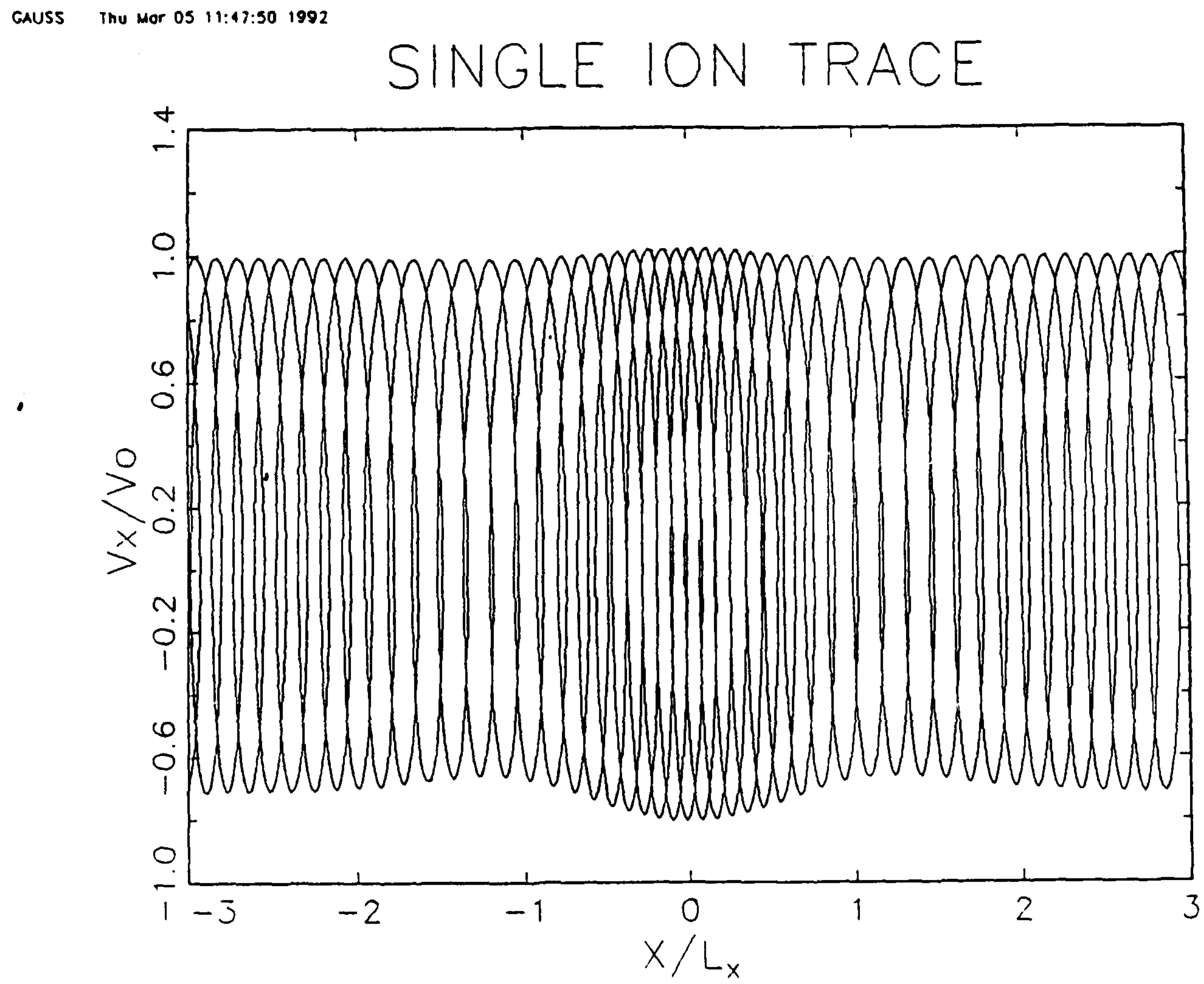

GAUSS Thu Mar 05 11:47:50 1992
SINGLE ION TRACE
1.4
1.0
0.6
0.2
-0.2
-0.6
-1.0
Vx/Vo
-3
-2
-1
0
1
2
3
X/Lx

FIGURE 9b

The Dynamics of Charged Particles in the Near Wake of a Very Negatively Charged Body–Laboratory Experiment and Numerical Simulation

M. Alvin Morgan
Chung Chan
David L. Cooke
Maurice F. Tautz

Reprinted from
IEEE TRANSACTIONS ON PLASMA SCIENCE
Vol. 17, No. 2, April 1989

The Dynamics of Charged Particles in the Near Wake of a Very Negatively Charged Body—Laboratory Experiment and Numerical Simulation

M. ALVIN MORGAN, CHUNG CHAN, SENIOR MEMBER, IEEE, DAVID L. COOKE, AND MAURICE F. TAUTZ

***Abstract*—A numerical simulation that is cylindrical in configuration space and 3-D (v_r, v_θ, v_z) in velocity space has been initiated to test a model for the near-wake dynamics of a very negatively charged body. The simulation parameters were closely matched to those of a laboratory experiment so that the results may be compared directly. It was found from the laboratory study that the electrons and ions can display different temporal features in the filling-in of the wake; and that they both can be found in the very near-wake region (within one body diameter) of an object with a highly negative body potential. We have also found that the temperature of the electrons in the very near wake could be somewhat colder than the ambient value, suggesting the possibility of a filtering mechanism being operative there.**

The simulation results to date largely corroborate the density findings in terms of the presence of an enhancement for both ions and electrons and in its location. There is reason to think too that additional agreements can be realized if two key elements—the inclusion of a 2-component, source electron distribution in the simulation and an understanding of the perturbation imposed by the diagnostic probe itself on the experiment—can be achieved. This is an ongoing process. Results from both the laboratory experiment and the numerical simulation will be presented, and a model that accommodates these findings will be discussed.

I. INTRODUCTION

THE need to further understand the plasma environment surrounding spacecrafts has been recognized for sometime now. With the resumption of shuttle flights into near-earth orbit, and the wide variety of experiments that are to be carried out in its wake or within that of the planned space station, it is becoming imperative that this information be acquired. Hester and Sonin [1], Samir *et al.* [2], and Stone [3] are foremost among those who have reported on experiments that seek to relate laboratory wake phenomena to the space environment. Others, including Martin [4] and Parker [5] have sought to gain some insight into the physics of plasma wakes by means of numerical simulation. To date, however, there has not been much attention given to corroborating numerical simulation results with laboratory findings. A key reason for wanting to do this would be to obtain some assurance that a numerical model can indeed provide results that are realistic: one could actually test the code with some known parameters and compare the results. Conversely, if the model's efficacy is established, then one might want to see how well the laboratory results conform to the model.

This paper is an update of our ongoing effort to understand the dynamics of charged particles in the near wake of a very negatively charged body. In previous publications, we reported on the temporal evolution of electron and ion streams within one body radius in the wake of a metallic disc placed in a flowing plasma [6]; and on the variability of the electron temperature in the same region depending on the characteristics of the surrounding plasma [7]. Here, we briefly review these recent and entirely unanticipated findings, present some results from a steady-state numerical simulation (that incorporated much of the experimental parameters, including the finite boundary and the wall potential) which corroborate the steady-state, electron, and ion density findings, and propose a model that links these results together. The organization of the subsequent material is as follows: Section II contains a brief description of the experimental configuration and the experimental results. Section III describes in short order the numerical model and technique that were used to carry out a computer simulation of the experimental scenario. The simulation results achieved to date are also presented. A discussion of the laboratory and simulation results then follow, in the closing Section IV.

II. EXPERIMENTAL CONFIGURATION AND RESULTS

Our experiments were performed in a pulsed plasma stream that was produced in the modified double plasma device shown in Fig. 1. The object used was a thin (thickness < 0.5 cm) aluminum disc of radius ≅ 3.25 cm. It was suspended in the middle of the stream 5.0 cm from the plasma entrance into the target chamber. Readers are referred to previous publications for details on the experimental set-up and diagnostics [6], and on the specifics of the generated plasma [7]. For the particle density studies, the typical operating parameters were: Plasma source density $n_0 \cong 10^9$ cm^{-3}; average plasma stream (target)

Manuscript received August 27, 1988; revised January 23, 1989. The work of M.A. Morgan and C. Chan was partially supported by NASA under Grant no. NAGW 1572 and by the Air Force Geophysics Laboratory under Contract no. F19628-85-K-0053.

M. A. Morgan and C. Chan are with the Center for Electromagnetics Research, Department of Electrical and Computer Engineering, Northeastern University, 235 Forsyth Bldg., Boston, MA 02115.

D. L. Cooke is with the Air Force Geophysics Laboratory, Space Physics Division, Spacecraft Interactions Branch, Hanscom Air Force Base, Bedford, MA 01731.

M. F. Tautz is with Radex, Inc., 192 Log Hill Road, Carlisle, MA 01741.

IEEE Log Number 8927086.

0093-3813/89/0400-0220$01.00 © 1989 IEEE

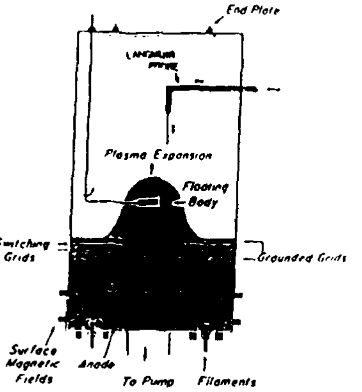

Fig. 1. Schematic of the experimental device.

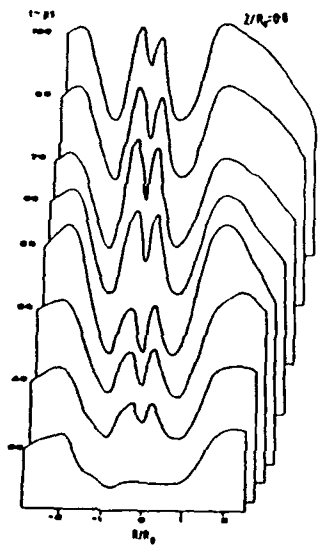

Fig. 2. $A < 1$: Time evolving measured electron current density profiles at $Z/R_0 = 0.8$.

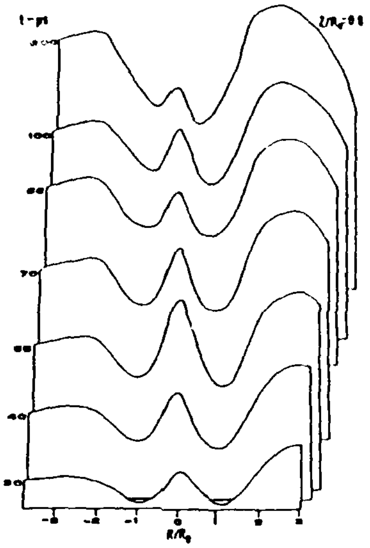

Fig. 3. $A < 1$: Time evolving measured ion current density profiles at $Z/R_0 = 0.8$.

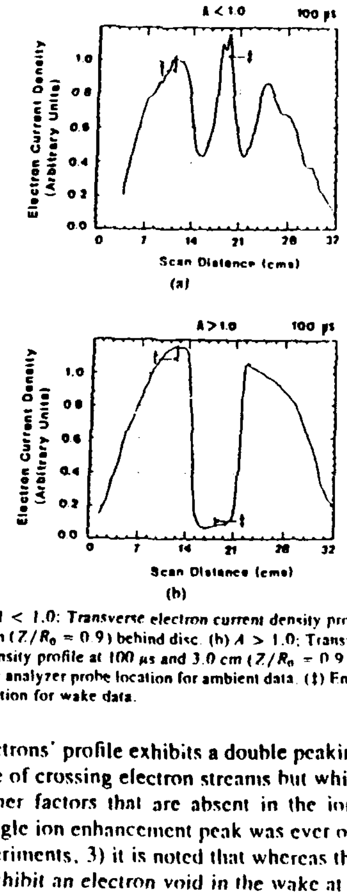

Fig. 4. (a) $A < 1.0$: Transverse electron current density profile at 100 μs and 3.0 cm ($Z/R_0 = 0.9$) behind disc. (b) $A > 1.0$: Transverse electron current density profile at 100 μs and 3.0 cm ($Z/R_0 = 0.9$) behind disc. (↑) Energy analyzer probe location for ambient data. (↕) Energy analyzer probe location for wake data.

density $n_i \cong 10^5$-10^7 cm^{-3}; ambient electron temperature $T_e \cong 2$-4 eV and ion temperature $T_i \lesssim 0.3$ eV; ion flow velocity $(v_i) = 1 \rightarrow 2c_s$, where c_s is the ion-acoustic velocity; Debye length $(\lambda_D) \cong 0.33$ cm; and the steady-state floating potential of the object was $\cong -20 \rightarrow -25$ V. The ratio of the ion flow energy to the object potential energy—subsequently referred to as the A parameter—was < 1.0.

Figs. 2 and 3 are illustrative of the results obtained for electron and ion current density in this plasma regime. The figures both infer particle density at a fixed location ($Z/R_0 = 0.8$) in time, from 30 to 100 μs for the electrons and to 500 μs for the ions. The salient points here are that 1) a strong enhancement in density for both particles in the wake is evident at this location. Indeed, it can be seen that at 70 μs for the electrons and 55 μs for the ions, the wake density exceeds the ambient density in magnitude, 2) the electrons' profile exhibits a double peaking feature, suggestive of crossing electron streams but which may be due to other factors that are absent in the ion profiles. Only a single ion enhancement peak was ever observed in these experiments, 3) it is noted that whereas the electron profiles exhibit an electron void in the wake at 30 μs, the

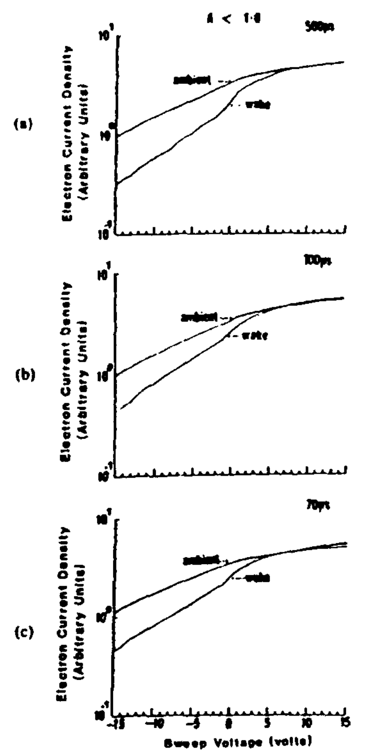

Fig. 5. $A < 1.0$; Energy analyzer probe traces of ambient and wake, electron data at 3.0 cm ($Z/R_0 = 0.9$) and time (a) 500 μs; (b) 100 μs; and (c) 70 μs.

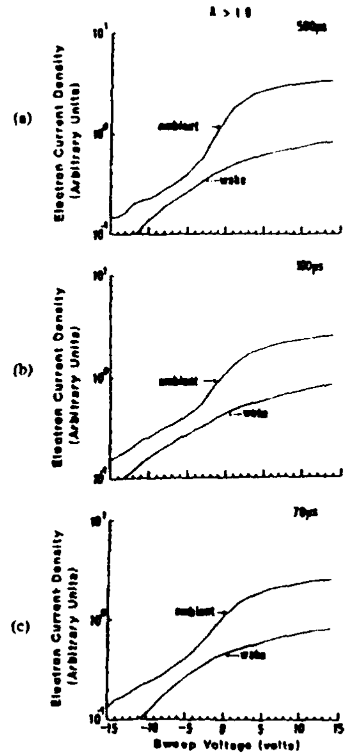

Fig. 6. $A < 1.0$; Energy analyzer probe traces of ambient and wake, electron data at 3.0 cm ($Z/R_0 = 0.9$) and time (a) 500 μs; (b) 100 μs; and (c) 70 μs.

equivalent ion profile displays a significant ion enhancement. This strongly suggests that particle enhancement occurs first with the ions and subsequently with the electrons.

In the electron temperature experiments two plasma regimes were investigated. One regime corresponded to that used for the aforementioned temporal studies as outlined above. In the other, v_s was increased to $3 \rightarrow 5c_s$ and ϕ_B was ≈ -10 V, such that $A = 2.0 \rightarrow 3.0$, or $A > 1.0$. Fig. 4(a) for the $A < 1.0$ regime and Fig. 4(b) for $A > 1.0$ effectively summarize the contrast between the two plasma regimes in terms of the near-wake density. They show the electron current density profiles as obtained by scanning transversely at 3.0 cm ($Z/R_0 = 0.9$) behind the disc; as can be seen in Fig. 4(b), the density profile displays a void in the wake with respect to the ambient density. This is in sharp contrast to the profile shown in Fig. 4(a) for which a density enhancement in the region is clearly evident.

Figs. 5 and 6 show the electron energy distribution for the $A < 1.0$ and $A > 1.0$ regimes, respectively, at the location ($Z/R_0 = 0.9$) of Fig. 4. It was found that in both regimes the energy distribution consists of a Maxwellian bulk population at the plasma potential, and another population of hotter-tail electrons. However, the location at which this is true is different for the two regimes. As a result, while the ambient temperature is clearly colder than that of the wake region in the $A > 1.0$ regime, the converse is true in the $A < 1.0$ instance. It is seen then that for $A < 1$, a large-density enhancement in the near wake corresponds to cold ambient electrons being drawn into the region. On the other hand, in the absence of any near-wake density enhancement, the electron temperature in the region could be even hotter than the ambient value due to the presence of a hot-tail component in the bulk electron distribution of the flowing plasma.

III. Numerical Model, Simulation Technique, and Simulation Results

In order to further verify the results that were achieved in the experiments, a full computer simulation of the experimental scenario was initiated. The approach taken was to model the plasma kinetically; that is, the net motion of many interacting particles was regarded as the determining factor in the plasma flow. The laws of mechanics are therefore applied to the individual particles of the ensemble, and statistical techniques are then used to determine the net movement of the bulk plasma. As such, the relevant equations that govern particle behavior in a rarefied plasma flow with singly ionized ions and electrons surrounding an object are 1) the Vlasov equations for both ions and electrons which provide the local values of both species, and 2) Poisson's equation, which governs the electric potential. Since the thermal velocity of the electrons ($v_{the} \cong 10^8$ cm/s) significantly exceeds the plasma-streaming velocity, which is on the order of the ion-acoustic velocity (i.e., $v_p \approx 2c_s = (5)10^5$ cm/s, where c_s = ion-acoustic velocity), it is therefore usual to consider the electrons to be in thermal equilibrium and to have a Maxwell-Boltzmann energy distribution so that

$$f_e(x, v, t) = n_0\left(\frac{m_e}{2\pi kT}\right)^{1/2} \cdot \exp\left[\left(e\Phi(x, t) - \frac{1}{2} m_e v^2\right)\Big/ KT_e\right] \quad (1)$$

where n = initial stream electron density, and v = electron thermal velocity.

The local electron density is then given by

$$n_e(x, t) = n_0 \exp\left[\left(e\Phi(x, t)/KT_e\right)\right]. \quad (2)$$

The ion-energy distribution cannot be as easily specified, for there is no ready form in which the ion density can be expressed. The local ion density is thus expressed as

$$n_i = \int_{-\infty}^{+\infty} f_i \, dv \quad (3)$$

where f_i is to be determined.

Substituting (2) and (3) into Poisson's equation, one gets

$$\nabla^2\Phi = 4\pi e\left[n_0 \exp\left(e\Phi/KT_e\right) - \int f_i \, dv\right] \quad (4)$$

which is solved along with the Vlasov equation for ions,

$$\frac{\partial f_i}{\partial t} + v_i \cdot \nabla f_i + \frac{e}{m_i} \nabla\Phi \cdot \nabla_v f_i = 0. \quad (5)$$

It is then necessary to solve (4) and (5), subject to the appropriate boundary conditions, to get self-consistent values for n_e, n_i, and Φ.

In general, four boundary conditions are required to obtain a solution. These are as follows:

1) The potential on the body; i.e., $\Phi(R) = \Phi_s$, where R = body radius, and Φ_s = surface potential.
2) The potential far away from the object, usually expressed as $\Phi(\infty, t)$, but necessarily the boundary potential in a bounded plasma.
3) The distribution function for ions, far away from the object $f_i(\infty, v)$; also, it is just the distribution function for ions at the edge in a bounded plasma.
4) The distribution that describes the charged ions leaving the surface of the object—$f_i(R, v_R > 0)$; where v_R = velocity of the emitted ion at the boundary of the object; i.e., at the body radius R.

Generally, all of the above information cannot be readily known and some assumptions must be made. For boundary condition 4, for example, it was assumed that the object surface is perfectly conducting to incident ions and secondary emission was ignored; $f_i(R, v_R > 0)$ was therefore set to zero. $f_i(\infty, V)$, on the other hand, was specified to be a drifting Maxwellian, given by

$$f_\infty = \left(\frac{m}{2\pi KT}\right) \exp - \left(\frac{m}{2KT}(v_i - v_s)^2\right)$$

where v_s is the plasma flow velocity.

The boundary potential was set at $-1\ KT_e$, which roughly corresponded to the actual experimental chamber-wall sheath value and the object body potential was set at a steady-state value of -20 V.

The actual solution technique used was the "inside-out" method [8]. Particles were followed from a point within the wake, then back outside into the ambient plasma in a time-independent fashion. With no time dependency the distribution function along the particle tracks is constrained to be whatever it is specified to be in the source region, thus affording a means of solving Vlasov's equation to obtain particle densities. The program used was the Mesothermal Auroral CHarging (MACH) program. It is an adaptation of TDWAKE, a program originally developed for the National Aeronautics and Space Administration (NASA). Currently in the possession of the Space Physics Division of the U.S. Air Force Geophysics Laboratory, MACH was developed in part to study the sheath structures surrounding large bodies in space. It is 2-D (R, Z) in configuration space and 3-D (v_x, v_y, v_z) in velocity space.

Computations were carried out in a cylindrical mesh centered on the object, and the Vlasov and Poisson equations were solved to produce electron density, ion density, total density, and electric potential at each iteration node point. The machine on which the program was executed was a RIDGE-32 supermini computer.

The steady-state results for the electron and ion density, as obtained by inputting the parameters for the $A < 1.0$ regime of the experimental study and iterating in a cylindrical space scaled to the dimensions of the plasma chamber, are shown in Figs. 7 and 8, respectively. Corresponding plots from data taken at 500 μs (the longest time for which experimental data was available, and which is essentially steady state in the experiment) are shown in Figs. 9 and 10. It is clearly seen in the experimental results that a density enhancement occurs in the wake region of both species; in addition, the location at which this is true is roughly equivalent, for it occurs between $Z/R_0 \approx 0.6 \rightarrow 1.2$ for the electrons, and between $Z/R_0 \approx 0.5 \rightarrow 1.0$ for the ions. In the simulation results, some density enhancement is also seen in the wake region. The location at which this occurs, however, is a little further downstream from that of the experimental results, at $Z/R_0 = 1.6 \rightarrow 2.1$ for ions and $Z/R_0 \approx 1.7 \rightarrow 2.1$ for electrons. It is noted too that in the electron profiles of Fig. 7 there

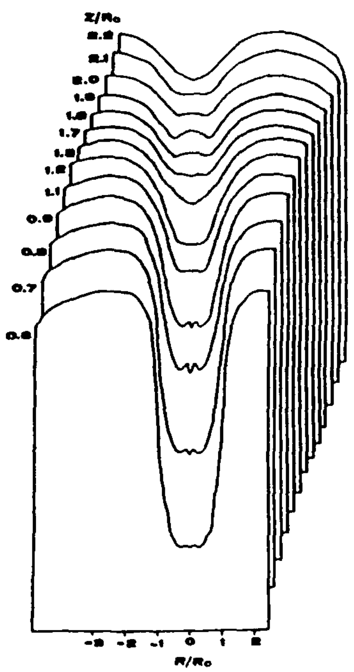

Fig. 7. $A < 1$; Two-dimensional electron number density profiles from simulation in the steady state.

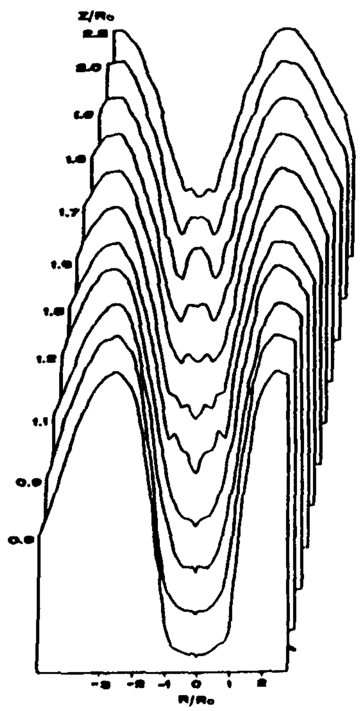

Fig. 8. $A < 1$; Two-dimensional ion number density profiles from simulation in a steady state.

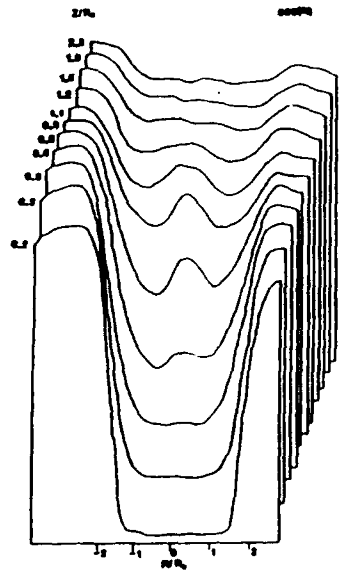

Fig. 9. $A < 1$; Two-dimensional electron current density profiles from experiment at 500 μs.

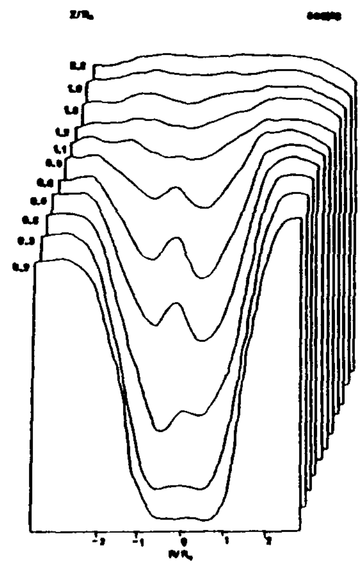

Fig. 10. $A < 1$; Two-dimensional ion current density profiles from experiment at 500 μs.

is some apparent enhancement at $Z/R_0 \approx 0.7 \rightarrow 1.0$ which is in very close accord with the experimental results. The amplitude of this feature with respect to the ambient density is considerably less than was observed in the corresponding experimental result however, and further effort is required to fully resolve this feature in order to determine exactly what is occurring there. One possible

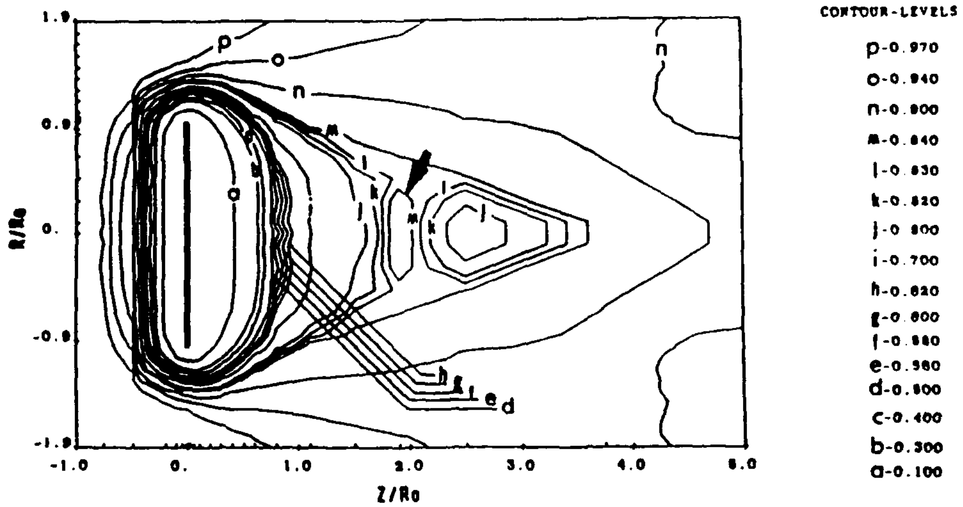

Fig. 11. $A < 1$; Two-dimensional electron density contours from simulation in a steady state.

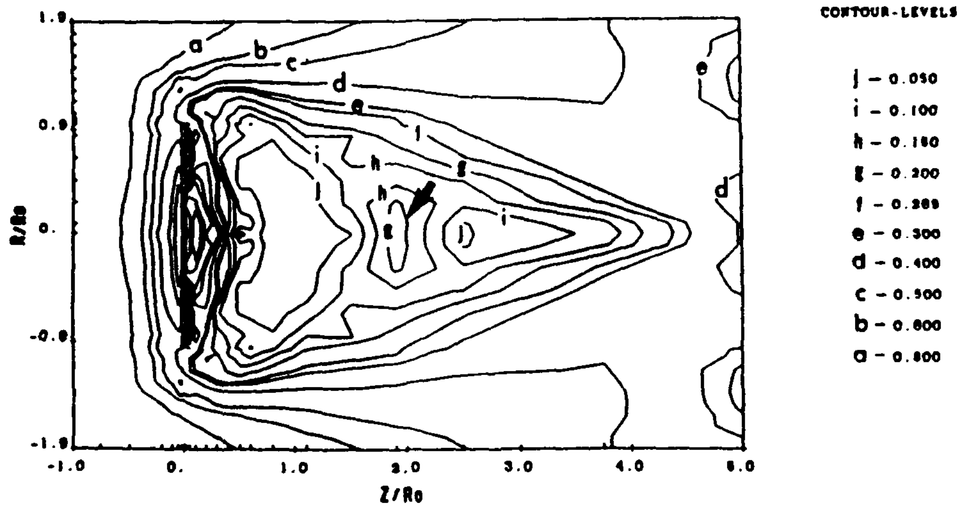

Fig. 12. $A < 1$; Two-dimensional ion density contours from simulation in a steady state.

explanation could lie in the fact that actual number densities were calculated in the simulation, while current density was the actual quantity measured in the experiments.

A different perspective of the information in Figs. 7 and 8 is shown in Figs. 11 and 12. These figures essentially show the 2-D density contours of the electrons and ions, respectively; in both, the density-enhancement regions (indicated by an arrow) can be clearly seen. The unnumbered contours to the left of $Z/R_0 \approx 0.5$ are indicative of ions impinging directly onto the backside of the object and creating a region of significant density enhancement in the process. Such a feature could not be observed in the experimental results because of the single-sided nature of the Langmuir probe that was used to make the density measurements. This is due to the fact that the trajectories of the particles that give rise to it would have impacted directly onto the backside of the probe which was covered with an insulating ceramic coating. This does serve to illustrate very nicely, however, how numerical simulations can direct experimental work, for the presence of such impinging ions will certainly be allowed for and possibly be detected in subsequent laboratory investigations.

IV. Discussion of Laboratory and Simulation Results

Although the experimental ion and electron current density profiles are similar in their essential features to the numerical profiles, there is a significant difference in their magnitudes. To begin with, the experimental data shows a much larger electron current density enhancement in the wake when compared to the electron-density enhancement seen in the numerical data. This might be explained by the fact that: a) Electron current density was the quantity measured in the experiment, while the actual electron number density was calculated in the simulation. As such, then, the velocity of the wake electrons could play a role in the observed differences in magnitude; b) there could also be some secondary electron emission from the backside of the disc, which is being impacted by ions. These electrons would contribute additionally to the enhancement of the wake electron current density as measured in the laboratory. Since secondary emission was not considered in the numerical simulation, this added enhancement effect would therefore not be a factor in the simulation results; c) another matter that could have some bearing on the observed differences is that the physical presence of a probe in the wake region of an object will influence to some extent the very parameters which the probe seeks to measure. Perturbations of this type are particularly noteworthy in these experiments, for the physics of Langmuir probes in the wake of a larger object is currently not well understood. To illustrate, it is noted that the wake of the probe could conceivably interact with the wake of the disc in such a manner that some of the observed difference between the experiment and simulation data might be attributed to the perturbing influence of the probe. We are currently engaged in studying how such effects could potentially arise by comparing the obtained I-V characteristic of a Langmuir probe that is physically immersed in a plasma (supported on a conducting probe shaft) with those obtained from numerical simulations of a probe-like object that is biased at varying potentials to collect electron current in the wake of a larger object. It is hoped that along with the wall effects, which have also been included in the simulation parameters, we will arrive at a better understanding of laboratory wake dynamics in the presence of diagnostic probes.

The picture that emerges from the experimental and simulation data then, regarding the dynamics of electrons and ions in the near wake, is a somewhat more involved process than that depicted in what has become the standard view of the near-wake environment. From that perspective, ions follow straight-line or "ballistic" trajectories in going past an object immersed in a collisionless plasma flow and cross the geometric axis of the object somewhere in the mid- to far-wake region. The near wake (the region in the immediate vicinity of the object and extending out to roughly $Z/R_0 < 4$) is thought to be ion free. These are the underlying assumptions in the works of several authors, including Taylor [9], Martin [10], Könemann [11], and Stone [12].

One difficulty with this standard viewpoint is the fact that for plasma-flow regimes in which the potential energy of the object exceeds the kinetic-flow energy of the plasma stream—i.e., when $A < 1.0$-ion trajectories will not follow ballistic paths, and as seen in Figs. 2-6, 9, and 10—ions do enter into the near-wake region. Such conditions could arise from the charging of a spacecraft during the emission of a charged-particle beam or during an auroral event.

The results indicate that if an $A < 1.0$ scenario suddenly comes about, ions will be attracted to the object, and under the influence of the surrounding charge sheath, which initially is large in extent (on the order of the object radius prior to the arrival of the main bulk plasma), will follow a curved trajectory into the region behind the object. This focusing action is enhanced by the fact that the sheath contracts as the plasma density increases at the object location (the final Debye length is ≤ 0.33 cms in our experiment), for the contracting sheath serves to pull ions even closer to the object. Indeed, it is seen from the simulation data that some ion trajectories impinge directly onto the backside of the object, even in a steady state.

The excess positive space charge generated by the buildup of ions just behind the object—clearly seen in Fig. 12—subsequently serve to attract more electrons to the area. This is supported by the experimental data in Figs. 2 and 3. As was pointed out in Section II, not only do the ions move into the wake region before the electrons, but the electron density is at a maximum at a later time than the corresponding time for the ions; it is this mechanism that is thought to bring about a colder-than-ambient electron temperature in the near-wake region.

Of course, the electrons can never directly impact the object, as the ions easily can, unless they possess energy sufficient to overcome the object's potential barrier. It can be expected that the electrons will be ultimately reflected at the point where the potential barrier equals their kinetic energy. For an electron population that is perfectly Boltzmann in distribution, the 1 KTe potential contour will be roughly the closest that electrons can be expected to approach the object. For an electron distribution that has a hot tail component, as was the case in the experiments, it might be expected that electrons would approach even closer to the object. With electron densities on the order of 10^7 cm^{-3}, the Debye length was ≈ 0.3 cm, which corresponded to a location of $Z/R_0 = 0.1$. It would therefore seem possible for electrons to approach to within $Z/R_0 < 1.0$, even in steady state, and that both ions and electrons would be present in the near wake. The steady-state results seem to indicate this to be true.

ACKNOWLEDGMENT

The authors would like to acknowledge the contribution of Prof. U. Samir, whose suggestions provided the initial impetus for this work; Dr. W. Burke, for his support and encouragement in this endeavor, and Dr. K. Wright for some helpful discussions along the way. We would also like to thank J. Genevich and R. Allen for their technical assistance in carrying out the experiments.

REFERENCES

[1] S. D. Hester and A. A. Sonin, "A laboratory study of the electrodynamic influences on the wakes of ionospheric satellites," *AIAA J.*, vol. 8, pp. 1090-1098, 1969.

[2] U. Samir, W. A. Oran, and N. H. Stone, "Laboratory simulation of space aerodynamic phenomena: Satellite wake studies," *Rarefied Gas Dynamics*, vol. 2, 1974.

[3] N. H. Stone, "The aerodynamics of bodies in a rarefied ionized gas, with applications to spacecraft environmental dynamics," NASA, TP-1933, 1981.

[4] A. R. Martin, "Numerical solutions to the problem of charged particle flow around an ionospheric spacecraft," *Planet. Space Sci.*, vol. 22, pp. 121-141, 1974.

[5] L. W. Parker, "Computation of collisonless steady-state plasma flow past a charged disk," NASA, Washington, DC, CR-144159, 1976.

[6] C. Chan, M. A. Morgan, and R. C. Allen, "Electron dynamics in the near wake of a conducting body," *IEEE Trans. Plasma Sci.*, vol. PS-14, no. 6, pp. 915-924, 1986.

[7] M. A. Morgan, C. Chan, and R. C. Allen, "A laboratory study of the electron temperature in the near wake of a conducting body," *Geophys. Res. Lett.*, vol. 14, no. 11, pp. 1170-1175, 1987.

[8] L. W. Parker, "Computation of collisionless steady-state plasma flow past charged disks," NASA, CR-133159, 1976.

[9] J. C. Taylor, "Disturbance of a rarefied plasma by a supersonic body on the basis of the Poisson-Vlasov equations—I," *Planet. Space Sci.*, vol. 15, pp. 155-187, 1967.

[10] A. R. Martin, "Numerical solutions to the problem of charged particle flow around an ionospheric spacecraft," *Planet. Space Sci.*, vol. 22, pp. 121-141, 1974.

[11] B. Kõnemann, "The collisionless flow of unmagnetized plasmas around bodies," *J. Plasma Phys.*, vol. 20, pp. 17-30, 1978.

[12] N. H. Stone, "The plasma wake of mesonic conducting bodies, part I: An experimental parametric study of ion focusing by the plasma sheath," *J. Plasma Phys.*, vol. 25, pp. 351-371, 1981.

M. Alvin Morgan was born on Montserrat, in the British West Indies, on May 19, 1956. He received the B.S.E.E and M.S.E.E degrees from Northeastern University, Boston, MA, in 1984 and 1988, respectively. He is currently a Research Assistant in the Department of Electrical and Computer Engineering at Northeastern, where he is working towards the Ph.D. degree. His research interests are in collisionless plasma dynamics, diagnostics and simulation in general, and wake phenomena in particular.

Chung Chan (S'80-M'81-SM'88) was born in Canton, China, on October 23, 1956, and received the B.S. degree in electrical engineering from North Dakota State University, Fargo, in 1978, and the M.S. and Ph.D. degrees in electrical and computer engineering from the University of Iowa, Iowa City, in 1980 and 1981, respectively.

From 1981 to 1984 he served as a Research Scientist in the Phaedrus Tandem Mirror at the University of Wisconsin in Madison. In September 1984, he joined the faculty of Northeastern University, Boston, where he currently holds the rank of Associate Professor. He is currently the Director of the Plasma Science and the Microelectronic Laboratories at Northeastern University. He is also a principal investigator on research projects supported by the National Science Foundation, the Air Force, the Office of Naval Research, Sematech, the Department of Energy, the National Aeronautics and Space Administration, and a number of industrial companies.

Dr. Chan received the IEEE Outstanding Graduate Student Award in 1981 for his research work on laboratory plasmas. He has published 40 refereed papers and presented more than 40 conference papers on topics related to novel plasma devices, space plasma simulations, nonlinear plasma phenomena, plasma processing, microelectronic fabrication, and novel plasma diagnostic techniques. He holds membership in Tau Beta Pi, AVS, APS, AGU and NY Academy of Science.

David L. Cooke was born in Abilene, TX, on December 17, 1951. He received the B.A. degree from McMurry College, Abilene, in 1974. Both M.S. (1977) and Ph.D. (1980) degrees were received from Rice University, Houston TX.

He is currently working in Spacecraft Interactions, on the staff in the Space Physics Division at the Air Force Geophysics Laboratory, Hanscom AFB, MA. His research interests include plasma kinetics, plasma-spacecraft interactions, plasma kinetic simulations, ionization phenomena, and time travel.

Maurice F. Tautz was born in Victoria, BC, Canada, on October 29, 1941. He received the B.Sc. and M.S. degrees from the University of Victoria in 1964 and 1968, respectively. He obtained the Ph.D. degree from Northeastern University, Boston, in 1976, in the field of elementary particle physics.

He worked for a few years as a Postdoctoral Fellow at Northeastern, on physics experiments being carried out at Fermilab. Since then, he has been at the Air Force Geophysics Laboratory, where his main research interest is in computer simulations of spacecraft charging problems.